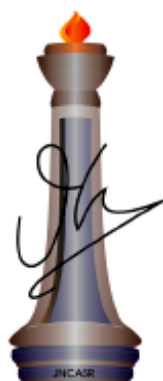

Design and Synthesis of Arylene Diimide Derived Organic Triplet Harvesters

A Thesis Submitted for the Degree of

Doctor of Philosophy

By

Swadhin Garain



New Chemistry Unit

Jawaharlal Nehru Centre for Advanced Scientific Research

(A Deemed University)

Bangalore - 560064 (INDIA)

July 2022

Design and Synthesis of Arylene Diimide Derived Organic Triplet Harvesters

A Thesis Submitted for the Degree of

Doctor of Philosophy

By

Swadhin Garain

UNDER THE SUPERVISION OF

Prof. Subi J. George

New Chemistry Unit

Jawaharlal Nehru Centre for Advanced Scientific Research

(A Deemed University)

Bangalore-560064 (INDIA)

July 2022

Dedicated to my Father

DECLARATION

I hereby declare that the matter embodied in the thesis entitled “*Design and Synthesis of Arylene Diimide Derived Organic Triplet Harvesters*” is the result of investigations carried out by me at the New Chemistry Unit, Jawaharlal Nehru Centre for Advanced Scientific Research, Bangalore, India under the supervision of **Prof. Subi J. George** and that it has not been submitted elsewhere for the award of any degree or diploma.

In keeping with the general practice in reporting the scientific observations, due acknowledgment has been made whenever the work described is based on the findings of other fellow researchers. Any omission that might have occurred due to oversight or error is in judgement is regretted.

Swadhin Garain

Mr. Swadhin Garain

(Ph. D. Student)



**Jawaharlal Nehru Centre for
Advanced Scientific Research**

Prof. Subi J. George
New Chemistry Unit
Jawaharlal Nehru Centre for Advanced
Scientific Research (JNCASR)
Bangalore-560064, India
Phone : +91 80 2208 2964
Fax: + 91 80 22082627
E-mail: george@jncasr.ac.in
Date: June 25, 2022

CERTIFICATE

I hereby certify that the matter embodied in this thesis entitled “*Design and Synthesis of Arylene Diimide Derived Organic Triplet Harvesters*” has been carried out by **Mr. Swadhin Garain** at the New Chemistry Unit, Jawaharlal Nehru Centre for Advanced Scientific Research, Bangalore, India under my supervision and that it has not been submitted elsewhere for the award of any degree or diploma.

Prof. Subi Jacob George
(Research Supervisor)

ACKNOWLEDGMENTS

During my Ph.D., I have been helped by a large number of people to whom I will always be grateful. Firstly, I would like to offer my most sincere thanks to one person who has stayed with me from the beginning to the end of my Ph.D., my research supervisor, Prof. Subi Jacob George. I am thankful to him for introducing me to the field of ambient triplet harvesting and for giving me the freedom to work on various problems. His ever-enthusiastic nature, constant encouragement, and support have helped me successfully complete this work.

I would like to express my gratitude to Prof. C. N. R. Rao, FRS for being a constant source of inspiration. His lectures on the history of science have been an experience of a lifetime. I am also grateful to him for creating such a vibrant research atmosphere to carry out this work.

My special thanks to my labmates, the Suprachem group members: Dr. Venkat, Dr. Mohit, Dr. Chidambar, Dr. Bhawani, Dr. Krishnendu, Dr. Ananya, Dr. Suman, Dr. Shikha, Souvik, Angshuman, Satyajit, Darshana, Saikat, Papiya, Vandana, Dr. Raju, Dr. Sushmitha, Dr. Sopan, Dr. Shagufi, Vijay, Bhawna, Chahat for their co-operation, valuable discussions and for creating a friendly atmosphere in the lab. Working with them was an absolute pleasure.

I am thankful to all the faculty members of NCU and CPMU for their guidance and support.

It is a great pleasure to thank my collaborators: Prof. Swapan K. Pati (JNCASR), Dr. Sarit S. Agasti (JNCASR), Prof. K. S. Narayan (JNCASR), Dr. Dinesh Kabra (IITB), Mr. Bidhan Chandra Garain (JNCASR), Mr. Soumen Pradhan (JNCASR), Ms. Gopa Sardar (IITB), Mr. Sinay Simanta Behera (JNCASR), for fruitful collaborations.

I am thankful to Prof. Subi J. George, Prof. S. Rajaram, Prof. Sarit S. Agasti, Prof. Chandrabhas Narayana from JNCASR, Prof. Mahavir Singh, and Prof. S. P. Sharma from IISc for their coursework.

I am thankful to Prof. Sridhar Rajaram, Prof. Sarit Agasti, Prof. Swapan K. Pati, and Mr. Bidhan Chandra Garain for valuable discussions.

I sincerely thank all my teachers, especially from “Indian Institute of Technology Madras” and “Visva-Bharati University,” for their encouragement at various stages of my academic career.

I am thankful to the following people for various technical assistance: Mrs. Usha (TEM); Mr. Mahesh (NMR), Mr. Deepak (NMR); Shivakumar (HRMS), and Mrs. Gayathri (Spectrofluorometer).

I am thankful to Dr. Suman Kuila, Dr. Aritra Sarkar, Dr. Meenal Kataria, Dr. Sopan M. Wagalgave, Dr. Shagufi Naz Ansari, and Anju for working with me on various projects.

I am grateful to summer and project students: Jishnu, Neha, Likhita, Anagha, Arnab, Priyank, Aiswarya, and Ananya for working with me on various projects.

I am thankful to the academic and administrative staff of JNCASR for their assistance.

I am thankful to my friends Arunava, Risov, Sanchita, Souvik, Rajib, Paribesh, Debu, Sudip, Debottam, Mainak, Sreyan, Manodeep, and All JNCASR friends for their unconditional support

Besides the research life, I am thankful to Prof. Subi J. George and his family members for their hospitality and affection.

*I am thankful to my Mother, Elder sister, Sanchari for their love and support and my **Father** for his hidden blessing.*

Financial assistance from the Council of Scientific & Industrial Research (CSIR) is gratefully acknowledged.

Swadhin

PREFACE

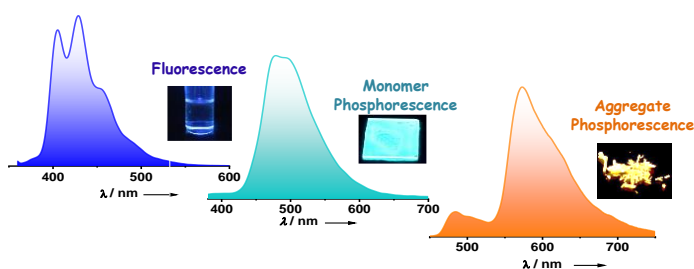
This thesis presents the design strategies and synthesis of purely organic chromophores for ambient triplet harvesting. We have attempted to synthesize various heavy-atom substituted, intra and intermolecular donor-acceptor chromophores based on arylene mono and diimides, mostly pyromellitic diimides. Thus, it includes the synthesis of small organic chromophores and, finally, investigating its phosphorescence and delayed fluorescence properties aided by spectroscopic, single-crystal X-ray diffraction analysis and computational investigations.

The thesis is divided into seven chapters. Where chapter 1 is the introduction, and Chapter 2 to 7 is divided into part A and part B.

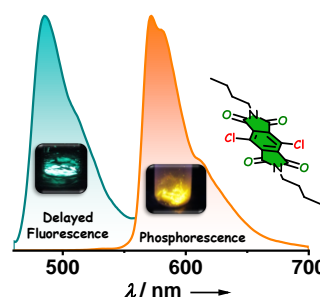
Chapter 1 presents triplet harvesting from purely organic chromophores under ambient conditions via room-temperature phosphorescence (RTP) and delayed fluorescence (DF) which is the key for achieving maximum efficiency in organic light-emitting diodes (OLEDs). In addition, due to the highly oxygen-sensitive nature and high lifetime of the triplets, they are very promising for various optical sensing and bioimaging applications. In this regard, developing alternative “metal-free” organic triplet emitters are more interesting and a promising alternative to the expensive and toxic organometallic phosphors. However, most organic chromophores suffer from meager quantum yield as their triplets are susceptible to vibrational and oxygen-mediated quenching. In this respect, alternative exquisite design strategies are required to achieve high quantum yield organic phosphors for further advancement in this field in amorphous and solution states. In this Chapter, we will be discussing the fundamental theory of phosphorescence and various mechanisms for delayed fluorescence in detail. Also, we will provide an overview of the design principles of such triplet emitting materials.

Part A includes chapters 2 to 6, where we have discussed different ways to harvest the triplet excitons and investigated the non-covalent donor-acceptor charge-transfer (CT) strategy to achieve phosphorescence from the CT states.

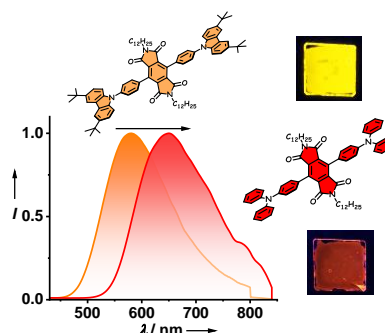
Chapter 2.1 presents arylene diimide derived ambient organic phosphors which are seldom reported despite their potential structural characteristics to facilitate the triplet harvesting. In this context, highly efficient room temperature phosphorescence (RTP) from simple, heavy-atom substituted pyromellitic diimide derivatives in amorphous matrix and crystalline state is presented here. Multiple intermolecular halogen bonding interactions among these phosphors, such as halogen-carbonyl and halogen- π resulted in the modulation of phosphorescence, cyan emission from monomeric state and orange-red emission from its aggregated state, to yield dual RTP emission. Remarkably, the air-stable phosphorescence presented here shown one of the highest quantum yields (~48%) among various organics in orange-red emissive region.



Chapter 2.2 presents a delayed fluorescence via triplet-triplet annihilation (TTA) and phosphorescence from the same molecular crystal, which is rarely achieved. Herein, we realized efficient cyan delayed fluorescence and orange-red phosphorescence emission from structurally simple chloro substituted pyromellitic diimide in the crystalline state with a quantum efficiency of 22% in air. Multiple halogens bonding interactions, halogen- π , and extended π - π interactions are responsible for efficient delayed fluorescence via TTA and phosphorescence emission with exceptional air and thermal stability.

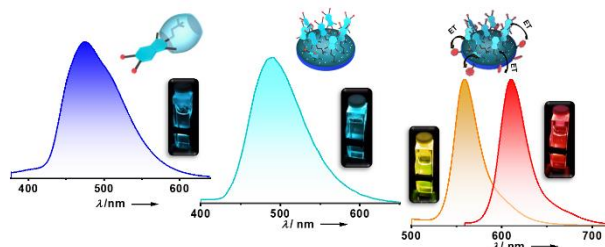


Chapter 3 presents a systematic investigation on donor-acceptor CT design based on these electron-deficient pyromellitic diimides are shown to exhibit small singlet-triplet gap facilitating efficient thermally activated delayed fluorescence (TADF) properties which is the another way to harvest the triplets. The theoretical calculation was performed to reinforce the role of the donor (phenyl carbazole) and acceptor (pyromellitic diimides) in maintaining both the



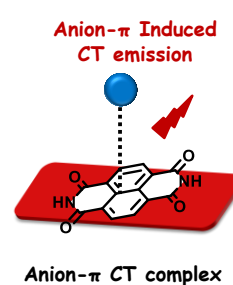
strong CT nature of the molecules and oscillator strength of emission. Moreover, analysis of the emissive phosphorescence bands of these molecules suggests that the confinement of CT states within the vicinity of locally-excited triplet states is crucial to harvest the triplet excitons via TADF process.

Chapter 4 shows solution-phase room-temperature phosphorescence (RTP) from organic phosphors which is seldom realized. Herein we achieve one of the highest quantum yield solution state RTP (~41.8 %) in water, from a structurally simple phthalimide phosphor, by employing an organic-inorganic supramolecular scaffolding strategy. We further use these

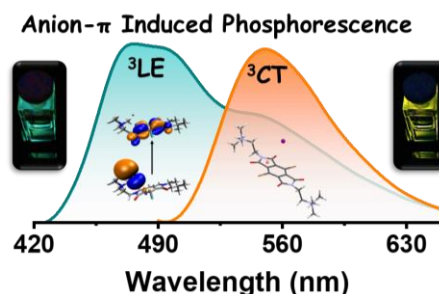


supramolecular hybrid phosphors as a light-harvesting scaffold to achieve delayed fluorescence from orthogonally anchored Sulforhodamine acceptor dyes via an efficient triplet to singlet Förster resonance energy transfer (TS-FRET), which is rarely achieved in solution. Electrostatic cross-linking of the inorganic scaffold at higher concentrations further facilitates the formation of self-standing hydrogels with efficient RTP and energy-transfer mediated long-lived fluorescence.

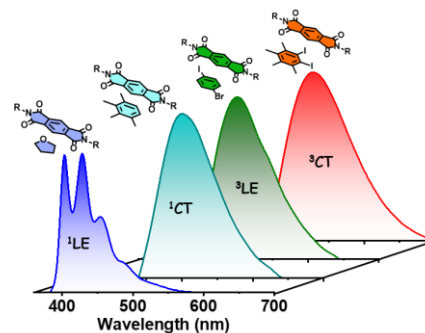
Chapter 5.1 we show the manipulation the optical properties of the chromophores via anion- π interaction which is difficult and summoning. Although anion- π induced formation of CT ground is known in the naphthalene diimide family, however, emissive CT state is rare and requires an elegant molecular design strategy. In this regard, we present the formation of anion- π induced CT ground state and subsequent realization of a unique through space red-emissive 1 CT state formation from π -acidic naphthalene diimides (NDIs) in aqueous solution. The clever molecular design strategy having counter iodide ions creates a perfect microenvironment to achieve an emissive CT state rather than the charge-separated state. To a greater extent, we exploit the emissive CT state in the aqueous phase for sensitive detection of insulin protein aggregate and successfully utilize it as a polarity-sensitive fluorescence marker.



Chapter 5.2 presents modulation of the emission features by toggling between the excited states using anion- π interactions. In this chapter we propose an anion- π based molecular design for the introduction of emissive singlet and triplet CT excited states, thereby expanding the functional scope of these weak supramolecular interactions. We investigate the anion- π induced emission from the singlet (^1CT) and triplet (^3CT) charge-transfer states of a dibromo di-cationic pyromellitic diimide derivative. Remarkably, we accomplish dual room temperature phosphorescence emission from the anion- π mediated ^3CT state along with the locally excited triplet state (^3LE) in the solution phase, using an organic-inorganic supramolecular scaffolding strategy. Comprehensive steady-state and time-resolved spectroscopy along with theoretical calculations provide detailed insights into the excited state manifolds of the phosphor. We envisage that the present study will expedite new molecular designs based on weak intermolecular interactions for the excited state engineering of organic chromophores to facilitate ambient triplet harvesting and CT emission.



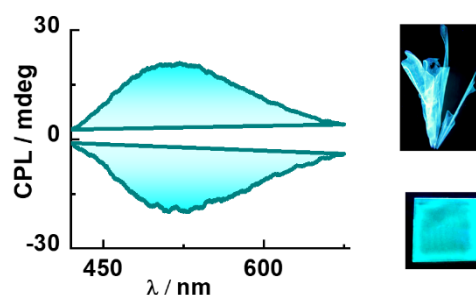
Chapter 6. In this chapter, we introduce a modular, non-covalent approach to bias the entire excited state landscape of an organic molecule using tunable ‘through-space charge-transfer’ interactions with appropriate donors. Although CT donor-acceptor complexes have been extensively explored as functional and supramolecular motifs in the realm of soft organic materials, they could not imprint their potentiality in the field of luminescent materials, and it still remains as a challenge. Thus, in this chapter, we investigate the modulation of the excited state emission characteristics of a simple pyromellitic diimide derivative on complexation with appropriate donor molecules of varying electronic characteristics to demonstrate the selective harvesting of emission from its locally excited (LE) and CT singlet and triplet states. Remarkably, co-crystallization of the pyromellitic diimide with heavy-atom substituted and electron-rich aromatic donors leads to an unprecedented ambient CT phosphorescence with impressive efficiency and notable



lifetime. Further, gradual minimizing of the electron-donating strength of the donors from 1,4-diiodo-2,3,5,6-tetramethylbenzene (or 1,2-diiodo-3,4,5,6-tetramethylbenzene) to 1,2-diiodo-4,5-dimethylbenzene and 1-bromo-4-iodobenzene, modulates the source of ambient phosphorescence emission from ^3CT excited state to ^3LE excited state. Through comprehensive spectroscopic, theoretical studies, and single-crystal analyses, we elucidate the unparalleled role of intermolecular donor-acceptor interactions to toggle between the emissive excited states and stabilize the triplet excitons. We envisage that the present study will be able to provide new and innovative dimensions to the existing molecular designs employed for triplet harvesting.

Part B includes chapter 7, where we have discussed circularly polarized phosphorescence (CPP) from solution processable film. We have shown the design strategies to achieve CPP from the LE and CT state.

Chapter 7.1 Chiral organic phosphors with circularly polarized room temperature phosphorescence (CPP) provide new prospects to the realm of circularly polarized luminescence (CPL) materials, owing to the long-lived triplet states and persistent emission. Although several molecular designs show efficient room temperature phosphorescence (RTP), realization of ambient organic CPP remains a formidable challenge. In this chapter, we introduce a chiral bischromophoric phosphor design, by appending molecular phosphors to chiral diaminocyclohexane core, to realize ambient CPP emission. Thus, solution processable polymer films of the *trans*-1,2-diaminocyclohexane (DAC) chiral cores with heavy-atom substituted pyromellitic diimide phosphors, exhibits one of the most efficient exclusive CPP emission with high phosphorescence quantum yield (~18% in air and 46% under vacuum) and significant luminescence dissymmetry factor ($|g_{\text{lum}}| \sim 4.0 \times 10^{-3}$).



Chapter 7.2 Achieving the phosphorescence from long-lived CT states via intermolecular donor-acceptor molecular design is challenging. In this chapter, we have presented CPP from triplet CT state which is extremely rare. To realize the CPP from ^3CT state, we used a bis-chromophoric molecular design with *trans*-1,2-diaminocyclohexane chiral core and heavy bromo substituted pyromellitic diimides phosphor as acceptor and phenyl carbazole as an achiral donor. Thus, solution-processable films exhibit the most efficient exclusive CPP emission with high phosphorescence quantum yield ($\sim 40\%$ in air) and significant luminescence dissymmetry factor ($|\text{g}_{\text{lum}}| \sim 1.5 \times 10^{-2}$). We hypothesized that CT-based intermolecular donor-acceptor molecular design helps us to achieve efficient $|\text{g}_{\text{lum}}|$ value.

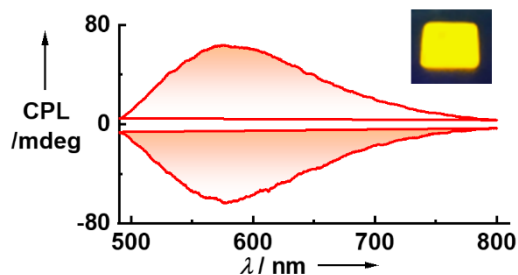


TABLE OF CONTENTS

Declaration	i
Certificate.....	iii
Acknowledgment	v
Preface.....	vii

Chapter-1

Design Strategies for Ambient Triplet Harvesters

Abstract.....	3
1.1. Different Excited State Processes	4
1.2. Why Triplet Harvesting?.....	7
1.3. Different Ways of Triplet Harvesting?	9
1.3.1. Phosphorescence	9
1.3.1.1. Design Strategy for Accessing the Triplets.....	9
1.3.1.2. Stabilization of the Triplets	11
1.3.1.2.1. Crystallization of the Phosphor	11
1.3.1.2.2. Embedding the Phosphor in the Rigid Host or the Polymeric Matrix	14
1.3.1.2.3. Phosphor in a Rigid Host.....	15
1.3.1.2.4. Phosphor in the Polymeric Matrix.....	16
1.3.1.2.5. Host-guest Strategy	20
1.3.2. Thermally Activated Delayed Fluorescence (TADF)	23
1.3.2.1. Design-strategy for TADF Emitters	24
1.3.3. Triplet-Triplet Annihilation (TTA)	25
1.3.3.1. Design-strategy for TTA-induced Delayed Fluorescence Emitters	26
1.3.4. Stabilization of the Triplets in Solution	27
1.3.4.1. Self-assembly Approach.....	28

1.3.4.2. Host-guest Strategy	30
1.3.4.3. Supramolecular Scaffolding Approach	31
1.4. Application of Organic Triplets	32
1.4.1. Organic Light-Emitting Diodes	33
1.4.2: Time-Resolved Bio-imaging	35
1.4.3: Sensing	37
1.5. Delayed Sensitization.....	37
1.6. Circularly Polarized Luminescence	43
1.7. Molecular Design Strategy: Why Arylene Diimides?	45
1.7.1. Design Strategy for Arylene Diimides Derived Ambient Triplet Harvesters ..	47
1.8. Conclusion:	48
1.9. References:.....	49

PART-A

Chapter-2.1

Ambient Dual Phosphorescence from Heavy atom Substituted Pyromellitic Diimides

Abstract	60
2.1.1. Introduction	61
2.1.2. Molecular Design	62
2.1.3. Theoretical Calculations:	62
2.1.4. Spectroscopic Studies in Solution-state:	64
2.1.5. Ambient Monomeric and Aggregated Room Temperature Phosphorescence in Polymer Matrix and Crystalline State	65
2.1.6. Conclusion	71
2.1.7. Experimental Section	72
2.1.7.1. General Methods.....	72

2.1.7.1. Protocol of Sample Preparation	73
2.1.8. Synthetic Schemes and Procedures	74
2.1.9. References:	79

Chapter-2.2

Delayed Fluorescence via Triplet-triplet Annihilation from a Pyromellitic Diimide Phosphor

Abstract	85
2.2.1. Introduction	86
2.2.2. Molecular Design	88
2.2.3. Theoretical Calculations	89
2.2.4. Spectroscopic Studies in Solution-state	90
2.2.5. Ambient Phosphorescence in Polymer Matrix	91
2.2.6. Ambient Triplet-Triplet Annihilation Induced Delayed Fluorescence and Phosphorescence in Aggregated State	92
2.2.7. Single-crystal X-ray Crystallography Analysis	96
2.2.8. Theoretical Calculations of CIPmDI Dimer	97
2.2.9. TTA Induced Delayed Fluorescence in HPmDI Single Crystal	98
2.2.10. Conclusion	99
2.2.11. Experimental Section	100
2.2.11.1. General Methods	100
2.2.11.1. Protocol of Sample Preparation	102
2.2.12. Synthetic Schemes and Procedures	102
2.2.13. References	114

Chapter-3

Thermally Activated Delayed Fluorescence: Color Tunable Delayed Fluorescence from Core-substituted Pyromellitic Diimides

Abstract	116
3.1. Introduction	117
3.2. Design Strategy	118
3.3. Spectroscopic Studies in Solution-state	119
3.4. Ambient Dual TADF and Phosphorescence in Polymer Matrix	121
3.5. Conclusion	125
3.6. Experimental Section	125
3.6.1. General Methods.....	125
3.6.2. Protocol of Sample Preparation	126
3.7. Synthetic Schemes and Procedures.....	127
3.8. References.....	133

Chapter-4

Solution-state Phosphorescence and Delayed Sensitization via Supramolecular Scaffolding

Abstract	138
4.1. Introduction	139
4.2. Molecular Design	140
4.3. Spectroscopic Studies in Solution-state	141
4.4. Ambient Solution-state Room Temperature Phosphorescence using Host-guest Strategy	143
4.5. Ambient Solution-state Room Temperature Phosphorescence in Laponite using Supramolecular Scaffolding.....	146
4.6. Triplet to Singlet Förster Resonance Energy Transfer via Delayed Sensitization....	147

4.7. Ambient Phosphorescence and Delayed Fluorescence in Hybrid Hydro Gel	151
4.8. Conclusion	154
4.9. Experimental Section	154
4.9.1. General Methods.....	154
4.9.2. Protocol of Sample Preparation	155
4.10. Synthetic Schemes and Procedures.....	156
4.11. References.....	160

Chapter-5.1

Anion- π Induced Charge-transfer Emission from Cationic Naphthalene Diimide

Abstract.....	166
5.1.1. Introduction	167
5.1.2. Molecular Design	168
5.1.3. Spectroscopic Studies in Solution-state:.....	168
5.1.4. High-resolution Electrospray Ionization Mass Spectrometry (ESI-MS) and Single-crystal X-ray Crystallography Analysis.....	170
5.1.5. Theoretical Calculations	171
5.1.6. Sensing by Anion- π Induced Through Space CT Emission	172
5.1.7. Conclusion	175
5.1.8. Experimental Section	176
5.1.8.1. General Methods.....	176
5.1.8.2. Protocol of Sample Preparation	177
5.1.9. Synthetic Schemes and Procedures.....	178
5.1.10. References:.....	178

Chapter-5.2

Anion- π Induced Phosphorescence from Charge-transfer States

Abstract.....	183
5.2.1. Introduction	184
5.2.2. Molecular Design	186
5.2.3. Spectroscopic Studies in Solution-state.....	187
5.2.4. High-resolution Electrospray Ionization Mass Spectrometry (ESI-MS), Single-crystal X-ray Crystallography Analysis and Theoretical Calculations.....	188
5.2.5. Phosphorescence Study of BrPmDI-LP hybrid in Solution.....	190
5.2.6. Phosphorescence Study of BrPmDI-LP Hybrid as Drop-casted Films.....	193
5.2.7. Conclusion	199
5.2.8. Experimental Section.....	199
5.2.8.1. General Methods.....	199
5.2.8.1. Protocol of Sample Preparation.....	201
5.2.9. Synthetic Schemes and Procedures.....	201
5.2.10. References.....	208

Chapter-6

Biasing the Excited State Manifold via Non-covalent Donor-Acceptor Approach

Abstract.....	214
6.1. Introduction	215
6.2. Molecular Design	217
6.3. Spectroscopic Studies in Solution-state: Formation of ¹ LE and ¹ CT States.....	218
6.4. Spectroscopic Studies of <i>A+D₁</i> and <i>A+D₂</i> Co-crystals: Formation of ³ CT States...	220
6.5. Single-crystal X-ray Crystallography Analysis and Theoretical Calculations	228
6.6. Spectroscopic Studies of <i>A+D₃</i> Co-crystals	229

6.7. Spectroscopic Studies of $A+D_4$ and $A+D_5$ Co-crystals: Formation of 3LE States ...	230
6.8. Conclusion	233
6.9. Experimental Section	223
6.9.1. General Methods.....	223
6.9.2. Protocol of Sample Preparation	225
6.10. Synthetic Schemes and Procedures.....	225
6.11. References.....	228

PART:B

Chapter-7.1

Circularly Polarized Phosphorescence from Pyromellitic Diimides

Abstract.....	248
7.1.1. Introduction	249
7.1.2. Molecular Design	250
7.1.3. Spectroscopic Studies in Solution-state:.....	251
7.1.4. Ambient Monomeric Room Temperature Phosphorescence in Polymer Matrix...	253
7.1.5. Theoretical Calculations	257
7.1.6. Circularly Polarized Phosphorescence in Processable Films.....	258
7.1.7. Conclusion	260
7.1.8. Experimental Section	261
7.1.8.1. General Methods.....	261
7.1.8.2. Protocol of Sample Preparation	262
7.1.9. Synthetic Schemes and Procedures.....	263
7.1.10. References:.....	274

Chapter-7.2

Circularly Polarized Room Temperature Phosphorescence from Charge-Transfer State Via Non-covalent Donor-Acceptor Approach

Abstract.....	281
7.2.1. Introduction	282
7.2.2. Molecular Design	283
7.2.3. Formation of Ground State CT Complex.....	284
7.2.4. Spectroscopic Studies in Thin Films: Formation of ³ CT state.....	285
7.2.5. Chiroptical Properties in Thin Films: Circularly Polarized Phosphorescence from Charge-transfer State	288
7.2.6. Conclusion	291
7.2.7. Experimental Section.....	292
7.2.7.1. General Methods.....	292
7.2.7.2. Protocol of Sample Preparation.....	292
7.2.8. Synthetic Schemes and Procedures.....	293
7.2.9. References.....	293
Curriculum Vitae	297
List of Publications	299

CHAPTER 1

Introduction:

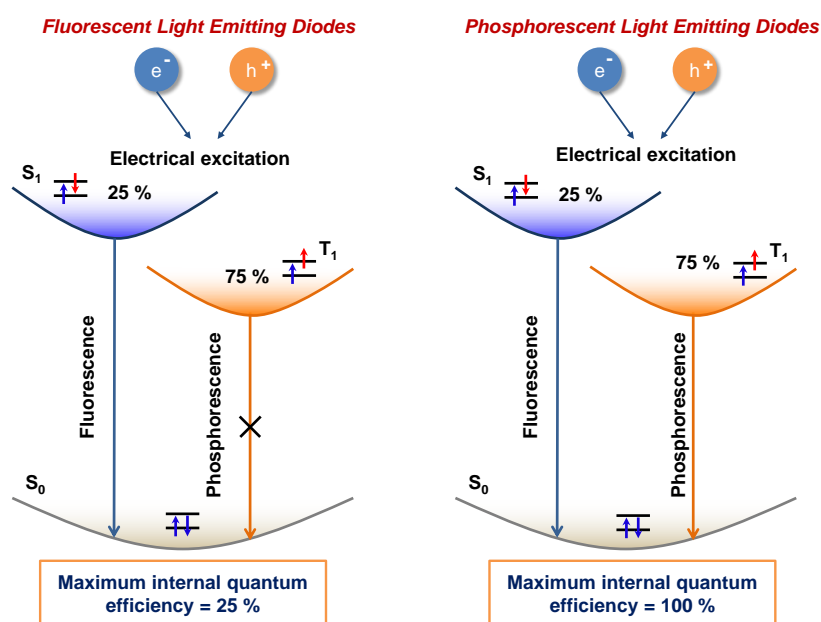
Design Strategies for Ambient Triplet Harvesters

CHAPTER 1

Design Strategies for Ambient Triplet Harvesters

Abstract

The introduction chapter presents triplet harvesting from purely organic chromophores under ambient conditions via room-temperature Phosphorescence (RTP) and delayed fluorescence (DF), which is the key to achieve maximum efficiency in organic light-emitting diodes (OLEDs). In addition, due to high oxygen-sensitive nature and - lifetime of the triplets, they are very promising in various optical sensing and bioimaging applications. In this regard, developing alternative “metal-free” organic triplet emitters is more exciting and these emitters make promising alternative to the expensive and toxic organometallic phosphors. However, most of the organic chromophores suffer from meagre quantum yield as their triplets are susceptible to vibrational and oxygen-mediated quenching. In this respect, alternative exquisite design strategies are required to achieve high quantum yield organic phosphors that function in both amorphous and solution states for further advancement in this field. In this chapter, we will discuss the fundamental theory of phosphorescence and various mechanisms for delayed fluorescence. Further, we will discuss the strategy to access the triplets and their stabilization. Also, we will provide an overview of the design principles of such triplet emitting materials.



1. Introduction:

1.1. Different Excited State Processes:

The thesis describes different efficient ways of triplet harvesting of purely organic chromophores. Firstly, we have discussed the various excited-state processes for detailed understanding.^[1,2] In an organic chromophore, the transition process happens between two electronic states (Figure 1.1). The singlet or triplet electronic state is designated by considering the electron's spatial coordinates and the position of the nuclei.^[1,2] In quantum mechanics, spin angular momentum is a vector quantity represented by the operator \hat{S} . For a two-electron system, there are four possible spin eigen states of \hat{S} is possible.^[1,2] The first spin wavefunction has eigenvalues $S = 0$, and spin multiplicity $M = 1$ ($M = 2S + 1$). It has only a single possible value of its z-component, i.e., eigenvalue $M_s = 0$, and is called singlet.^[1,2] Quantum mechanically it can be written as $1/\sqrt{2}\{|\uparrow\downarrow\rangle - |\downarrow\uparrow\rangle\}$.^[1,2] The next three spin wavefunctions have eigenvalues $S = 1$ and $M = 3$. They only differ in the z-component of the spin, which can take one of three eigenvalues ($M_s = 1, 0, -1$).^[1,2] This arrangement is therefore called triplet.^[1,2] The three plausible states are $|\uparrow\uparrow\rangle$, $|\downarrow\downarrow\rangle$ and $1/\sqrt{2}\{|\uparrow\downarrow\rangle + |\downarrow\uparrow\rangle\}$ according to the quantum mechanics.^[1,2] The ground state of an organic molecule is a singlet state; hence, the electrons will have antiparallel paired spins.^[1,2] However, they could have an antiparallel or parallel spin in the excited state as they have no restriction of the spin orientation rule.^[1,2] According to the occupation of the electron in the orbitals, the orbitals are classified as the highest occupied molecular orbital (HOMO) and lowest unoccupied molecular orbitals (LUMO) in the electronic state.^[1,2] The LUMO is empty in the ground singlet state. Upon photo excitation, an electron of the HOMO in the ground singlet state (S_0) goes to the LUMO in the excited singlet state (S_1 or S_n).^[1,2] The transition always happens from the low energy vibrational levels to the high energy excited state, followed by the Boltzmann distribution.^[1,2] The Boltzmann distribution describes that the maximum population resides in the lowest vibrational level of the singlet state (S_0).^[1,2] However, a direct transition from the singlet ground state (S_0) to the excited triplet state (T_n) is not possible due to the spin-forbidden nature of the transition, where total angular momentum is not conserved.^[1,2] The photo excitation process is very fast and is in the femtosecond order ($t \sim 10^{-15}$ seconds).^[1,2] After absorbing the light, a molecule goes to the higher energy excited state e.g., S_2 , S_3 or higher (Figure 1.1).^[1,2] However, the system

wants to come to equilibrium from the non-equilibrium high energy singlet state and starts dissipating the energy gained upon light absorption (Figure 1.1).^[1,2] First, the molecules started dissipating their energy via vibrational relaxation (Figure 1.1).^[1,2] Vibrational relaxation is a non-radiative process that happens between the same electronic states.^[1,2] The molecules relax by releasing thermal energy or transferring their energy to the neighbouring molecule.^[1,2] The time scale of this process is $\sim 10^{-13}$ to 10^{-11} seconds.^[1,2] Further, the excited electrons relax to the lowest excited singlet state (S_1), following Kasha's Rule via the internal conversion (IC) process (Figure 1.1).^[2,3] IC is a non-radiative transition between two electronic states of the same spin-multiplicity. The process is fast, having a time scale of $\sim 10^{-11}$ to 10^{-19} seconds.^[1,2] When the IC happens, it always competes with fluorescence or the inter-system crossing (ISC) process.^[1,2] However, when IC becomes complete, the molecules come to the low energy excited state and then gets de-excited either radiatively or non-radiatively to the ground singlet state (S_0) and maintain the spin multiplicity (Figure 1.1).^[1,2] The non-radiative way is the loss of energy via heat to the surrounding solvent molecule intermolecularly or the same molecule intramolecularly.^[1,2] If the transition happens radiatively, then the process is called fluorescence.^[1,2] According to Kasha's Rule, molecules always emit from low energy excited state ($S_1 \rightarrow S_0$) (Figure 1.1).^[3] Prof. Michael Kasha stated that emission (fluorescence or phosphorescence) always takes place from the lowest vibrational level of the first excited singlet state (S_1) to the ground singlet state (S_0).^[3] It is noteworthy that if the distribution of HOMO and LUMO becomes almost the same before and after the transition, it is called the local excited (LE) state and follows the Frank Condon principle.^[1,2] However, the excited electrons from the singlet state can also undergo an ISC process during the IC process to the nearest excited triplet state ($T_n, n > 1$) and eventually go to the low-lying T_1 state (Figure 1.1).^[1,2] The process of ISC is essential in the context of whole work described in the thesis, i.e., to harvest the triplets, and is defines as the non-radiative transition between the two spin states having different spin multiplicities. ISC is formally a forbidden transition as the spin changes, but orbital angular momentum is not changing, so total angular momentum is not conserved.^[1,2] For ISC to happen, the molecules require to follow El Sayed's rule so as to have a significant amount of spin-orbit coupling matrix element (SOCME), so that orbital angular momentum will change and in resultant total angular momentum will be conserved.^[4] Typically, the time scale of the ISC process is $\sim 10^{-10}$ to 10^{-8} seconds;^[1,2] however, it is

extremely dependent on hetero atom and heavy atom in the molecular design, which we will discuss in detail later in this chapter.

Upon ISC, when the molecules reach the low energy triplet state (T_1), the radiative transition of excited electrons from the T_1 state to the singlet ground state (S_0) occurs, known as phosphorescence (Figure 1.1).^[1,2] In contrast to fluorescence, which happens very fast (~nano second timescale), phosphorescence is slow with a typical time scale of microseconds to a few seconds owing to its spin-forbidden nature.^[1,2] Thus, the situation demands specific additional criteria to be satisfied to get efficient phosphorescence from organic chromophores under air.^[5] This includes (i) Efficient SOC and high ISC rate between the S_1 and T_n states to populate the triplet and (ii) Stabilizing the triplet excitons by the suppression of non-radiative decay pathways from T_1 to S_0 .^[5] Due to the very high lifetime of the triplet, they are susceptible to intermolecular collisions with the surrounding molecules (e. g. with solvent molecules), which facilitates non-radiative relaxation, and the triplet loses its energy by heat.^[1,2] Further, the triplet of a molecule is easily quenched by the molecular oxygen in the air due to the triplet nature of both by the triplet-to-triplet dexter energy transfer process.^[1,2,5] However, the main objective of the thesis is to harvest the triplet under ambient conditions, so the current dissertation will describe the methods to prevent the triplet quenching and stabilization of the triplets and describes the molecular design strategy for efficient ambient triplet harvesting.

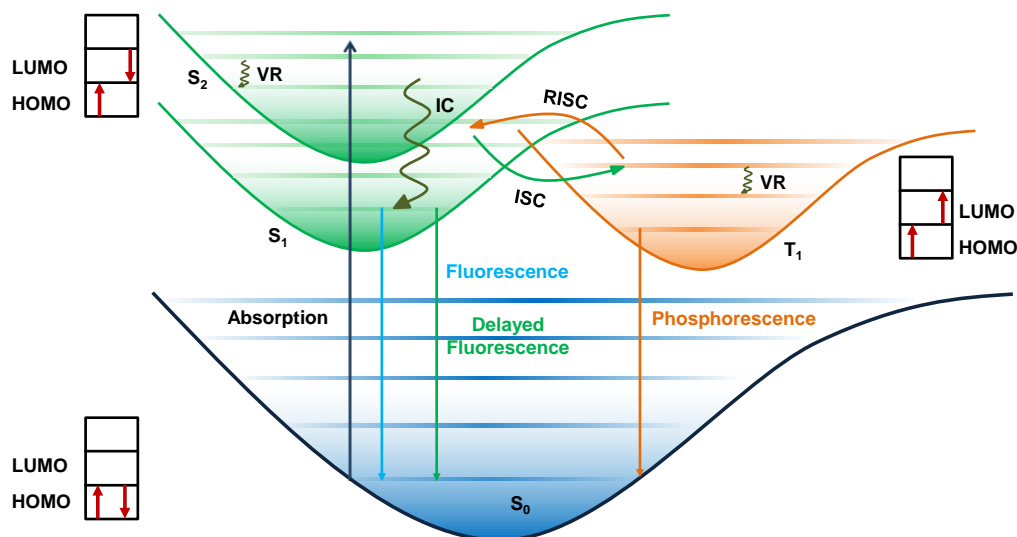


Figure 1.1. The Perrin-Jablonski diagram showing the most crucial excited state transitions (both radiative and non-radiative) upon absorption of a photon. The spin configurations are also shown for the S_0 , S_1 , and T_1 states.

1.2. Why Triplet Harvesting?

Finding a suitable emitter for Organic Light Emitting Diodes (OLEDs) is one of the most challenging research areas in scientific and industrial interests.^[6] Usage of OLED displays can endow multiple advantages due to its low cost, high lifetime, eco-friendly nature and potential to manufacture thin, flat, flexible displays.^[6] According to Fermi-Dirac spin-statistics, there would be 25 % singlet excitons and 75 % triplet excitons in an organic luminescent molecule upon excitation (Figure 1.2).^[6] Unfortunately, these triplet excitons are non-emissive in most organic molecules. On the other hand, fluorescent emitting materials can convert only 25% of the singlet excitons into photons in an electroluminescent device known as ‘first-generation emitters’ in OLEDs resulting in only 25% of the maximum internal quantum efficiency (IQE) (Figure 1.2).^[6a,b] However, the low IQE of the fluorescent materials prompted researchers to develop high-efficiency phosphorescent emitting materials that have a high IQE (Figure 1.2).^[6,7] The phosphorescent materials can convert both singlet and triplet excitons into photons, generated by hole and electron injection by a radiative transition process.^[6] Therefore, theoretically, 100% IQE can be reached provided there is no loss process during the radiative transition (Figure 1.2).^[6] These emitters are called ‘second-generation emitters’ in OLEDs because they can offer higher IQE than the ‘first-generation emitters’.^[6,7] Although 100 % IQE is theoretically possible, organic phosphors suffer from meager

quantum yield, and the device efficiency is not excellent because long-lifetime generates high-efficiency roll-off.^[6] Third-generation materials, i.e., thermally activated delayed fluorescence (TADF) molecules, are superior to phosphorescent materials in this regard. TADF materials also theoretically possess 100 % internal quantum efficiency and the efficient utilization of triplet exciton, efficient quantum yield, good stability, ease in fabrication, heavy atom-free molecular design, and most importantly, low-efficiency roll-off made them superior candidates for OLEDs.^[6] Notably, an IQE of 62.5 % can also be reached via triplet-triplet annihilation (TTA) induced delayed fluorescence, where a bi-molecular process of two triplet collisions generates a high-energy singlet state.^[8] Other than OLEDs, the high lifetime of the triplets and oxygen-sensitive nature of the organic phosphors make them suitable for diverse applications such as bioimaging, sensing, singlet oxygen production, photodynamic therapy, photocatalysis, and optical sensing.^[5] The field of bio-imaging benefitted the most in this context.^[5]

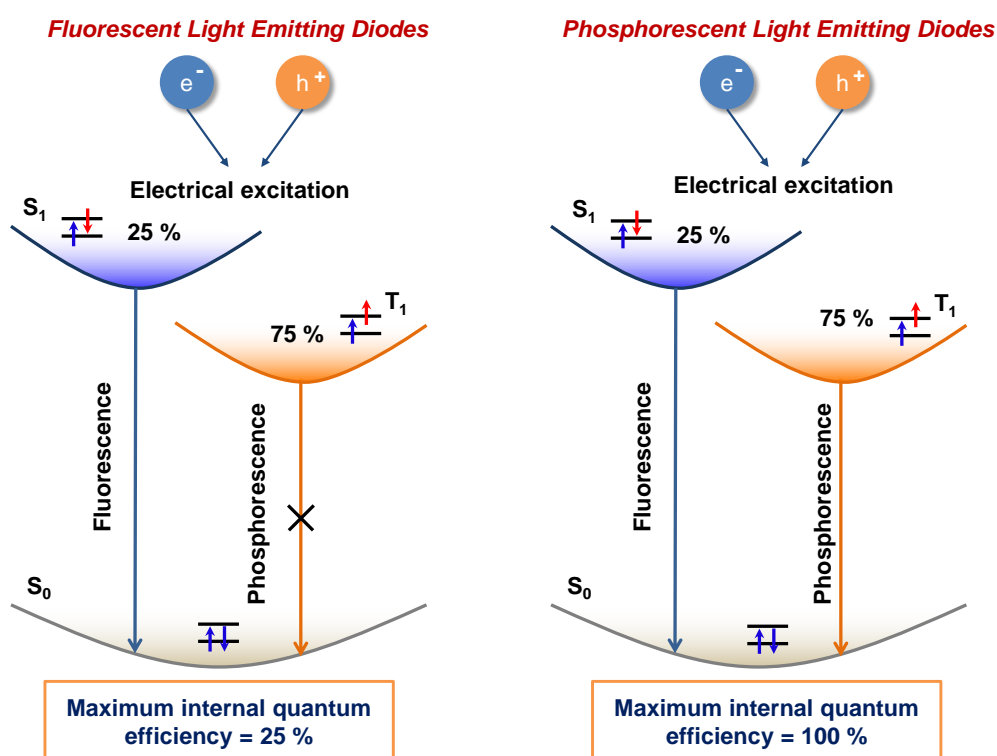


Figure 1.2. The simplified Jablonski diagram showing the utilization of singlet and triplet excitons upon electrical excitation.

1.3. Different Ways of Triplet Harvesting?

The triplets can be harvested majorly in three different ways, i) Phosphorescence,^[5] ii) TADF,^[6] and iii) TTA,^[7] as discussed in earlier section. We will discuss the photophysical process behind it and the molecular design strategy in this part.

1.3.1. Phosphorescence

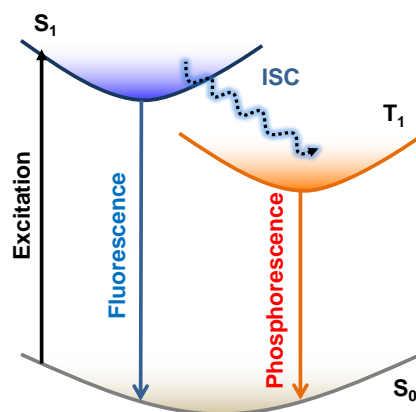


Figure 1.3. The simplified Jablonski diagram showing the phosphorescence process upon photo excitation.

1.3.1.1. Design Strategy for Accessing the Triplets:

Phosphorescence is a radiative transition process occurring from an excited triplet state to the ground singlet state of an organic molecule.^[1,5] Owing to the spin-forbidden nature of the emission, it possesses a high emission lifetime (usually in the order of microseconds to seconds). In addition, phosphorescence often leads to a very high Stokes shift due to energetically low-lying T₁ states, described in the simplified Jablonski diagram in Figure 1.3.^[1,2] Traditionally, organometallic complexes possessing heavy-metal atoms, e.g., Ru, Ir, Pt, etc., are extensively used to facilitate the spin-orbit coupling (SOC) between S₁-T_n states, leading to very efficient and fast ISC. However, these metals are highly toxic and less abundant (Ir is the 3rd rarest element on earth), making this class of emitters cost-effective.^[5] As a result, the focus of this research field has inclined steeply towards metal-free pure organic emitters from organometallic complexes.^[5] In the past decade, new pure organic chromophores have grown tremendously as potential room-temperature phosphorescence (RTP) emitters developed.^[5] However, to access the triplets of organic phosphor high SOC and ISC rate is required due to the spin forbidden triplet to singlet transition. ISC is a spin forbidden process due to the spin angular

momentum change upon spin flipping.^[1,5] For efficient ISC, significant singlet-triplet mixing is necessary, which is dependent on the SOC proportionally and inversely proportional to the singlet-triplet energy gap. Quantum mechanically singlet-triplet mixing can be expressed by,

$$\delta = \frac{\langle {}^3\Psi | H_{SO} | {}^1\Psi \rangle}{|E_{S_1} - E_{S_2}|}$$

δ , suggest the singlet-triplet mixing by first-order spin-orbit coupling according to the perturbation theory. ${}^1\Psi$ and ${}^3\Psi$ represent singlet and triplet wavefunction participating in ISC.^[9] H_{SO} is the spin-orbit coupling Hamiltonian, and E_{S_1} and E_{T_1} are the low-energy singlet and triplet excited states.^[9] So, the mathematical expression suggests that high SOC and low singlet-triplet energy gap (ΔE_{ST}) will mix the singlet and triplet state efficiently, and the ISC rate will increase.^[1,9] Further, the H_{SO} can be written as,

$$H_{SO} = -\frac{Z^4 e^2}{8\pi\epsilon_0 m_e^2 c^2} \mathbf{l} \cdot \mathbf{s}$$

where e is the elementary charge of an electron, ϵ_0 is the permittivity of the vacuum, m is the mass of an electron, c is the speed of light, and Z is the atomic number of the nucleus.^[1,10] When the electron's spin is influenced by the electron's motion around the nucleus, then strong SOC takes place, which changes the orientation of electrons' spin due to the generation of strong electromagnetic force.^[1,10] Thus, to increase the SOC significantly, Z is crucial since H_{SO} is proportional to Z^4 and highly sensitive to the charge/size of the nucleus.^[1,10] Heavy atoms like I, Br, and Cl can generate strong electromagnetic forces, thus considered as heavy atoms.^[1,10] So, in purely organic chromophores, the SOC can be enhanced by introducing heavy atoms in the π -conjugated core of the chromophores in the molecular backbone.^[5]

Further, to enhance the ISC rate, i.e., the spin flipping process, the dot product of orbital and spin total angular momentum ($\mathbf{l} \cdot \mathbf{s}$) plays a crucial role. During the ISC process, there is a change of spin angular momentum (s); however, for electronic transition to happen, there should be a change in the total angular momentum so that the total angular momentum will be conserved.^[1] To alleviate the scenario, Prof. Mostafa El-Sayed, in his seminal works in 1960, postulated a rule which tells that 'The rate of ISC will be fast when there is at the change in their respective molecular orbital (MO) configuration' (Figure 1.4).^[4] The rate of ISC will be fast when the singlet is of π - π^* and the triplet is of n - π^* in nature or vice versa, and the rate of ISC will be slow when both the singlet or

triplet will be π - π^* or n - π^* in nature (Figure 1.4).^[4] So, the ISC rate can be significantly enhanced in purely organic chromophores by introducing a hetero atom with a lone pair of electrons.^[5] For example, hetero atoms like Oxygen, Nitrogen, Sulphur, or a group like a carbonyl or a sulphonyl in the π -conjugated core of the chromophores in the molecular structure ensures the conservation of total angular momentum, an essential criterion for achieving an electronic transition between states of two different spin multiplicities (Figure 1.4).^[5]

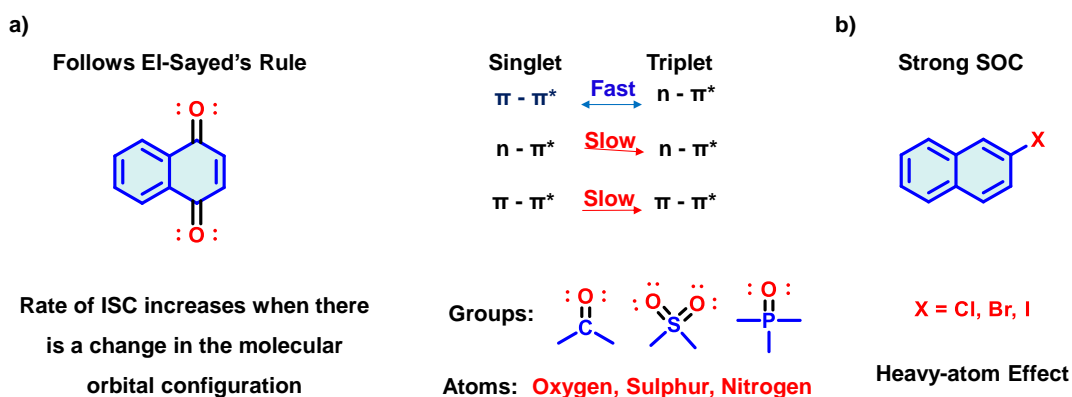


Figure 1.4. Molecular structure and plausible functional groups or atoms that will increase the a) ISC by following El-Sayed and b) SOC via heavy atom effect between singlet and triplet states.

1.3.1.2. Stabilization of the Triplets:

Once strong SOC and an efficient ISC are achieved in an organic molecule, the next challenge is stabilizing those resulting triplets from vibrational dissipation and molecular oxygen using various approaches. In this regard, crystallization^[11] of the phosphors or embedding the phosphor in the polymeric host^[12,13] or host-guest^[14] strategy would be beneficial

1.3.1.2.1. Crystallization of the Phosphor:

It has been shown that highly-ordered, rigid, and dense networks of molecules in a crystalline sample reduce the vibrational motions of the individual molecules efficiently and prevent oxygen diffusion.^[11] In that regard, pioneering works by Tang, Kim, and Huang and their co-workers have established efficacy using simple molecular design principles. ‘Directed heavy atom effect’ and ‘H-aggregation’ in a highly organized

crystalline assembly via H-aggregation are considered as a grand strategy for determining the triplet stability (Figures 1.5,1.6).^[11a-c]

Tang and co-workers realized ambient phosphorescence via crystallization from various benzophenone derivatives with an excellent quantum efficiency of ~40 % at room temperature (Figure 1.5a).^[11a] Upon crystallization, different non-covalent interactions effectively lock the conformational flexibility of the phosphors, leading to unprecedented phosphorescence under air (Figures 1.5b-c).^[11a] This pioneering ‘crystallization-induced phosphorescence’ is considered the foundation of the entire field of the ambient organic phosphors.^[11a]

Further pioneering work is done by Kim and co-workers and develops a unique ‘directed heavy-atom effect’ approach in the host-guest co-crystal where the crucial role played by halogen bonding is established.^[11b] Authors have used a dibromo aromatic compound as the host and the aromatic aldehyde as a guest in the bi-component crystalline assembly (Figure 1.5e).^[11b] The halogen-bonding induced external heavy atom effect helped to increase the SOC and ISC significantly, which will help to achieve efficient green phosphorescence emission ($\Phi_P = 56\%$) in the air at room temperature (Figures 1.5f,g).^[11b]

H-aggregation between the phosphor molecules is another way to achieve an efficient triplet yield, which was first proposed by Huang and co-workers (Figures 1.6a,b).^[11c] They have shown that strong H-aggregation between the phosphor molecules increases the number of ISC channels, increasing the phosphorescence efficiency without any heavy atom (Figure 1.6c).^[11b] Bryce and co-workers further showed that intermolecular electronic coupling between two different excited state configurations ($n-\pi^*$ and $\pi-\pi^*$) in the closely-packed crystalline assembly would be helpful for efficient ISC in a highly twisted donor-acceptor system.^[11i]

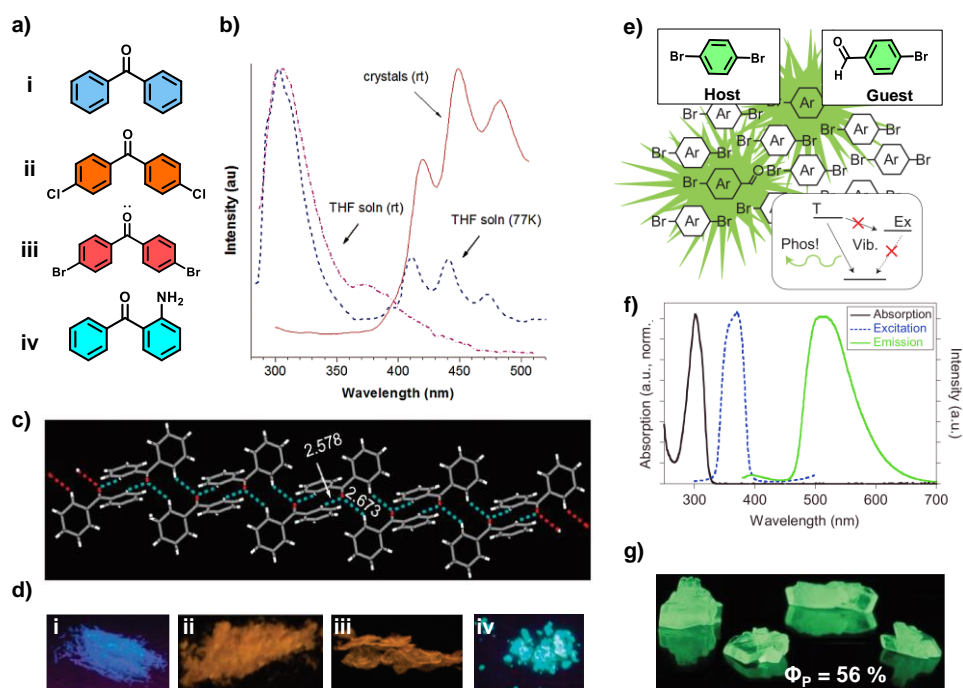


Figure 1.5. a) Molecular structures of Benzophenone derivatives (i to iv). b) Emission spectra of Benzophenone in the THF solution, THF solution at 77 K and crystalline state at room temperature ($[c] = 1 \mu\text{M}$, $\lambda_{exc.} = 270 \text{ nm}$). c) Extended arrangement of Benzophenone crystal driven by C-H...O hydrogen bonds (marked by dotted lines). d) Photographs of Benzophenone derivatives (i to iv) in the crystalline state under 365 nm UV light illumination at room temperature. e) Schematic representation of directed heavy atom organic phosphorescence and its design principle, where the host, a dibrominated analogue to the chromophore and the chromophore is diluted by substitution into the host crystal. f) Absorption, excitation and emission spectra of the crystals. UV absorption comes from host, which constitutes over 99.99 wt.% of the crystal, but excitation comes from guest. g) Photograph of mixed crystals grown from slow evaporation of a 0.001 wt% host/guest mixture in hexanes solution, under 365 nm UV light. (Reproduced from reference 11a and 11b).

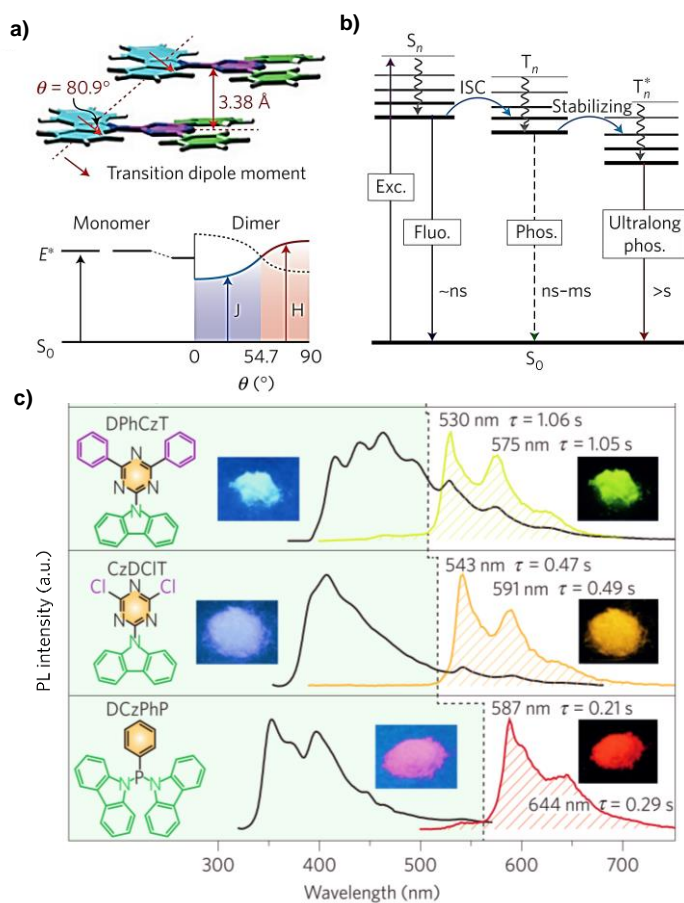


Figure 1.6. a) Single-crystal structures of **DPhCzT** showing the formation of *H*-aggregates as evident by the measured angle (θ) of 80.9° between the transition dipoles and interconnected axis and schematic energy diagram of *J*-aggregation ($\theta < 54.7^\circ$) and *H*-aggregation ($\theta > 54.7^\circ$). The blue and red solid curves represent the exciton energy levels of allowed transition for *J*- and *H*-aggregation, respectively. The dotted curve refers to the corresponding exciton energy level of forbidden transition. b) Proposed energy diagram for fluorescence, phosphorescence and ultralong phosphorescence of **DPhCzT** aggregates. c) The steady-state emission spectra (left) and ultralong phosphorescence spectra (right) of a series of specially designed molecules. Insets show the corresponding photographs taken before (left) and after (right) the excitation source is turned off ($\lambda_{exc.} = 365 \text{ nm}$). (Reproduced from reference 11c).

1.3.1.2.2. Embedding the Phosphor in the Rigid Host or the Polymeric Matrix:

So far, studies on crystal-phase RTP have been investigated to achieve very high efficiency and a lifetime of up to several seconds.^[11] However, despite these

breakthrough achievements from these classes of organic RTP emitters, their processability is poor and often requires stringent growth conditions. Therefore, the researchers in this community have actively pursued a more general and convenient strategy to obtain RTP in an amorphous and solution-processable film state.^[12,13] For stabilizing the triplets in an amorphous state, rigid matrices are necessary to decrease the vibrational dissipation and oxygen diffusion.^[12,13] The rigid host could be either a small molecule host like a steroid (e. g., β -estradiol)^[12] or a glassy polymer (e. g., polymethylmethacrylate (PMMA)^[13], polyvinyl alcohol (PVA).^[14]

1.3.1.2.3. Phosphor in a Rigid Host:

Adachi and co-workers designed and synthesized a series of aromatic polynuclear hydrocarbon (PAH) phosphors as a guest and used steroidal host molecules such as β -estradiol (Figure 1.7a).^[12a] These host molecules have high triplet energy (because of short π -conjugation length); hence, non-radiative loss due to triplet-triplet Dexter energy transfer is minimized. In addition, they possess a rigid cyclic fused-ring structure and strong hydrogen-bonding interactions in their solid films.^[12a] Such structural characteristics benefit the suppressed molecular motions, hinder oxygen diffusion to a great extent, and help in dispersing the guest phosphors very efficiently. Hence, aggregation-caused quenching can be remarkably minimized. The authors showed that deuteration of the phosphor molecules substantially reduces the non-radiative decay rate. In addition, substituting the phosphors with a secondary amino group enhances intersystem crossing from the S_1 state to the T_1 state (El-Sayed's Rule) without increasing the non-radiative decay rate (Figure 1.6a). As a result, the host-guest systems presented in this seminal work provide a slow non-radiative deactivation pathway from the T_1 state at room temperature and effective intersystem crossing from the S_1 state to the T_1 state. These factors resulted in an efficient persistent, color-tunable afterglow RTP with a quantum yield of over 10 % and above 1 second lifetime in air (Figure 1.7b).^[12a]

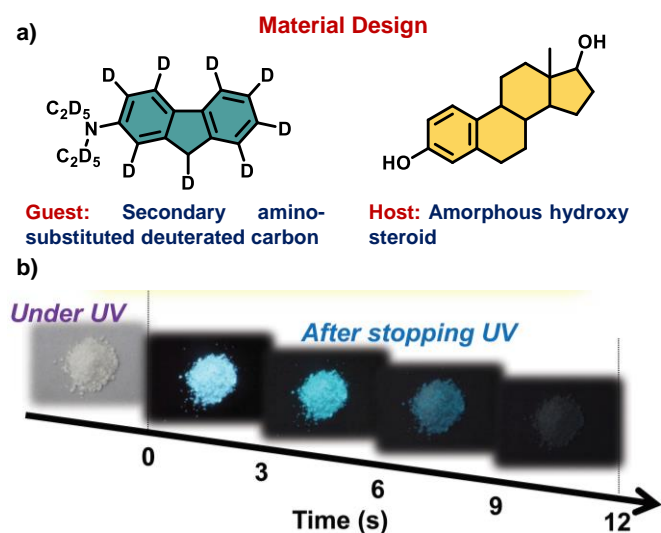


Figure 1.7. a) Organic phosphor design based on hydroxyl steroid host and a deuterated guest, b) Guest showing efficient persistent RTP in presence of rigid host in air (Reproduced from reference 12a).

1.3.1.2.4. Phosphor in the Polymeric Matrix:

Unlike their small-molecule counterparts, non-conjugated amorphous polymers offer better rigidity, high triplet energy, and more straightforward processing methodologies. One of the most widely used polymer host systems for this purpose is polymethyl methacrylate (PMMA), with high glass transition temperature ($T_g = 108\text{ }^\circ\text{C}$) and high triplet energy ($\sim 3.1\text{ eV}$), suggesting their ability to form rigid glasses as well as an excellent comprehensive band-gap host material.

Reineke and co-workers studied commercially available hole-transporting materials, i.e. (N,N'-Bis(naphthalen-1-yl)-N,N' bis(phenyl)benzidine (**NPB**)) as good phosphorescent emitters when dispersed in PMMA matrices at very low concentrations (Figure 1.8a).^[13a] The low concentration of the phosphors is maintained to prevent aggregation-caused quenching effects.^[13a] However, due to the oxygen-sensitive nature of the phosphorescence emission, **NPB**-doped PMMA films do not show phosphorescence emission (Figures 1.8b-d). Further, they have coated **NPB**-doped PMMA layer with an O₂-barrier layer (ethylene-vinyl alcohol copolymer) (Figure 1.8e). They achieved a very high photoluminescence quantum yield from PMMA hybrid films with a very high lifetime with visible afterglow characteristics (Figures 1.8f,g).^[13a] Further, they have utilized it as a unique 'programmable luminescent tag' by using the reversible afterglow phosphorescence emission highly sensitive to oxygen.^[13a]

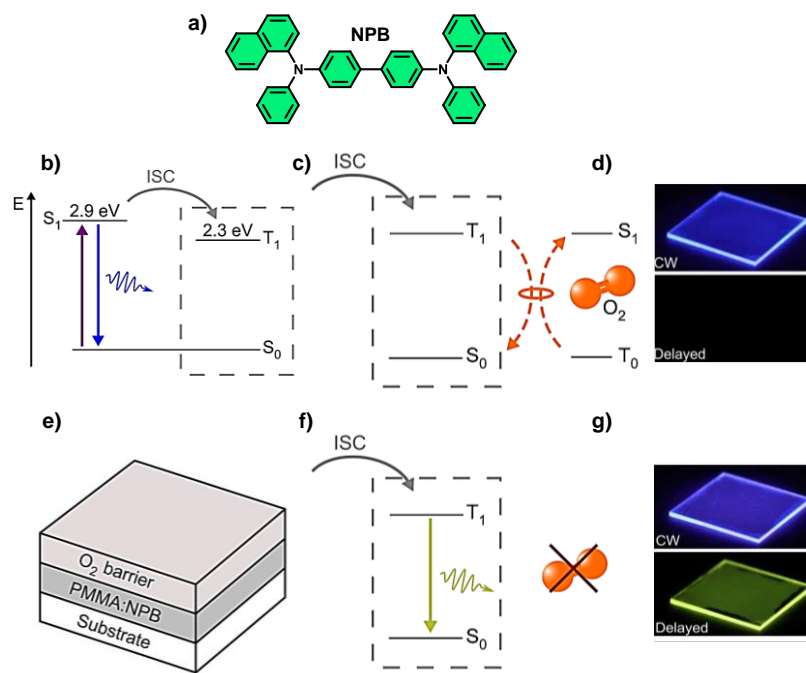


Figure 1.8. a) Molecular structures of **NPB**. b) Schematic representation of simplified Jablonski diagram showing upon photo-excitation, excited singlet state (S_1) of **NPB** generates which leads to fluorescence or ISC to the excited triplet state (T_1). c) In the absence of an oxygen barrier T_1 state of **NPB** depopulates in the presence of oxygen via the triplet-triplet dexter energy transfer process, and d) shows only fluorescence emission, no phosphorescence. e-f) Upon putting oxygen barrier, T_1 state of **NPB** does not depopulate with surrounding oxygen, and g) shows visible greenish-yellow phosphorescence. (Reproduced from reference 13a).

Kim and co-workers also realized solution-processable RTP by embedding 2,5-dihexyloxy-4-bromobenzaldehyde (**Br6A**) into isotactic PMMA with a phosphorescence efficiency of 7.5 % at room-temperature (Figure 1.9).^[13e] The reduced beta (β)-relaxation of isotactic PMMA most efficiently suppresses vibrational triplet decay.

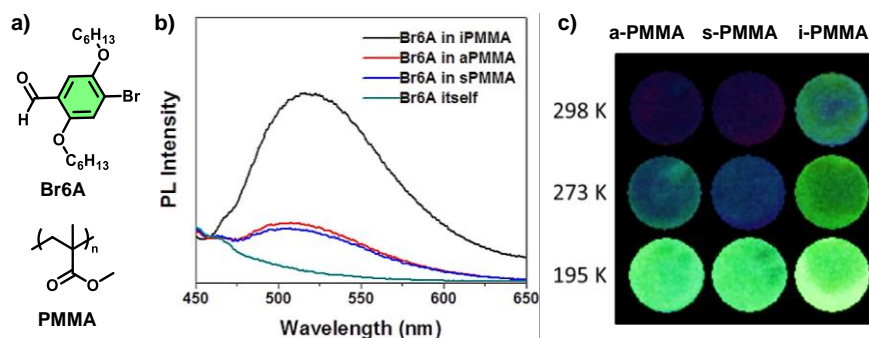


Figure 1.9. a) Molecular structures of **Br6A** and **PMMA** matrix. b) Emission spectra of **Br6A** alone and when doped into the isotactic **PMMA** (*i*-**PMMA**), syndiotactic **PMMA** (*s*-**PMMA**), and atactic **PMMA** (*a*-**PMMA**). c) Phosphorescence emission of **Br6A** embedded into isotactic, syndiotactic, and atactic **PMMA** at three different temperatures. (Reproduced from reference 13e).

Other than **PMMA**, Poly(vinyl alcohol) (**PVA**) has emerged as a popular choice as a host matrix for designing amorphous afterglow RTP emitters in recent years. **PVA** is a water-soluble polymer used extensively in composites due to its high transparency, tensile strength, flexibility, and good oxygen barrier performances. The most notable difference between **PMMA** and **PVA** is the possibility of a more robust packing of suitable guest phosphors provided by supramolecular interactions such as hydrogen-bonding and ion-dipole interactions, possible due to the presence of multiple polar hydroxyl groups in **PVA**.

In this regard, Kim, and co-workers utilized bromo-aldehyde core, functionalized with carboxylic acid side-chains (Figure 1.10a).^[14a] The carboxylic acid groups were known to form strong hydrogen bonding with the **PVA** matrix and result in reduced vibrational relaxations (Figures 1.10a,b).^[14a] In addition, the author proposed unique halogen bonding with the neighbouring phosphor molecules, which is well organized in the **PVA** matrix (Figure 1.10b).^[14a] Strong hydrogen bonding and the halogen-bonding interaction reduced the vibrational dissipation and increased the SOC via external heavy atom effect; both factors helped realize excellent phosphorescence quantum efficiency of over ~24 % in air (Figure 1.10b).^[14a] Further, the author shows the importance of carboxylic acid side-chains by eliminating the carboxylic acid group into a long alkyl chain where feeble phosphorescence was observed (Figures 1.10a,b).^[14a]

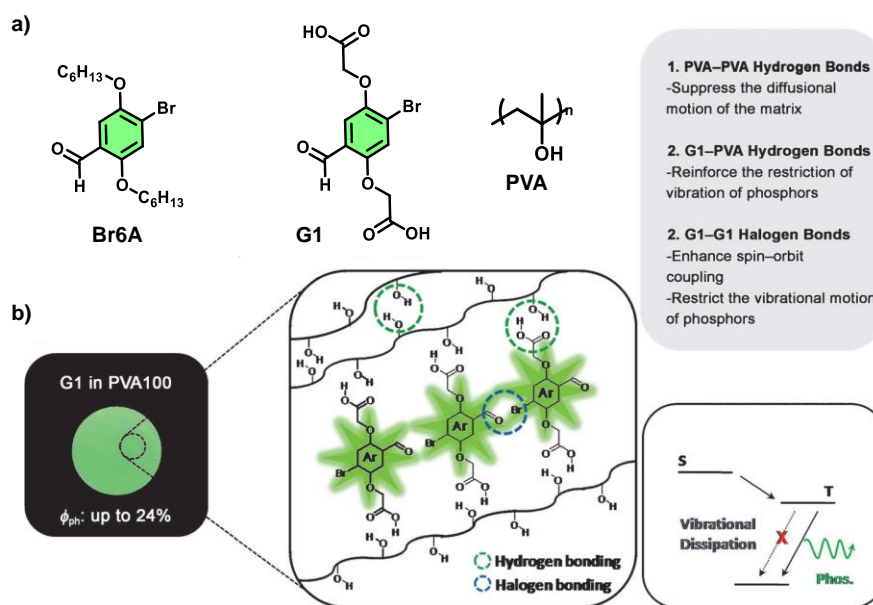


Figure 1.10. a) Molecular structures of **Br6A**, **G1**, and **PVA**. b) Photograph of phosphorescence emission under 365 nm UV-lamp and schematic illustration of phosphorescence processes in the **G1-PVA** hybrid film. (Reproduced from reference 14a)

Zhao and co-workers also have taken advantage of the rigidity of the PVA matrix and strong oxygen barrier ability to conduct more extensive research on afterglow phosphorescence from heavy-atom free phosphors (Figure 1.11a).^[14b] Authors have developed planar poly nuclear aromatic compounds based on carbazole, dibenzofuran, and dibenzothiophene derivatives (Figure 1.11a).^[14b] The hetero atom having lone pair of electrons helped in an effective ISC process by following El Sayeds' rule. The planar carbazole derivative showed efficient cyan phosphorescence emission with a lifetime of more than 2 seconds, with an afterglow duration of more than 20 seconds (Figure 1.11a).^[14b] Further, authors have developed excitation-dependent afterglow emission from pyrene derivatives by controlling the H-bonding interaction (Figure 1.11b).^[14c]

In this regard, our group demonstrated blue afterglow phosphors by cleverly choosing organic chromophores triazatruxene (**TAT**) with very high triplet energy and dispersing them in low concentrations in rigid polymer, polyvinyl alcohol (Figure 1.12).^[14d]

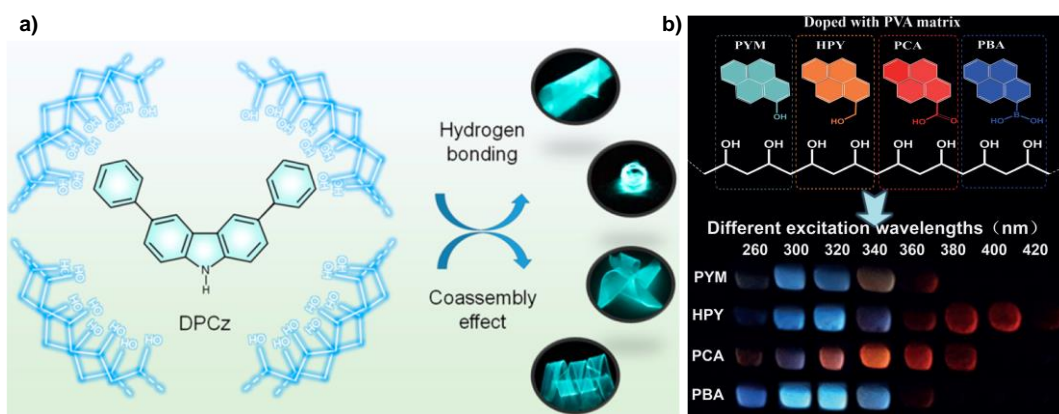


Figure 1.11. a) Molecular structures of *DPCz* and photographs of *DPCz-PVA* hybrid showing cyan long-lived phosphorescence using 254 nm UV-lamp excitation. b) Molecular structures of different pyrene derivatives and their photographs of excitation-dependent long-lived phosphorescence emission upon different phosphor concentrations in the PVA matrix. (Reproduced from reference 14b and 14c).

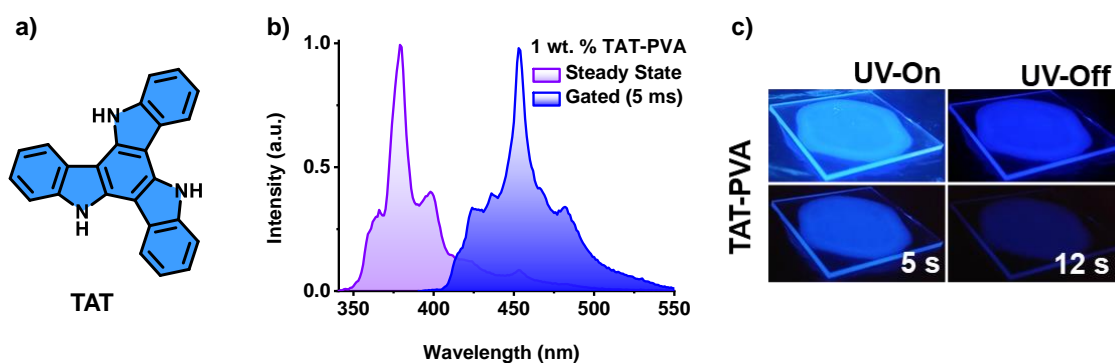


Figure 1.12. a) Molecular structures of triazatruxene derivative (*TAT*). b) Normalized steady-state and gated emission spectra of *TAT-PVA* hybrid film ($\lambda_{exc.} = 330$ nm, delay time = 5 ms) and c) corresponding photographs showing pure blue phosphorescence emission. (Reproduced from reference 14d).

1.3.1.2.5. Host-guest Strategy:

Employing supramolecular host-guest interactions has been one of the most innovative approaches to achieve RTP under ambient conditions. In this approach, the macrocyclic host molecule forms a stable inclusion complex with the guest molecule using various non-covalent interactions like hydrophobic, ion-dipole, etc. (Figure 1.13a).

Recently Liu and co-workers illustrated highly efficient RTP from bromophenyl-methyl-pyridinium molecule inside the **CB[6]** (Figure 1.13b).^[16a,b] They have shown

that bromophenyl-methyl-pyridinium molecule shows weak phosphorescence efficiency of 4.6 % in the crystalline state.^[16a] The phosphorescence efficiency increased to 81.2 % upon complexation with **CB[6]** (Figure 1.13b).^[16a,b] A similar strategy is bestowed from the same group to achieve afterglow emission from the phenyl-methyl-pyridinium molecule by removing the heavy atom from the core (Figures 1.13c,d).^[16b]

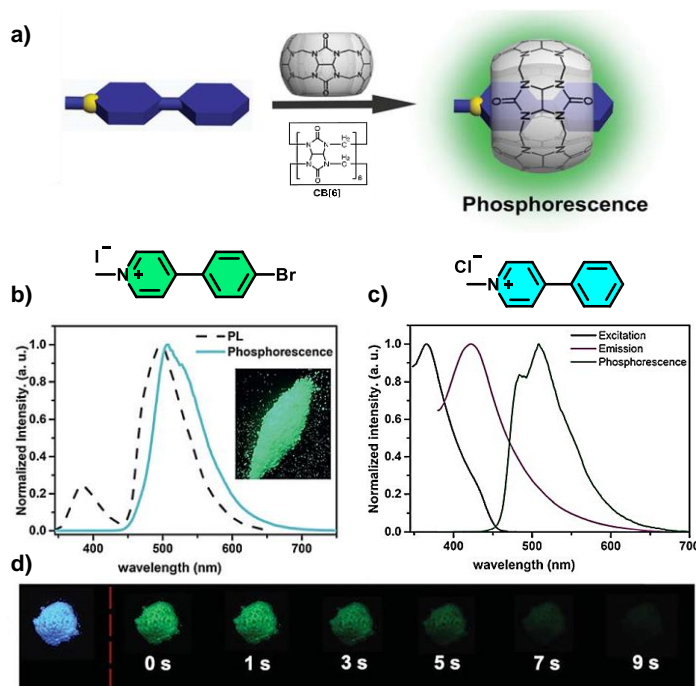


Figure 1.13. a) Schematic representation of phosphor, CB[6] complex. b) Molecular structure and its corresponding steady-state emission (black dashed line) and gated emission (cyan solid line) spectra upon complexation with CB[6] ($\lambda_{exc.} = 334$ nm, inset: photograph of phosphor, CB[6] complex under 365 nm UV light). c) Molecular structure and its corresponding excitation (black line), steady-state emission (grey line) and gated emission (green line) spectra upon complexation with CB[6] ($\lambda_{exc.} = 366$ nm). d) Afterglow emission of phosphor, CB[6] complex under 365 nm UV light. (Reproduced from reference 15a-c).

In another seminal work from the same group, ultra-long phosphorescent material ('supramolecular pins') with astonishingly high efficiency of 99.38 % was constructed using a similar molecular architecture with phenyl pyridinium moiety (Figure 1.14a).^[16c] Here, two phenyl pyridinium molecules are linked via an alkyl chain, where one is thioether substituted, while the other is substituted with a bromine atom (Figure 1.14a).^[16c] The whole moiety is trapped inside **CB[8]**, resulting in the gradual appearance

of new red-shifted bands in both absorption and emission spectrum that hint towards the formation of an effective CT assembly.^[16c] Authors speculate that an efficient intramolecular charge (ICT) transfer happens between the thioether-substituted phenylpyridinium moiety, which acts as the donor, to the bromo-substituted phenylpyridinium moiety, which acts as the acceptor (Figure 1.14a).^[16c] Phosphorescence quantum yield of 12.10 % achieved with **CB[8]** alone was enhanced to 99.38 % with a lifetime of 110.3 ms upon mixing phenylpyridinium/**CB[8]** complex with polyacrylamide (PAM), PVA and γ -CD in a treated filter paper (Figure 1.14b).^[16c] When **CB[8]** binding and rigid matrix encapsulation stiffens the phosphor from vibration dissipation and oxygen quenching of the triplet state, the alkyl bridge helps in the ‘molecular folding’ that further facilitates π - π stacking, ICT, and halogen bonding (Figure 1.14a).^[16c]

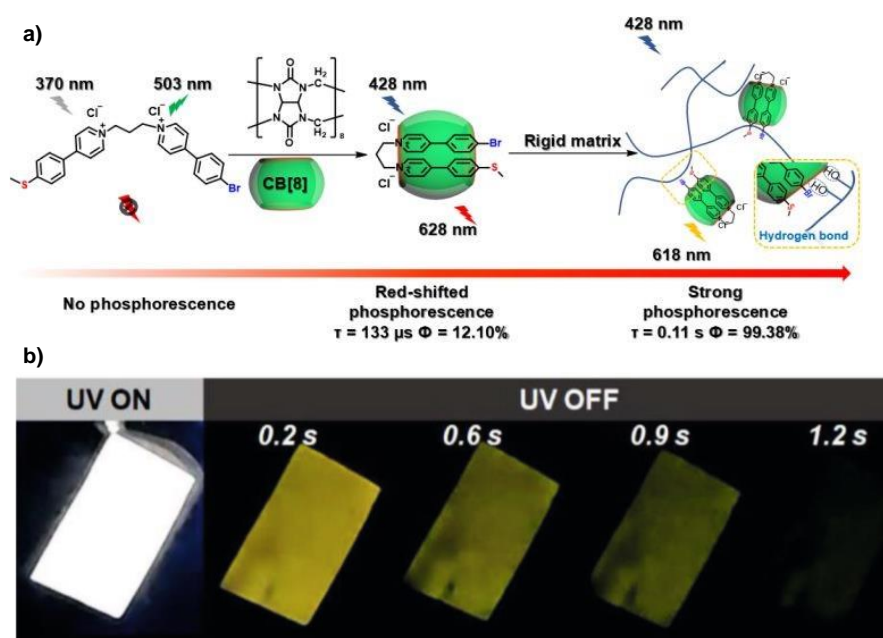


Figure 1.14. a) Schematic representation of supramolecular pin formation and its complexation in presence of rigid matrix. b) Afterglow images of filter paper embedded with phosphor/**CB[8]** assemblies under 365 nm UV light. (Reproduced from reference 15d).

1.3.2. Thermally Activated Delayed Fluorescence (TADF):

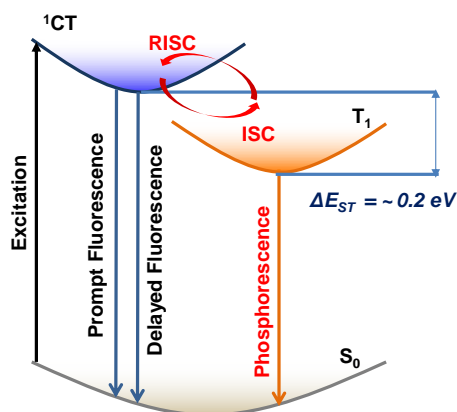


Figure 1.15. The simplified Jablonski diagram shows the TADF process upon photo-excitation.

Thermally activated delayed fluorescence (TADF) is another efficient way to harvest the triplet excitons where a maximum of 100 % IQE can be achieved (Figure 1.15).^[6] In recent days, TADF materials are promising triplet harvesters due to narrow emissions, high stability, easy fabrication, and most importantly, they do not require any heavy metals that are costly and toxic.^[6] However, the main challenge is to design a promising TADF molecule is having a small ΔE_{ST} value, a low lifetime, intense fluorescence, and satisfying all other conditions for becoming an excellent OLED emitter material like high external quantum efficiency, high quantum yield in the solid state, narrow emission, etc.^[6,16]

The concept of TADF is not new; in the textbook, it is written as E-type delayed fluorescence. In 1929 Perrin was first reported, and it was further studied in 1961 in Eosin molecule by Hatachard and co-workers.^[17] However, Adachi and co-workers re-investigated the concept of TADF and showed a potential OLED emitter using Sn^{4+} based porphyrin complex.^[18] Further, in 2012, the same group made a path-breaking work by proposing a general design strategy of TADF molecule using purely organic chromophores (Figure 1.15).^[6a] The basic theory of the TADF phenomenon demands less energy gap between the singlet and triplet excited state (ΔE_{ST}) so that it will fall within the range of the usual room temperature energy (~ 25.6 meV when $T = 298$ K).^[6] Then there will be a high equilibrium between ISC and the reverse intersystem crossing process (RISC). Subsequently, the non-emissive 75 % triplet excitons without going

through non-radiative pathways can be converted to singlet excitons, resulting in a maximum of 100 % IQE.^[6] The rate of RISC can be written as,

$$k_{\text{RISC}} \propto e^{\frac{-\Delta E_{\text{ST}}}{k_{\text{B}}T}}$$

where k_{B} is the Boltzmann Constant, T is temperature, and ΔE_{ST} is the energy gap between the lowest excited singlet and triplet states. k_{RISC} is exponentially proportional to $(-\Delta E_{\text{ST}}/k_{\text{B}}T)$.^[6] A decrease in ΔE_{ST} will increase the k_{RISC} , and an increase in temperature will increase TADF efficiency.^[6] The energy gap should ideally be tens of meV for an efficient RISC process.^[6] Further, the delayed fluorescence lifetime is related to k_{RISC} by the relation $k_{\text{RISC}} = 1/\tau_{\text{D}}$.^[6]

1.3.2.1. Design-strategy for Thermally Activated Delayed Fluorescence (TADF) Emitters:

In purely organic chromophores decrease in ΔE_{ST} , is possible by purposefully forming of charge transfer (CT) state by introducing an electron-rich donor and electron-deficient acceptor (Figure 1.16).^[6,16] Further, reduction of ΔE_{ST} is possible by reducing the overlap between the HOMO of the donor and the LUMO of the acceptor (Figure 1.16).^[6] Theoretically, the singlet and triplet energy depend on the i. energy difference between HOMO and LUMO orbitals, ii. electron repulsion energy (K) and iii. exchange energy (J), and can be written as,

$$E_{\text{S}_1} = E_{\text{HOMO}} - E_{\text{LUMO}} + K + J$$

$$E_{\text{T}_1} = E_{\text{HOMO}} - E_{\text{LUMO}} + K - J$$

$$\Delta E_{\text{ST}} = E_{\text{S}_1} - E_{\text{T}_1} + 2J$$

ΔE_{ST} is directly related to exchange energy (J), so to reduce the ΔE_{ST} , reduction of the exchange energy between the electrons residing in HOMO and LUMO orbitals is necessary (Figure 1.16a).^[6,16] Further, the oscillator strength (f) of emission is directly proportional to the exchange energy (J), and then oscillator strength (f) also depends on the orbital overlap between HOMO and LUMO (Figure 1.16a).^[6,16] Thus, the reduction of oscillator strength (f) is necessary to reduce the ΔE_{ST} , which is possible if the donor and acceptor are spatially separated (Figure 1.16a).^[6] So, selecting a suitable bridging moiety will help to maintain the proper angle (close to 90°) between donor and acceptor in a covalently attached system (Figure 1.16b).^[6] Although present theories of the TADF are still not widely accepted, few organic systems reported in the literature show efficient

TADF emission; however, their ΔE_{ST} is very high. Further, finding the triplet state from where the RISC happens is also necessary. RISC from locally excited triplet (3LE) states of either donor or acceptor is standard; however, evidences are there of forming charge transfer triplet (3CT) state.^[16e] Although RISC from 3CT and 1CT is unfavourable due to forbidden spin-orbit coupling (SOC). Some recent theoretical findings show that forbidden spin-orbit coupling (SOC) between 3CT and 1CT states gets favoured by vibronically coupled states of 3CT and 3LE .^[6]

a) Design-strategy:

$$E_{S_1} = E_{HOMO-LUMO} + K + J$$

$$E_{T_1} = E_{HOMO-LUMO} + K - J$$

$$\Delta E_{ST} = E_{S_1} - E_{T_1} = 2J$$

K = electron repulsion energy
J = The exchange energy

- I. Oscillator Strength (f) of emission depends on the orbital overlap between HOMO and LUMO and $f \propto J$.
- II. A proper balance between the twist angle and frontier orbital overlap is necessary.
- III. Decreasing the overlap between the HOMO and LUMO by spatial separation of these frontier orbitals.

b) Molecular Design:

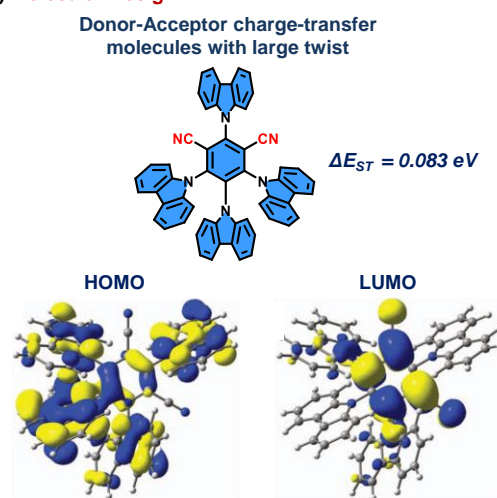


Figure 1.16. The a) necessary criteria and b) plausible molecular design for a covalently bound donor-acceptor molecular design. (Reproduced from reference 6a).

1.3.3. Triplet-Triplet Annihilation (TTA):

Delayed fluorescence via triplet-triplet annihilation (TTA) is also another efficient way to harvest the triplet excitons (Figure 1.12).^[8] Two triplet excitons upon bimolecular collision result in a high-energy singlet exciton in this mechanism.^[8] For generating an excited singlet state, the two triplet energy should be more than or equal to singlet energy ($2T_1 \geq S_1$) (Figure 1.17).^[8] So that maintaining a considerable energy gap between the lowest singlet and triplet excited states is necessary.^[8] Efficient triplet formation ability and essential energy requirement are not easy for purely organic chromophores, resulting in minimal molecular design. Hence till now, anthracene and related derivatives only show TTA-induced delayed fluorescence.^[8c] Although, in triplet harvesting, the TTA-induced delayed fluorescence is more efficient than the fluorescence emitter as the

maximum IQE of 62.5 % can be achieved utilizing this process ($25 \% + 0.5 \times 75 \% = 62.5 \%$), however further advancement of the field is required (Figure 1.17).^[8]

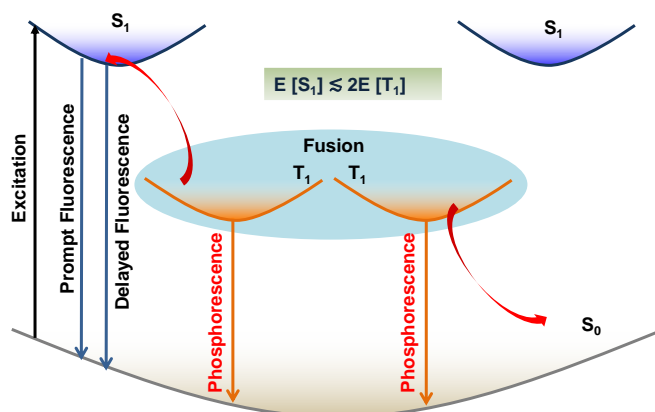


Figure 1.17. The simplified Jablonski diagram showing the TTA process upon photo excitation.

1.3.3.1. Design-strategy for TTA-induced Delayed Fluorescence Emitters:

The necessary conditions for the TTA-induced delayed fluorescence process in the solid-state are i) efficient ISC rate to generate the triplet and ii) long triplet diffusion length with efficient triplet migration.^[19] Perepichka and co-workers recently realized TTA-induced delayed fluorescence in acridone derivatives in the crystalline state (Figure 1.18).^[19a] They found one-dimensional slipped π -stacks (3.41 Å) of N-substituted acridone derivatives with the parallel alignment of transition dipole showed TTA-induced delayed fluorescence (Figures 1.17a,b).^[19a] Further, to validate the concept of long-range π ordering, they substituted the N position of acridone with a bulky group (Figure 1.18b).^[19a] They observed that delayed fluorescence is diminished due to breaking π ordering.^[19a] However, the delayed fluorescence efficiency of the system is very less and dominated mainly by the phosphorescence emission with very low quantum efficiency (Figure 1.18c).^[19a]

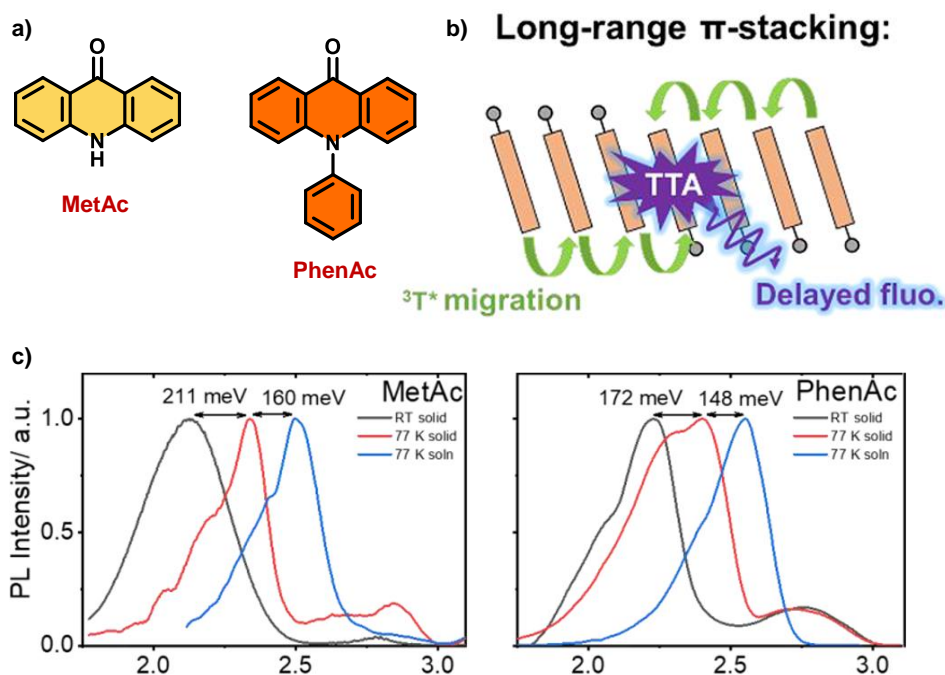


Figure 1.18. a) Molecular structure and plausible mechanism for TTA process in the crystalline state. c) Gated emission spectra (delay time = 1ms) of acridone derivatives in CHCl_3 glass matrices at 77 K, in crystalline powders at room temperature and in solid-state at 77K showing dual phosphorescence and DF. (Reproduced from reference 19a).

1.3.4. Stabilization of the Triplets in Solution:

Phosphorescence in the crystalline state and the solution-processable amorphous state have already been established.^[5,11-13] However, some of the latest applications demand phosphorescence to be achieved in the solution state. The high lifetime, large Stokes-shift, and oxygen-sensitive nature of the organic phosphors make them suitable for bioimaging, sensing, singlet oxygen production, photodynamic therapy, photocatalysis, and optical sensing.^[5] Harvesting triplet excitons via harnessing phosphorescence in the solution state is necessary to realize these applications. Stabilization of triplets in the solution is arduous due to the highly susceptible nature of the triplet state via various deactivation factors such as vibrational dissipation, molecular oxygen, and so on. The non-radiative deactivation is rampant due to higher collisional quenching and unrestricted vibrational and rotational motions of the phosphor molecules.^[5] Moreover, here, dissolved oxygen also serves as a vicious quenching factor; thus, phosphor has to be protected from oxygen to achieve RTP in the solution. All these factors make solution-state phosphorescence a holy grail that can be achieved only after addressing the

challenges. To alleviate this scenario, we will focus on how supramolecular chemistry can solve these fundamental issues to harness the triplet excitons for realizing RTP in the solution state and preferably in the aqueous phase (Figure 1.19).

Heavy and hetero-atom substituted molecular design principles are not only the sole criteria, but the rigidity and oxygen tolerance of the chromophores by employing various non-covalent interactions can also be the critical factors in achieving solution state phosphorescence. In this regard, different supramolecular approaches like i. constructing assemblies or creating rigid microenvironments via self-assembly, ii. host-guest interactions, and iii. organic-inorganic hybrid co-assembly approaches would be ideal for attaining solution state phosphorescence at room temperature (Figure 1.19).

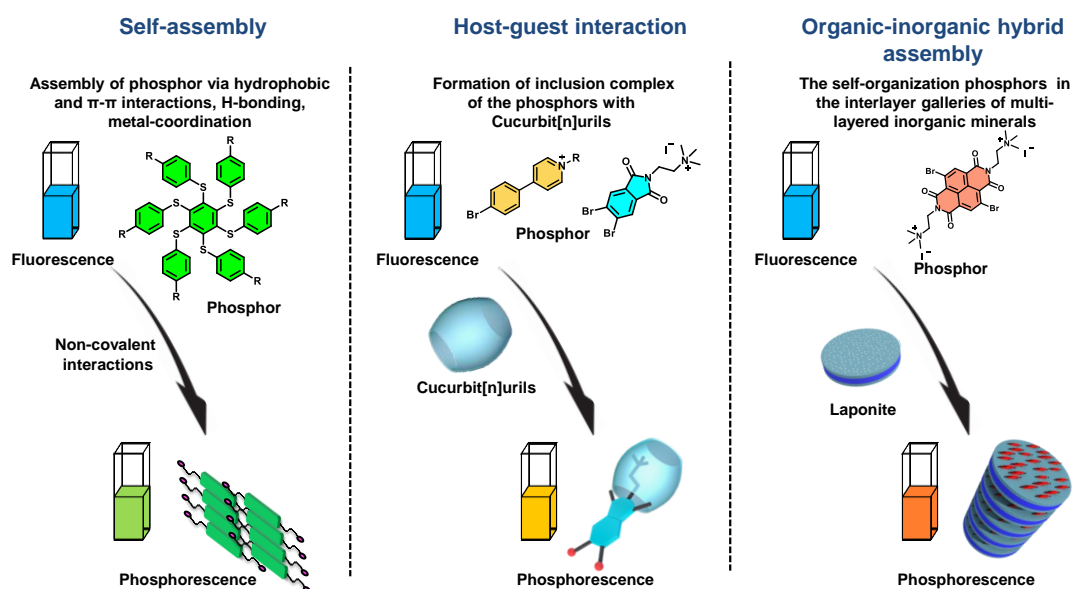


Figure 1.19. Various supramolecular approaches to realize ambient room temperature phosphorescence in solution.

1.3.4.1. Self-assembly Approach:

Ambient phosphorescence from organic phosphors in the crystalline state is mainly attributed to the reduced vibrational degrees of freedom of the molecules in the networks, which is achieved through various non-covalent interactions, for example, π - π interactions, H-bonding, and halogen bonding.^[11] Theoretical insights of some of these excitonically-coupled aggregated systems suggest that the intermolecular interactions also open up more ISC channels between the lowest singlet and nearest triplet states than the isolated chromophores, improving the ISC rates.^[11c] Recently, various research

groups have attempted molecular organizations of phosphors in a solution state to realize efficient ambient RTP. The initial breakthrough using this approach was first made by Ceroni and co-workers, using hexathiobenzene molecule with six terpyridine (tpy) groups at the periphery (Figure 1.20a).^[20a] Upon coordination with Mg^{2+} , they observed a turned-on RTP emission after forming a rigid metal-coordinated supramolecular polymer which restricted the phosphor molecules' conformational flexibility by inhibiting the intramolecular rotations (Figure 1.20a).^[20a] Upon adding $Mg(ClO_4)_2$ salt in the THF solution of the phosphor, a new red-shifted emission band ($\lambda_{max.} = 545 \text{ nm}$, $\Phi = 10\%$) with a lifetime of $5.3 \mu\text{s}$ in air-equilibrated solution suggests the phosphorescence nature of the emission (Figure 1.20b).^[20a]

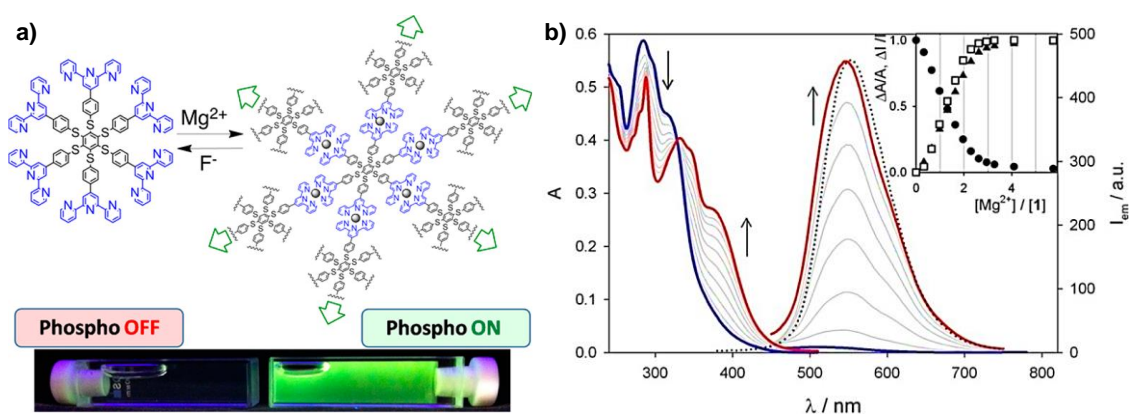


Figure 1.20. a) Molecular structure, schematic representation of Mg^{+2} coordination, and photograph of the coordination polymer in presence of UV light. b) Absorption and phosphorescence spectra of the phosphor upon titration with a 2.70 mM of $Mg(ClO_4)_2$ in THF solution ($\lambda_{exc.} = 326 \text{ nm}$). (Reproduced from reference 20a).

In another work, a water-soluble derivative of a hexathiobenzene derivative with multiple carboxylate groups at the periphery has been used (Figure 1.21a).^[20b] In monomer state, the aqueous solution of this molecule does not show any RTP; however, upon photo-excitation, there is a conformational change in the excited state geometry from its ground state structure which leads to a more hydrophobic and long-lived dark state (Figure 1.21b).^[20a] The long-lifetime (pico-second/nano-second) of the dark state enables the possibility of intermolecular interactions (pico-second or sub-pico-second), leading to the formation of aggregates upon photo excitation, which are shown to be more stable than the individual monomers (Figures 1.20b,c).^[20a] Therefore, the disassociation rate of these aggregates was slower than the rate of formation of the aggregation upon

photo excitation, thereby facilitating the aggregation-induced phosphorescence (AIP).^[20a]

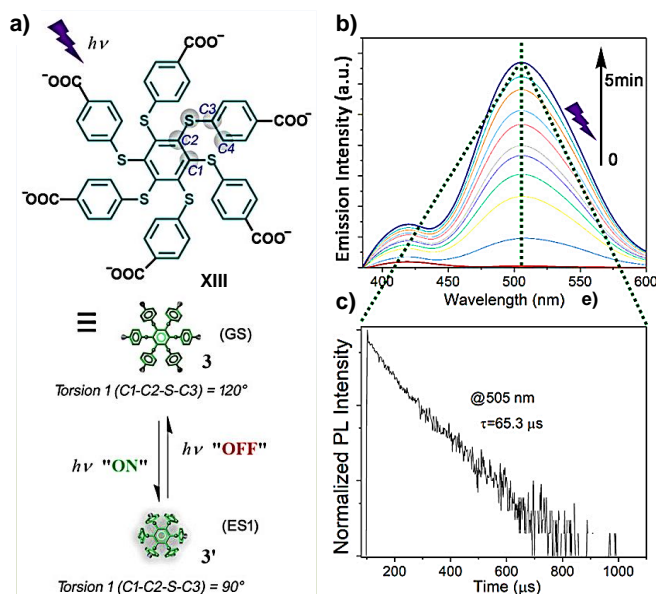


Figure 1.21. a) Molecular structure and schematic representation of photo excitation-controlled aggregation-induced phosphorescence in the water. d) Emission enhancement and lifetime decay plot ($\lambda_{\text{collected}} = 505 \text{ nm}$) of the phosphor in water upon prolonged UV irradiation ($[c] = 0.01 \text{ mM}$, $\lambda_{\text{exc.}} = 365 \text{ nm}$). (Reproduced from reference 20b).

1.3.4.2. Host-guest Strategy:

In this approach, the macrocyclic host molecule forms a stable inclusion complex with the guest molecule, using various non-covalent interactions like hydrophobic, ion-dipole, etc.^[21] Minimizing the vibrational dissipation and oxygen-mediated quenching of guest triplets by confining them in a rigid microenvironment inside the host molecule's cavity is crucial for achieving solution state RTP. The binding ability between the host macrocycles and phosphors significantly influences the RTP emission efficiency.^[21] Stronger host-guest binding interactions usually give rise to a higher quantum yield for the RTP emission. Cucurbit[n]urils (**CB**) is a class of host molecules with a higher binding constant with the guest molecules.^[21] Tian and co-workers showed a pH-responsive RTP emission based on **CB[7]** as a molecular shuttle in the bromo-substituted isoquinoline derivative which show efficient green phosphorescence at higher pH (Figures 1.21a,b).^[21a] Similarly, in another attempt, the same group illustrated a yellow RTP emission and a single component white light emission in an aqueous solution from

a heavy-atom-substituted triazine derivative in the presence of **CB[8]** host (Figures 1.16c-e).^[21b]

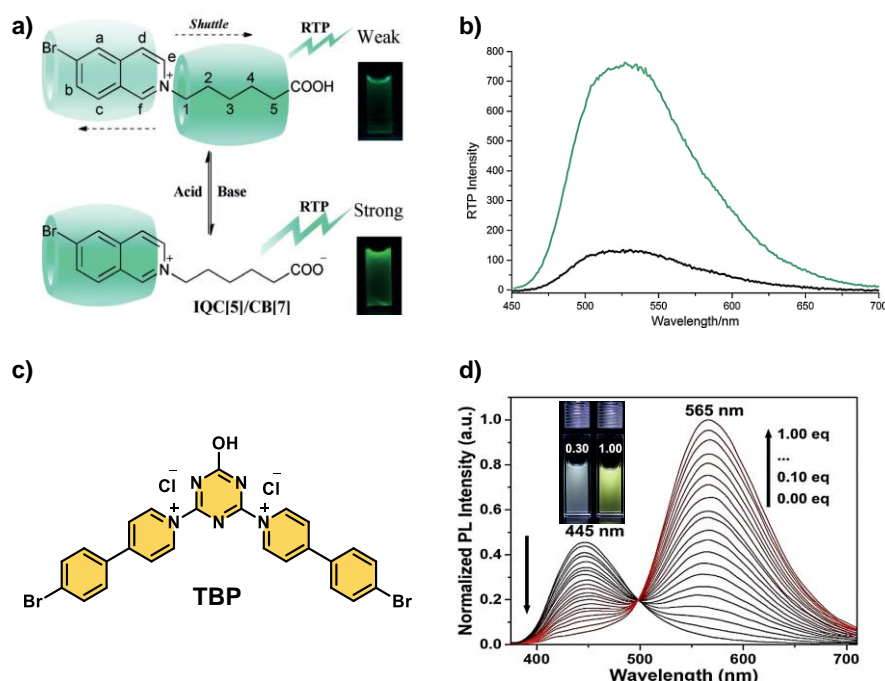


Figure 1.22. a) Schematic representation of **ICQ[5]-CB[7]** complexation modulated by pH. b) Phosphorescence emission spectra of the binary **ICQ[5]/CB[7]** complex in water at pH 3.7 (black line) and pH 6.9 (green line) ($[\text{ICQ[5]}]=0.075 \text{ mM}$, $[\text{CB[7]}]=0.12 \text{ mM}$, $\lambda_{\text{exc.}} = 300 \text{ nm}$). c) Molecular structure of **TBP**. d) Emission spectra of **TBP** upon addition of 0 to 1 eqv. **CB[8]**. (Reproduced from reference 21a and 21b).

1.3.4.3. Supramolecular Scaffolding Approach:

The self-organization of organic chromophores in the interlayer galleries of multi-layered inorganic minerals is a novel approach for ambient triplet harvesting in aqueous media (Figure 1.23)^[22a] The controlled and rigid organization is possible by co-assembling the organic phosphor in the inorganic silicate template (Figures 1.22a-c).^[22a] In this approach, limited diffusional motion through the nano-scale periodic galleries in the template and restricted oxygen diffusion in the interlayer galleries serve to achieve efficient ambient phosphorescence in the solution (Figure 1.23c).^[22a]

Recently, our group has reported RTP from bromo-substituted naphthalene diimides in laponite (**LP**) clay particles via a unique supramolecular scaffolding approach (Figure 1.23).^[22b] **LPs** are multi-layered inorganic materials that can act as a platform where organic dye molecules can self-organize inside the interlayer galleries (Figure

1.23c).^[22b] **LP** particles have a diameter of 25 nm and thickness of 0.9 nm with orthogonal negative and positive charges at the surfaces and edges, respectively (Figure 1.23b).^[22] The electro statistically driven ‘House of Cards’ packing in **LP** particles can be prevented by exfoliating them in an aqueous solution, followed by neutralizing the positive charges using sodium polyacrylate to co-assemble later with cationic phosphors via ionic self-assembly (Figure 1.23c).^[22b] **BrNDI** in the laponite hybrids with a new red-shifted emission band centered at 613 nm ($\lambda_{exc.} = 380$ nm) having a lifetime of 347 μ s, which proved the phosphorescence nature of the emission (Figures 1.22d,e).

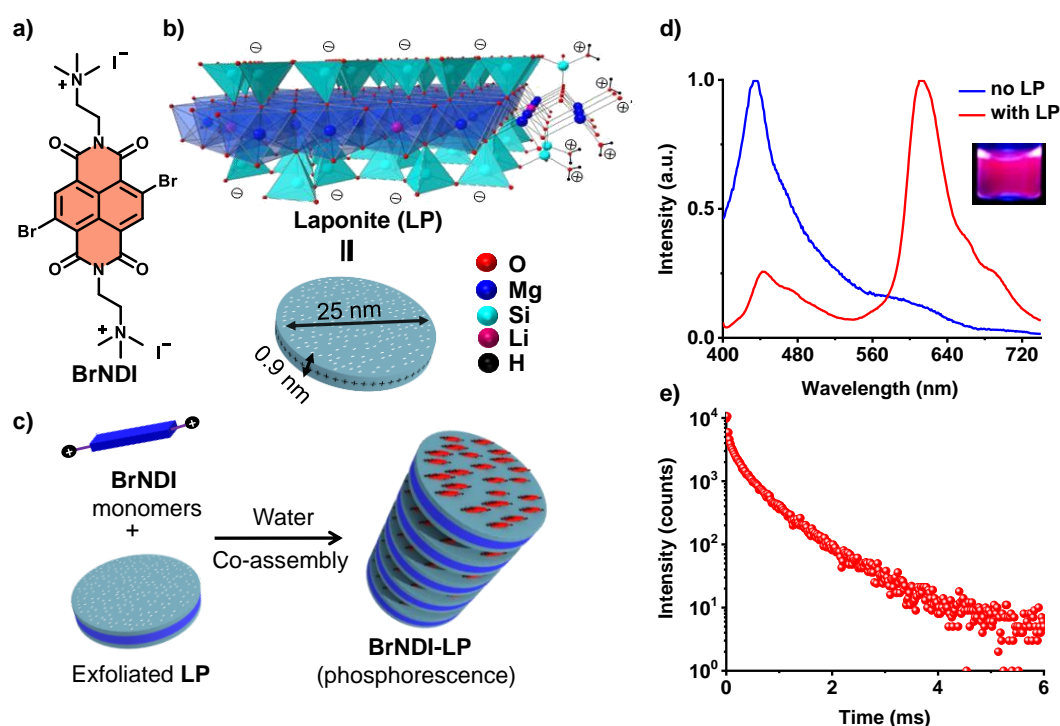


Figure 1.23. a) Molecular structures of **BrNDI**. b) Schematic representation of Laponite (**LP**) structure. c) Proposed schematic of the ionic hybrid co-assembly of exfoliated **LP** nanoplates and cationic phosphor in water (blue colour along the edges represents that the **LP** nanoplates are wrapping with anionic polymer). d) Normalized emission spectra and e) lifetime decay profile of **BrNDI-LP** hybrids (**LP**=2.25 wt%, $\lambda_{exc.}$ =380 nm) in water. Inset of (d) shows the photographs of **BrNDI-LP** hybrids in the solution state under 365 nm UV irradiation ($[BrNDI]=0.1$ mM). (Reproduced from reference 22b).

1.4: Application of Organic Triplets:

Organic optoelectronic materials are of profound interest due to the plethora of applications endowed by them. Emerging applications of these classes of materials outweigh the traditional device applications in LEDs, further reinforcing their importance

in the contemporary scientific community.^[5,6] Along with OLEDs, organic phosphors have diverse applications in bio-imaging, sensing, and data encryption.^[5] Due to the long lifetime of the triplet, they can easily avoid the autofluorescence of the cell. Bio-imaging in the biological realm gained momentum and benefited most after achieving solution state phosphorescence.^[5] The additional oxygen-sensitive nature of the triplet and afterglow phosphors opened a new dimension to sensing and anticounterfeiting.^[5]

1.4.1. Organic Light-Emitting Diodes:

The utilization of triplet excitons in purely organic chromophores made significant advancements in the OLEDs technology due to the dramatic enhancement of the overall device efficiency.^[7] Previously fluorescence LEDs were used for potential commercial applications.^[7a] In the 1990s phosphorescent LED field gained attention in the optoelectronic community when device fabrication started with the organometallic complexes.^[7b-d] However, due to the low device stability, poor processibility, and non-flexible nature of the organometallic phosphors they were replaced by purely organic phosphorescent and TADF materials.^[6] The easy low-temperature fabrication, highly stable and flexible nature of purely organic phosphorescent and TADF emitters, have overcome the popularity of the organometallic LED.^[5,6] Adachi and co-workers made efficient dual-color afterglow phosphorescent OLEDs using 3-(N-carbazolyl)-androst-2-ene as host and deuterated N,N'-bis(3 methylphenyl)-N,N'-bis(phenyl)-9,9-dimethylfluorene guest molecules (Figure 1.24a).^[23] The co-deposited film shows exhibits blue fluorescence and green afterglow phosphorescence under photo-excitation (Figure 1.24b).^[23] Further, the authors have used coronene-d₁₂ as a guest, showing a phosphorescence lifetime of 4.3 seconds.^[23] Next, the authors have utilized the co-doped mixture of host-guest in the emitting layer of OLED to obtain electroluminescence behaviour (Figures 1.23a,b).^[23] The device shows blue emission upon application of voltage, and interestingly when the power supply is switched off device exhibits persistent green emission (Figures 1.23b,c).^[23]

However, due to the long lifetime and low phosphorescence quantum yield, organic phosphorescence materials are not very efficient for the OLEDs (Figure 1.24d).^[6] A long phosphorescence lifetime always increases the possibility of triplet-triplet or triplet-singlet collision, forming non-emissive singlets and decreasing the device efficiency (Figure 1.24e).^[6] So, organic materials with low lifetime and high quantum

yield are desirable for further advancement of the field.^[6] In this regard, TADF materials are very efficient due to their low delayed lifetime and very high quantum efficiency and are now at the front in OLED technology.^[6]

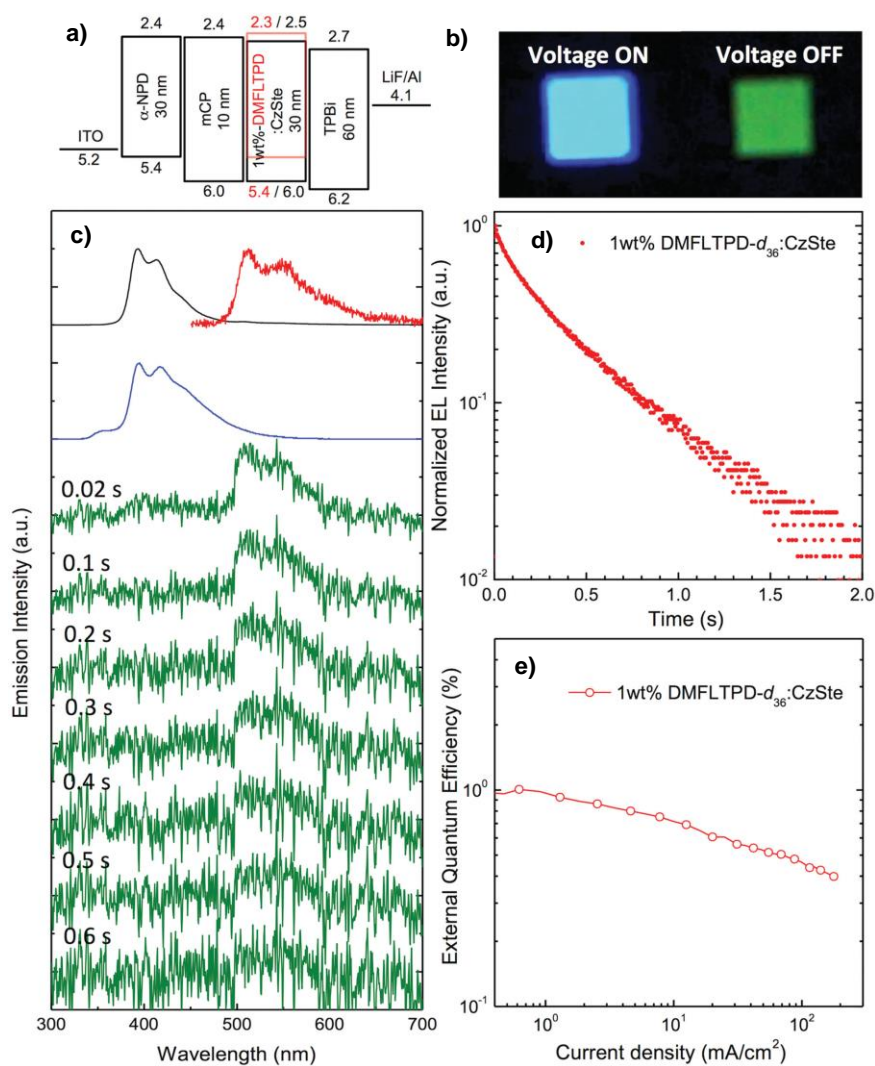


Figure 1.24. a) Schematic representation of an OLED device structure. b) Electroluminescence characterisations of the OLED showing blue emission upon application of voltage, and exhibits persistent green emission upon switching off. c) Steady-state photo-luminescence (black) and phosphorescence (red) spectra of a doped CzSte film, and electro luminescence spectra of the OLED during (blue) and after (green) electrical excitation. d) Long-lived lifetime decay profile of device after the applied voltage was turned off. e) External quantum efficiency vs. current density characteristics of the OLED. (Reproduced from reference 23).

1.4.2. Time-Resolved Bio-imaging:

Solution-state RTP, especially in aqueous media, has immense importance in the realms of bio-imaging; among this, time-resolved bio-imaging is in the front.^[5] Liu and co-workers have used the phosphorescent nature of bromophenyl-methyl-pyridinium and stabilized it in an aqueous solution to achieve their goal of bio-imaging.^[24a] First, the authors have attached the bromophenyl-methyl-pyridinium (**BrBP**) molecules with hyaluronic acid (**HA**) and made a polymer out of it, showing blue fluorescence at 380 nm but no phosphorescence emission (Figure 1.25a).^[24a] A green phosphorescence appears upon the addition of **CB[8]** into the solution of the polymer (Figure 1.25a).^[24a] Authors have hypothesized that the synergistic effect of strong host-guest interaction with **BrBP** and **CB[8]** and hydrogen bonding with the **HA** chain restrict the movement of the phosphors and reduce their vibrational motion, which results phosphorescence efficiency of 7.58 % with a lifetime of 4.33 ms. Further authors have utilized the **HABrBp-CB[8]** conjugated for tumor cell imaging (Figure 1.25b).^[24a]

Using a different approach, Wu and co-workers reported solution state RTP in a new class of donor-acceptor type charge-transfer emitting organic nanoparticles based on difluoroboron β -diketonate (acceptor) and carbazole (donor) (Figure 1.25c).^[24b] The strong charge-transfer (CT) nature of the molecules studied in this report ensured a red-shifted absorption maximum in the visible wavelength region.^[24a] These absorption features of the CT-derivatives and the additional long-lived emission from these molecules make them potential candidates for remarkable advancement in the field as novel bio-imaging probes. The authors observed no RTP for the molecularly dissolved samples of these derivatives in THF (Figure 1.25d).^[24a] However, with the utilization of a nano precipitation method in solvent (THF)/anti-solvent (water) medium, they successfully synthesized well-dispersed self-assembled nanoparticles with an average diameter of 105 nm (**H-NpCzBF₂NPs**), 85 nm (**Br-NpCzBF₂NPs**), 110 nm (**I-NpCzBF₂NPs**), as evident from the scanning electron microscopy.^[24a] These aggregated NPs were capable of showing solution state RTP by visible light excitation (Figure 1.25d).^[24a] Upon excitation at 470 nm resulted in bright red-emitting RTP from **H-NpCzBF₂NP** ($\lambda_{\text{max}} = 610$ nm), **Br-NpCzBF₂NP** ($\lambda_{\text{max}} = 620$ nm), and **I-NpCzBF₂NP** ($\lambda_{\text{max}} = 622$ nm), respectively (Figure 1.25d).^[24a] Further insights from TD-DFT calculations showed that the increased number of ISC channels was partly responsible for better triplet state formation in the nanoparticles as compared to the monomer state.

The authors further explored the nanoparticles as plausible bio-imaging probes utilizing the confocal laser scanning microscopy (CLSM) of *I-NpCzBF₂NP*-loaded HeLa cells.^[24a] They observed the emission from both green (500-550 nm) and red (570-620 nm) channels by the CLSM technique upon excitation with a 488 nm laser (Figure 1.25e).^[24a] This observation demonstrates that the *I-NpCzBF₂NP* nanoparticles had successfully penetrated through the cell membrane and entered the cell cytoplasm.^[24a]

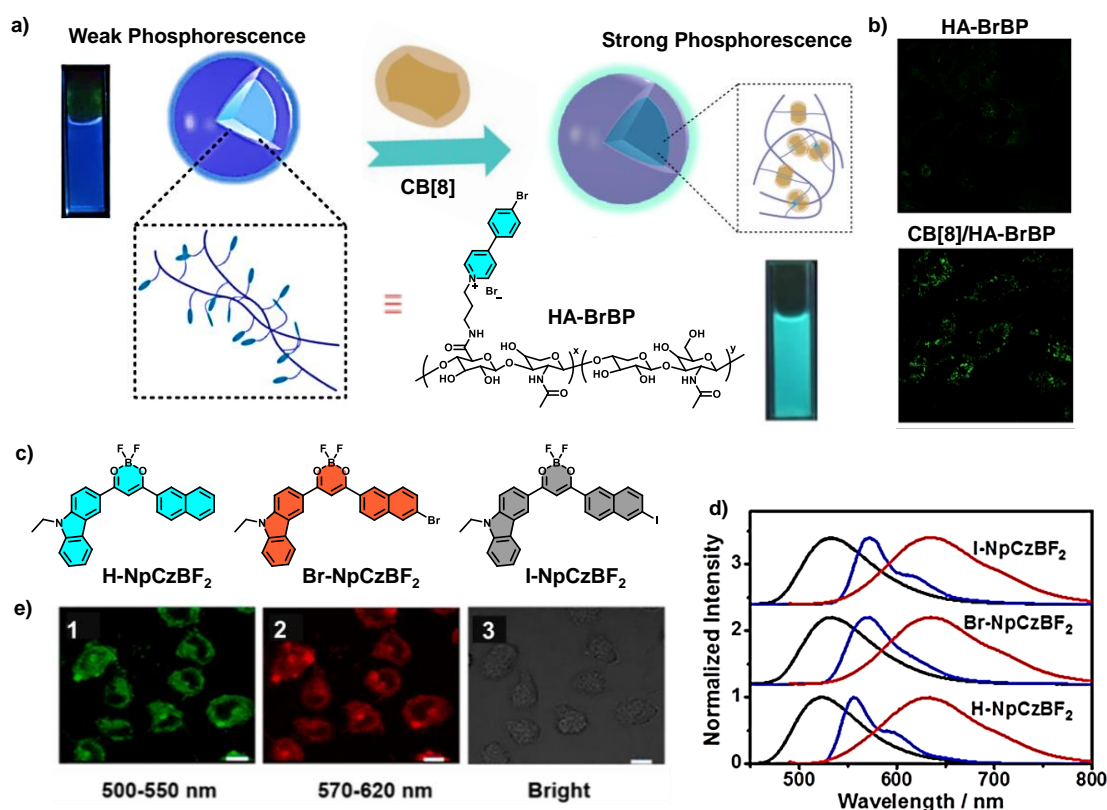


Figure 1.25. a) Schematic representation of *HABrBP/CB[8]* complexation, *HABrBP* showing weak and strong phosphorescence before and after complexation respectively. b) Confocal microscopy images of A549 cells incubated with *HABrBP* (above) and with *CB[8]/HABrBP* ($[HABrBP] = 25 \mu\text{M}$, $[CB[8]] = 12.5 \mu\text{M}$). c) Molecular structures of *H-NpCzBF₂*, *Br-NpCzBF₂* and *I-NpCzBF₂*. b) Normalized fluorescence in THF (black line, $[c] = 10 \mu\text{M}$), phosphorescence spectra at 77 K in THF (blue line, $[c] = 10 \mu\text{M}$), and phosphorescence spectra of *H-NpCzBF₂*, *Br-NpCzBF₂* and *I-NpCzBF₂* nanoparticles in water (red line, $\lambda_{exc.} = 470 \text{ nm}$, delay time = 0.1 ms, $[c] = 1 \text{ mM}$, red line). c) Confocal luminescence images of HeLa cells incubated with *I-NpCzBF₂* ($[c]=1 \mu\text{M}$ in water, $\lambda_{exc.} = 488 \text{ nm}$, scale bar: 10 μm). (Reproduced from reference 24a and 24b).

1.4.3: Sensing:

Triplets of an organic molecule are highly sensitive to oxygen, making them suitable candidates for the oxygen sensor in physiological conditions.^[25] Ceroni and co-workers have demonstrated that silica-PEG NPs embedded with persulfurated benzene chromophores can act as an oxygen sensor in the physiological oxygen range in water (Figure 1.26a).^[25a] Authors have synthesized carboxylic end substituted hexathiobenzene skeleton modified with (3-aminopropyl) triethoxysilane (Figure 1.26a).^[25a] Then, silica PEG NPs encapsulated chromophores to form a rigid supramolecular microenvironment inside the NPs cavity showing green phosphorescence emission in oxygenated aqueous solution was further used for oxygen sensing study.^[25a] The phosphorescence lifetime and quantum yield were increased upon deoxygenation, which is completely reversible upon reoxygenation.^[25a] The Stern-Volmer quenching plot was measured at two different temperatures (22°C and 36.6°C) in an aqueous buffer solution (Figure 1.26b).^[25a] The partial pressure of oxygen measured the oxygen concentration, and the lifetime decay rate was measured by quenching of lifetime.^[25a]

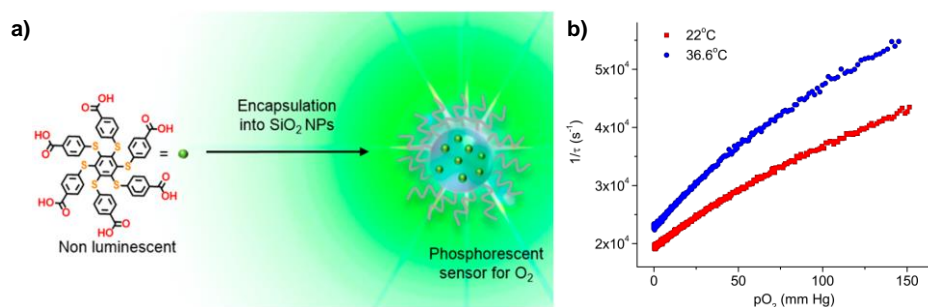


Figure 1.26. a) Molecular structure and schematic representation of phosphor doped silica nanoparticles. b) Stern-Volmer oxygen quenching plots of phosphor doped silica nanoparticles measured in buffer solutions ($[phosphate] = 20\text{ mM}$, $pH = 7.2$). (Reproduced from reference 25a).

1.5. Delayed Sensitization: Another Efficient Way to Achieve Colour Tunable Delayed Fluorescence:

In the earlier discussion, we have mainly discussed the effectiveness of specific rigid polymers or small molecule hosts in suppressing the non-radiative deactivation pathways in simple heteroatom-containing aromatic organic chromophores with high triplet yields.^[11-15] However, it is worth noting that, to date, most of these chromophores emit

either green or yellow phosphorescence, whereas blue or red/NIR organic phosphors are very rare.^[11-14] In this regard, blue afterglow phosphors have been demonstrated by our group and Zhao's group discussed in section 1.3.1.2.2.^[14b-e] On the other hand, red/NIR afterglow emitters based on purely organic molecules remain a massive challenge as low-energy triplets are susceptible to more available non-radiative transitions in these wavelength regions. Therefore, exploring different ways to achieve afterglow in the red/NIR regions is imperative. Achieving metal-free ambient red/NIR afterglow is the key to advancing the bio-imaging technologies, in addition to night-vision or communication technologies that still depend on rare-earth metals. One of the most efficient ways to achieve red/NIR emission is by using Förster Resonance Energy Transfer (FRET) from high-energy energy donor molecules to suitable dye molecules that emit in these regions (Figure 1.27).^[26] Moreover, successfully demonstrating this FRET process also benefits using a pool of commercially available dye molecules, avoiding tedious synthetic procedures. 'Delayed fluorescence' emission can be envisioned as a delayed sensitization of singlet excited states of commercially available fluorescent dyes by the long-lived triplet state of donor molecules (Figure 1.27).^[26b,c] The afterglow delayed fluorescence can be realized using the phosphorescence-FRET technique.^[26b,c] The extent of the afterglow duration is dependent on the phosphorescence lifetime of the triplet sensitizer acting as the FRET donor in this process.^[26] This FRET mechanism has been well investigated in high-energy fluorescence (as donors) and commercially available fluorescent dyes for white light emission and other functions. Förster proposed the theoretical description of FRET in the 1940s. FRET is a non-radiative dipole-dipole coupling between energy donor and acceptor molecules (Figure 1.27a).^[2] Its rate is dependent on the inverse sixth power of the distance between donor and acceptor molecules.^[2] It is interesting to note that traditionally studies and applications of FRET have been majorly dominated by singlet-to-singlet energy transfer (S-S FRET) as it is a quantum-mechanically allowed transition between two spin-states of the same multiplicity.^[2] However, it is also to be noted that given the spin-orbit coupling is strong in any molecule that allows an intense phosphorescence (T_1-S_0) emission.^[26] It is potentially a suitable donor for the triplet-to-singlet energy transfer (TS-FRET) process (Figure 1.22b).^[2, 26] This is possible because an appreciable dipolar coupling interaction is possible in such cases.^[26] In fact, because of this strong SOC aided

by the heavy-transition metals in organometallic complexes, TS-FRET has been extensively used in these classes of materials for decades.^[2]

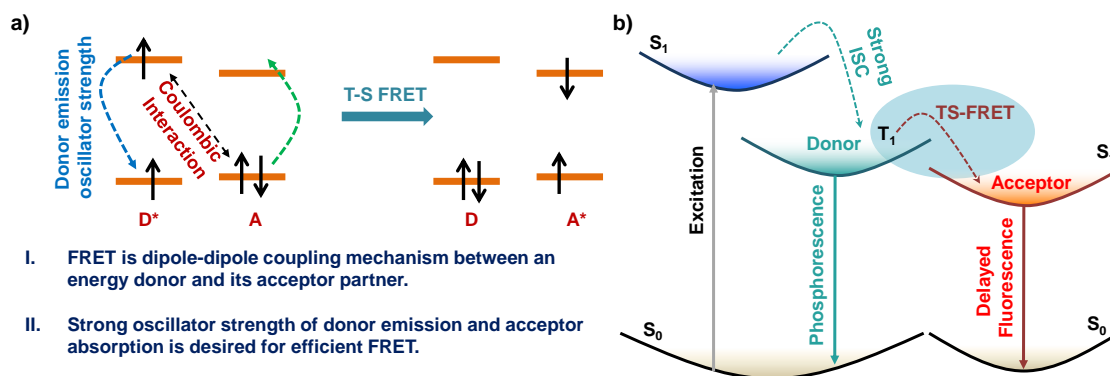


Figure 1.27. The a) necessary criteria and b) simplified Jablonski diagram for the phosphorescence FRET process.

Interestingly, such protocol has long been overlooked in metal-free organic phosphors until 2019 by Reineke and co-workers.^[26b] The authors proposed a simultaneous SS-FRET and TS-FRET process between a purely organic bioluminescent (emit both by fluorescence and RTP) chromophore (**NPB**) as a donor and a commercially available red-emitting dye as an acceptor (Figures 1.27a,b).^[26b] The choice of the donor (**NPB**) and acceptor molecules was based on the spectral overlap of donor emission and acceptor absorption wavelengths.^[26b] The authors used low-concentration donor molecules dispersed in a rigid amorphous PMMA matrix to observe maximum RTP intensity while avoiding aggregation-caused quenching.^[26b] In PMMA, the donor showed fluorescence and phosphorescence, suggesting its bi-luminescent character (Figure 1.28c).^[26b] In general, non-radiative FRET is characterized by a gradual decrease of donor radiative lifetime with increasing weight percentages of the acceptor loading (Figures 1.27d,f).^[26b] As evident from Figures 1.22e,g, the donor's fluorescence and RTP lifetimes decrease with the gradual increase of acceptor loading, which is also accompanied by a decrease in its total emission intensity (Figures 1.27d,f).^[26b] Interestingly, the authors also showed a gradual red-shift in the time-gated emission profile (Figure 1.28f).^[26b] These observations point toward the simultaneous SS-FRET and TS-FRET occurring in two purely organic chromophores, which are also visible by the naked eye (Figure 1.28g).^[26b]

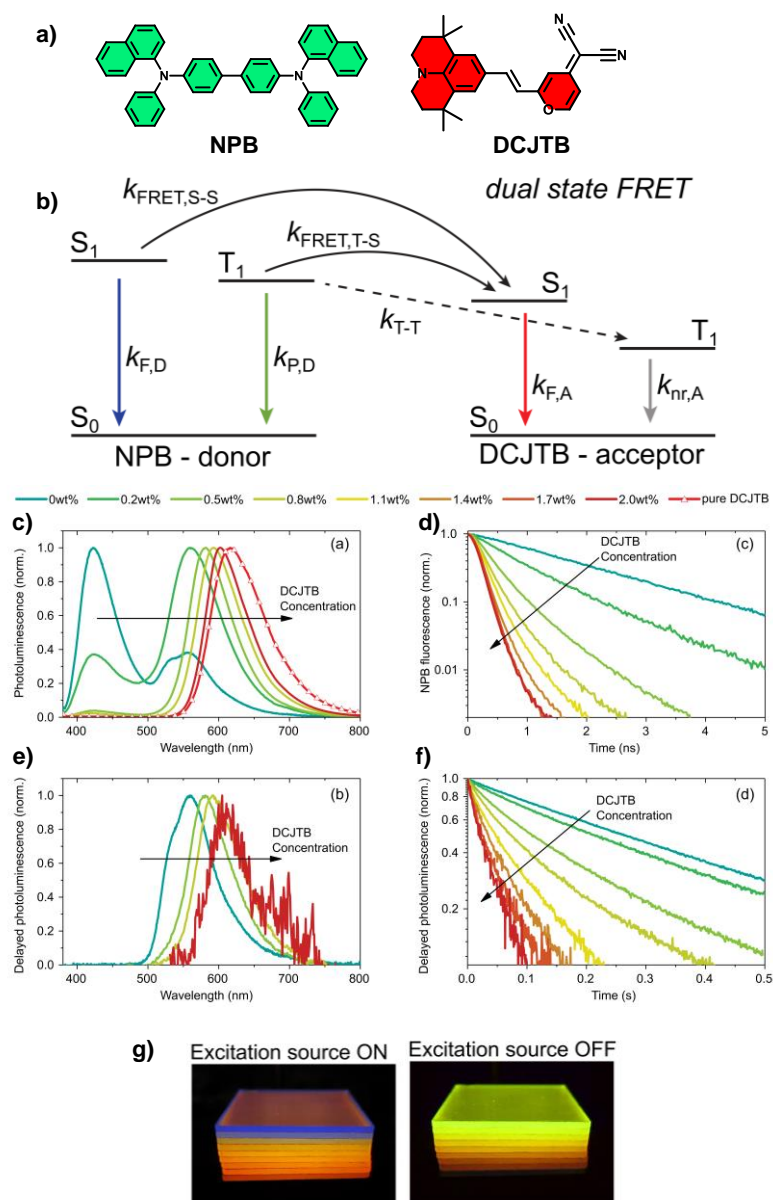


Figure 1.28. a) Molecular structure for SS and TS-FRET pair. b) Simple Jablonski diagram showing schematic representation of SS and TS-FRET process. Normalized c) steady-state and e) delayed emission spectra show a red-shift of the acceptor emission upon increasing the acceptor concentration with a concomitant decrease of the donor emission, suggesting SS-FRET and long-lived emission suggesting TS-FRET process. Decrease in the donor's d) fluorescence lifetime and f) phosphorescence lifetime attested to the SS and TS-FRET process, respectively. g) Photographs of SS and TS-FRET process. (Reproduced from reference 26a).

In that regard, our group developed a highly efficient afterglow phosphor based on coronene tetracarboxylic derivative (CS), which emits yellowish-green afterglow with

an excellent quantum efficiency (~25 %) and an ultralong lifetime of over 2.4 s in air, when dispersed in low concentration in PVA (Figures 1.28a-c).^[26c] Further, we exploited the PVA as a host to co-organize other water-soluble organic dyes capable of forming hydrogen bonding; hence, close proximity between the donor (**CS**) and acceptor molecules could be ensured.^[26c] As discussed earlier, these factors are pre-requisites for efficient TS-FRET and were successfully shown through various time-resolved experiments (Figure 1.29d). Yellow-emitting **SRG** and red-emitting **SR101** dyes were used as FRET acceptors in the system, and over 80 % energy transfer was achieved with maximum photoluminescence quantum efficiency of over 50 % (Figures 1.28b-d).^[26c] The afterglow fluorescence can also be visualized by the naked eye and was shown to be air-stable for months (Figure 1.29e). Unlike the previous system, SS-FRET was negligible in this case due to the high ISC efficiency of **CS** and larger spectral overlap between the donor phosphorescence and acceptor absorption wavelengths.^[26c] Although TS-FRET has long been overlooked for any suitable applications in the realm of afterglow emission, in the past couple of years it has been advancing with a great pace both in terms of molecular design and applications in bio-imaging.

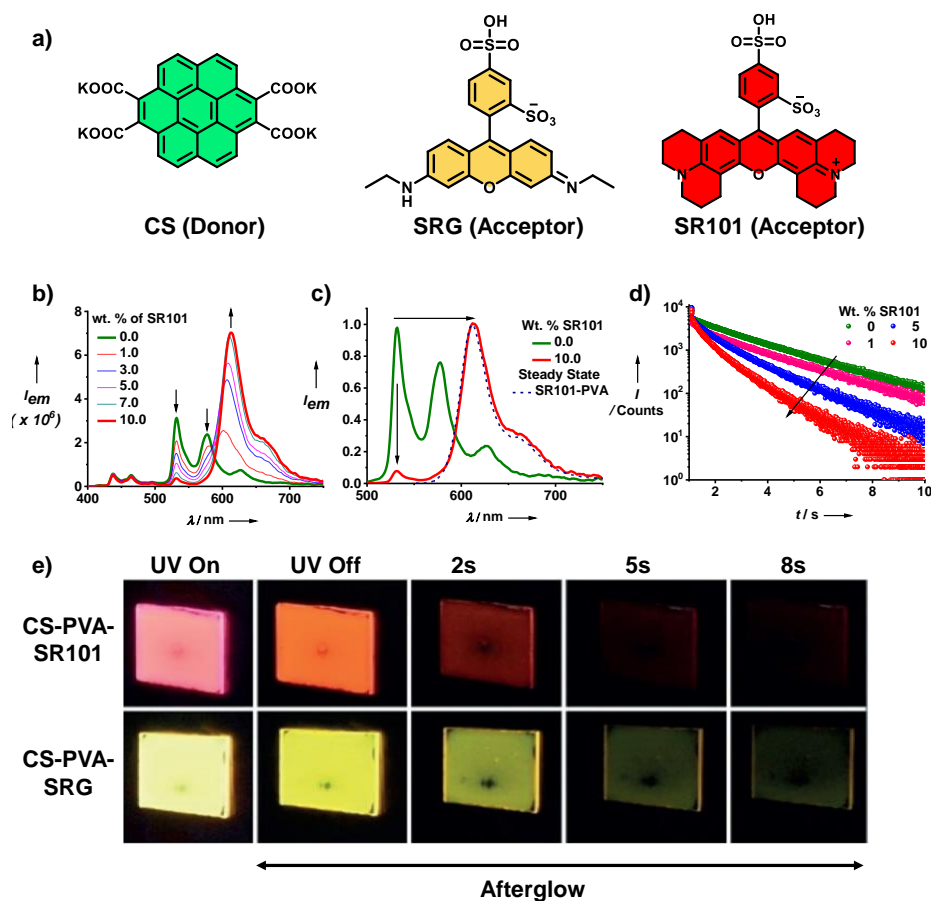


Figure 1.29. a) Molecular structure of the phosphorescence energy donor (CS) and fluorescence energy acceptor (SRG and SR101). b) Steady-state emission spectra show a red-shift of the acceptor emission upon increasing the acceptor concentration with a concomitant decrease of the donor emission, suggesting the energy-transfer process. c) Delayed emission spectra show the plausibility of phosphorescence energy transfer. d) Decrease in the donor's phosphorescence lifetime attested to the plausibility of phosphorescence energy transfer. e) Photographs show visual detection of delayed sensitization. (Reproduced from reference 26b).

1.6. Circularly Polarized Luminescence:

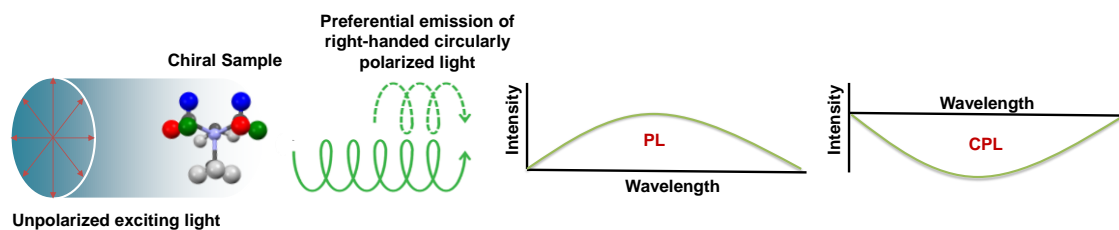


Figure 1.30. a) Schematic representation shows CPL emission from chiral organic chromophores. b) Importance of CPL emitter in CP-OLEDs. (Reproduced from reference 27h).

Circularly polarized luminescence (CPL) materials recently gained particular attention in the scientific community due to their several advantages in asymmetric synthesis, chiroptical materials, three-dimensional (3D) display, chiral optoelectronic devices, and spintronics.^[27] Chiroptical properties of a chiral molecule in the ground state are measured by the circular dichroism (CD) spectroscopy which measures the differential absorption of right- and left-handed circularly polarized light.^[27] The magnitude of CD is determined by a parameter called absorption dissymmetry factor ($|g_{CD}|$) and mathematically written as

$$|g_{CD}| = \frac{2(\epsilon_L - \epsilon_R)}{(\epsilon_L + \epsilon_R)}$$

where ϵ_L and ϵ_R are the molar absorption coefficients for the left- and right-handed CP light, respectively.^[27] Experimentally, the value of $|g_{CD}|$ is defined as an equation

$$|g_{CD}| = \frac{\theta}{A \times 32980}$$

However, to realize CPL emission, either the chiral moiety should be emissive or the chiral molecule attached to the chromophores should be emissive, where strong chiral induction from the chiral core to the luminophore is necessary.^[27] The parameter measures the CPL activity of a chiral molecule called the luminescence dissymmetry factor ($|g_{lum}|$). Mathematically it can be written as

$$|g_{lum}| = \frac{2(I_L - I_R)}{(I_L + I_R)}$$

I_L and I_R are the intensity of left- and right-handed circularly polarized light, respectively. Theoretically, the maximum possible $|g_{lum}|$ value ranges from +2 to -2.^[27] Although several chiral units are available in the organic literature, a proper choice of chiral moiety

and luminophores is necessary to make a good CPL active material.^[27] To design an efficient CPL active small organic chromophore, covalent bonding between the chiral part with the chromophores are most viable strategy.^[27] Also, chromophores should be close to chiral moiety for efficient chiral induction to happen.^[27] In the literature, the self-assembly strategy is considered one of the most efficient strategies for CPL activity from purely organic chromophores due to its ability to form ordered structures.^[27] Non-covalent interaction between chiral host and achiral guest or vice-versa can also be an efficient approach for CPL activity.

In anti-reflectance technology, CPL active materials are in the front due to their ability to generate circularly polarized light (Figure 1.30).^[27] Generally, a polarizer and quarter-wave plate are required to produce circularly polarized light.^[27] However, an OLED device composed of a polarizer and quarter-wave plate absorbs half of the emission from LED, and device efficiency decreases.^[27] On the other hand, most of the CPL active purely organic molecules are fluorescent emitters.^[28] But the current OLED technology demands a phosphorescence emitter or TADF emitter to achieve high external quantum efficiency (EQE).^[27] So, a smart design strategy is required for further development of the field. In addition, efficient $|g_{lum}|$ is also required for efficient circularly polarized OLEDs.^[27] Unfortunately, most of the small organic molecules suffer from the low $|g_{lum}|$ value due to their low magnetic and high electric dipole transition moments. The $|g_{lum}|$ value is directly proportional to the magnetic transition dipole moments and inversely proportional to the electric transition dipole moment.^[27] The simplified form of $|g_{lum}|$ is

$$|g_{lum}| = \frac{m \cos \theta}{\mu}$$

where θ is the angle between magnetic and electric transition dipole moments. The simple way to increase the $|g_{lum}|$ is by decreasing the electrical transition dipole moment and increasing the magnetic transition dipole moment.^[29a,b] In this regard formation of CT states can decrease the electrical transition dipole moment as it is a forbidden transition and increases the magnetic transition.^[29a,b] Both factors can increase an organic molecule's overall $|g_{lum}|$ value.^[29a,b] Further few strategies, including Förster resonance energy transfer (FRET) and triplet-triplet-annihilation, can also increase the $|g_{lum}|$ value.^[29c-e]

1.7. Molecular Design Strategy: Why Arylene Diimides?

In our work, we have harvested the triplet exciton using various arylene diimides, especially pyromellitic diimides. Arylene diimide is a particular class of molecule where the presence of four carbonyl groups in the molecular design inherently makes the system electron deficient.^[30] Scientists have taken advantage of this type of material and made them suitable candidates for electron-deficient n-type semiconductors.^[31] Further in organic field-effect transistors (OFETs), photovoltaic, batteries arylene diimides are front due to their high air stability.^[31] However, among the various arylene diimides, perylene diimides (PDIs) and naphthalene diimides (NDIs) gained special recognition in supramolecular chemistry.^[32] Matile and co-workers extensively investigated the NDIs for anion- π recognition and made significant contribution in anion- π catalysis and anion-transport.^[33] Würthner and co-workers extensively studied PDIs for self-assembly and optoelectronic applications.^[34] Further, due to the electron-deficient nature, arylene diimides can easily form stable radical anions, which is very useful in catalysis and artificial photosynthesis.^[35] In addition, the energy levels of any arylene diimides can be easily tuned by core-substitution, which already opens a plethora of opportunities in the optoelectronic realm.^[30b,c] Tunable fluorescence of core-substituted NDIs helped to achieve the different function including energy transfer and circularly polarized luminescence in solution.^[31e]

However, the use of arylene diimides in the OLED technology in terms of triplet harvesting (phosphorescence, TADF, or TTA) is unexplored. We hypothesize that arylene diimide or mono imide would be perfect for triplet harvesters because the class of molecules inherently possesses a significant ISC rate. Also, the core can be easily substituted by the heavy atom to increase the SOC, which will help to access the triplets in cryogenic conditions.

1.7.1. Why Pyromellitic Diimides?

We first checked the phosphorescence properties of all heavy atom substituted arylene diimides (PDIs, NDIs, and PmDIs) in cryogenic conditions to validate our hypothesis (Figure 1.31a). We have realized that the NDIs have triplets in the red region (~580 nm to 750 nm) region and PmDIs have triplets in the cyan (~450 nm to 600 nm) region, which we can access in the cryogenic conditions using liquid nitrogen (Figure 1.31b).^[22a]

However, we have not found any triplets of PDIs in the visible region. Keeping this in mind, our lab first explored the triplets of NDIs via phosphorescence and TADF.^[22a,36] Using a unique supramolecular scaffolding approach, our group has reported RTP from bromo-substituted NDIs in laponite clay particles.^[22a] Detailed we have discussed earlier in section 1.3.5.3., how we can efficiently harvest the triplet in solution.^[22a]

Further donor-acceptor-based molecular design strategy helps us to achieve red-emitting delayed fluorescence from core-substituted NDIs.^[36] Although we have harvested the triplet excitons of NDIs via phosphorescence and TADF, the efficiency of triplet emission is not excellent (~4% in **LP** film for phosphorescence and ~10 % for TADF in air).^[22a,36] We hypothesize that, due to the sizeable singlet-triplet energy gap (ΔE_{ST}), triplet excitons are getting wasted via a non-radiative decay channel during the ISC process (Figure 1.31b). As we have earlier discussed in section 1.3.1.1., ΔE_{ST} should be less for efficient triplet harvesting. So that we have moved further to the smallest member of arylene diimide i.e, pyromellitic diimides, due to low ΔE_{ST} . The chance of triplet exciton loss during the ISC process is more petite in PmDIs, and we have mainly focused on this derivative in the entire thesis and showed different ways of triplet harvesting.

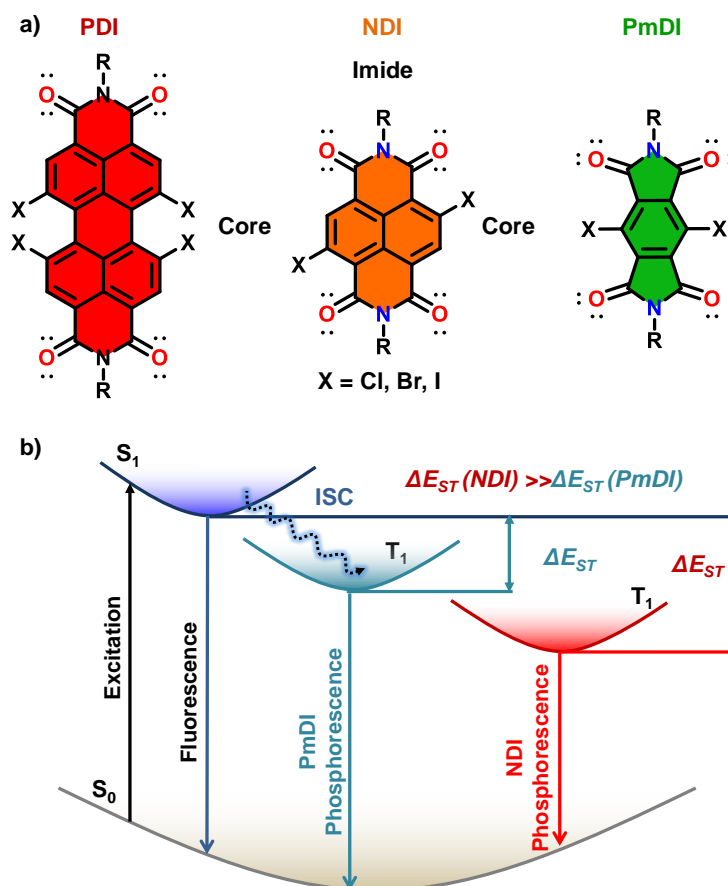


Figure 1.31. a) Molecular structures of different arylene diimides. b) Simplified Jablonski diagram showing the qualitative singlet and triplet energy level of NDIs and PmDIs and their singlet to triplet to energy difference.

1.7.2. Design Strategy for Arylene Diimides Derived Ambient Triplet Harvesters:

The strategy mentioned earlier i. Increment of SOC between S_1 and T_n states by incorporating the heavy-atom and ii. Increasing the ISC rate between S_1 and T_n states by incorporating the hetero-atom or introducing the carbonyl/sulphonyl group will help to access the triplet under cryogenic conditions or under an inert atmosphere. We believe that PmDIs would be the best choice due to the presence of four carbonyl groups also, minimum ΔE_{ST} will increase the ISC rate significantly without much non-radiative loss. Further easy core substitution with the heavy atom will increase the SOC and benefit ambient triplet harvesting via phosphorescence applying the suitable stabilization technique.

Further minimization of ΔE_{ST} is required for TADF molecules for efficient RISC to happen we have already discussed in section 1.3.2. The conventional strategy to make charge transfer molecules having electron-rich donor moiety and electron-poor acceptor moiety with a large dihedral angle between them can be applied. The PmDI will play the role of acceptor here. By selecting the suitable spacer between donor and PmDIs dihedral angle can be controlled, which will help to reduce the ΔE_{ST} further. An appropriate choice of a donor can give color tunability.

Further, we envisage that planar PmDIs with small π surfaces can form long-range π stacking upon short alkyl chain substitution in the imide position. This will be helpful for excellent triplet migration in the crystalline state. Triplet migration can generate TTA-induced delayed fluorescence. The detailed process we have discussed earlier in section 1.3.2.

1.8. Conclusion:

In conclusion, in this chapter, we have started the discussion with various excited state processes as we believe that a proper understanding of the basic photophysical process is required. Next, we discussed the importance of triplet harvesting, the design strategy to access the triplets, and different stabilization processes for ambient triplet harvesting, mainly via phosphorescence and delayed fluorescence. The fundamental design principles in these examples consider two steps: first, designing the phosphors for high ISC rates, ensuring the high triplet state density, and second, suppressing the non-radiative pathways for bright RTP emission. We showed that in the initial years, crystal-phase RTP had seen tremendous growth; however, limitations such as solution-processability issues shifted the focus on the amorphous state and solution-processable RTP material design. Furthermore, we focused on how efficient TADF emitters can be designed for third-generation OLEDs by covalently attached donor-acceptor design. Next, we have tried to shed light on advancing more challenging ‘solution state RTP’ under ambient conditions. We presented those supramolecular self-assembly strategies are used in most of the examples in this area to harness RTP in the solution state and showed how the bio-imaging field is benefitted the most. Next, we have discussed the design strategy based on arylene diimides and envisioned that every plausible triplet harvesting could be bestowed using this molecular design. Phosphorescence FRET technique and CPL are discussed further to achieve color-tunable delayed fluorescence

from commercially available fluorescence emitters and circularly polarized triplet emission from purely organic chromophores, respectively.

1.9. References:

[1] a) G. Baryshnikov, B. Minaev, H. Ågren, *Chem. Rev.* **2017**, *117*, 6500-6537; b) T. Itoh, *Chem. Rev.* **2012**, *112*, 4541-4568; c) A. Köhler, H. Bässler, *Mater. Sci. Eng. R Rep.* **2009**, *66*, 71-109.

[2] J. R. Lakowicz, *Principles of Fluorescence Spectroscopy* (3rd ed.), Springer, **2011**.

[3] M. Kasha, *Disc. Farad. Soc.*, **1950**, *9*, 14-19.

[4] a) S. K. Lower, M. A. El-Sayed, *Chem. Rev.* **1966**, *66*, 199-241; b) M. A. El-Sayed, *J. Chem. Phys.* **1963**, *38*, 2834-2838; c) M. A. El-Sayed, *J. Chem. Phys.* **1963**, *38*, 3032-3036.

[5] a) G. N. Lewis, M. Kasha *J. Am. Chem. Soc.* **1944**, *66*, 2100-2116; b) G. N. Lewis, D. Lipkin, T. T. Magel, *J. Am. Chem. Soc.* **1941**, *63*, 3005-3018. c) S. Hirata, *Adv. Opt. Mater.* **2017**, *5*, 1700116; d) W. Zhao, Z. He, W. Y. Lam, Jacky, Q. Peng, H. Ma, Z. Shuai, G. Bai, J. Hao, B. Z. Tang, *Chem* **2016**, *1*, 592-602; e) S. Xu, R. Chen, C. Zheng, W. Huang, *Adv. Mater.* **2016**, *28*, 9920-9940; f) W. Zhao, Z. He, B. Z. Tang, *Nat. Rev. Mater.* **2020**, *5*, 869-885; g) X. Ma, J. Wang, H. Tian, *Acc. Chem. Res.* **2019**, *52*, 738-748; h) T. Zhang, X. Ma, H. Wu, L. Zhu, Y. Zhao, H. Tian, *Angew. Chem., Int. Ed.* **2020**, *59*, 11206-11216; i) Y. Wang, H. Gao, J. Yang, M. Fang, D. Ding, B. Tang, Z. Li, *Adv. Mater.* **2021**, *33*, 2007811.

[6] a) H. Uoyama, K. Goushi, K. Shizu, H. Nomura, C. Adachi, *Nature* **2012**, *492*, 234-238; b) M. Y. Wong, E. Zysman-Colman, *Adv. Mater.* **2017**, *29*, 1605444; c) Y. Tao, K. Yuan, T. Chen, P. Xu, H. Li, R. Chen, C. Zheng, L. Zhang, W. Huang, *Adv. Mater.* **2014**, *26*, 7931-7958; d) Y. Tao, K. Yuan, T. Chen, P. Xu, H. Li, R. Chen, C. Zheng, L. Zhang, W. Huang, *Adv. Mater.* **2014**, *26*, 7931-7958; e) Y. Im, M. Kim, Y. J. Cho, J.-A. Seo, K. S. Yook, J. Y. Lee, *Chem. Mater.* **2017**, *29*, 1946-1963; f) T. J. Penfold, F. B. Dias, A. P. Monkman, *Chem. Commun.* **2018**, *54*, 3926-3935; g) Y. Liu, C. Li, Z. Ren, S. Yan, M. R. Bryce, *Nat. Rev. Mater.* **2018**, *3*, 18020.

[7] a) C. W. Tang, S. A. Van Slyke, *App. Phys. Lett.* **1987**, *51*, 913-915; b) J. H. Burroughes, D. D. Bradley, A. R. Brown, R. N. Marks, K. Mackay, R. H. Friend, P. L.

Burn, A. B. Holmes, *Nature* **1990**, *347*, 539-541; c) M. A. Baldo, D. F. O'Brien, Y. You, A. Shoustikov, S. Sibley, M. E. Thompson, S. R. Forrest, *Nature* **1998**, *395*, 151-154; d) C. Adachi, M. A. Baldo, S. R. Forrest, M. E. Thompson, *Appl. Phys. Lett.* **2000**, *77*, 904-906.

[8] a) C. Gao, W. W. H. Wong, Z. Qin, S. C. Lo, E. B. Namdas, H. Dong, W. Hu, *Adv. Mater.* **2021**, *33*, 2100704; b) P. Bharmoria, H. Bildirir, K. Moth-Poulsen, *Chem. Soc. Rev.* **2020**, *49*, 6529-6554; c) D. Di, L. Yang, J. M. Richter, L. Meraldi, R. M. Altamimi, A. Y. Alyamani, D. Credgington, K. P. Musselman, J. L. MacManus Driscoll, R. H. Friend, *Adv. Mater.* **2017**, *29*, 1605987; d) A. Dey, D. Kabra, *ACS Appl. Mater. Interfaces* **2018**, *10*, 38287-38293; e) C. J. Chiang, A. Kimyonok, M. K. Etherington, G. C. Griffiths, V. Jankus, F. Turksoy, A. P. Monkman, *Adv. Funct. Mater.* **2013**, *23*, 739-746.

[9] P. W. Atkins, R. S. Friedman, *Molecular Quantum Mechanics* (Oxford University Press, New York, NY) **1997**.

[10] D. S. McClure, *J. Chem. Phys.* **1949**, *17*, 905-913.

[11] a) W. Z. Yuan, X. Y. Shen, H. Zhao, J. W. Y. Lam, L. Tang, P. Lu, C. Wang, Y. Liu, Z. Wang, Q. Zheng, J. Z. Sun, Y. Ma, B. Z. Tang, *J. Phys. Chem. C* **2010**, *114*, 6090-6099; b) O. Bolton, K. Lee, H.-J. Kim, K. Y. Lin, J. Kim, *Nat. Chem.* **2011**, *3*, 205-210; c) Z. An, C. Zheng, Y. Tao, R. Chen, H. Shi, T. Chen, Z. Wang, H. Li, R. Deng, X. Liu, W. Huang, *Nat. Mater.* **2015**, *14*, 685-690; d) A. D. Nidhankar, Goudappagouda, D. S. Mohana Kumari, S. K. Chaubey, R. Nayak, R. G. Gonnade, G. V. P. Kumar, R. Krishnan, S. S. Babu, *Angew. Chem. Int. Ed.* **2020**, *59*, 13079-13085; e) L. Gu, H. Shi, L. Bian, M. Gu, K. Ling, X. Wang, H. Ma, S. Cai, W. Ning, L. Fu, H. Wang, S. Wang, Y. Gao, W. Yao, F. Huo, Y. Tao, Z. An, X. Liu, W. Huang, *Nat. Photonics* **2019**, *13*, 406-411; f) J. Yang, X. Zhen, B. Wang, X. Gao, Z. Ren, J. Wang, Y. Xie, J. Li, Q. Peng, K. Pu, Z. Li, *Nat. Commun.* **2018**, *9*, 840; g) Y. Wang, J. Yang, Y. Tian, M. Fang, Q. Liao, L. Wang, W. Hu, B. Z. Tang, Z. Li, *Chem. Sci.* **2020**, *11*, 833-838; h) E. Hamzehpoor, D. F. Perepichka, *Angew. Chem. Int. Ed.* **2020**, *59*, 9977-9981; i) Z. Yang, Z. Mao, X. Zhang, D. Ou, Y. Mu, Y. Zhang, C. Zhao, S. Liu, Z. Chi, J. Xu, Y. C. Wu, P. Y. Lu, A. Lien, M. R. Bryce, *Angew. Chem. Int. Ed.* **2016**, *55*, 2181-2185.

[12] a) S. Hirata, K. Totani, J. Zhang, T. Yamashita, H. Kaji, S. R. Marder, T. Watanabe, C. Adachi, *Adv. Funct. Mater.* **2013**, *23*, 3386-3397; b) S. Hirata, M. Vacha, *Adv. Opt.*

- Mater.* **2017**, *5*, 1600996; c) S. Hirata, K. Totani, H. Kaji, M. Vacha, T. Watanabe, C. Adachi, *Adv. Opt. Mater.* **2013**, *1*, 438-442; d) I. Bhattacharjee, K. Hayashi, S. Hirata, *JACS Au* **2021**, *7*, 945-954; e) I. Bhattacharjee, S. Hirata, *Adv. Mater.* **2020**, *32*, 2001348.
- [13] a) M. Gmelch, H. Thomas, F. Fries, S. Reineke, *Sci. adv.* **2019**, *5*, eaau7310; b) M. Louis, H. Thomas, M. Gmelch, A. Haft, F. Fries, S. Reineke, *Adv. Mater.* **2019**, *31*, 1807887; c) H. Thomas, D. L. Pastoetter, M. Gmelch, T. Achenbach, A. Schlögl, M. Louis, X. Feng, S. Reineke, *Adv. Mater.* **2020**, *32*, 2000880; d) Y Li, L. Jiang, W. Liu, S. Xu, T.-Y. Li, F. Fries, O. Zeika, Y. Zou, C. Ramanan, S. Lenk, R. Scholz, D. Andrienko, X. Feng, K. Leo, S. Reineke, *Adv. Mater.* **2021**, *33*, 210184; e) D. Lee, O. Bolton, B. C. Kim, J. H. Youk, S. Takayama, J. Kim, *J. Am. Chem. Soc.* **2013**, *135*, 6325-6329.
- [14] a) M. S. Kwon, D. Lee, S. Seo, J. Jung, J. Kim, *Angew. Chem. Int. Ed.* **2014**, *53*, 11177-11181; b) L. Gu, W. Ye, X. Liang, A. Lv, H. Ma, M. Singh, W. Jia, Z. Shen, Y. Guo, Y. Gao, H. Chen, D. Wang, Y. Wu, J. Liu, H. Wang, X.-Y. Zheng, Z. An, W. Huang, Y. Zhao, *J. Am. Chem. Soc.* **2021**, *143*, 18527-18535; c) Y. Su, Y.; Y. Zhang, Z. Wang, W. Gao, P. Jia, D. Zhang, C. Yang, Y. Li, Y. Zhao, *Angew. Chem. Int. Ed.* **2020**, *59*, 9967-9971; d) S. Kuila, S. Garain, S. Bandi, S. J. George, *Adv. Funct. Mater.* **2020**, *30*, 2003693.
- [15] a) Z.-Y. Zhang, Y. Chen, Y. Liu, *Angew. Chem. Int. Ed.* **2019**, *58*, 6028-6032; b) Z.-Y. Zhang, Y. Liu, *Chem. Sci.* **2019**, *10*, 7773-7778; c) X.-K. Ma, W. Zhang, Z. Liu, H. Zhang, B. Zhang, Y. Liu, *Adv. Mater.* **2021**, *33*, 2007476; d) W-L. Zhou, W. Lina, Y. Chena, Y. Liu, *Chem. Sci.* **2022**, DOI:10.1039/D2SC01770A.
- [16] a) P. L. dos Santos, M. K. Etherington, A. P. Monkman, *J. Mater. Chem. C* **2018**, *6*, 4842-4853; b) P. L. dos Santos, F. B. Dias, A. P. Monkman, *J. Phys. Chem. C* **2016**, *120*, 18259-18267; c) F. B. Dias, J. Santos, D. R. Graves, P. Data, R. S. Nobuyasu, M. A. Fox, A. S. Batsanov, T. Palmeira, M. N. Berberan-Santos, M. R. Bryce, A. P. Monkman, *Adv. Sci.* **2016**, *3*, 1600080; d) T. Ogiwara, Y. Wakukawa, T. Ikoma, *J. Phys. Chem. A* **2015**, *119*, 3415-3418; e) J. U. Kim, I. S. Park, C.-Y. Chan, M. Tanaka, Y. Tsuchiya, H. Nakanotani, C. Adachi, *Nat. Commun.* **2020**, *11*, 1765; f) M. K. Etherington, J. Gibson, H. F. Higginbotham, T. J. Penfold, A. P. Monkman, *Nat. Commun.* **2016**, *7*, 13680; g) J. Gibson, A. P. Monkman, T. J. Penfold, *Chem Phys Chem* **2016**, *17*, 2956-2961; h) E.

W. Evans, Y. Olivier, Y. Puttison, W. K. Myers, T. J. Hele, S. M. Menke, T. H. Thomas, D. Credgington, D. Beljonne, R. H. Friend, *J. Phys. Chem. Lett.* **2018**, *9*, 4053-4058.

[17] C. A. Parker, C. G. Hatchard, *Trans. Faraday Soc.*, **1961**, *57*, 1894-1904.

[18] A. Endo, M. Ogasawara, A. Takahashi, D. Yokoyama, Y. Kato, C. Adachi, *Adv. Mater.* **2009**, *21*, 4802-4806.

[19] a) E. Hamzehpoor, C. Ruchlin, Y. Tao, J. E. Ramos-Sanchez, H. M. Titi, G. Cosa, D. F. Perepichka, *J. Phys. Chem. Lett.* **2021**, *12*, 6431-6438; b) O. V. Mikhnenko, P. W. M. Blom, T.-Q. Nguyen, *Energy Environ. Sci.* **2015**, *8*, 1867-1888; c) T. Serevičius, R. Komskis, P. Adomėnas, O. Adomėnienė, G. Kreiza, V. Jankauskas, K. Kazlauskas, A. Miasojedovas, V. Jankus, A. Monkman, S. Juršėnas, *J. Phys. Chem. C* **2017**, *121*, 8515-8524.

[20] a) A. Fermi, G. Bergamini, M. Roy, M. Gingras, P. Ceroni, *J. Am. Chem. Soc.* **2014**, *136*, 6395-6400; b) X. Jia, C. Shao, X. Bai, Q. Zhou, B. Wu, L. Wang, B. Yue, H. Zhu, L. Zhu, *PNAS* **2019**, *116*, 4816.

[21] a) Y. Gong, H. Chen, X. Ma, H. Tian, *Chem Phys Chem* **2016**, *17*, 1934-1938; b) J. Wang, Z. Huang, X. Ma, H. Tian, *Angew. Chem. Int. Ed.* **2020**, *59*, 9928-9933.

[22] a) K. V. Rao, A. Jain, S. J. George, *J. Mater. Chem. C* **2014**, *2*, 3055-3064; b) S. Kuila, K. V. Rao, S. Garain, P. K. Samanta, S. Das, S. K. Pati, M. Eswaramoorthy, S. J. George, *Angew. Chem. Int. Ed.* **2018**, *57*, 17115-17119.

[23] R. Kabe, N. Notsuka, K. Yoshida, C. Adachi, *Adv. Mater.* **2016**, *28*, 655-660.

[24] a) W.-L. Zhou, Y. Chen, Q. Yu, H. Zhang, Z.-X. Liu, X.-Y. Dai, J.-J. Li, Y. Liu, *Nat. Commun.* **2020**, *11*, 4655; b) F. Wang, W. J. Guo, H. Y. Xiao, Q. Z. Yang, B. Chen, Y. Z. Chen, C. H. Tung, L. Z. Wu, *Adv. Funct. Mater.* **2020**, *30*, 1907282.

[25] a) M. Villa, B. Del Secco, L. Ravotto, M. Roy, E. Rampazzo, N. Zaccheroni, L. Prodi, M. Gingras, S. A. Vinogradov, P. Ceroni, *J. Phys. Chem. C* **2019**, *123*, 29884-29890. b) Y. Yu, M. S. Kwon, J. Jung, Y. Zeng, M. Kim, K. Chung, J. Gierschner, J. H. Youk, S. M. Borisov, J. Kim, *Angew. Chem. Int. Ed.* **2017**, *56*, 16207-16212.

[26] a) A. Cravencenco, M. Hertzog, C. Ye, M. N. Iqbal, U. Mueller, L. Eriksson, K. Børjesson, *Sci. Adv.* **2019**, *5*, eaaw5978; b) A. Kirch, M. Gmelch, S. Reineke, *J. Phys.*

Chem. Lett. **2019**, *10*, 310-315; c) S. Kuila, S. J. George, *Angew. Chem. Int. Ed.* **2020**, *59*, 9393-9397.

[27] a) R. Farshchi, M. Ramsteiner, J. Herfort, A. Tahraoui, H. T. Grahn, *Appl. Phys. Lett.* **2011**, *98*, 162508; b) C. S. Wang, H. S. Fei, Y. Qiu, Y. Q. Yang, Z. Q. Wei, *Appl. Phys. Lett.* **1999**, *74*, 19-21; c) D.-Y. Kim, *J. Korean Phys. Soc.* **2006**, *49*, 505-508; d) C. Wagenknecht, C.-M. Li, A. Reingruber, X.-H. Bao, A. Goebel, Y.-A. Chen, Q. Zhang, K. Chen, J.-W. Pan, *Nat. Photonics* **2010**, *4*, 549-552. e) J. Han, S. Guo, H. Lu, S. Liu, Q. Zhao, W. Huang, *Adv. Opt. Mater.* **2018**, *6*, 1800538; f) X. Li, Y. Xie, Z. Li, *Adv. Photonics Res.* **2021**, *2*, 2000136; g) J. Roose, B. Z. Tang, K. S. Wong, *Small* **2016**, *12*, 6495-6512; h) Y. Sang, J. Han, T. Zhao, P. Duan, M. Liu, *Adv. Mater* **2020**, *32*, 1900110; i) J. Kumar, T. Nakashima, T. Kawai, *J. Phys. Chem. Lett.* **2015**, *6*, 3445-3452; j) Y. Imai, Y. Nakano, T. Kawai, J. Yuasa, *Angew. Chem. Int. Ed.* **2018**, *57*, 8973-8978; k) G. Albano, G. Pescitelli, L. Di Bari, *Chem. Rev.* **2020**, *120*, 10145-10243, l) L. Wan, J. Wade, X. Shi, S. Xu, M. J. Fuchter, A. J. Campbell, *Appl. Mater. Interfaces* **2020**, *12*, 39471-39478.

[28] a) J. Kumar, H. Tsumatori, J. Yuasa, T. Kawai, T. Nakashima, *Angew. Chem. Int. Ed.* **2015**, *54*, 5943-5947; b) J. Kumar, T. Nakashima, H. Tsumatori, T. Kawai, *J. Phys. Chem. Lett.* **2014**, *5*, 316-321; c) S. Sarkar, B. Narayan, S. J. George, *Chem Nano Mat* **2020**, *6*, 1169-1174; d) S. Hu, L. Hu, X. Zhu, Y. Wang, M. Liu, *Angew. Chem. Int. Ed* **2021**, *60*, 19451-19457; e) H. Zhang, J. Han, X. Jin, P. Duan, *Angew. Chem. Int. Ed.* **2021**, *60*, 4575-4580; f) S. Zheng, J. Han, X. Jin, Q. Ye, J. Zhou, P. Duan, M. Liu, *Angew. Chem. Int. Ed* **2021**, *60*, 22711-22716; g) E. E. Greciano, R. Rodríguez, K. Maeda, L. Sánchez, *Chem. Commun.* **2020**, *56*, 2244-2247; h) Z. Li, Y. Han, F. Nie, M. Liu, H. Zhong, F. Wang, *Angew. Chem. Int. Ed.* **2021**, *60*, 8212-8219; i) K. Takaishi, K. Iwachido, R. Takehana, M. Uchiyama, T. Ema, *J. Am. Chem. Soc.* **2019**, *141*, 6185-6190; j) K. Takaishi, S. Murakami, K. Iwachido, T. Ema, *Chem. Sci.* **2021**, *12*, 14570-14576; k) P. Liao, S. Zang, T. Wu, H. Jin, W. Wang, J. Huang, B.Z. Tang, Y. Yan, *Nat. Commun.* **2021**, *12*, 1-9; l) M. Li, S. H. Li, D. Zhang, M. Cai, L. Duan, M. K. Fung, C. F. Chen, *Angew. Chem. Int. Ed.* **2018**, *57*, 2889-2893.

[29] a) J. Han, D. Yang, X. Jin, Y. Jiang, M. Liu, P. Duan, *Angew. Chem. Int. Ed.* **2019**, *58*, 7013-7019; b) S. Inagaki, K. Yamamura, K. Nakasuji, T. Nakazawa, I. Murata, *J. Am. Chem. Soc.* **1981**, *103*, 2093-2094; c) L. Ji, Y. Sang, G. Ouyang, D. Yang, P. Duan,

Y. Jiang, M. Liu, *Angew. Chem., Int. Ed.* **2019**, *58*, 844-848; d) J. Han, P. Duan, X. Li, M. Liu, *J. Am. Chem. Soc.* **2017**, *139*, 9783-9786; d) J. Wade, J. Brandt, D. Reger, F. Zinna, K. Amsharov, N. Jux, D. Andrews, M. J. Fuchter, *Angew. Chem., Int. Ed.* **2021**, *60*, 222-227; e) D. Yang, P. Duan, L. Zhang, M. Liu, *Nat. Commun.* **2017**, *8*, 15727.

[30] a) S. V. Bhosale, C. H. Jani, S. J. Langford, *Chem. Soc. Rev.* **2008**, *37*, 331-342; b) F. Werthner, S. Ahmed, C. Thalacker, T. Debaerdemaeker, *Chem. Eur. J.* **2002**, *8*, 4742-4750; c) N. Sakai, J. Mareda, E. Vauthey, S. Matile, *Chem. Commun.* **2010**, *46*, 4225-4237; d) S. M. Luo, K. A. Stellmach, S. M. Ikuzwe, D. D. Cao, *J. Org. Chem.* **2019**, *84*, 10362-1037.

[31] a) J. H. Oh, S.-L. Suraru, W.-Y. Lee, M. Kçnemann, H. W. Hçffken, C. Rçger, R. Schmidt, Y. Chung, W.-C. Chen, F. Wùrthner, Z. Bao, *Adv. Funct. Mater.* **2010**, *20*, 2148-2156; b) T. He, M. Stolte, F. Wùrthner, *Adv. Mater.* **2013**, *25*, 6951-6955; c) H. Yan, Z. Chen, Y. Zheng, C. Newman, J. R. Quinn, F. Dçtz, M. Kastler, A. Facchetti, *Nature* **2009**, *457*, 679-686.

[32] a) S.-L. Suraru, F. Wùrthner, *Angew. Chem. Int. Ed.* **2014**, *53*, 7428-7448; b) C. Rçger, F. Wùrthner, *J. Org. Chem.* **2007**, *72*, 8070-8075; c) R. S. K. Kishore, V. Ravikumar, G. Bernardinelli, N. Sakai, S. Matile, *J. Org. Chem.* **2008**, *73*, 738-740; d) A. Takai, T. Yasuda, T. Ishizuka, T. Kojima, M. Takeuchi, *Angew. Chem. Int. Ed.* **2013**, *52*, 9167-9171; e) A. Sarkar, S. Dhiman, A. Chalishazar, S. J. George, *Angew. Chem. Int. Ed.* **2017**, *56*, 13767-13771; f) B. Narayan, K. K. Bejagam, S. Balasubramanian, S. J. George, *Angew. Chem. Int. Ed.* **2015**, *54*, 13053-13057; g) S. Sarkar, A. Sarkar, S. J. George, *Angew. Chem. Int. Ed.* **2020**, *59*, 19841-19845; h) S. Sarkar, A. Sarkar, A. Som, S. S. Agasti, S. J. George, *J. Am. Chem. Soc.*, **2021**, *143*, 11777-11787;

[33] a) R. E. Dawson, A. Hennig, D. P. Weimann, D. Emery, S. Gabutti, J. Montenegro, V. Ravikumar, M. Mayor, J. Mareda, C. A. Schalley, S. Matile, *Nat. Chem.* **2010**, *2*, 533-538; b) A. Vargas Jentsch, D. Emery, J. Mareda, P. Metrangolo, G. Resnati, S. Matile, *Angew. Chem. Int. Ed.* **2011**, *50*, 11675-11678; c) M. Paraja, S. Matile, *Angew. Chem. Int. Ed.* **2020**, *59*, 6273-6377; d) L. Liu, Y. Cotelle, A.-B. Bornhof, C. Besnard, N. Sakai, S. Matile, *Angew. Chem. Int. Ed.* **2017**, *56*, 13066-13069; e) Y. Cotelle, S. Benz, A.-J. Avestro, T. R. Ward, N. Sakai, S. Matile, *Angew. Chem. Int. Ed.* **2016**, *55*, 4275-4279.

[34]a) M. M. Safont-Sempere, P. Osswald, M. Stolte, M. Grüne, M. Renz, M. Kaupp, K. Radacki, H. Braunschweig, F. Würthner, *J. Am. Chem. Soc.* **2011**, *133*, 9580-959; b) M. Wehner, F. Würthner, *Nat. Rev. Chem.* **2020**, *4*, 38-53; c) S. Ogi, V. Stepanenko, J. Thein, F. Würthner, *J. Am. Chem. Soc.* **2016**, *138*, 670-678; d) S. Ogi, V. Stepanenko, K. Sugiyasu, M. Takeuchi, F. Würthner, *J. Am. Chem. Soc.* **2015**, *137*, 3300-330.

[35] a) P. D. Frischmann, K. Mahata, F. Würthner, *Chem. Soc. Rev.* **2013**, *42*, 1847-1870; b) S. Guha, S. Saha, *J. Am. Chem. Soc.* **2010**, *132*, 17674-17677; c)

[36] S. Kuila, A. Ghorai, P. K. Samanta, R. B. K. Siram, S. K. Pati, K. S. Narayan, S. J. George, *Chem. Eur. J.* **2019**, *25*, 16007-16011.

PART A

CHAPTER 2.1

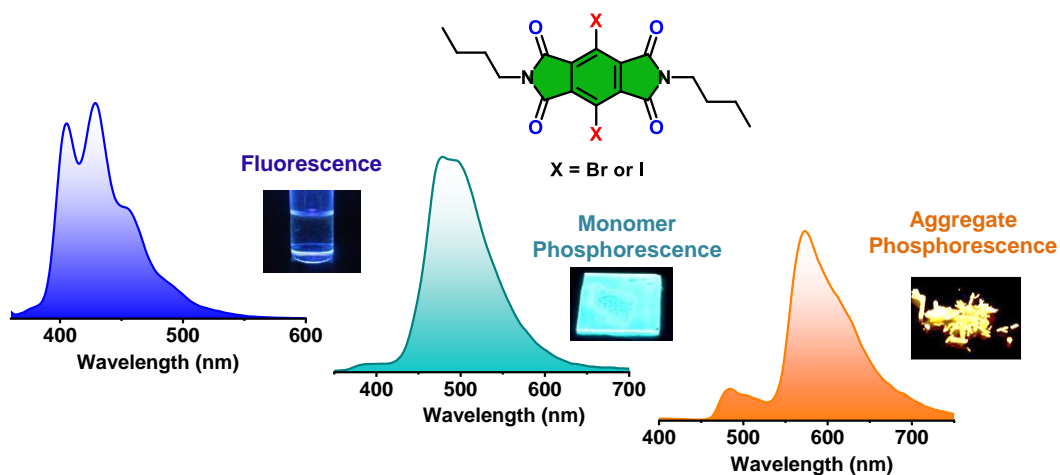
Ambient Dual Phosphorescence from Heavy atom Substituted Pyromellitic Diimides

CHAPTER 2.1

Ambient Dual Phosphorescence from Heavy atom Substituted Pyromellitic Diimides*

Abstract

Arylene diimide derived ambient organic phosphors are seldom reported despite their potential structural characteristics to facilitate the triplet harvesting. In this context, highly efficient room temperature phosphorescence (RTP) from simple, heavy-atom substituted pyromellitic diimide derivatives in amorphous matrix and crystalline state is presented here. Multiple intermolecular halogen bonding interactions among these phosphors, such as halogen-carbonyl and halogen- π resulted in the modulation of phosphorescence, cyan emission from monomeric state and orange-red emission from its aggregated state, to yield twin RTP emission. Remarkably, the air-stable phosphorescence presented here shows one of the highest phosphorescence quantum yield (~48%) among various organics reported in the orange-red emissive region.



*Manuscript based on this work is published in *Angew. Chem. Int. Ed.* **2021**, *60*, 12323-12327.

2.1.1. Introduction:

Design of ambient organic phosphors is one of the most actively pursued research in recent times as promising alternative to the toxic, metal-based organometallic phosphors for various applications.^[1] One of the important challenges in realizing the RTP from organic molecules is to stabilize the triplet states by minimizing the vibrational and oxygen mediated triplet quenching.^[1a] Recently, very elegant design strategies in this direction have been reported to achieve ambient RTP from organic phosphors both in their crystalline states^[2] and by embedding them in polymeric matrix^[3] or in various supramolecular scaffolds.^[4] However, new molecular designs with high quantum yield phosphors are required for the further advancement in this field. Since phosphorescence is a spin-forbidden process, a strong spin-orbit coupling (SOC) is considered as a basic requisite to promote the intersystem crossing process (ISC) between a singlet (S_n) and triplet state (T_n).^[1a,5] In this respect, we envisage that arylene diimides are an important class of molecules to be explored, with its multiple carbonyl groups in the backbone and with the diverse synthetic strategies available for their core-substitution with heavy atoms to increase the SOC and thus the resultant ISC efficiency.^[6] Although arylene diimides have been extensively investigated for various optoelectronic applications as electron-deficient semiconductors, their ambient triplet harvesting properties are rarely explored.^[7] While arylene monoimides such as naphthalene monoimides and phthalimide derivatives are recently shown to exhibit ambient RTP, corresponding diimide derivatives are seldom exploited for triplet harvesting.^[8] In this context, our group has recently reported the ambient triplet harvesting of core-substituted naphthalene diimides via RTP^[4h] and thermally activated delayed fluorescence (TADF).^[9]

Further we envision that, well-studied supramolecular chemistry of arylene diimides would give an opportunity to realize multimode phosphorescence via tuneable intermolecular interactions. Recently, (supramolecular) aggregation of organic phosphors has been elegantly used by the groups of Huang^[2c,10] and Yang^[11] for realizing dual-mode phosphorescence, which is of great importance for various applications such as white-light phosphorescence.^[3i,12] In this chapter, we show novel heavy-atom core-substituted pyromellitic diimide (**PmDI**) derivatives, as efficient orange-red ambient RTP emitters stable in air (Figure 2.1.1).

Such intense RTP emission with one of the highest quantum yield (~48 %) in the long-wavelength region of the visible spectrum is unprecedented. Further, we show that the phosphorescence emission could be modulated from cyan in the monomeric state to orange-red in aggregated state of the phosphors, by exploiting various intermolecular halogen bonding interactions such as halogen- π and halogen-carbonyl interactions, which facilitates the stacking of the phosphors and increases the SOC significantly. Although triplet harvesting of **PmDI** has recently been explored as polymer phosphors, small molecule-based phosphors are not yet reported.^[13]

2.1.2. Molecular Design:

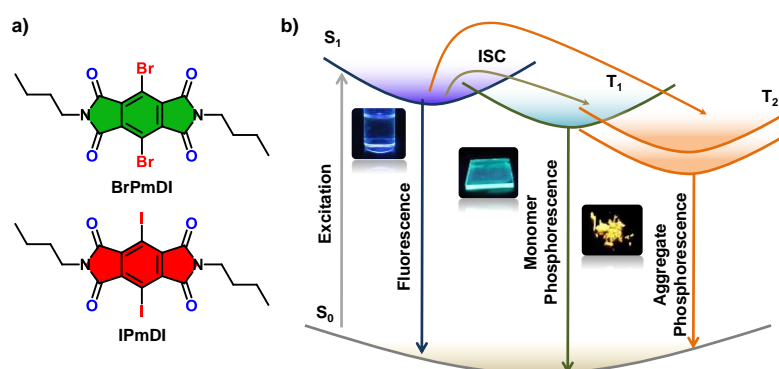


Figure 2.1.1. a) Molecular structures of **BrPmDI** and **IPmDI**. b) Simplified Jablonski diagram to explain the monomer and aggregated phosphorescence and other photophysical processes.

Here we have designed and synthesized two heavy-atom substituted pyromellitic diimide derivatives (**BrPmDI** and **IPmDI**) from a durene derivative and were fully characterized by NMR, mass spectrometry, and single-crystal X-ray diffraction (Figure 2.1.1 and Scheme 2.1). We envision that the four carbonyl groups in the molecular design and core substitution with heavy atoms will help to increase the ISC rate and SOC significantly.

2.1.3. Theoretical Calculations:

The fundamental prerequisite for the triplet emission in arylene diimide based systems is to access the triplet excited state. Therefore, in order to have a qualitative understanding of ISC efficiency in **PmDI** derivatives showed here, we investigated their excited state characteristics by detailed TDDFT calculations using CAM-B3LYP exchange correlation functional (Figure 2.1.2). The rate of ISC is dependent on the SOC strength

and this is estimated quantitatively by calculating the SOC matrix element (SOCME) between S_1 and its closely lying triplet states (T_n). In both these cases, multiple triplet states are present below the S_1 excited state and thus providing a thermodynamically favourable ISC route (Figure 2.1.2). In **BrPmDI**, there are two main contributing pathways for ISC according to the corresponding SOC matrix element (Figure 2.1.2a). These are S_1 ($n-\pi^*$) to T_6 ($\pi-\pi^*$) and S_1 to T_2 , where corresponding calculated SOCME are 16 and 526 cm^{-1} , respectively (Figure 2.1.2a). It is important to note that the closely-lying T_5 and T_4 possess the similar molecular orbital (MO) configuration as that of S_1 and this does not follow El-Sayed rule; therefore, the magnitude is much lower than that between S_1 and T_2 having different electron-hole configurations (Figure 2.1.2.a). In addition, both these transitions are also facilitated by the presence of heavy Br atoms. For **IPmDI** monomers, the ISC pathway is facilitated by close-lying S_1 - T_2 which follow El-Sayed rule and since iodine is expected to show a stronger heavy-atom effect as compared to bromine, the magnitude of SOCME is three times higher than **BrPmDI** (Figure 2.1.2.b).

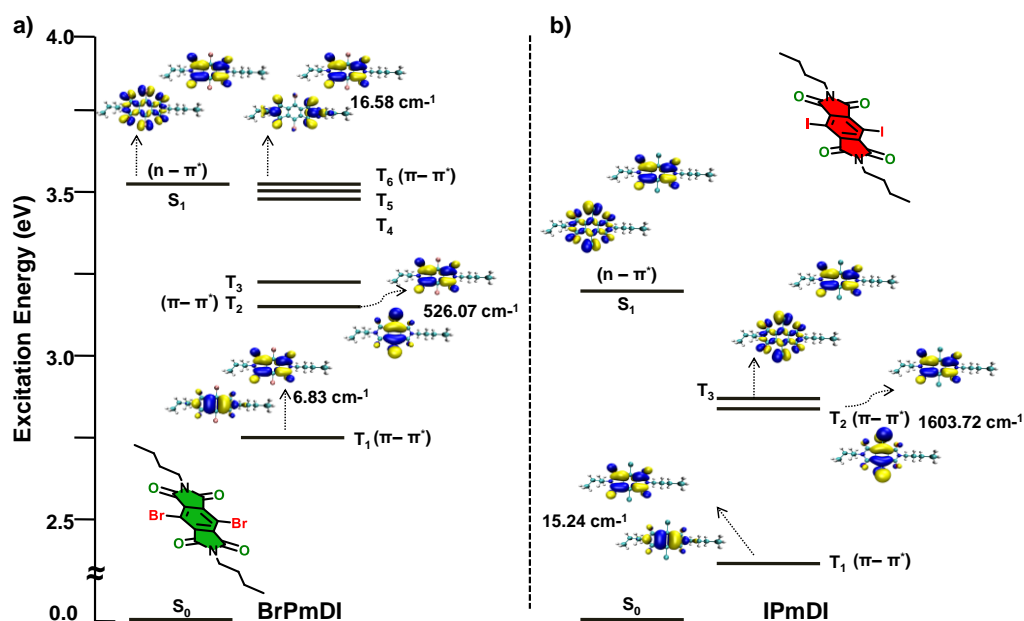


Figure 2.1.2. Ground state geometries, relative excitation energies and their corresponding hole, electron wavefunctions and SOC matrix elements for both monomeric a) **BrPmDI**, b) **IPmDI** were optimized using B3LYP functional in conjunction with 6-31+g(d) basis set for C, N, O, H and LANL2DZ basis set for Br with effective core potential (Hole and electron wavefunctions are shown below and above in the schematic, respectively).

2.1.4. Spectroscopic Studies in Solution-state:

Spectroscopic characterization of **BrPmDI** and **IPmDI** in solution was subsequently performed using steady-state and time-resolved emission experiments. In solution state (THF, 0.05 mM), absorption spectra of **BrPmDI** and **IPmDI** showed characteristic S_0 - S_2 (π - π^*) transition with a maximum at 360 nm and 380 nm, respectively (Figures 2.1.3a,d).^[13] In solution, both molecules exhibited only weak fluorescence emission in the 400-550 nm regions with a short average lifetime of ~ 0.8 ns (Figures 2.1.3a,b,d,e). On the other hand, when the experiments were performed at 77 K (THF) in the glassy matrix to reduce the vibrational dissipation, red-shifted emission in the 425 to 700 nm region with an emission maximum at 504 and 507 nm for **BrPmDI** ($\tau_{\text{avg}} = 7.7$ ms) and **IPmDI**, ($\tau_{\text{avg}} = 1.9$ ms), respectively was observed (Figures 2.1.3c,f). The high lifetime of this red-shifted emission suggests its phosphorescence origin.

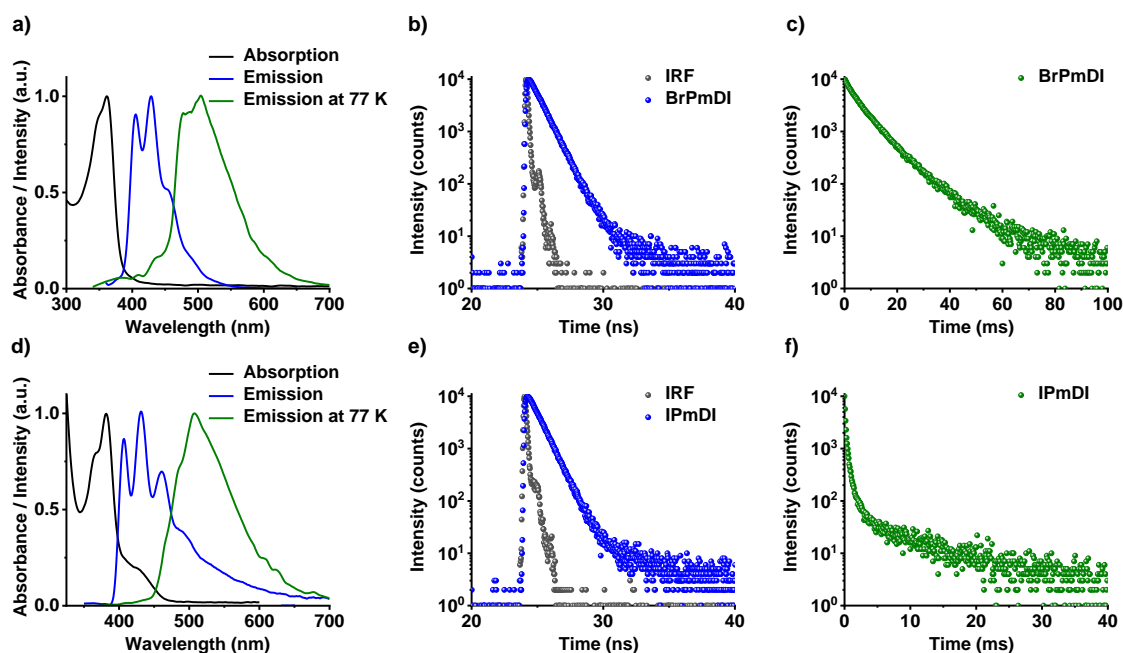


Figure 2.1.3. Normalized absorption and emission spectra at room temperature and emission spectra at 77 K of a) **BrPmDI** and d) **IPmDI** in THF solution ($[c] = 0.05$ mM, $\lambda_{\text{exc.}} = 330$ nm and 350 nm for **BrPmDI** and **IPmDI**, respectively). Fluorescence lifetime decay profiles of b) **BrPmDI** and e) **IPmDI** in THF ($[c] = 0.05$ mM, $\lambda_{\text{exc.}} = 373$ nm, $\lambda_{\text{collected}} = 450$ nm). Phosphorescence lifetime decay profiles of c) **BrPmDI** and f) **IPmDI** in THF at 77 K ($[c] = 0.05$ mM, $\lambda_{\text{exc.}} = 330$ and 350 nm for **BrPmDI** and **IPmDI**, respectively, $\lambda_{\text{collected}} = 500$ nm).

2.1.5. Ambient Monomeric and Aggregated Room Temperature Phosphorescence in Polymer Matrix and Crystalline State:

To harvest the triplets by minimizing the vibrational dissipation under ambient conditions, we first dispersed the molecules in poly(methylmethacrylate) (PMMA) matrix, an amorphous polymeric host known to stabilize RTP, at very low concentrations. (1 wt.% with respect to PMMA).^[3a] Remarkably, a strong cyan emission was observed for both PMMA films with maximum at 480 and 487 nm, respectively under ambient conditions (Figures 2.1.4a,d). High lifetime of these red-shifted emissions (1.4 ms and 6.3 μ s for **BrPmDI** and **IPmDI**, respectively) and its similarity with that of the emission of the pure molecules in frozen THF at 77 K clearly suggest the phosphorescence origin from monomeric states (Figures 2.1.4a,d,c,f). In addition these molecule also show very weak fluorescence emission in the 380 nm to 430 nm region (Figures 2.1.4a,d). The absolute phosphorescence quantum efficiencies of **BrPmDI** and **IPmDI** in 1 wt. % PMMA matrix were 18 % and 2 %, respectively, under air. Therefore, it is evident that a strong internal heavy-atom effect is operative in these derivatives to facilitate substantial ISC and subsequent efficient RTP in amorphous matrix. We hypothesized that higher phosphorescence efficiency of the **BrPmDI** compared to the **IPmDI** in 1 wt. % PMMA matrix is due to higher ISC rate (k_{ISC}), lower non-radiative decay rate (k_{nr}) and more number of ISC channels present in monomeric state (Figures 2.1.2). It is worth mentioning that 1 wt. % amorphous films of **BrPmDI** when under vacuum, displayed an impressive phosphorescence quantum yield of 54 %. Interestingly, on increasing the concentration of these phosphors in the PMMA matrix (5 to 50 wt. % with respect to PMMA) gradual appearance of a red-shifted emission (orange-red region) with maximum at 576 and 585 nm for **BrPmDI** and **IPmDI**, respectively, with the concomitant disappearance of monomeric cyan phosphorescence, was observed (Figures 2.1.4b,e). The lifetime in the millisecond time scale for these films suggests the phosphorescence modulation of these phosphors via intermolecular interactions ($\tau_{avg.} = 5.2, 0.32$ ms and $\Phi_p = 17.5$ %, 30 % for **BrPmDI** and **IPmDI**, respectively in 50 wt. % with respect to PMMA under air) (Figures 2.1.4c,f). Drop-casted films of **BrPmDI** and **IPmDI** showed similar emission features with lower quantum yield, which confirms the emission from aggregated phosphors. Aggregation of phosphors in the polymer matrix at higher wt. % is further evident from the increased scattering and red-shift in the absorption spectra as well as red-shifted excitation spectra monitored at 650 nm (Figure

2.1.5). We envisage that the presence of multiple non-covalent interactions in the aggregated state stabilizes the triplet energy level.^[10,11]

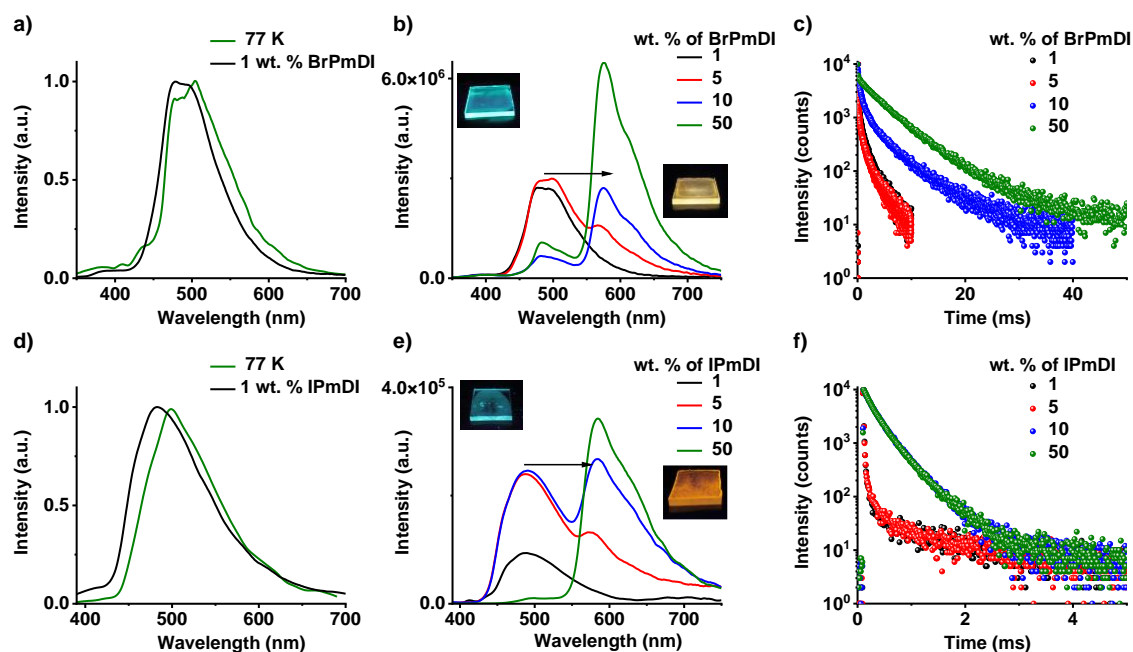


Figure 2.1.4. Normalized emission spectra of a) **BrPmDI** and d) **IPmDI** in frozen THF at 77 K, in PMMA films with 1 wt. % of phosphors. Emission spectra of PMMA films doped with different wt. % of b) **BrPmDI** and e) **IPmDI**, respectively. (Inset: photographs of **BrPmDI** and **IPmDI** in PMMA films with 1 wt. % and 50 wt. % of phosphors under 365 nm UV-lamp excitation). Lifetime decay profile of PMMA films doped with different wt. % of c) **BrPmDI** and f) **IPmDI** respectively. ($\lambda_{exc.} = 330$ and 350 nm for **BrPmDI** and **IPmDI**, respectively, $\lambda_{collected} = 500$ nm for monomer and 650 nm for aggregate).

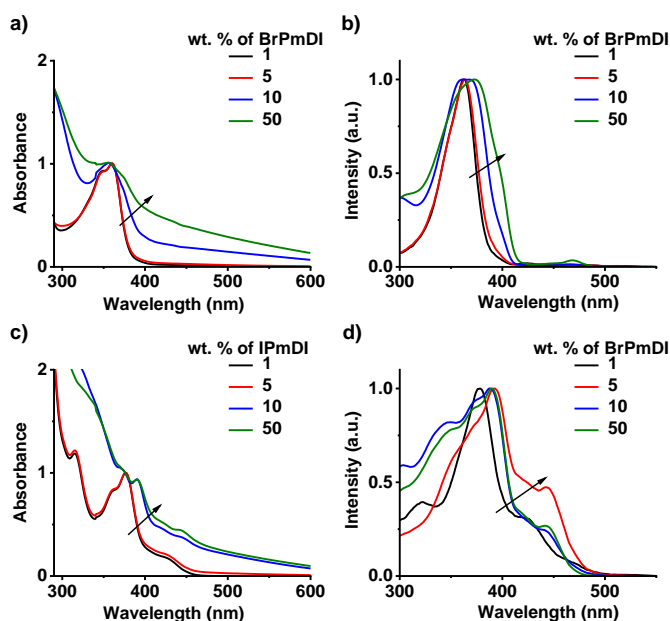


Figure 2.1.5. Normalized absorption spectra of PMMA films doped with different wt. % of a) **BrPmDI** and c) **IPmDI**, respectively. ($\lambda_{\text{monitored}} = 600 \text{ nm}$). Normalized excitation spectra of PMMA films doped with different wt. % of b) **BrPmDI** and d) **IPmDI**, respectively.

To characterize the various intermolecular interactions in the stacked state of these phosphors, single crystals of **BrPmDI** and **IPmDI** were further investigated. Interestingly, single crystals of **BrPmDI** and **IPmDI** showed intense orange-red phosphorescence emission with a maximum at 576 and 585 nm for **BrPmDI** and **IPmDI**, respectively, similar to that of the PMMA films with aggregated phosphors (Figures 2.1.6a,b,d,e). The high lifetimes of 11.4 ms and 0.61 ms for **BrPmDI** and **IPmDI** crystals, respectively and gated emission spectra (delay time = 0.5 ms) confirms the phosphorescent nature of the emission (Figures 2.1.6b,c,e,f). Selective excitation of the aggregated absorption at 450 nm also resulted in similar red-sifted phosphorescence emission suggesting the assembled state of the phosphors in crystals (Figures 2.1.6b,e). Remarkably, both **BrPmDI** and **IPmDI** crystals showed high absolute phosphorescence quantum efficiencies of 26 % and 48 %, respectively, under air, which is the highest phosphorescence quantum yield in the arylene diimide family and also one of the highest phosphorescence quantum yields reported in the orange-red region among various ambient organic phosphors. Remarkably, the phosphorescence quantum yield of **IPmDI** crystals has increased to 68 % under vacuum. Higher phosphorescence quantum efficiency of **IPmDI** crystals compared to the **BrPmDI** could be attributed to a stronger

SOC and high ISC rate (k_{ISC}) in the former, which is also supported by its faster phosphorescence lifetime (Figures 2.1.6c,f) as expected in heavy-atom organic phosphors.

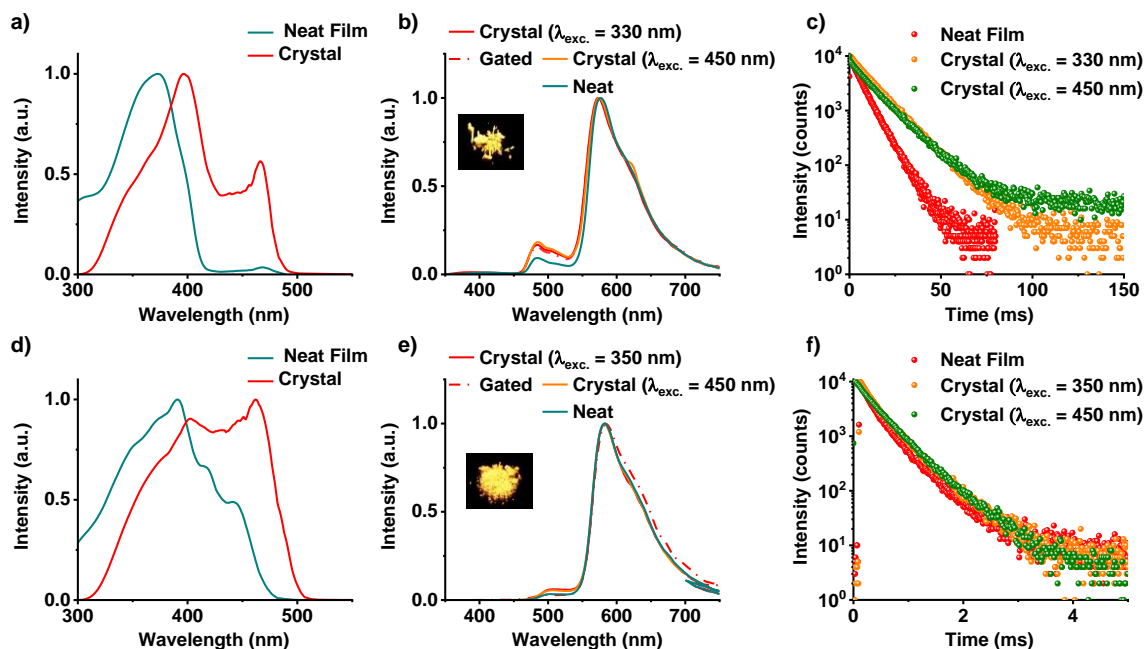


Figure 2.1.6. Normalized excitation spectra of drop-casted neat films and crystals of a) **BrPmDI** and d) **IPmDI**. Normalized steady-state and gated emission spectra of b) **BrPmDI** and e) **IPmDI**. Phosphorescence lifetime decay profiles of c) **BrPmDI** and f) **IPmDI** of drop-casted neat films and in crystalline state, ($\lambda_{monitored} = 650$ nm, $\lambda_{collected} = 650$ nm, $\lambda_{exc.} = 330$ nm and 350 nm for **BrPmDI** and **IPmDI**, respectively, for selective excitation $\lambda_{exc.} = 450$ nm, all experiments were performed in air).

X-ray diffraction analysis of the crystals further provided insights into the molecular organization of the phosphors in the aggregated state. Single crystals of **BrPmDI** exhibited a layered slip-stacked molecular organization with an interlayer distance of 3.8 Å (Figure 2.1.7) which justifies the stabilization of orange-red emissive, red-shifted phosphorescence of the aggregated state in the crystalline phase. Further stacked arrangement of phosphors is stabilized by the halogen- π (C \cdots Br, 3.5 Å) and the interdigitated alkyl chains between molecules of adjacent layers (Figures 2.1.7a-c). In addition, within each layer, these molecules are connected by C=O \cdots Br intermolecular non-covalent interactions (3.1 Å) (Figure 2.1.7b). It has been well-established that halogen bonding can enhance the SOC by external heavy-atom effect.^[2a] We envisage that, rigid 3D network due to the various non-covalent interactions specially halogen

bonding help the triplet stabilization via minimizing the vibrational dissipation and by enhancing the SOC. In addition, strong intra-molecular $C=O\cdots Br$ (3.2 Å) (Figure 2.1.7b) interactions can also contribute to high SOC even in the molecular dispersed and glassy matrix. Similar organization was also observed in the crystals of **IPmDI** (Figures 2.1.7d-f). Since the crystal packing is similar in both molecules (Figure 2.1.7) with closely matching short-contact distances, we envision that the extent of the external/ internal heavy-atom effect determines the differences in their RTP intensity.

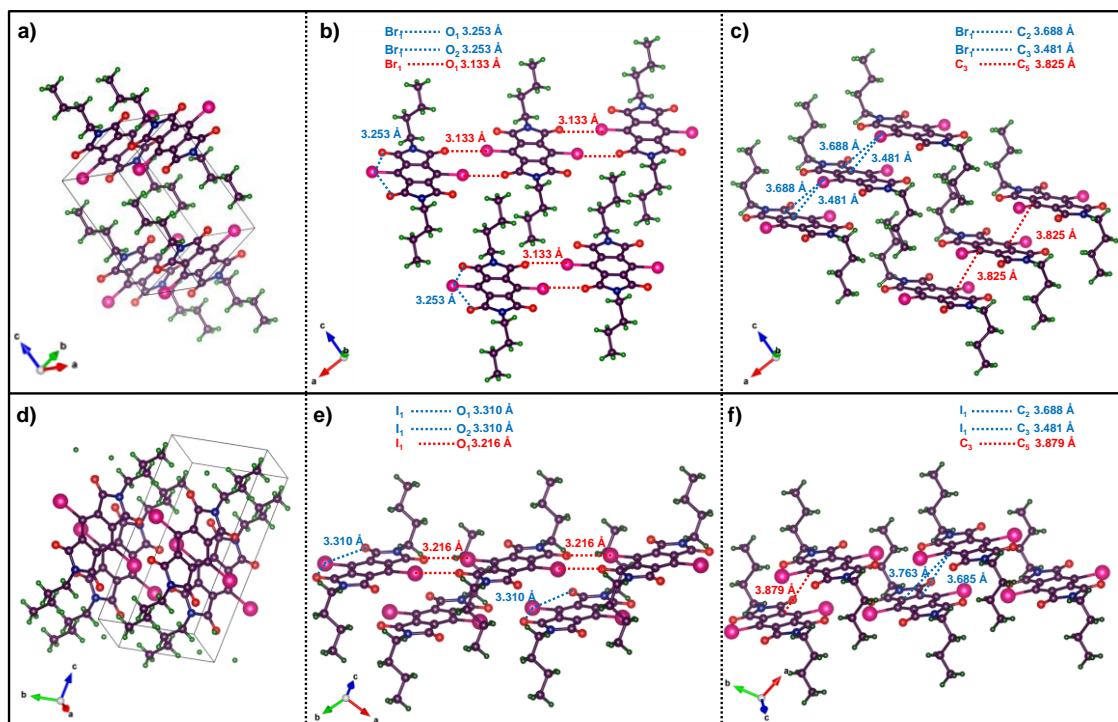


Figure 2.1.7. a,d) Unit cell, b,e) slipped stacked arrangement showing various intermolecular interactions, c,f) intramolecular and intermolecular halogen-carbonyl interaction of **BrPmDI** (1st row) and **IPmDI** (2nd row) single crystals.

To validate the stabilization of triplets in the crystal state we have performed time-dependent density functional theory (TDDFT) calculations (Figure 2.1.8). The calculated energy levels of the optimized geometry of the first excited triplet state of dimeric **BrPmDI**s support the observed red shift in phosphorescence in the aggregated state (Figures 2.1.8). Upon aggregation, number of intersystem crossing channels increases significantly as evident from the ground state optimized geometries of **BrPmDI** dimers (Figure 2.1.8.), which could be one of the reasons for the high phosphorescence efficiency in the crystalline state compared to the monomeric state. Further, reduced

density gradient (RDG) plot of the dimeric triplet state also clearly shows the intra- and intermolecular non-covalent interactions observed in the crystalline state, which can enhance the ISC/SOC efficiency (Figures 2.1.9a-c).

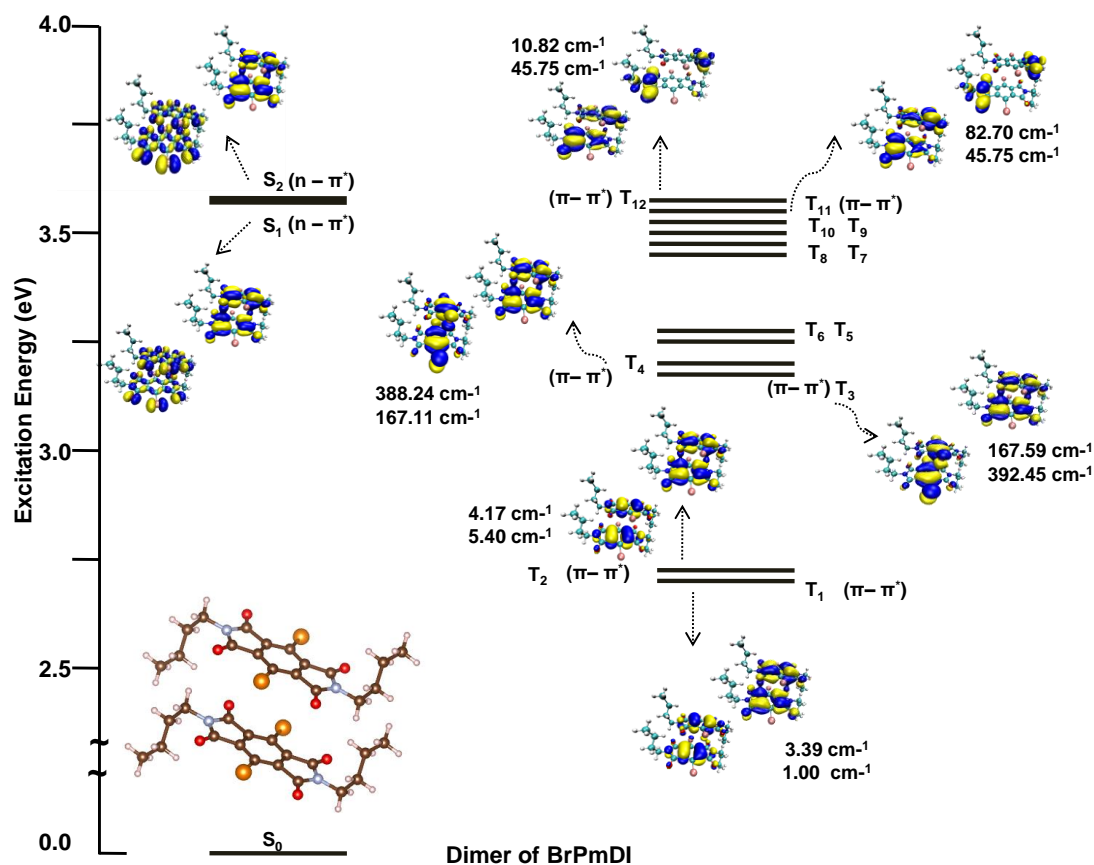


Figure 2.1.8. a) Ground state geometries, relative excitation energies and their corresponding hole, electron wavefunctions and SOC matrix elements for dimeric **BrPmDI** were optimized using *B3LYP* functional in conjunction with *6-31+g(d)* basis set for C, N, O, H and *LANL2DZ* basis set for Br with effective core potential (Hole and electron wavefunctions are shown below and above in the schematic, respectively).

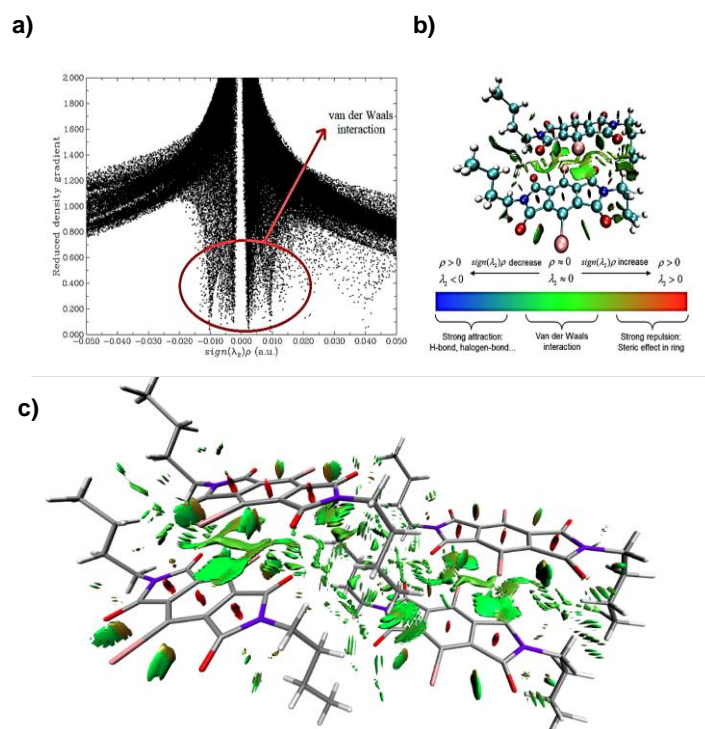


Figure 2.1.9. a) Plots of the reduced density gradient versus the electron density multiplied by the sign of the second Hessian eigenvalue b,c) Gradient isosurfaces ($s = 0.5$ au). The surfaces are colored on a blue-green-red scale according to values of $\text{sign}(\lambda_2)\rho$. Blue indicates strong attractive interactions, and red indicates strong nonbonded overlap.

2.1.6. Conclusions:

In conclusion, we have introduced a new class of small organic molecule based efficient, ambient organic phosphors from the smallest member of the arylene diimide family, i.e., pyromellitic diimides, by a rational “heavy-atom” substitution strategy. The **PmDI** derivatives reported here showed high phosphorescence quantum yield (~48 % and ~68 %, in air and vacuum, respectively) with exceptional air stability. Further, the tunable phosphorescence emission could also be achieved by the stacking of phosphors using multiple intermolecular halogen bonding interactions. Although many organic room temperature phosphors are reported recently, the present system is unique with respect to its new molecular design, high quantum yield and halogen bonding induced tunable phosphorescence.^[1f] We envisage that arylene diimide phosphors, with its rich chemistry of core-substitution and appropriate molecular structure conducive for efficient SOC and ISC, offer plethora of opportunities in the frontier research area of organic phosphors.

2.1.7. Experimental Section:

2.1.7.1. General Methods:

NMR Measurements: ^1H and ^{13}C NMR spectra were recorded on a BRUKER AVANCE-400 Fourier transformation spectrometer with 400 and 100 MHz, respectively. The spectra were calibrated with respect to the residual solvent peaks. The chemical shifts are reported in parts per million (ppm) with respect to TMS. Short notations used are s for singlet, d for doublet, t for triplet, q for quartet and m for multiplet.

Optical Measurements: Electronic absorption spectra were recorded on a Perkin Elmer Lambda 900 UV-Vis-NIR spectrometer and emission spectra were recorded on FLS1000 spectrometer, Edinburgh Instruments. Solution state UV-Vis and emission spectra were recorded in 1 mm path length cuvette. Fluorescence spectra of films were recorded in front-face geometry to avoid self-absorption.

Lifetime measurements and quantum yield: Fluorescence lifetimes were performed on a Horiba Delta Flex time-correlated single-photon-counting (TCSPC) instrument. A 373 nm LED laser diode with a pulse repetition rate of 1 MHz was used as the light source. The instrument response function (IRF) was collected using a scatterer (Ludox AS40 colloidal silica, Sigma-Aldrich). Phosphorescence lifetime ($\lambda_{\text{exc.}} = 330\text{nm}, 350\text{ nm}, 430\text{ nm}$ and 450 nm) and gated emission were measured on FLS1000 spectrometer, Edinburgh Instruments equipped with a micro flash-lamp (μF2) set-up. Quantum yields were measured using an integrating sphere in the same instrument.

High Resolution Mass Spectroscopy (HRMS): HR-MS was carried out using Agilent Technologies 6538 UHD Accurate-Mass Q-TOFLC/MS.

Matrix-Assisted Laser Desorption Ionization (MALDI): MALDI was performed on a Bruker daltonics Autoflex Speed MALDI TOF System (GT0263G201) spectrometer using trans-2-[3-(4-tert-Butylphenyl)-2-methyl-2-propenylidene] malononitrile (DCTB) as the matrix.

Single Crystal X-ray Crystallography: Suitable single crystals of both **BrPmDI**, and **IPmDI** were selected and mounted on a Rigaku Saturn 724+ CCD diffractometer at 150 K using paratone oil for unit cell determination and intensity data collection. Data integration and indexing was carried out using CrysAlisPro software. Using Olex^[14a], the

structure was solved with the ShelXT^[14b] structure solution program using Intrinsic Phasing. The complete refinement of the structures were carried out with the ShelXL^[14c] refinement package using Least Squares minimization.

Computational Details: Ground State (S_0) of **BrPmDI** and **IPmDI** monomer molecules were optimized using density functional theory (DFT) and electronic absorption spectra were calculated using time-dependent density functional theory (TD-DFT) as implemented in the Gaussian 16 software.^[15a] Ground state (S_0) optimization and frequency calculations were performed employing B3LYP^[15b-d] exchange functional with 6-31+g(d) basis set except for Br and I, for which LANL2DZ basis set was used with the corresponding effective core potential (ECP). While the excited state calculations were performed using long-range corrected CAM-B3LYP^[15e] exchange-correlation functional with the same basis sets as mentioned before. Ground state frequency calculations were performed to confirm the absence of any unstable normal mode. The first singlet excited state (S_1) of monomers were optimized at the TD-DFT level of theory. While the first triplet excited states (T_1) were also optimized at the TD-DFT level of theory within the Tamm-Dancoff approximation (TDA) to overcome the triplet instability issue.^[15f] The spin-orbit coupling (SOC) effect was considered to be a perturbation of the scalar relativistic Kohn-Sham orbitals after SCF and TD-DFT calculations (pSOC-TDDFT).^[15g-i] The SOC matrix elements were calculated using B3LYP with a Slater-type all-electron TZP basis set for all atoms as implemented in the ADF package.^[15j] Reduced density gradient (RDG) plot calculations were done using Multiwfn 3.6 package.^[15k]

2.1.7.2. Protocol of Sample Preparation:

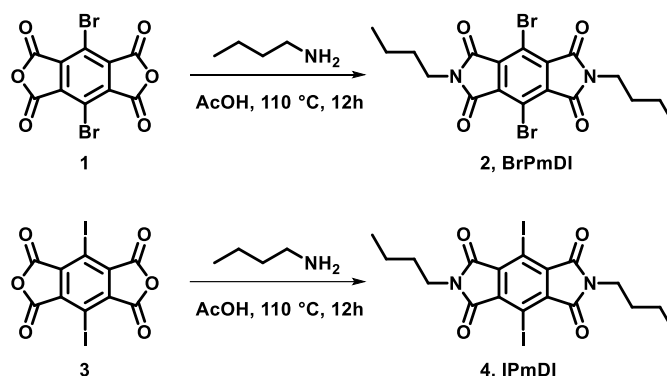
All solution state studies were performed keeping the final concentration of the samples to 0.05 mM from a stock solution of THF (1 mM). For thin films, **BrPmDI** and **IPmDI** molecules (3 mg each) were mixed with appropriate amount of PMMA (depending on the weight ratio) in a total 2 ml chloroform solution. (For example, 1 wt. % dye: PMMA consists of 3 mg dye in 300 mg PMMA). This mixture was then heated at 50 °C for 10 minutes, followed by sonication (5 minutes) to completely dissolve all the components. Then, 0.5 mL of this solution was drop-casted on a clean glass substrate. Finally, the drop-casted thin films were dried at 60 °C for 30 minutes prior to the photophysical

studies. For the phosphorescence studies of the crystal, a small amount of the crystal was placed in between two quartz plates.

2.1.8. Synthetic Schemes and Procedures:

Materials: Pyromellitic dianhydride (PMDA) and [Bis(trifluoroacetoxy)iodo] benzene (BTI) was purchased from Sigma Aldrich; Durene, *n*-Butylamine and Potassium Permanganate were purchased from Alfa-Aesar; Pyridine, Acetic acid, Bromine and Iodine were purchased from Spectrochem and used without further purification.

Synthetic Scheme:



Scheme 2.1. Synthetic scheme for *BrPmDI* and *IPmDI*.

Synthetic Procedures:

Compound **1** and **3** were synthesized according to the literature procedure.^[16]

Synthesis of BrPmDI: Compound **1** (0.50 g, 1.3 mmol) was taken in a 100 mL round bottom flask and 25 mL acetic acid was added into it and stirred at room temperature for 30 minutes. *n*-Butylamine (0.25 g, 3.3 mmol) was added to the reaction mixture and stirred for 12 hours at 110 °C. After completion of the reaction, 100 mL of water was added to get gray coloured precipitate. The precipitate was filtered and dried under vacuum for 10 hours. Column chromatography was performed using 1-5 % methanol in chloroform as an eluent to get the pure product as greenish white solid (0.48 g, 74 % yield).

¹H NMR (CDCl₃, 400 MHz), δ (ppm) = 3.73 (t, 4H, J = 7.4 Hz), 1.72-1.64 (m, 4H), 1.42-1.32 (m, 4H), 0.96 (t, 6H, J = 7.4 Hz); ¹³C NMR (CDCl₃, 100 MHz), δ (ppm) = 163.8, 136.5, 114.4, 39.2, 30.6, 20.4, 13.9. HRMS (APCI): m/z calculated for C₁₈H₁₈Br₂N₂O₄: 485.9613: observed 486.9807 [M+H]⁺, MALDI-TOF (DCTB matrix, negative mode): m/z calculated for C₁₈H₁₈Br₂N₂O₄: 485.9613: observed 486.514 [M]⁻.

Synthesis of IPmDI: Compound **3** (0.50 g, 1.06 mmol) was taken in a 100 mL round bottom flask and 25 mL acetic acid was added to it and stirred at room temperature for 30 minutes. *n*-Butylamine (0.17 g, 2.34 mmol) was added into the reaction mixture and stirred for 12 hours at 110 °C. After completion of the reaction 100 mL of water was added to get gray coloured precipitate. The precipitate was filtered and dried under vacuum for 10 hours. Column chromatography was performed using 1-5 % methanol in chloroform as an eluent to get the pure product as yellow solid (0.38 g, 62 % yield).

^1H NMR (CDCl_3 , 400 MHz), δ (ppm) = 3.73 (t, 4H, $J = 7.4$ Hz), 1.72-1.64 (m, 4H), 1.42-1.32 (m, 4H), 0.96 (t, 6H, $J = 7.4$ Hz); ^{13}C NMR (CDCl_3 , 100 MHz), δ (ppm) = 163.8, 136.5, 114.4, 39.2, 30.6, 20.4, 13.9. MALDI-TOF (DCTB matrix, negative mode): m/z calculated for $\text{C}_{18}\text{H}_{18}\text{I}_2\text{N}_2\text{O}_4$: 579.9376; observed 579.277 [M].

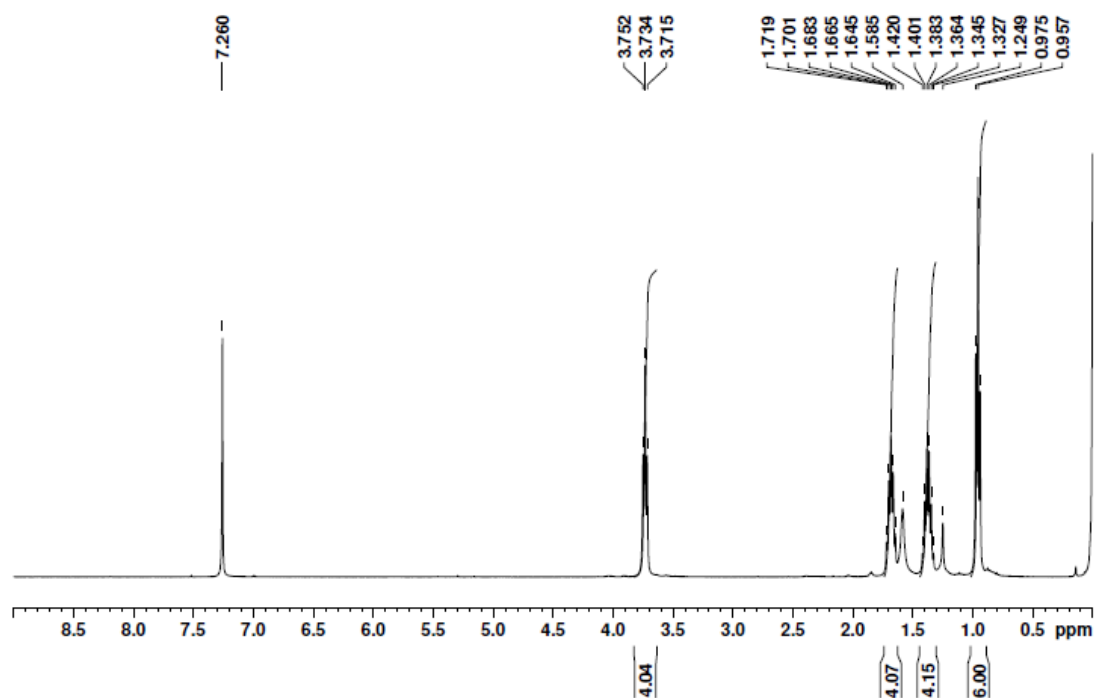


Figure 2.1.10. ^1H NMR spectrum of **BrPmDI** in CDCl_3 .

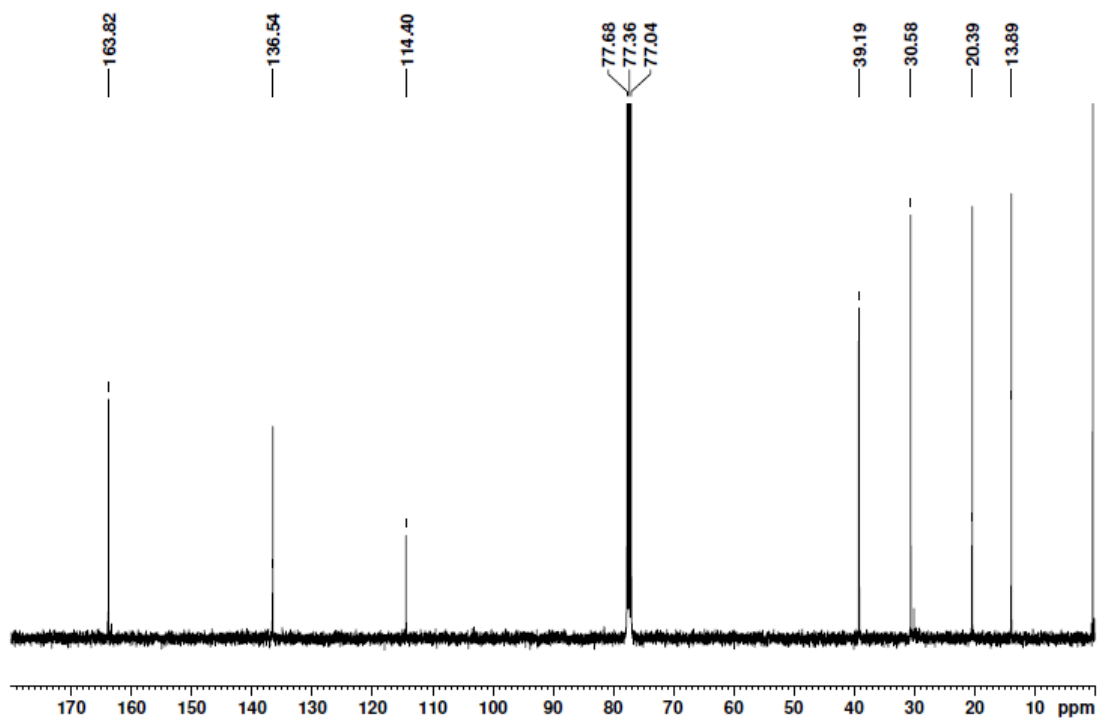


Figure 2.1.11. ^{13}C NMR spectrum of *BrPmDI* in CDCl_3 .

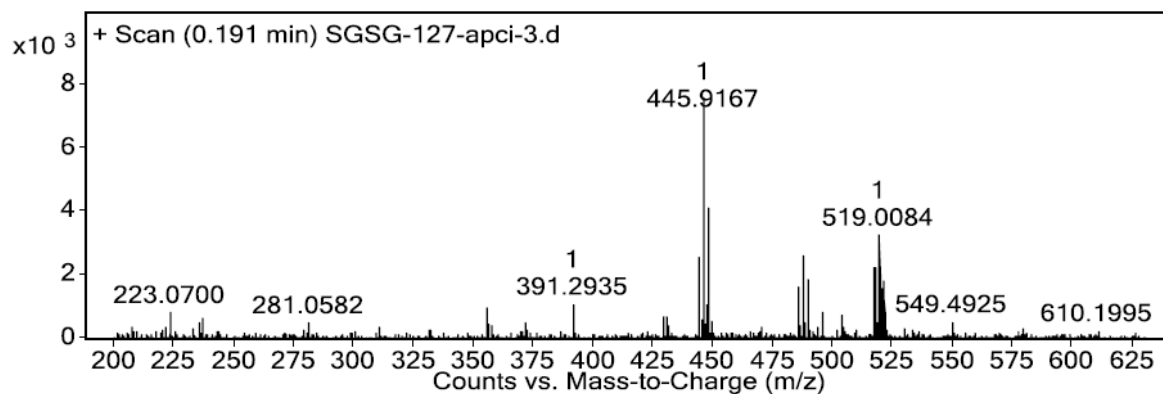


Figure 2.1.12. APCI-HR-MS spectrum of *BrPmDI*.

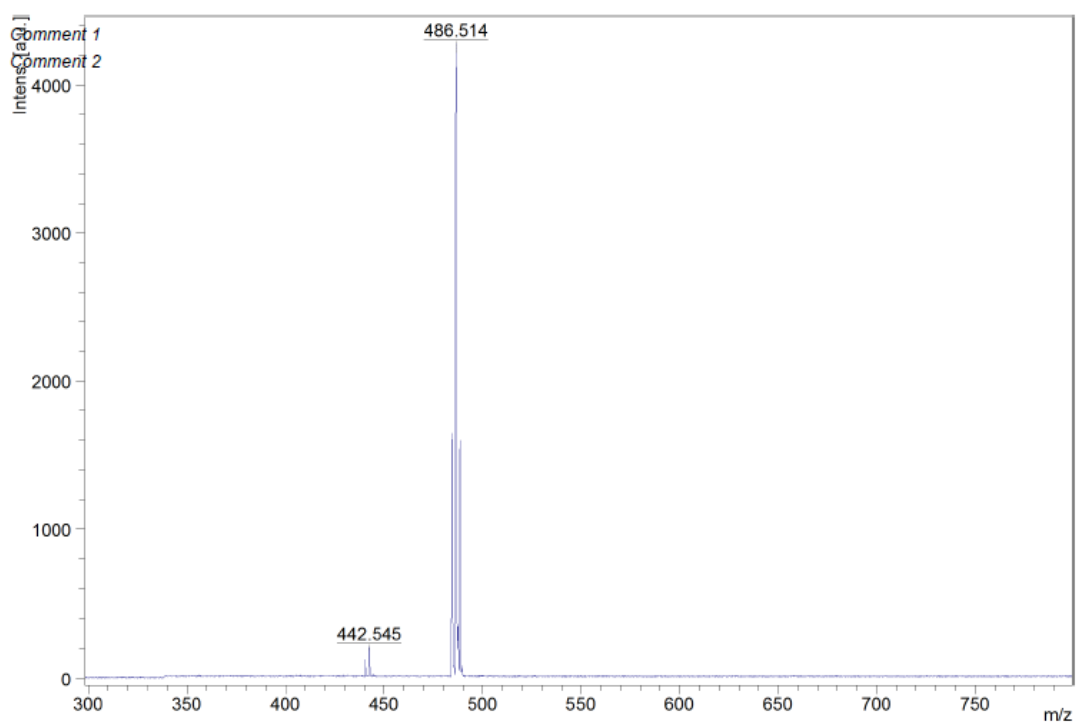


Figure 2.1.13. MALDI spectrum of *BrPmDI*.

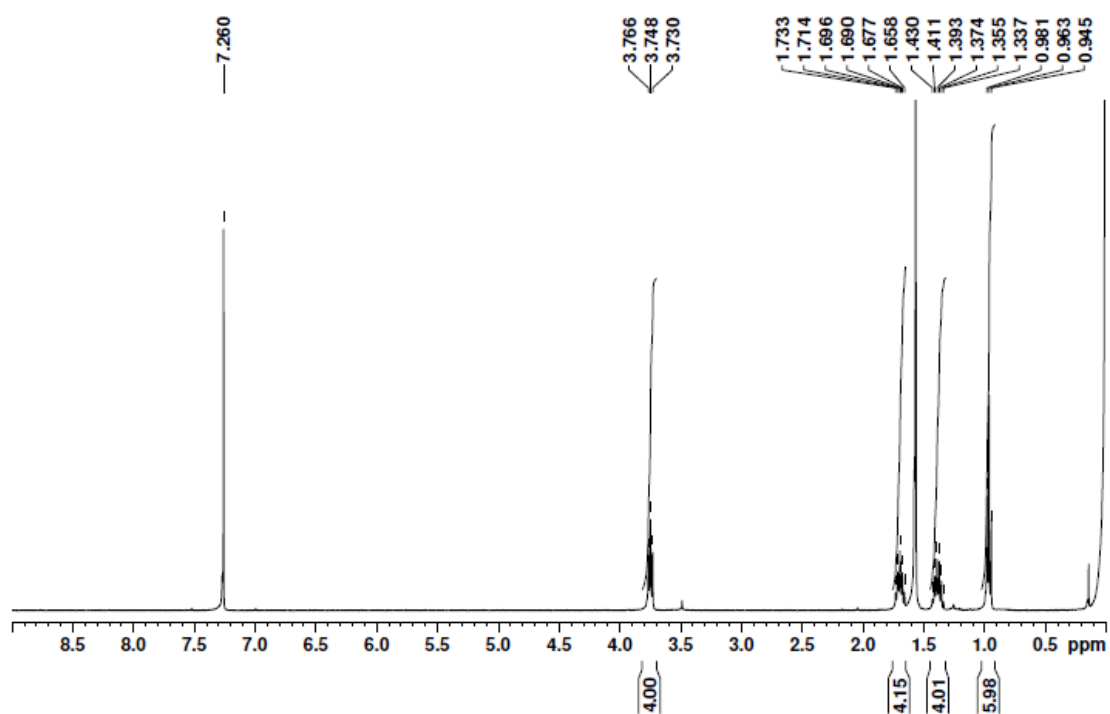


Figure 2.1.14. ^1H NMR spectrum of *IPmDI* in CDCl_3 .

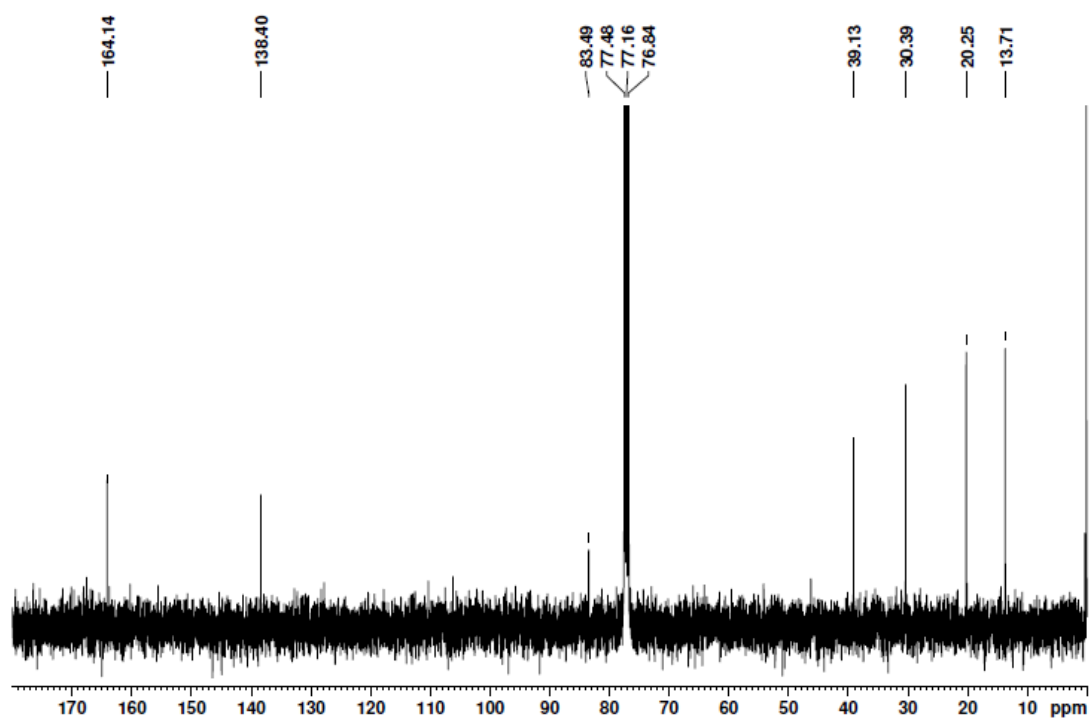


Figure 2.1.15. ^{13}C NMR spectrum of IPmDI in CDCl_3 .

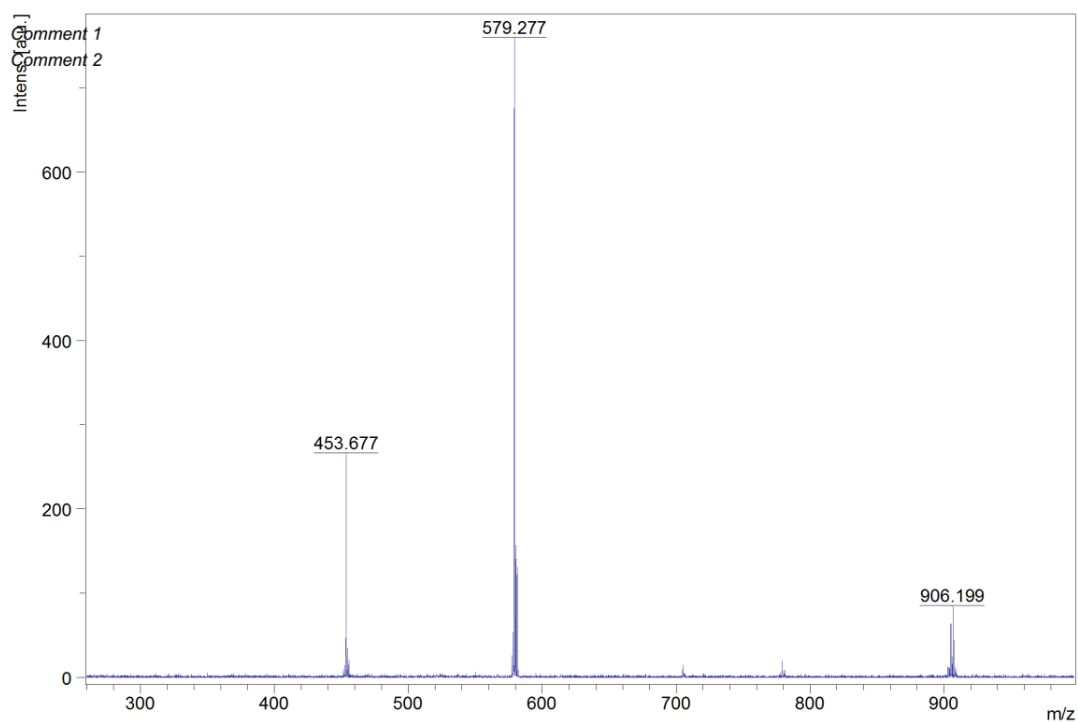


Figure 2.1.16. MALDI spectrum of IPmDI.

2.1.9. References:

[1] a) S. Hirata, *Adv. Opt. Mater.* **2017**, *5*, 1700116; b) Kenry, C. Chen, B. Liu, *Nat. Commun.* **2019**, *10*, 2111; c) W. Zhao, Z. He, J. W. Y. Lam, Q. Peng, H. Ma, Z. Shuai, G. Bai, J. Hao, Ben Z. Tang, *Chem* **2016**, *1*, 592-602; d) T. Zhang, X. Ma, H. Wu, L. Zhu, Y. Zhao, H. Tian, *Angew. Chem. Int. Ed.* **2020**, *59*, 11206-11216; e) S. Xu, R. Chen, C. Zheng, W. Huang, *Adv. Mater.* **2016**, *28*, 9920-9940; f) X. Ma, J. Wang, H. Tian, *Acc. Chem. Res.* **2019**, *52*, 738-748.

[2] a) O. Bolton, K. Lee, H.-J. Kim, K. Y. Lin, J. Kim, *Nat. Chem.* **2011**, *3*, 205-210; b) W. Z. Yuan, X. Y. Shen, H. Zhao, J. W. Y. Lam, L. Tang, P. Lu, C. Wang, Y. Liu, Z. Wang, Q. Zheng, J. Z. Sun, Y. Ma, B. Z. Tang, *J. Phys. Chem. C* **2010**, *114*, 6090-6099; c) Z. An, C. Zheng, Y. Tao, R. Chen, H. Shi, T. Chen, Z. Wang, H. Li, R. Deng, X. Liu, W. Huang, *Nat. Mater.* **2015**, *14*, 685-690; d) A. D. Nidhankar, Goudappagouda, D. S. Mohana Kumari, S. K. Chaubey, R. Nayak, R. G. Gonnade, G. V. P. Kumar, R. Krishnan, S. S. Babu, *Angew. Chem. Int. Ed.* **2020**, *59*, 13079-13085; e) L. Gu, H. Shi, L. Bian, M. Gu, K. Ling, X. Wang, H. Ma, S. Cai, W. Ning, L. Fu, H. Wang, S. Wang, Y. Gao, W. Yao, F. Huo, Y. Tao, Z. An, X. Liu, W. Huang, *Nat. Photonics* **2019**, *13*, 406-411; f) J. Yang, X. Zhen, B. Wang, X. Gao, Z. Ren, J. Wang, Y. Xie, J. Li, Q. Peng, K. Pu, Z. Li, *Nat. Commun.* **2018**, *9*, 840; g) Y. Wang, J. Yang, Y. Tian, M. Fang, Q. Liao, L. Wang, W. Hu, B. Z. Tang, Z. Li, *Chem. Sci.* **2020**, *11*, 833-838; h) E. Hamzehpoor, D. F. Perepichka, *Angew. Chem. Int. Ed.* **2020**, *59*, 9977-9981.

[3] a) D. Lee, O. Bolton, B. C. Kim, J. H. Youk, S. Takayama, J. Kim, *J. Am. Chem. Soc.* **2013**, *135*, 6325-6329; b) Y. Su, Y. Zhang, Z. Wang, W. Gao, P. Jia, D. Zhang, C. Yang, Y. Li, Y. Zhao, *Angew. Chem. Int. Ed.* **2020**, *59*, 9967-9971; c) H. Wu, W. Chi, Z. Chen, G. Liu, L. Gu, A. K. Bindra, G. Yang, X. Liu, Y. Zhao, *Adv. Funct. Mater.* **2019**, *29*, 1807243; d) Y. Su, S. Z. F. Phua, Y. Li, X. Zhou, D. Jana, G. Liu, W. Q. Lim, W. K. Ong, C. Yang, Y. Zhao, *Sci. adv.* **2018**, *4*, eaas9732; e) M. Louis, H. Thomas, M. Gmelch, A. Haft, F. Fries, S. Reineke, *Adv. Mater.* **2019**, *31*, 1807887; f) H. Thomas, D. L. Pastoetter, M. Gmelch, T. Achenbach, A. Schlögl, M. Louis, X. Feng, S. Reineke, *Adv. Mater.* **2020**, *32*, 2000880; g) M. Gmelch, H. Thomas, F. Fries, S. Reineke, *Sci. adv.* **2019**, *5*, eaau7310; h) A. Kirch, M. Gmelch, S. Reineke, *J. Phys. Chem. Lett.* **2019**, *10*, 310-315; i) S. Kuila, S. J. George, *Angew. Chem. Int. Ed.* **2020**, *59*, 9393-9397.

[4] a) X. Yao, J. Wang, D. Jiao, Z. Huang, O. Mhirsi, F. Lossada, L. Chen, B. Haehnle, A. J. C. Kuehne, X. Ma, H. Tian, A. Walther, *Adv. Mater.* **2020**, 2005973; b) Z. Li, Y. Han, F. Wang, *Nat. Commun.* **2019**, *10*, 3735; c) Z. Li, Y. Han, F. Nie, M. Liu, H. Zhong, F. Wang, *Angew. Chem. Int. Ed.* **2021**, 10.1002/anie.202015846; d) J. Wang, Z. Huang, X. Ma, H. Tian, *Angew. Chem. Int. Ed.* **2020**, *59*, 9928-9933; e) D. Li, F. Lu, J. Wang, W. Hu, X.-M. Cao, X. Ma, H. Tian, *J. Am. Chem. Soc.* **2018**, *140*, 1916-1923; f) Z.-Y. Zhang, Y. Chen, Y. Liu, *Angew. Chem. Int. Ed.* **2019**, *58*, 6028-6032; *Angew. Chem.* **2019**, *131*, 6089-6093; g) H. Chen, X. Ma, S. Wu, H. Tian, *Angew. Chem. Int. Ed.* **2014**, *53*, 14149-14152; h) S. Kuila, K. V. Rao, S. Garain, P. K. Samanta, S. Das, S. K. Pati, M. Eswaramoorthy, S. J. George, *Angew. Chem. Int. Ed.* **2018**, *57*, 17115-17119; i) F.-F. Shen, Y. Chen, X. Dai, H.-Y. Zhang, B. Zhang, Y. Liu, Y. Liu, *Chem. Sci.* **2021**, 10.1039/d0sc05343k.

[5] J. Xu, A. Takai, Y. Kobayashi, M. Takeuchi, *Chem. Commun.* **2013**, *49*, 8447-8449.

[6] a) N. Sakai, J. Mareda, E. Vauthey, S. Matile, *Chem. Commun.* **2010**, *46*, 4225-4237; b) F. Würthner, S. Ahmed, C. Thalacker, T. Debaerdemaeker, *Chem. Eur. J.* **2002**, *8*, 4742-4750.

[7] a) J. H. Oh, S. L. Suraru, W.-Y. Lee, M. Könemann, H. W. Höffken, C. Röger, R. Schmidt, Y. Chung, W.-C. Chen, F. Würthner, Z. Bao, *Adv. Funct. Mater.* **2010**, *20*, 2148-2156; b) A. Nowak-Król, K. Shoyama, M. Stolte, F. Würthner, *Chem. Commun.* **2018**, *54*, 13763-13772; c) Q. Zheng, J. Huang, A. Sarjeant, H. E. Katz, *J. Am. Chem. Soc.* **2008**, *130*, 14410-14411.

[8] a) X. Chen, C. Xu, T. Wang, C. Zhou, J. Du, Z. Wang, H. Xu, T. Xie, G. Bi, J. Jiang, X. Zhang, J. N. Demas, C. O. Trindle, Y. Luo, G. Zhang, *Angew. Chem. Int. Ed.* **2016**, *55*, 9872-9876; b) B. Chen, W. Huang, H. Su, H. Miao, X. Zhang, G. Zhang, *Angew. Chem. Int. Ed.* **2020**, *59*, 10023-10026; c) X. Lin, J. Wang, B. Ding, X. Ma, H. Tian, *Angew. Chem. Int. Ed.* **2020**, 10.1002/anie.202012298.

[9] S. Kuila, A. Ghorai, P. K. Samanta, R. B. K. Siram, S. K. Pati, K. S. Narayan, S. J. George, *Chem. Eur. J.* **2019**, *25*, 16007-16011.

[10] F. Li, S. Guo, Y. Qin, Y. Shi, M. Han, Z. An, S. Liu, Q. Zhao, W. Huang, *Adv. Opt. Mater.* **2019**, *7*, 1900511.

- [11] Y. Wen, H. Liu, S. Zhang, Y. Gao, Y. Yan, B. Yang, *J. Mater. Chem. C* **2019**, *7*, 12502-12508.
- [12] a) Z. He, W. Zhao, J. W. Y. Lam, Q. Peng, H. Ma, G. Liang, Z. Shuai, B. Z. Tang, *Nat. Commun.* **2017**, *8*, 416; b) S. Hirata, M. Vacha, *Adv. Opt. Mater.* **2017**, *5*, 1600996; c) S. Kuila, S. Garain, S. Bandi, S. J. George, *Adv. Funct. Mater.* **2020**, *30*, 2003693;
- [13] K. Kanosue, S. Ando, *ACS Macro Lett.* **2016**, *5*, 1301-1305.
- [14] a) O. V. Dolomanov, L. J. Bourhis, R. J. Gildea, J. A. Howard, H. Puschmann, *J. Appl. Cryst.* **2009**, *42*, 339-341; b) G. M. Sheldrick, *Acta Crystallogr., Sect. A: Found. Adv* **2014**, *70*, C1437; c) G. M. Sheldrick, *Acta Crystallogr. C* **2015**, *71*, 3-8.
- [15] a) Gaussian 16, Revision A.03, M. J. Frisch, G. W. Trucks, H. B. Schlegel, G. E. Scuseria, M. A. Robb, J. R. Cheeseman, G. Scalmani, V. Barone, G. A. Petersson, H. Nakatsuji, X. Li, M. Caricato, A. V. Marenich, J. Bloino, B. G. Janesko, R. Gomperts, B. Mennucci, H. P. Hratchian, J. V. Ortiz, A. F. Izmaylov, J. L. Williams; F. Ding; F. Lipparini, F. Egidi, J. Goings, B. Peng, A. Petrone, T. Henderson, D. Ranasinghe, V. G. Zakrzewski, J. Gao, N. Rega, G. Zheng, W. Liang, M. Hada, M. Ehara, K. Toyota, R. Fukuda, J. Hasegawa, M. Ishida, T. Nakajima, Y. Honda, O. Kitao, H. Nakai, T. Vreven, K. Throssell, J. A. Montgomery Jr., J. E. Peralta, F. Ogliaro, M. J. Bearpark, J. J. Heyd, E. N. Brothers, K. N. Kudin, V. N. Staroverov, T. A. Keith, R. Kobayashi, J. Normand, K. Raghavachari, A. P. Rendell, J. C. Burant, S. S. Iyengar, J. Tomasi, M. Cossi, J. M. Millam, M. Klene, C. Adamo, R. Cammi, J. W. Ochterski, R. L. Martin, K. Morokuma, O. Farkas, J. B. Foresman, D. J. Fox, Gaussian, Inc., Wallingford CT, **2016**; b) A. D. Becke, *J. Chem. Phys.* **1993**, *98*, 1372-1377; c) C. Lee, W. Yang, R. G. Parr, *Phys. Rev. B* **1988**, *37*, 785-789; d) B. Miehlich, A. Savin, H. Stoll, H. Preuss, *Chem. Phys. Lett.* **1989**, *157*, 200-206; e) T. Yanai, D. P. Tew, N. C. Handy, *Chem. Phys. Lett.* **2004**, *393*, 51-57; f) T. Yanai, D. P. Tew, N. C. Handy, *Chem. Phys. Lett.* **2004**, *393*, 51-57; g) S. Hirata, M. Head-Gordon, *Chem. Phys. Lett.* **1999**, *314*, 291-299-57; h) E. van Lenthe, R. Van Leeuwen, E. J. Baerends, *Int. J. Quan. Chem.* **1996**, *57*, 281-293; i) E. van Lenthe, J. G. Snijders, E. J. Baerends, *J. Chem. Phys.* **1996**, *105*, 6505-6516; j) F. Wang, T. Ziegler, E. van Lenthe, S. van Gisbergen, E. J. Baerends, *J. Chem. Phys.* **2005**, *122*, 204103-204112; k) ADF2017, SCM, *Theoretical Chemistry*, Vrije Universiteit, Amsterdam, The Netherlands, <http://www.scm.com>.

[16] D. Cao, M. Hong, A. K. Blackburn, Z. Liu, J. M. Holcroft, J. F. Stoddard, *Chem. Sci.* **2014**, *5*, 4242–4248.

CHAPTER 2.2

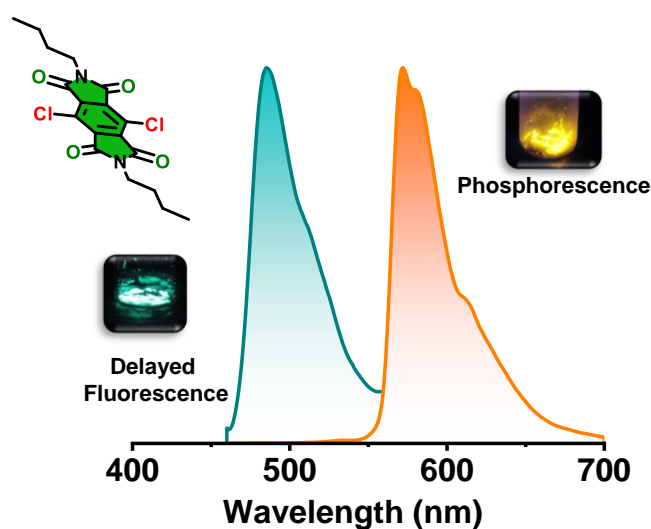
Delayed Fluorescence via Triplet-triplet Annihilation from a Pyromellitic Diimide Phosphor

CHAPTER 2.2

Delayed Fluorescence via Triplet-triplet Annihilation from a Pyromellitic Diimide Phosphor*

Abstract

Triplet harvesting via triplet-triplet annihilation (TTA) induced delayed fluorescence and phosphorescence from the same molecular crystal is rarely observed. Herein we realize efficient cyan afterglow delayed fluorescence and orange-red phosphorescence emission from structurally simple chloro substituted pyromellitic diimide in the crystalline state with an excellent quantum efficiency of 22 % in air. Multiple intermolecular halogen bonding interactions are responsible for efficient orange-red phosphorescence in the aggregated state by increasing intersystem crossing (ISC) channel and spin-orbit coupling (SOC). Detailed spectroscopic studies reveal that dominant cyan emission in the crystalline state is induced by the TTA process, which is further evident from laser intensity-dependent study. We envision that long-range π -stacking of the chromophores helps triplet migration along (010) plane that results in efficient TTA induced delayed fluorescence from sensitizer free purely organic phosphor



*Manuscript based on this work is under preparation.

2.2.1. Introduction:

In recent days, the scientific community has been eagerly waiting for the new efficient, purely organic triplet harvesters, especially organic phosphors due to the potential applications in optoelectronic display, devices, bioimaging, and perfect alternatives to the toxic heavy metal-based inorganic and organometallic complex.^[1] However, purely organic phosphors demand an efficient inter-system crossing (ISC) rate and significant spin-orbit coupling (SOC) for triplet emission.^[1] Therefore, along with the elegant molecular design strategy, a thoughtful stabilization process needs to be addressed for efficient ambient triplet harvesting due to instability of the triplet exciton towards vibrational and oxygen quenching.^[1] Thus, so far, crystallization of the phosphors,^[2] embedding the phosphors into the polymeric matrices,^[3] the host-guest strategy^[4] have become most popular in the scientific realm for stabilizing the triplets. Hitherto, delayed fluorescence via thermally activated delayed fluorescence (TADF) and triplet-triplet annihilation (TTA) are also another efficient ways to harvest the triplet excitons.^[5,6] Spatially separated covalently attached donor-acceptor molecular design strategy becomes the grand strategy to achieve TADF emission by reducing energy gap via generation of intermediate singlet charge-transfer (¹CT) state.^[5,7] While, there are only a few molecular designs available for TTA process where two triplets (of the annihilator) will fuse together and generate an excited singlet that will emit via delayed fluorescence without a sensitizer.^[8] Plausibly, the TTA process is complicated for purely organic emitters due to the involvement of a multistep photophysical process.^[6a,b] In most cases, the optoelectronic realm considered the TTA process as trespassers in delayed emission as the generated excited singlet via the TTA process becomes non-emissive in nature.^[9] Moreover, scientists believe that TTA is one of the reasons for triplet quenching which decreases the device efficiency.^[9] Although, TTA-based up-conversion is a well-known phenomenon in literature due to its ability to give anti-stokes emission and become a pervasive research field.^[6a,ba,10] The ability to upconvert the near-infra-red (NIR) light into UV-visible light is advantageous in bioimaging^[11a,b] and photo redox-catalysis^[11c] due to the excellent penetration power of the NIR light. However, the process requires a sensitizer and annihilator, where the sensitizer generates a triplet and transfers its triplet energy to the annihilator via the triplet-to-triplet dexter energy transfer process.^[6a,b10a] Then the triplet of the two annihilators collides together and generates an excited singlet which emits.^[6a,b10a]

However, in this two-component system, a sensitizer is necessary to breed the triplet, which is based on the typical toxic heavy-metal based organometallic complex.^[6a,b10a] On top of that, limited choice of sensitizer design prefers only metal porphyrin complex or few organo-metallic complex.^[6a,b10a] Moreover, the multistep process demands efficient Dexter energy transfer efficiency between sensitizer and annihilator for efficient triplet collision of annihilator.^[6a,b10a] However, there is a significant chance of triplet quenching which cannot be avoided. In this regard, sensitizer-free, purely organic chromophores can be envisioned to be a perfect choice of TTA emitter where the triplet loss can be mitigated. Although it is rare, which could be due to the formation of non-emissive singlets, the process still demands an elegant molecular design strategy for further advancement of the field. We envisage that only the purely organic phosphors can satisfy the criteria as it is an efficient triplet emitter, and the possibility of triplet collision exists.

In this chapter, we have designed a chloro substituted pyromellitic diimide (**CIPmDI**) derivative which shows dual highly efficient cyan delayed fluorescence emission and orange-red phosphorescence emission in the amorphous film and in the crystalline state with an excellent photoluminescence quantum yield of 22 % in air. It is noteworthy here that we have observed efficient monomeric phosphorescence emission in the polymeric matrix with very low doping concentration having phosphorescence quantum yield of 30 %. Detailed spectroscopic analysis revealed that delayed fluorescence is originated via TTA process which is further evident from the laser intensity dependent study. We hypothesized that long range π -stacking with small π - π distance of the **CIPmDI** along (010) plane increases the plausibility of triplet collision via efficient triplet migration. The dual delayed fluorescence via TTA and phosphorescence emission from a single molecule in the crystalline state is very difficult to realize and rarely observed.

2.2.2. Molecular Design:

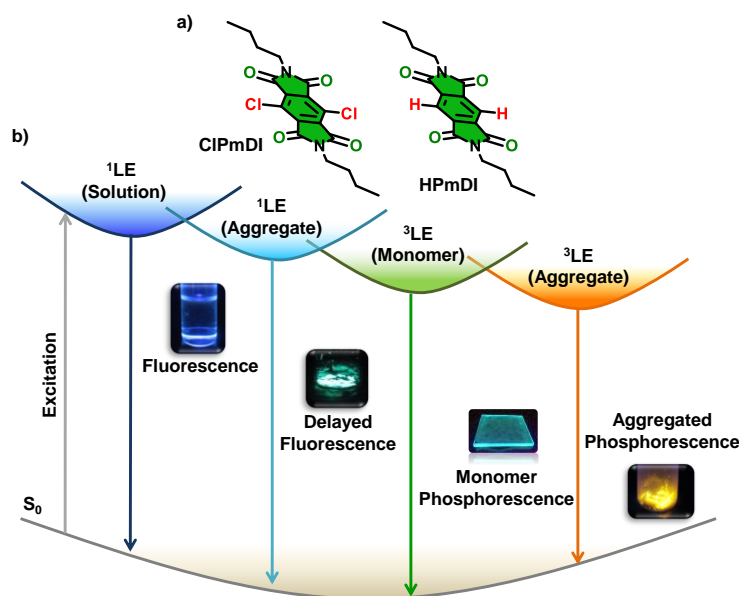


Figure 2.2.1 a) Molecular structures of **CIPmDI** and **HPmDI**. b) Simplified Jablonski diagram showing 1LE fluorescence in solution (THF), 3LE phosphorescence in PMMA matrix, delayed fluorescence, and phosphorescence simultaneously in the crystalline state.

Our group recently made a significant contribution in the burgeoning field of organic phosphor and came up with various arylene diimides especially pyromellitic diimide derivatives for efficient phosphorescence emission in the crystalline, amorphous, and solution state.^[12] Arylene diimides are special class of molecules with which increases the ISC rate significantly as the nascent molecule bears multiple carbonyl groups inherently, and π -core that can be easy substituted with heavy atoms to increase the SOC significantly.^[12] Recently we have observed dual phosphorescence emission from bromo and iodo substituted pyromellitic diimides in the monomeric and aggregated state.^[12d] In this chapter we have synthesized **CIPmDI** from a durene derivative, and it was fully characterized by nuclear magnetic resonance spectroscopy (NMR), mass spectrometry, and single-crystal X-ray diffraction (Scheme 2.2) to harvest the triplet exciton via TTA induced delayed fluorescence. The necessary conditions for the TTA process are i) efficient ISC rate to generate the triplet and ii) long triplet diffusion length with efficient triplet migration.^[13] We envisaged that organic phosphor would be the perfect choice for the TTA process as an efficient ISC rate is observed upon heavy or hetero atom substitution. Long-range ordering of π stacking is also possible by

selective choice of phosphor. Keeping this in mind, we have alleviated the scenario using **CIPmDI**, where efficient ISC is expected due to the presence of multiple carbonyl groups in the molecular design.

2.2.3. Theoretical Calculations:

We have synthesized **CIPmDI** from a durene derivative and was fully characterized by nuclear magnetic resonance spectroscopy (NMR), mass spectrometry, and single-crystal X-ray diffraction (Scheme 2.2.1). The fundamental prerequisites of a triplet emitter are following El Sayed's rule and having significant SOCME between singlet and triplet state so that the ISC rate will be fast. The computed natural transition orbitals (NTOs) of **CIPmDI** in the monomeric state show that S_1 is $n-\pi^*$ in nature and T_3 and T_1 are $\pi-\pi^*$ in nature (Figure 2.2.2). Change in the molecular orbital configuration from singlet to triplet state suggests efficient ISC from S_1 to T_3 and T_1 states. Furthermore, very high SOCME values between $S_1 \rightarrow T_3$ and $S_1 \rightarrow T_1$ (94.78 cm^{-1} and 7.46 cm^{-1} , respectively) will help to access the triplet under cryogenic conditions or inert atmosphere (Figure 2.2.2). We envisage that the designed **CIPmDI** will show efficient phosphorescence emission in the solid-state under ambient conditions.

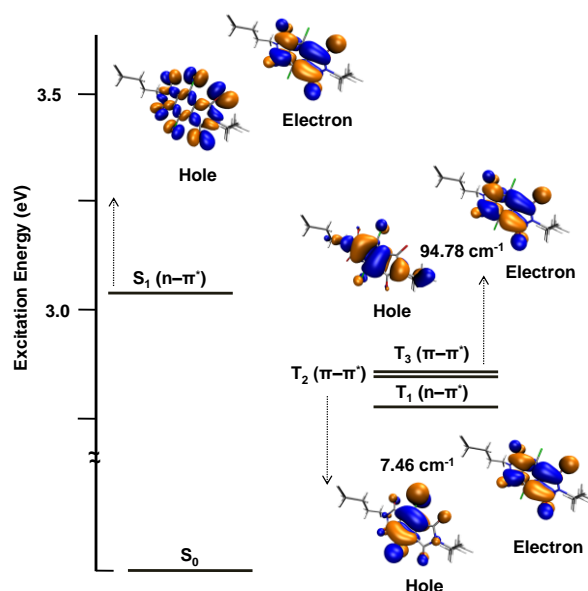


Figure 2.2.2 Ground state geometries, relative excitation energies and their corresponding hole, electron wavefunctions, and SOC matrix elements for **CIPmDI** optimized using *B3LYP* functional in conjunction with *6-31+g(d)* basis set for C, N, O, H and *LANL2DZ* basis set for Cl with effective core potential (Hole and electron wavefunctions are shown below and above in the schematic, respectively).

2.2.4. Spectroscopic Studies in Solution-state:

We have done spectroscopic characterization of these molecules in solution and solid states and subsequently performed steady-state and time-resolved emission experiments for detailed understanding. Photophysical studies of **CIPmDI** in tetrahydrofuran (THF) at a concentration of 0.05 mM showed a characteristic π - π^* absorption band in the 280 to 375 nm region (Figure 2.2.3a). Corresponding emission spectra in THF ($\lambda_{exc.} = 340$ nm) showed weak fluorescence emission in the 380 nm to 550 nm region (Figure 2.2.3a), with a short average lifetime of ~ 0.78 ns (Figure 2.2.3b). Sharp vibronic features in the emission spectra suggest locally excited nature of the emission, similar to the previously reported derivatives. However, due to the inefficient ISC, vibrational, and oxygen quenching, we have not observed any phosphorescence emission and long lifetime components at room temperature in the solution state. Next, to access the triplets and to understand the phosphorescence emission in the monomeric state, we have reduced the vibrational dissipation by freezing the THF solution (0.05 mM) at 77 K and performed the experiments. A red-shifted, highly intense emission band in the 450 to 650 nm region with an emission maximum at 500 nm was observed along with the locally excited fluorescence band in the high energy region (Figure 2.2.3a). The corresponding lifetime decay experiment of the red-shifted emission shows an average lifetime of ~ 131 ms, suggesting excellent stabilization of triplets at low temperatures (Figure 2.2.3c).

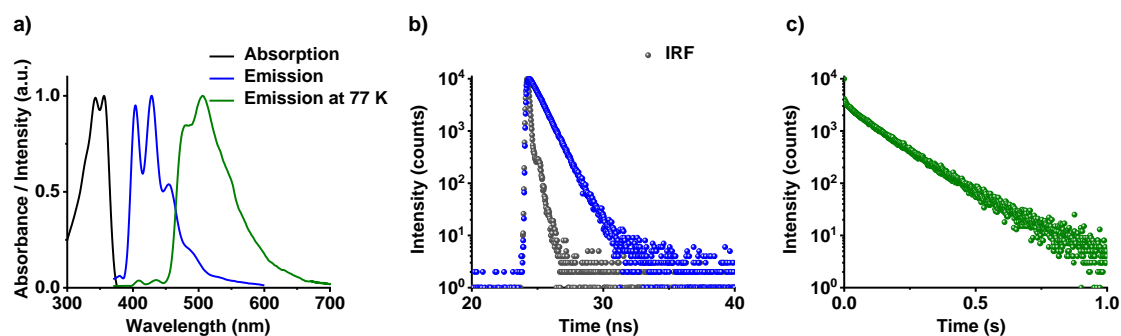


Figure 2.2.3. a) Normalized absorption (black line), fluorescence emission (blue line) and phosphorescence emission (at 77 K, green line) spectra, b) fluorescence ($\lambda_{exc.} = 373$ nm, $\lambda_{collected} = 430$ nm) and c) phosphorescence ($\lambda_{exc.} = 340$ nm, $\lambda_{collected} = 500$ nm) lifetime decay profile of **CIPmDI** ($[c] = 0.05$ mM, $\lambda_{exc.} = 340$ nm).

2.2.5. Ambient Phosphorescence in Polymer Matrix:

However, to harvest the triplets under ambient conditions in processable polymer films, we first dispersed **CIPmDI** in poly(methylmethacrylate) (PMMA) matrix at very low concentrations (1 wt.% with respect to PMMA). PMMA is an amorphous polymeric host known to stabilize triplet excitons by minimizing vibrational dissipation and from oxygen quenching, thereby enhancing the triplet contribution of the total emission.^[3a,12b] We realized a strong emission band in the 400-700 nm region with a maximum of 500 nm (Figure 2.2.4a). The high lifetime of this red-shifted emission ($\tau_{\text{avg.}} = 2.3$ ms) and its resemblance with that of the emission of the pure molecules in frozen THF at 77 K hints toward the phosphorescence nature of emission in the monomeric state (Figures 2.2.4a,b). To confirm the phosphorescence nature of the emission we performed the photophysical study in a vacuum (Figures 2.2.4c,d). The significant enhancement in the photo-luminescence emission intensity (7.42-fold) and lifetime (from $\tau_{\text{avg.}} = 2.3$ ms to $\tau_{\text{avg.}} = 31.8$ ms) confirms the phosphorescence nature of the emission (Figures 2.2.4c,d). This significant enhancement of emission intensity and lifetime explicitly indicates the contribution of triplet excitons in the emission mechanism, as these excitons are prone to substantial quenching in the presence of oxygen.^[1] Next, to attest to the phosphorescence nature of the emission in the monomeric state, we have performed a temperature-dependent study (1 wt. % of **CIPmDI** in PMMA). The gradual increase in the overall emission intensity and lifetime with decreasing temperatures (from 300 K to 20 K) reaffirms the phosphorescence nature of the emission as reduced vibrational dissipation at lower temperatures increases the phosphorescence efficiency (Figures 2.2.4e,f). Therefore, we hypothesized that the ubiquities of four carbonyl groups inherently in the molecular structure of PmDI and the heavy-atom effect of chlorine atom is operative here to result in substantial ISC with efficient SOCME between singlet and triplet state are sufficient enough to show efficient ambient RTP in a processable polymer film. The absolute phosphorescence quantum efficiency of 1 wt. % of **CIPmDI** in PMMA is 4 % in air which is increased to 30 % in oxygen free atmosphere.

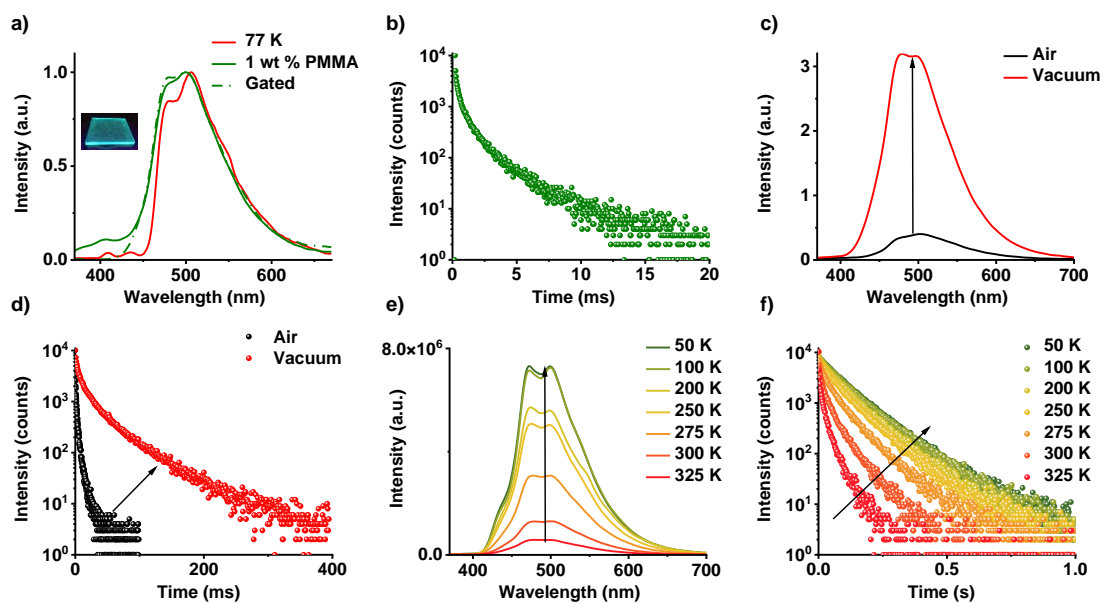


Figure 2.2.4. a) Normalized steady-state emission spectrum (green line), gated emission spectrum (green dot line), emission spectrum at 77 K (red line) and b) lifetime decay profile of **CIPmDI** in PMMA matrix. c) Steady-state emission spectra, and d) lifetime decay profile of **CIPmDI** in PMMA matrix in air and vacuum. Temperature-dependent e) emission spectra and f) lifetime decay profile of **CIPmDI** in PMMA matrix ($\lambda_{exc.} = 340 \text{ nm}$, $\lambda_{collected} = 500 \text{ nm}$, 1 wt. % **CIPmDI** doped in PMMA matrix is used to perform all the experiments).

2.2.6. Ambient Triplet-Triplet Annihilation Induced Delayed Fluorescence and Phosphorescence in the Aggregated State:

Interestingly, gradual evolution of a new red-shifted band (orange-red region) in the emission spectra with maximum at 578 nm is observed upon increasing the doping concentration of **CIPmDI** in the PMMA matrix (5 to 50 wt.% with respect to PMMA) (Figure 2.2.5a). We envisaged the same is due to the phosphor's aggregation at the higher concentration in the PMMA matrix. Further red-shift in the excitation spectra, when monitored at 650 nm, confirms the aggregation propensity of the molecule at higher concentrations (Figure 2.2.5b). However, the milli second scale lifetime of the new red-shifted band suggests its delayed character of the emission (Figure 2.2.5c). Surprisingly the higher energy emission band becomes narrower and blue-shifted compared to the original monomeric phosphorescence band, and the maximum shifted to 483 nm with increasing the doping concentration of **CIPmDI** in the PMMA matrix (Figure 2.2.5a). Further to understand in detail, we have monitored excitation spectra at

470 nm, and astonishingly the excitation spectra are red-shifted compared to the monomeric **CIPmDI** in PMMA matrix (Figure 2.2.5d). Time-resolved emission decay experiments of the 50 wt. % doped **CIPmDI** film shows a high emission lifetime, which differs from the monomeric phosphorescence lifetime (Figure 2.2.5c). The observations suggest that the origin of the high energy emission band for higher wt. % of **CIPmDI** doped in PMMA is different from the monomeric 1 wt. % of **CIPmDI** in PMMA and originating upon aggregation of the chromophores in high doping concentration.

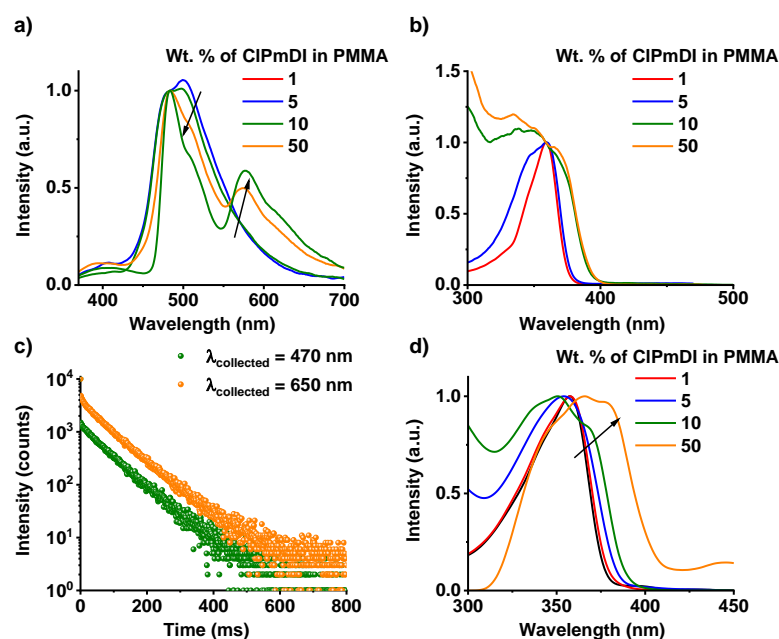


Figure 2.2.5. a) Normalized steady-state emission spectra of PMMA films with different wt. of **CIPmDI**. b) Normalized steady-state excitation spectra of **CIPmDI** monitored at 650 nm. c) lifetime decay profile of 50 wt.% **CIPmDI** doped PMMA film. d) Normalized steady-state excitation spectra of **CIPmDI** monitored at 470 nm. ($\lambda_{\text{exc.}} = 340$ nm, all experiments were performed under air).

To understand the dual emission behavior in detail in the aggregated state, we have studied **CIPmDI** in the crystalline state (Figure 2.2.6). Interestingly, the single crystal of **CIPmDI** showed greenish-yellow emission with dual emission bands centered at 483 and 578 nm, respectively, similar to the emission obtained for the PMMA films with high doping concentration of the phosphor (Figure 2.2.6a). High lifetime values of 111 ms and 118 ms were obtained when we performed lifetime decay at 470 nm and 650 nm, respectively, hinting towards the long-lived nature of the emission, which is further confirmed by the gated emission spectra (delay time = 1 ms)

(Figures 2.2.6b,c). The excitation spectra in the crystalline state clearly show the aggregated band, and we observed a similar emission spectral feature upon selectively excited at the aggregated band ($\lambda_{\text{exc.}} = 450$ nm) (Figures 2.2.6a,c). **CIPmDI** in the crystalline state show a high photoluminescence quantum yield of 22 % in air and 24.5 % under vacuum.

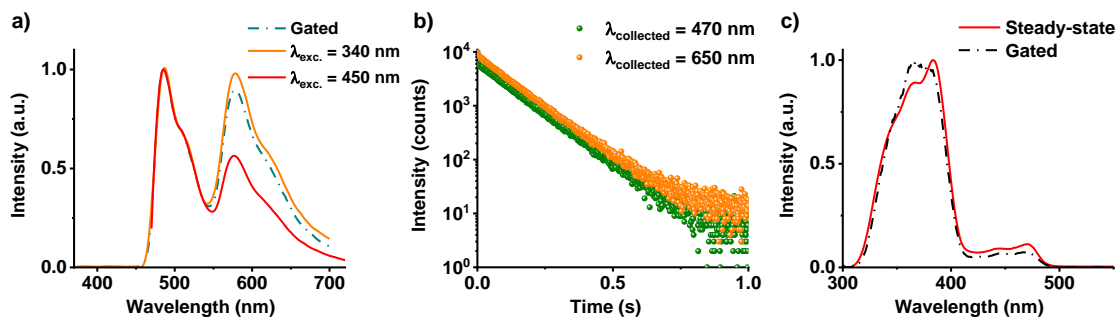


Figure 2.2.6. a) Normalized steady-state and gated emission spectra, b) lifetime decay profile and c) excitation spectra of **CIPmDI** in the crystalline state ($\lambda_{\text{exc.}} = 340$ nm, delay time = 1 ms, all experiments were performed under air).

However, to understand the detailed delayed nature of the dual emission bands centered at 483 and 578 nm, respectively, we have performed the temperature-dependent experiment of **CIPmDI** in the crystalline state which is the most efficient tool to differentiate between delayed fluorescence and phosphorescence. Intensified emission intensity and lifetime upon decreasing the temperature (from 340 K to 20 K) attested the phosphorescence nature of the low energy emission band ($\lambda_{\text{maximum}} = 578$ nm) which is plausibly the aggregated phosphorescence observed previously for bromo and iodo substituted PmDIs (Figures 2.2.7a,b). In contrast, the emission intensity and lifetime of the high energy emission band ($\lambda_{\text{maximum}} = 483$ nm) gradually decreases with a decrease in temperature hints towards the delayed nature of the emission (Figures 2.2.7a,c). We hypothesized that these opposite trends of the two bands in temperature-dependent experiments unambiguously confirm that two mechanisms are operative in the crystalline state. Further, the delayed emission spectra at two extreme temperatures (20 K and 340 K) were carried out to calculate the triplet to singlet energy gap (ΔE_{ST}) to further understand the delayed nature of the high energy emission band (Figure 2.2.7d). We envisioned that the plausible nature of the delayed emission could be TADF, TTA or delayed fluorescence via hot exciton transfer. The calculated ΔE_{ST} is

~ 430 meV is significantly high and rules out the plausibility of TADF emission as reverse intersystem crossing will be inefficient here (Figure 2.2.7d).

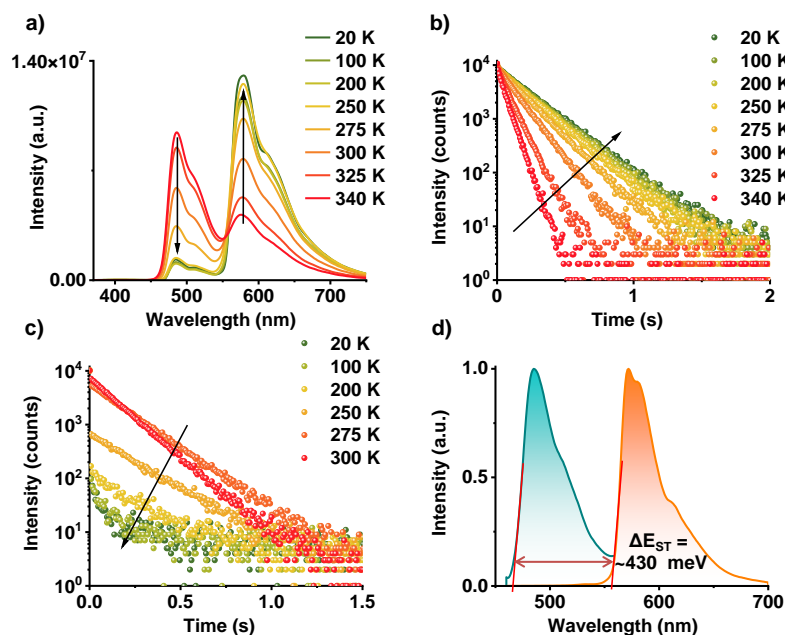


Figure 2.2.7. Temperature dependent a) steady-state emission spectra, b) phosphorescence lifetime decay profile ($\lambda_{\text{collected}} = 650$ nm), and c) delayed fluorescence ($\lambda_{\text{collected}} = 470$ nm) lifetime decay profile of **CIPmDI** in crystalline state. d) Delayed emission spectra at 340 K (cyan line), at 20 K (orange line) of **CIPmDI** in crystalline state ($\lambda_{\text{exc.}} = 340$ nm, delay time = 1 ms, all experiments were performed under vacuum).

We realized that laser intensity dependent study will be perfect here to conclude possible delayed fluorescence mechanism. The laser intensity dependent study of the **CIPmDI** in the crystalline state showed that the high energy emission band ($\lambda_{\text{maximum}} = 483$ nm) dominates at high laser intensity and gradually decreases upon decreasing laser power (Figures 2.2.8a.). At the low laser intensity peak reversal is realized and phosphorescence peak dominates which is clearer when we have normalized the emission spectra at 578 nm (Figures 2.2.8b). The quadratic relationship between triplet population and emission intensity of the higher energy band is due to the involvement of two triplets in the up-conversion process (Figures 2.2.8c,d). The laser intensity dependent study rules out the plausibility of the TADF and delayed fluorescence via hot exciton transfer mechanism where linear relationship with between triplet population and emission intensity is expected.

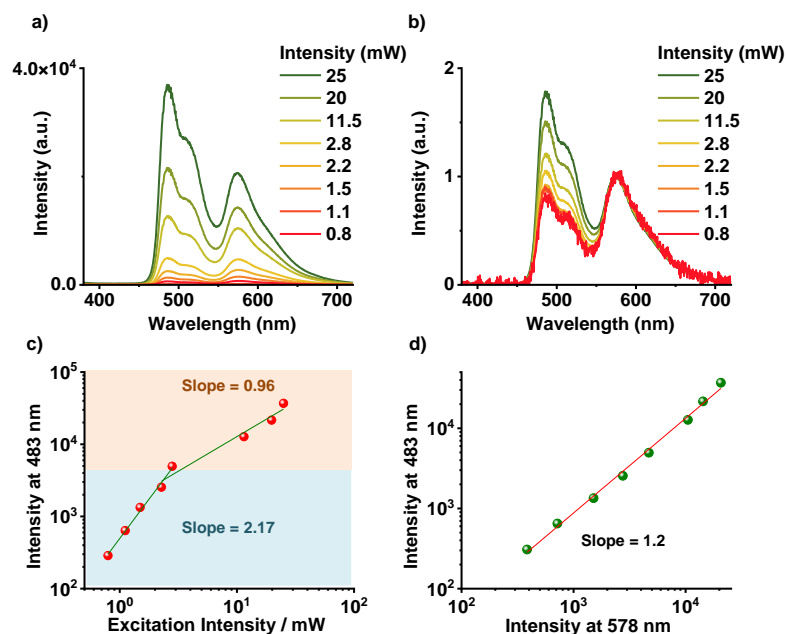


Figure 2.2.8. Excitation intensity-dependent a) steady-state emission spectra and b) normalized steady-state emission spectra (normalized at 578 nm) of **CIPmDI** in the crystalline state. The corresponding double-logarithmic plot of c) TTA-induced delayed fluorescence versus laser excitation power and d) TTA-induced delayed fluorescence versus phosphorescence peak intensity. ($\lambda_{exc.} = 355 \text{ nm}$).

2.2.7. Single-crystal X-ray Crystallography Analysis:

Further, to understand the impact of the molecular organization on the delayed fluorescence and phosphorescence emission, we have solved the crystal structure of **CIPmDI** (Figure 2.2.9a). We observed multiple intra (3.178 Å) and intramolecular (3.057 Å) halogen-carbonyl interactions present in the lateral direction that helped to form extended arrangement in the same plane (Figure 2.2.9b). Further slipped stacked organization is observed with a π - π distance of 3.886 Å along the (010) plane (Figure 2.2.9c). Halogen- π (3.484 Å) and halogen-halogen (3.885 Å) interactions with the help of π - π interaction formed an extended arrangement (Figure 2.2.9c). We hypothesized that multiple halogen bonding interactions form a rigid 3D network of chromophores, decreasing vibrational dissipation and increasing the SOC significantly to stabilize the triplets.

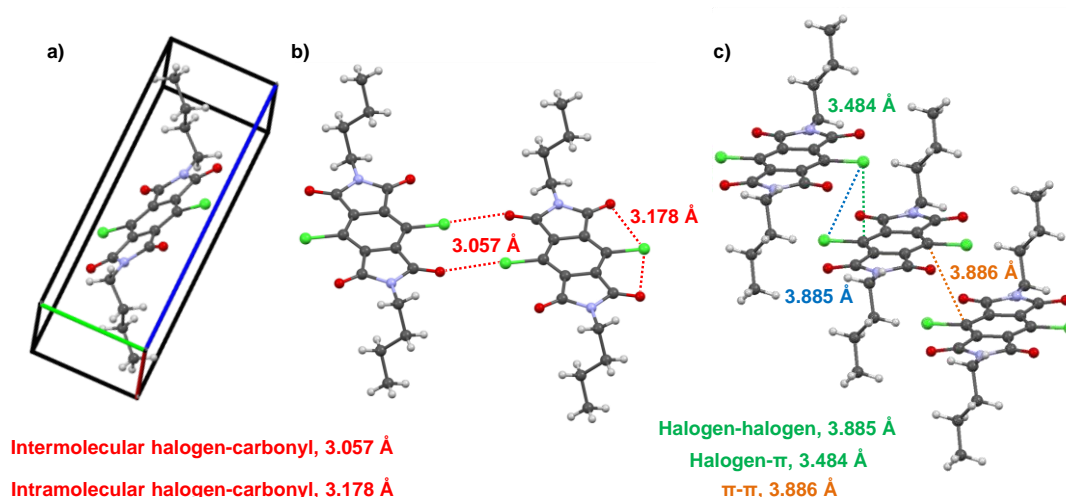


Figure 2.2.9. a) Unit cell, b) intramolecular and intermolecular halogen-carbonyl interaction and c) slipped stacked arrangement showing various halogen bonding interactions and π - π stacking of CIPmDI single crystal.

2.2.8. Theoretical Calculations of CIPmDI Dimer:

Further, to understand the role of intermolecular interaction and halogen bonding interaction in phosphorescence emission, we have computed NTOs of dimeric CIPmDI (Figure 2.2.10). Theoretical calculations coincide with our experimental findings and precisely explain that an increased number of intersystem crossing channels and significant SOCME is responsible for efficient phosphorescence emission of the crystalline state (Figure 2.2.10). Although intermolecular halogen bonding interactions and computed NTOs explain the efficient phosphorescence in the crystalline state, further understanding is required to explain efficient TTA delayed fluorescence in the crystalline state.

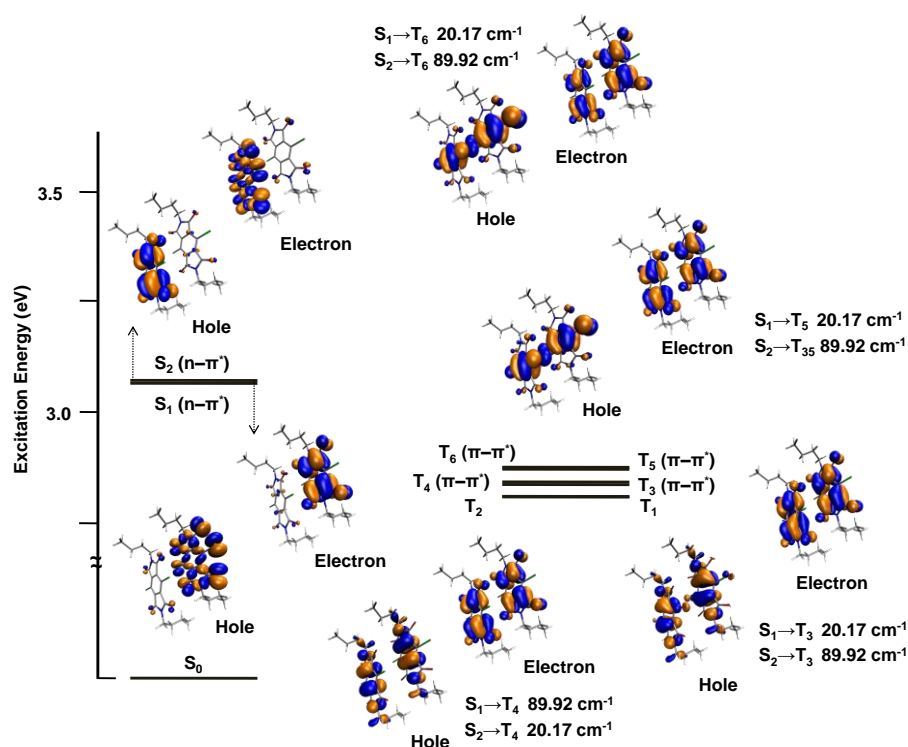


Figure 2.2.10. Ground state geometries, relative excitation energies and their corresponding hole, electron wavefunctions, and SOC matrix elements for dimeric **ClPmDI** optimized using *B3LYP* functional in conjunction with 6-31+g(d) basis set for C, N, O, H and LANL2DZ basis set for Cl with effective core potential.

2.2.9. TTA Induced Delayed Fluorescence in HPmDI Single Crystal:

ClPmDI shows efficient ambient phosphorescence in the orange-red region in the crystalline state. Further, we have observed long-range π stacking with a π - π distance of 3.886 Å driven by multiple halogen bonding interactions along the (010) plane and we envisage efficient triplet migration along this plane (Figure 2.2.11). We have made the control molecule **HPmDI** without any heavy atom in the core for proof of concept. We observed dual delayed fluorescence (Figures 2.2.12a,b) and phosphorescence (Figures 2.2.12a,c) behavior from the **HPmDI** derivative similar to the **ClPmDI** derivative. Similar molecular packing with long-range ordering is realized with a π - π distance of 3.406 Å (Figure 2.2.12d). We can hypothesize that the long-range order of π stacking is essential for efficient triplet migration, which is responsible for TTA to occur. Although **HPmDI** meets the criteria of long-range π -stacking, due to the absence of heavy atoms in the molecular design, its TTA efficiency is less. We hypothesized that

along with the long-range ordering of π -stacks, efficient triplet generation is also essential for triplet fusion.

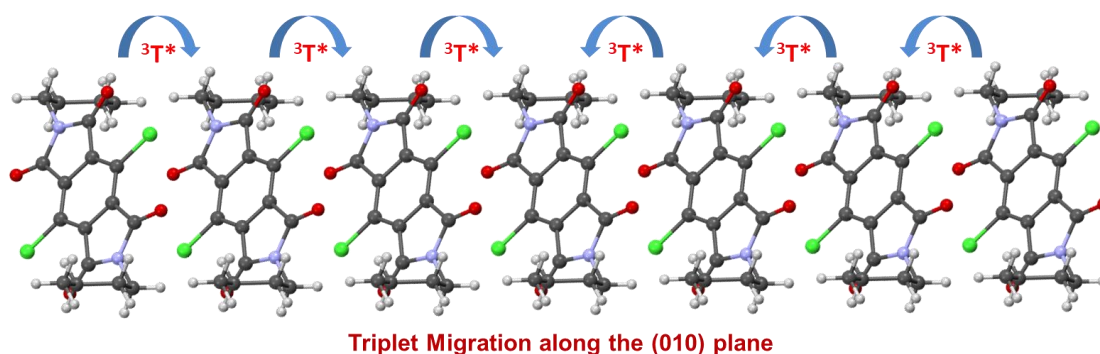


Figure 2.2.11. Long-range slipped stacked arrangement showing the plausible way of triplet migration in *CIPmDI* single crystal.

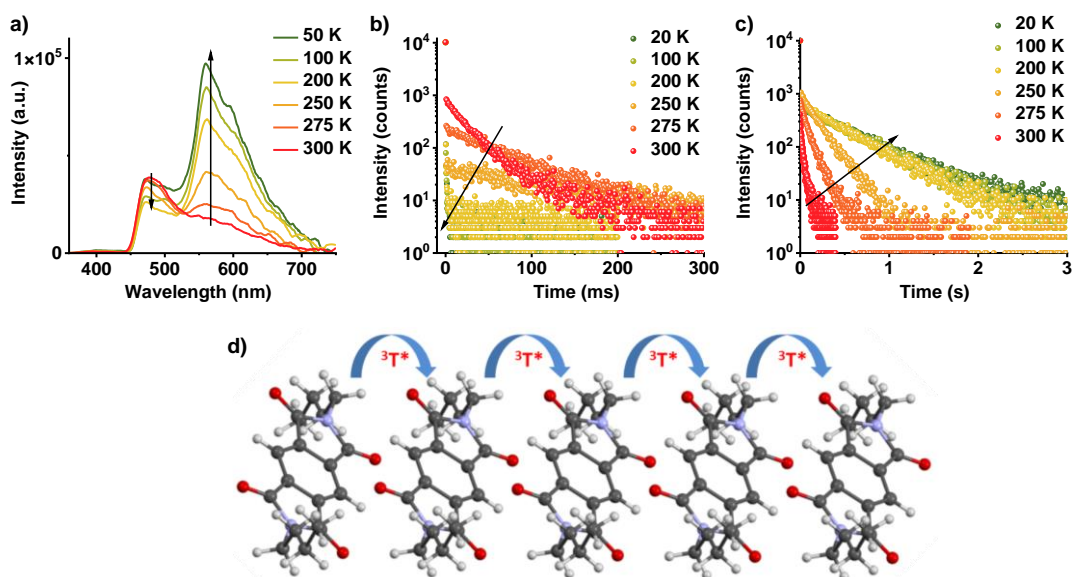


Figure 2.2.12. Temperature-dependent a) gated emission spectra, b) delayed fluorescence ($\lambda_{\text{collected}} = 470$ nm) and c) phosphorescence lifetime decay profile ($\lambda_{\text{collected}} = 650$ nm) of *HPmDI* in the crystalline state. d) Long-range slipped stacked arrangement showing plausible way of triplet migration in *HPmDI* single crystal. ($\lambda_{\text{exc.}} = 340$ nm, gate time = 1 ms, all experiments were performed under vacuum).

2.2.10. Conclusions:

In conclusion, here, we have achieved efficient dual delayed fluorescence and phosphorescence from structurally simple chloro substituted pyromellitic diimides in the aggregated state with high photoluminescence quantum yield of 22 % with

excellent thermal and air stability. Detailed spectroscopy, crystal structure, and laser intensity-dependent study affiliated the strong delayed cyan emission in the crystalline state is induced by the TTA process where orange-red emission is due to phosphorescence. Multiple halogen bonding interactions (halogen-carbonyl, halogen- π) increased the number of ISC channels and SOC significantly and helped to achieve efficient orange red-emitting phosphorescence emission. Further long-range slipped stacking driven by halogen- π and π - π interaction along the (010) plane is helpful to meet the criteria for efficient triplet migration by increasing triplet diffusion length for triplet fusion to occur which resulted in efficient delayed fluorescence in the aggregated and crystalline state. Further study of the control molecule **HPmDI** suggested that along with the long-range π stacking, efficient ISC is also necessary for TTA-induced delayed fluorescence in purely organic chromophores. We envisioned that an elegant molecular design of organic phosphor would be the ideal choice for sensitizer-free TTA-induced delayed fluorescence to occur due to their excellent triplet formation ability. We hope that the current hypothesis of heavy-atom substituted organic phosphor having long-range π stacking will open many opportunities to achieve TTA-based delayed fluorescence in the near future.

2.2.11. Experimental Section:

2.2.11.1. General Methods:

NMR Measurements: ^1H and ^{13}C NMR spectra were recorded on a BRUKER AVANCE-400 Fourier transformation spectrometer with 400 and 100 MHz, respectively. The spectra were calibrated with respect to the residual solvent peaks. The chemical shifts are reported in parts per million (ppm) with respect to TMS. Short notations used are s for singlet, d for doublet, t for triplet, q for quartet, and m for multiplet.

Optical Measurements: Electronic absorption spectra were recorded on a Perkin Elmer Lambda 900 UV-Vis-NIR spectrometer, and emission spectra were recorded on FLS1000 spectrometer, Edinburgh Instruments. Solution state UV-Vis and emission spectra were recorded in 1 mm path length cuvette. Fluorescence spectra of films were recorded in front-face geometry to avoid self-absorption.

Lifetime Measurements and Quantum Yield: Fluorescence lifetimes were performed on a Horiba Delta Flex time-correlated single-photon-counting (TCSPC) instrument. A

373 nm LED laser diode with a pulse repetition rate of 1 MHz was used as the light source. The instrument response function (IRF) was collected using a scatterer (Ludox AS40 colloidal silica, Sigma-Aldrich). Phosphorescence lifetime ($\lambda_{\text{exc.}} = 340$ and 440 nm) and gated emission were measured on FLS1000 spectrometer, Edinburgh Instruments equipped with a micro flash-lamp ($\mu\text{F}2$) set-up. Quantum yields were estimated using an integrating sphere in the same instrument.

High Resolution Mass Spectroscopy (HRMS): HR-MS was carried out using Agilent Technologies 6538 UHD Accurate-Mass Q-TOFLC/MS.

Matrix-Assisted Laser Desorption Ionization (MALDI): MALDI was performed on a Bruker daltonics Autoflex Speed MALDI TOF System (GT0263G201) spectrometer using trans-2-[3-(4-tert-Butylphenyl)-2-methyl-2-propenylidene] malononitrile (DCTB) as the matrix.

Single crystal X-ray crystallography: Suitable single crystal of the **CIPmDI** and **HPmDI** compound was mounted on a thin glass fibre with commercially available super glue. Intensity data were collected at 302 K on a Bruker Smart X2 APEX II CCD diffractometer having a normal focus, 2.4 kW sealed tube X-ray source with graphite monochromatic Mo-K α radiation ($\lambda = 0.71073$ Å) operating at 50 kV and 30 mA, with ω scan mode an exposure time of 1 s per frame. The programme SAINT was used for integration of diffraction profiles, and absorption correction was made with SADABS programme. All the structure were solved by direct method, and refinement were done with full matrix least square on F^2 using SHELXL-2014 and Olex2 software. All of the non-hydrogen atoms were refined anisotropically.

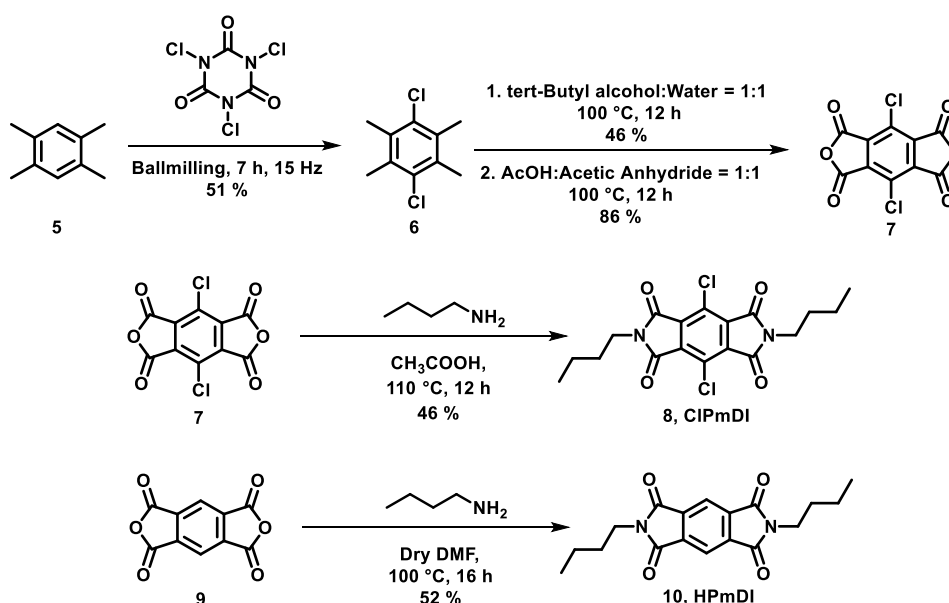
Computational Details: Ground State (S_0) of **CIPmDI** monomer molecules were optimized using density functional theory (DFT), and electronic absorption spectra were calculated using time-dependent density functional theory (TD-DFT) as implemented in the Gaussian 16 software.^[14a] Ground state (S_0) optimization and frequency calculations were performed employing B3LYP^[14b-d] exchange functional with 6-31+g(d) basis set except for Br and I, for which LANL2DZ basis set was used with the corresponding effective core potential (ECP). While the excited-state calculations were performed using long-range corrected CAM-B3LYP^[14e] exchange-correlation functional with the same basis sets as mentioned before. Ground state frequency calculations were performed to confirm the absence of any unstable normal

mode. The first singlet excited state (S_1) of monomers was optimized at the TD-DFT level of theory. While the first triplet excited states (T_1) were also optimized at the TD-DFT level of theory within the Tamm-Dancoff approximation (TDA) to overcome the triplet instability issue.^[14f] The spin-orbit coupling (SOC) effect was considered to be a perturbation of the scalar relativistic Kohn-Sham orbitals after SCF and TD-DFT calculations (pSOC-TDDFT).^[14g-i] The SOC matrix elements were calculated using B3LYP with a Slater-type all-electron TZP basis set for all atoms as implemented in the ADF package.^[14j]

2.2.11.2. Protocol of Sample Preparation:

All solution state studies were performed, keeping the final concentration of the samples to 0.05 mM from a stock solution of THF (1 mM). For thin films, **CIPmDI** molecules (3 mg each) were mixed with appropriate amount of PMMA (depending on the weight ratio) in a total 2 ml chloroform solution. (For example, 1 wt. % dye: PMMA consists of 3 mg dye in 300 mg PMMA). This mixture was then heated at 50 °C for 10 minutes, followed by sonication (5 minutes) to completely dissolve all the components. Then, 0.5 mL of this solution was drop-casted on a clean glass substrate. Finally, the drop-casted thin films were dried at 60 °C for 30 minutes prior to the photophysical studies. For the phosphorescence studies of the crystal, a small amount of the crystal was placed in between two quartz plates.

2.2.12. Synthetic Schemes and Procedures:



Scheme 2.2. Synthetic schemes of CIPmDI and HPmDI.

Materials: Pyromellitic dianhydride was purchased from Sigma-Aldrich, Durene, *n*-Butylamine, and Potassium Permanganate were purchased from Alfa-Aesar. Trichloro cyanuric acid was purchased from TCI, Acetic acid and *tert*-butyl alcohol were purchased from Spectrochem and used without further purification.

Synthetic Procedures:

Synthetic procedure for CIPmDI and HPmDI:

Synthesis of 6: Durene (**5**) (4 g, 29.80 mmol) and trichlorocyanuric acid (TCCA) (3.8 g, 20.86 mmol) were ball-milled at room temperature for 7 hours at 15 Hz rotation speed. The reaction mixture was dissolved in dichloromethane (DCM) and filtered. The filtrate was evaporated to get an off-white solid. Column chromatography was performed using *n*-hexane as an eluent to get the pure product as a white solid (3.1 g, 51 % yield).

^1H NMR (CDCl_3 , 400 MHz) δ (ppm)=2.38 (s, 6H); ^{13}C NMR (CDCl_3 , 100 MHz), δ (ppm) = 133.4, 133.1, 18.2.

Synthesis of 7: In a 250 ml 2 neck round bottom flask, compound **6** (3 g, 14.78 mmol) was taken. 60 ml (1:1 v/v) *tert*-Butyl alcohol and water were added into it. Then the temperature was increased to 90 °C. Potassium permanganate (KMnO_4) was added in portions over 1 hour. The reaction was stirred for 24 hours. The mixture was cooled to room temperature, and 10 ml of ethanol was added to quench the unreacted KMnO_4 . The mixture was filtered via celite filtration. Drop by drop, concentrated HCl was added to it to make pH~ 2. The filtrate was evaporated under reduced pressure, and 300ml acetone was added into it. The mixture was again stirred for 12 hours at room temperature. The mixture was filtered, and the filtrate was evaporated to get a white solid as product (2.2 g, 46% yield). We proceed to the next step without further purification.

In a 100 ml round bottom flask, white solid (2.2 g, 6.8 mmol) was taken. 60 ml acetic acid and acetic anhydride (1:1 v/v) were added. Then the reaction mixture was stirred for 12 hours at 100 °C. Acetic acid and acetic anhydride were evaporated under reduced pressure to get a pale-yellow product (1.9 g, 97 % yield). Due to the very low solubility, we proceed to the next step without any further purification.

Synthesis of CIPmDI: In a 100 ml round bottom flask, compound **7** (0.5 g, 1.74 mmol) was taken, and 25 ml acetic acid was added to it. The mixture was stirred for 15

minutes. *n*-butyl amine (280 mg, 3.83 mmol) was mixed with 10 ml acetic acid and added dropwise into the mixture. The reaction mixture was stirred at 110 °C for 16 hours. The mixture was cooled to room temperature and poured into ice-cold water to get the white precipitate. The solid was filtered, and column chromatography was performed using chloroform as an eluent to get the pure product as an off-white solid (420 mg, 61 % yield).

^1H NMR (CDCl_3 , 400 MHz) δ (ppm) = 3.73 (t, 4H, $J = 7.4$ Hz), 1.72-1.65 (m, 4H), 1.42-1.33 (m, 4H), 0.96 (t, 6H, $J = 7.4$ Hz); ^{13}C NMR (CDCl_3 , 100 MHz), δ (ppm) = 163.2, 134.7, 127.1, 38.7, 30.3, 20.0, 13.6; APCI-HR-MS (negative mode): m/z calculated for $\text{C}_{18}\text{H}_{18}\text{Cl}_2\text{N}_2\text{O}_4$: 396.0644, found: 396.0369 [M].

Synthesis of HPmDI: In a 100 ml round bottom flask, compound **9** (0.50 g, 2.4 mmol) was taken in a 100 ml round bottom flask, and 50 mL of dry DMF was added into it and stirred at room temperature for 30 minutes. Then *n*-butylamine (0.37g, 5.1 mmol) was added into the reaction mixture, and it was allowed to stir for 16 hours at 100°C. After completion of the reaction, 100 ml water was added to this reaction mixture to result in a white precipitate. The precipitate was then filtered and dried under vacuum for 10 hours. The white crude solid was then purified by silica-gel (100-200 mesh) column chromatography using chloroform as an eluent to obtain the pure product as white solid (0.39 g, 52 % yield).

^1H NMR (CDCl_3 , 400 MHz), δ (ppm) = 8.25 (s, 2H), 3.73 (t, 4H, $J = 7.4$ Hz), 1.72-1.64 (m, 4H), 1.41-1.32 (m, 4H), 0.97 (t, 6H, $J = 7.4$ Hz); ^{13}C NMR (CDCl_3 , 100 MHz), δ (ppm) = 166.3, 137.3, 118.1, 38.5, 30.5, 20.1, 13.6. HRMS (ESI): m/z calcd. for $\text{C}_{18}\text{H}_{20}\text{N}_2\text{O}_4$ 328.1423: observed 329.1493 [$\text{M}+\text{H}$].

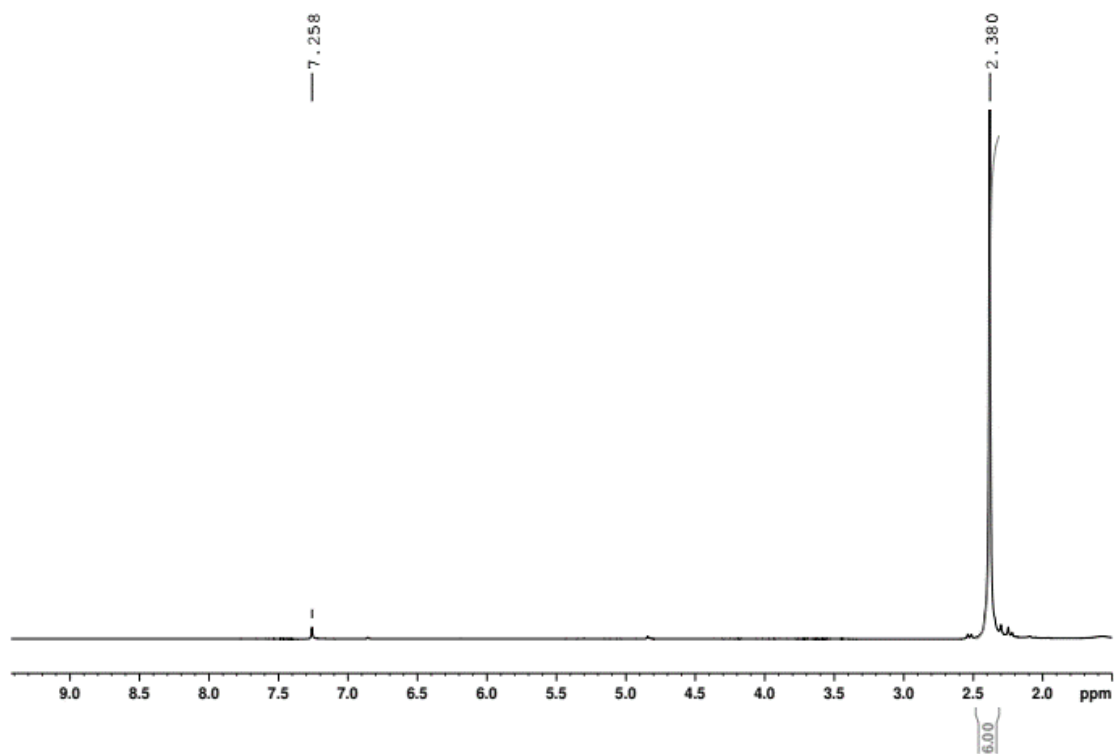


Figure 2.2.13. ^1H NMR spectrum of **6** in CDCl_3 .

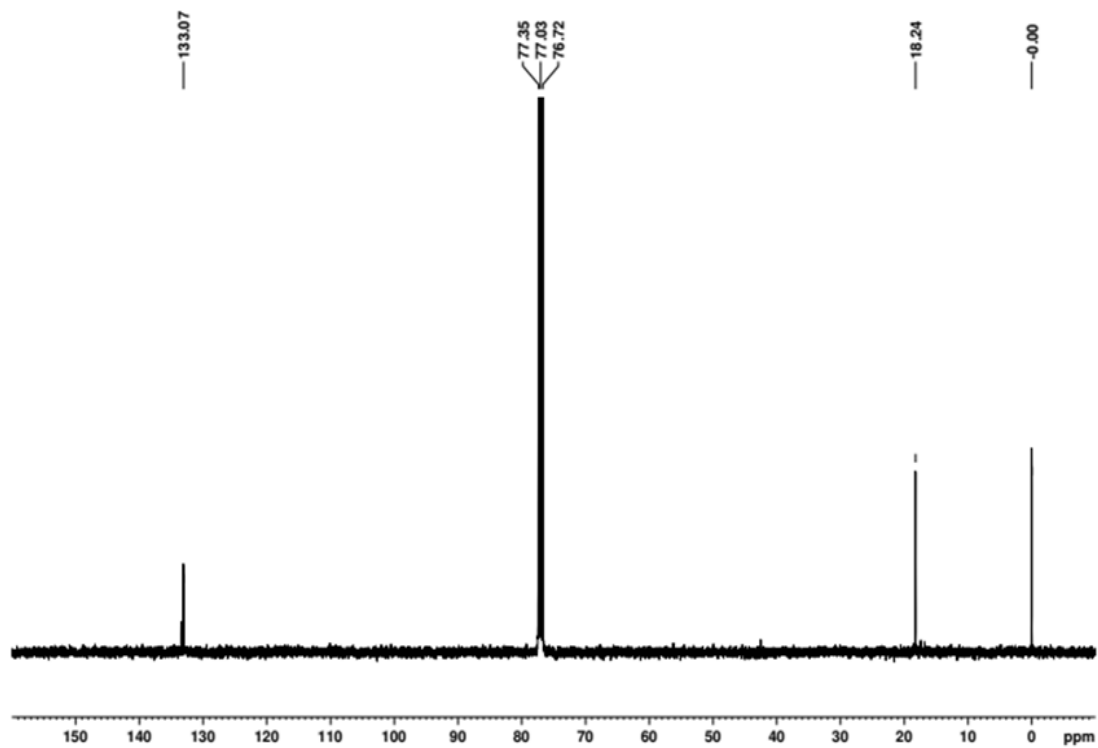


Figure 2.2.14. ^{13}C NMR spectrum of **6** in CDCl_3 .

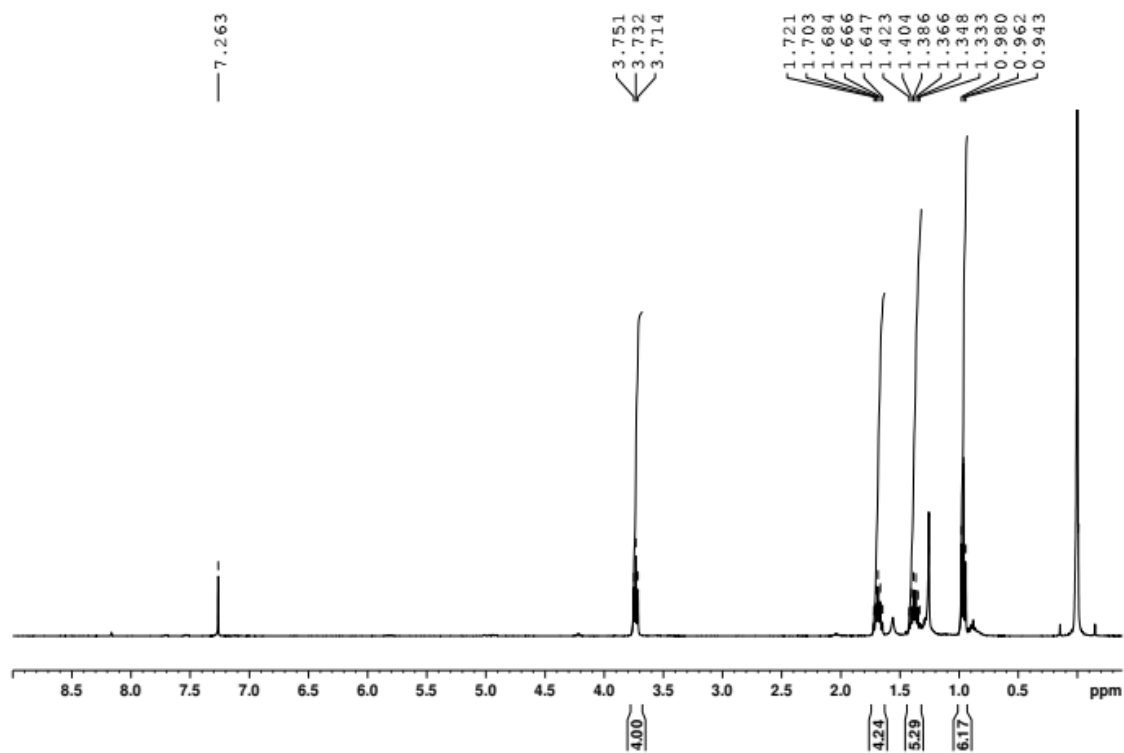


Figure 2.2.15. ^1H NMR spectrum of *CIPmDI* in CDCl_3 .

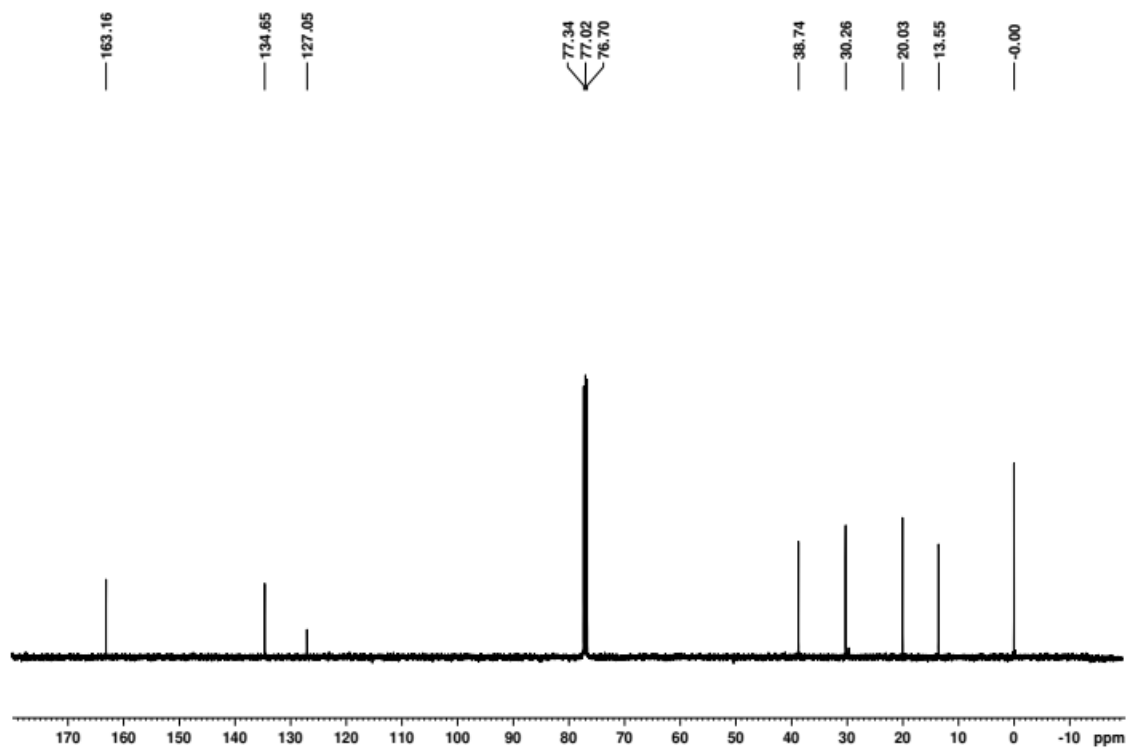


Figure 2.2.16. ^{13}C NMR spectrum of *CIPmDI* in CDCl_3 .

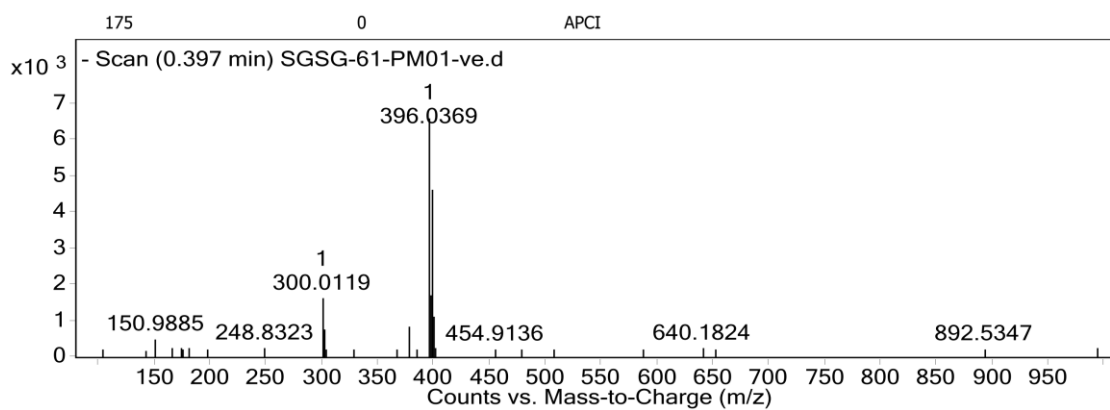


Figure 2.2.17. HR-MS spectrum of *CIPmDI* in APCI mode.

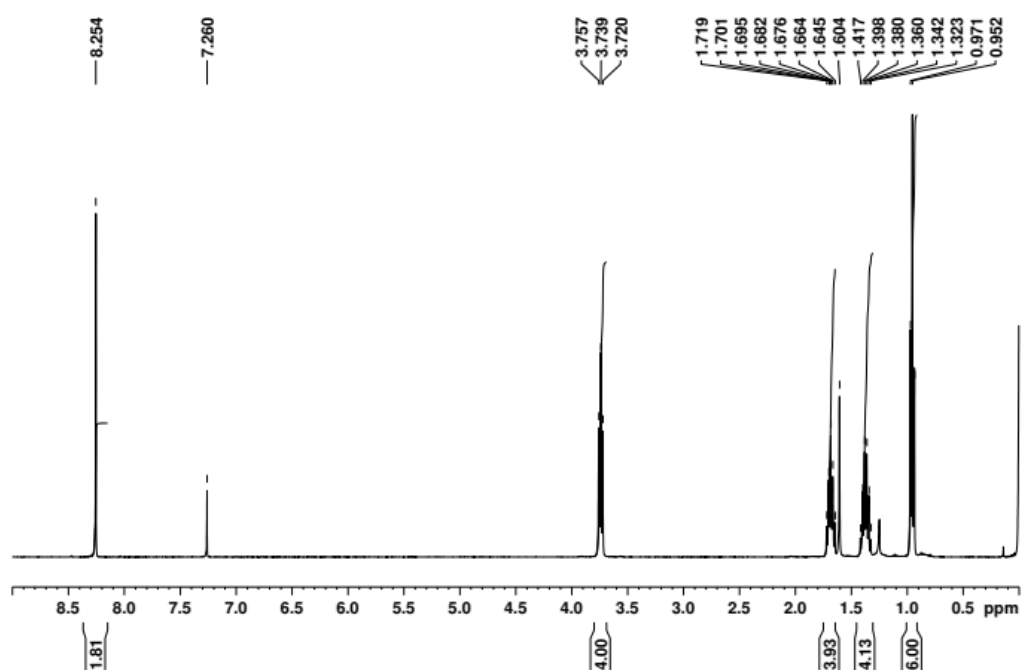


Figure 2.2.18. ¹H NMR spectrum of *HPmDI* in CDCl₃.

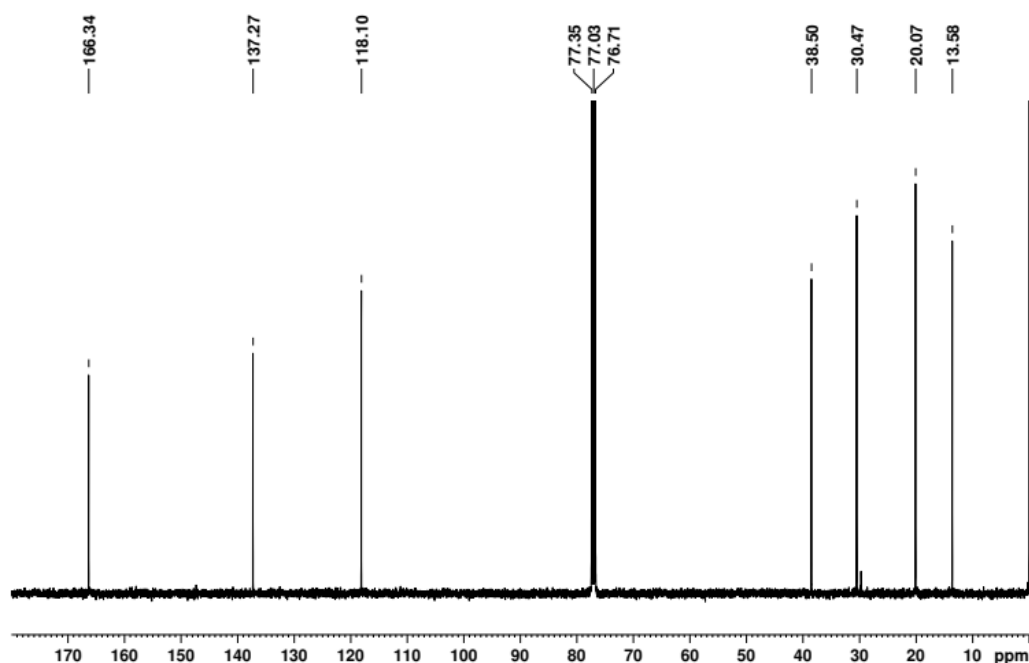


Figure 2.2.19. ^{13}C NMR spectrum of *HPmDI* in CDCl_3 .

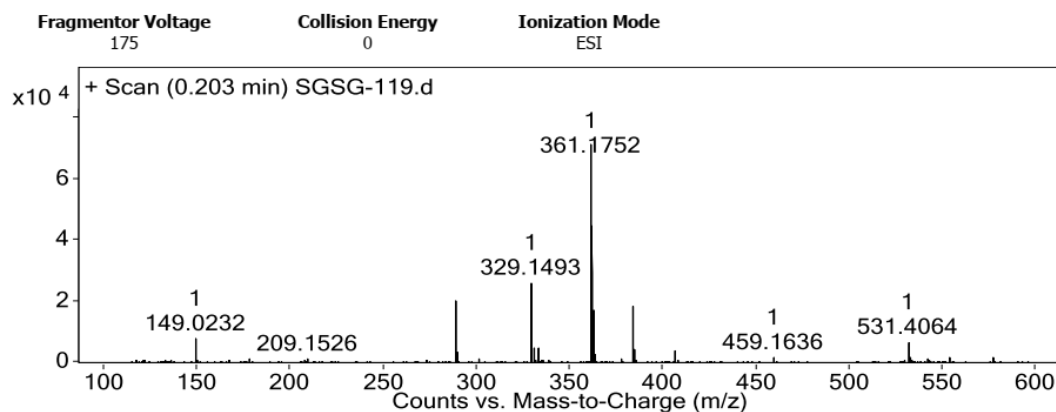


Figure 2.2.20. ESI-HRMS spectrum of *HPmDI*.

2.2.13. References:

- [1] a) S. Hirata, *Adv. Opt. Mater.* **2017**, *5*, 1700116; b) M. Y. Wong, E. Zysman-Colman, *Adv. Mat.* **2017**, *29*, 1605444; c) W. Zhao, Z. He, W. Y. Lam, Jacky, Q. Peng, H. Ma, Z. Shuai, G. Bai, J. Hao, B. Z. Tang, *Chem* **2016**, *1*, 592-602; d) S. Xu, R. Chen, C. Zheng, W. Huang, *Adv. Mater.* **2016**, *28*, 9920-9940; e) W. Zhao, Z. He, B. Z. Tang, *Nat. Rev. Mater.* **2020**, *5*, 869-885; f) X. Ma, J. Wang, H. Tian, *Acc. Chem. Res.* **2019**, *52*, 738-748; g) T. Zhang, X. Ma, H. Wu, L. Zhu, Y. Zhao, H. Tian, *Angew. Chem., Int. Ed.* **2020**, *59*, 11206-11216; h) Y. Wang, H. Gao, J. Yang, M. Fang, D. Ding, B. Tang, Z. Li, *Adv. Mater.* **2021**, *33*, 2007811.

- [2] a) O. Bolton, K. Lee, J-H. Kim, K.Y. Lin, J. Kim, *Nat. Chem.* **2011**, *3*, 205-210; b) Z. An, C. Zheng, Y. Tao, R. Chen, H. Shi, T. Chen, Z. Wang, H. Li, R. Deng, X. Liu, W. Huang, *Nat. Mater.* **2015**, *14*, 685-690; c) Y. Tao, R. Chen, H. Li, J. Yuan, Y. Wan, H. Jiang, C. Chen, Y. Si, C. Zheng, B. Yang, G. Xing, W. Huang, *Adv. Mater.* **2018**, *30*, 1803856; d) S. Cai, H. Shi, J. Li, L. Gu, Y. N. Z. Cheng, S. Wang, W. Xiong, L. Li, Z. An, W. Huang, *Adv. Mater.* **2017**, *29*, 1701244; e) P. Alam, T. S. Cheung, N. L. C. Leung, J. Zhang, J. Guo, L. Du, R. T. K. Kwok, J. W. Y. Lam, Z. Zeng, D. L. Phillips, H. H. Y. Sung, I. D. Williams, B. Z. Tang, *J. Am. Chem. Soc.* **2022**, *144*, 3050-3062; f) Y. Gong, G. Chen, Q. Peng, W. Z. Yuan, Y. Xie, S. Li, Y. Zhang, B. Z. Tang, *Adv. Mater.* **2015**, *27*, 6195-6201; g) P. Alam, N. Leung, J. Liu, X. Zhang, Z. He, R. T. K. Kwok, J. W. Y. Lam, H. H. Y. Sung, I. D. Williams, Q. Peng, B. Z. Tang, *Adv. Mater.* **2020**, *32*, 2001026; h) Y. Xie, Y. Ge, Q. Peng, C. Li, Q. Li, Z. Li, *Adv. Mater.* **2017**, *29*, 1606829; i) Q. Liao, Q. Gao, J. Wang, Y. Gong, Q. Peng, Y. Tian, Y. Fan, H. Guo, D. Ding, Q. Li, Z. Li, *Angew. Chem. Int. Ed.* **2020**, *59*, 9946-9951; j) J. Ren, Y. Wang, Y. Tian, Z. Liu, X. Xiao, J. Yang, M. Fang, Z. Li, *Angew. Chem. Int. Ed.* **2021**, *60*, 12335-12340.
- [3] a) M. S. Kwon, D. Lee, S. Seo, J. Jung, J. Kim, *Angew. Chem. Int. Ed.* **2014**, *53*, 11177-11181; b) S. Kuila, S. Garain, S. Bandi, S. J. George, *Adv. Funct. Mater.* **2020**, *30*, 2003693; c) H. Wu, W. Chi, Z. Chen, G. Liu, L. Gu, A. K. Bindra, G. Yang, X. Liu, Y. Zhao, *Adv. Funct. Mater.* **2019**, *29*, 1807243; d) Z. Wang, Y. Zhang, C. Wang, X. Zheng, Y. Zheng, L. Gao, C. Yang, Y. Li, L. Qu, Y. Zhao, *Adv. Mater.* **2020**, *32*, 1907355; f) Y. Su, Y. Zhang, Z. Wang, W. Gao, P. Jia, D. Zhang, C. Yang, Y. Li, Y. Zhao, *Angew. Chem. Int. Ed.* **2020**, *59*, 9967-9971; e) C. Wang, Y. Zhang, Z. Wang, Y. Zheng, X. Zheng, L. Gao, Q. Zhou, J. Hao, B. Pi, Q. Li, C. Yang, Y. Li, K. Wang, Y. Zhao, *Adv. Funct. Mater.* **2022**, *32*, 2111941; f) S. Cai, Z. Sun, H. Wang, X. Yao, H. Ma, W. Jia, S. Wang, Z. Li, H. Shi, Z. An, Y. Ishida, T. Aida, W. Huang, *J. Am. Chem. Soc.* **2021**, *143*, 16256-16263; g) M. Louis, H. Thomas, M. Gmelch, A. Haft, F. Fries, S. Reineke, *Adv. Mater.* **2019**, *31*, 1807887; h) H. Thomas, D. L. Pastoetter, M. Gmelch, T. Achenbach, A. Schlögl, M. Louis, X. Feng, S. Reineke, *Adv. Mater.* **2020**, *32*, 2000880.
- [4] a) J. Wang, Z. D. Li, F. Lu, J. Wang, W. Hu, X. M. Cao, X. Ma, H. Tian, *J. Am. Chem. Soc.* **2018**, *140*, 1916-1923; b) Huang, X. Ma, H. Tian, *Angew. Chem. Int. Ed.* **2020**, *59*, 9928-9933; c) X. Yao, J. Wang, D. Jiao, Z. Huang, O. Mhirs, F. Lossada, L. Chen, B. Haehnle, A. J. C. Kuehne, X. Ma, H. Tian, A. Walther, *Adv. Mater.* **2020**,

2005973; d) Z. Y. Zhang, Y. Chen, Y. Liu, *Angew. Chem. Int. Ed.* **2019**, *58*, 6028-6032; e) M. Huo, X. Y. Dai, Y. Liu, *Angew. Chem., Int. Ed.* **2021**, *60*, 27171-27177; f) Z.-Y. Zhang, W.-W. Xu, W.-S. Xu, J. Niu, X.-H. Sun, Y. Liu, *Angew. Chem. Int. Ed.* **2020**, *59*, 18748-18754; g) X. K. Ma, W. Zhang, Z. Liu, H. Zhang, B. Zhang, Y. Liu, *Adv. Mater.* **2021**, *33*, 2007476; h) Z. Li, Y. Han, F. Nie, M. Liu, H. Zhong, F. Wang, *Angew. Chem. Int. Ed.* **2021**, *60*, 8212-8219; i) Z. Li, Y. Han, F. Wang, *Nat. Commun.* **2019**, *10*, 3735; j) S. Kuila, K. V. Rao, S. Garain, P. K. Samanta, S. Das, S. K. Pati, M. Eswaramoorthy, S. J. George, *Angew. Chem. Int. Ed.* **2018**, *57*, 17115-17119; k) S. Garain, B. C. Garain, M. Eswaramoorthy, S. K. Pati, S. J. George, *Angew. Chem. Int. Ed.* **2021**, *60*, 19720-19724.

[5] a) H. Uoyama, K. Goushi, K. Shizu, H. Nomura, C. Adachi, *Nature* **2012**, *492*, 234-238; b) M. Y. Wong, E. Zysman-Colman, *Adv. Mater.* **2017**, *29*, 1605444; c) Y. Tao, K. Yuan, T. Chen, P. Xu, H. Li, R. Chen, C. Zheng, L. Zhang, W. Huang, *Adv. Mater.* **2014**, *26*, 7931-7958; d) Y. Tao, K. Yuan, T. Chen, P. Xu, H. Li, R. Chen, C. Zheng, L. Zhang, W. Huang, *Adv. Mater.* **2014**, *26*, 7931-7958; e) Y. Im, M. Kim, Y. J. Cho, J.-A. Seo, K. S. Yook, J. Y. Lee, *Chem. Mater.* **2017**, *29*, 1946-1963; f) T. J. Penfold, F. B. Dias, A. P. Monkman, *Chem. Commun.* **2018**, *54*, 3926-3935; g) Y. Liu, C. Li, Z. Ren, S. Yan, M. R. Bryce, *Nat. Rev. Mater.* **2018**, *3*, 18020.

[6] a) C. Gao, W. W. H. Wong, Z. Qin, S. C. Lo, E. B. Namdas, H. Dong, W. Hu, *Adv. Mater.* **2021**, *33*, 2100704; b) P. Bharmoria, H. Bildirir, K. Moth-Poulsen, *Chem. Soc. Rev.* **2020**, *49*, 6529-6554; c) D. Di, L. Yang, J. M. Richter, L. Meraldi, R. M. Altamimi, A. Y. Alyamani, D. Credginton, K. P. Musselman, J. L. MacManus Driscoll, R. H. Friend, *Adv. Mater.* **2017**, *29*, 1605987; d) A. Dey, D. Kabra, *ACS Appl. Mater. Interfaces* **2018**, *10*, 38287-38293; e) C. J. Chiang, A. Kimyonok, M. K. Etherington, G. C. Griffiths, V. Jankus, F. Turksoy, A. P. Monkman, *Adv. Funct. Mater.* **2013**, *23*, 739-746.

[7] a) P. L. dos Santos, M. K. Etherington, A. P. Monkman, *J. Mater. Chem. C* **2018**, *6*, 4842-4853; b) P. L. dos Santos, F. B. Dias, A. P. Monkman, *J. Phys. Chem. C* **2016**, *120*, 18259-18267; c) F. B. Dias, J. Santos, D. R. Graves, P. Data, R. S. Nobuyasu, M. A. Fox, A. S. Batsanov, T. Palmeira, M. N. Berberan-Santos, M. R. Bryce, A. P. Monkman, *Adv. Sci.* **2016**, *3*, 1600080; d) T. Ogiwara, Y. Wakukawa, T. Ikoma, *J. Phys. Chem. A* **2015**, *119*, 3415-3418; e) J. U. Kim, I. S. Park, C.-Y. Chan, M. Tanaka, Y. Tsuchiya, H. Nakanotani, C. Adachi, *Nat. Commun.* **2020**, *11*, 1765; f) M. K. Etherington, J. Gibson, H. F. Higginbotham, T. J. Penfold, A. P. Monkman, *Nat.*

Commun. **2016**, *7*, 13680; g) J. Gibson, A. P. Monkman, T. J. Penfold, *Chem Phys Chem* **2016**, *17*, 2956-2961; h) E. W. Evans, Y. Olivier, Y. Puttisong, W. K. Myers, T. J. Hele, S. M. Menke, T. H. Thomas, D. Credgington, D. Beljonne, R. H. Friend, *J. Phys. Chem. Lett.* **2018**, *9*, 4053-4058.

[8] a) E. Hamzehpoor, C. Ruchlin, Y. Tao, J. E. Ramos-Sanchez, H. M. Titi, G. Cosa, D. F. Perepichka, *J. Phys. Chem. Lett.* **2021**, *12*, 6431-6438; b) X. G. Wu, C. Y. Huan, D. G. Chen, D. H. Liu, C. C. Wu, K. J. Chou, B. Zhang, Y. F. Wang, Y. Liu, E. Y. Li, W. G. Zhu, P. T. Chou, *Nat. Commun.* **2020**, *11*, 2145.

[9] a) C. Murawski, K. Leo, M. C. Gather, *Adv. Mater.* **2013**, *25*, 6801-6827; b) B. Zee, Y. Li, G. J. A. H. Wetzelaer, P. W. M. Blom, *Adv. Opt. Mater.*, **2021**, *9*, 2100249.

[10] a) N. Yanai, N. Kimizuka, *Acc. Chem. Res.* **2017**, *50*, 2487-2495; b) S. Amemori, Y. Sasaki, N. Yanai, N. Kimizuka, *J. Am. Chem. Soc.* **2016**, *138*, 8702-8705; c) P. Bharmoria, S. Hisamitsu, H. Nagatomi, T. Ogawa, M.-a. Morikawa, N. Yanai, N. Kimizuka, *J. Am. Chem. Soc.* **2018**, *140*, 10848-10855.

[11] a) Q. Liu, T. S. Yang, W. Feng, F. Y. Li, *J. Am. Chem. Soc.* **2012**, *134*, 5390-5397; b) O. S. Kwon, H. S. Song, J. Conde, H.-I. Kim, N. Artzi, J.-H. Kim, *ACS Nano* **2016**, *10*, 1512-1521; c) B. D. Ravetz, A. B. Pun, E. M. Churchill, D. N. Congreve, T. Rovis, L. M. Campos, *Nature* **2019**, *565*, 343-346.

[12] a) S. Kuila, K. V. Rao, S. Garain, P. K. Samanta, S. Das, S. K. Pati, M. Eswaramoorthy, S. J. George, *Angew. Chem. Int. Ed.* **2018**, *57*, 17115-17119; b) S. Garain, B. C. Garain, M. Eswaramoorthy, S. K. Pati, S. J. George, *Angew. Chem. Int. Ed.* **2021**, *60*, 19720-19724; c) S. Kuila, A. Ghorai, P. K. Samanta, R. B. K. Siram, S. K. Pati, K. S. Narayan, S. J. George, *Chem. Eur. J.* **2019**, *25*, 16007-16011 d) S. Garain, S. Kuila, B. C. Garain, M. Kataria, A. Borah, S. K. Pati, S. J. George, *Angew. Chem. Int. Ed.* **2021**, *60*, 12323-12327; e) S. Garain, S. Sarkar, B. C. Garain, S. K. Pati, S. J. George, *Angew. Chem. Int. Ed.* **2022**, DOI: 10.1002/anie.202115773; f) S. Kuila, S. Garain, G. Banappanavar, B. C. Garain, D. Kabra, S. K. Pati, S. J. George, *J. Phys. Chem. B* **2021**, *125*, 4520-4526.

[13] a) O. V. Mikhnenko, P. W. M. Blom, T.-Q. Nguyen, *Energy Environ. Sci.* **2015**, *8*, 1867-1888; b) T. Serevičius, R. Komskis, P. Adomėnas, O. Adomėnienė, G. Kreiza, V. Jankauskas, K. Kazlauskas, A. Miasojedovas, V. Jankus, A. Monkman, S. Juršėnas, *J. Phys. Chem. C* **2017**, *121*, 8515-8524.

[14] a) Gaussian 16, Revision A.03, M. J. Frisch, G. W. Trucks, H. B. Schlegel, G. E. Scuseria, M. A. Robb, J. R. Cheeseman, G. Scalmani, V. Barone, G. A. Petersson, H.

Nakatsuji, X. Li, M. Caricato, A. V. Marenich, J. Bloino, B. G. Janesko, R. Gomperts, B. Mennucci, H. P. Hratchian, J. V. Ortiz, A. F. Izmaylov, J. L. Williams; F. Ding; F. Lipparini, F. Egidi, J. Goings, B. Peng, A. Petrone, T. Henderson, D. Ranasinghe, V.G. Zakrzewski, J. Gao, N. Rega, G. Zheng, W. Liang, M. Hada, M. Ehara, K. Toyota, R. Fukuda, J. Hasegawa, M. Ishida, T. Nakajima, Y. Honda, O. Kitao, H. Nakai, T. Vreven, K. Throssell, J. A. Montgomery Jr., J. E. Peralta, F. Ogliaro, M. J. Bearpark, J. J. Heyd, E. N. Brothers, K. N. Kudin, V. N. Staroverov, T. A. Keith, R. Kobayashi, J. Normand, K. Raghavachari, A. P. Rendell, J. C. Burant, S. S. Iyengar, J. Tomasi, M. Cossi, J. M. Millam, M. Klene, C. Adamo, R. Cammi, J. W. Ochterski, R. L. Martin, K. Morokuma, O. Farkas, J. B. Foresman, D. J. Fox, Gaussian, Inc., Wallingford CT, **2016**; b) A. D. Becke, *J. Chem. Phys.* **1993**, *98*, 1372–1377; c) C. Lee, W. Yang, R. G. Parr, *Phys. Rev. B* **1988**, *37*, 785–789; d) B. Miehlich, A. Savin, H. Stoll, H. Preuss, *Chem. Phys. Lett.* **1989**, *157*, 200–206; e) T. Yanai, D. P. Tew, N. C. Handy, *Chem. Phys. Lett.* **2004**, *393*, 51–57; f) T. Yanai, D. P. Tew, N. C. Handy, *Chem. Phys. Lett.* **2004**, *393*, 51–57; g) S. Hirata, M. Head-Gordon, *Chem. Phys. Lett.* **1999**, *314*, 291–299–57; h) E. van Lenthe, R. Van Leeuwen, E. J. Baerends, *Int. J. Quan. Chem.* **1996**, *57*, 281–293; i) E. van Lenthe, J. G. Snijders, E. J. Baerends, *J. Chem. Phys.* **1996**, *105*, 6505–6516; j) F. Wang, T. Ziegler, E. van Lenthe, S. van Gisbergen, E. J. Baerends, *J. Chem. Phys.* **2005**, *122*, 204103–204112.

CHAPTER 3

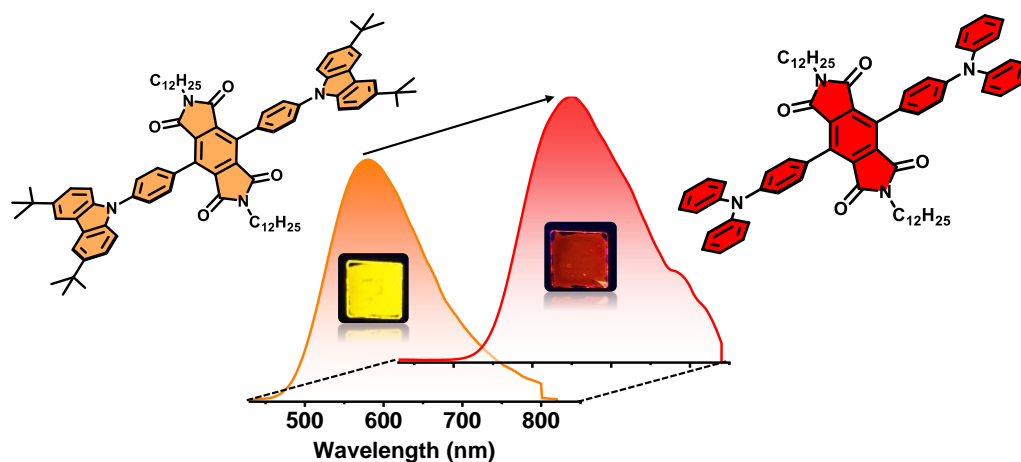
Thermally Activated Delayed Fluorescence: Color Tunable Delayed Fluorescence from Core-substituted Pyromellitic Diimides

CHAPTER 3

Thermally Activated Delayed Fluorescence: Color Tunable Delayed Fluorescence from Core-substituted Pyromellitic Diimides*

Abstract

Thermally activated delayed fluorescence (TADF) is alternate way to harvest the triplet exciton to achieve 100 % internal quantum efficiency. This chapter presents a systematic investigation of donor-acceptor charge-transfer (CT) design based on the electron-deficient pyromellitic diimides and electron-rich phenyl carbazole, and triphenylamine that has shown to exhibit small singlet-triplet gap facilitating efficient thermally activated delayed fluorescence (TADF) properties. Theoretical calculation was performed to understand the role of the donor (phenyl carbazole) and acceptor (pyromellitic diimides) in maintaining the strong CT nature of the molecules. Moreover, a detailed photophysical analyses of the emissive bands of the current molecules suggest the presence of dual TADF and phosphorescence emission at room temperature.



*Manuscript based on this work is under preparation.

3.1. Introduction:

Recently, the scientific community has been eagerly waiting for the new efficient purely organic triplet harvesters due to their paramount importance in optoelectronic display, devices and bioimaging.^[1] However, harvesting the triplet excitons from purely organic materials are difficult and challenging compared to the heavy atom based toxic organometallic phosphors.^[2] Despite the challenges involved, profound interest to harvest the triplet excitons from purely organic chromophores is due to their relatively high air stability, processability and large number of molecular designs with tuneable emission.^[1] In this respect, phosphorescence,^[3] TADF^[4] and triplet-triplet annihilation (TTA)^[5] are becoming the efficient approaches to harvest the triplet excitons effectively from purely organic emitters. Among these three-processes, maximum internal quantum efficiency (IQE) 100 % can be achieved via phosphorescence and TADF.^[1] However, most of the phosphorescence reported in the literature are in the crystalline state and suffers from meagre quantum efficiency so that TADF materials are preceding in harvesting the triplets due to their high quantum yield and solution-processability.^[4] Designing efficient TADF emitters require clever molecular design strategies with covalently linked spatially separated donor and acceptor, which spontaneously form emissive charge-transfer states to reduce the singlet-triplet energy gap (ΔE_{ST}) for efficient reverse inter system crossing (RISC).^[1,4] However, most of the TADF emission delayed fluorescence under deaerated conditions as triplets are very susceptible to quenching in air due to the triplet nature of the oxygen. Additionally, there are very rare molecular designs present that can show ambient dual TADF and phosphorescence.^[6] It is essential to understand the role of the triplet state which is responsible for delayed fluorescence emission. In this regard the objective of the chapter is to achieve dual TADF and room temperature phosphorescence (RTP) simultaneously from the same emitter, and in addition, understanding the role of locally excited (³LE) or ³CT for delayed emission.^[1-4]

To alleviate the scenario here, we have used pyromellitic diimide (PmDI) as an acceptor, which is the smallest congener of the arylene diimide family, having efficient triplet formation ability due to the presence of four carbonyl groups which enhances the ISC by following El Sayed's rule.^[7] On the other hand, the core of the PmDIs can be easily substituted by the aromatic planar donor by the C-C coupling reaction. Here we

have used phenyl carbazole (CzPh) and triphenylamine (TPA) as the donors and designed core-substituted PmDI derivatives **CzPhPmDI** and **TPAPmDI** via Suzuki coupling reaction. A systematic photophysical study reveals that both the molecules show intramolecular charge transfer (ICT) character in both the ground and excited states. Further, the dispersed molecules in the PMMA matrix at very low concentrations showed efficient triplet harvesting properties at room temperature. Further, a temperature-dependent study attested the triplet harvesting via dual TADF and phosphorescence with an efficient quantum efficiency of 30 % and 16 % under ambient conditions with excellent color tunability for **CzPhPmDI** and **TPAPmDI**, respectively.

3.2. Molecular Design:

The basic design principle for a TADF emitter consists of an electron-rich donor and electron-deficient acceptor where the donor and acceptor should be spatially separated to decrease the ΔE_{ST} . The covalent donor-acceptor molecular design will form an intermediate CT state which will help to reduce the ΔE_{ST} (Figures 3.1a,b). In this chapter, we have used **PmDI** as an acceptor and phenyl carbazole (**CzPh**), triphenylamine (**TPA**) as donor to achieve the color tuneable TADF upon varying the donor strength (Figures 3.1a,b). Further to understand the ground state geometries, we have performed time-dependent density functional theory (TDDFT). The obtained natural transition orbitals (NTOs) show that donor and acceptor are spatially separated at a significant angle between them (Figures 3.1c,d). On the other hand, NTOs show that HOMO is located on the donor part of the chromophores, and the LUMO located on the acceptor part, that suggests the propensity of CT state formation (Figures 3.1c,d). The calculated oscillator strength for **CzPhPmDI** and **TPAPmDI** are $f=0.0003$ and 0.0213 , respectively, which are significant enough to obtain the ICT band in the UV-Visible absorption spectra.

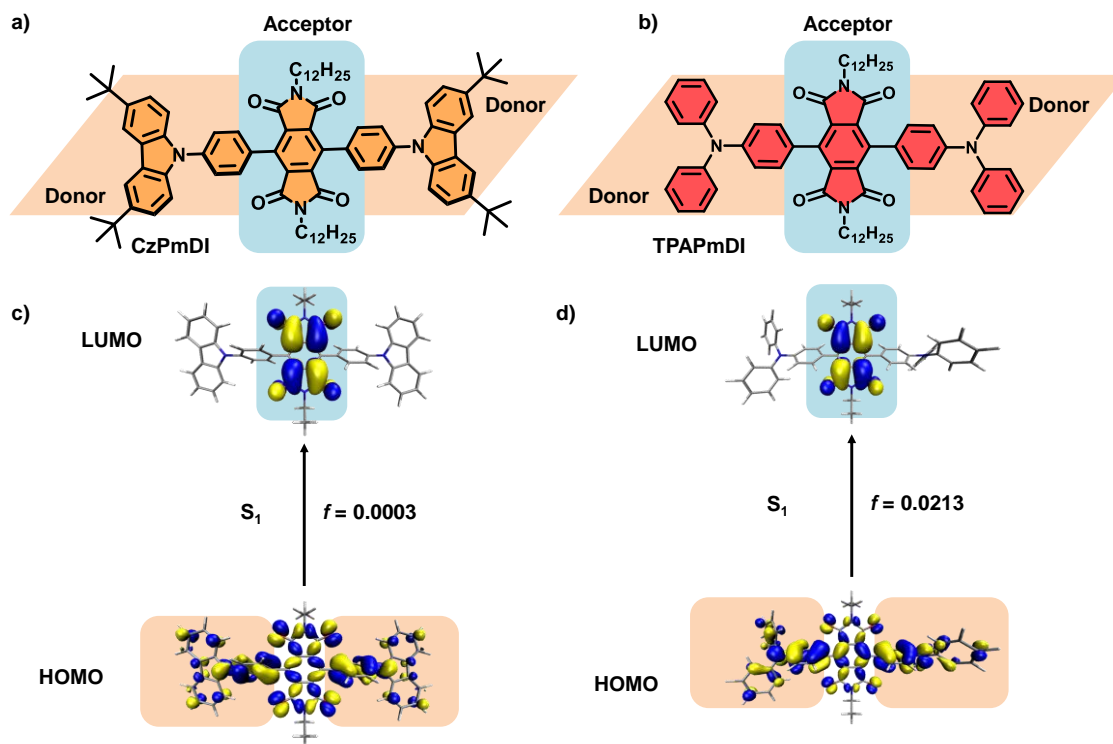


Figure 3.1 a,b) Molecular structures of **CzPhPmDI** and **TPAPmDI**. Natural transition orbitals for S_1 state at the optimized S_0 geometry for optical absorption of c) **CzPhPmDI** and d) **TPAPmDI**, calculated using $\omega^*B97XD/6-31+g(d)$ level of theory in vacuum. Hole and electron wave functions and the oscillator strength for the transition (f) are also provided.

3.3. Spectroscopic Studies in Solution-state:

The core substituted pyromellitic derivatives **CzPhPmDI** and **TPAPmDI**, were synthesized and characterized by nuclear magnetic resonance spectroscopy (NMR) and mass spectrometry. To understand the detailed photophysical properties of **CzPhPmDI** and **TPAPmDI**, first, we have done a systematic investigation in the solution state ($[c] = 0.05$ mM) (Figure 3.2). Further, to understand the intermolecular charge-transfer (ICT) nature of the emission, we have performed studies in methylcyclohexane (MCH) and toluene. UV-Visible absorption spectra showed the π - π^* absorption band at 320 nm to 420 nm region and 350 nm to 450 nm region for **CzPhPmDI** and **TPAPmDI**, respectively, in both MCH and toluene (Figures 3.2a,d). Along with the strong π - π^* absorption band, a weak band at 420 nm to 530 nm and 450 to 580 nm observed for **CzPhPmDI** and **TPAPmDI**, respectively, which we hypothesized as ICT band (Figures 3.2a,d). Corresponding emission spectra ($\lambda_{exc.} = 405$ nm) of **CzPhPmDI** show an

emission maximum at 625 nm, which is bathochromically shifted to 685 nm in more polar solvent toluene, suggesting the ICT nature of the **CzPhPmDI** emission (Figure 3.2b). A similar bathochromic shift is also observed for the **TPAPmDI** derivative upon changing solvent polarity from MCH to toluene (Figure 3.2e). CT nature of the emission is further supported by the lifetime decay experiments upon direct excitation at the CT band, which showed an average lifetime of 3.85 ns (toluene) and 2.90 ns (MCH) for **CzPhPmDI** and **TPAPmDI**, respectively (Figures 3.2c,f, Table 3.1). However, we have not observed any delayed fluorescence in the solution state.

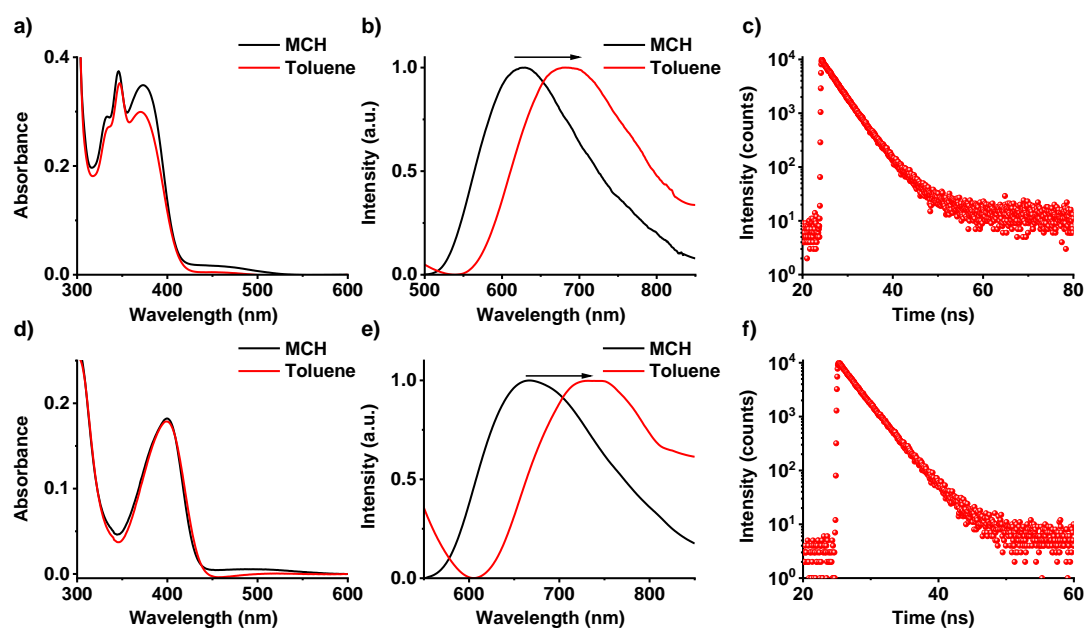


Figure 3.2. Normalized absorption a) **CzPhPmDI**, d) **TPAPmDI** and corresponding emission spectra of b) **CzPhPmDI**, e) **TPAPmDI** in MCH and toluene. Lifetime decay profile of c) **CzPhPmDI**, f) **TPAPmDI** in toluene and MCH, respectively ($\lambda_{exc.} = 480$ nm, $\lambda_{collected} = 650$ nm) ($[c] = 0.05$ mM, $\lambda_{exc.} = 405$ nm).

Table 3.1 Summary of fluorescence decay of **CzPhPmDI** and **TPAPmDI** in solution.

System	Solvent	$\lambda_{exc.}$ (nm)	$\lambda_{monitored}$ (nm)	τ_1 (ns)	τ_2 (ns)	τ_3 (ns)	$\tau_{avg.}$ (ns)
CzPhPmDI	<i>TOL</i>	480	650	3.54 (92 %)	7.48 (8 %)	-	3.86
TPAPmDI	<i>MCH</i>	480	650	2.68 (98 %)	15.06 (2 %)	-	2.93

3.4. Ambient Dual TADF and Phosphorescence in Polymer Matrix:

However, to harvest the triplets under ambient conditions, we first dispersed **CzPhPmDI** and **TPAPmDI** in poly(methylmethacrylate) (PMMA) matrix at very low concentrations (1 wt.% with respect to PMMA). PMMA is an amorphous polymeric host that stabilizes triplet excitons by minimizing vibrational dissipation, thereby facilitating triplet harvesting. We observed strong emission at 450-800 nm region with a maximum at 590 nm and 650 nm for **CzPhPmDI** and **TPAPmDI** respectively (Figures 3.3a,d). A high lifetime component of this emission $\tau_{\text{avg.}} = 1.86 \mu\text{s}$ and $1.18 \mu\text{s}$ for **CzPhPmDI** ($\lambda_{\text{exc.}} = 405 \text{ nm}$, $\lambda_{\text{collected}} = 590 \text{ nm}$) and **TPAPmDI** ($\lambda_{\text{exc.}} = 405 \text{ nm}$, $\lambda_{\text{collected}} = 650 \text{ nm}$) respectively, suggests the plausibility of delayed emission via TADF (Figures 3.3c,f, Table 3.2). It is interesting to mention here that TADF emission is always composed of prompt and delayed emission from ^1CT state; similarly, in the present case, we have also observed the prompt lifetime of 68 ns and 8.56 ns for **CzPhPmDI** and **TPAPmDI**, respectively. Further to understand the delayed nature of the emission, we have performed temperature-dependent lifetime decay experiments. For a TADF emitter, we can expect a decrease in lifetime decay upon decreasing the temperature due to a decrease in thermal energy reduce the RISC rate. The experimental observation matches our hypothesis, and we observed the decrease in the initial decay in the lifetime decay profile for both the **CzPhPmDI** and **TPAPmDI** upon decreasing the temperature ($\lambda_{\text{exc.}} = 405 \text{ nm}$, $\lambda_{\text{collected}} = 590 \text{ nm}$ and 650 nm for **CzPhPmDI** and **TPAPmDI**, respectively) attesting the TADF contribution in the total emission (Figures 3.3a,d). However, we do notice that the long-range decay component in the lifetime decay profile increases upon decreasing the temperature, which assuaged us to investigate the phosphorescence contribution to the total emission (Figures 3.4a,d). To validate our observation, we have performed a temperature-dependent study to understand the phosphorescence nature of the emission. The gradual increase in overall emission intensity and lifetime (from $\tau_{\text{avg.}} = 7.7 \mu\text{s}$ at 300 K to $\tau_{\text{avg.}} = 17 \mu\text{s}$ at 20 K and $\tau_{\text{avg.}} = 6.3 \mu\text{s}$ at 300 K to $\tau_{\text{avg.}} = 45.8 \mu\text{s}$ at 20 K for **CzPhPmDI** and **TPAPmDI** respectively) upon decreasing temperature reaffirms the phosphorescence nature of the emission (Figures 3.4b,c,e,f, Table 3.3), as reduced vibrational dissipation at lower temperature increases the phosphorescence efficiency. The experiments suggest that the overall emission has dual delayed and phosphorescence contribution. Although observation of phosphorescence emission from a TADF emitter at very low temperature is obvious and there should be a triplet state

involved from where the RISC should occur. However, observation of dual TADF and phosphorescence emission simultaneously at room temperature is rare and seldom reported. We hypothesized that the phosphorescence emission originates from the locally excited triplet state (^3LE) of overall chromophores, results in the generation of the red-shifted ^3LE state compared to the individual donor and acceptor. It is important to mention here that the calculated energy difference between singlet and triplet state (ΔE_{ST}) is ~ 0.05 eV and ~ 0.09 eV for **CzPhPmDI** and **TPAPmDI**, respectively, and the ^3LE state is higher in energy than the ^1CT state which is violating the Hund's rule (Figure 3.5). Although ΔE_{ST} in the current molecules is quite low and meets the criteria of efficient RISC, we believe that the RISC is happening from the ^3CT state, which is prone to form in donor-acceptor type molecular design. However, we have not experimentally observed the phosphorescence from a lower-lying ^3CT state due to the inherently low oscillator strength of the ^3CT excited state. We have shown a simplified Jablonski diagram and hypothesized that ^3LE and ^3CT states are vibronically coupled, and ^3CT indeed plays a role in the efficient RISC process (Figure 3.6).

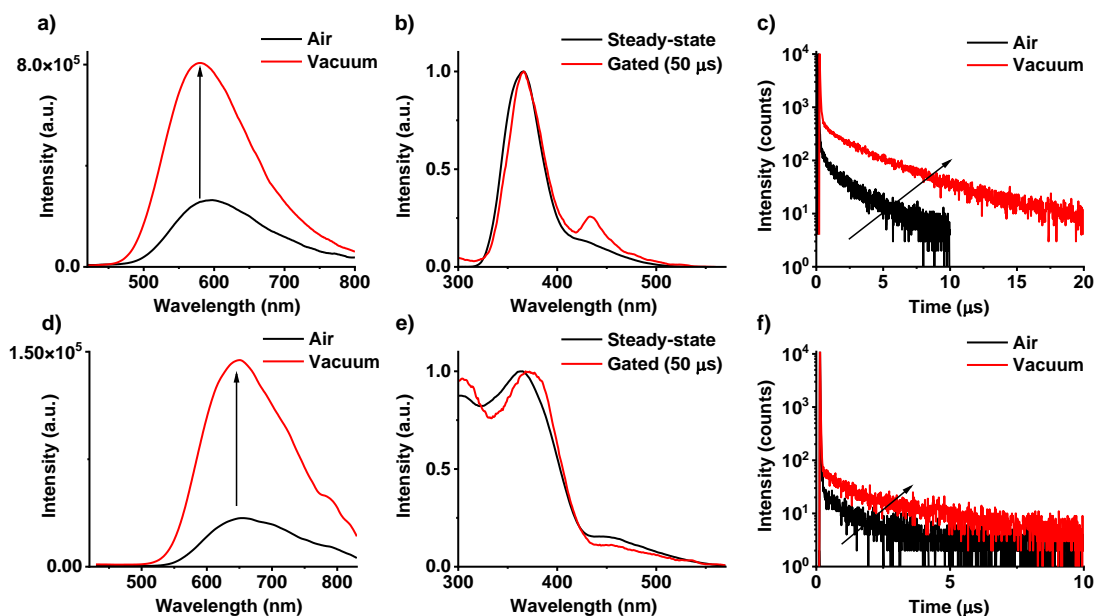


Figure 3.3. Steady-state emission spectra of a) **CzPhPmDI** and d) **TPAPmDI** in air and vacuum. Steady-state and gated excitation spectra of b) **CzPhPmDI** and e) **TPAPmDI** in air. Lifetime decay profile of c) **CzPhPmDI**, f) **TPAPmDI** respectively in air and vacuum ($\lambda_{\text{exc.}} = 405$ nm, $\lambda_{\text{collected}} = 590$ nm and 650 nm for **CzPhPmDI** and **TPAPmDI** respectively, $\lambda_{\text{monitored}} = 650$ nm, delay time = 50 μs).

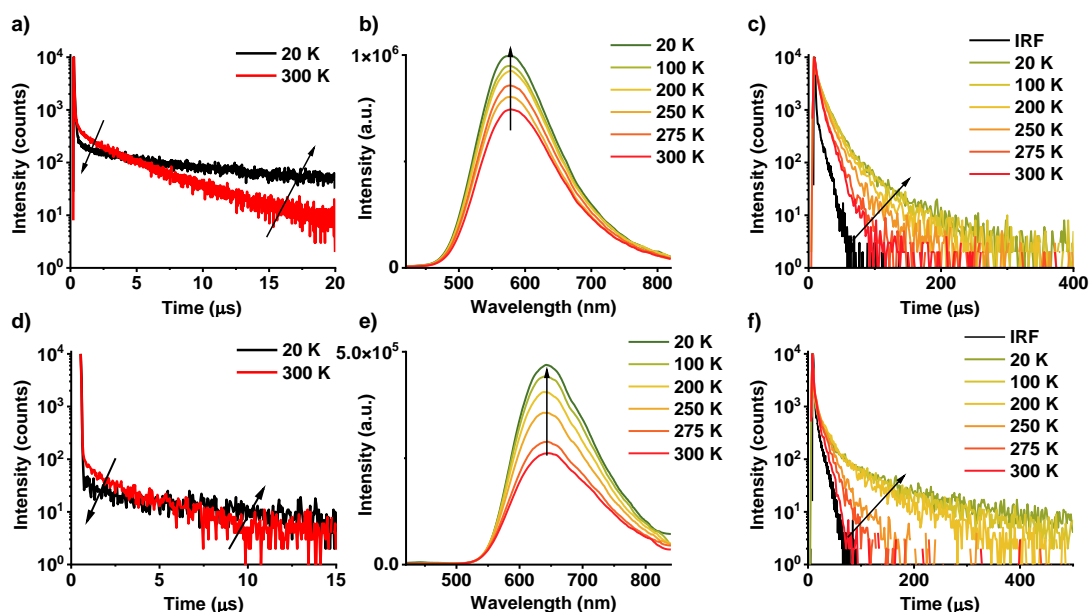


Figure 3.4. Temperature dependent studies of *CzPhPmDI* and *TPAPmDI* as doped PMMA films. TADF lifetime decay profile of a) *CzPhPmDI*, c) *TPAPmDI* in 20 K and 300 K ($\lambda_{exc.} = 405$ nm, $\lambda_{collected} = 590$ nm and 650 nm for *CzPhPmDI* and *TPAPmDI* respectively). Steady-state emission spectra of b) *CzPhPmDI* and e) *TPAPmDI*. Phosphorescence lifetime decay profile of c) *CzPhPmDI*, f) *TPAPmDI*. ($\lambda_{exc.} = 405$ nm, $\lambda_{collected} = 540$ nm and 590 nm for *CzPhPmDI* and *TPAPmDI* respectively) For all cases 1 wt.% of compounds in PMMA matrix was used.

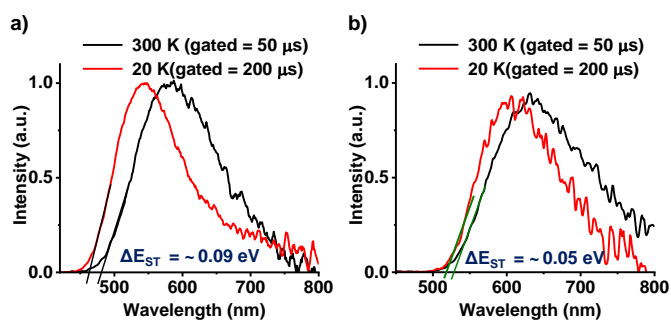


Figure 3.5. Experimental singlet-triplet energy gap (ΔE_{ST}) calculation of a) *CzPhPmDI* and b) *TPAPmDI* (calculated from phosphorescence spectra at 20 K and delayed emission spectra at 300 K showing $\Delta E_{ST} \sim 0.09$ eV and ~ 0.05 eV respectively for *CzPhPmDI* and b) *TPAPmDI*, $\lambda_{exc.} = 405$ nm). For all cases 1 wt.% of compounds in PMMA matrix was used.

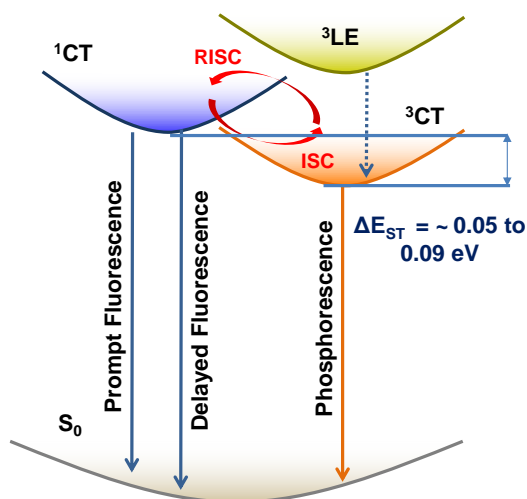


Figure 3.6. Simplified Jablonski diagram showing prompt fluorescence, delayed fluorescence via TADF and Phosphorescence emission also depicting the plausible way of RISC mechanism.

Table 3.2 Summary of delayed fluorescence decay of 1 wt.% **CzPhPmDI** and **TPAPmDI** doped in PMMA.

System		$\lambda_{\text{exc.}}$ (nm)	$\lambda_{\text{monitored}}$ (nm)	τ_1 (ns)	τ_2 (μ s)	τ_3 (μ s)
CzPhPmDI	Air	405	590	68 (20 %)	1.86 (80 %)	-
CzPhPmDI	Vacuum	405	590	155 (98 %)	3.62 (92 %)	-
TPAPmDI	Air	405	650	8.56 (80 %)	36.59 ns (6 %)	1.18 (14 %)
TPAPmDI	Vacuum	405	650	11.28 (57 %)	0.4 (8 %)	4.02 (35 %)

Table 3.3 Summary of phosphorescence decay of 1 wt.% **CzPhPmDI** and **TPAPmDI** doped in PMMA.

System	Temperature	$\lambda_{\text{exc.}}$ (nm)	$\lambda_{\text{monitored}}$ (nm)	τ_1 (μs)	τ_2 (μs)	τ_3 (μs)	$\tau_{\text{avg.}}$ (μs)
CzPhPmDI	20 K	405	540	1.85 (14 %)	13.52 (80 %)	50.00 (14 %)	17.00
CzPhPmDI	300 K	405	540	2.94 (35 %)	10.35 (65 %)	-	7.75
TPAPmDI	20 K	405	590	1.36 (36 %)	17.08 (36 %)	139.9 (28 %)	45.80
TPAPmDI	300 K	405	590	1.65 (47 %)	10.39 (53 %)	-	6.28

3.5. Conclusions:

In conclusion, in this chapter, we have discussed an indirect way to harvest the triplet exciton via TADF. Theoretical calculation predicts that the structurally simple donor-acceptor-based design of core-substituted PmDIs (**CzPhPmDI** and **TPAPmDI**) showed the plausibility of CT state formation, which is proved by the detailed spectroscopic studies in the solution state in different solvents. Further, spectroscopic studies in the solid-state (**CzPhPmDI** and **TPAPmDI** doped in the PMMA matrix at very low concentration) reveal the emission of both **CzPhPmDI** and **TPAPmDI** composed of dual TADF and phosphorescence at room temperature which is confirmed by the temperature-dependent studies of the films in vacuum. We envisaged that PmDI is an efficient acceptor core that can be easily used for triplet harvesting by combining with the suitable donor molecules to achieve color-tunable TADF emission. We believe that the donor-acceptor-based strategy can be easily extended to the through-space TADF design shortly.

3.6. Experimental Section:

3.6.1. General Methods:

NMR Measurements: ^1H and ^{13}C NMR spectra were recorded on a BRUKER AVANCE-400 Fourier transformation spectrometer with 400 and 100 MHz respectively.

The spectra were calibrated with respect to the residual solvent peaks. The chemical shifts are reported in parts per million (ppm) with respect to TMS. Short notations used are, s for singlet, d for doublet, t for triplet, q for quartet and m for multiplet.

Optical Measurements: Electronic absorption spectra were recorded on a Perkin Elmer Lambda 900 UV-Vis-NIR spectrometer and emission spectra were recorded on FLS1000 spectrometer, Edinburgh Instruments. Solution state UV-Vis and emission spectra were recorded in 1 mm path length cuvette. Fluorescence spectra of films were recorded in front-face geometry to avoid self-absorption.

Lifetime Measurements and Quantum yield: Fluorescence lifetimes were performed on a Horiba Delta Flex time-correlated single-photon-counting (TCSPC) instrument. A 480 nm LED laser diode with a pulse repetition rate of 1 MHz was used as the light source. The instrument response function (IRF) was collected using a scatterer (Ludox AS40 colloidal silica, Sigma-Aldrich). Phosphorescence lifetime ($\lambda_{exc.} = 330$ and 350 nm) and gated emission were measured on FLS1000 spectrometer, Edinburgh Instruments equipped with a micro flash-lamp ($\mu F2$) set-up. Quantum yields were measured using an integrating sphere in the same instrument.

High Resolution Mass Spectrometry (HRMS): HR-MS was carried out using Agilent Technologies 6538 UHD Accurate-Mass Q-TOFLC/MS.

Matrix-Assisted Laser Desorption Ionization (MALDI): MALDI was performed on a Bruker daltonics Autoflex Speed MALDI TOF System (GT0263G201) spectrometer using trans-2-[3-(4-tert-Butylphenyl)-2-methyl-2-propenylidene] malononitrile (DCTB) as the matrix.

3.6.2. Protocol of Sample Preparation:

All solution state studies were performed keeping the final concentration of the samples to 0.05 mM from a stock solution of $CHCl_3$ (1 mM). For thin films, **CzPhPmDI** and **TPAPmDI** molecules (3 mg each) were mixed with appropriate amount of PMMA (depending on the weight ratio) in total 2 mL chloroform solution. (For example, 1 wt. % dye: PMMA consists of 3 mg dye in 300 mg PMMA). This mixture was then heated at 50 °C for 10 minutes followed by sonication (5 minutes) to completely dissolve all the components. Then, 0.5 mL of this solution was drop-casted on a clean glass substrate.

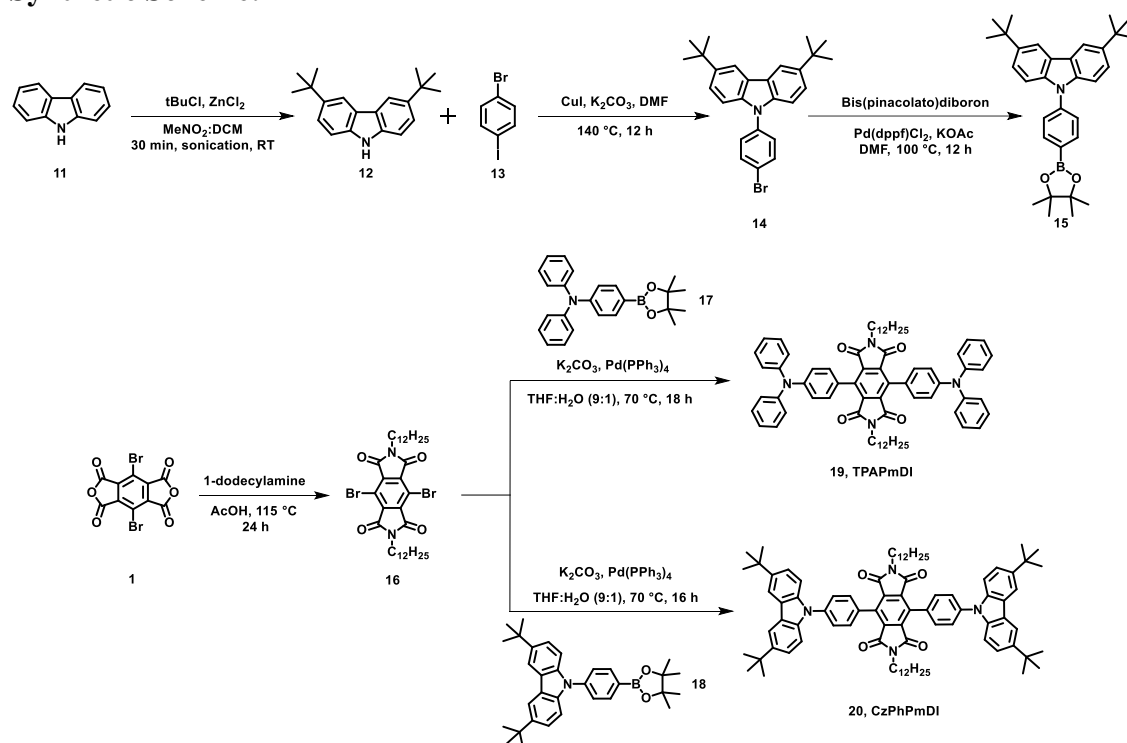
Finally, the drop-casted thin films were dried at 60 °C for 30 minutes prior to the photophysical studies.

3.7. Synthetic Schemes and Procedures:

The synthesis of **CzPhPmDI** and **TPAPmDI** is shown in Scheme 3.

Materials: The reagents and solvents were purchased from vendors and used directly. The starting materials 4-(diphenylamino)phenylboronic acid pinacol ester and dodecylamine were purchased from Sigma Aldrich; 1-bromo-4-iodobenzene, tetrakis(triphenylphosphine)palladium and 1,1'-Bis(diphenylphosphino)ferrocene[dichloropalladium (II)] were purchased from TCI; other all reagents and solvents were purchased from local vendors. Solvents used for various reactions were dried using a commercial solvent purification/drying system.

Synthetic Scheme:



Scheme 3. Synthetic scheme for **TPAPmDI** and **CzPhPmDI**.

Synthetic Procedures:

Compound 2-5 and 6 were synthesized according to the literature procedure. ^[7a,8]

Synthesis of 16: Compound 1 (0.50 g, 1.3 mmol) was taken in a 100 mL round bottom flask and 20 mL acetic acid was added into it and stirred at room temperature for 15 minutes. dodecylamine (0.739 g, 3.99 mmol) was added to the reaction mixture and stirred for 24 hours at 115°C . After completing the reaction, 100 mL of ice-cold water

was added to get white colored precipitate. The precipitate was filtered and dried under a vacuum. Column chromatography was performed using 30-40 % chloroform in hexane as an eluent to get the pure product as white solid (0.739 g, 76 % yield).

^1H NMR (400 MHz, CDCl_3) δ (ppm) 3.74-3.71 (t, $J = 7.31$ Hz, 4H), 1.71-1.68 (m, 4H), 1.33-1.25 (m, 36H), 0.89-0.86 (t, $J = 6.98$ Hz, 6H); ^{13}C NMR (100 MHz, CDCl_3) δ (ppm) 163.48, 136.22, 114.08, 39.17, 31.92, 29.73, 29.62, 29.55, 29.43, 29.34, 29.10, 28.21, 26.82, 22.69, 14.11; MALDI-TOF (negative mode): m/z calculated for $\text{C}_{34}\text{H}_{50}\text{Br}_2\text{N}_2\text{O}_4$: 710.211; observed 709.856 $[\text{M}]^-$.

Synthesis of TPAPmDI: In a 100 mL vacuum-dried round bottom flask, K_2CO_3 (116.6 mg, 0.84 mmol) and $\text{Pd}(\text{PPh}_3)_4$ (3.2 mg, 2.81 μmol) were added to the solution of compound **7** (100 mg, 0.14 mmol) and *N,N*-Diphenyl-4-(4,4,5,5-tetramethyl-1,3,2-dioxaborolan-2-yl)aniline (**17**) (130 mg, 0.35 mmol) in THF: H_2O (15 mL; 9:1 v/v) solvent mixture under nitrogen atmosphere. The reaction mixture was stirred at 70 °C for 18 hours. Progress of the reaction was monitored by TLC. After completion, the reaction mixture was diluted with water and extracted with dichloromethane (2×20 mL). The combined organic layers were washed with water followed by brine and dried over anhydrous NaSO_4 . The organic layer was filtered and concentrated under reduced pressure. The residue was purified by silica gel column chromatography eluting with 40 % dichloromethane in hexane to afford **TPAPmDI** as a brown solid (78 mg, 53%).

^1H NMR (400 MHz, CDCl_3) δ (ppm) 7.32-7.28 (m, 12H), 7.24-7.22 (m, 8H), 7.15-7.06 (m, 8H), 3.59-3.55 (t, $J = 7.23$ Hz, 4H), 1.64-1.58 (m, 4H), 1.27-1.23 (m, 36H), 0.88-0.85 (t, $J = 6.74$ Hz, 6H); ^{13}C NMR (100 MHz, CDCl_3) δ (ppm) 165.67, 148.69, 147.35, 137.34, 134.36, 130.75, 129.42, 125.51, 123.61, 123.30, 120.54, 38.56, 31.90, 29.71, 29.61, 29.55, 29.47, 29.33, 29.15, 28.41, 26.96, 22.68, 14.11; MALDI-TOF (negative mode): m/z calculated for $\text{C}_{70}\text{H}_{78}\text{N}_4\text{O}_4$: 1038.602; observed 1038.722 $[\text{M}]^-$.

Synthesis of CzPhPmDI: In a 100 mL vacuum-dried round bottom flask, K_2CO_3 (116 mg, 0.84 mmol) and $\text{Pd}(\text{PPh}_3)_4$ (3.2 mg, 2.81 μmol) were added to the solution of compound **7** (100 mg, 0.14 mmol) and compound **18** (149 mg, 0.309 mmol) in THF: H_2O (15 mL; 9:1 v/v) solvent mixture under nitrogen atmosphere. The reaction mixture was stirred at 70 °C for 16 hours. Progress of the reaction was monitored by TLC. After completion, the reaction mixture was diluted with water and extracted with dichloromethane (2×20 mL). The combined organic layers were washed with water

followed by brine, and dried over anhydrous NaSO₄. The organic layer was filtered and concentrated under reduced pressure. The residue was purified by silica gel column chromatography eluting with 30 % dichloromethane in hexane to afford CzPmDI as a yellow solid (85 mg, 48%).

¹H NMR (400 MHz, CDCl₃) δ (ppm) 8.17-8.16 (d, *J* = 1.54 Hz, 4H), 7.76-7.69 (m, 8H), 7.59-7.57 (d, *J* = 8.62 Hz, 4H), 7.52-7.49 (dd, *J* = 1.89 Hz, 8.66 Hz, 4H), 3.66-3.62 (t, *J* = 7.56 Hz, 4H), 1.70-1.62 (m, 4H), 1.49 (s, 36H), 1.33-1.23 (m, 36H), 0.87-0.83 (t, *J* = 6.68 Hz, 6H); ¹³C NMR (100 MHz, CDCl₃) δ (ppm) 165.42, 143.13, 139.62, 139.25, 139.06, 134.58, 131.19, 128.96, 125.58, 123.68, 123.62, 120.39, 117.94, 116.22, 115.51, 109.64, 34.77, 32.04, 31.90, 29.61, 29.56, 29.49, 29.33, 29.16, 26.98, 22.67, 14.09; MALDI-TOF: *m/z* calculated for C₈₆H₁₀₆N₄O₄: 1258.821; observed 1259.347 [M+H]⁺.

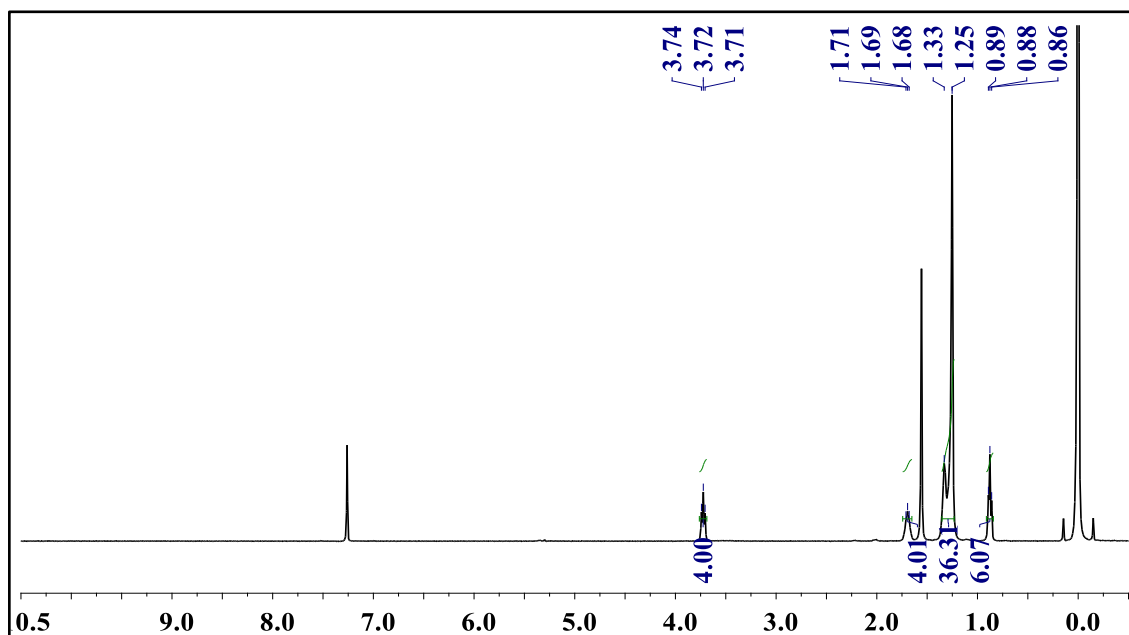


Figure 3.7. ¹H NMR spectrum of compound **16** in CDCl₃.

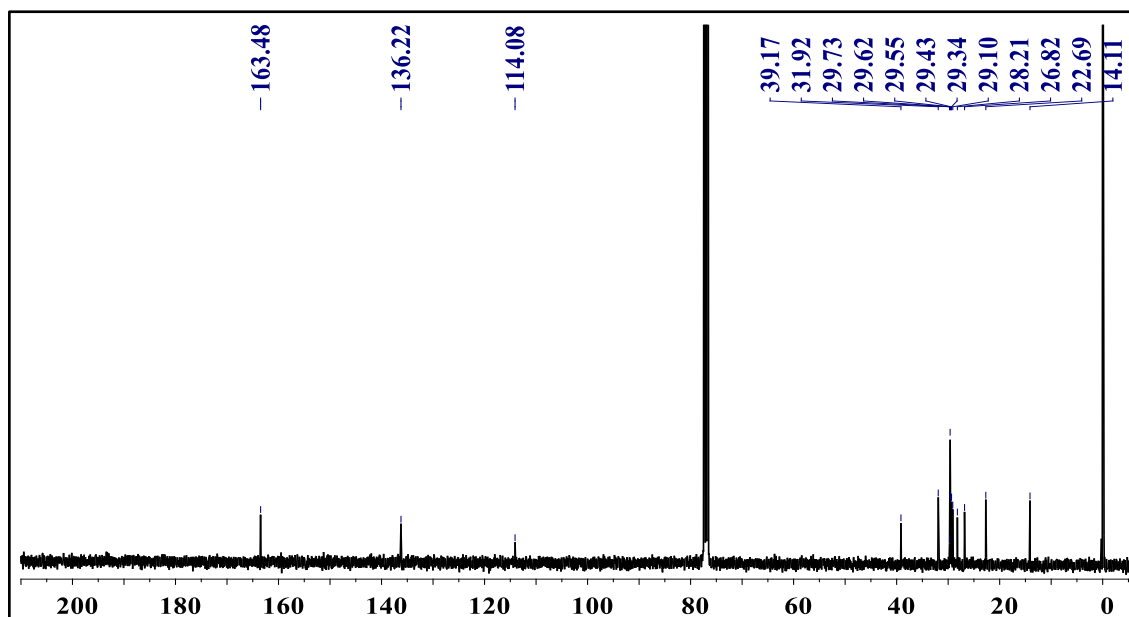


Figure 3.8. ^{13}C NMR spectrum of compound **16** in CDCl_3 .

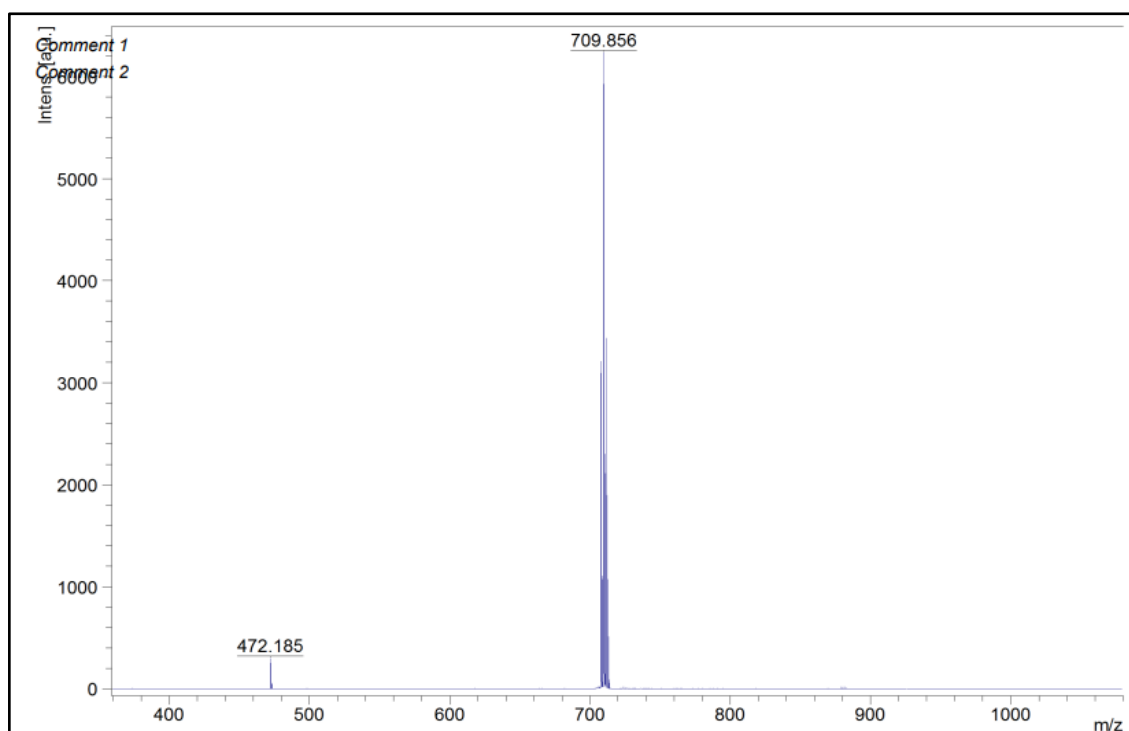


Figure 3.9. MALDI spectrum of compound **16**.

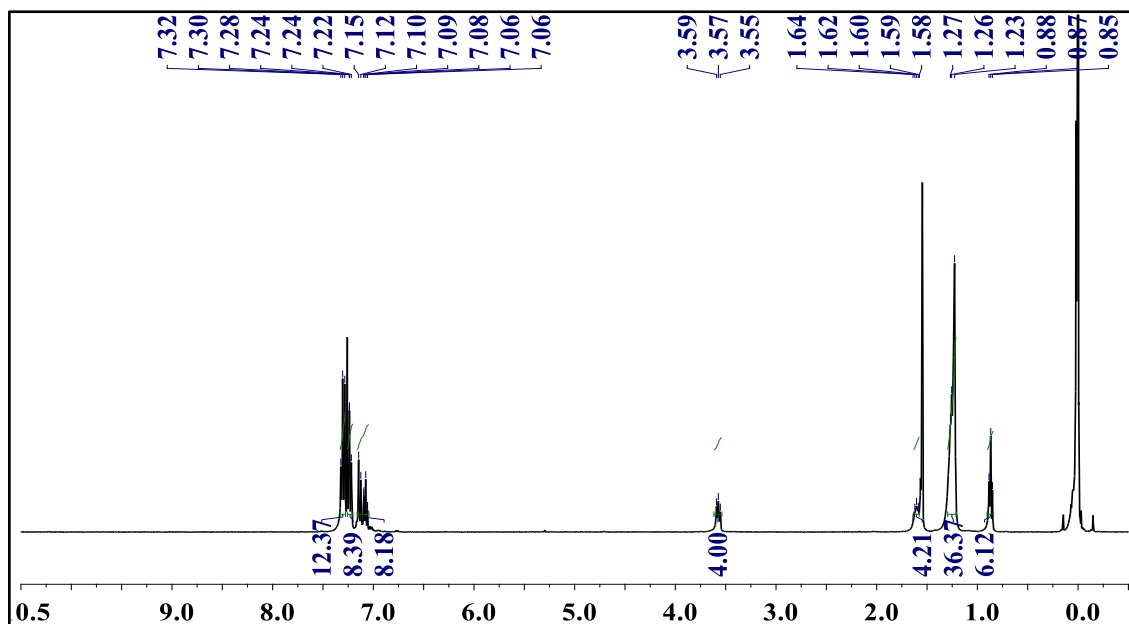


Figure 3.10. ¹H NMR spectrum of TPAPmDI in CDCl₃.

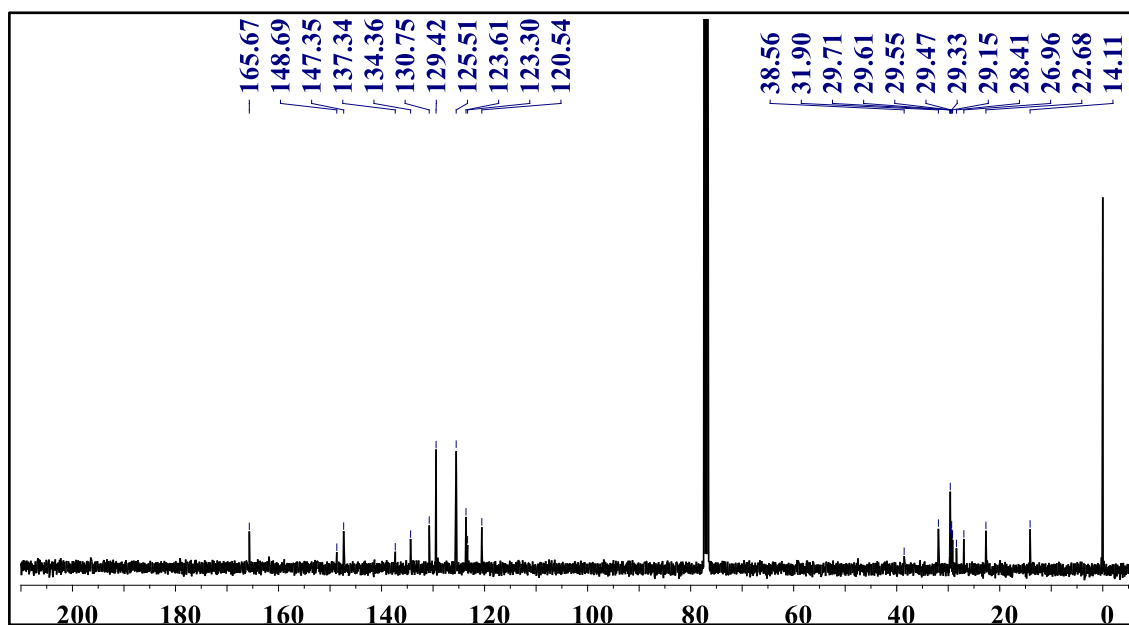


Figure 3.11. ¹³C NMR spectrum of TPAPmDI in CDCl₃.

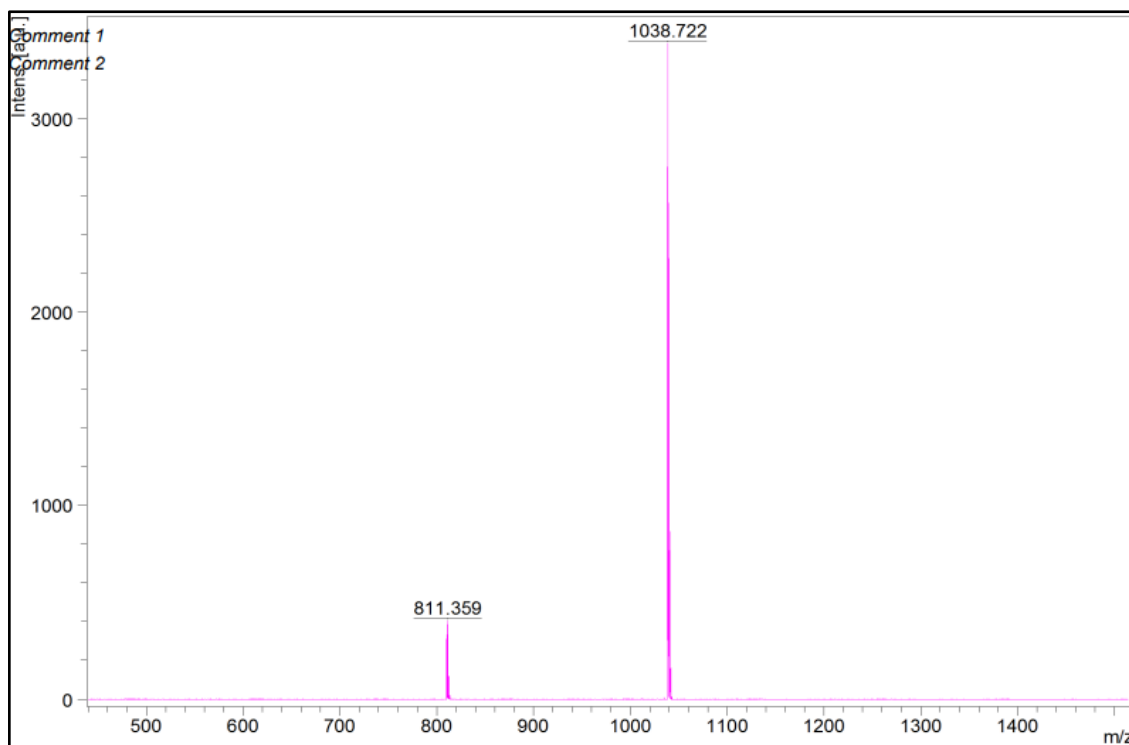


Figure 3.12. MALDI spectrum of TPAPmDI

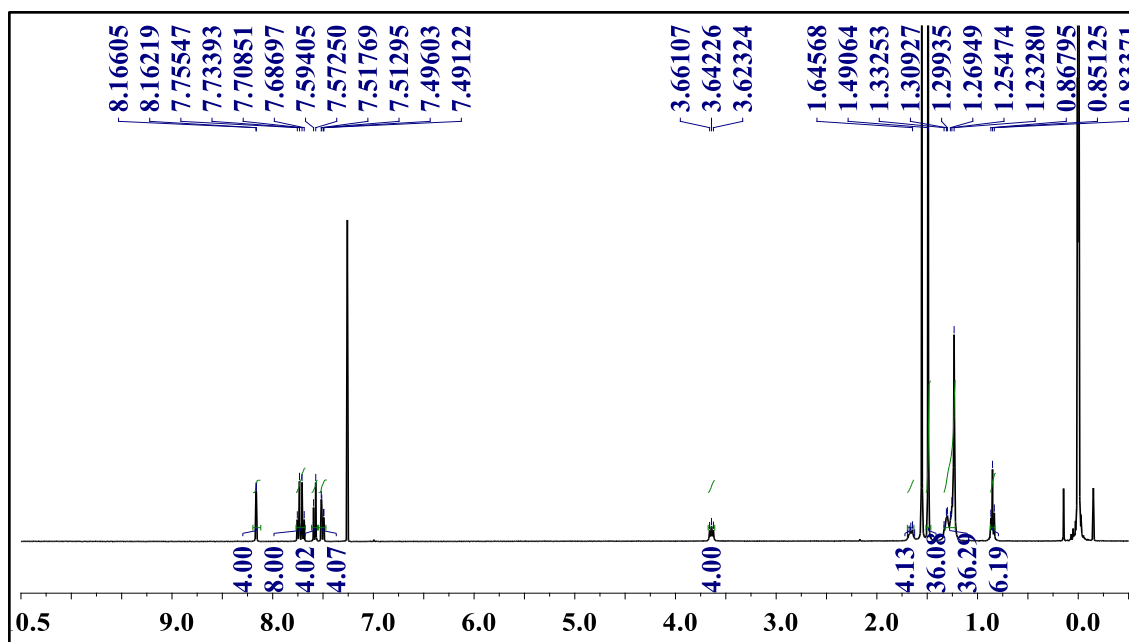


Figure 3.13. ^1H NMR spectrum of CzPhPmDI in CDCl_3 .

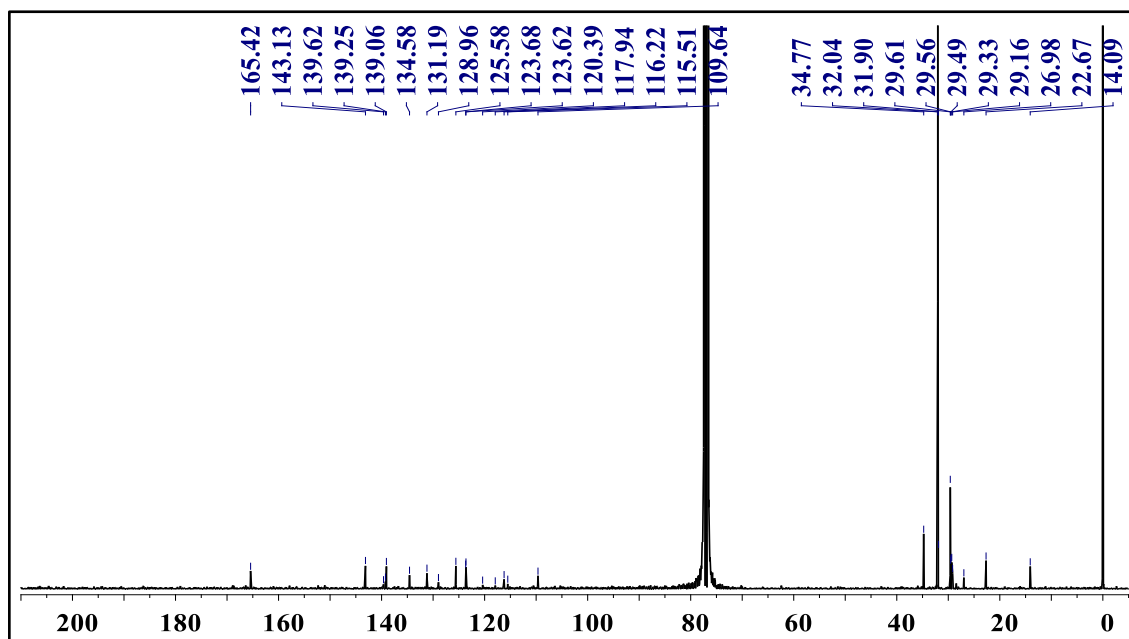


Figure 3.14. ^{13}C NMR spectrum of CzPhPmDI in CDCl_3 .

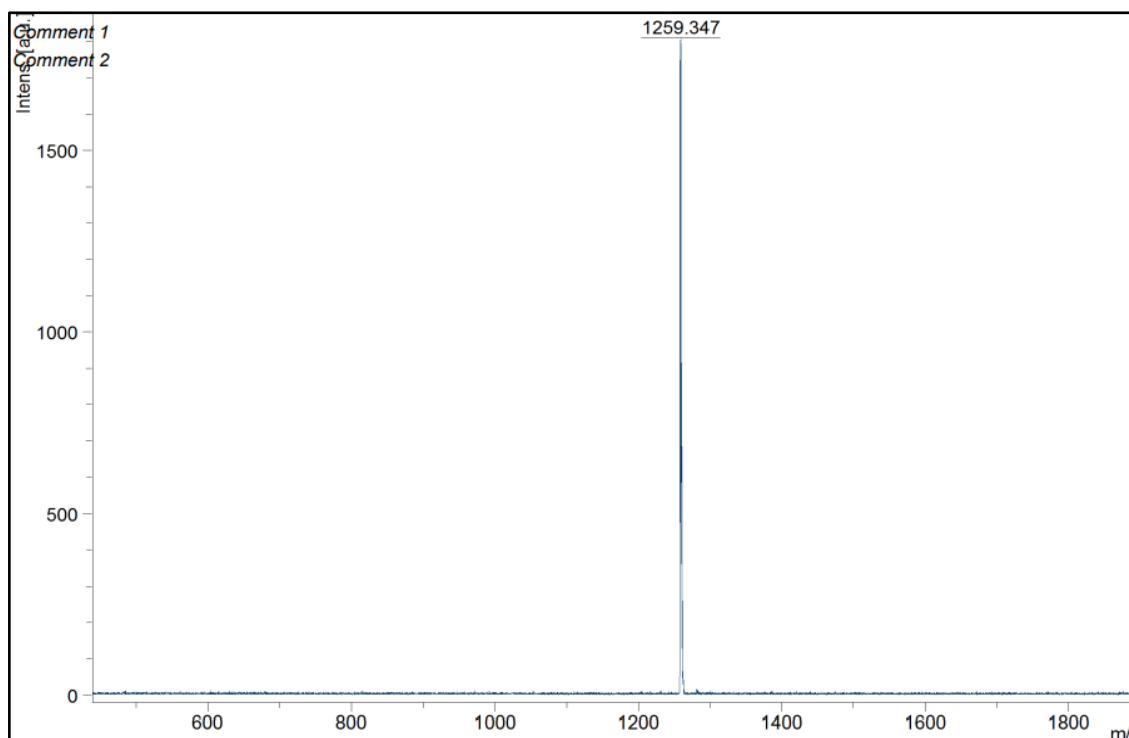


Figure 3.15. MALDI spectrum of CzPhPmDI

3.8. References:

- [1] a) H. Uoyama, K. Goushi, K. Shizu, H. Nomura, C. Adachi, *Nature* **2012**, 492, 234-238; b) M. Y. Wong, E. Zysman-Colman, *Adv. Mater.* **2017**, 29, 1605444; c) Y. Tao, K. Yuan, T. Chen, P. Xu, H. Li, R. Chen, C. Zheng, L. Zhang, W. Huang, *Adv. Mater.* **2014**,

26, 7931-7958; d) Y. Tao, K. Yuan, T. Chen, P. Xu, H. Li, R. Chen, C. Zheng, L. Zhang, W. Huang, *Adv. Mater.* **2014**, *26*, 7931-7958; e) Y. Im, M. Kim, Y. J. Cho, J.-A. Seo, K. S. Yook, J. Y. Lee, *Chem. Mater.* **2017**, *29*, 1946-1963; f) T. J. Penfold, F. B. Dias, A. P. Monkman, *Chem. Commun.* **2018**, *54*, 3926-3935; g) Y. Liu, C. Li, Z. Ren, S. Yan, M. R. Bryce, *Nat. Rev. Mater.* **2018**, *3*, 18020.

[2] a) S. Hirata, *Adv. Opt. Mater.* **2017**, *5*, 1700116; b) Kenry, C. Chen, B. Liu, *Nat. Commun.* **2019**, *10*, 2111; c) W. Zhao, Z. He, J. W. Y. Lam, Q. Peng, H. Ma, Z. Shuai, G. Bai, J. Hao, Ben Z. Tang, *Chem* **2016**, *1*, 592-602; d) T. Zhang, X. Ma, H. Wu, L. Zhu, Y. Zhao, H. Tian, *Angew. Chem. Int. Ed.* **2020**, *59*, 11206-11216; e) S. Xu, R. Chen, C. Zheng, W. Huang, *Adv. Mater.* **2016**, *28*, 9920-9940; f) X. Ma, J. Wang, H. Tian, *Acc. Chem. Res.* **2019**, *52*, 738-748.

[3] a) O. Bolton, K. Lee, J.-H. Kim, K.Y. Lin, J. Kim, *Nat. Chem.* **2011**, *3*, 205-210; b) D. Lee, O. Bolton, B. C. Kim, J. H. Youk, S. Takayama, J. Kim, *J. Am. Chem. Soc.* **2013**, *135*, 6325-6329; c) Z. An, C. Zheng, Y. Tao, R. Chen, H. Shi, T. Chen, Z. Wang, H. Li, R. Deng, X. Liu, W. Huang, *Nat. Mater.* **2015**, *14*, 685-690; d) Z. He, W. Zhao, J. W. Y. Lam, Q. Peng, H. Ma, G. Liang, Z. Shuai, B. Z. Tang, *Nat. Commun.* **2017**, *8*, 416; e) Q. Liao, Q. Gao, J. Wang, Y. Gong, Q. Peng, Y. Tian, Y. Fan, H. Guo, D. Ding, Q. Li, Z. Li, *Angew. Chem. Int. Ed.* **2020**, *59*, 9946-9951; f) J. Ren, Y. Wang, Y. Tian, Z. Liu, X. Xiao, J. Yang, M. Fang, Z. Li, *Angew. Chem. Int. Ed.* **2021**, *60*, 12335-12340; g) S. Kuila, S. Garain, S. Bandi, S. J. George, *Adv. Funct. Mater.* **2020**, *30*, 2003693; h) S. Kuila, S. J. George, *Angew. Chem. Int. Ed.* **2020**, *59*, 9393-9397; i) L. Gu, W. Ye, X. Liang, A. Lv, H. Ma, M. Singh, W. Jia, Z. Shen, Y. Guo, Y. Gao, H. Chen, D. Wang, Y. Wu, J. Liu, H. Wang, X.-Y. Zheng, Z. An, W. Huang, Y. Zhao, *J. Am. Chem. Soc.* **2021**, *143*, 18527-18535; j) Y. Su, Y.; Y. Zhang, Z. Wang, W. Gao, P. Jia, D. Zhang, C. Yang, Y. Li, Y. Zhao, *Angew. Chem. Int. Ed.* **2020**, *59*, 9967-9971; k) Y. Su, S. Z. F. Phua, Y. Li, X. Zhou, D. Jana, G. Liu, W. Q. Lim, W. K. Ong, C. Yang, Y. Zhao, *Sci. adv.* **2018**, *4*, eaas9732; l) A. Kirch, M. Gmelch, S. Reineke, *S. J. Phys. Chem. Lett.* **2019**, *10*, 310-315; m) S. Sun, J. Wang, L. Ma, X. Ma, H. Tian, *Angew. Chem. Int. Ed.* **2021**, *60*, 18557-18560.

[4] a) P. L. dos Santos, M. K. Etherington, A. P. Monkman, *J. Mater. Chem. C* **2018**, *6*, 4842-4853; b) P. L. dos Santos, F. B. Dias, A. P. Monkman, *J. Phys. Chem. C* **2016**, *120*, 18259-18267; c) F. B. Dias, J. Santos, D. R. Graves, P. Data, R. S. Nobuyasu, M. A. Fox,

A. S. Batsanov, T. Palmeira, M. N. Berberan-Santos, M. R. Bryce, A. P. Monkman, *Adv. Sci.* **2016**, *3*, 1600080; d) T. Ogiwara, Y. Wakukawa, T. Ikoma, *J. Phys. Chem. A* **2015**, *119*, 3415-3418; e) J. U. Kim, I. S. Park, C.-Y. Chan, M. Tanaka, Y. Tsuchiya, H. Nakanotani, C. Adachi, *Nat. Commun.* **2020**, *11*, 1765; f) M. K. Etherington, J. Gibson, H. F. Higginbotham, T. J. Penfold, A. P. Monkman, *Nat. Commun.* **2016**, *7*, 13680; g) J. Gibson, A. P. Monkman, T. J. Penfold, *Chem Phys Chem* **2016**, *17*, 2956-2961; h) E. W. Evans, Y. Olivier, Y. Puttisong, W. K. Myers, T. J. Hele, S. M. Menke, T. H. Thomas, D. Credginton, D. Beljonne, R. H. Friend, *J. Phys. Chem. Lett.* **2018**, *9*, 4053-4058.

[5] a) D. Di, L. Yang, J. M. Richter, L. Meraldi, R. M. Altamimi, A. Y. Alyamani, D. Credginton, K. P. Musselman, J. L. MacManus Driscoll, R. H. Friend, *Adv. Mater.* **2017**, *29*, 1605987; b) A. Dey, D. Kabra, *ACS Appl. Mater. Interfaces* **2018**, *10*, 38287-38293; c) C. J. Chiang, A. Kimyonok, M. K. Etherington, G. C. Griffiths, V. Jankus, F. Turksay, A. P. Monkman, *Adv. Funct. Mater.* **2013**, *23*, 739-746; d) E. Hamzehpoor, C. Ruchlin, Y. Tao, J. E. Ramos-Sanchez, H. M. Titi, G. Cosa, D. F. Perepichka, *J. Phys. Chem. Lett.* **2021**, *12*, 6431-6438; e) X. G. Wu, C. Y. Huan, D. G. Chen, D. H. Liu, C. C. Wu, K. J. Chou, B. Zhang, Y. F. Wang, Y. Liu, E. Y. Li, W. G. Zhu, P. T. Chou, *Nat. Commun.* **2020**, *11*, 2145.

[6] a) S. Hirata, M. Vacha, *Adv. Opt. Mater.* **2017**, *5*, 1600996; b) S. Kuila, S. Garain, G. Banappanavar, B. C. Garain, D. Kabra, S. K. Pati, S. J. George, *J. Phys. Chem. B* **2021**, *125*, 4520-4526; c) S. Kuila, A. Ghorai, P. K. Samanta, R. B. K. Siram, S. K. Pati, K. S. Narayan, S. J. George, *Chem. Eur. J.* **2019**, *25*, 16007-16011.

[7] a) S. Garain, S. Kuila, B. C. Garain, M. Kataria, A. Borah, S. K. Pati, S. J. George, *Angew. Chem. Int. Ed.* **2021**, *60*, 12323-12327; b) S. Garain, S. Sarkar, B. C. Garain, S. K. Pati, S. J. George, *Angew. Chem. Int. Ed.* **2022**, DOI: 10.1002/anie.202115773. c) S. Garain, B. C. Garain, M. Eswaramoorthy, S. K. Pati, S. J. George, *Angew. Chem. Int. Ed.* **2021**, *60*, 19720-19724; d) (a) S. Kuila, K. V. Rao, S. Garain, P. K. Samanta, S. Das, S. K. Pati, M. Eswaramoorthy, S. J. George, *Angew. Chem. Int. Ed.* **2018**, *57*, 17115-17119.

[8] a) P. Therdkatanyuphong, P. Chasing, C. Kaiyasuan, S. Boonnab, T. Sudyoasuk, V. Promarak, *Adv. Funct. Mater.* **2020**, *30*, 2002481; b) L. Zhao, S. Wang, J. Lü, J. Ding, L. Wang, *J. Mater. Chem. C*, **2017**, *5*, 9753.

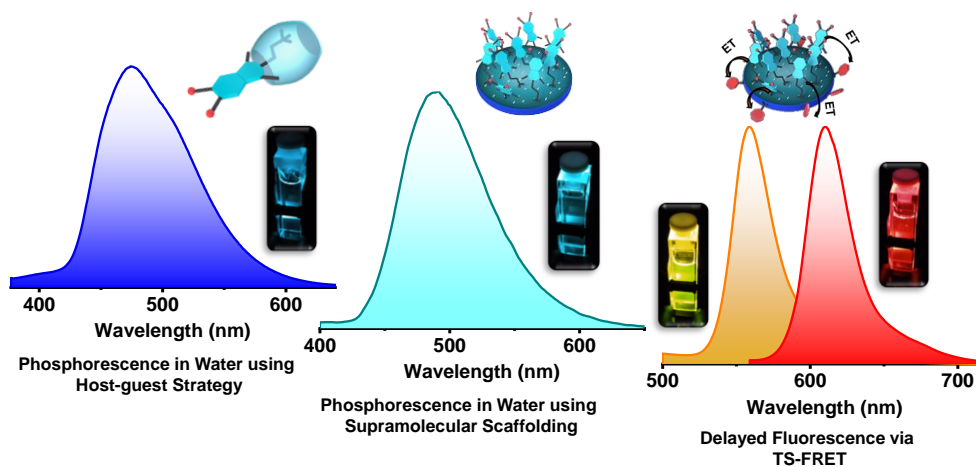
CHAPTER 4
Solution-state Phosphorescence and Delayed Sensitization via
Supramolecular Scaffolding

CHAPTER 4

Solution-state Phosphorescence and Delayed Sensitization via Supramolecular Scaffolding*

Abstract

Solution phase room-temperature phosphorescence (RTP) from organic phosphors is seldom realized. In this Chapter we discuss one of the highest efficient solution state RTP (~41.8 %) in water, from a structurally simple phthalimide phosphor, by employing an organic-inorganic supramolecular scaffolding strategy. We further use these supramolecular hybrid phosphors as a light-harvesting scaffold to achieve delayed fluorescence from orthogonally anchored sulforhodamine acceptor dyes via an efficient triplet to singlet Förster resonance energy transfer (TS-FRET), which is rarely achieved in solution. Electrostatic cross-linking of the inorganic scaffold at higher concentrations further facilitates the formation of self-standing hydrogels with efficient RTP and energy-transfer mediated long-lived fluorescence.



*Manuscript based on this work is published in *Angew. Chem. Int. Ed.* **2021**, 60, 19720-19724.

4.1. Introduction:

Recent years have witnessed a rapid surge in the research field of purely organic room-temperature phosphors by minimizing the triplet deactivation of the chromophores, which possess efficient inter-system crossing (ISC) efficiency and high triplet quantum yield, because of their likely applications in bioimaging, sensing and light-emitting materials.^[1] This has been often achieved by suppressing the molecular motion in their crystalline states^[2] or by embedding them in polymer matrices,^[3] which minimizes the vibrational and oxygen mediated non-radiative quenching of the triplet states. However, the next challenge in this field is the realization of efficient RTP in solution and gel phases, which is of paramount importance for exploring applications of organic phosphors in the biological realm.^[4] One elegant strategy to achieve RTP in these “soft-phases” would be to construct supramolecular microenvironments to arrest the dynamics and the vibrational dissipation of the phosphors either by non-covalent encapsulation or scaffolding.^[5] Thus far, the most successful strategy in this direction is the host-guest approach to encapsulate the phosphors through hydrophobic and other specific non-covalent interactions.^[6] Ma, Tian and co-workers have shown that well-known hydrophobic hosts, cyclodextrin and cucurbituril (CB), could harvest the triplets of a variety of organic phosphors, both in solution and gel phases.^[7] Liu and co-workers have extended CB host-guest complexation strategy to phenyl-pyridinium derivatives to extract efficient RTP in solution.^[8] Our group has recently introduced an organic-inorganic hybrid strategy to achieve aqueous phase phosphorescence, wherein inter-layer galleries of soluble inorganic materials were used as scaffolds to non-covalently anchor and rigidify the phosphors apart from providing a barrier to oxygen.^[9] However, most of the solution state phosphorescence reported so far exhibits low quantum yield compared to their crystalline or film states.^[10] Although Liu and co-workers have recently reported the highest quantum yield in the film state using a host-guest “supramolecular pin” strategy, the corresponding solution exhibits only one-eighth of this efficiency.^[11] Thus, further development of solution state phosphors demands an improvement in its efficiency under ambient conditions.

To alleviate this scenario, herein, we present highly efficient ambient RTP from a simple heavy atom substituted cationic phthalimide derivative (**CPthBr**) in aqueous solution with a remarkable phosphorescence quantum yield of ~41.8 %, using a supramolecular anchoring approach. Such intense RTP emission in the low-wavelength

region is one of the highest yield reported to date for organic phosphors in fluid phases. We show the ambient RTP of **CPthBr** in aqueous solution by host-guest encapsulation with cucurbit[7]uril (**CB[7]**) and also by the electrostatic supramolecular scaffolding using negatively charged laponite (**LP**) clays (Figure 4.1). Further, we utilize these phosphor-**LP** hybrids as efficient light-harvesting scaffolds by the orthogonal functionalization of the **LP** nanoclays with negatively charged fluorescent dyes (Figure 4.1). These multi-component donor- acceptor hybrids show delayed fluorescence from the acceptor molecule by an efficient TS-FRET which is seldom reported in the solution phase.^[8b] Interestingly, we also show that, at higher concentration, these **LP**-phosphor hybrids form self-standing hydrogels which also shows highly efficient phosphorescence and tuneable long-lived fluorescence by the delayed sensitization of the singlets of various acceptor dyes.

4.2. Molecular Design:

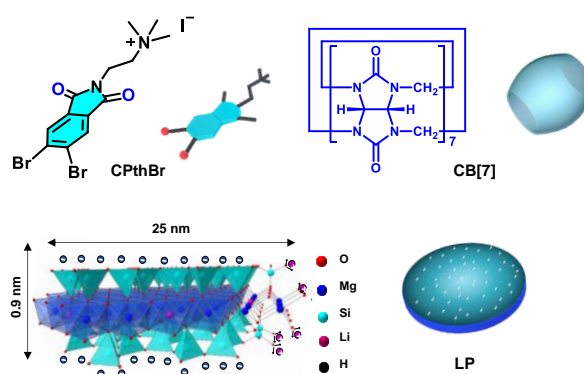


Figure 4.1. Molecular structures of **CPthBr** and schematic representation of **CPthBr**, **CB[7]** and **LP**.

First, we have synthesized a water-soluble, heavy-atom bromo-substituted phthalimide derivative, **CPthBr**, bearing cationic trimethylammonium group at the imide position and was fully characterized using nuclear magnetic resonance spectroscopy (NMR), high-resolution mass spectrometry (HR-MS) and high-performance liquid chromatography (HPLC) (See synthetic scheme 4 and experimental section). The molecular structures and schematic representation of **CB[7]** and **LP** nanoparticles are shown in Figure 4.1. In this work, we have used water-soluble **CB[7]** as host and **LP** clay nanoplates as the inorganic scaffold. Hence to promote the host-guest interaction and ionic self-assembly, the phosphors (**CPthBr**) was functionalized with quaternary ammonium cation groups. Another important feature of these chromophores

includes aromatic carbonyl groups and Br-atoms in the core, which is envisioned to promote efficient ISC and significant spin-orbit coupling (SOC) between singlet and triplet states.

4.3. Spectroscopic Studies in Solution-state:

CPthBr in water ($[c] = 0.1 \text{ mM}$) exhibited characteristic π - π^* absorption ($\lambda_{\text{max.}} = 306 \text{ nm}$) and weak monomer fluorescence emission in the 370-570 nm region ($\lambda_{\text{max.}} = 420 \text{ nm}$) (Figures 4.2a,b). The weak emission with a maximum at 520 nm obtained by the selective excitation at 404 nm and the corresponding excitation spectrum confirms the presence of aggregated molecules (Figures 4.2c,d). The time-resolved fluorescence decay experiments further showed the fluorescence lifetime of monomer and aggregate as 3.39 ns and 5.31 ns, respectively (Figures 4.2e,f). Further detailed light-scattering and microscopic studies have revealed that the molecules are aggregated in water to give thin two-dimensional sheet-like nanostructures (Figures 4.3a,b). The triplet emissive character of **CPthBr** was evident in the glassy matrix of THF at 77 K ($[c] = 0.05 \text{ M}$), which showed red-shifted phosphorescence emission with a maximum at 470 nm and with a long average lifetime of 6.2 ms (Figures 4.3c,d). This observation is consistent with the molecular design with carbonyl group and heavy atom to facilitate an efficient SOC and ISC (Figure 4.3e). Theoretical studies using time-dependent density functional theory (TD-DFT) further showed that the major contributing ISC channels in this molecular system would be S_1 (n - π^*) to T_4 (π - π^*), T_3 (π - π^*) and T_1 (π - π^*) which follows El Sayed's rule to allow the spin forbidden singlet-to-triplet transition (Figure 4.3e). The calculated spin-orbit coupling matrix element (SOCME) between S_1 to T_4 , T_3 and T_1 are found to be 27.42, 18.23 and 14.71 cm^{-1} , respectively (Figure 4.3e).

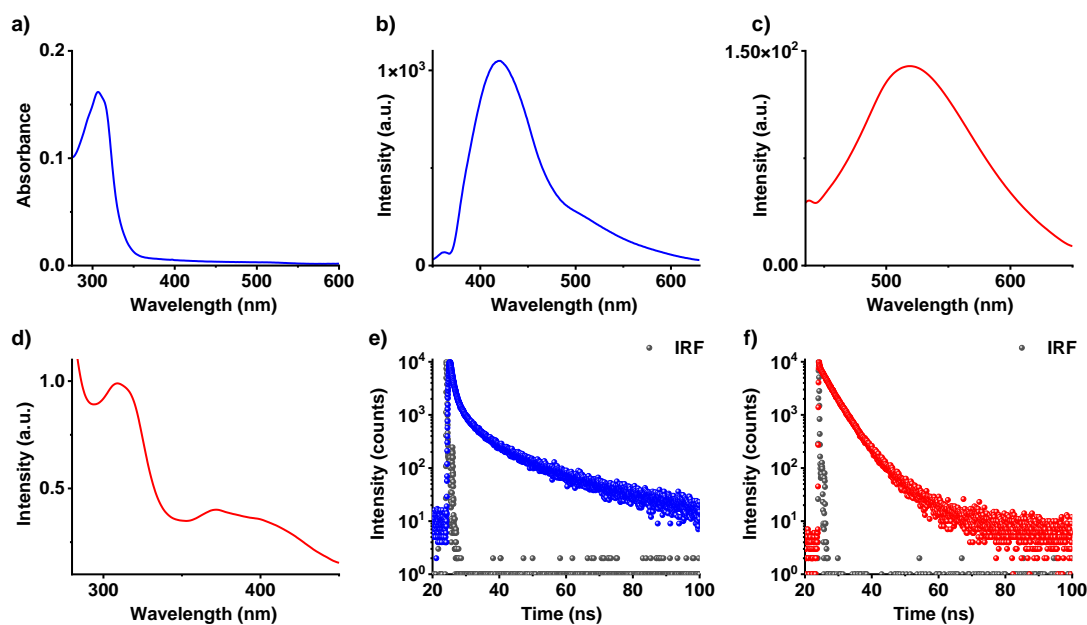


Figure 4.2. a) Absorption spectrum, b) emission spectrum at $\lambda_{exc.} = 310$ nm, c) emission spectrum at $\lambda_{exc.} = 404$ nm, d) excitation spectrum ($\lambda_{monitored} = 530$ nm), e) lifetime decay plot obtained by $\lambda_{exc.} = 286$ nm, $\lambda_{collected} = 370$ nm and f) lifetime decay plot obtained by $\lambda_{exc.} = 404$ nm, $\lambda_{collected} = 530$ nm of **CPhBr** in water ($[c] = 0.1$ mM). IRF = Instrument response function.

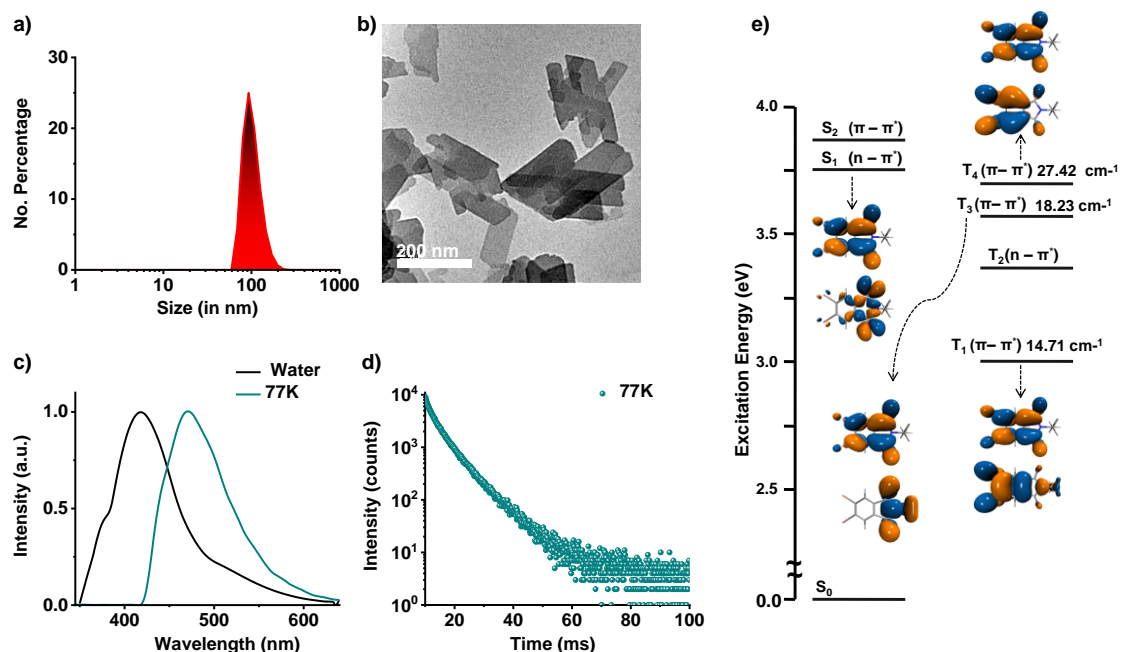


Figure 4.3. a) Dynamic Light Scattering (DLS) data depicting size of **CPthBr** (0.1 mM) in presence of **CB[7]**, b) TEM image of **CPthBr** (0.1 mM) in aqueous solution. c) Steady state emission spectra of **CPthBr** ($\lambda_{exc.} = 310$ nm, black line at room-temperature in water, dark cyan line = 77 K in THF). d) Time-resolved decay profile of **CPthBr** in THF (0.05 mM) at 77 K ($\lambda_{exc.} = 310$ nm, $\lambda_{collected} = 530$ nm, $\tau_{avg.} = 6.2$ ms). e) Relative excitation energies and their corresponding hole (below) and electron (above) wavefunctions and SOCME values of **CPthBr** (without cationic trimethylammonium group) obtained from TD-DFT calculation using CAM-B3LYP functional in conjunction with 6-31+g(d) basis set for C, H, N, O, and LANL2DZ basis set for Br with effective core potential.

4.4. Ambient Solution-state Room Temperature Phosphorescence using Host-guest Strategy:

Next, we endeavoured the ambient triplet harvesting from **CPthBr** in solution by minimizing the vibrational dissipation using various supramolecular strategies. First, the host-guest complexation of **CPthBr** ($[c] = 0.1$ mM) with **CB[7]**, by exploiting the high binding constant of the ammonium groups with the rim carbonyl groups of CB host, through ion-dipole interactions is attempted.^[12] Upon titration with **CB[7]**, a new red-shifted emission band with a maximum at 475 nm is observed with the gradual disappearance of monomer fluorescence, similar to the emission in the glassy matrix hinting towards the solution state phosphorescence from **CPthBr-CB[7]** complexes

(Figures 4.4a,b). The time-gated emission spectrum (delay time = 50 μ s), which showed similar emission features as that of the steady-state emission and the long average lifetime of 104 μ s, confirmed the solution phase RTP (Figures 4.4b,c).

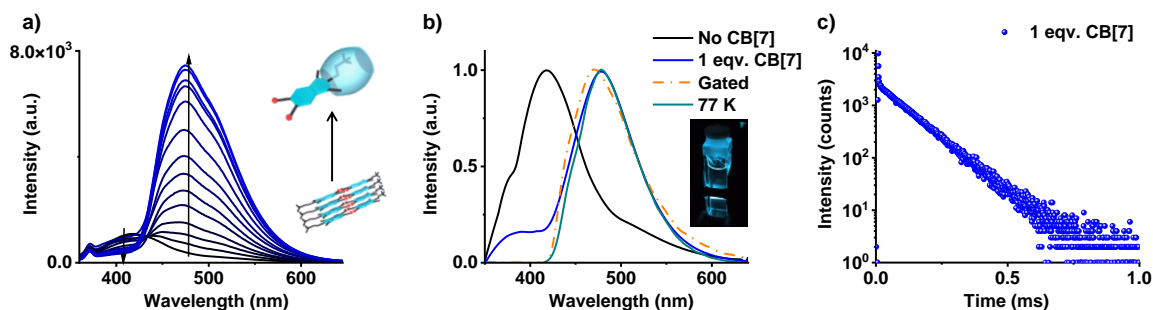


Figure 4.4. a) Photoluminescence titration study of the **CPthBr** with increasing equivalents (0 eqv. to 1.4 eqv.) of **CB[7]** in water. Inset: schematic showing interaction of **CPthBr** in the absence and presence of **CB[7]**. b) Steady-state (black line = without **CB[7]**), green line = 77 K, 1:1 **CPthBr-CB[7]** complex = blue line) and gated emission spectra of **CPthBr** in water. Inset: photograph of 1:1 **CPthBr-CB[7]** complex upon 310 nm Xe lamp excitation. c) Lifetime decay plot of 1:1 **CPthBr-CB[7]** complex.

The formation of a stable **CPthBr-CB[7]** host-guest complex with a 1:1 stoichiometry was confirmed by HR-MS and NMR analyses (Figure 4.5). ESI-HR-MS of the complex showed 1553.2875 m/z, a mass corresponding to the formation of 1:1 host-guest complex, which is also confirmed by the similarity between the experimentally observed and simulated isotopic patterns (Figures 4.5a,b). Tandem mass spectroscopy (MS/MS) experiments of the complex ion (**CPthBr-CB[7]**) showed a high stability for the complex, as very high accelerating voltages were required to disassociate the complex to individual molecular ions (Figure 4.5c). The up-field shift of H_a , H_b and H_c from 4.131 to 3.298 ppm ($\Delta\delta = 0.833$ ppm), from 3.621 to 2.703 ppm ($\Delta\delta = 0.918$ ppm) and from 3.200 to 3.125 ppm ($\Delta\delta = 0.075$ ppm), respectively suggests the formation **CPthBr-CB[7]** host-guest complex (Figure 4.5d). Again splitting of the **CB[7]** proton into two sets of equivalent proton ($CH_{[2]}$ from 5.753 and 5.714 ppm to 5.729, 5.690 ppm and 5.635, 5.596 ppm respectively and $CH_{[3]}$ from 4.189 and 4.151 ppm to 4.166, 4.128 ppm and 4.086, 4.047 ppm, respectively) and up-field shift ($CH_{[1]}$ from 5.477 to 5.399 ppm) also suggests asymmetric charge density environment of the **CB[7]** proton (Figure 4.5d).

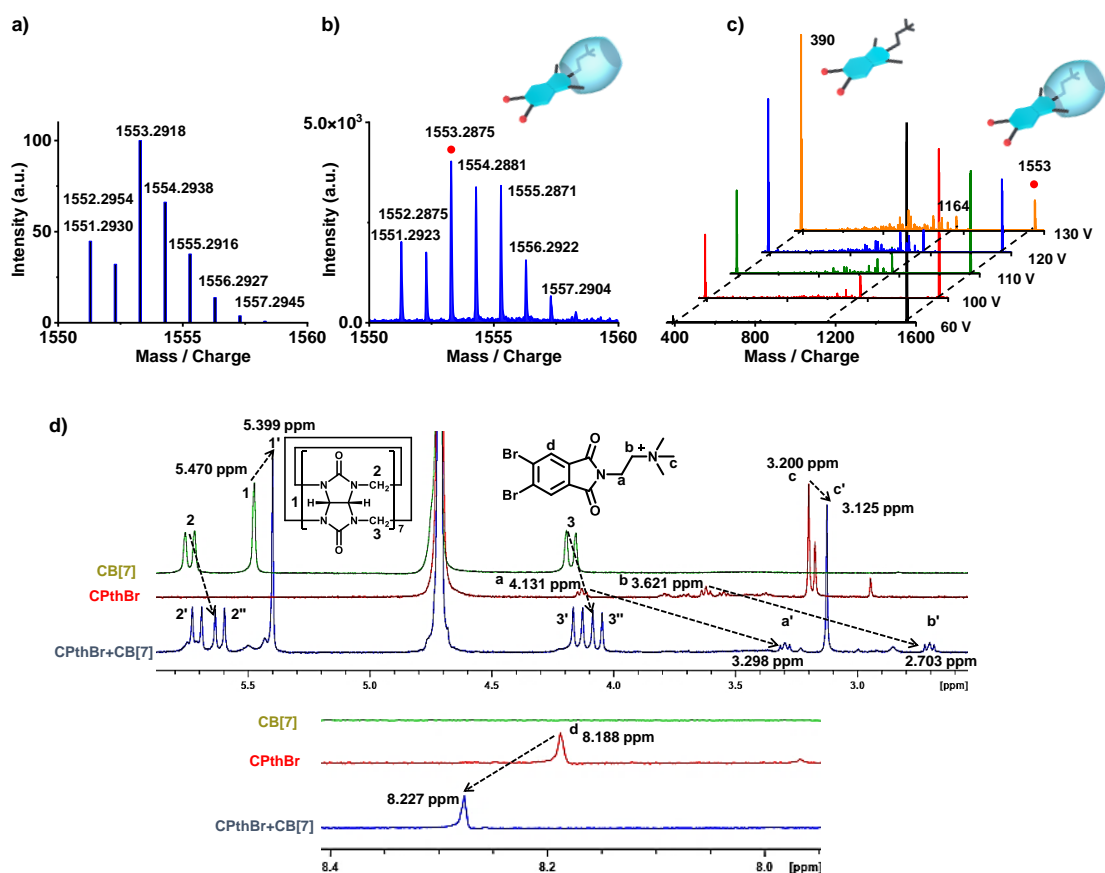


Figure 4.5. a) Simulated and b) experimental high-resolution ESI-MS isotopic pattern of 1:1 *CPthBr*-*CB*[7] complex. c) ESI tandem MS/MS pattern of 1:1 *CPthBr*-*CB*[7] complex ion (1553.2875, m/z) upon varying accelerating voltage. d) ^1H NMR spectra of *CB* [7], *CPthBr* and 1:1 *CPthBr*-*CB*[7] complex in D_2O (0.1 mM).

However, the absolute phosphorescence quantum yield (Φ_{P}) of this complex in water is found to be only 6 %. The Φ_{P} of this complex have further been enhanced to 13 % under inert atmosphere and 14 % in film state by incorporating to a polyvinyl alcohol (PVA) matrix, suggesting the possibility of improving the Φ_{P} by reducing the oxygen diffusion and arresting the vibrational dissipation to a greater extent, respectively (Figure 4.6).

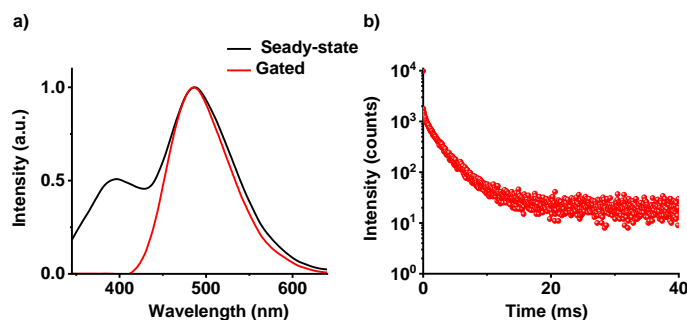


Figure 4.6. a) Steady-state, gated emission spectra and b) lifetime decay profile of 1:1 **CPthBr-CB[7]** complex by incorporating into a polyvinyl alcohol (PVA) matrix. ($\lambda_{exc.} = 310 \text{ nm}$, $\lambda_{collected} = 530 \text{ nm}$).

4.5. Ambient Solution-state Room Temperature Phosphorescence in Laponite using Supramolecular Scaffolding:

To increase the solution phase Φ_P of **CPthBr**, next an organic-inorganic supramolecular scaffolding strategy previously reported by our group is attempted,^[9] wherein the negatively charged surface of **LP** nano-clays is used as a template to anchor the cationic phosphors. The dual-charged disc-shaped nano-clays, with a negative charge at the surface and positive charge at the rim (edge), were first exfoliated in water by wrapping the positive charges at the rim with anionic sodium polyacrylate polymer, thus preventing the electrostatically driven clay networks.^[13] Zeta potential studies showed a decrease in the negative charge of the **LP** nanoplates, upon increasing the **CPthBr** concentration, suggesting the hybrid co-assembly (Figure 4.7a). Titration of an aqueous solution of **CPthBr** ($[c] = 0.5 \text{ mM}$) with increasing wt. % of **LP** (0.125 wt. % shows gradual appearance of an intense cyan phosphorescence ($\lambda_{max.} = 487 \text{ nm}$), (Figure 4.7b). The high lifetime of 1.62 ms and gated emission spectrum (delay time = 0.5 ms) confirms the phosphorescence nature of this emission (Figures 4.7c,d). Maximum phosphorescence was observed with 6 wt. % of **LP** and the corresponding hybrid solution showed a remarkable Φ_P of 41.8 % under ambient conditions and could be improved further to 43 % upon purging the solution with nitrogen. It should be mentioned that hybrids with 6 wt.% is a viscous (85 mPaS) solution, due to the electrostatically driven interaction between the laponite nanoclays. However, the hybrids with lower wt. % of laponite (2.25 wt. %), which behaves like normal solution (1.40 mPaS) also showed impressive Φ_P of 36 %. Further we envisage that, the less quantum yield of the previously reported systems using **LP** templates could be due to

their less number of ISC channels and low SOCME value compared to the present system.^[9,10f] Anchoring of the cationic phosphors to the clay surface minimizes the vibrational motion of the phosphors and spatially separates the phosphors to reduce the inter-phosphor interactions, thus yielding a very high phosphorescence intensity.

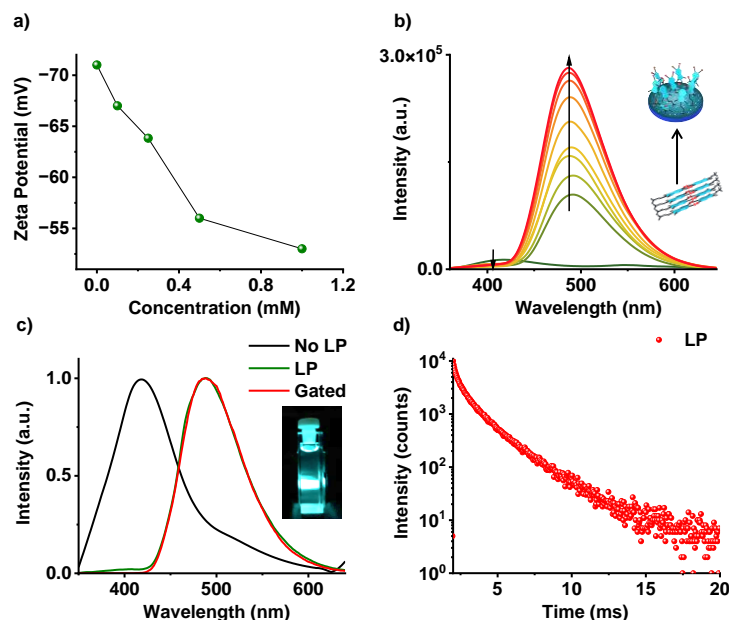


Figure 4.7. a) Zeta potential of *CPhBr-LP* hybrids upon titration in aqueous solution (LP = 2.25 wt. %). b) Photoluminescence titration study of the *CPhBr* with increasing the LP wt. % (0.125 wt. % to 6 wt. %) in an aqueous solution. Inset: schematic showing interaction of *CPhBr* in absence and presence of LP. c) Steady-state and gated emission spectra of *CPhBr-LP* hybrids. Inset: photograph of *CPhBr-LP* hybrid upon 310 nm Xe lamp excitation. d) Lifetime decay plot of *CPhBr-LP* hybrid (LP = 6 wt. %). (In all cases $\lambda_{exc.} = 310$ nm, $\lambda_{collected} = 530$ nm).

4.6. Triplet to Singlet Förster Resonance Energy Transfer via Delayed Sensitization:

Recently TS-FRET has emerged as an efficient strategy to achieve long-lived tunable fluorescence by a delayed sensitization process.^[3g] However, an efficient TS-FRET in organic systems requires significant oscillator strength for the donor (D) phosphorescence to facilitate the dipole-dipole coupling with an acceptor (A) (Figure 4.8a).^[3e,g] Further, TS-FRET also demands the spatial closeness of D and A molecules and hence has been reported mostly in condensed states such as in films.^[3e,g] To achieve the TS-FRET in solution, we envisage that LP with complementary charges at

its surface and edges provide an unprecedented scaffold to orthogonally anchor and to spatially separate the cationic D and anionic A dyes without any electrostatically driven ground-state interactions (Figure 4.8b). Thus, negatively charged Sulforhodamine G (**SRG**) and Sulforhodamine101 (**SR101**) with high fluorescence quantum yield and with good spectral overlap with the **CPthBr** triplet emission were selected as the acceptors (Figure 4.8c). The simplified Jablonski explains the TS-FRET process in figure 4.8d, where **CPthBr** transfers its triplet exciton to the fluorescence acceptor.

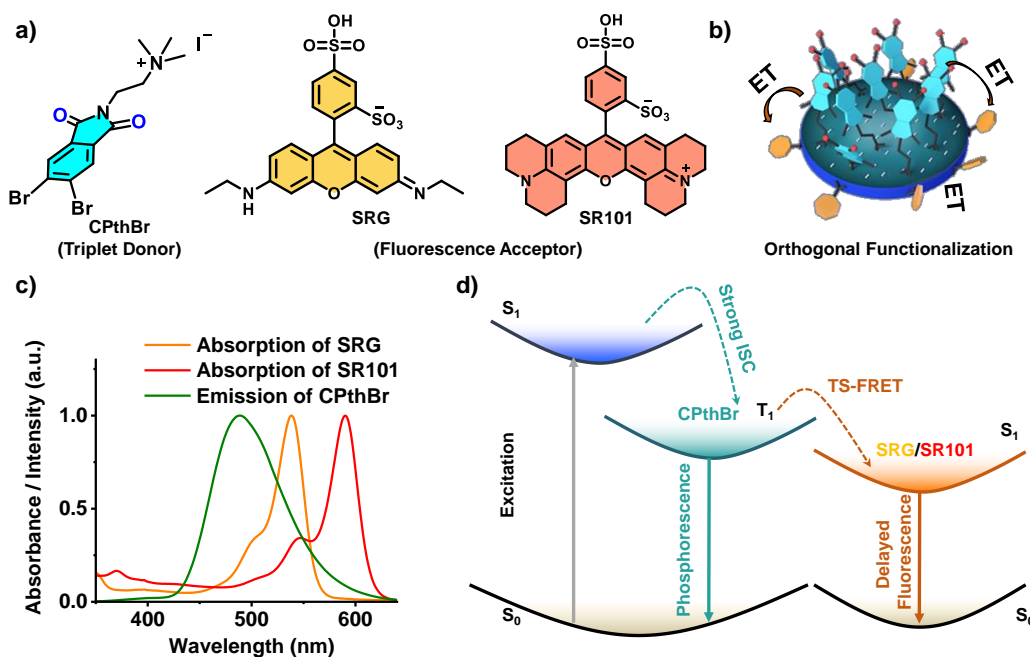


Figure 4.8. a) Molecular structures for TS-FRET donor (**CPthBr**) and fluorescence acceptor (**SRG**, **SR101**). b) Schematic showing TS-FRET from **CPthBr** to **SRG** dyes. c) Spectral overlap of **CPthBr** phosphorescence ($[c] = 0.5$ mM) with the absorption spectra of **SRG** and **SR101** ($[c] = 0.05$ mM) in **LP** hybrids. d) Simplified Jablonski diagram explains the TS-FRET process.

To explore the TS-FRET process, the concentration of the A molecules (0.005 to 0.05 mM) in **CPthBr-LP** hybrid solution (0.5 mM in 2.25 wt. %) was gradually increased (Figures 4.9a,b). The emission intensity of **SRG** ($\lambda_{\text{max.}} = 560$ nm) and **SR101** ($\lambda_{\text{max.}} = 610$ nm) showed a gradual increase with a concomitant decrease of the **CPthBr** phosphorescence upon increasing D:A composition from 100:1 to 100:10, which hint toward a TS-FRET in the solution state (Figures 4.9a,b). Time-resolved decay experiments showed a decrease in the phosphorescence lifetime of the donor from 1.03 ms to 0.698 ms and 0.418 ms in the 100:10 D:A hybrid solution of **SRG** and **SR101**,

respectively, and thus rules out the possibility of any trivial energy transfer process (Figures 4.9c,d). Interestingly, the gated spectrum (delay time = 50 μ s) clearly showed that emission from the acceptor had delayed fluorescence characteristics, which clearly demonstrates the delayed sensitization process and TS-FRET (Figures 4.9e,f).

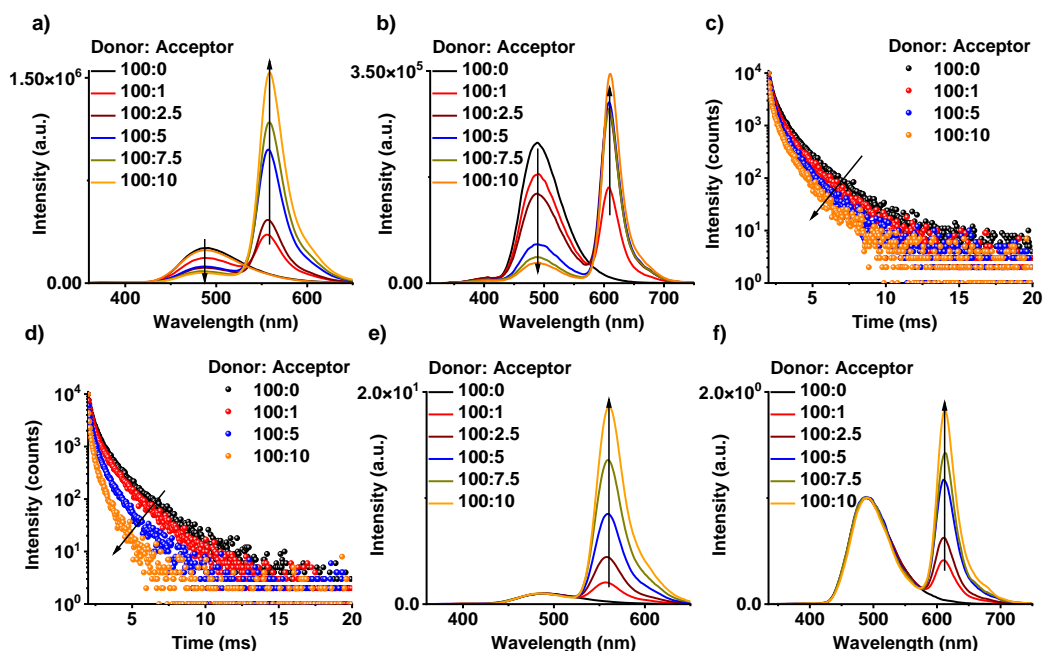


Figure 4.9. a,b) Steady-state emission spectra, c,d) lifetime decay profiles and e,f) gated emission spectra of **CPthBr-SRG-LP** and **CPthBr-SR101-LP** hybrids, respectively with increasing the doping concentration of **SRG** and **SR101** in aqueous solution. ($\lambda_{exc.} = 310$ nm, $\lambda_{collected.} = 490$ nm, delay time = 50 μ s, for all cases **LP** = 2.25 wt. %, *IRF* = Instrument response function).

Accordingly, the lifetime of **SRG** and **SR101** scaffolded on to **CPthBr-LP** hybrids are found to be 163.5 μ s and 60.4 μ s, respectively (Figure 4.10a). On the other hand, direct excitation of these hybrids leads to the prompt fluorescence in the ns timescale ($\tau_{avg.} = 4.25$ ns and 4.75 ns for **SRG** and **SR101**, respectively), unambiguously indicating that the delayed fluorescence occurs through the sensitization of the singlets (Figure 4.10b). The efficiency of the energy transfer was calculated to be ~32% and ~60% for **SRG** and **SR101**, respectively (D:A = 100:10), (Table 4.1). The role of laponite scaffolding in creating microenvironments with spatially separated D and A chromophores is crucial to achieve the same as no energy transfer was observed in the absence of **LP** template.

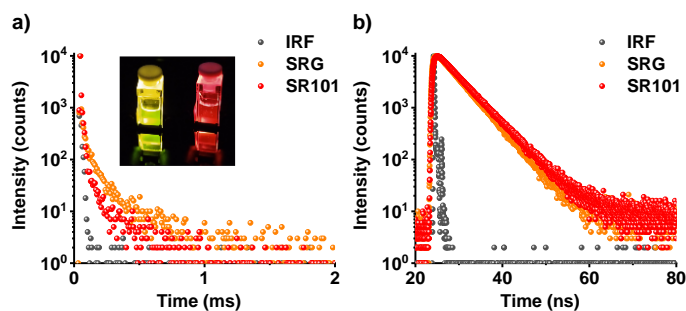


Figure 4.10. a) Delayed fluorescence lifetime decay profiles of **CPthBr-SRG-LP** and **CPthBr-SR101-LP** hybrids ($\lambda_{exc.} = 310$ nm, $\lambda_{collected} = 640$ nm, and $\lambda_{collected} = 670$ nm for **CPthBr-SRG-LP** and **CPthBr-SR101-LP**, respectively). Inset: photographs of **CPthBr-SRG-LP** and **CPthBr-SR101-LP** hybrids, respectively upon 310 nm Xe lamp excitation. (D:A = 10:1). b) Lifetime decay profiles of **CPthBr-SRG-LP** and **CPthBr-SR101-LP** hybrids in aqueous solution ($[c] = 0.05$ mM, $\lambda_{exc.} = 532$ nm, $\lambda_{collected} = 640$ nm and 670 nm for **CPthBr-SRG-LP** and **CPthBr-SR101-LP**, respectively, for all cases **LP** = 2.25 wt. %, IRF = Instrument response function).

An increase of the acceptor emission in the gated emission spectra upon increasing the acceptor concentration suggests the TS-FRET is operative in the **LP** scaffolded drop-casted films on quartz substrates (Figures 4.11a,b). Further, the decrease of the donor lifetime and high delayed fluorescence lifetime of the acceptor confirms the TS-FRET in the **CPthBr-SRG-LP** hybrids in the film state, suggesting spatial separation of D and A and efficient TS-FRET also be retained in the drop-casted films (Figures 4.11c-f).

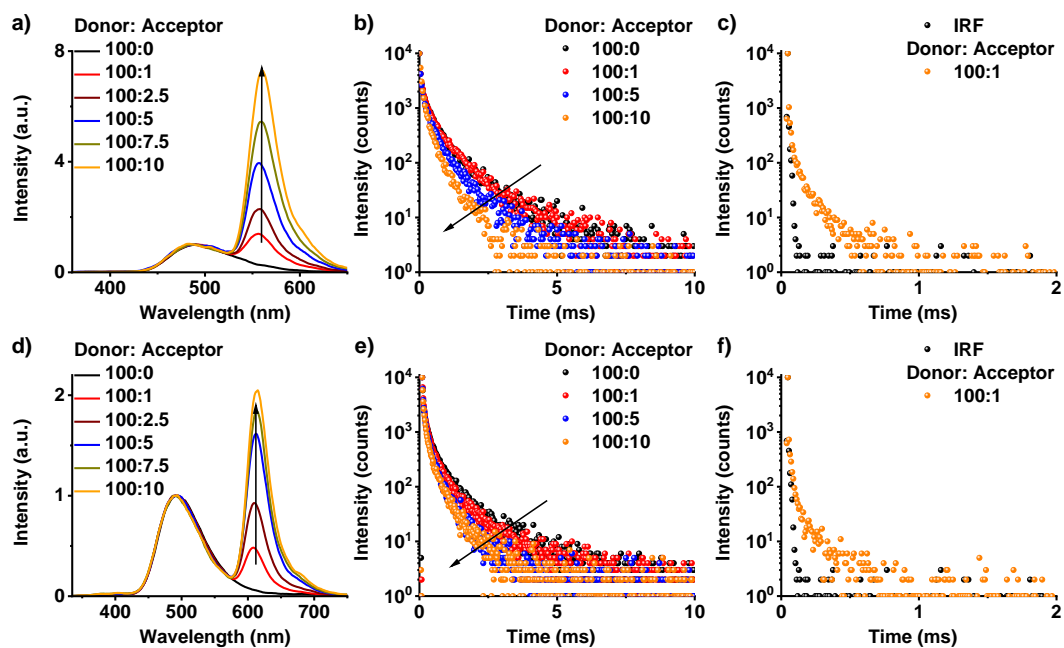


Figure 4.11. a,d) Gated emission spectra ($\lambda_{exc.} = 310$ nm, delay time = 50 μ s), b,e) lifetime decay profiles ($\lambda_{exc.} = 310$ nm, $\lambda_{collected.} = 490$ nm) and d,f) delayed fluorescence lifetime decay plot ($\lambda_{exc.} = 310$ nm, $\lambda_{collected.} = 640$ nm and $\lambda_{collected.} = 670$ nm for **CPthBr-SRG-LP** and **CPthBr-SR101-LP**, respectively) of drop casted thin film of **CPthBr-SRG-LP** and **CPthBr-SR101-LP** hybrids, respectively (LP = 2.25 wt. %, [C] of **CPthBr** = 0.5 mM, IRF = Instrument response function).

4.7. Ambient Phosphorescence and Delayed Fluorescence in Hybrid Hydro Gel:

LP scaffold is known to form unique self-standing supramolecular hydrogel at higher concentrations through an electrostatically driven house of card organization fostered by its differentially charged surfaces. Thus, it can be used to make soft-hybrid-based phosphorescent hydrogels.^[9] First, phosphorescent hydrogels of **CPthBr** ([C] = 0.5 mM) were made by the co-assembly with 10 wt.% of LP, which exhibits a cyan phosphorescence with an average lifetime of 1.34 ms and Φ_P of 34.2% (Figures 4.12a,b). Similarly, yellow and orange emitting hydrogels could be made by exploiting the TS-FRET process in these **CPthBr-LP** hydrogels by incorporating **SRG** and **SR101** dyes (D:A = 100:10), respectively (Figure 4.12a,b). Corresponding **SRG** and **SR101** hydrogels exhibit delayed fluorescence with an average lifetime of 162 μ s and 55 μ s, respectively, and with Φ_P 's of 81% and 37% with **SRG** and **SR101** dye, respectively (Figure 4.12c, Table 4.1). Phosphorescent hydrogels are seldom reported, and the

organic-inorganic hybrid co-assembly presents an attractive strategy to make self-standing luminescent hydrogels.

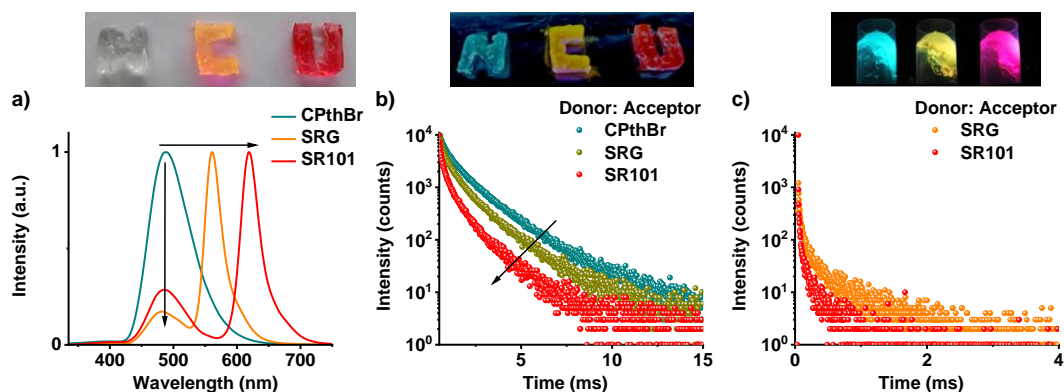


Figure 4.12. a) Normalized gated emission spectra and b) lifetime decay profiles ($\lambda_{exc.} = 310 \text{ nm}$, $\lambda_{collected} = 500 \text{ nm}$) of **CPthBr**, 10:1 **CPthBr-SRG-LP** and **CPthBr-SR101-LP** hybrid hydrogels, respectively. c) delayed fluorescence lifetime decay profiles ($\lambda_{exc.} = 310 \text{ nm}$, $\lambda_{collected} = 640 \text{ nm}$ and 670 nm for **CPthBr-SRG-LP** and **CPthBr-SR101-LP**, respectively) of 10:1 **CPthBr-SRG-LP** and **CPthBr-SR101-LP** hybrid hydrogels, respectively. Top inset: Photographs of self-standing hydrogel and 'NCU' is written under visible light and under 254 nm UV light using hydrogel. (LP = 10 wt.% for hydrogels, all photographs were taken under 256 nm UV lamp excitation, IRF = Instrument response function).

Table 4.1. Summary of energy transfer (Φ_{ET}) efficiency.

Acceptor	Physical State	Donor (C PthBr) and Acceptor (SR G or SR 101) Ratio	Average Lifetime (in ms) of C PthBr at 490 nm ($\lambda_{exc.} = 310$ nm)	Energy Transfer Efficiency (%)
-	Liquid	100:0	1.030	-
SR G	Liquid	100:1	0.910	11.7
SR G	Liquid	100:5	0.809	21.5
SR G	Liquid	100:10	0.698	32.2
SR 101	Liquid	100:1	0.877	14.9
SR 101	Liquid	100:5	0.621	39.7
SR 101	Liquid	100:10	0.418	59.4
-	Solid (Thin Film)	100:0	0.558	-
SR G	Solid (Thin Film)	100:1	0.469	15.9
SR G	Solid (Thin Film)	100:5	0.386	30.8
SR G	Solid (Thin Film)	100:10	0.288	48.4
SR 101	Solid (Thin Film)	100:1	0.348	37.6
SR 101	Solid (Thin Film)	100:5	0.227	59.3
SR 101	Solid (Thin Film)	100:10	0.184	67.0
-	Gel	100:0	1.340	-
SR G	Gel	100:10	1.060	20.9
SR 101	Gel	100:10	0.74	44.8

The energy transfer efficiency was calculated from the following equation: $\Phi_{ET} = 1 - \langle \tau_{DA} \rangle / \langle \tau_D \rangle$. Here, $\langle \tau_{DA} \rangle$ is the lifetime of the donor in the presence of the acceptor, and $\langle \tau_D \rangle$ is the lifetime of the donor without any acceptor.

4.8. Conclusions:

In conclusion, we have reported an efficient RTP emission in an aqueous solution and amorphous hydrogel, from a simple phthalimide derivative using a soluble inorganic silicate template to anchor the phosphor molecules. This strategy has resulted in one of the highest solution and gel phase phosphorescence quantum yields reported till date, under ambient conditions. The laponite-phosphor soft-hybrids could further be used as an efficient light-harvesting scaffold by co-anchoring negatively charged Sulforhodamine dyes, utilizing the facially separated, complementary charges of the nanoclay scaffold. Consequently, the TS-FRET between the triplet state of phosphor and the singlet state of the fluorescent dyes have resulted in long-lived singlet emission by a delayed sensitization process both in solution and gel states, which is rarely reported for purely organic systems. We envisage that this study would steer active research in solution-state phosphors and their use for imaging and sensing applications in biological systems.

4.9. Experimental Section:

4.9.1. General Methods:

NMR Measurements: ^1H and ^{13}C NMR spectra were recorded on a BRUKER AVANCE-400 Fourier transformation spectrometer with 400 and 100 MHz, respectively. The spectra were calibrated with respect to the residual solvent peaks. The chemical shifts are reported in parts per million (ppm) with respect to TMS. Short notations used are, s for singlet, d for doublet, t for triplet, q for quartet and m for multiplet.

Optical Measurements: Electronic absorption spectra were recorded on a Perkin Elmer Lambda 900 UV-Vis-NIR spectrometer and emission spectra were recorded on FLS1000 spectrometer, Edinburgh Instruments. Solution state UV-Vis and emission spectra were recorded in 1 mm path length cuvette. Fluorescence spectra of films were recorded in front-face geometry to avoid self-absorption.

Lifetime Measurements and Quantum yield: Fluorescence lifetimes were performed on a Horiba Delta Flex time-correlated single-photon-counting (TCSPC) instrument. A 286 nm diode and 404 nm, 532 nm laser diode with a pulse repetition rate of 1 MHz were used as the light source. The instrument response function (IRF) was collected by

using a scatterer (Ludox AS40 colloidal silica, Sigma-Aldrich). Phosphorescence lifetime ($\lambda_{exc.} = 310$ nm) and gated emission were measured on FLS1000 spectrometer, Edinburgh Instruments equipped with a micro flash-lamp (μ F2) set-up. Quantum yields were measured using an integrating sphere in the same instrument.

High Resolution Mass Spectrometry (HRMS): HR-MS was carried out using Agilent Technologies 6538 UHD Accurate-Mass Q-TOFLC/MS.

High Performance Liquid Chromatography (HPLC): HPLC was carried out using Agilent 1260 infinity quaternary HPLC system equipped with analytical ZORBAX Eclipse plus C18 column (4.6 mm \times 100 mm, 3.5 micron).

Computational Details: Ground State (S_0) of **CPthBr** molecule was optimized using density functional theory (DFT) and electronic absorption spectra were calculated using time-dependent density functional theory (TD-DFT) as implemented in the Gaussian 16 software.^[14a] Ground state (S_0) optimization and frequency calculation was performed employing B3LYP^[14b-d] exchange functional with 6-31+g(d) basis set except for Br for which LANL2DZ basis set was used with the corresponding effective core potential (ECP). While the excited state calculations were also performed B3LYP exchange-correlation functional with the same basis sets as mentioned before. Ground state frequency calculation was performed to confirm the absence of any unstable normal mode. The first singlet excited state (S_1) was optimized at the TD-DFT level of theory. While the first triplet excited states (T_1) were also optimized at the TD-DFT level of theory within the Tamm-Dancoff approximation (TDA) to overcome the triplet instability issue.^[14e] The spin-orbit coupling (SOC) effect was considered to be a perturbation of the scalar relativistic Kohn-Sham orbitals after SCF and TD-DFT calculations (pSOC-TD-DFT).^[14f-h] The SOC matrix elements were calculated using B3LYP with a Slater-type all-electron TZP basis set for all atoms as implemented in the ADF package.^[14i]

4.9.2. Protocol of Sample Preparation:

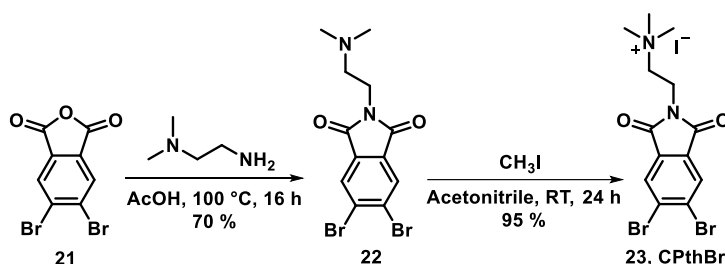
All solution state studies and phosphorescence studies of **CPthBr** in the presence of **CB[7]** were performed, keeping the final concentration of the samples at 0.1 mM. 1 mM **CPthBr** and 0.2 mM **CB[7]** in an aqueous solution was used as a stock solution. Phosphorescence studies of **CPthBr** with **LP** were performed, keeping the final concentration of the samples at 0.5 mM, using a stock solution of 5 mM **CPthBr**

and 7 wt. % **LP** in water (suspending 630 mg of **LP** in 9 mL millipore distilled aqueous solution under intense sonication followed by treating the suspension with 24 mg of sodium polyacrylate). The phosphorescent hydrogel was prepared using 10 wt. % **LP**. For the TS-FRET studies, the required amount of **SRG** and **SR101** was added into 0.5 mM **CPthBr-LP** hybrids (**LP** = 2.25 wt. %) and sonicated for 5 minutes to get a clear hybrid solution. 0.1 mM **SRG** and **SR101** in an aqueous solution were used as a stock solution. For thin film preparation, hybrid solutions were drop casted on clean quartz substrates and dried under vacuum overnight at 50 °C.

4.10. Synthetic Schemes and Procedures:

Materials: *o*-Xylene and *N, N'*-dimethylethylenediamine were purchased from Alfa-Aesar; Pyridine, Acetic acid, Bromine and Potassium Permanganate were purchased from Spectrochem, India and used without further purification.

Synthetic Scheme:



Scheme 4. Synthetic scheme for CPthBr.

Synthetic Procedures:

Compound **21** was synthesized according to the literature procedure.^[15]

Synthesis of compound 22: Dibromophthalic anhydride (**21**) (500 mg, 1.63 mmol) was taken in a 100 mL round bottom flask, and 25 mL acetic acid was added into it and stirred at room temperature for 30 minutes. *N, N'*-dimethylethylenediamine (180.0 mg, 2.04 mmol) was added to the reaction mixture and allowed to reflux for 16 hours. Subsequently aqueous solution was added to the reaction mixture, and acetic acid was neutralized by sodium bicarbonate and the compound was extracted with chloroform. The chloroform was evaporated under reduced pressure and dried under vacuum for 10 hours. Column chromatography was performed using 1 to 5 % methanol in chloroform as an eluent to get the pure product as white solid (430 mg, 70 % yield).

^1H NMR (CDCl_3 , 400 MHz), δ (ppm) = 8.07 (s, 1H), 3.79 (t, 2H, $J = 6.4$ Hz), 2.57 (t, 2H, $J = 6.4$ Hz), 2.26 (s, 6H); ^{13}C NMR (CDCl_3 , 100 MHz), δ (ppm) = 166.5, 131.9, 131.2, 128.4, 56.8, 45.4, 36.5. HRMS (ESI): m/z calculated for $\text{C}_{12}\text{H}_{12}\text{Br}_2\text{N}_2\text{O}_2$: 375.9245; observed 376.9312 $[\text{M}+\text{H}]^+$.

Synthesis of compound CPthBr: In a 100 mL round bottom flask, compound **22** (400 mg, 1.29 mmol) and methyl iodide (0.8 mL, 12.9 mmol) were added. 50 mL chloroform was added into it and stirred for 24 hours at room temperature. The white precipitate formed during the reaction was filtered, washed with diethyl ether, and dried under vacuum to give pure compound **CPthBr** (523 mg, 95% yield).

^1H NMR ($\text{DMSO}-d_6$, 400 MHz), δ (ppm) = 8.32 (s, 1H), 4.02 (t, 2H, $J = 6.8$ Hz), 3.60 (t, 2H, $J = 7.0$ Hz), 3.16 (s, 9H); ^{13}C NMR ($\text{DMSO}-d_6$, 100 MHz), δ (ppm) = 165.8, 132.0, 130.7, 128.2, 61.8, 52.5, 31.7. HRMS (ESI): m/z calculated for $\text{C}_{13}\text{H}_{13}\text{Br}_2\text{N}_2\text{O}_3$: 390.9474; observed 390.9491 $[\text{M}]^+$.

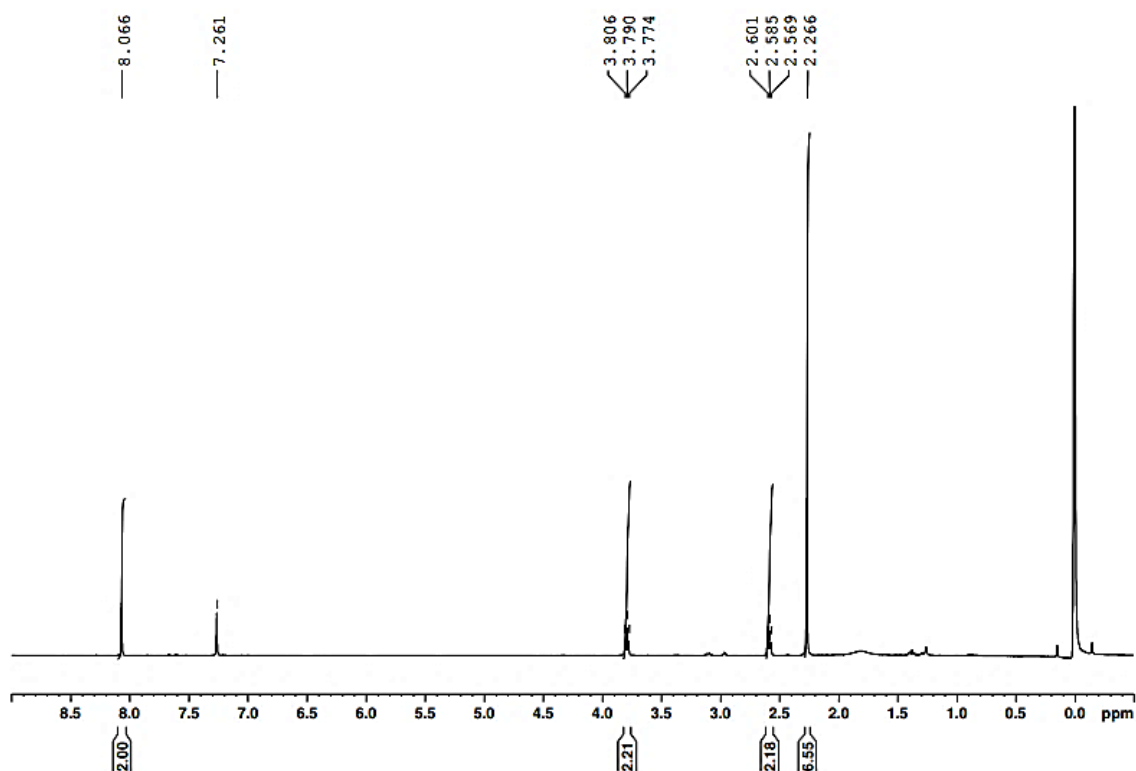


Figure 4.13. ^1H NMR spectrum of **22** in CDCl_3 .

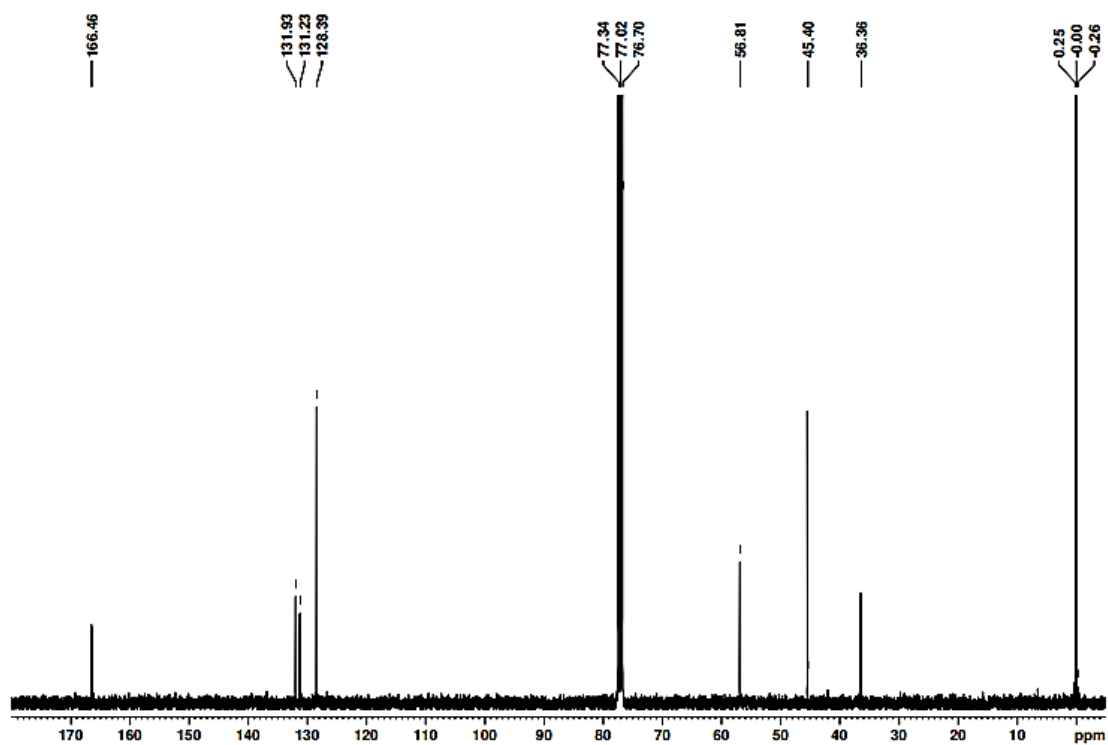


Figure 4.14. ^{13}C NMR spectrum of **22** in CDCl_3 .

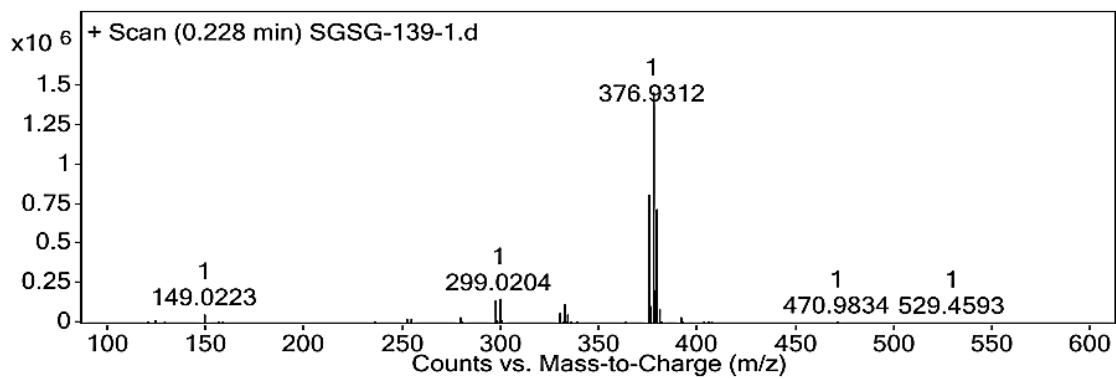


Figure 4.15. ESI-HR-MS spectrum of **22**.

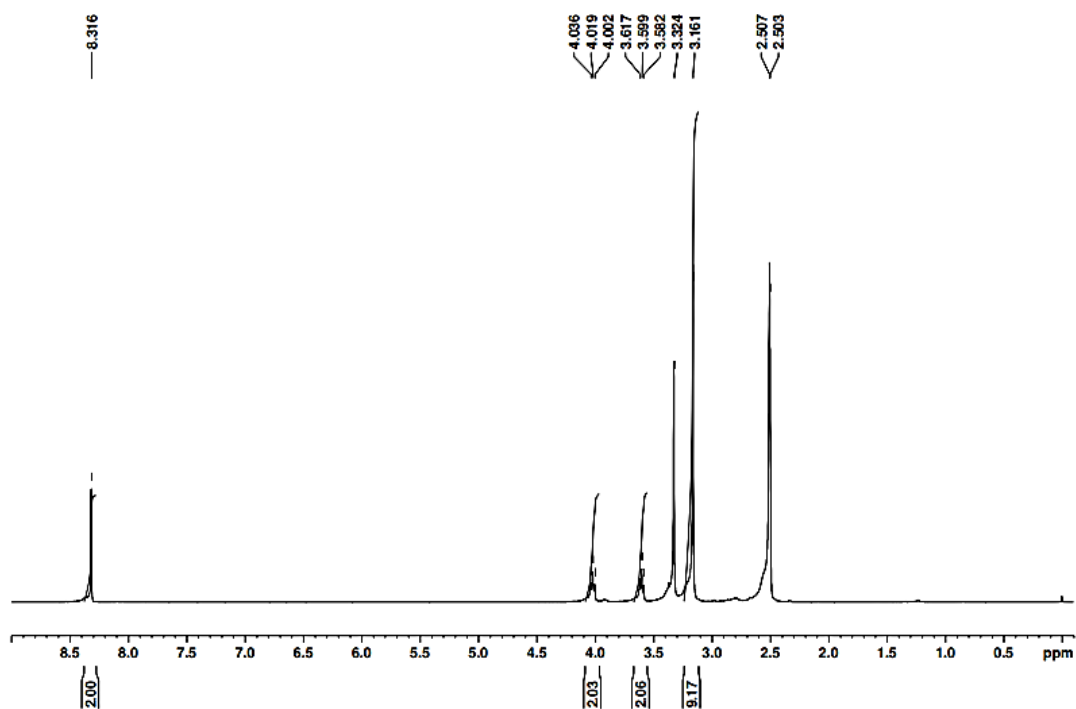


Figure 4.16. ^1H NMR spectrum of CPthBr in DMSO- d_6 .

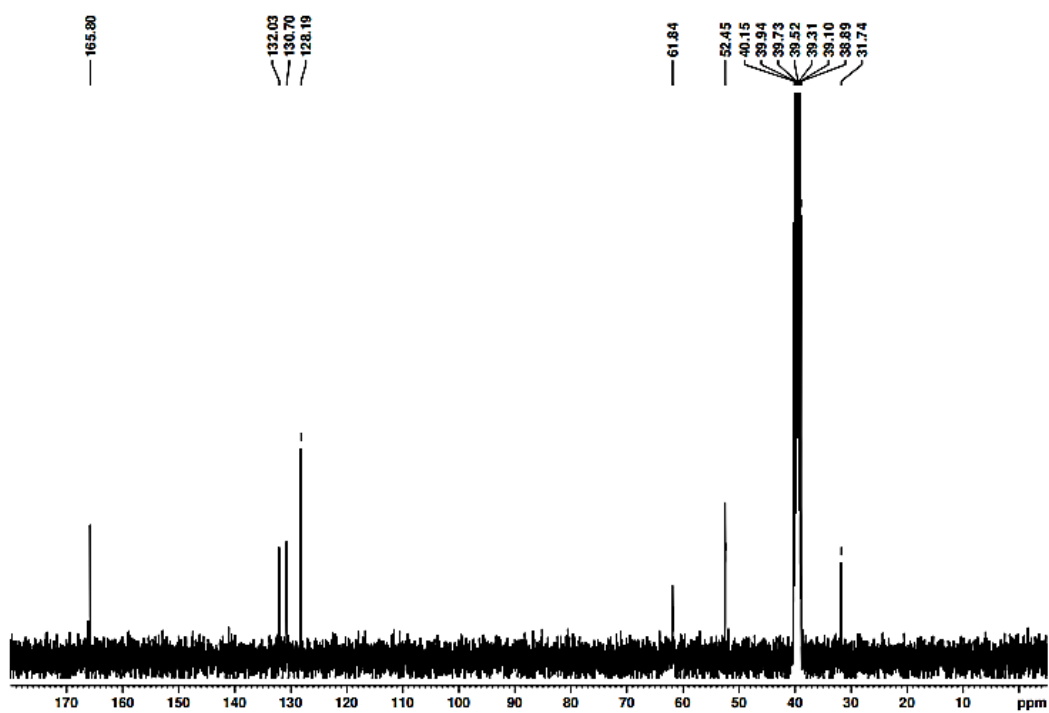


Figure 4.17. ^{13}C NMR spectrum of CPthBr in DMSO- d_6 .

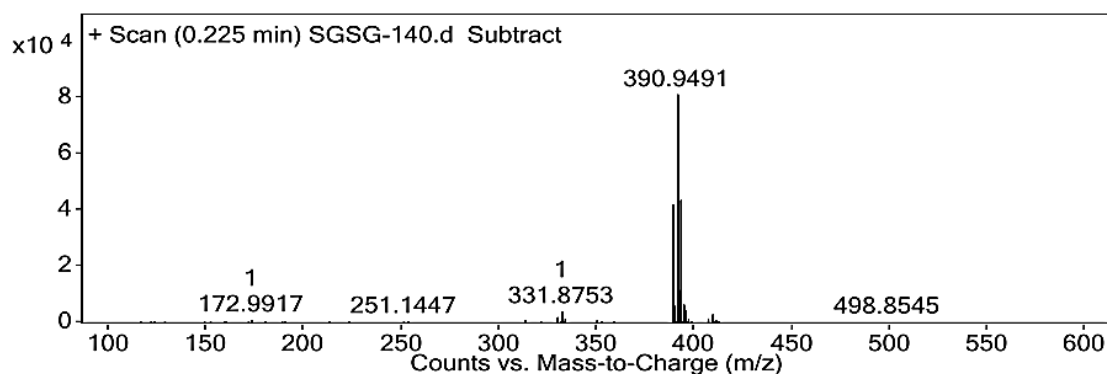


Figure 4.18. ESI-HR-MS spectrum of *CPthBr*.

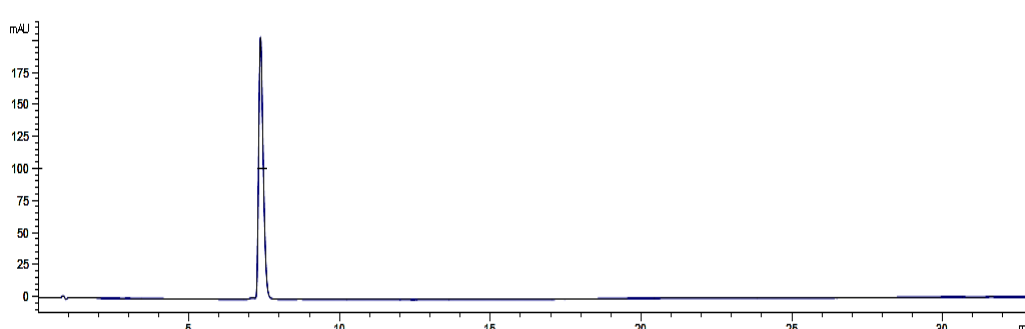


Figure 4.19. HPLC profile of *CPthBr* ($[c] = 0.5 \text{ mM}$, A gradient elution of acetonitrile from 80-100% in aqueous solution was used by monitoring at 310 nm).

4.11. References:

[1] a) W. Zhao, Z. He, Jacky W. Y. Lam, Q. Peng, H. Ma, Z. Shuai, G. Bai, J. Hao, Ben Z. Tang, *Chem* **2016**, *1*, 592-602; b) S. Xu, R. Chen, C. Zheng, W. Huang, *Adv. Mater.* **2016**, *28*, 9920-9940; c) S. Hirata, *Adv. Opt. Mater.* **2017**, *5*, 1700116; d) T. Zhang, X. Ma, H. Wu, L. Zhu, Y. Zhao, H. Tian, *Angew. Chem. Int. Ed.* **2020**, *59*, 11206-11216; e) W. Zhao, Z. He, B. Z. Tang, *Nat. Rev. Mater.* **2020**, *5*, 869-885; f) A. D. Nidhankar, Goudappagouda, V. C. Wakchaure, S. S. Babu, *Chem. Sci.* **2021**, *12*, 4216-4236.

[2] a) W. Z. Yuan, X. Y. Shen, H. Zhao, J. W. Y. Lam, L. Tang, P. Lu, C. Wang, Y. Liu, Z. Wang, Q. Zheng, J. Z. Sun, Y. Ma, B. Z. Tang, *J. Phys. Chem. C* **2010**, *114*, 6090-6099; b) O. Bolton, K. Lee, H.-J. Kim, K. Y. Lin, J. Kim, *Nat. Chem.* **2011**, *3*, 205-210; c) Z. An, C. Zheng, Y. Tao, R. Chen, H. Shi, T. Chen, Z. Wang, H. Li, R. Deng, X. Liu, W. Huang, *Nat. Mater.* **2015**, *14*, 685-690; d) Y. Xiong, Z. Zhao, W. Zhao, H. Ma, Q. Peng, Z. He, X. Zhang, Y. Chen, X. He, J. W. Y. Lam, B. Z. Tang, *Angew. Chem. Int. Ed.* **2018**, *57*, 7997-8001; e) He, W. Zhao, J. W. Y. Lam, Q. Peng,

H. Ma, G. Liang, Z. Shuai, B. Z. Tang, *Nat. Commun.* **2017**, *8*, 416; f) Y. Gong, G. Chen, Q. Peng, W. Z. Yuan, Y. Xie, S. Li, Y. Zhang, B. Z. Tang, *Adv. Mater.* **2015**, *27*, 6195-6201; g) B. Chen, W. Huang, H. Su, H. Miao, X. Zhang, G. Zhang, *Angew. Chem. Int. Ed.* **2020**, *59*, 10023-10026; h) S. Garain, S. Kuila, B. C. Garain, M. Kataria, A. Borah, S. K. Pati, S. J. George, *Angew. Chem. Int. Ed.* **2021**, *60*, 12323-12327; i) A. D. Nidhankar, Goudappagouda, D. S. Mohana Kumari, S. K. Chaubey, R. Nayak, R. G. Gonnade, G. V. P. Kumar, R. Krishnan, S. S. Babu, *Angew. Chem. Int. Ed.* **2020**, *59*, 13079-13085; j) Q. Liao, Q. Gao, J. Wang, Y. Gong, Q. Peng, Y. Tian, Y. Fan, H. Guo, D. Ding, Q. Li, Z. Li, *Angew. Chem. Int. Ed.* **2020**, *59*, 9946-9951.

[3] a) D. Lee, O. Bolton, B. C. Kim, J. H. Youk, S. Takayama, J. Kim, *J. Am. Chem. Soc.* **2013**, *135*, 6325; b) Y. Su, Y. Zhang, Z. Wang, W. Gao, P. Jia, D. Zhang, C. Yang, Y. Li, Y. Zhao, *Angew. Chem. Int. Ed.* **2020**, *59*, 9967-9971; c) H. Wu, W. Chi, Z. Chen, G. Liu, L. Gu, A. K. Bindra, G. Yang, X. Liu, Y. Zhao, *Adv. Funct. Mater.* **2019**, *29*, 1807243; d) H. Thomas, D. L. Pastoetter, M. Gmelch, T. Achenbach, A. Schlögl, M. Louis, X. Feng, S. Reineke, *Adv. Mater.* **2020**, *32*, 2000880; e) A. Kirch, M. Gmelch, S. Reineke, *J. Phys. Chem. Lett.* **2019**, *10*, 310-315; f) S. Kuila, S. Garain, S. Bandi, S. J. George, *Adv. Funct. Mater.* **2020**, *30*, 2003693; g) S. Kuila, S. J. George, *Angew. Chem. Int. Ed.* **2020**, *59*, 9393-9397; 9393-9397.

[4] a) J. Zhi, Q. Zhou, H. Shi, Z. An, W. Huang, *Chem. Asian J.* **2020**, *15*, 947-957; b) Q. Dang, Y. Jiang, J. Wang, J. Wang, Q. Zhang, M. Zhang, S. Luo, Y. Xie, K. Pu, Q. Li, Z. Li, *Adv. Mater.* **2020**, *32*, 2006752; c) Y. Wang, H. Gao, J. Yang, M. Fang, D. Ding, B. Z. Tang, Z. Li, *Adv. Mater.* **2021**, *33*, 2007811.

[5] a) D. Li, F. Lu, J. Wang, W. Hu, X.-M. Cao, X. Ma, H. Tian, *J. Am. Chem. Soc.* **2018**, *140*, 1916-1923; b) X. Yao, J. Wang, D. Jiao, Z. Huang, O. Mhirsi, F. Lossada, L. Chen, B. Haehnle, A. J. C. Kuehne, X. Ma, H. Tian, A. Walther, *Adv. Mater.* **2020**, 2005973; c) Y. Gong, H. Chen, X. Ma, H. Tian, *ChemPhysChem* **2016**, *17*, 1934-1938; d) Z.-Y. Zhang, W.-W. Xu, W.-S. Xu, J. Niu, X.-H. Sun, Y. Liu, *Angew. Chem. Int. Ed.* **2020**, *59*, 18748-18754.

[6] a) Z. Li, Y. Han, F. Wang, *Nat. Commun.* **2019**, *10*, 3735; b) Z. Li, Y. Han, F. Nie, M. Liu, H. Zhong, F. Wang, *Angew. Chem. Int. Ed.* **2021**, *60*, 8212-8219; c) Z.-Y. Zhang, Y. Chen, Y. Liu, *Angew. Chem. Int. Ed.* **2019**, *58*, 6028-6032; d) Z.-Y. Zhang, Y. Liu, *Chem. Sci.* **2019**, *10*, 7773-7778.

- [7] a) J. Wang, Z. Huang, X. Ma, H. Tian, *Angew. Chem. Int. Ed.* **2020**, *59*, 9928-9933; b) H. Chen, X. Ma, S. Wu, H. Tian, *Angew. Chem. Int. Ed.* **2014**, *53*, 14149-14152.
- [8] a) W.-L. Zhou, Y. Chen, Q. Yu, H. Zhang, Z.-X. Liu, X.-Y. Dai, J.-J. Li, Y. Liu, *Nat. Commun.* **2020**, *11*, 4655; b) F.-F. Shen, Y. Chen, X. Dai, H.-Y. Zhang, B. Zhang, Y. Liu, Y. Liu, *Chem. Sci.* **2021**, *12*, 1851-1857.
- [9] S. Kuila, K. V. Rao, S. Garain, P. K. Samanta, S. Das, S. K. Pati, M. Eswaramoorthy, S. J. George, *Angew. Chem. Int. Ed.* **2018**, *57*, 17115-17119.
- [10] a) J. Xu, A. Takai, Y. Kobayashi, M. Takeuchi, *Chem. Commun.* **2013**, *49*, 8447-8449; b) G. D. Gutierrez, G. T. Sazama, T. Wu, M. A. Baldo, T. M. Swager, *J. Org. Chem.* **2016**, *81*, 4789-4796; c) C. Feng, S. Li, L. Fu, X. Xiao, Z. Xu, Q. Liao, Y. Wu, J. Yao, H. Fu, *J. Phys. Chem. Lett.* **2020**, *11*, 8246-8251; d) A. Lv, W. Ye, X. Jiang, N. Gan, H. Shi, W. Yao, H. Ma, Z. An, W. Huang, *J. Phys. Chem. Lett.* **2019**, *10*, 1037-1042; e) A. Fermi, G. Bergamini, M. Roy, M. Gingras, P. Ceroni, *J. Am. Chem. Soc.* **2014**, *136*, 6395-6400; f) Y. Deng, P. Li, J. Li, D. Sun, H. Li, *ACS Appl. Mater. Interfaces* **2021**, *13*, 14407-14416; g) H. Shu, H. Li, J. Rao, L. Chen, X. Wang, X. Wu, H. Tian, H. Tong, L. Wang, *J. Mater. Chem. C* **2020**, *8*, 14360-14364.
- [11] X.-K. Ma, W. Zhang, Z. Liu, H. Zhang, B. Zhang, Y. Liu, *Adv. Mater.* **2021**, *33*, 2007476.
- [12] a) S. J. Barrow, S. Kasera, M. J. Rowland, J. del Barrio, O. A. Scherman, *Chemical Reviews* **2015**, *115*, 12320-12406; b) Y. H. Ko, H. Kim, Y. Kim, K. Kim, *Angew. Chem. Int. Ed.* **2008**, *47*, 4106-4109.
- [13] K. V. Rao, A. Jain, S. J. George, *J. Mater. Chem. C* **2014**, *2*, 3055-3064.
- [14] a) Gaussian 16, Revision A.03, M. J. Frisch, G. W. Trucks, H. B. Schlegel, G. E. Scuseria, M. A. Robb, J. R. Cheeseman, G. Scalmani, V. Barone, G. A. Petersson, H. Nakatsuji, X. Li, M. Caricato, A. V. Marenich, J. Bloino, B. G. Janesko, R. Gomperts, B. Mennucci, H. P. Hratchian, J. V. Ortiz, A. F. Izmaylov, J. L. Williams, F. Ding, F. Lipparini, F. Egidi, J. Goings, B. Peng, A. Petrone, T. Henderson, D. Ranasinghe, V. G. Zakrzewski, J. Gao, N. Rega, G. Zheng, W. Liang, M. Hada, M. Ehara, K. Toyota, R. Fukuda, J. Hasegawa, M. Ishida, T. Nakajima, Y. Honda, O. Kitao, H. Nakai, T. Vreven, K. Throssell, J. A. Montgomery Jr., J. E. Peralta, F. Ogliaro, M. J. Bearpark, J. J. Heyd, E. N. Brothers, K. N. Kudin, V. N. Staroverov, T. A. Keith, R. Kobayashi, J.

Normand, K. Raghavachari, A. P. Rendell, J. C. Burant, S. S. Iyengar, J. Tomasi, M. Cossi, J. M. Millam, M. Klene, C. Adamo, R. Cammi, J. W. Ochterski, R. L. Martin, K. Morokuma, O. Farkas, J. B. Foresman, D. J. Fox, Gaussian, Inc., Wallingford CT, **2016**; b) A. D. Becke, *J. Chem. Phys.* **1993**, *98*, 1372–1377; c) C. Lee, W. Yang, R. G. Parr, *Phys. Rev. B* **1988**, *37*, 785–789; d) B. Miehlich, A. Savin, H. Stoll, H. Preuss, *Chem. Phys. Lett.* **1989**, *157*, 200–206; e) S. Hirata, M. Head-Gordon, *Chem. Phys. Lett.* **1999**, *314*, 291–299; f) E. van Lenthe, R. Van Leeuwen, E. J. Baerends, *Int. J. Quan. Chem.* **1996**, *57*, 281–293; g) E. van Lenthe, J. G. Snijders, E. J. Baerends, *J. Chem. Phys.* **1996**, *105*, 6505–6516; h) F. Wang, T. Ziegler, E. van Lenthe, S. van Gisbergen, E. J. Baerends, *J. Chem. Phys.* **2005**, *122*, 204103–204112; i) S. Shyshkanov, T. N. Nguyen, F. M. Ebrahim, K. C. Stylianou, P. J. Dyson, *Angew. Chem. Int. Ed.* **2019**, *58*, 5371–5375.

[15] X. Huang, M. Hu, X. Zhao, C. Li, Z. Yuan, X. Liu, C. Cai, Y. Zhang, Y. Hu, Y. Chen, *Organic Letters* **2019**, *21*, 3382–3386.

CHAPTER 5.1

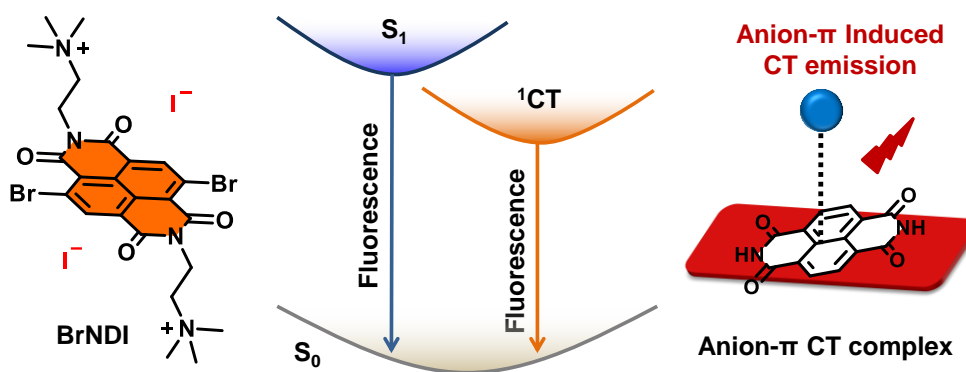
Anion- π Induced Charge-transfer Emission from Cationic Naphthalene Diimide

CHAPTER 5.1

Anion- π Induced Charge-transfer Emission from Cationic Naphthalene Diimide*

Abstract

Manipulating the optical properties of the chromophores via anion- π interaction is difficult and summoning. Although anion- π induced formation of charge-transfer (CT) ground is known in the naphthalene diimide family, however, emissive CT state is rare and requires an elegant molecular design strategy. In this regard, we present the formation of anion- π induced CT ground state and subsequent realization of a unique through space red-emissive ^1CT state formation from π -acidic naphthalene diimides (NDIs) in aqueous solution. The clever molecular design strategy having counter iodide ions creates a perfect microenvironment to achieve an emissive CT state rather than the charge-separated state. To a greater extent, we exploit the emissive CT state in the aqueous phase for sensitive detection of insulin protein aggregate and successfully utilize it as a polarity-sensitive fluorescence marker.



*Manuscript based on this work is under preparation

5.1.1. Introduction:

Anion- π interactions between electron-deficient arenes and anions have emerged as an important non-covalent interaction over the last decade and provided new scopes in the study of self-assembly and molecular recognition.^[1] The meteoric rise in anion- π research is due to its functional relevance in distinct frontier research areas of materials science,^[2] supramolecular chemistry,^[3] and chemical biology.^[4] The recent surge in this field was propelled by the contributions of Matile and co-workers using electron-deficient arylene diimide systems, with respect to the experimental probing of these weak interactions and with unique applications in selective anion transport^[5] and anion- π catalysis.^[6] Most of these results have been revealed, using naphthalene diimide derivatives owing to the diverse electronic character of its π -acidic surface, which can be easily tweaked by the structural modifications at the core.^[7] Anion- π induced ground-state charge transfer between anions and electron deficient NDIs was also exploited for anion sensing using associated colour changes.^[8] Surprisingly, anion- π induced modulation of emission properties by the creation of charge-transfer excited states has not been explored, despite the unique fluorescent characteristics of core-substituted NDIs. We envision that anion- π induced emissive charge-transfer states would further expand the functional scope of these weak interactions especially in the burgeoning area of ambient triplet harvesting of organic chromophores.^[9] Further, anion- π induced emission with charge-transfer character would provide a new mechanism to polarity-sensitive fluoroprobes, which often relies on intramolecular charge-transfer (ICT) or twisted intramolecular charge-transfer (TICT) based fluorescence signalling from covalently connected push-pull fluorophores.^[10]

In this chapter we present a unique anion- π induced red-emissive charge-transfer fluorescence from a cationic NDI derivative with bromo groups at the core and trimethyl ammonium groups at the imide position and iodide ions as the counter ions, in water. We have previously reported this molecule for harvesting aqueous phase phosphorescence from the locally excited triplet state (³LE), by scaffolding in the interlayer galleries of the layered clay materials.^[11] Although, we have postulated the presence of charge-transfer interactions in this molecule, a detailed study was not performed. In the present investigation, with detailed experimental and theoretical studies, we unambiguously prove the Anion- π interactions between the counter anions and electron deficient NDI

core, which leads to dual fluorescence originating from the locally excited (^1LE) and anion- π induced charge-transfer (^1CT). Further, we demonstrate that the solvatochromic nature of the CT emission can be used as a novel polarity sensitive fluorescence mechanism to probe and visualize the hydrophobic regimes of protein aggregates.

5.1.2. Molecular Design:

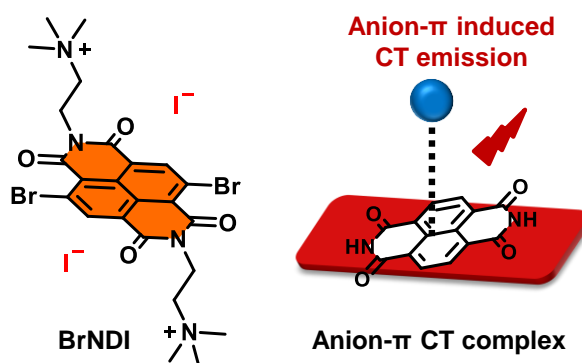


Figure 5.1.1. Molecular structure of **BrNDI** with counter iodide ions and schematic representation showing the formation of the Anion- π CT complex.

In this chapter, we synthesized a water-soluble, naphthalene diimide derivative, **BrNDI**, bearing cationic trimethylammonium group at the imide position. In the molecular design, the quaternary ammonium cations having iodide counter ions are envisioned to house the perfect microenvironment for Anion- π interaction with the π -acidic NDI core with high binding affinity.

5.1.3. Spectroscopic Studies in Solution-state:

First, we have performed detailed photophysical studies of **BrNDI** in water ($[c] = 0.1$ mM). Absorption spectrum showed π - π^* transition with vibronic maxima at 366 nm and 411 nm typical of molecularly dissolved NDI chromophores (Figure 5.1.2a). In addition, it also showed of a weak broad absorption in the 450 nm to 600 nm region, characteristic of anion- π induced CT band in NDIs (Figure 5.1.2a). Interestingly, **BrNDI** exhibits dual emission ($\lambda_{\text{exc.}} = 320$ nm) maxima at 436 nm and 620 nm (Figure 5.1.2b). The high-energy emission band is characteristic of the locally excited (^1LE) emission of unsubstituted NDI molecules, which is also evident from the excitation spectrum monitored at this emission ($\lambda_{\text{monitored}} = 430$ nm) (Figure 5.1.2c). On the other hand, the excitation spectrum monitored at the red-shifted emission ($\lambda_{\text{monitored}} = 650$ nm) matched

with the red-shifted broad absorption spectrum in the 450-600 nm, hinting towards its anion- π induced CT origin (Figure 5.1.2d). Further exclusive formation of the this red-shifted emission upon the direction excitation of the CT absorption at 510 nm, supported its CT origin (Figure 5.1.2d). Lifetime decay profiles showed average fluorescence lifetimes of 0.04 ns and 1.3 ns, respectively for the ^1LE and ^1CT emission and the higher lifetime of the latter is in consistent its CT character (Figure 5.1.2e). As expected, CT fluorescence is strongly dependent on the solvent polarity and large Stokes shifts are observed in water (~ 110 nm) (Figure 5.1.2f). Further the Stokes shift of **BrNDI** in water (~ 110 nm) is larger than that in relatively less polar acetonitrile (~ 80 nm), which further confirms the CT character of the excited states of **BrNDI** (Figure 5.1.2f).

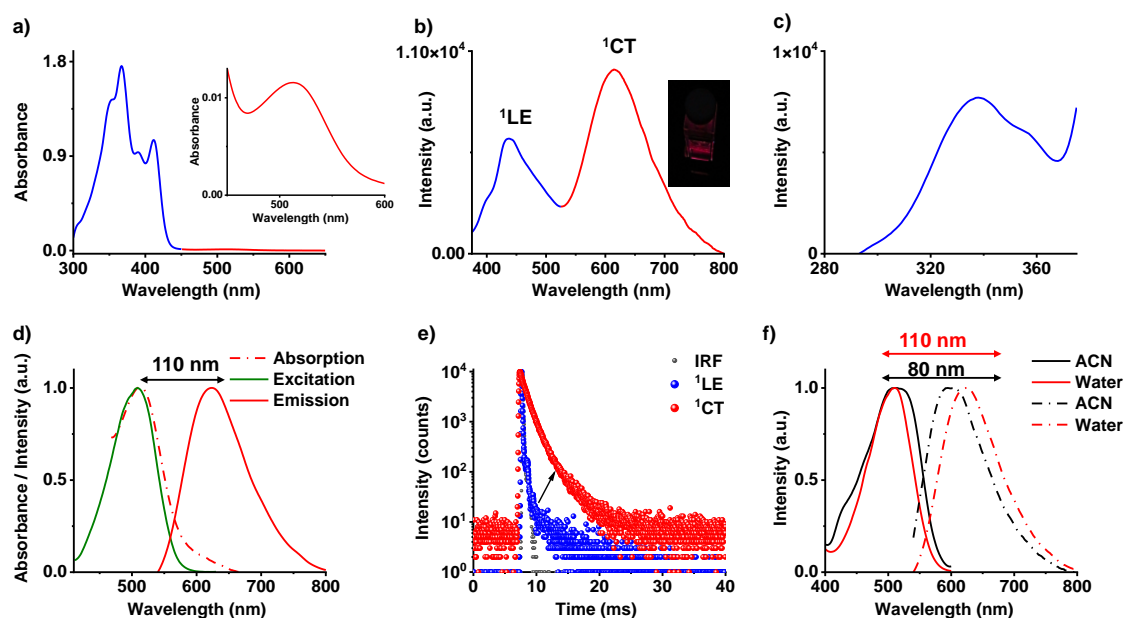


Figure 5.1.2. a) Absorption (blue line) and zoomed in anion- π induced CT absorption (inset, red line) of **BrNDI** in water. b) Steady-state emission spectrum ($\lambda_{exc.} = 320$ nm) and c) excitation spectrum ($\lambda_{monitored} = 440$ nm) of **BrNDI** in water. d) Normalized anion- π induced CT absorption spectrum, excitation spectrum ($\lambda_{monitored} = 650$ nm) and emission spectrum upon selective excitation at the CT band ($\lambda_{exc.} = 510$ nm) of **BrNDI** in water. e) lifetime decay profile ($\lambda_{exc.} = 373$ nm and 532 nm, $\lambda_{collected} = 430$ nm and 650 nm for ^1LE and ^1CT emission respectively) of **BrNDI** in water. f) Normalized excitation spectra ($\lambda_{monitored} = 650$ nm) and emission spectra upon selective excitation at the CT band ($\lambda_{exc.} = 510$ nm) in polar solvent water and relatively non-polar solvent acetonitrile. ($[c] = 0.1$ mM). Inset of b) shows the photograph of the red CT fluorescence obtained by 370 nm Xe lamp excitation

5.1.4. High-resolution Electrospray Ionization Mass Spectrometry (ESI-MS) and Single-crystal X-ray Crystallography Analysis:

High-resolution electrospray ionization mass spectrometry (ESI-MS) is one of the methods to probe anion- π interaction. Hence, we performed ESI-MS experiments in the positive ion mode. Interestingly, the ESI-MS spectrum of **BrNDI** in water showed the presence of [**BrNDI-I**]⁺ complex-ion at 722.9477 m/z which is similar to the simulated isotopic patterns corroborated the anion- π interaction in **BrNDI** (Figures 5.1.3a,b). Further, tandem mass spectrometry (MS/MS) experiments on the complex-ion peak showed its dissociation into individual components with increased accelerating voltage (Figure 5.1.3c). ESI-MS and MS/MS experiments affirm anion-binding with the π -acidic arylene diimides (Figures 5.1.3a-c).

Single-crystal X-ray crystallography analysis in the solid-state is the easiest method to prove anion- π interaction due to the proximity of the anions and π surface and where there is no possibility of solvent caging of the anions. Hence, we have grown **BrNDI** single crystal in water at room temperature. The single-crystal X-ray crystallographic data of **BrNDI** unveils the iodides ions are at the top of the π surface with the closest distance between iodide ion and π surface is 3.705 Å, unequivocally proves the subsistence of anion- π interaction (Figures 5.1.3d-f). Along with the anion- π interaction, π --- π (3.461 Å) and halogen--- π (3.475 Å) interactions is observed in a layered a slip-stacked arrangement and Iodide ions are embedded and stabilized in a vein via anion--- π interactions in a layered structure (Figures 5.1.3e,f). The crystal structure analyses offer us forthright experimental evidence of anion--- π interactions in the ground state.

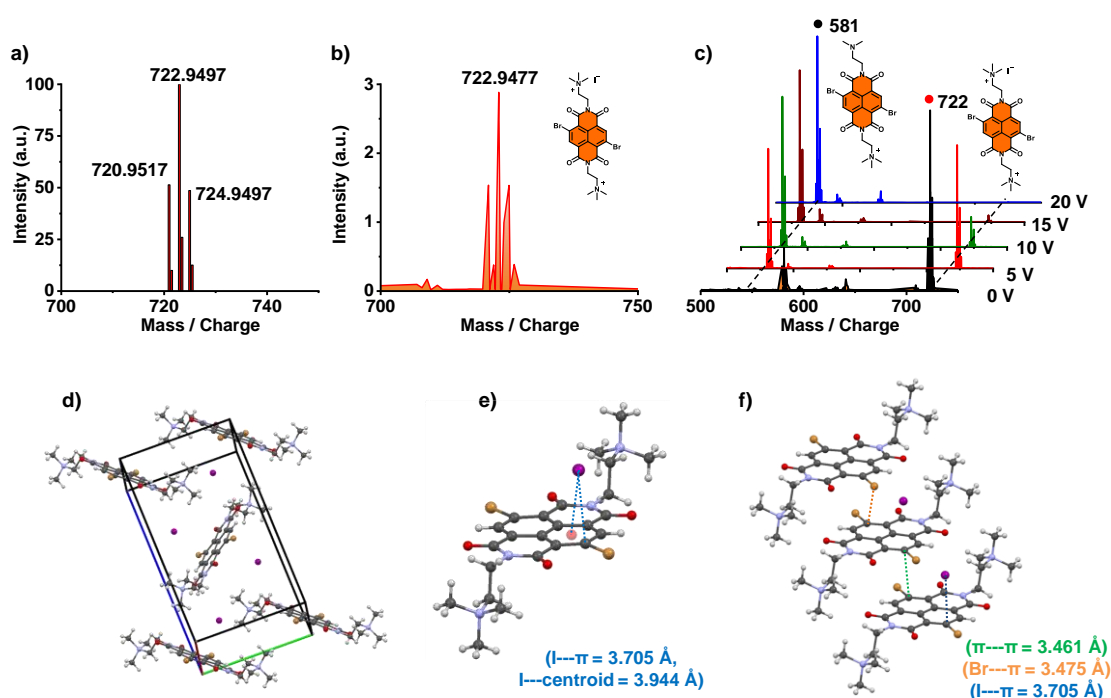


Figure 5.1.3. a) Simulated isotropic pattern and b) high-resolution ESI-MS spectrum of the $[\text{BrNDI-I}]^+$ anion- π complex (722.9477, m/z). c) ESI tandem MS/MS pattern of $[\text{BrNDI-I}]^+$ anion- π complex (722.9477, m/z) upon varying accelerating voltage. d) Unit cell of **BrNDI** single crystal. e) Single-crystal X-ray crystallographic structure showing anion- π interaction between iodide ion and π surface with a closest distance of 3.705 Å (blue line). f) Slipped π -stacked layered molecular arrangement of **BrNDI** driven by halogen- π ($\text{Br} \cdots \pi$, orange line), $\pi \cdots \pi$ (green line) and anion- π (blue lines) interactions.

5.1.5. Theoretical Calculations:

To interpret the experimental observations, we have performed time-dependent density functional theory (TD-DFT) calculations on the anion- π complexes of **BrNDI** with iodide counter anion using CAM-B3LYP exchange-correlation functional. The presence of CT interaction from iodide (donor) to the NDI core (acceptor) is clear from the computed natural transition orbitals (NTOs) of the first excited singlet state where hole is located on the iodide ion and electron is on the π surface (Figure 5.1.4a). Furthermore, the reduced density gradient (RDG) plot of the complex-ion clearly shows the intermolecular non-covalent interactions between iodide ion and π surface helps us to culminate the anion- π induced formation of CT complex (Figure 5.1.4b).

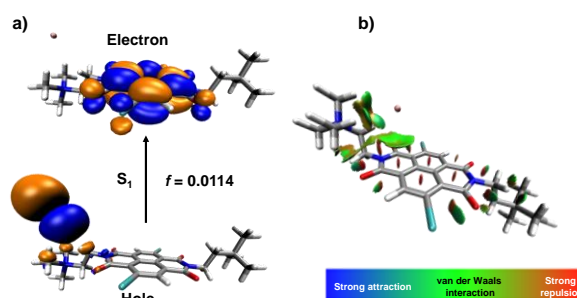


Figure 5.1.4. a) Computed natural transition orbitals (NTOs) of **BrNDI** showing CT complex, calculated for first excited singlet state using TD-CAM-B3LYP/6-31+g(d) level of theory. b) Gradient iso-surfaces ($s = 0.5$ au) of **BrNDI** showing non-covalent interaction between iodide ion and π surface (Blue, green, and red indicates attractive, van der Waals and non-bonding interactions, respectively).

5.1.6. Sensing by Anion- π Induced Through Space CT Emission:

The anion- π interactions are different than most of the reported examples, as it is induced by the counterions, and hence an equivalent concentration of the anions is able to induce an efficient anion- π interaction. We hypothesize that the position of trimethyl ammonium groups houses a perfect environment for iodide ions to weakly co-ordinate with the π -acidic surface and prevent it from completely getting converted into a charge-separated state. We have further validated our hypothesis by exchanging the iodide counter ion with the weakly co-ordinating anion BF_4^- . Broad absorption band at low energy region, dual emission feature in the emission spectrum, and broad red-shifted emission band upon selective excitation at the CT band similar to **BrNDI** help us to realize that the CT emission exists even upon exchanging the weakly co-ordinating BF_4^- ion (Figures 5.1.5a-c). As a result, in the present case, the anion- π interactions are present in a wide range of concentrations, even in the solution phase (Figures 5.1.5d,e). It is interesting to mention that CT emission persists even at a very low concentration (2.5 μM) of the solution, although the relative intensity of the CT emission with respect to the LE emission decreased upon decreasing the concentration as expected from a weakened interaction (Figure 5.1.5e). Existence of the through space emissive CT state at very low concentration and its bathochromic shift of ~ 20 nm in less polar acetonitrile solvent prompted us to utilize **BrNDI** as a polarity-sensitive fluorescence marker (Figure 5.1.5f). It is well studied that solvatochromic dyes work efficiently in the intercellular environment and change their colour upon polarity changes from hydrophilic to

hydrophobic regions.^[12] Keeping this in mind, we have applied the novel anion- π induced through space CT emission of **BrNDI** for sensitive protein fibril detection. Recently, the sensitive detection of protein aggregate is one of the most active research areas being pursued due to their paramount importance for detecting Alzheimer's, Parkinson's, and Huntington's diseases.^[13] In the present study, we have utilized insulin as a model protein composed of two peptide chains having 51 amino acid residues that readily undergo fibrilization under various destabilizing conditions (like high temperature, low pH, shaking, stirring, and so on) and which forms extended β -sheet structure via self-assembly and prepared insulin oligomer and fibril solution in presence of 0.1 mM **BrNDI** using 1mM native insulin.^[14] Then we kept it in a heating bath for 5 hours and 96 hours at 70 °C in 10 mM sodium phosphate buffer (pH-7.4) to prepare insulin oligomer and fibril respectively. After removing from the heating bath, we kept the solutions for overnight at room temperature to prior photophysical experiments. Detailed spectroscopic analysis revealed a significant bathochromic shift of the emission maximum from 620 nm to 590 nm and 580 nm is observed from water ([c] of **BrNDI** = 0.1 mM) to insulin oligomer and fibrillar solution respectively ($\lambda_{exc.} = 510$ nm, [c] of **BrNDI** in insulin solution = 12 μ M) (Figure 5.1.6a). We hypothesized that the bathochromic shift is observed because the change in polarity from hydrophilic to the hydrophobic environment leads to apparent orange emissivity in hydrophobic insulin fibril solution. Time resolved emission decay profile further analyses the CT nature of the broad-band (Figure 5.1.6b). However, a substantial increase in CT emission intensity ($\lambda_{exc.} = 320$ nm) is realized along with the sizeable bathochromic shift (Figure 5.1.6c). It is exciting to mention that the relative intensity ratio of 1CT to 1LE ($^1CT:^1LE$) changes from 1.64 to 34.7 from hydrophilic water to hydrophobic insulin fibril solution (Figure 5.1.6c). We hypothesized that significant increase in the CT emission intensity (1CT) compared to the (1LE) even at a very low concentration of **BrNDI** ([c] of **BrNDI** in insulin solution = 12 μ M) in insulin solution could be because of increasing the iodide ion's local concentration in the confined microenvironments enhances ground state interaction, leading to enhanced CT emission. To avoid any optical artifact (for example self-absorption) we have used 10/2 mm cuvette and performed repeated experiments by changing excitation and emission slit width and rotating the cuvette to 90° (Figure 5.1.6d). It is noteworthy to mention that novel molecular design presented here having high binding affinity ($K_a = 10^4$ M⁻¹) with π -surface leads to enhanced CT emission even

at very low concentration of **BrNDI** in protein solution which is not possible using externally added ion due to the low their low binding ability.^[5a] However, the successful spectroscopic detection provoked us to image the insulin oligomers and fibrils using confocal microscopy (Figure 5.1.6e). The clear oligomeric and fibrillar structure is obtained upon visible light excitation ($\lambda_{exc.} = 514$ nm), suggesting the binding of **BrNDI** in the fibrillar network and making it a potential visible light excited polarity sensitive fluorescence marker (Figure 5.1.6e). Further spectral evaluation from the confocal image of fibrillar structure matches with the emission spectrum of the insulin fibril solution attested the origin of fibrillar emission comes from the CT states of **BrNDI** (Figure 5.1.6f).

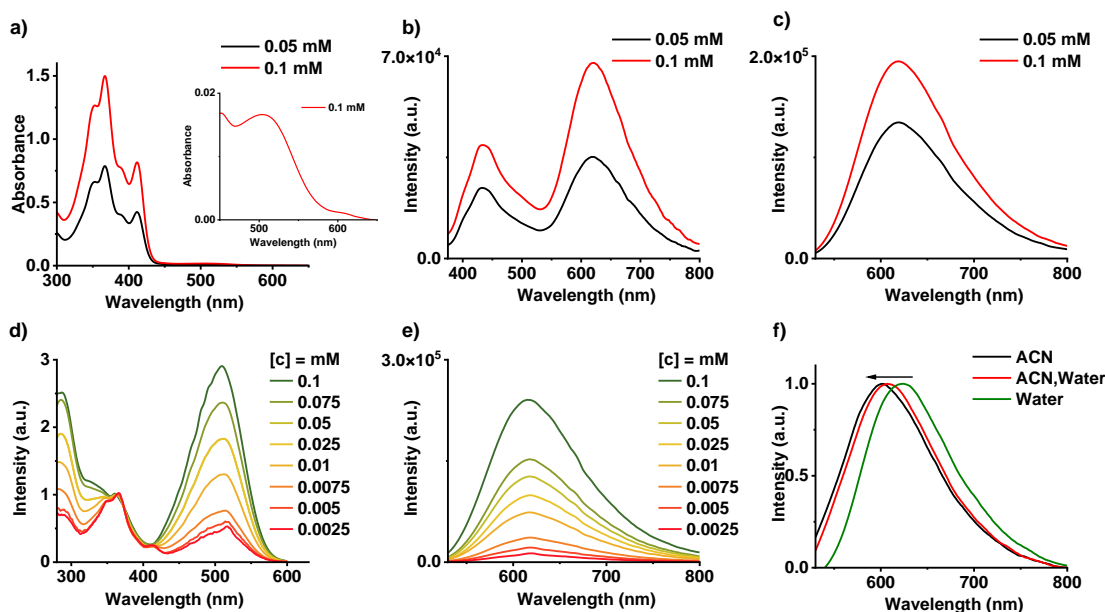


Figure 5.1.5 a) Absorption spectra (Inset: Zoomed in absorption spectrum showing CT band), b) emission spectra ($\lambda_{exc.} = 320$ nm) and c) emission spectra upon selective excitation at the CT band ($\lambda_{exc.} = 510$ nm) of **BrNDI-BF₄** in water at two different concentrations. d) Normalized excitation spectra ($\lambda_{monitored.} = 650$ nm) and e) emission spectra upon selective excitation at the CT band ($\lambda_{exc.} = 510$ nm) of **BrNDI** in different concentration. f) Solvatochromism study of **BrNDI** in ACN, 50% ACN-water and water ($[c] = 0.1$ mM) upon selective excitation at the CT band ($\lambda_{exc.} = 510$ nm).

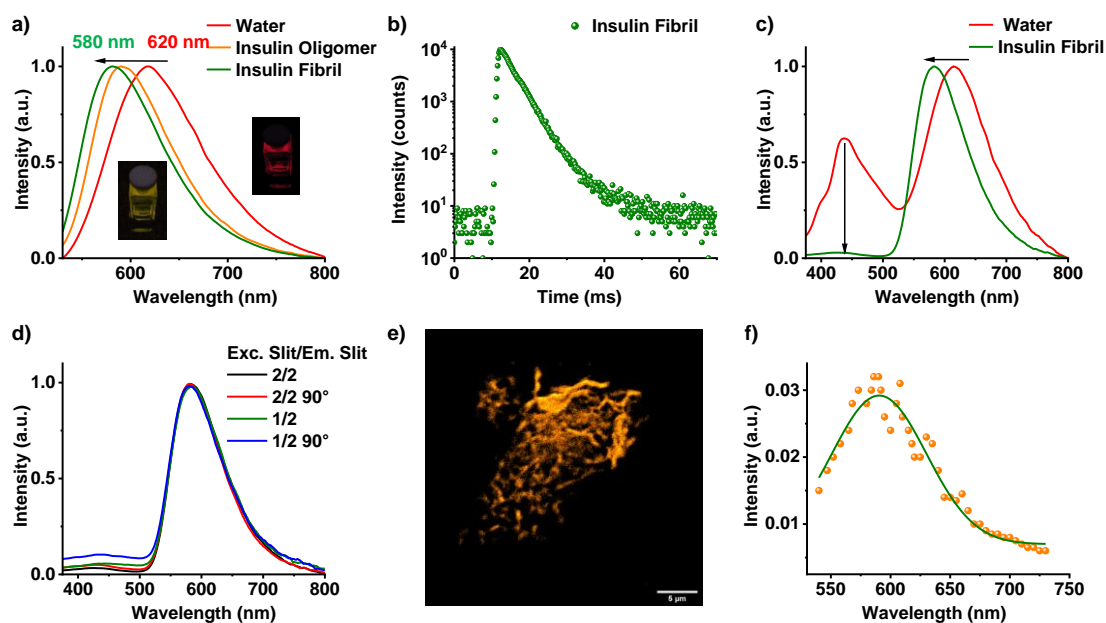


Figure 5.1.6 a) Normalized emission spectra of **BrNDI** in water ($[c] = 0.1 \text{ mM}$), in presence of insulin oligomer and fibril ($[c] = 12 \text{ }\mu\text{M}$) upon selective excitation at CT band ($\lambda_{exc.} = 510 \text{ nm}$, Inset: photograph of insulin fibril (orange) and oligomer (red) upon 370 nm Xe lamp excitation in presence of **BrNDI**). b) Lifetime decay profile of **BrNDI** in presence of insulin fibril ($[c] = 12 \text{ }\mu\text{M}$, $\lambda_{exc.} = 510 \text{ nm}$, $\lambda_{collected} = 650 \text{ nm}$). c) Normalized emission spectra of **BrNDI** in water ($[c] = 0.1 \text{ mM}$) and in presence of insulin fibril ($[c] = 12 \text{ }\mu\text{M}$) ($\lambda_{exc.} = 320 \text{ nm}$). d) Emission spectra of **BrNDI** in insulin fibril ($[c] = 12 \text{ }\mu\text{M}$) upon changing the slit width and rotating the cuvette to 90° to avoid self-absorption ($\lambda_{exc.} = 320 \text{ nm}$, all the experiments we performed in $10/2 \text{ mm}$ cuvette in front-face geometry). e) Confocal microscopy image showing the fibrillar structure of insulin protein in presence of **BrNDI** ($\lambda_{exc.} = 514 \text{ nm}$). f) Emission spectra evolution from confocal image of insulin fibril showing anion- π induced CT emission.

5.1.7. Conclusions:

In conclusion, detailed spectroscopy, single-crystal XRD analysis, and mass-spectrometry assuage us to mitigate anion- π interactions between electron-rich anion and electron-deficient NDI core, leading to emissive CT states. The controlled modulation of CT state via ingenious molecular design strategy emanated red emission in water. Further, we have utilized the novel anion- π induced emissive through space CT as a polarity-sensitive fluorescent marker for visualizing insulin protein aggregate. The proposed result will give a new dimension in molecular design strategies to modulate the

triplet states for ambient triplet harvesting via phosphorescence from CT triplet state (^3CT) and thermally activated delayed fluorescence to a greater extent.

5.1.8. Experimental Section:

5.1.8.1. General Methods:

NMR Measurements: ^1H and ^{13}C NMR ^1H and ^{13}C NMR spectra were recorded on a BRUKER AVANCE-400 Fourier transformation spectrometer with 400 and 100 MHz respectively. The spectra are calibrated with respect to the residual solvent peaks. The chemical shifts are reported in parts per million (ppm) with respect to TMS. Short notations used are, s for singlet, d for doublet, t for triplet, q for quartet and m for multiplet.

Optical Measurements: Electronic absorption spectra were recorded on Jasco V-750 UV-Visible spectrophotometer and emission spectra were recorded on FLS1000 spectrometer, Edinburgh Instruments. Solution state emission spectra were recorded in 10/2 mm path length cuvette in front-face geometry to avoid self-absorption. Fluorescence lifetimes were performed on a same instrument. A 510 nm LED diode with a pulse repetition rate of 1 MHz was used as the light source.

Confocal Laser Scanning Microscopy (LCSM): Confocal microscopy imaging was done at room temperature using Leica TCS SP8 laser scanning confocal microscope with a laser excitation of $\lambda_{\text{exc.}} = 514$ nm. Imaging was performed using Leica oil-immersion objectives: HC PL APO CS2 63x with numerical aperture (NA) 1.40. Fluorescence light was specially filtered with emission filters (TD 488/561/633) and imaged with HVD detector. Confocal images were processed using LAS X (Leica) and image J software.

Lifetime Measurements and Quantum yield: Fluorescence lifetimes were performed on a Horiba Delta Flex time-correlated single-photon-counting (TCSPC) instrument. A 373 nm and 532 nm LED diode with a pulse repetition rate of 1 MHz was used as the light source. The instrument response function (IRF) was collected using a scatterer (Ludox AS40 colloidal silica, Sigma-Aldrich).

Single Crystal X-ray Crystallography: Suitable single crystal of the **BrNDI** compound was mounted on a thin glass fibre with commercially available super glue. Intensity data were collected Bruker D8 VENTURE diffractometer equipped with a PHOTON detector

and graphite-monochromated Mo-K α radiation ($\lambda = 0.71073 \text{ \AA}$, 50 kV, 1mA) at 100 K. APEX III software was used to collect, reduce and integrate the raw data. The direct method was used for solving crystal structure, followed by full-matrix least-squares refinements against F2 (all data HKLF 4 format) using the SHELXL 2014/7^{R1} and difference Fourier synthesis and least-squares refinement revealed the positions of the non-hydrogen atoms. All nonhydrogen atoms were refined anisotropically and remaining hydrogen atoms were placed in geometrically constrained positions and refined with isotropic temperature factors, generally $1.2 \times U_{eq}$ of their parent atoms. Molecular structure drawings were prepared using the program Mercury (version 3.1). We have selected the best crystal; however, few alerts are generated and can't be resolved despite several attempts due to the weak diffraction of crystals.

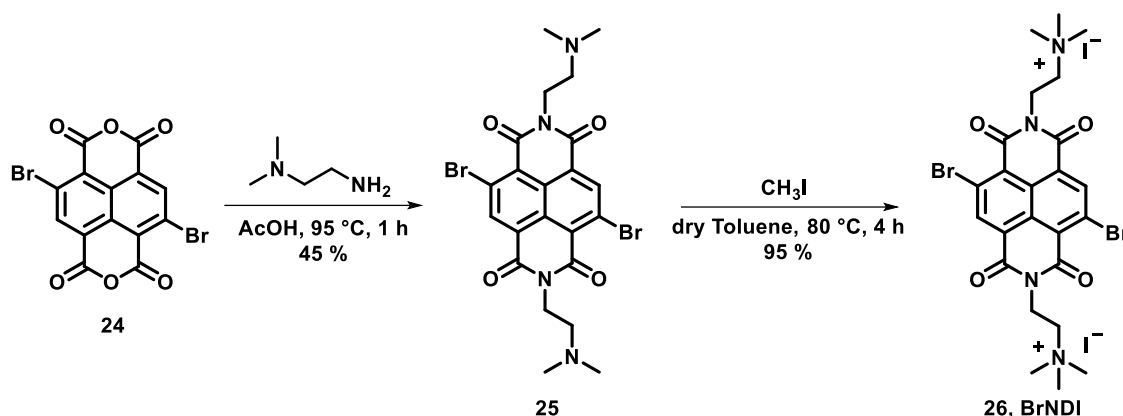
Computational Details: Ground State (S_0) of **BrNDI** molecules was optimized using density functional theory (DFT) and electronic absorption spectra was calculated using time-dependent density functional theory (TD-DFT) as implemented in the Gaussian 16 software considering solvent effect.^[15] Ground state (S_0) optimization and frequency calculation was performed employing B3LYP^[16-18] exchange functional with 6-31+g(d) basis set except for Br and I for which LANL2DZ basis set was used with the corresponding effective core potential (ECP) in gas phase. While the excited state calculations were performed using CAMB3LYP exchange-correlation functional with the same basis sets as mentioned before. The first singlet excited state (S_1) was optimized at the TD-DFT level of theory. While the first triplet excited states (T_1) were also optimized at the TD-DFT level of theory within the Tamm-Dancoff approximation (TDA) to overcome the triplet instability issue.^[19] The solvent (acetonitrile) effects were taken into accounts by the polarized continuum model (PCM) using the integral equation formalism variant (IEFPCM).^[20] Reduced density gradient (RDG) plot calculations were done using Multiwfn 3.6 package.^[21]

5.1.8.2. Protocol of Sample Preparation:

All solution state studies of **BrNDI** were performed, using the study concentration of the samples at 0.0025 mM to 0.1 mM, where 0.5 mM **BrNDI** was used as a stock solution. Insulin oligomer and fibril stock solutions were prepared using 0.1 mM **BrNDI** and 1mM native insulin. Then kept it in a heating bath for 5 hours and 96 hours at 70 °C in 10 mM sodium phosphate buffer (pH-7.4) to prepare insulin oligomer and fibril solutions,

respectively. After removing them from the heating bath, we kept the solutions overnight at room temperature before photophysical experiments. Then all the solution state studies of **BrNDI** were performed, using the study concentration of the samples at 12 μM to 3 μM . 12 μM solution of insulin oligomer and fibril were drop casted on clean glass substrate for confocal imaging.

5.1.9. Synthetic Scheme and Procedures:



Scheme 5.1. Synthetic scheme for BrNDI.

Compound **24**, **25** and **BrNDI** was synthesized according to literature procedure.^[11]

5.1.10. References:

1. a) A. Frontera, P. Gamez, M. Mascal, T. J. Mooibroek, J. Reedijk, *Angew. Chem. Int. Ed.* **2011**, *50*, 9564-9583; b) N. H. Evans, P. D. Beer, *Angew. Chem. Int. Ed.* **2014**, *53*, 11716-11754; c) Y. Zhao, Y. Cotelle, L. Liu, J. Lopez-Andarias, A.-B. Bornhof, M. Akamatsu, N. Sakai, S. Matile, *Acc. Chem. Res.* **2018**, *51*, 2255-2263.
2. Wang, X. Gu, P. Zhang, X. Huang, X. Zheng, M. Chen, H. Feng, R. T. K. Kwok, J. W. Y. Lam, B. Z. Tang, *J. Am. Chem. Soc.* **2017**, *139*, 16974-16979.
3. a) Q. He, Y.-F. Ao, Z.-T. Huang, D.-X. Wang, *Angew. Chem. Int. Ed.* **2015**, *54*, 11785-11790; b) B. Jiang, W. Wang, Y. Zhang, Y. Lu, C. W. Zhang, G. Q. Yin, X. L. Zhao, L. Xu, H. Tan, X. Li, G. X. Jin, H. B. Yang, *Angew. Chem. Int. Ed.* **2017**, *56*, 14438-14442.
4. C. Estarellas, A. Frontera, D. Quino-nero, P. M. Deya, *Angew. Chem. Int. Ed.* **2011**, *50*, 415-418.
5. a) R. E. Dawson, A. Hennig, D. P. Weimann, D. Emery, S. Gabutti, J. Montenegro, V. Ravikumar, M. Mayor, J. Mareda, C. A. Schalley, S. Matile, *Nat. Chem.* **2010**, *2*, 533-

538; b) A. Vargas Jentzsch, D. Emery, J. Mareda, P. Metrangolo, G. Resnati, S. Matile, *Angew. Chem. Int. Ed.* **2011**, *50*, 11675-11678.

6) a) M. Paraja, S. Matile, *Angew. Chem. Int. Ed.* **2020**, *59*, 6273-6377; b) L. Liu, Y. Cotelle, A.-B. Bornhof, C. Besnard, N. Sakai, S. Matile, *Angew. Chem. Int. Ed.* **2017**, *56*, 13066-13069; c) Y. Cotelle, S. Benz, A.-J. Avestro, T. R. Ward, N. Sakai, S. Matile, *Angew. Chem. Int. Ed.* **2016**, *55*, 4275-4279.

7) a) N. Sakai, J. Mareda, E. Vauthey, S. Matile, *Chem. Commun.* **2010**, *46*, 4225-4237; b) F. Würthner, S. Ahmed, C. Thalacker, T. Debaerdemaeker, *Chem. Eur. J.* **2002**, *8*, 4742-4750.

8) a) S. Guha, S. Saha, *J. Am. Chem. Soc.* **2010**, *132*, 17674-17677; b) S. Guha, F. S. Goodson, L. J. Corson, S. Saha, *J. Am. Chem. Soc.* **2012**, *134*, 13679-13691.

9) a) W. Z. Yuan, X. Y. Shen, H. Zhao, J. W. Y. Lam, L. Tang, P. Lu, C. Wang, Y. Liu, Z. Wang, Q. Zheng, J. Z. Sun, Y. Ma, B. Z. Tang, *J. Phys. Chem. C* **2010**, *114*, 6090-6099; b) O. Bolton, K. Lee, H.-J. Kim, K. Y. Lin, J. Kim, *Nat. Chem.* **2011**, *3*, 205-210; c) Z. An, C. Zheng, Y. Tao, R. Chen, H. Shi, T. Chen, Z. Wang, H. Li, R. Deng, X. Liu, W. Huang, *Nat. Mater.* **2015**, *14*, 685-690; *130*, 8129-8133; d) S. Garain, S. Kuila, B. C. Garain, M. Kataria, A. Borah, S. K. Pati, S. J. George, *Angew. Chem. Int. Ed.* **2021**, *60*, 12323-12327; e) S. Kuila, K. V. Rao, S. Garain, P. K. Samanta, S. Das, S. K. Pati, M. Eswaramoorthy, S. J. George, *Angew. Chem. Int. Ed.* **2018**, *57*, 17115-17119; f) S. Garain, B. C. Garain, M. Eswaramoorthy, S. K. Pati, S. J. George, *Angew. Chem. Int. Ed.* **2021**, *60*, 19720-19724; g) S. Garain, S. Sarkar, B. C. Garain S. K. Pati, S. J. George, *Angew. Chem. Int. Ed.* **2022**, DOI: 10.1002/anie.202115773.

10) a) K. Rotkiewicz, K. H. Grellmann, Z. R. Grabowski, *Chem. Phys. Lett.* **1973**, *19*, 315-318; b) Z. R. Grabowski, K. Rotkiewicz, W. Rettig, *Chem. Rev.* **2003**, *103*, 3899-4032; c) C. Reichardt, *Chem. Rev.* **1994**, *94*, 2319-2358.

11) S. Kuila, K. V. Rao, S. Garain, P. K. Samanta, S. Das, S. K. Pati, M. Eswaramoorthy, S. J. George, *Angew. Chem. Int. Ed.* **2018**, *57*, 17115-17119.

12) M. Dell'Acqua, L. Ronda, R. Piano, S. Pellegrino, F. Clerici, E. Rossi, A. Mozzarelli, M. L. Gelmi and G. Abbiati, *J. Org. Chem.*, **2015**, *80*, 10939-10954.

13) M. Shoji, T. E. Golde, J. Ghiso, T. T. Cheung, S. Estus, L. M. Shaffer, X.-D. Cai, D. M. McKay, R. Tintner, B. Frangione, S. G. Younkin, *Science* **1992**, 258, 126-129; b) H. Le Vine III, *Protein Sci.* **1993**, 2, 404-410.

14) M. R. Sawaya, M. P. Hughes, J. A. Rodriguez, R. Riek, D. S. Eisenberg, *Cell* **2021**, 184, 4857-4873.

15) a) Gaussian 16, Revision C.01, Frisch, M. J.; Trucks, G. W.; Schlegel, H. B.; Scuseria, G. E.; Robb, M. A.; Cheeseman, J. R.; Scalmani, G.; Barone, V.; Petersson, G. A.; Nakatsuji, H.; Li, X.; Caricato, M.; Marenich, A. V.; Bloino, J.; Janesko, B. G.; Gomperts, R.; Mennucci, B.; Hratchian, H. P.; Ortiz, J. V.; Izmaylov, A. F.; Sonnenberg, J. L.; Williams-Young, D.; Ding, F.; Lipparini, F.; Egidi, F.; Goings, J.; Peng, B.; Petrone, A.; Henderson, T.; Ranasinghe, D.; Zakrzewski, V. G.; Gao, J.; Rega, N.; Zheng, G.; Liang, W.; Hada, M.; Ehara, M.; Toyota, K.; Fukuda, R.; Hasegawa, J.; Ishida, M.; Nakajima, T.; Honda, Y.; Kitao, O.; Nakai, H.; Vreven, T.; Throssell, K.; Montgomery, J. A., Jr.; Peralta, J. E.; Ogliaro, F.; Bearpark, M. J.; Heyd, J. J.; Brothers, E. N.; Kudin, K. N.; Staroverov, V. N.; Keith, T. A.; Kobayashi, R.; Normand, J.; Raghavachari, K.; Rendell, A. P.; Burant, J. C.; Iyengar, S. S.; Tomasi, J.; Cossi, M.; Millam, J. M.; Klene, M.; Adamo, C.; Cammi, R.; Ochterski, J. W.; Martin, R. L.; Morokuma, K.; Farkas, O.; Foresman, J. B.; Fox, D. J. Gaussian, Inc., Wallingford CT, **2016**; b) Becke, A. D., A new mixing of Hartree-Fock and local density-functional theories. *J. Chem. Phys.* **1993**, 98, 1372-1377; c) Lee, C.; Yang, W.; Parr, R. G., Development of the Colle-Salvetti correlation-energy formula into a functional of the electron density. *Phys. Rev. B* **1988**, 37, 785-789; d) Miehlich, B.; Savin, A.; Stoll, H.; Preuss, H., Results obtained with the correlation energy density functionals of Becke and Lee, Yang and Parr. *Chem. Phys. Lett.* **1989**, 157, 200-206; e) Hirata, S.; Head-Gordon, M., Time-dependent density functional theory within the Tamm-Dancoff approximation. *Chem. Phys. Lett.* **1999**, 314, 291-299; f) Scalmani, G.; Frisch, M. J., *Ab initio* non-relativistic spin dynamics, *J. Chem. Phys.* **1996**, 104, 281-293; g) T. Lu, F. Chen, *J. Comput. Chem.* **2012**, 33, 580-592.

CHAPTER 5.2

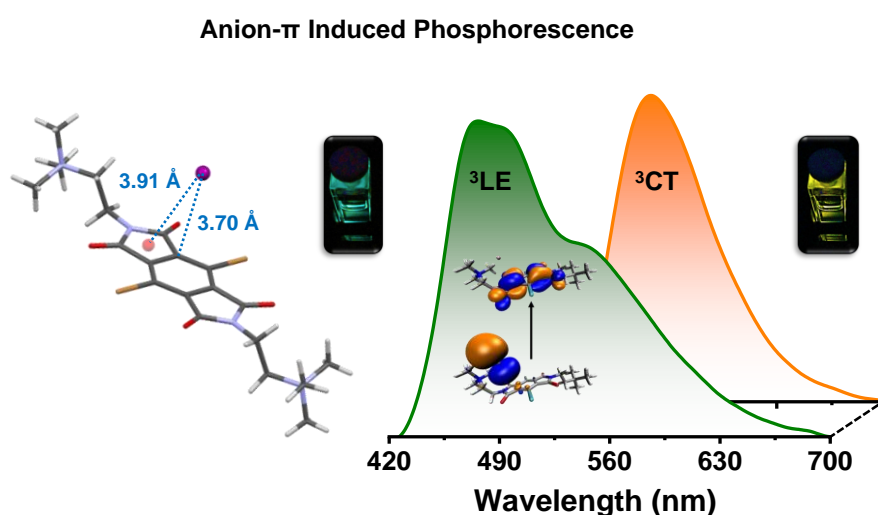
Anion- π Induced Phosphorescence from Charge-transfer States

CHAPTER 5.2

Anion- π Induced Phosphorescence from Charge-transfer States*

Abstract

The burgeoning non-covalent interactions between π -acidic aromatic surfaces and anions have been recently shown to have unique functional relevance in anion transport, ion sensing and organocatalysis. Despite its potential to instigate charge-transfer (CT) states, modulation of the emission features by toggling between the excited states using anion- π interactions is not yet explored. On the other hand, excited states with CT characteristics play an important role in the ambient triplet harvesting of organic chromophores. In this context, in this chapter we propose an anion- π based molecular design for the introduction of emissive singlet and triplet CT excited states, thereby expanding the functional scope of these weak supramolecular interactions. In the present study, we investigate the anion- π induced emission from the singlet (1CT) and triplet (3CT) CT states of a dibromo di-cationic pyromellitic diimide derivative. Remarkably, we accomplish dual room temperature phosphorescence emission from the anion- π mediated 3CT state along with the locally excited triplet state (3LE) in solution



* Manuscript based on this work is published in *J. Am. Chem. Soc.* **2022**, *144*, 10854-10861.

phase, using an organic-inorganic supramolecular scaffolding strategy. Comprehensive steady-state and time-resolved spectroscopy along with theoretical calculations provide detailed insights into the excited state manifolds of the phosphor. We envisage that the present study will expedite new molecular designs based on weak intermolecular interactions for the excited state engineering of organic chromophores to facilitate ambient triplet harvesting and CT emission.

5.2.1. Introduction:

Anion- π interactions between π -acidic aromatic surfaces having positive quadrupole moments with anions, have recently attracted immense attention in supramolecular chemistry.^[1] In contrast to the corresponding complementary interaction between cations and π -basic aromatic surfaces, anion- π interactions are less explored due to the difficulties in accessing anion- π contacts. Despite its whimsical nature, the recent past has witnessed a meteoric rise in the number of reports on the occurrence and plausible functional relevance of anion- π interactions.^[2] The seminal work by Matile and co-workers provided the experimental evidence for the existence of anion- π interactions using electron-deficient naphthalene diimides (NDIs).^[3] Further they also demonstrated the functional relevance of this burgeoning interaction by demonstrating its importance in modulating the anion transport across the bilayer membrane.^[1d,3] With this pioneering work, Matile group continued to exploit the possibilities of anion- π interactions for various functional outcomes, primarily for catalysis.^[4] The explicit contributions of anion- π interactions in catalysis are by stabilizing the negatively charged intermediate with catalysts that are π -acidic in nature. Hitherto, anion- π interactions have been utilized for catalysing multifarious reactions such as enolate, enamine, iminium, and enantioselective chemistry.^[4] In addition to these, Saha and co-workers have also exploited the anion- π interactions-based fluoride ion sensors, using the ground state charge-transfer (CT) interaction between arylene diimides and anions.^[5] In the present work, we expand the functional scope of anion- π interactions and propose that these weak interactions can be utilized to realize both fluorescence and ambient phosphorescence.

More recently, there has been an expeditious upsurge in harvesting the ambient triplet states of purely organic chromophores due to their ease of processability and non-toxicity, compared to its organometallic counterparts.^[6] The ambient triplet harvesting in organic systems have been achieved usually via three important photophysical processes:

phosphorescence^[7], triplet-triplet fusion (TTF)^[8] and thermally activated delayed fluorescence (TADF).^[9] Various efficient (supra)molecular designs have been recently introduced to minimize the vibrational and oxygen quenching of triplet states to harvest room temperature phosphorescence from organic chromophores owning high triplet yields.^[10] On the other hand, reverse inter-system crossing (RISC) mediated TADF has also been realized from elegantly designed donor-acceptor molecular systems by modulating the energy gap between singlet and triplet states.^[10] It is well understood that both singlet (¹CT) and triplet (³CT) CT states play a decisive role in biasing the excited state manifold to facilitate the triplet harvesting.^[9] Hence, we envisage that the anion- π induced interactions would provide an alternative and simple molecular design to mediate the triplet harvesting pathways through CT states. In addition, this supramolecular strategy can also boost the inter-system crossing (ISC) efficiency of the organic chromophores through external heavy atom effect provided by the non-covalently bound anions. Generally, the spin forbidden nature of triplet emission demands a significant ISC efficiency and strong spin-orbit coupling (SOC) between singlet and triplet states, which can be satisfied via hetero and heavy atom substitution in the molecular design.^[6] In this context, arylene diimides are the finest class of chromophores to investigate anion- π induced CT states, with their electron deficient character and versatile synthetic flexibility available to tune the electronic and optical characteristics via core-substitution.^[11] Recently, we have shown that triplet excitons can be efficiently harvested from arylene diimide cores such as naphthalene diimides (NDIs) and pyromellitic diimides (PmDIs), via room-temperature phosphorescence^[10a,12] and TADF.^[13] The multiple carbonyl groups present in the molecular design and easy core substitution with heavy atoms accelerate the ISC process and increase the SOC significantly in these derivatives.^[10a,12] Thus, keeping in mind the π -acidity and triplet character of arylene diimides, herein we investigate the anion- π induced modulation of the optical properties of a di-cationic PmDI derivative, with heavy-atom core substitution and iodide counterions (**BrPmDI**). The easier accessibility to the triplet states of PmDIs compared to the NDIs and their facile synthetic route make them an ideal choice to investigate anion- π interaction.

In this contribution, we show an unprecedented anion- π interaction induced emissive singlet and triplet CT states from **BrPmDI** under ambient conditions, thereby expanding the functional relevance of these weak interactions towards the optical

functionality of organic materials. Efficient CT interaction between the counter iodide anions with the PmDI core leads to the ground state CT absorption and corresponding CT fluorescence (^1CT) in aqueous solution. On the other hand, supramolecular scaffolding of **BrPmDI** inside the inorganic hybrids to stabilize the triplet states from oxygen and vibrational quenching, leads to a dual solution phase phosphorescence emission from both the locally excited (^3LE) and the anion- π induced CT (^3CT) triplet states. To the best of our knowledge, this is the first report on anion- π induced phosphorescence properties accomplished from organic phosphors under ambient conditions.

5.2.2. Molecular Design:

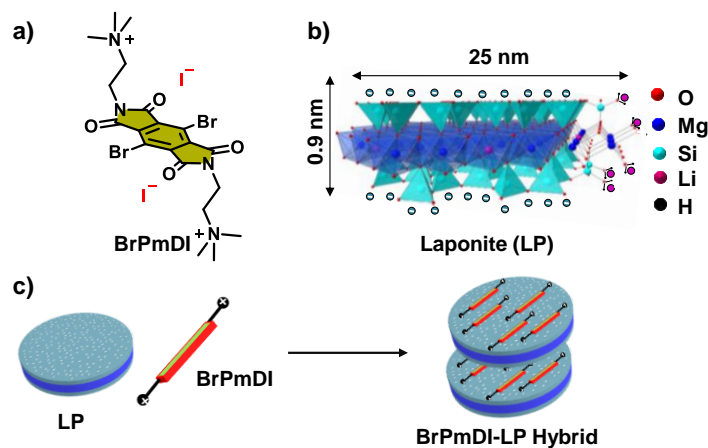


Figure 5.2.1. a) Molecular structure of **BrPmDI** with counter iodide ions. b) Schematic representation of Laponite (LP) nanodisc structure. c) Schematic representation showing formation of hybrid co-assembly between **BrPmDI** and LP.

The PmDI derivative, **BrPmDI**, (Figure 5.2.1) is appended with trimethyl ammonium cationic moiety at the imide position with iodide counter ions and core-substituted with bromine heavy atoms. **BrPmDI** was synthesized according to synthetic procedure shown in synthetic scheme 5.2.1 and was fully characterized by nuclear magnetic resonance spectroscopy (NMR), high-resolution mass spectrometry (HRMS), and was checked for purity by high-performance liquid chromatography (HPLC). The negatively charged surface of LP nanoplates can easily bind electrostatically with complementarily charged **BrPmDI** having positively quaternary ammonium groups appended to its imide position and providing them a confined environment in the interlayer galleries of LP. The cationic

BrPmDI molecule can organize in the interlayer galleries of **LP** nanoplates and is envisioned to harvest the triplet excitons via phosphorescence.

5.2.3. Spectroscopic Studies in Solution-state:

BrPmDI exhibited characteristic π - π^* absorption bands with a maximum at 366 nm in water ($[c] = 0.1$ mM) (Figure 5.2.2a). A closer look at the absorption spectrum showed a very broad, weak, red-shifted band ranging from 450 nm to 600 nm, in addition to the π - π^* transitions (Figure 5.2.2a). Similar spectral features were attributed to the anion- π interactions for electron-deficient NDI derivatives with various anions reported by Matile and co-workers,^[3] hinting towards similar interactions between the counter iodide ions with the electron deficient arylene diimide core. Remarkably, the steady-state emission spectrum in water displayed dual emission with maxima at 427 nm and 605 nm (Figure 5.2.2b, $\lambda_{\text{exc.}} = 320$ nm). Further, the blue shifted emission centered around 430 nm is characteristic of the fluorescence emission from LE singlet state of these derivatives (^1LE), which is also confirmed by the excitation spectrum collected at this emission (Figure 5.2.2c). On the other hand, excitation spectrum collected at the red-shifted emission by monitoring at 650 nm, showed a maximum at 480 nm which is closely matching with the corresponding, red-shifted band of absorption spectrum (Figure 5.2.2d). This result confirms the anion- π interaction induced emissive CT complexation between iodide counter anion and π -acidic PmDI core. This is further supported by the emission measurements performed by the selective excitation at the broadband ($\lambda_{\text{exc.}} = 470$ nm), which showed the exclusive formation of the red-shifted emission band spanning from 500 nm to 750 nm region in both cases (Figure 5.2.2b). Hence it can be inferred that the origin of the red-shifted emission band is due to the anion- π induced CT fluorescence (^1CT). For further understanding, the lifetime decay measurements were performed by selectively exciting at the LE ($\lambda_{\text{exc.}} = 373$ nm) and CT bands ($\lambda_{\text{exc.}} = 480$ nm) (Figures 5.2.2e). Notably, the lifetime analyses of the high energy band ($\lambda_{\text{collected}} = 430$ nm) showed a lifetime of 0.9 ns, while the low energy red-shifted band ($\lambda_{\text{collected}} = 650$ nm) showed an increased lifetime of 5.2 ns (Figures 5.2.2e). The enhanced lifetime of the red-shifted band reiterated the anion- π induced formation of emissive CT state. In addition, solvatochromic changes in the emission maximum further reaffirm the CT nature of the emission occurring at higher wavelengths (Figures 5.2.2f).

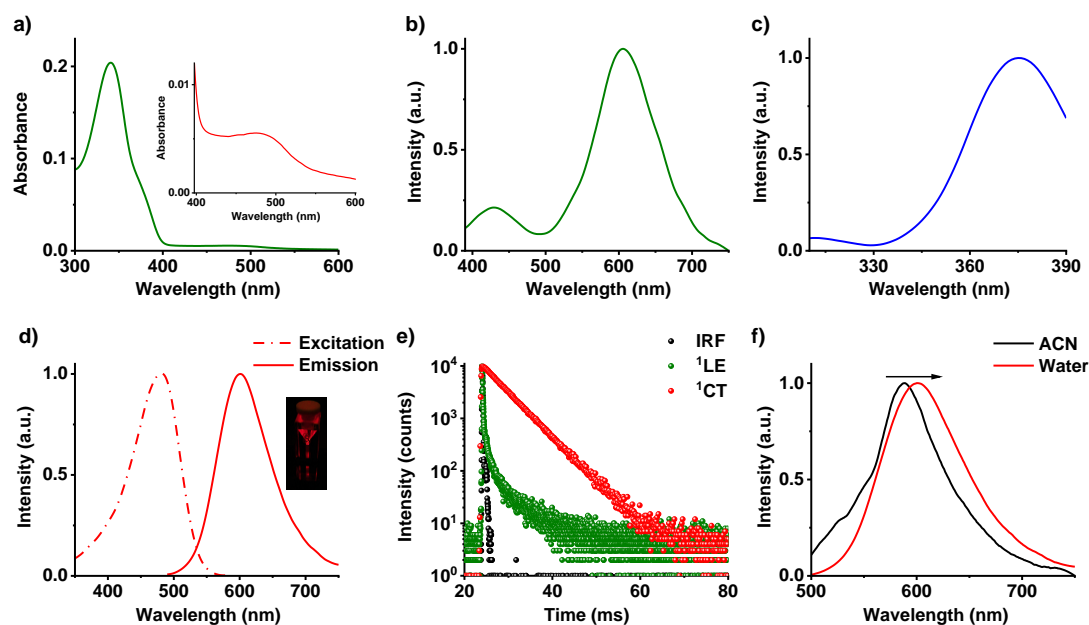


Figure 5.2.2. Spectroscopic characterization of **BrPmDI**. a) Absorption (inset: zoomed in anion- π induced CT absorption), b) steady-state emission ($\lambda_{exc.} = 320$ nm), normalized excitation ($\lambda_{collected} = 420$ nm), d) normalized excitation ($\lambda_{collected} = 650$ nm) and emission spectra ($\lambda_{exc.} = 470$ nm) of the CT state and f) fluorescence lifetime decay profiles of both 1LE and 1CT emissions ($\lambda_{exc.} = 373$ nm, 480 nm and $\lambda_{collected} = 420$ nm, 650 nm for 1LE and 1CT , respectively), f) normalized emission spectra ($\lambda_{exc.} = 510$ nm) in polar solvent water and relatively non-polar solvent acetonitrile. ($[c] = 0.1$ mM, IRF is the instrument response function. Inset of d) shows the photograph of the red CT fluorescence obtained by 370 nm Xe lamp excitation.

5.2.4. High-resolution Electrospray Ionization Mass Spectrometry (ESI-MS), Single-crystal X-ray Crystallography Analysis and Theoretical Calculations:

To further probe the counter anion induced anion- π interactions in the cationic **BrPmDI**, high-resolution electrospray ionization mass spectrometry (ESI-HRMS) was performed in the positive ion mode (Figure 5.2.3).^[3] Interestingly, the ESI-MS analyses of **BrPmDI** showed peak at 672.9305 m/z which is similar to the simulated isotopic patterns, corresponding to the anion- π complex with intact counter ions (Figures 5.2.3a,b). Tandem mass spectrometry (MS/MS) experiments on the complex ion peak further showed that its dissociation into individual components indeed requires increased accelerating voltages (Figure 5.2.3c).

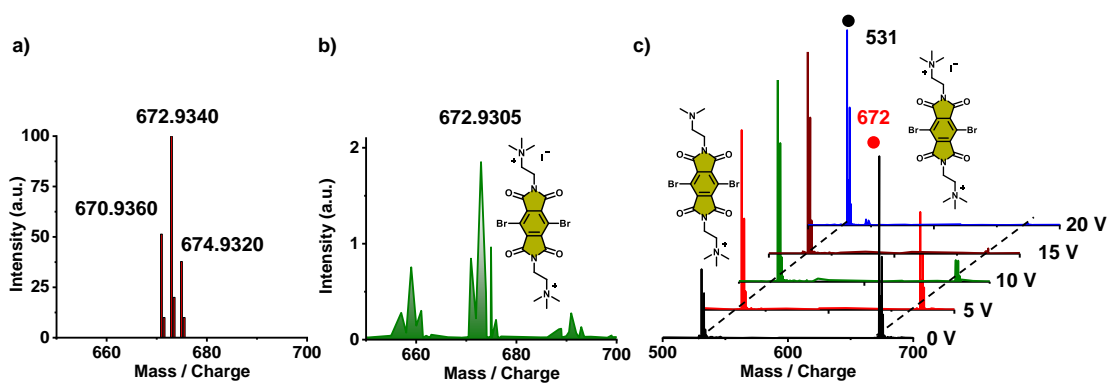


Figure 5.2.3. a) Simulated isotropic pattern and b) high-resolution ESI-MS spectrum of the $[\text{BrPmDI-I}]^+$ anion- π complex (672.9305, m/z). c) ESI tandem MS/MS pattern of $[\text{BrPmDI-I}]^+$ anion- π complex (672.9305, m/z) upon varying accelerating voltage.

The presence of anion- π interaction was further unambiguously proven by the single crystal X-ray diffraction studies (Figures 5.2.4a,b). Single crystals of **BrPmDI** displayed a layered molecular organization with a slip-stacked arrangement (Figure 5.2.4a). The distance between the interlayers was observed to be 3.88 Å and I⁻ ions were embedded and stabilized in a channel via anion- π interactions with contact distances of 3.69 Å, thus providing the direct evidence of anion- π CT complex (Figures 5.2.4b). In addition, supramolecular arrangement of **BrPmDI** was further stabilized by various halogen bonding interactions such as, C=O \cdots Br (3.91 Å), Br \cdots Br (3.94 Å) and Br \cdots π (3.88 Å) (Figure 5.2.4a). Theoretical studies also supported these experimental observations, where natural transition orbitals (NTO) of **BrPmDI** obtained from the TDDFT calculations using CAMB3LYP functional showed localization of hole and electron on the iodide ion and PmDI π -surface, respectively suggesting the presence of CT transition (Figure 5.2.4c). The calculated oscillator strength ($f = 0.012$) is significant enough to observe the CT band in UV-Vis absorption spectrum.

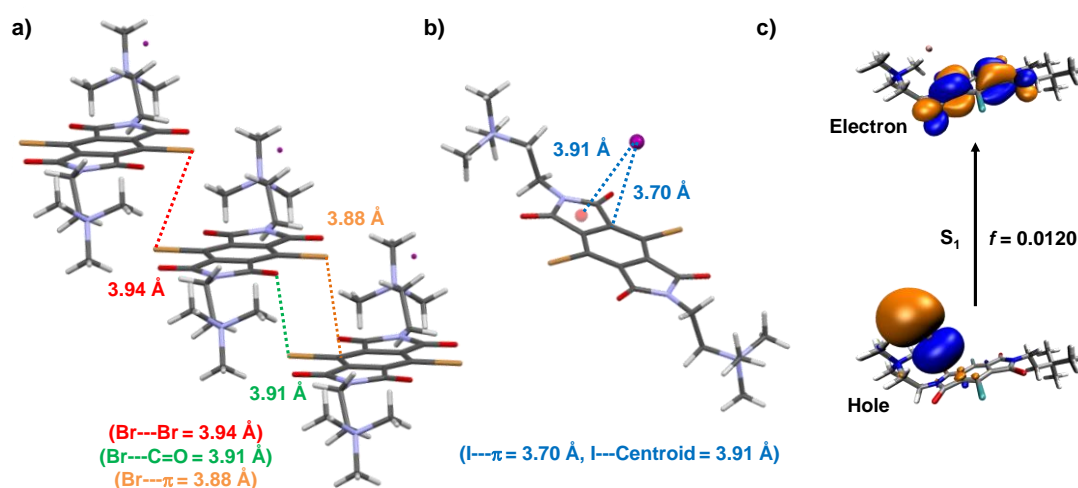


Figure 5.2.4. *a-b*) Single crystal X-ray diffraction data of **BrPmDI**: *a*) Slipped π -stacked layered molecular arrangement of **PmDI** driven by various halogen bonding interactions such **Br---Br** (marked with red lines), **Br---C=O** (marked with green lines) and **Br--- π** (marked with orange lines) and *b*) anion- π contacts (marked with blue lines). *c*) Natural transition orbitals (NTOs) of **BrPmDI** and iodide complex for first excited singlet state (S_1), calculated at TD-CAM-B3LYP level in conjunction with 6-31+g(d) basis set for C, N, O, H and LANL2DZ basis set for Br and I with effective core potential.

5.2.5. Phosphorescence Study of BrPmDI-LP hybrid in Solution:

The studies so far substantiated that anion- π interactions can indeed stabilize the CT states in arylene diimides, leading to CT emission from singlet states (^1CT). In the recent past it has been shown that CT triplet states play an important role in harvesting triplets via phosphorescence or TADF.^[8,12] So, we have further explored the possibility of anion- π induced CT states to instigate the triplet harvesting in arylene diimides. Recently, we have introduced an efficient supramolecular scaffolding approach by utilizing laponite nanoplates, to stabilize the triplet states of arylene diimides by reducing the vibrational and oxygen quenching.^[10a,h] Laponite (**LP**) is an inorganic, water soluble silicate-based nano-template with structural rigidity and nanoscale periodicity that can organize small molecules inside the interlayer galleries.^[14] These dual charged disc-shaped nanoplates were exfoliated in aqueous solution after neutralizing the positively charged edges with sodium polyacrylate to prevent the electrostatically driven clay network formation.^[14] Next, the hybrid co-assembly between **BrPmDI** and **LP** nanoplates (**BrPmDI-LP**) in water was probed using spectroscopic studies. Systematic titration studies were carried out to identify the composition of the co-assembly with maximum emission intensity and

accordingly subsequent studies were performed with 1.00 mM solution of **BrPmDI** in 5 wt.% of **LP** (Figure 5.2.5a). Interestingly emission spectrum of the aqueous solution of the **BrPmDI-LP** co-assembly, showed a dual emission with maxima at 470 nm and 560 nm, along with a weak insignificant emission in the range of 390 nm to 430 nm corresponding to the ^1LE emission (Figure 5.2.5b). The gated emission spectrum ($\lambda_{\text{exc.}} = 370$ nm, delay time = 50 μs) was identical to the steady-state emission spectrum, which further confirmed the delayed character of the emission (Figure 5.2.5b). The emission collected at 470 nm ($\lambda_{\text{exc.}} = 370$ nm) showed an average lifetime of 0.37 ms, hinting towards the phosphorescence nature of the emission (Figure 5.2.5c). Temperature dependent lifetime decay profiles (283 K to 353 K), further confirmed the phosphorescence nature of the emission in **LP** hybrid solution (Figure 5.2.5d). Further the redshift of this emission ($\lambda_{\text{max.}} = 470$ nm) compared to the singlet LE fluorescence ($\lambda_{\text{max.}} = 427$ nm) suggest that this could be originated from the triplet LE state, which is confirmed by the steady-state and gated excitation spectra monitored at 470 nm (Figure 5.2.5e). The cyan phosphorescence emission of **BrPmDI** is similar to our previously reported ^3LE of PmDI derivatives,^[12] which reiterates the ^3LE origin of the emission (Figure 5.2.5b). The absolute phosphorescence quantum efficiency of 1 mM **BrPmDI** in 5 wt.% **LP** is found to be ~5.4 %.

A deeper examination of the steady-state and gated emission spectra revealed the presence of another emission band with a maximum at 560 nm, along with the ^3LE emission centered at 470 nm (Figure 5.2.5b). Interestingly, the excitation spectrum collected at 650 nm emission displayed a broadband in the 465 nm to 575 nm region, corresponding to the CT absorption, along with the LE band, indicating the CT nature of the latter emission band (^1CT or ^3CT), which is of different origin compared to the ^3LE emission at 470 nm (Figure 5.2.5e). In addition, the selective excitation of the lower energy band at 470 nm also resulted in the exclusive formation of this red-shifted emission (Figure 5.2.5b). Time-resolved decay experiments showed that this red-shifted emission consists of CT fluorescence with an average lifetime of 7.17 ns which is very high than the ^1LE fluorescence and a long-lived emission with an average lifetime of 0.23 ms, suggesting the involvement of triplet CT states (^3CT) (Figures 5.2.5c,f). Further, we have carried out time-resolved excitation spectra monitored at 650 nm to understand the involvement of CT state (Figure 5.2.6a). With the time evolution (0 ms to 9.5 ms) the LE state contribution gradually decreased with a concomitant rise in the red-shifted CT band

in the excitation spectra (Figure 5.2.6a). The gradual formation of long-lived emissive CT states was further evident from the time-resolved emission spectra ($\lambda_{\text{exc.}} = 370$ nm) (Figure 5.2.6b). Theoretical calculations revealed that the NTOs (calculated from the TDDFT, using CAMB3LYP functional) of **BrPmDI** triplet state have a hybrid character where the LE state is dominated by π - π^* transition and excited CT state arises due to the presence of counter iodide ion (Figure 5.2.6c). The significant change in orbital involvement in the excitations (hole) of S_1 and T_1 facilitates high ISC from S_1 to T_1 .

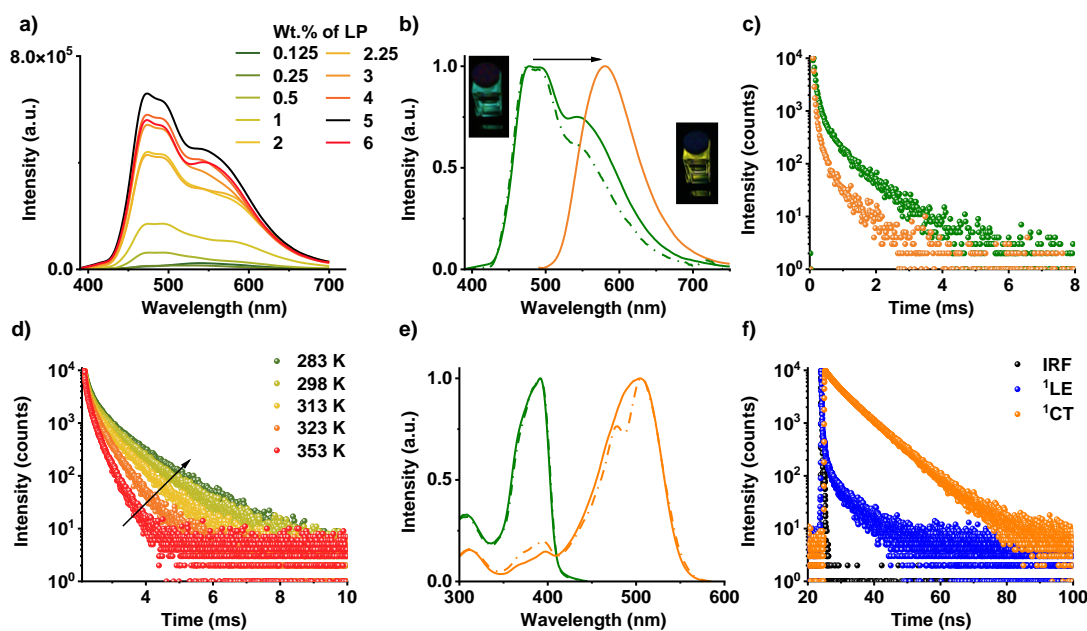


Figure 5.2.5. Dual Phosphorescence of **BrPmDI-LP** hybrid in aqueous solution. a) Steady-state emission spectra ($\lambda_{\text{exc.}} = 370$ nm) of **BrPmDI-LP** hybrids in solution with increasing **LP** wt.%. b) Normalized steady-state (solid line), gated (dashed line) emission spectra upon $\lambda_{\text{exc.}} = 370$ nm (green line) showing the contribution from both LE and CT emissions. The emission from CT upon direct excitation at $\lambda_{\text{exc.}} = 470$ nm (orange line) is also shown. Inset: photograph of **BrPmDI-LP** hybrid solution upon Xe lamp excitation with 330 nm and 470 nm. c) Lifetime decay profile for LE (green, $\lambda_{\text{collected}} = 470$ nm) and CT (orange, $\lambda_{\text{collected}} = 650$ nm) emissions at $\lambda_{\text{exc.}} = 370$ nm. d) Temperature dependent lifetime decay profile ($\lambda_{\text{exc.}} = 355$ nm, $\lambda_{\text{collected}} = 470$ nm). e) Normalized steady-state (solid lines) and gated excitation spectra (dashed lines) for LE (green line, $\lambda_{\text{monitored}} = 470$ nm) and CT (orange line, $\lambda_{\text{monitored}} = 650$ nm) emissions. Lifetime decay profile of **BrPmDI-LP** hybrid in aqueous solution. f) ^1LE fluorescence (blue, $\lambda_{\text{exc.}} = 373$ nm, $\lambda_{\text{collected}} = 410$ nm, $\tau_{\text{avg.}} = 1.18$ ns) and ^1CT fluorescence (orange, $\lambda_{\text{exc.}} = 480$ nm, $\lambda_{\text{collected}} = 650$ nm) and f) long-lived CT emission ($\lambda_{\text{exc.}} = 470$ nm, $\lambda_{\text{collected}} = 650$ nm).

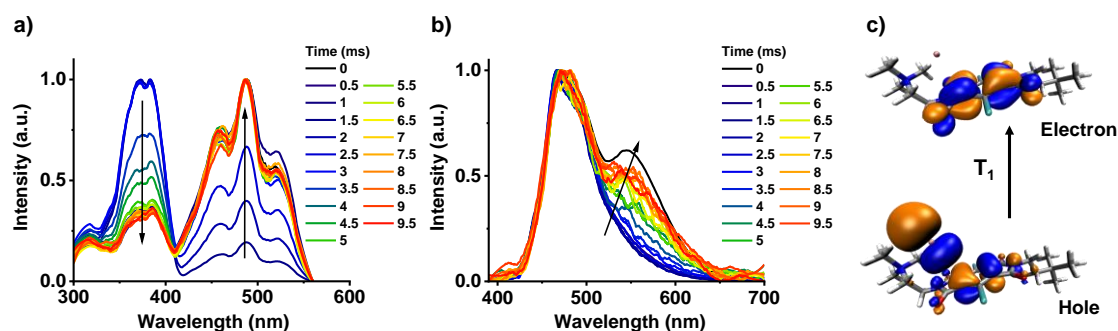


Figure 5.2.6. Dual Phosphorescence of **BrPmDI-LP** hybrid in aqueous solution: Time resolved a) excitation ($\lambda_{\text{monitored}} = 650 \text{ nm}$) and b) emission spectra ($\lambda_{\text{exc.}} = 370 \text{ nm}$). Arrows indicate the spectral changes with time. c) Natural transition orbitals (NTOs) **BrPmDI** and iodide complex for first excited triplet state (T_1), calculated at TD-CAM-B3LYP level in conjunction with 6-31+g(d) basis set for C, N, O, H and LANL2LDZ basis set for Br and I with effective core potential showing both LE and CT character. Concentration of the hybrid solution used 1 mM of **BrPmDI-LP** and 5 wt.% **LP** in water. Delay time used in the gated spectra is 50 μs .

5.2.6. Phosphorescence Study of BrPmDI-LP Hybrid as Drop-casted Films:

The delayed CT emission at 560 nm could be composed of either ^3CT phosphorescence or a delayed emission from the ^1CT state. To perform the photophysical study in the absence of oxygen and at different temperatures for investigating the involvement of ^3CT states in delayed CT emission, we have made the film by drop-casting the hybrid solution onto a quartz plate. Similar to the hybrid solution, the steady-state and gated emission spectra ($\lambda_{\text{exc.}} = 370 \text{ nm}$ and 470 nm, delay time = 50 μs) of the film showed the presence of ^3LE emission at 470 nm along with the CT emission band at 560 nm, which was also obtained by the direct excitation at the CT band (Figure 5.2.7a). Steady-state excitation spectra ($\lambda_{\text{monitored}} = 470 \text{ nm}$ and 650 nm) displayed a broad CT absorption band, along with the LE band similar to the hybrid solution (Figure 5.2.7b). Further delayed excitation spectra ($\lambda_{\text{monitored}} = 470 \text{ nm}$ and 650 nm, delay time = 50 μs) confirmed the contribution of the LE and CT absorption to the former and latter long-lived emission bands, respectively (Figure 5.2.7b). The triplet nature of the broad band was further evaluated by performing the photophysical experiments under vacuum, where emission intensities were increased by 3.64x and 1.64x folds, and lifetimes were increased from 0.62 ms to 0.89 ms and 0.65 ms to 0.99 ms when excited at 370 nm and 470 nm, respectively

(Figures 5.2.7c-f). However, to attest the phosphorescence nature of the emission, we have performed temperature-dependent studies of the film. (Figure 5.2.8). The increase in the resultant intensity of the emission in both steady-state and gated emission and corresponding lifetime with the decrease in temperature for both the LE ($\lambda_{\text{exc.}} = 370$ nm) and CT ($\lambda_{\text{exc.}} = 470$ nm) emission components, substantiate the phosphorescence nature of the delayed emission (Figure 5.2.8). The temperature-dependent studies further helped us to culminate that the red-shifted band can be explained as the anion- π induced formation triplet CT state (^3CT). The absolute phosphorescence quantum efficiency of **BrPmDI-LP** hybrid film is found to be $\sim 11\%$, which increased to $\sim 40\%$ in a vacuum. Further study of **BrPmDI** in the glassy matrix (acetonitrile) at 77 K showed both the triplet state emissions (^3LE and ^3CT) with high lifetime components similar to laponite hybrids (Figure 5.2.9a,b). We have also observed the presence of a very fast short lifetime component along with a long-lived feature in the decay profile in the film state with an average lifetime of around $1.4 \mu\text{s}$ ($\lambda_{\text{exc.}} = 373$ nm, $\lambda_{\text{collected}} = 650$ nm) (Figure 5.2.9c). In the time-gated emission spectra at shorter time scales (such as $0.5 \mu\text{s}$ and $1 \mu\text{s}$), a predominant emission of the CT states with a maximum at 550 nm was observed, suggesting the presence of delayed fluorescence from the ^1CT states, which disappeared at higher timescales (Figure 5.2.9d). Although the close proximity of ^3CT ($\lambda_{\text{maximum}} = 550$ nm) and ^1CT ($\lambda_{\text{maximum}} = 560$ nm) states with a smaller energy gap ($\Delta E_{\text{ST}} = \sim 0.05$ eV) suggest the possibility of a TADF pathway for this delayed emission (Figure 5.2.9e) we could not provide a convincing experimental support for the same with temperature dependent studies due to the significant contribution from the phosphorescence emission (Figure 5.2.8). These results further suggests that anion- π induced CT states may be used for the design of through space TADF systems, which emerged recently as an alternative molecular design to the well-studied covalently linked donor-acceptors systems.^[15] Since anion- π interactions are well known to be dependent on the nature of the anions, we further investigated the role of the counter ions on the observed phosphorescence. Thus, we have synthesised **BrPmDI** having different counter ions such as Br^- , BF_4^- , and BPh_4^- . The hybrids of these molecules with **LP**, **BrPmDI-Br-LP**, **BrPmDI-BF₄-LP** and **BrPmDI-BPh₄-LP**, in solution showed similar ^3LE emission behaviour suggesting the negligible external heavy atom effect from the iodide counter ion for the parent molecule (Figure 5.2.9f). However, the formation of ^3CT state is largely influenced by the counter ion as visible in the emission spectra, where the emission with maximum around 560 nm

is decreased significantly when bulky BPh_4^- ion was used (Figure 5.2.9f). In resultant, these experiments suggest that the ^3CT emission is more influenced by the ability of the counter anions to induce the CT states rather than the external heavy atom to stabilize the triplet states. However, the existence of CT interaction even after exchanging with the bulky counter ion is due to the higher association constant of the counter ion compared to the externally added anions reported in literature.^[3]

In summary, based on the detailed spectroscopic studies, we realized all the possible excited states of **BrPmDI** in LP hybrids, i.e., ^1LE (390-430 nm), ^1CT (560 nm), ^3LE (470 nm), ^3CT (550 nm). It is worth mentioning that the maximum of ^1CT state in the LP scaffold is blue-shifted ($\lambda_{\text{maximum}} = 560$ nm) compared to that in aqueous solution ($\lambda_{\text{maximum}} = 605$ nm), which could be due to the less polar nature of the interlayer galleries of LP as a result of its secluded microenvironment. However, we envisage that in polar solvents the CT fluorescence is more stabilized to give a much more red-shifted emission at 605 nm. Although the singlet and triplet states are closely spaced in these hybrids, experimental results suggested a low-lying ^1CT compared to the ^3CT , which could be due to the difference in the molecular geometry of the CT complex in these two excited states.

[16]

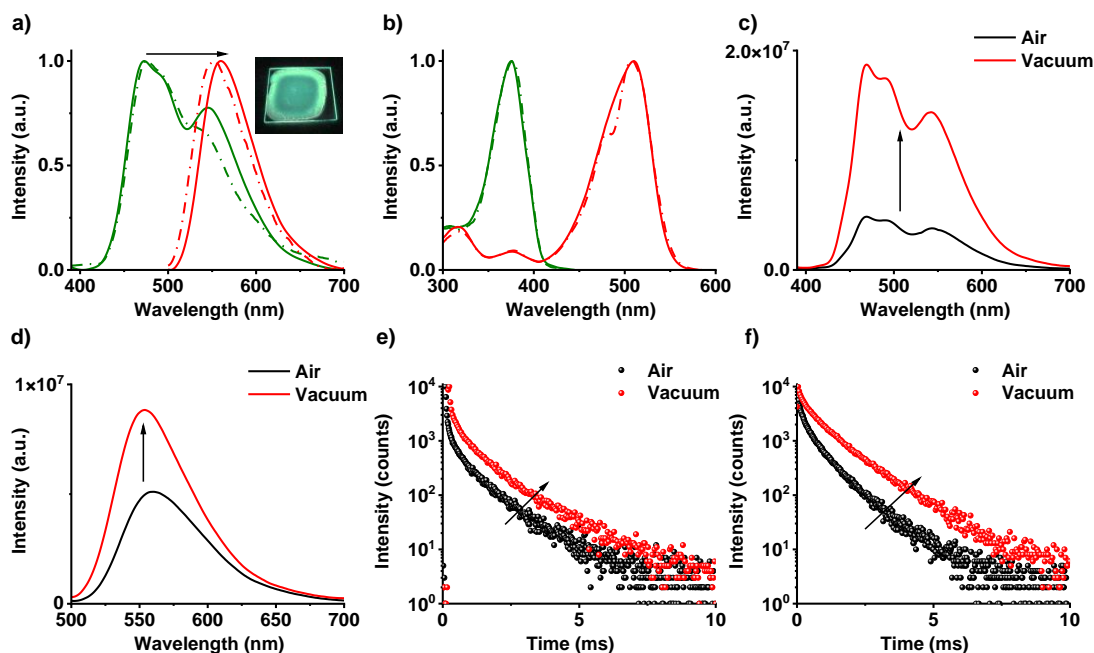


Figure 5.2.7. Dual Phosphorescence of **BrPmDI-LP** hybrid as drop-casted films: a) Normalized steady-state (solid line), gated (dashed line) emission spectra upon $\lambda_{exc.} = 370$ nm (green line) showing the contribution from both LE and CT emissions. Corresponding steady-state (solid line) and gated (dashed line) CT emission upon direct excitation at $\lambda_{exc.} = 470$ nm (orange line) is also shown. Inset shows the photograph of **BrPmDI-LP** hybrid film upon 365 nm UV light irradiation. b) Normalized steady-state (solid lines) and gated excitation spectra (dashed lines) for LE (green line, $\lambda_{monitored} = 470$ nm) and CT (orange line, $\lambda_{monitored} = 650$ nm) emissions. Steady-state emission spectra under air and vacuum c) $\lambda_{exc.} = 370$ nm, d) $\lambda_{exc.} = 470$ nm. Lifetime decay profiles of e) 3LE phosphorescence ($\lambda_{exc.} = 370$ nm, $\lambda_{collected} = 470$ nm) and f) long-lived CT emission ($\lambda_{exc.} = 370$ nm, $\lambda_{collected} = 650$ nm). Concentration of the hybrid solution used for drop-casting is 1 mM of **BrPmDI-LP** and 5 wt.% **LP** in water.

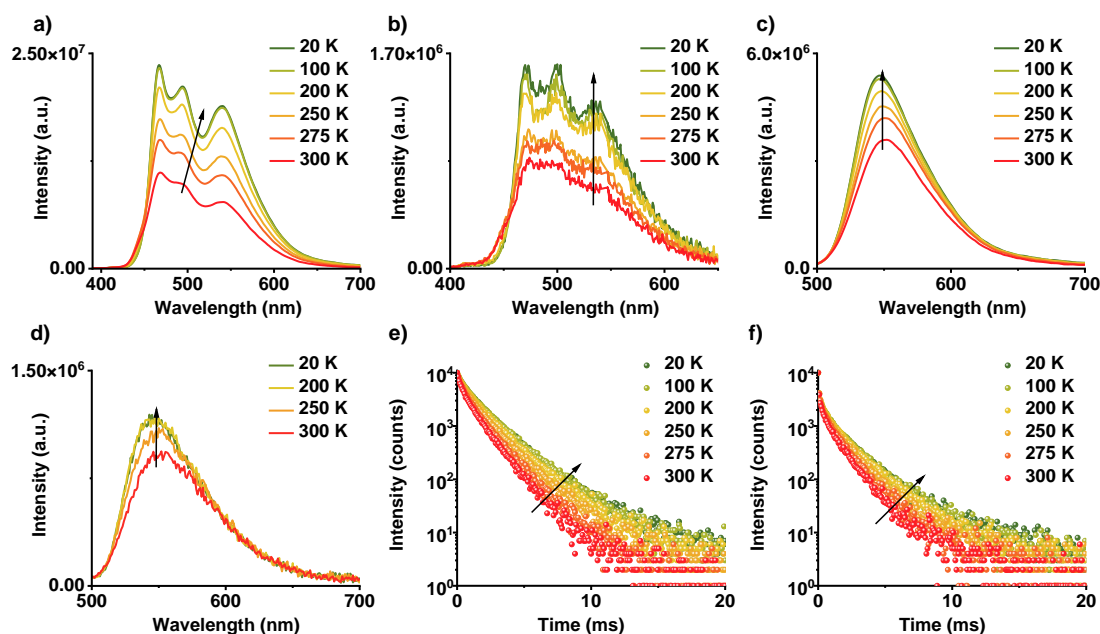


Figure 5.2.8. Temperature dependent studies of **BrPmDI-LP** hybrid as drop-casted films: Steady-state emission spectra at a) $\lambda_{exc.} = 370$ nm excitation. b) Delayed emission spectra ($\lambda_{exc.} = 370$ nm, delay time = 50 μ s) of the CT emission. Steady-state emission spectra at c) $\lambda_{exc.} = 470$ nm excitation. d) Delayed emission spectra ($\lambda_{exc.} = 470$ nm, delay time = 50 μ s) of the CT emission. Lifetime decay profiles of e) 3LE phosphorescence ($\lambda_{exc.} = 370$ nm, $\lambda_{collected} = 470$ nm) and f) 3CT phosphorescence ($\lambda_{exc.} = 370$ nm, $\lambda_{collected} = 650$ nm). Concentration of the hybrid solution used for drop-casting is 1 mM of **BrPmDI-LP** and 5 wt.% **LP** in water.

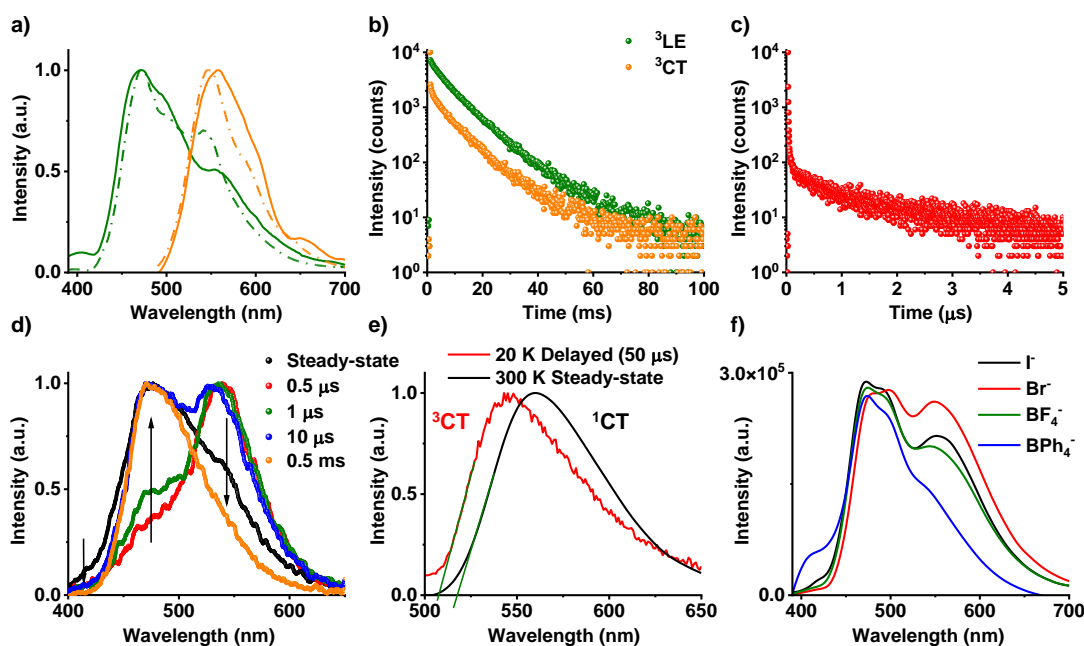


Figure 5.2.9. a) Normalized steady-state (solid line), gated (dashed line, delay time = 0.1 ms) emission spectra upon $\lambda_{\text{exc.}} = 340$ nm (green line) showing the contribution from both LE and CT emissions of **BrPmDI** in acetonitrile glassy matrix under cryogenic conditions at 77 K. The emission from CT upon direct excitation at $\lambda_{\text{exc.}} = 470$ nm (orange line) is also shown. b) Lifetime decay profile for LE (green, $\lambda_{\text{collected}} = 470$ nm) and CT (orange, $\lambda_{\text{collected}} = 650$ nm) emissions at $\lambda_{\text{exc.}} = 340$ nm of **BrPmDI** in acetonitrile glassy matrix under cryogenic conditions at 77 K. c) Lifetime decay profile ($\lambda_{\text{exc.}} = 373$ nm, $\lambda_{\text{collected}} = 650$ nm) of the film, which attributed to delayed fluorescence character. d) Normalized steady-state and delayed emission spectra (delay time = 0.5 μs to 0.5 ms) of **BrPmDI-LP** hybrid as drop-casted films at 300 K ($\lambda_{\text{exc.}} = 355$ nm). e) Experimental singlet triplet energy gap (ΔE_{ST}) calculation of **BrPmDI-LP** hybrid as drop-casted films (calculated from delayed emission spectra at 20 K and steady state emission spectra at 300 K showing $\Delta E_{\text{ST}} = 0.05$ eV, $\lambda_{\text{exc.}} = 470$ nm, concentration of the hybrid solution used for drop-casting is 1 mM of **BrPmDI-LP** and 5 wt.% **LP** in water). f) Steady-state emission spectra upon $\lambda_{\text{exc.}} = 370$ nm (green line) showing the contribution from both LE and CT emissions of **BrPmDI-LP**, **BrPmDI-Br-LP**, **BrPmDI-BF₄-LP** and **BrPmDI-BPh₄-LP** hybrid in aqueous solution, and the CT emission contribution is least for **BrPmDI-BPh₄-LP** i.e., in presence of bulky counterion.

5.2.7. Conclusions:

In conclusion, we have reported the anion- π interaction induced emissive CT states in a simple electron-deficient di-cationic pyromellitic diimide derivative with electron rich counter iodide anion. **BrPmDI** in aqueous solution exhibited anion- π induced CT absorption and corresponding CT fluorescence (^1CT), indicating the potential of these interactions in imparting the emissive CT states to electron-deficient arylene diimides. Inspired by the high triplet yields of PmDI derivatives, triplet stabilization of **BrPmDI** was further attempted by a supramolecular scaffolding strategy in the interlayer galleries of clay nanosheets in solution to minimize the vibrational and oxygen quenching of the triplet states. Interestingly, the resulting **BrPmDI-LP** hybrids exhibited ambient phosphorescence in the solution state. A deeper examination unravelled dual phosphorescence emission: cyan emissive phosphorescence from locally excited triplet state and an orange-emissive emission from the anion- π induced ^3CT state. This anion- π induced triplet CT emission is unprecedented, and it was unambiguously validated with a series of steady state and time resolved emission experiments. We envisage that the red-shifted CT phosphorescence emission in the solution state opens a plethora of opportunities in the field of bioimaging and sensing. But more importantly, we believe that anion- π induced formation of emissive CT states indeed offers an exciting molecular design for purely organic phosphors with tunable emission.

5.2.8. Experimental Section:

5.2.8.1. General Methods:

NMR Measurements: ^1H and ^{13}C NMR spectra were recorded on a BRUKER AVANCE-400 Fourier transformation spectrometer with 400 and 100 MHz respectively. The spectra were calibrated with respect to the residual solvent peaks. The chemical shifts are reported in parts per million (ppm) with respect to TMS. Short notations used are, s for singlet, d for doublet, t for triplet.

Optical Measurements: Electronic absorption spectra were recorded on Jasco V-750 UV-Visible spectrophotometer and emission spectra were recorded on FLS1000 spectrometer, Edinburgh Instruments. Solution state UV-Vis and emission spectra were recorded in 10 mm path length cuvette. Fluorescence spectra of the films were recorded in front-face geometry to avoid self-absorption.

Lifetime Measurements and Quantum yield: Fluorescence lifetimes were performed on a Horiba Delta Flex time-correlated single-photon-counting (TCSPC) instrument. A 373 nm diode and 480 nm laser diode with a pulse repetition rate of 1 MHz was used as the light source. The instrument response function (IRF) was collected using a scatterer (Ludox AS40 colloidal silica, Sigma-Aldrich). Phosphorescence lifetime ($\lambda_{\text{exc.}} = 370$ nm and 470 nm), gated emission and time-resolved excitation and emission were measured on FLS1000 spectrometer, Edinburgh Instruments equipped with a micro flash-lamp (μF2) set-up. Quantum yields were measured using an integrating sphere in the same instrument. Delayed PL (delay time = 0.5 μs , 1 μs , 10 μs and 0.5 ms) is performed using a 355 nm excitation source (repetition rate: 1 kHz and pulse width of ~ 0.8 ns) from Innolas) with a continuous neutral density filter, and the delayed PL is collected using gated Andor iCCD as described earlier.^[17]

High Resolution Mass Spectrometry (HR-MS): HR-MS was carried out using Agilent Technologies 6538 UHD Accurate-Mass Q-TOFLC/MS.

High Performance Liquid Chromatography (HPLC): HPLC was carried out using Agilent 1260 infinity quaternary HPLC system equipped with analytical ZORBAX Eclipse plus C18 column (4.6 mm \times 100 mm, 3.5 micron).

Single Crystal X-ray Crystallography: Suitable single crystal of the **BrPmDI** was mounted on a thin glass fibre with commercially available super glue. Intensity data were collected Bruker D8 VENTURE diffractometer equipped with a PHOTON detector and graphite-monochromated Mo-K α radiation ($\lambda = 0.71073$ Å, 50 kV, 1mA) at 100 K. APEX III software was used to collect, reduce and integrate the raw data. The direct method was used for solving crystal structure, followed by full-matrix least-squares refinements against F2 (all data HKLF 4 format) using the SHELXL 2014/7^{R1} and difference Fourier synthesis and least-squares refinement revealed the positions of the non-hydrogen atoms. All nonhydrogen atoms were refined anisotropically and remaining hydrogen atoms were placed in geometrically constrained positions and refined with isotropic temperature factors, generally 1.2 \times U_{eq} of their parent atoms. Molecular structure drawings were prepared using the program Mercury (version 3.1).

Computational Details: Ground State (S_0) of **BrPmDI** molecules was optimized using density functional theory (DFT) and electronic absorption spectra was calculated using time-dependent density functional theory (TD-DFT) as implemented in the Gaussian 16

software considering solvent effect.^[18a] Ground state (S_0) optimization and frequency calculation was performed employing B3LYP^[18b-d] exchange functional with 6-31+g(d) basis set except for Br and I for which LANL2DZ basis set was used with the corresponding effective core potential (ECP) in gas phase. While the excited state calculations were performed using CAMB3LYP exchange-correlation functional with the same basis sets as mentioned before. The first singlet excited state (S_1) was optimized at the TD-DFT level of theory. While the first triplet excited states (T_1) were also optimized at the TD-DFT level of theory within the Tamm-Dancoff approximation (TDA) to overcome the triplet instability issue.^[18e] The solvent (acetonitrile) effects were taken into accounts by the polarized continuum model (PCM) using the integral equation formalism variant (IEFPCM).^[18f]

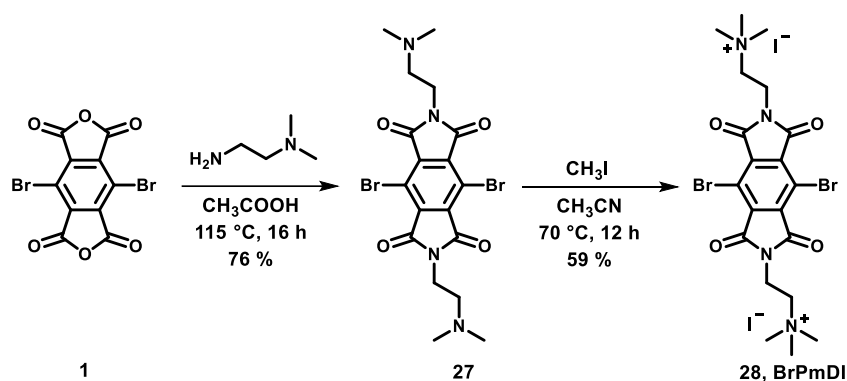
5.2.8.2. Protocol of Sample Preparation:

All solution state studies of **BrPmDI** were performed, using the study concentration of the samples at 0.05 and mM 0.1 mM, where 0.5 mM **BrPmDI** were used as a stock solution.

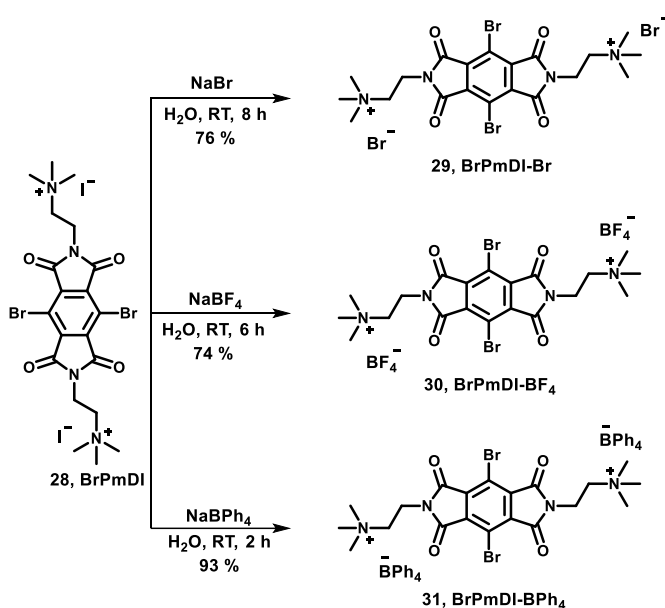
Phosphorescence studies of **BrPmDI/BrPmDI-BF₄** with **LP** were performed, keeping the final concentration of the samples at 1 mM, using a stock solution of 5 mM **BrPmDI/BrPmDI-BF₄** and 7 wt. % **LP** in water (suspending 630 mg of **LP** in 9 mL millipore distilled aqueous solution under intense sonication followed by treating the suspension with 24 mg of sodium polyacrylate). For thin film preparation, hybrid solutions were drop casted on clean quartz substrates and dried under vacuum overnight at 50 °C.

5.2.9. Synthetic Schemes and Procedures:

Dibromo-pyromellitic dianhydride was purchased from TCI; N,N-dimethyl ethylene diamine was purchased from Alfa-Aesar; methyl iodide, acetonitrile and acetic acid were purchased from local vendors and used without further purification.



Scheme 5.2.1. Synthetic scheme for **BrPmDI**.



Scheme 5.2.2. Synthetic scheme for **BrPmDI-Br**, **BrPmDI-BF₄** and **BrPmDI-BPh₄**

Synthesis of 27: Dibromo-pyromellitic dianhydride (**1**) (100 mg, 0.266 mmol) was added into the 10 mL glacial acetic acid in a 25 mL round bottom flask and stirred at room temperature for 10 minutes. N, N-dimethyl ethylene diamine (70 mg, 0.798 mmol) was added into the reaction mixture and stirred for 16 hours at 115 °C. After completing the reaction, acetic acid was removed under a high vacuum using a rotary evaporator, and the crude product was precipitated in a DCM/hexane mixture (10:1). The precipitate was filtered and washed with hexane and diethyl ether several times and dried under vacuum to afford **2** (105 mg, 76%) as a yellowish-white solid.

^1H NMR (400 MHz, CDCl_3) δ (ppm) 3.85 (t, 4H, $J = 8$ Hz), 2.62 (t, 4H, $J = 8$ Hz), 2.27 (s, 12H); ^{13}C NMR (100 MHz, CDCl_3) δ (ppm) 163.50, 136.24, 114.13, 56.60, 45.48, 36.95; HRMS (ESI): m/z calculated for $\text{C}_{18}\text{H}_{20}\text{Br}_2\text{N}_4\text{O}_4$: 515.9831; observed 516.9896 $[\text{M}+\text{H}]^+$.

Synthesis of BrPmDI: Compound **27** (100 mg, 0.193 mmol) was dissolved in 20 mL of acetonitrile: chloroform (1:1) mixture. Then, excess methyl iodide was added and stirred at 70 °C for 12 hours. The obtained suspension was evaporated under vacuum using a rotary evaporator and washed with chloroform and hexane to get **BrPmDI** (90 mg, 59%) as a crimson solid.

^1H NMR (400 MHz, DMSO) δ (ppm) 4.13 (t, 4H, $J = 7$ Hz), 3.62 (t, 4H, $J = 7$ Hz), 3.20 (s, 18H); ^{13}C NMR (100 MHz, DMSO) δ (ppm) 163.41, 135.83, 113.35, 61.70, 52.79, 31.87; HRMS (ESI): m/z calculated for $\text{C}_{20}\text{H}_{26}\text{Br}_2\text{N}_4\text{O}_4\text{I}_2$: 799.8390; observed 672.9340 $[\text{M}-\text{I}]^+$, 531.0045 $[\text{M}-2\text{I}-\text{CH}_3]^+$.

Synthesis of BrPmDI-Br: BrPmDI: (5 mg, 6.25 μmol) was dissolved in 5 mL distilled water and stirred for 5 min and subsequently NaBr (6.43 mg, 62.5 μmol) was added to it. The reaction mixture was stirred for 8 h at room temperature to obtain a pale-yellow solution. The excess solvent was removed under vacuum and the crude compound was washed (2-3 times) with ethanol to remove excess NaBr and dried under vacuum to obtain **BrPmDI-Br** (3.39 mg, 76%) as a colorless solid. HRMS (ESI): m/z calculated for $\text{C}_{20}\text{H}_{26}\text{Br}_4\text{N}_4\text{O}_4$: 705.8647; observed $[\text{M}-\text{Br}]^+$ 626.9429, $[\text{M}-2\text{Br}-\text{CH}_3]^+$ 531.0034.

Synthesis of BrPmDI-BF₄: BrPmDI: (15 mg, 0.01 mmol) was dissolved in 10 mL distilled water and stirred for 5 min and subsequently NaBF₄ (0.03 mmol) was added to it. The reaction mixture was stirred for 6 h at room temperature to obtain a light brown precipitate. The excess solvent was removed under vacuum and the crude compound was washed (2-3 times) with methanol to remove excess NaBF₄ and dried under vacuum to obtain **BrPmDI-BF₄** (10 mg, 74%) as a light-yellow solid. HRMS (ESI): m/z calculated for $\text{C}_{20}\text{H}_{26}\text{Br}_2\text{N}_4\text{O}_4\text{B}_2\text{F}_8$ 720.0359; observed 633.0314 $[\text{M}-\text{BF}_4]^+$, 531.0047 $[\text{M}-2\text{BF}_4-\text{CH}_3]^+$

Synthesis of BrPmDI-BF₄: BrPmDI BrPmDI-I₂: (5 mg, 6.25 μmol) was dissolved in 5 mL water acetonitrile mixture (1:4 ratio) and stirred for 5 min, NaBPh₄ (21.39 mg, 62.5 μmol) was added to it. The reaction mixture was stirred for 2 h at room temperature to obtain a light-yellow precipitate. The precipitation was collected through filtration and the crude compound was washed (2-3 times) with ethanol to remove excess NaBPh₄ and dried under vacuum to obtain **BrPmDI-BPh₄** (6.92 mg, 93%) as a pale-yellow solid.

^1H NMR (400 MHz, DMSO- d_6) δ (ppm) 7.17 (br, s 16H), 6.94-6.80 (t, 16H, $J = 7.3$ Hz), 6.78-6.77 (t, 8H, $J = 7.1$ Hz), 4.06-4.02 (t, 4H, $J = 7$ Hz), 3.62-3.58 (t, 4H, $J = 7.4$ Hz), 3.18 (s, 18H); HRMS (ESI): m/z calculated for $\text{C}_{68}\text{H}_{66}\text{B}_2\text{Br}_2\text{N}_4\text{O}_4$: 1184.3616; observed 865.1925 $[\text{M}-\text{BPh}_4]^+$, 531.0027 $[\text{M}-2\text{BPh}_4-\text{CH}_3]^+$.

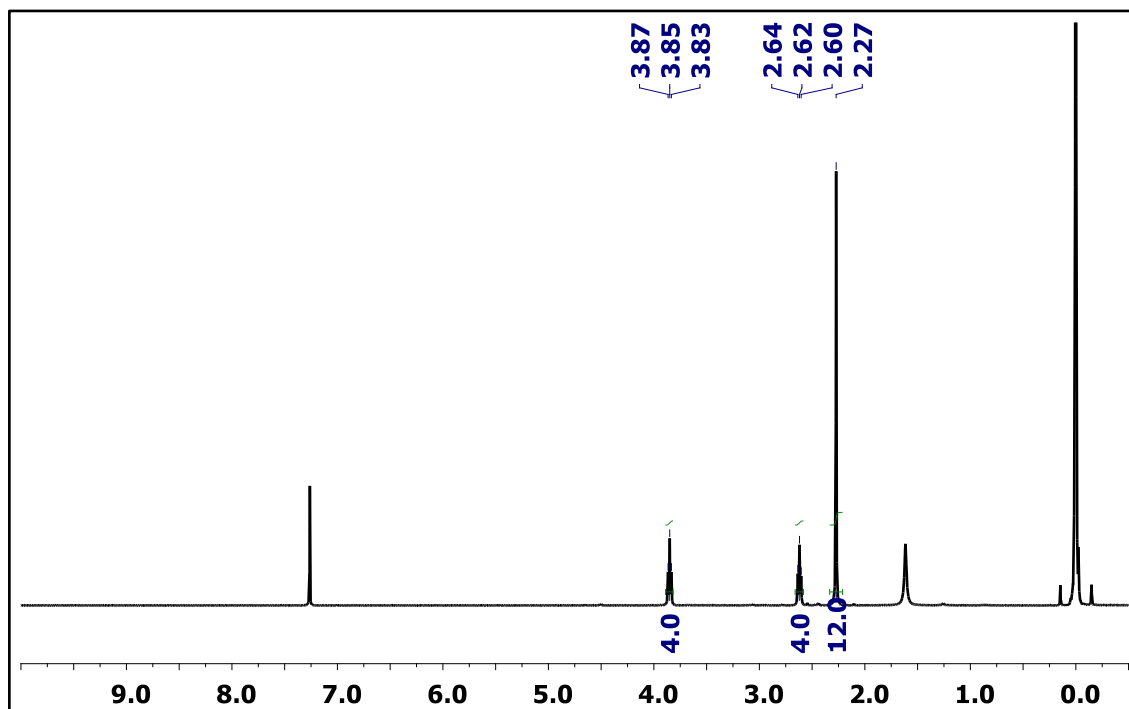


Figure 5.2.10. ^1H NMR spectrum of compound 27 in CDCl_3 .

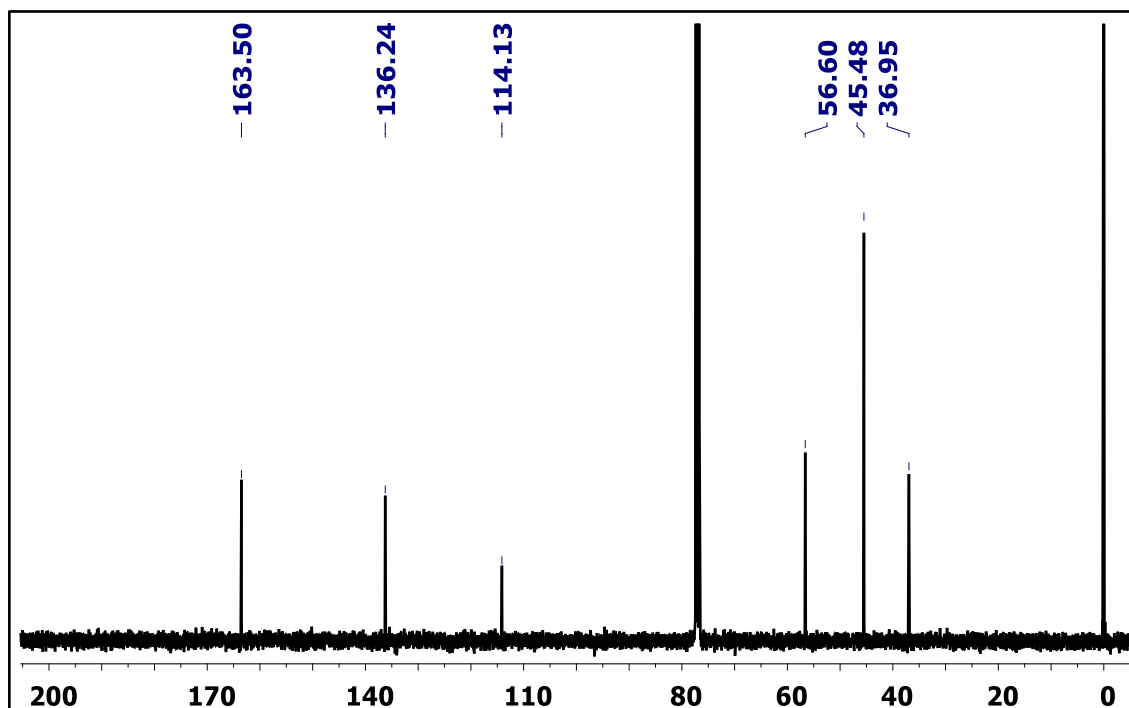


Figure 5.2.11. ^{13}C NMR spectrum of compound 27 in CDCl_3 .

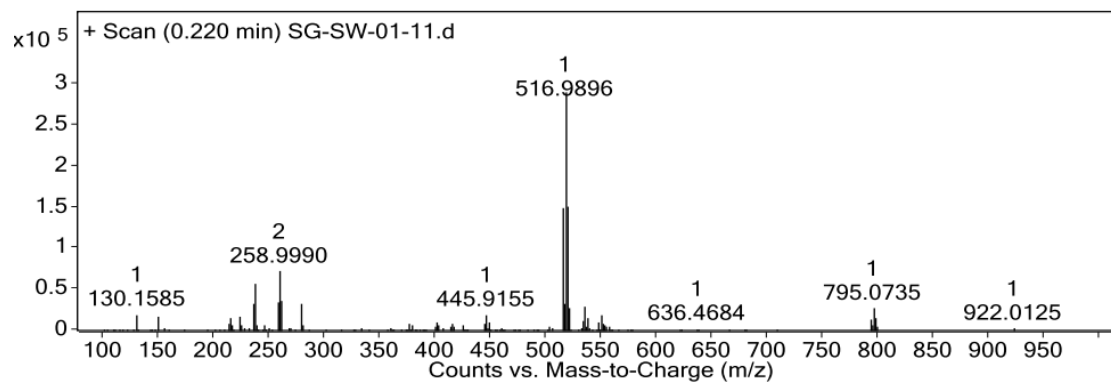


Figure 5.2.12. ESI-HRMS data of compound 27.

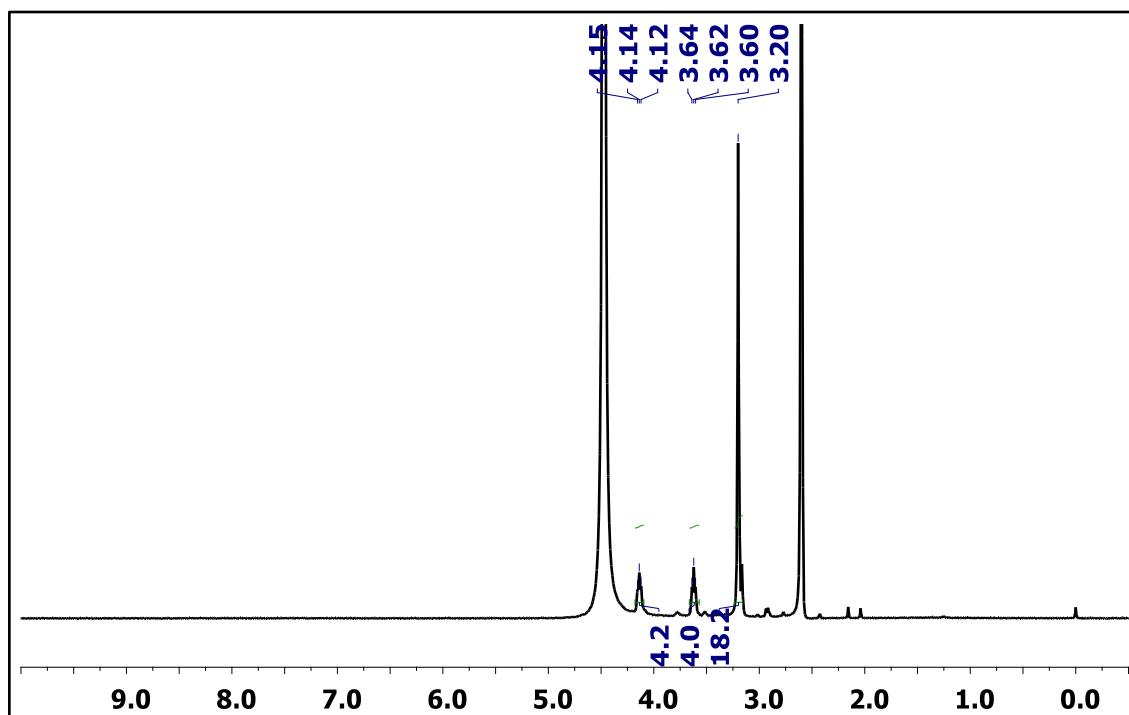


Figure 5.2.13. ^1H NMR spectrum of **BrPmDI** in $\text{DMSO-}D_6$.

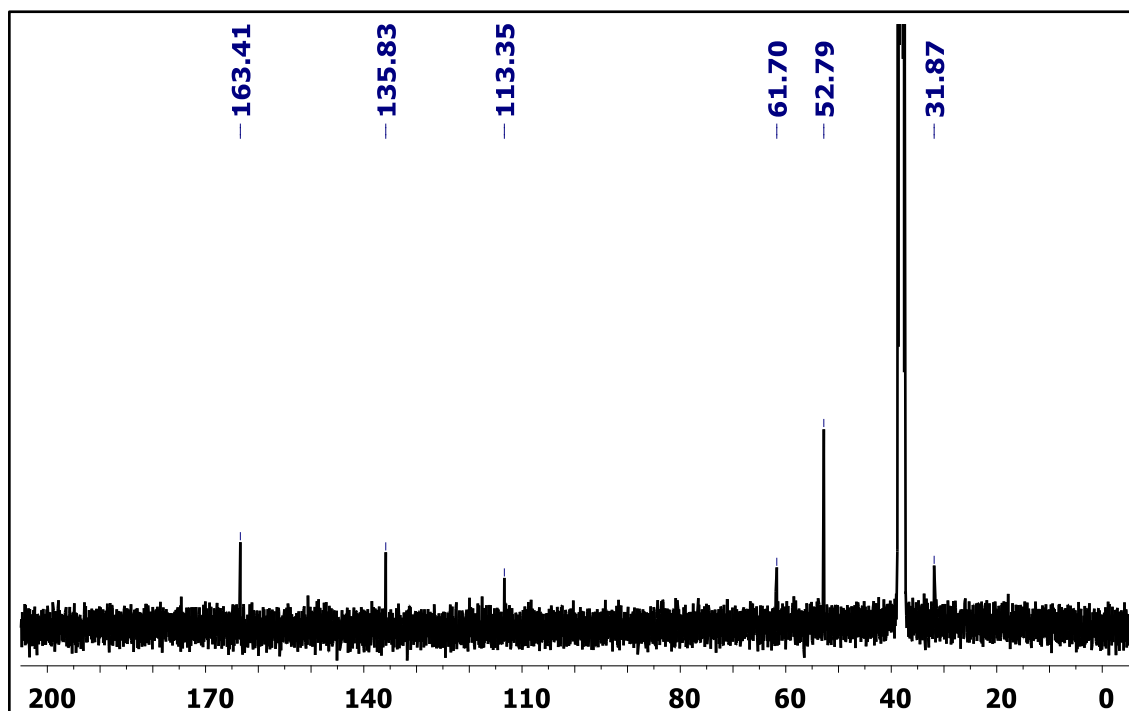


Figure 5.2.14. ^{13}C NMR spectrum of *BrPmDI* in $\text{DMSO-}D_6$.

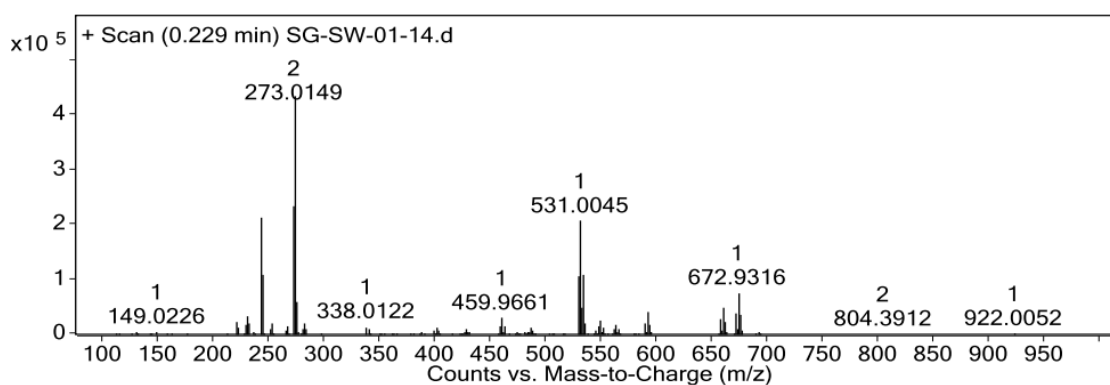


Figure 5.2.15. ESI-HRMS data of *BrPmDI*.

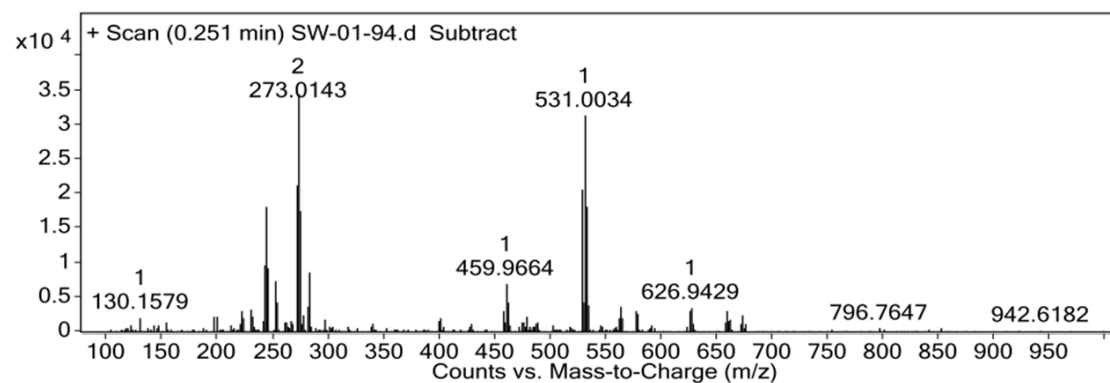


Figure 5.2.16. ESI-HRMS data of *BrPmDI-Br*.

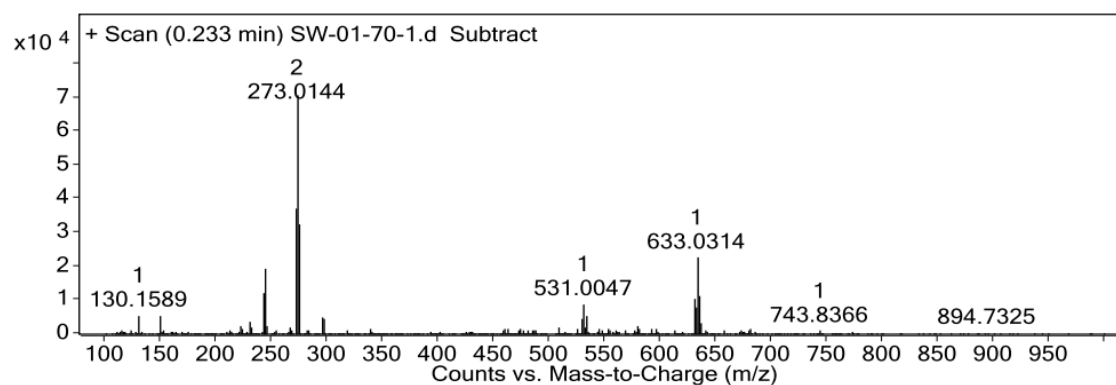


Figure 5.2.17. ESI-HRMS data of *BrPmDI-BF₄*.

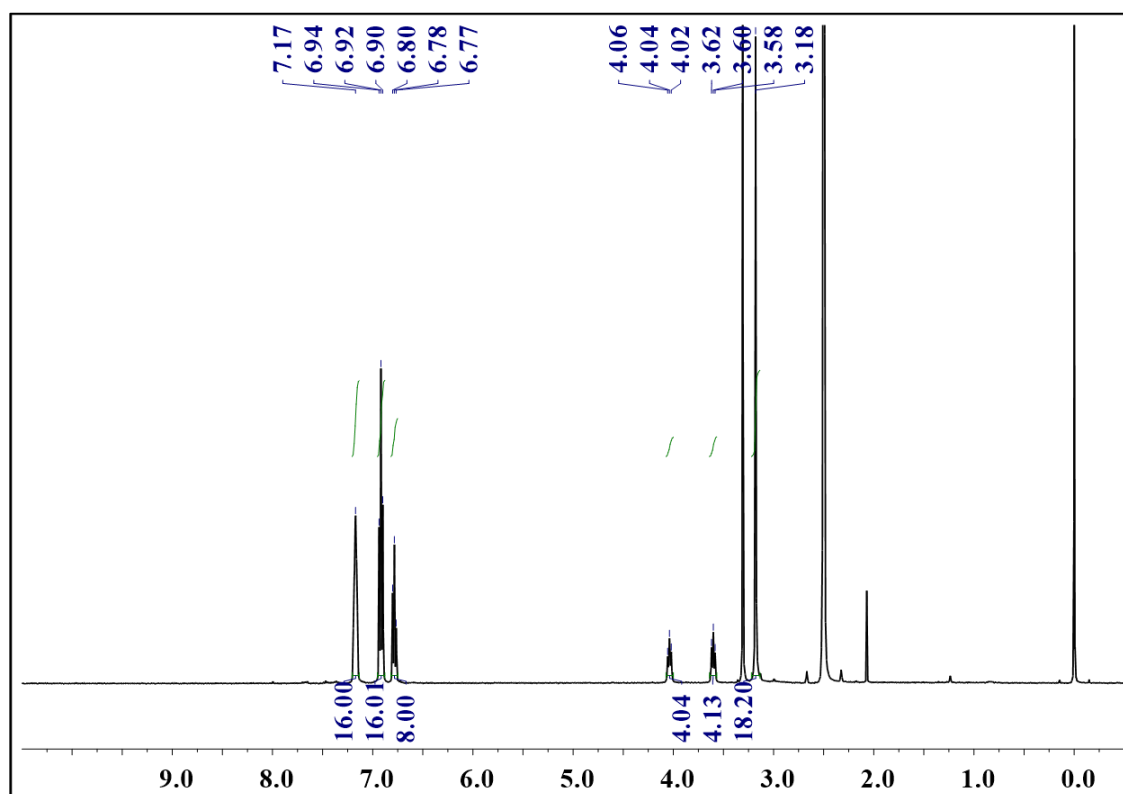


Figure 5.2.18. ¹H NMR spectrum of *BrPmDI-BPh₄* in DMSO-*D*₆.

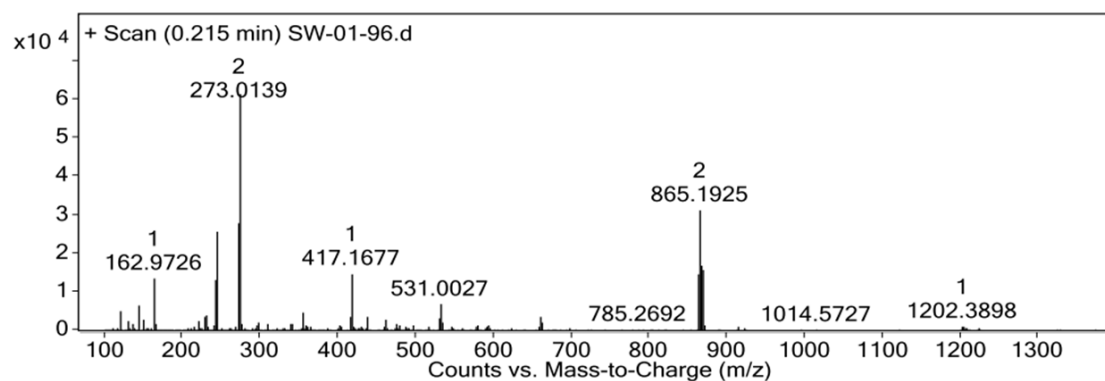


Figure 5.2.19. ESI-HRMS data of *BrPmDI-BPh₄*.

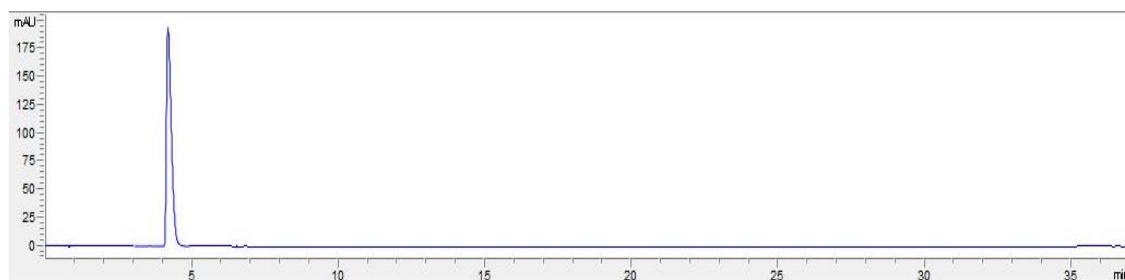


Figure 5.2.20. HPLC profile of **BrPmDI** ($[c] = 0.5 \text{ mM}$, A gradient elution of acetonitrile from 60-100% in aqueous solution was used by monitoring at 375 nm).

5.2.10. References:

[1]. (a) A. Frontera, P. Gamez, M. Mascal, T.J. Mooibroek, J. Reedijk, *Angew. Chem. Int. Ed.* **2011**, *50*, 9564-9583; (b) Y. Zhao, Y. Cotelte, N. Sakai, S. Matile, *J. Am. Chem. Soc.* **2016**, *138*, 4270-4277; (c) B. L. Schottel, H. T. Chifotides, K. R. Dunbar, *Chem. Soc. Rev.* **2008**, *37*, 68-83; (d) A. Vargas Jentsch, A. Hennig, J. Mareda, S. Matile, *Acc. Chem. Res.* **2013**, *46*, 2791-2800.

[2] (a) Y. Zhao, Y. Cotelte, L. Liu, J. López-Andarias, A.-B. Bornhof, M. Akamatsu, N. Sakai, S. Matile, *Acc. Chem. Res.* **2018**, *51*, 2255-2263; (b) S. Saha, *Acc. Chem. Res.* **2018**, *51*, 2225-2236.

[3] R. E. Dawson, A. Hennig, D. P. Weimann, D. Emery, V. Ravikumar, J. Montenegro, T. Takeuchi, S. Gabutti, M. Mayor, J. Mareda, C. A. Schalley, S. Matile, *Nat. Chem.* **2010**, *2*, 533-538.

[4] (a) Y. Zhao, N. Sakai, S. Matile, *Nat. Commun.* **2014**, *5*, 3911; (b) Y. Zhao, Y. Cotelte, A.-J. Avestro, N. Sakai, S. Matile, *J. Am. Chem. Soc.* **2015**, *137*, 11582-11585; (c) L. Liu, Y. Cotelte, A.-J. Avestro, N. Sakai, S. Matile, *J. Am. Chem. Soc.* **2016**, *138*, 7876-7879; (d) Y. Cotelte, V. Lebrun, N. Sakai, T. R. Ward, S. Matile, *ACS Cent. Sci.* **2016**, *2*, 388-393.

[5] (a) S. Guha, S. Saha, *J. Am. Chem. Soc.* **2010**, *132*, 17674-17677; (b) S. Guha, F. S. Goodson, S. Roy, L. J. Corson, C. A. Gravenmier, S. Saha, *J. Am. Chem. Soc.* **2011**, *133*, 15256-15259.

[6] (a) W. Zhao, Z. He, W. Y. Lam, Jacky, Q. Peng, H. Ma, Z. Shuai, G. Bai, J. Hao, B. Z. Tang, *Chem* **2016**, *1*, 592-602; (b) S. Xu, R. Chen, C. Zheng, W. Huang, *Adv. Mater.* **2016**, *28*, 9920-9940; (c) W. Zhao, Z. He, B. Z. Tang, *Nat. Rev. Mater.* **2020**, *5*, 869-885;

(d) X. Ma, J. Wang, H. Tian, *Acc. Chem. Res.* **2019**, *52*, 738-748; (e) J. Yang, M. Fang, Z. Li, *Acc. Mater. Res.* **2021**, *2*, 644-654.

[7] (a) O. Bolton, K. Lee, J-H. Kim, K.Y. Lin, J. Kim, *Nat. Chem.* **2011**, *3*, 205-210; (b) D. Lee, O. Bolton, B. C. Kim, J. H. Youk, S. Takayama, J. Kim, *J. Am. Chem. Soc.* **2013**, *135*, 6325-6329; (c) Z. An, C. Zheng, Y. Tao, R. Chen, H. Shi, T. Chen, Z. Wang, H. Li, R. Deng, X. Liu, W. Huang, *Nat. Mater.* **2015**, *14*, 685-690; (d) Z. He, W. Zhao, J. W. Y. Lam, Q. Peng, H. Ma, G. Liang, Z. Shuai, B. Z. Tang, *Nat. Commun.* **2017**, *8*, 416; (e) Q. Liao, Q. Gao, J. Wang, Y. Gong, Q. Peng, Y. Tian, Y. Fan, H. Guo, D. Ding, Q. Li, Z. Li, *Angew. Chem. Int. Ed.* **2020**, *59*, 9946-9951; (f) J. Ren, Y. Wang, Y. Tian, Z. Liu, X. Xiao, J. Yang, M. Fang, Z. Li, *Angew. Chem. Int. Ed.* **2021**, *60*, 12335-12340; (g) S. Kuila, S. Garain, S. Bandi, S. J. George, *Adv. Funct. Mater.* **2020**, *30*, 2003693; (h) S. Kuila, S. J. George, *Angew. Chem. Int. Ed.* **2020**, *59*, 9393-9397; (i) L. Gu, W. Ye, X. Liang, A. Lv, H. Ma, M. Singh, W. Jia, Z. Shen, Y. Guo, Y. Gao, H. Chen, D. Wang, Y. Wu, J. Liu, H. Wang, X.-Y. Zheng, Z. An, W. Huang, Y. Zhao, *J. Am. Chem. Soc.* **2021**, *143*, 18527-18535; (j) Y. Su, Y.; Y. Zhang, Z. Wang, W. Gao, P. Jia, D. Zhang, C. Yang, Y. Li, Y. Zhao, *Angew. Chem. Int. Ed.* **2020**, *59*, 9967-9971; (k) Y. Su, S. Z. F. Phua, Y. Li, X. Zhou, D. Jana, G. Liu, W. Q. Lim, W. K. Ong, C. Yang, Y. Zhao, *Sci. adv.* **2018**, *4*, eaas9732; (l) A. Kirch, M. Gmelch, S. Reineke, *S. J. Phys. Chem. Lett.* **2019**, *10*, 310-315; (m) S. Sun, J. Wang, L. Ma, X. Ma, H. Tian, *Angew. Chem. Int. Ed.* **2021**, *60*, 18557-18560.

[8] a) D. Di, L. Yang, J. M. Richter, L. Meraldi, R. M. Altamimi, A. Y. Alyamani, D. Credgington, K. P. Musselman, J. L. MacManus Driscoll, R. H. Friend, *Adv. Mater.* **2017**, *29*, 1605987; b) A. Dey, D. Kabra, *ACS Appl. Mater. Interfaces* **2018**, *10*, 38287-38293.

[9] (a) H. Uoyama, K. Goushi, K. Shizu, H. Nomura, C. Adachi, *Nature* **2012**, *492*, 234-238; (b) M. Y. Wong, E. Zysman-Colman, *Adv. Mat.* **2017**, *29*, 1605444.

[10] (a) S. Kuila, K. V. Rao, S. Garain, P. K. Samanta, S. Das, S. K. Pati, M. Eswaramoorthy, S. J. George, *Angew. Chem. Int. Ed.* **2018**, *57*, 17115-17119; (b) Z. Y. Zhang, Y. Chen, Y. Liu, *Angew. Chem. Int. Ed.* **2019**, *58*, 6028-6032; (c) D. Li, F. Lu, J. Wang, W. Hu, X. M. Cao, X. Ma, H. Tian, *J. Am. Chem. Soc.* **2018**, *140*, 1916-1923; (d) X. Yao, J. Wang, D. Jiao, Z. Huang, O. Mhirsi, F. Lossada, L. Chen, B. Haehnle, A. J. C. Kuehne, X. Ma, H. Tian, A. Walther, *Adv. Mater.* **2020**, 2005973; (e) J. Wang, Z.

Huang, X. Ma, H. Tian, *Angew. Chem. Int. Ed.* **2020**, *59*, 9928-9933; (f) H. J. Yu, Q. Zhou, X. Dai, F. F. Shen, Y. M. Zhang, X. Xu, Y. Liu, *J. Am. Chem. Soc.* **2021**, *143*, 13887-13894; (g) X. K. Ma, W. Zhang, Z. Liu, H. Zhang, B. Zhang, Y. Liu, *Adv. Mater.* **2021**, *33*, 2007476; (h) S. Garain, B. C. Garain, M. Eswaramoorthy, S. K. Pati, S. J. George, *Angew. Chem. Int. Ed.* **2021**, *60*, 19720-19724; (i) Z. Li, Y. Han, F. Nie, M. Liu, H. Zhong, F. Wang, *Angew. Chem. Int. Ed.* **2021**, *60*, 8212-8219; (j) Z. Li, Y. Han, F. Wang, *Nat. Commun.* **2019**, *10*, 3735; (k) M. Huo, X. Y. Dai, Y. Liu, *Angew. Chem., Int. Ed.* **2021**, *60*, 27171-27177; (l) M. Huo, X. Y. Dai, Y. Liu, *Small* **2022**, *18*, 2104514.

[11] (a) N. Sakai, J. Mareda, E. Vauthey, S. Matile, *Chem. Commun.* **2010**, *46*, 4225-4237; (b) F. Würthner, S. Ahmed, C. Thalacker, T. Debaerdemaeker, *Chem. Eur. J.* **2002**, *8*, 4742-4750;

[12] (a) S. Garain, S. Kuila, B. C. Garain, M. Kataria, A. Borah, S. K. Pati, S. J. George, *Angew. Chem. Int. Ed.* **2021**, *60*, 12323-12327; (b) S. Garain, S. Sarkar, B. C. Garain, S. K. Pati, S. J. George, *Angew. Chem. Int. Ed.* **2022**, DOI: 10.1002/anie.202115773.

[13] S. Kuila, S. Garain, G. Banappanavar, B. C. Garain, D. Kabra, S. K. Pati, S. J. George, *J. Phys. Chem. B* **2021**, *125*, 4520-4526; (b) S. Kuila, A. Ghorai, P. K. Samanta, R. B. K. Siram, S. K. Pati, K. S. Narayan, S. J. George, *Chem. Eur. J.* **2019**, *25*, 16007-16011.

[14] K. V. Rao, a. Jain, S. J. George, *J. Mater. Chem. C* **2014**, *2*, 3055-3064.

[15] H. Tsujimoto, D. G. Ha, G. Markopoulos, H. S. Chae, M. A. Baldo, T. M. Swager, *J. Am. Chem. Soc.* **2017**, *139*, 4894-4900; (b) C. M. Tonge, Z. M. Hudson, *J. Am. Chem. Soc.* **2019**, *141*, 13970-13976; (c) Q. Li, J. Hu, J. Lv, X. Wang, S. Shao, L. Wang, X. Jing, F. Wang, *Angew. Chem. Int. Ed.* **2020**, *59*, 20174-20182.

[16] (a) S. Difley, D. Beljonne, T. Van Voorhis, *J. Am. Chem. Soc.* **2008**, *130*, 3420-3427; (b) P. de Silva, *J. Phys. Chem. Lett.* **2019**, *10*, 5674-5679.

[17] G. Banappanavar, S. Vaidya, U. Bothra, L. R. Hegde, K. P. Sharma, R. H. Friend, D. Kabra, *Applied Physics Reviews*, **2021**, *8*, 031415.

[18] a) Gaussian 16, Revision A.03, M. J. Frisch, G. W. Trucks, H. B. Schlegel, G. E. Scuseria, M. A. Robb, J. R. Cheeseman, G. Scalmani, V. Barone, G. A. Petersson, H. Nakatsuji, X. Li, M. Caricato, A. V. Marenich, J. Bloino, B. G. Janesko, R. Gomperts, B.

Mennucci, H. P. Hratchian, J. V. Ortiz, A. F. Izmaylov, J. L. Williams; F. Ding; F. Lipparini, F. Egidi, J. Goings, B. Peng, A. Petrone, T. Henderson, D. Ranasinghe, V. G. Zakrzewski, J. Gao, N. Rega, G. Zheng, W. Liang, M. Hada, M. Ehara, K. Toyota, R. Fukuda, J. Hasegawa, M. Ishida, T. Nakajima, Y. Honda, O. Kitao, H. Nakai, T. Vreven, K. Throssell, J. A. Montgomery Jr., J. E. Peralta, F. Ogliaro, M. J. Bearpark, J. J. Heyd, E. N. Brothers, K. N. Kudin, V. N. Staroverov, T. A. Keith, R. Kobayashi, J. Normand, K. Raghavachari, A. P. Rendell, J. C. Burant, S. S. Iyengar, J. Tomasi, M. Cossi, J. M. Millam, M. Klene, C. Adamo, R. Cammi, J. W. Ochterski, R. L. Martin, K. Morokuma, O. Farkas, J. B. Foresman, D. J. Fox, Gaussian, Inc., Wallingford CT, **2016**; b) A. D. Becke, *J. Chem. Phys.* **1993**, *98*, 1372; c) C. Lee, W. Yang, R. G. Parr, *Phys. Rev. B* **1988**, *37*, 785-789; d) B. Miehlich, A. Savin, H. Stoll, H. Preuss, *Chem. Phys. Lett.* **1989**, *157*, 200-206; e) S. Hirata, M. Head-Gordon, *Chem. Phys. Lett.* **1999**, *314*, 291-299; f) G. Scalmani, M. J. Frisch, *J. Chem. Phys.* **1996**, *57*, 281-293.

CHAPTER 6

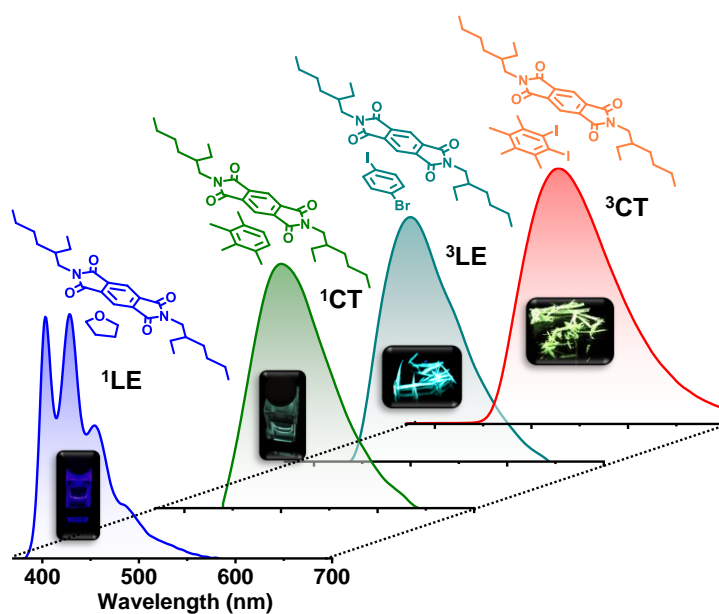
Biasing the Excited State Manifold via Non-covalent Donor- Acceptor Approach

CHAPTER 6

Biasing the Excited State Manifold via Non-covalent Donor-Acceptor Approach*

Abstract

Engineering the electronic excited state manifolds of organic molecules can give rise to various functional outcomes, including ambient triplet harvesting, that has received prodigious attention in the recent past. In this chapter, we introduce a modular, non-covalent approach to bias the entire excited state landscape of an organic molecule using tunable ‘through-space charge-transfer’ interactions with appropriate donors. Although charge-transfer (CT) donor-acceptor complexes have been extensively explored as functional and supramolecular motifs in the realm of soft organic materials, they could not imprint their potentiality in the field of luminescent materials, and it still remains as a challenge. Thus, in the present study, we investigate the modulation of the excited state emission characteristics of a simple pyromellitic diimide derivative on complexation with appropriate donor molecules of varying electronic characteristics to demonstrate the selective harvesting of emission from its locally excited (LE) and CT singlet and triplet states. Remarkably, co-crystallization of the pyromellitic diimide with heavy-atom substituted and electron-rich aromatic donors



*Manuscript based on this work is under revision in Chemical Sciences.

leads to an unprecedented ambient CT phosphorescence with impressive efficiency and notable lifetime. Further, gradual minimizing of the electron-donating strength of the donors from 1,4-diiodo-2,3,5,6-tetramethylbenzene (or 1,2-diiodo-3,4,5,6-tetramethylbenzene) to 1,2-diiodo-4,5-dimethylbenzene and 1-bromo-4-iodobenzene, modulates the source of ambient phosphorescence emission from 3CT excited state to 3LE excited state. Through comprehensive spectroscopic, theoretical studies, and single-crystal analyses, we elucidate the unparalleled role of intermolecular donor-acceptor interactions to toggle between the emissive excited states and stabilize the triplet excitons. We envisage that the present study will be able to provide new and innovative dimensions to the existing molecular designs employed for triplet harvesting.

6.1. Introduction:

Biasing the landscape of electronic excited state manifolds of organic molecular systems has paramount importance in controlling various photophysical processes and resultant functions. The necessity to harvest triplet excitons owing to their practical implications in organic lighting devices, sensing, and bioimaging has triggered interest in manipulating the singlet and triplet excited states by innovative molecular designs.^[1] Thus, the recent past has witnessed a renaissance in the field of ambient triplet harvesting by effectively tuning the excited state dynamics with pertinent introduction of elegant molecular designs. Generally, the triplet excitons are harvested via two major photophysical processes; phosphorescence^[2-4] and thermally activated delayed fluorescence (TADF).^[5] Often, CT states play an important role in these ambient triplet harvesting processes, where these states can assist the exciton transfer by acting as an intermediate state or excitons can be directly harvested from the CT states.^[5] In the present contribution, we propose a modular approach to realize efficient triplet harvesting, by toggling between the LE and CT states of an organic molecule by through-space CT interactions, in non-covalent co-crystal scaffolds of donor and acceptor molecules (Figure 6.1).

Supramolecular networks of CT co-crystals, with the co-facial organization of donor and acceptor chromophores,^[6] are an important class of organic functional materials and have been extensively explored in organic ferroelectrics^[7] and charge-transport.^[8] Further, the reversible dynamic nature of the CT interactions with tunable association constant, has been used for the design of various supramolecular materials,

such as molecular motors,^[9] supramolecular polymers^[10] and foldamers.^[11] Despite the functional and supramolecular diversities offered by CT complexes, their optical properties are relatively less explored as they often form non-fluorescent CT complexes or charge-separated states.^[12] Even though emissive CT states (¹CT) are reported, phosphorescence from triplet CT states is rarely encountered.^[12] Although, attempts have been made to achieve phosphorescence under cryogenic conditions from CT complexes,^[13] to the best of our knowledge, there are no reports on organic CT based ambient phosphors known to date.

Earlier, we have unveiled that the anomalous exciplex like emission emanating from the arylene diimides in the presence of aromatic solvents have clear CT characteristics, resulting from the ground-state CT complexation between electron-rich aromatic solvents and electron-deficient arylene diimide cores.^[14] Thus, to toggle between different excited states by the CT strategy, we have chosen a donor-acceptor intermolecular architecture with arylene diimides based on pyromellitic diimide as acceptor and various electron rich heavy atom substituted benzene as donor components. Apart from the countless opportunities offered by arylene diimides to tune their electronic properties by structural modification,^[15] the added advantage bestowed by pyromellitic diimides due to their facile synthetic route and high triplet yields,^[16] urged us to continue exploring their potentials as the acceptor in the CT system. The simplified Jablonski diagram (Figure 6.1) explains the possible electronic transitions realized by judiciously choosing the donor component to interact with pyromellitic diimide (**PmDI**). In presence of non-aromatic solvents like THF, **PmDI** exhibits its characteristic highly blue-shifted LE fluorescence (¹LE). This can be further pushed into CT fluorescence with the help of electron rich aromatic solvents with low ionization potential that can form emissive CT complex with **PmDI**, as observed previously with naphthalene diimide derivatives.^[14] Remarkably, the integration of heavy atom into the donor counterpart induces ambient locally-excited (³LE) phosphorescence of **PmDI** via external heavy atom effect. More interestingly, the coalescence of both the above concepts, i.e., introducing donor with strong electron-donating capacity with heavy atoms can trigger unique CT phosphorescence under ambient conditions, from the triplet ³CT states, (Figure 6.1). Therefore, we illustrate tunable ambient phosphorescence from a simple arylene diimide derivative by selectively tuning the excited state dynamics of the phosphor using a modular non-covalent organic co-crystal approach.

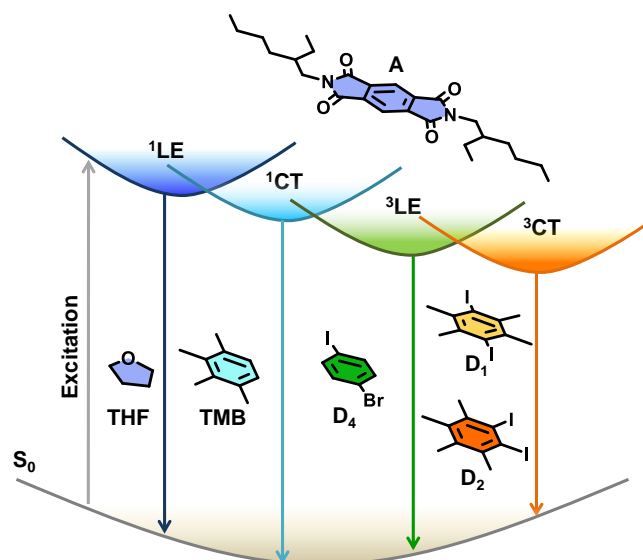


Figure 6.1. Schematic of the modular donor-acceptor co-assembly strategy to tune the excited state manifold of pyromellitic diimide (**PmDI**) phosphor. Molecular structure of acceptor (**PmDI**, **A**) and its tunable emission with different aromatic donors (**D**). Simplified Jablonski diagram showing various emission processes possible in the excited state.

6.2. Molecular Design:

In this chapter, we introduce a modular donor-acceptor co-crystal approach to realize the unprecedented ambient CT phosphorescence. In this co-crystal approach, we envision that the excited state manifold can be modulated by the structural engineering of either donor and acceptor molecular components, and thereby selectively harnessing emission from LE or CT triplet excited states. This can be realized by the simultaneous incorporation of heavy atoms into the individual components, and/or tuning the acceptor or donor strength. The former results in populating the triplet state by enhancing spin-orbit coupling (SOC), and thereby inter-system crossing (ISC) efficiency by external or internal heavy atom effect,^[1a] while the latter prompts the excitons to preferentially channel into the CT states.^[1b] Further, we envisage that the co-crystal organization stabilized by various intermolecular interactions, would harvest the triplets by minimizing the common triplet quenching vibrational pathways.^[1a,2a]

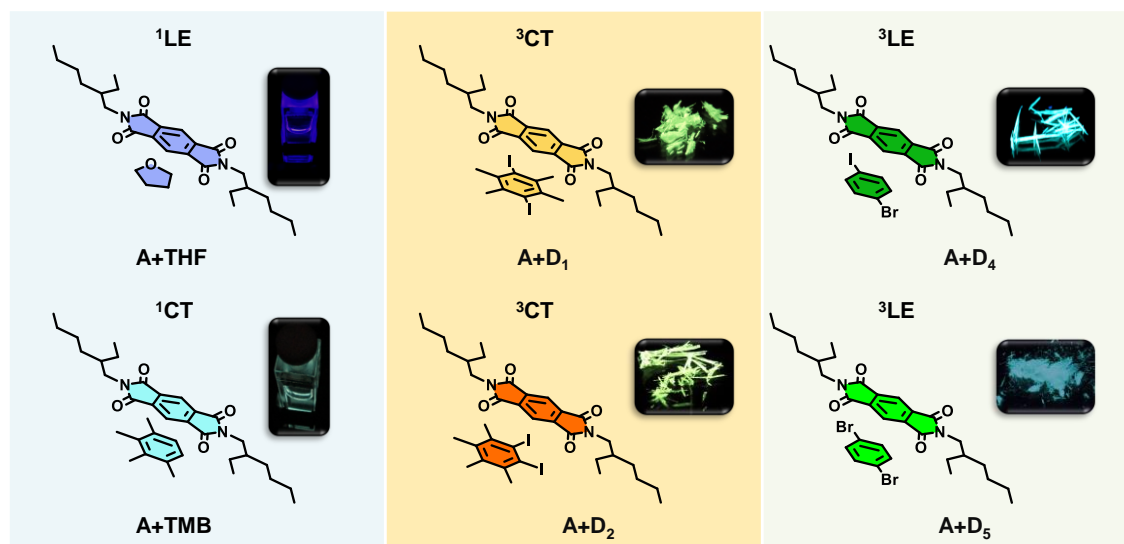


Figure 6.2. Molecular structure of acceptor (**PmDI**, **A**) and its tunable emission with different aromatic donors; locally excited fluorescence (1LE) in THF solution, charge-transfer (1CT) fluorescence in electron rich-aromatic solvents (TMB), locally excited phosphorescence (3LE) in 1-bromo-4-iodobenzene (**D₄**), 1,4-dibromo-benzene (**D₅**) and charge-transfer phosphorescence (3CT) in 1,4-diiodo-2,3,5,6-tetramethylbenzene (**D₁**), 1,2-diiodo-3,4,5,6-tetramethylbenzene (**D₂**). (Photographs of 1LE , 1CT emission obtained by 340 nm and 370 nm Xe lamp excitation and 3LE and 3CT phosphorescent co-crystals under 365 nm UV lamp).

6.3. Spectroscopic Studies in Solution-state: Formation of 1LE and 1CT States:

Pyromellitic diimide (**PmDI**) derivative without any heavy-atom substitution was chosen as the acceptor component for the present study (Figure 6.2). Initially, the CT complexation of **PmDI** with various aromatic solvents was investigated by detailed spectroscopic studies (Figure 6.3). In THF, **PmDI** showed an absorption maximum of 320 nm and a structured emission with vibronic maxima at 420 nm, 440 nm and 460 nm, characteristic of local excited (1LE) fluorescence of **PmDI** monomer (Figures 6.3a,b). Further investigation was carried out to unravel the differences in the spectroscopic properties of **PmDI** in the presence of various aromatic solvents which is crucial for the scope of the present investigation. As the electron donating capacities of the aromatic solvents were increased from benzene to 1,2,3,4-tetramethylbenzene (TMB), a new red-shifted absorption band appeared, with a maximum red-shift observed for TMB, which indicates the ground-state electronic interaction with the solvent molecules (Figure 6.2a).

The corresponding emission spectra upon exciting at the $\pi\text{-}\pi^*$ band ($\lambda_{\text{exc.}} = 320 \text{ nm}$) of **PmDI** in the same set of solvents exhibited dual emission bands, where the higher energy band corresponds to the ^1LE state of **PmDI**, whereas the new broad red-shifted emission can be correlated to the ^1CT emission (Figure 6.2b). This is further confirmed by the emission spectra obtained upon the direct excitation of the lower energy band in the absorption spectra, which showed structureless emission with a gradual red-shifted maxima, with the increase in the donor strength of solvent, while moving from toluene to tetramethylbenzene (Figure 6.2c). This is more evident from the plot of emission maximum vs ionization potential where a nearly linear trend (from toluene to TMB) was observed confirming the CT nature of the interaction between **PmDI** and various aromatic solvents (Figure 6.2d).^[17] These inferences fall in line with the previous results reported by our group^[14] and Kitagawa's group^[18] where emissive ground state CT complexes were formed between naphthalene diimides (NDIs) and various aromatic solvents. Furthermore, the time-resolved lifetime decay experiments showed average lifetimes of 0.86 ns in THF ($\lambda_{\text{exc.}} = 340 \text{ nm}$, $\lambda_{\text{collected}} = 420 \text{ nm}$) corresponding to the ^1LE state of **PmDI**, and 2.56 ns in TMB ($\lambda_{\text{exc.}} = 442 \text{ nm}$, $\lambda_{\text{collected}} = 500 \text{ nm}$), corresponding to the newly formed ^1CT state (Figure 6.2e). The increased lifetime in presence of TMB and other electron rich aromatic solvents, suggests the stabilization of the complex in electron donating solvents (Figure 6.2e) which reiterated the CT nature of the red-shifted emission.

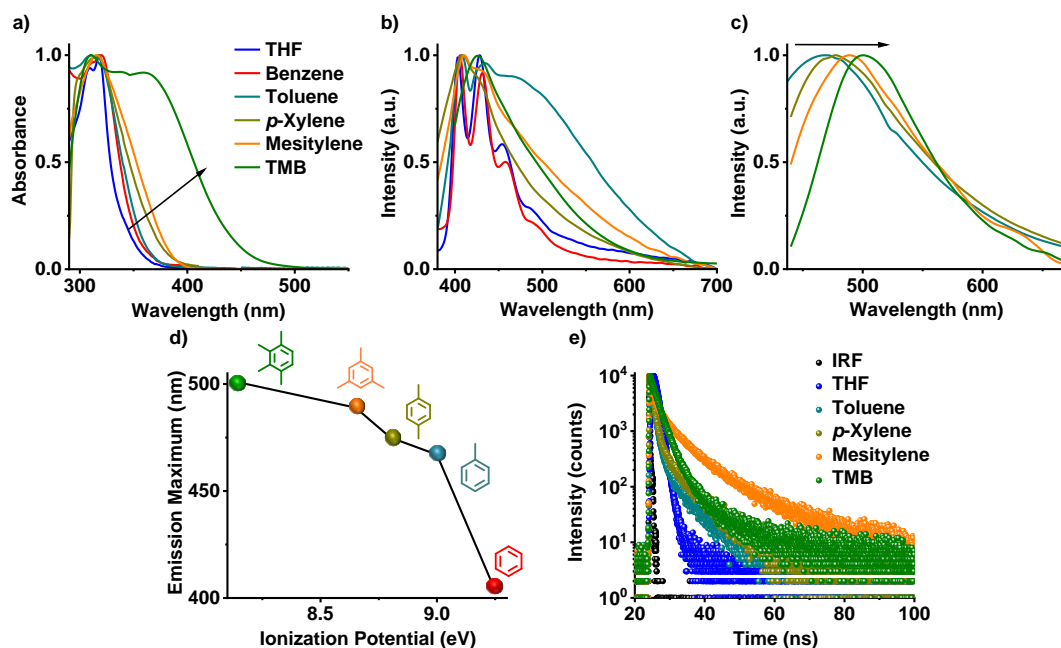


Figure 6.3. Solution state CT fluorescence of **PmDI** in electron rich aromatic solvents: a) Normalized absorption spectra of **PmDI** in various solvents, which shows the presence of ground state CT band in electron rich aromatic donors. b) Normalized steady-state emission spectra showing ¹LE emission in THF, benzene and broad, red-shifted CT emission band in electron-rich aromatic solvents (λ_{exc.} = 340 nm). c) Normalized emission spectra showing CT emission in electron-rich aromatic solvents upon selective excitation at the CT band (λ_{exc.} = 420 nm). d) Plot of emission maximum versus the ionization potential of various aromatic solvents under study, which shows that emission maximum becomes red-shifted upon decreasing the ionization potential of the solvent. e) Fluorescence lifetime decay profiles of **PmDI** in various solvents: ¹LE emission in THF (λ_{exc.} = 340 nm, λ_{collected} = 420 nm), ¹CT emission in toluene, p-xylene, mesitylene (λ_{exc.} = 404 nm, λ_{collected} = 500 nm) and TMB (λ_{exc.} = 442 nm, λ_{collected} = 500 nm), IRF is the instrument response function (τ_{avg.} = 1.82 ns, 2.62 ns and 6.42 ns for toluene, p-xylene and mesitylene, respectively).

6.4. Spectroscopic Studies of A+D₁ and A+D₂ Co-crystals: Formation of ³CT States:

Inspired by the emissive singlet CT state formed between the electron-rich aromatic solvents and **PmDI**, we made an attempt to realize phosphorescence from ³CT state, by donor-acceptor co-crystallization approach while modulating the donor characteristics, and thereby the intermolecular interactions. We have chosen the positional isomers based

on electron-rich aromatic donor TMB with heavy atom substitution, i.e., 1,4- diiodo-2,3,5,6-tetramethylbenzene (**D**₁) and 1,2-diiiodo-3,4,5,6- tetramethylbenzene (**D**₂), to facilitate ISC and hence to stabilize the ³CT state (Figure 6.2). The preliminary studies of **D**₂ with **PmDI** in solution state under cryogenic conditions exhibited a highly red-shifted band in the excitation spectra compared to the bare acceptor (**A**), suggesting the formation of CT complex even in solution under cryogenic conditions (Figure 6.4a). Emission spectrum of **A+D**₂ gets red-shifted by 44 nm ($\lambda_{\text{max.}} = 544$ nm) compared to **A** upon direct excitation at the CT band ($\lambda_{\text{exc.}} = 430$ nm) pointing towards the CT nature of the phosphorescence emission (Figure 6.4b). Unlike **A**, the sharp decay component in the lifetime decay plot of **A+D**₂ implies the formation of another state different from that of ³LE state, which could be the ³CT state (Figure 6.4c). However, we have successfully extracted the newly formed state upon selectively exciting at the CT band, which clearly shows a short lifetime component compared to the ³LE emission, and validated our hypothesis of ³CT state formation (Figure 6.4d). Therefore, 1:1 co-crystals of donor: acceptor (**A+D**₁ and **A+D**₂); where donor used is **D**₁ or **D**₂, and acceptor **PmDI** were grown, that resulted in beautiful greenish-yellow crystals (Figure 6.2). Subsequent photophysical studies of the co-crystals exhibited an evident, red-shifted band in the excitation spectra monitored at 560 nm, incongruous to individual donor and acceptor spectral characteristics (Figure 6.5a). The steady-state emission spectra when excited at 340 nm, showed an intense greenish-yellow emission with maxima centred at 520 nm and 528 nm for **A+D**₁ and **A+D**₂, respectively, whereas respective individual donors and acceptors were weakly emissive (Figure 6.5b). Notably, the gated emission spectra (delay time = 50 μ s) of the co-crystals and emission lifetimes ($\lambda_{\text{collected}} = 560$ nm) of 22.02 μ s and 12.24 μ s for **A+D**₁ and **A+D**₂, respectively, collected under 340 nm excitation, pointed towards the delayed nature of the emission that emanates from them (Figures 6.5c,d). Intensified emission and pro-longed lifetime in vacuum compared to ambient conditions confirmed the role played by triplet state in the emission of these co-crystals (Figure 6.6). The nature of the delayed emission was further validated by temperature dependent studies (Figure 6.7). The increased emission intensity and lifetime upon decreasing the temperature confirms the phosphorescent nature of the emission (Figure 6.7). In order to get further insights into the nature of the emission, we investigated photophysical characteristics of the individual components (Figure 6.8). Individual donors **D**₁ and **D**₂ in the crystal state were weakly emissive while the acceptor **PmDI** in

PMMA matrix at 20 K and in THF at 77 K under cryogenic conditions showed a maximum around 500 nm, corresponding to the phosphorescence emission from LE triplet state of (^3LE) of **PmDI** (Figures 6.8a,b). Remarkably, the delayed emission of the co-crystals is further red-shifted (**A+D₁** with λ_{maximum} at 520 nm and **A+D₂** with λ_{maximum} at 528 nm) and broadened, which ruled out the possibility of the co-crystal emission to be originating from the acceptor ^3LE emission and steered us to further investigate the role of CT states on the long-lived emission (Figure 6.8b). The key role played by CT process was investigated by selectively exciting at the CT band of the co-crystals at 430 nm (Figures 6.5d,6.8b). Similar emission spectral profiles and lifetime decay profiles observed upon selective excitation with that of the LE excitation at 340 nm, clearly substantiated the origin of long-lived emission to be the CT states formed by the donor-acceptor interactions (Figures 6.5d,6.8b,d). In addition, the closer examination of excitation spectra showed a significant contribution from the CT band (shaded portion) which is much more red-shifted than the individual LE states of both D and A (Figure 6.5a). Further, the temperature dependent studies carried out by the selective excitation at the CT band also displayed an increase in the emission intensity and lifetime at lower temperatures pointing towards phosphorescent nature of the CT emission (Figure 6.9). Upon amalgamating both the observations, it can be inferred that the phosphorescence emission of these co-crystals indeed originates from the ^3CT state of the donor-acceptor complex, and to the best of our knowledge this is the first report on ^3CT phosphorescence from organic co-crystals at room-temperature. The time-resolved excitation and emission (both excitation at LE and selective excitation at CT band) experiments did not show any changes in the spectral maxima at various time intervals and wholly matched with the delayed emission spectra while suggesting the exclusive contribution of the ^3CT state in the phosphorescence emission (Figure 6.10). It is noteworthy to mention that the proposed CT co-crystal approach is very efficient to exclusively realize ^3CT emission in clearing out the contributions from ^3LE and ^1LE states. Over and above to this, CT co-crystals exhibit exceptionally high phosphorescence quantum yields compared to that of individual components and were measured to be 46 % and 43 % in air, and 71 % and 65 % under vacuum, for **A+D₁** and **A+D₂**, respectively.

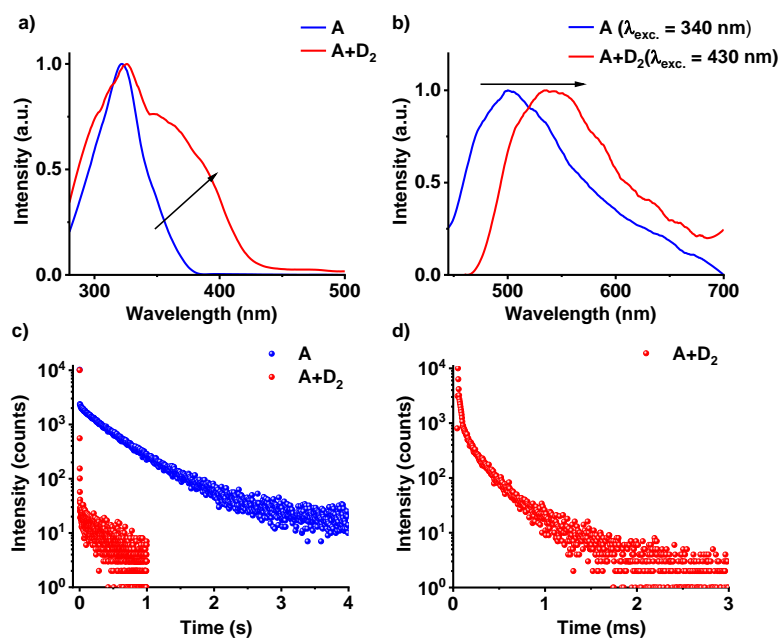


Figure 6.4. Comparison of the spectroscopic studies of $A+D_2$ complex and A alone at 77 K in THF glassy matrix: a) Excitation spectra ($\lambda_{\text{monitored}} = 560 \text{ nm}$), b) delayed emission spectra (delay time = 0.5 ms). Corresponding lifetime decay profiles when excited at c) $\lambda_{\text{exc.}} = 340 \text{ nm}$, ($\tau_{\text{avg.}} = 0.48 \text{ s}$ and for A alone and $\tau_{\text{avg.}} = 0.33 \text{ s}$ (excluding fast component) for $A+D_2$), and d) $\lambda_{\text{exc.}} = 430 \text{ nm}$ ($\tau_{\text{avg.}} = 0.16 \text{ ms}$). In both cases the emission was collected at 560 nm. (Concentration of each component is 0.1 mM).

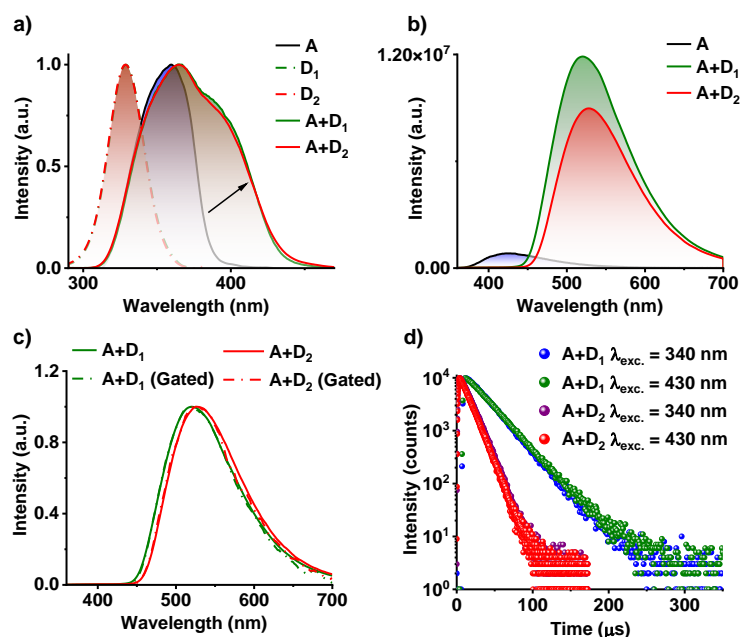


Figure 6.5. ^3CT Phosphorescence studies of $\text{A}+\text{D}_1$ and $\text{A}+\text{D}_2$ co-crystals: a) Normalized excitation spectra of individual donors (D_1 and D_2 , $\lambda_{\text{monitored}} = 420 \text{ nm}$), acceptor (A , $\lambda_{\text{monitored}} = 560 \text{ nm}$) and donor-acceptor co-crystal ($\text{A}+\text{D}_1$ and $\text{A}+\text{D}_2$, $\lambda_{\text{monitored}} = 560 \text{ nm}$), which shows the red-shifted band for donor-acceptor co-crystal compared to individual components suggesting the formation of CT complex. b) Steady-state emission spectra of the acceptor (A) and donor-acceptor co-crystal ($\text{A}+\text{D}_1$ and $\text{A}+\text{D}_2$), which shows the weakly emissive nature of bare acceptor and highly emissive nature of donor-acceptor pair ($\lambda_{\text{exc.}} = 340 \text{ nm}$). c) Normalized steady-state (solid line) and delayed (dotted line, delay time = $50 \mu\text{s}$) emission spectra of $\text{A}+\text{D}_1$ (green) and $\text{A}+\text{D}_2$ (red) co-crystal ($\lambda_{\text{exc.}} = 340 \text{ nm}$, $\lambda_{\text{monitored}} = 560 \text{ nm}$). d) Lifetime decay profile for $\text{A}+\text{D}_1$ and $\text{A}+\text{D}_2$ co-crystal upon excitation at 340 nm and selective excitation at CT band ($\lambda_{\text{exc.}} = 430 \text{ nm}$) ($\lambda_{\text{collected}} = 560 \text{ nm}$).

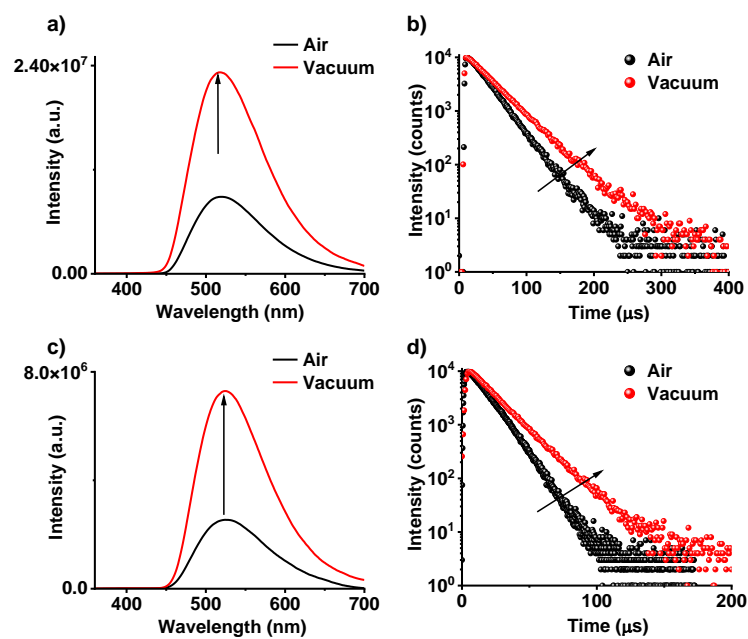


Figure 6.6. Spectroscopic studies of $A+D_1$ and $A+D_2$ co-crystals under air and vacuum: Steady-state emission spectra ($\lambda_{exc.} = 340$ nm) of a) $A+D_1$ and c) $A+D_2$ and corresponding lifetime decay profiles ($\lambda_{exc.} = 340$ nm, $\lambda_{collected} = 560$ nm) of b) $A+D_1$ ($\tau = 22.02$ μ s in air and 34.14 μ s in vacuum) and d) $A+D_2$ ($\tau = 12.24$ μ s in air and 17.39 μ s in vacuum).

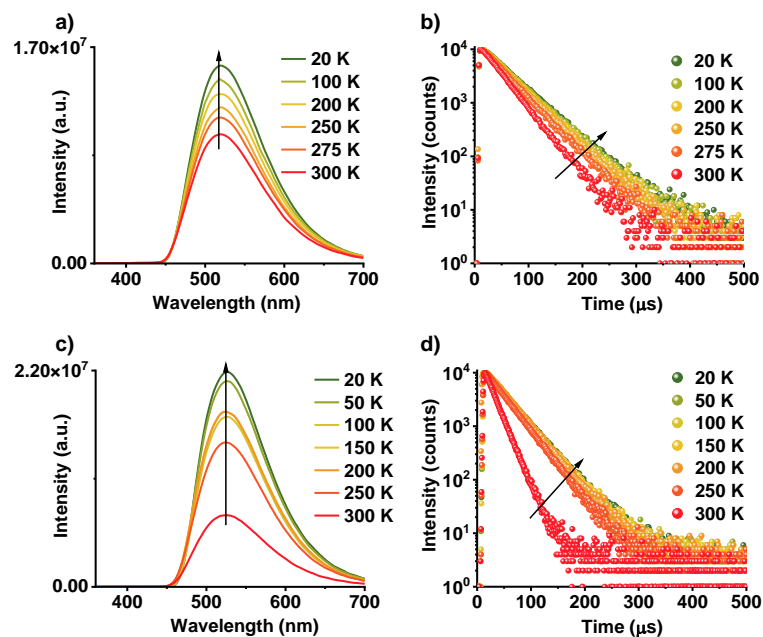


Figure 6.7. Temperature dependent studies of $A+D_1$ and $A+D_2$ co-crystals: Steady-state emission spectra ($\lambda_{exc.} = 340$ nm) of a) $A+D_1$ and c) $A+D_2$. Corresponding lifetime decay profiles ($\lambda_{exc.} = 340$ nm, $\lambda_{collected} = 560$ nm) of b) $A+D_1$ ($\tau = 48.47$ μ s at 20 K and 24.12 μ s at 300 K), and d) $A+D_2$ ($\tau = 35.83$ μ s at 20 K and 17.39 μ s at 300 K).

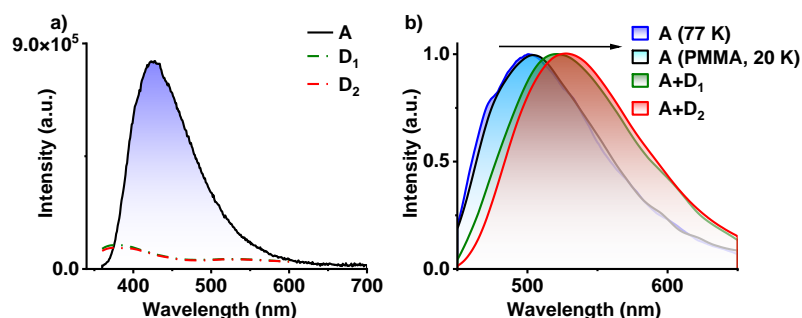


Figure 6.8. a) Steady-state emission spectra of individual donors (D_1 and D_2), acceptor (A) shows weakly emissive nature of individual donors and acceptor ($\lambda_{exc.} = 340$ nm). b) Comparison of 3LE phosphorescence of A alone and 3CT phosphorescence $A+D_1$ and $A+D_2$ co-crystals: delayed emission spectra of A at cryogenic conditions ($[c] = 0.05$ mM in THF), in PMMA matrix (1 wt.% of A doped in PMMA matrix) shows 3LE phosphorescence and $A+D_1$ and $A+D_2$ at ambient conditions show 3CT phosphorescence (delay time = 1 ms for A and 50 ms for $A+D_1$ and $A+D_2$, $\lambda_{exc.} = 340$ nm for A and 430 nm $A+D_1$ and $A+D_2$).

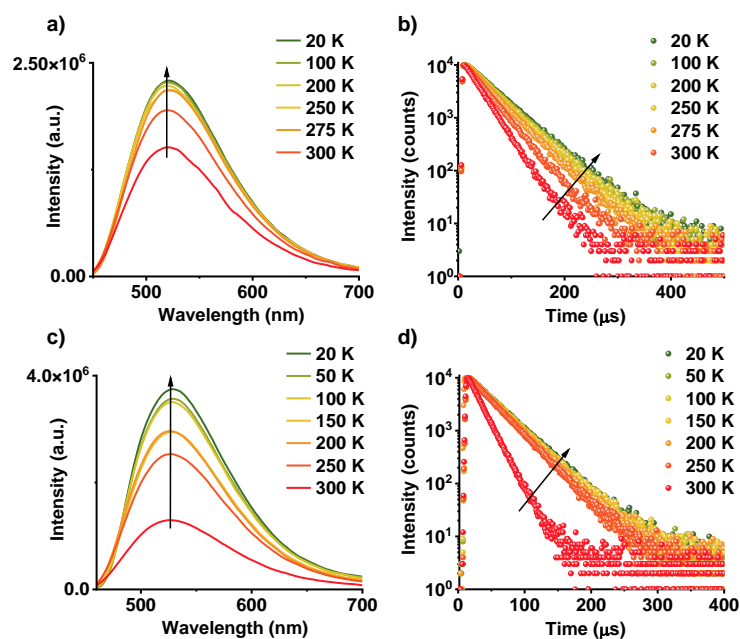


Figure 6.9. Temperature dependent studies of $A+D_1$ and $A+D_2$ co-crystals by the selective excitation at the CT absorption: Steady-state emission spectra ($\lambda_{exc.} = 430$ nm) of a) $A+D_1$ and c) $A+D_2$. Lifetime decay profiles ($\lambda_{exc.} = 430$ nm, $\lambda_{collected} = 560$ nm) of b) $A+D_1$ ($\tau = 49.39$ μ s at 20 K and 35.67 μ s at 300 K) and d) $A+D_2$ ($\tau = 35.38$ μ s at 20 K and 17.33 μ s at 300 K).

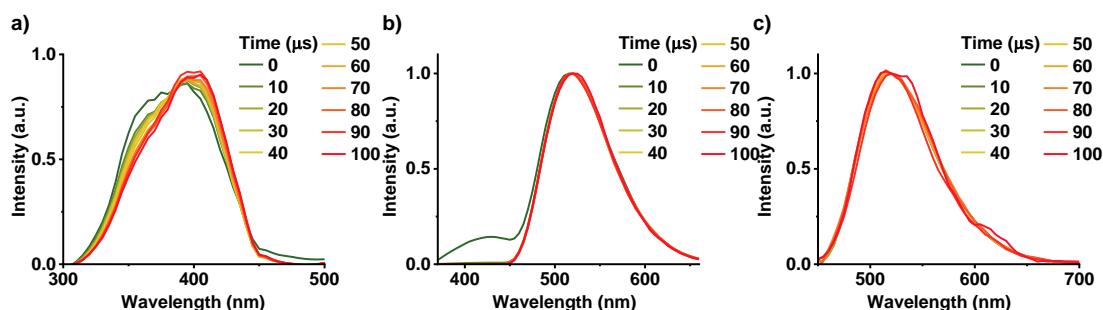


Figure 6.10. Time-resolved a) excitation spectra, ($\lambda_{monitored} = 560$ nm), b) emission spectra upon exciting at $\lambda_{exc.} = 340$ nm and c) upon selective excitation at the CT band ($\lambda_{exc.} = 430$ nm) of $A+D_1$ co-crystal.

6.5. Single-crystal X-ray Crystallography Analysis and Theoretical Calculations:

Further, we have attempted to characterize the molecular arrangement of donor and acceptor in the CT co-crystal by single-crystal X-ray diffraction (XRD) analysis (Figure 6.11a). We have observed that the donor and acceptor are arranged in a slipped stacked manner where the donor is partially stacked on top of the acceptor (Figure 6.11a). For example, in the case of **A+D₂**, a weak π - π interaction (4.281 Å) is present between donor and acceptor (Figures 6.11a). Interestingly, the two-iodine atoms of the donor (**D₂**) face the π -surface of **PmDI** with a distance of 3.849 Å suggesting the presence of strong halogen- π interaction (Figures 6.11a). Thus, the co-facial organization of the donor and acceptor components mediated by halogen- π and weak π - π interactions could be responsible for the intermolecular CT interaction observed in these co-crystals (Figures 6.11a). The interdigitated nature of **PmDI** alkyl chains of adjacent D-A stacks suggests that hydrophobic interactions between alkyl chains also play a crucial role in the non-covalent organization of the co-crystals (Figure 6.11a). Interestingly, we observed another type of halogen bonding interaction between iodine and carbonyl with a distance of 3.161 Å within the same layer of donor-acceptor pair (Figure 6.11b). We envisage that, these halogen bonding interactions in the co-crystal increase the SOC significantly and along with the CT interaction, facilitate the efficient harvesting of triplet excitons.

The presence of through-space CT interaction between **D₁** (donor) and **PmDI** (acceptor) via their co-facial organization is further validated from the computed natural transition orbitals (NTOs) of the first excited singlet state (**S₁**) where the hole is located on the **D₁** and electron on the π -surface of the acceptor (Figures 6.11c). The significant oscillator strength ($f = 0.0023$) with spatially separated highest occupied molecular orbitals (HOMO) and lowest unoccupied molecular orbitals (LUMO) leads to strong CT transition in the ground state (Figures 6.11b). Interestingly, HOMO and LUMO of first excited triplet state (**T₁**) were also located over donor and acceptor, respectively similar to **S₁** state suggesting the CT nature of **T₁** state of **A+D₁**. (Figures 6.11c). The calculated spin-orbit coupling matrix element (SOCME) between **S₁** and **T₁** is 34.212 cm⁻¹, which is significant enough to populate the triplet excitons to the ³CT state and thus helped to realize phosphorescence emission from a more thermodynamically stable state. Although the experimental energy gap between ³LE from ³CT is not very high, the presence of

heavy atoms decreases the vibronic coupling, and thus the repopulation of ^3LE from the ^3CT state is not favourable. Further the significant energy difference ($\Delta E_{\text{ST}} = \sim 110 \text{ meV}$) between ^1CT ($\lambda_{\text{maximum}} = 500 \text{ nm}$) and ^3CT ($\lambda_{\text{maximum}} = 528 \text{ nm}$) prevents the reverse intersystem crossing (RISC) to harvest triplets through the TADF pathway, thus leading to the exclusive ^3CT pathway for the triplet harvesting.

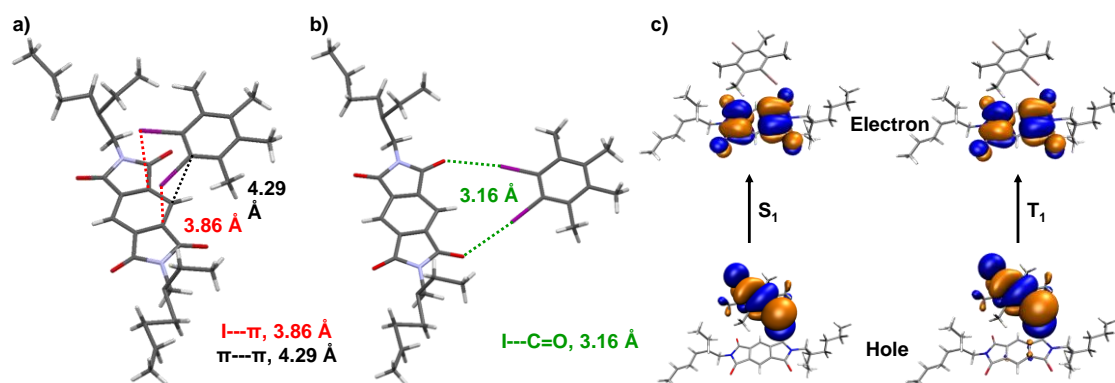


Figure 6.11. Single-crystal X-ray diffraction data of $\mathbf{A+D}_2$ co-crystal: Donor-acceptor arrangement of $\mathbf{A+D}_2$ pair, driven by various halogen bonding and weak $\pi\cdots\pi$ interactions, such as a) $\text{I}\cdots\pi$ (marked with red lines), $\pi\cdots\pi$ (marked with black lines) in a stack and b) $\text{I}\cdots\text{C}=\text{O}$ (marked with green lines) in the same plane. c) Theoretical calculations of $\mathbf{A+D}_1$: Natural transition orbitals (NTOs) of $\mathbf{A+D}_1$ pair for first excited singlet (S_1) and triplet state (T_1), calculated using TD-CAM-B3LYP level in conjunction with 6-31+g(d) basis set for C, N, O, H and LANL2DZ basis set showing CT character.

6.6. Spectroscopic Studies of $\mathbf{A+D}_3$ Co-crystals:

We have further realized that the CT complexation can be indeed applied to a wide subset of electron-rich donors with heavy-atom incorporated into them to harvest the ^3CT phosphorescence. For example, CT co-crystals of **PmDI** with another electron rich donor, with only two methyl groups and heavy atoms, 1,2-diiodo-4,5-dimethylbenzene (**D₃**), also exhibited similar results although we could not solve the crystal structure (Figure 6.12). It is worth noticing that, due to the reduced electron-rich character of **D₃**, compared to **D₁** or **D₂** the extent of CT strength was diminished, which is reflected as a blue-shift in the excitation spectrum and emission spectrum of $\mathbf{A+D}_3$ compared to that of the $\mathbf{A+D}_2$ cocrystal (Figures 6.12a,b). The Comparison between respective maxima of ^3LE phosphorescence of bare acceptor and ^3CT phosphorescence of $\mathbf{A+D}_3$ and $\mathbf{A+D}_2$ pair suggested that we can indeed modulate the ^3CT phosphorescence emission by changing

the donor strength (Figure 6.12b), which would be worth exploring with a different series of electron rich donor molecules.

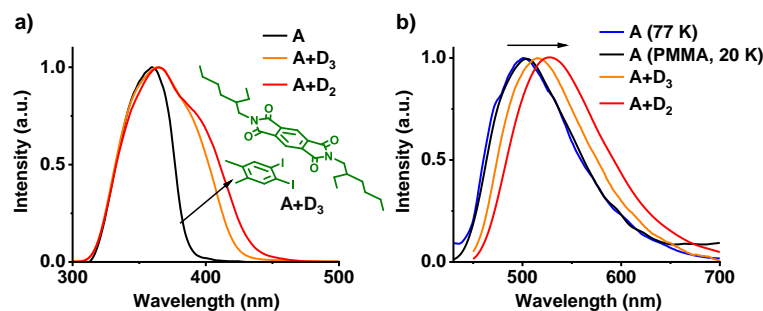


Figure 6.12. 3CT phosphorescence studies of $A+D_3$ co-crystals and comparison with the 3LE phosphorescence of A alone and 3CT phosphorescence $A+D_2$ co-crystals: a) Excitation spectra of acceptor (A) alone and donor-acceptor co-crystal $A+D_2$ (red line), $A+D_3$ (orange line), red-shifted band of donor-acceptor co-crystal compared to the bare acceptor (A) suggests the formation of CT state ($\lambda_{monitored} = 560$ nm). d) Delayed emission spectra of acceptor (A) alone at cryogenic conditions ($[c] = 0.05$ mM in THF) and in PMMA matrix (1 wt.% of A doped in PMMA matrix) show 3LE phosphorescence, and $A+D_2$ and $A+D_3$ in air show 3CT phosphorescence (delay time = 1 ms for A and 50 μ s for $A+D_2$ and $A+D_3$ co-crystals).

6.7. Spectroscopic Studies of $A+D_4$ and $A+D_5$ Co-crystals: Formation of 3LE States:

Finally, in order to confirm the role of the electron rich aromatic donors in stabilizing the 3CT state, we have utilized similar heavy atom substituted aromatic donor without any methyl substitution to decrease the donor strength (Inset of Figure 6.13a). Hence, we have grown 1:1 co-crystal of **PmDI** with 1-bromo-4-iodobenzene (**D4**) as the donor. In contrast to the previous observations, the excitation spectra of $A+D_4$ co-crystal monitored at 560 nm did not show any red-shifted band and was similar to the excitation spectra of acceptor **PmDI**, pointing towards the absence of a CT complexation. (Figure 6.13a). The resulting bright green crystals exhibited intense emission upon exciting at 340 nm with a maximum at 500 nm, unlike weakly emissive individual donor and acceptor (Figure 6.13b). The emission lifetime was measured out to be 0.38 ms ($\lambda_{exc.} = 340$ nm, $\lambda_{collected} = 560$ nm), and the gated emission spectra (delay time = 0.1 ms) indicated the presence of delayed component in the emission which was proven out to be

phosphorescence by the temperature dependent studies (Figures 6.13c-f). Surprisingly, the gated emission spectra of the co-crystals entirely replicated the phosphorescence spectrum of **PmDI** in PMMA, collected at 20 K under 340 nm excitation, suggesting the source of origin of emission of **A+D₄** to be the LE triplet state (³LE) of the **PmDI** (Figure 6.13d). Impressively, the phosphorescence quantum yield of **A+D₄** is 52 % in air and 70 % under vacuum, indicating a significant enhancement in the phosphorescence efficiency compared to that of **PmDI** alone which is weakly emissive in crystalline state. Single crystal XRD analysis helped us to explain the reason behind the excellent ³LE phosphorescence efficiency of the **A+D₄** co-crystal (Figure 6.14). The co-crystals showed layers of self-sorted donor and acceptor molecules, which are alternatively spaced in the lateral direction, directed by the halogen-carbonyl interactions (iodo-carbonyl and bromo-carbonyl) between the molecules within a layer (Figure 6.14a). In addition, four interlayer halogen-carbonyl interactions per donor molecules and, two each with the above and below layers, (together constituting a total of six halogen carbonyl interactions) were also observed (Figures 6.14b). We envisage that the presence of multiple halogen bonding interactions resulted in the significant enhancement of the SOC value via external heavy atom effect to achieve very high phosphorescence efficiency from ³LE state of **PmDI**. Further, in the absence of significant CT interactions, **A+D₄** molecules adapt a two-dimensional lateral organization, rather than an alternatively stacked arrangement observed in case of **A+D₂**. Further, we have used 1,4-dibromobenzene derivative (**D₅**) as a donor to deeply investigate the role of external heavy atom effect in triggering the ³LE phosphorescence. As expected, the emission spectra of **A+D₅** co-crystal was exactly similar to the ³LE phosphorescence of acceptor suggesting the origin of the phosphorescence emission to be ³LE in nature (Figure 6.15a). Although we could not obtain the crystals for **A+D₅**, powder XRD studies suggest that the packing of the donor and acceptor is similar in both **A+D₅** and **A+D₄** (Figure 6.15b). Intriguingly, **A+D₅** showed a quantum yield of 11 % in air, which is lesser than that of **A+D₄** (52%), signifying the pivotal role of external heavy atom in inducing efficient phosphorescence emission (³LE). We infer that the presence of heavier iodine in **A+D₄** in the place of bromine increased the SOC, which resulted in efficacious emission with higher quantum yield. Furthermore, the theoretical calculations of **A+D₅** also supported the observed spectroscopic properties which showed that CT interactions are absent between the donor and acceptor molecules (Figures 6.15c). The computed NTOs showed

that both the hole and electron are located on the π -surface of the acceptor for first excited singlet (S_1) and triplet (T_1) states, suggesting the LE transition (Figure 6.15c).

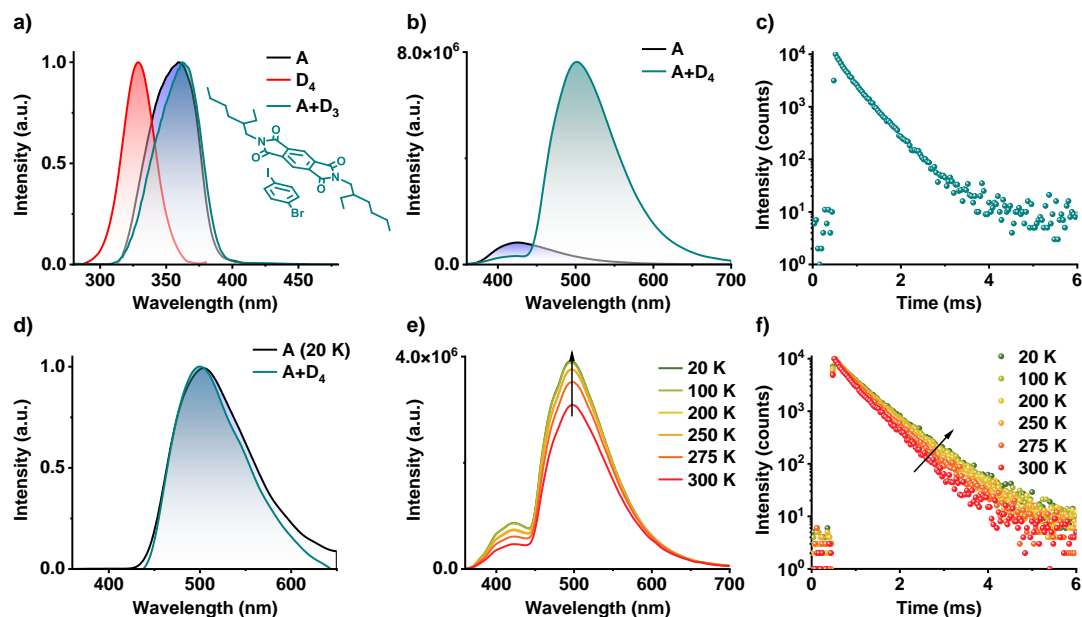


Figure 6.13. 3LE Phosphorescence studies of $A+D_4$ co-crystal: a) Excitation spectra of individual donor (D_4 , $\lambda_{monitored} = 420$ nm), acceptor (A , $\lambda_{monitored} = 560$ nm) and donor-acceptor co-crystal ($A+D_4$, $\lambda_{monitored} = 560$ nm), which suggest absence of CT band (Inset shows molecular structure for $A+D_4$ pair). b) Steady-state emission spectra of bare acceptor (A) and donor-acceptor pair ($A+D_4$) shows weakly emissive nature of acceptor and highly emissive nature of donor-acceptor co-crystal ($\lambda_{exc.} = 340$ nm). c) Lifetime decay profiles ($\lambda_{exc.} = 340$ nm, $\lambda_{collected} = 560$ nm) of $A+D_4$. d) Normalized delayed emission spectra of acceptor doped in PMMA matrix at 20 K (1 wt.% with respect to PMMA) and donor-acceptor pair at room temperature show the same emission maximum, hinting towards the 3LE emission ($\lambda_{exc.} = 340$ nm). e) Steady-state emission spectra ($\lambda_{exc.} = 340$ nm) and f) corresponding lifetime decay profile ($\lambda_{exc.} = 340$ nm, $\lambda_{collected} = 560$ nm, $\tau_{avg} = 0.61$ ms at 20 K and 0.49 at 300 K) at different temperatures.

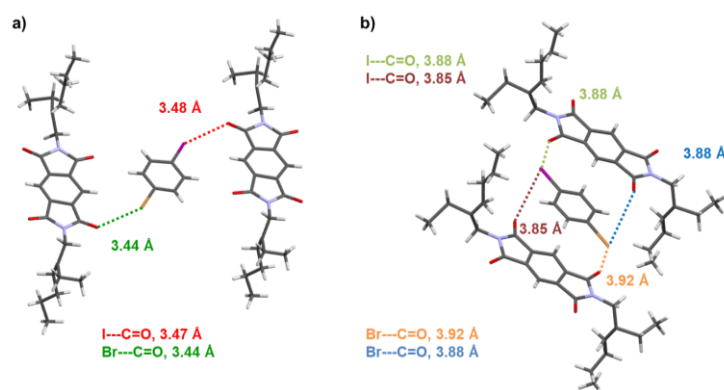


Figure 6.14. Single-crystal X-ray diffraction data of $A+D_4$ co-crystal: Donor-acceptor arrangement of $A+D_4$ pair, driven by halogen carbonyl interactions, a) $I\cdots C=O$ (marked with red lines) and $Br\cdots C=O$ (marked with green lines) in the same plane, b) $I\cdots C=O$ (marked with light-green and brown lines) and $Br\cdots C=O$ (marked with blue and orange lines) in the parallel plane.

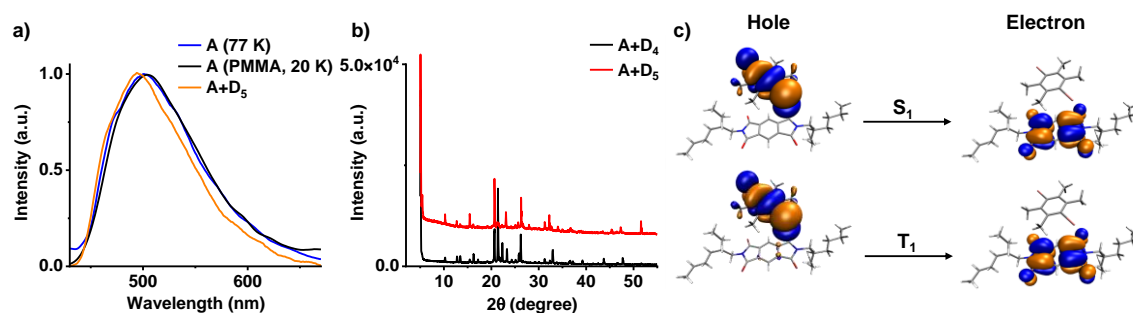


Figure 6.15. a) Normalized delayed emission spectra of acceptor (A) alone at 77 K in THF, doped in PMMA matrix at 20 K (1 wt.% with respect to PMMA) and $A+D_5$ at room temperature ($\lambda_{exc.} = 340$ nm, delay time = 1 ms). b) Powder XRD pattern of $A+D_4$ and $A+D_5$ co-crystals. c) Natural Transition Orbitals (NTOs) for $A+D_5$. Singlet and triplet states were calculated at TD-B3LYP level with 6-31+g(d) basis set for C, H, O and N and LANL2DZ basis set for I with effective core potential.

6.8. Conclusions:

In summary, we have reported room-temperature CT phosphorescence from organic donor-acceptor co-crystals for the first time using pyromellitic diimide as the acceptor and heavy atom-substituted aromatic molecules as donors. The detailed spectroscopic studies and further analyses suggested that the donor-acceptor non-covalent complexation is an efficient modular approach to manipulate the electronically excited states of molecules.

Firstly, we have shown that **PmDI** (acceptor) can form ground-state CT complex with different aromatic solvents which has led to the CT fluorescence emission from the newly formed ^1CT states in solution. The progressive traversing from non-aromatic solvents to highly electron-donating aromatic solvents has resulted in the shift of emission from ^1LE state to ^1CT states with maxima at 440 nm and 500 nm, respectively. Inspired from the potential of **PmDI** to form CT complexes and its effortless accessibility to triplet state, we further extrapolated the CT complexation of **PmDI** with heavy atom substituted electron-rich aromatic donors to extract ^3CT phosphorescence from the donor-acceptor complex under ambient conditions. Strikingly, the 1:1 co-crystal of **PmDI** with donors 1,4-diiodo-2,3,5,6-tetramethylbenzene (**D**₁) and 1,2-diiodo 3,4,5,6-tetramethylbenzene (**D**₂) exhibited an efficient greenish-yellow room-temperature phosphorescence emission from the CT states with appreciable quantum yields and lifetime. The exceptionally efficient phosphorescence emission from the CT co-crystal can be justified by the minimal vibrational dissipation of the triplet state and the enhanced rate of ISC facilitated by various intermolecular interactions between the donor and acceptor molecules in the long-range ordered alternate assembly. Although, very recently, a few examples on through-space CT based TADF have been reported,¹⁹ to the best of our knowledge, we have presented the first report on ^3CT phosphorescence realized under ambient conditions. Later, we have switched the ^3CT ($\lambda_{\text{maximum}} = 528$ nm) emission to ^3LE ($\lambda_{\text{maximum}} = 500$ nm) emission, similar to neat **PmDI** by utilizing heavy-atom substituted donors, 1-bromo-4-iodobenzene (**D**₄) and 1,4-dibromobenzene (**D**₅), with reduced donor strength. Remarkably, we have also realized that the co-crystallization strategy that not only modulate the origin of excited state emission, but also significantly amplify the ^3LE emission compared to neat **PmDI** via external heavy-atom effect.

In a concise, we can conclude that the supramolecular strategy based on through-space CT interactions, delineated in the current study can be cleverly used as tool to modulate between the various excited state manifolds of arylene diimide acceptors by the judicious choice of donors. We envisage that the current study also opens up an innovative way for generating ^1CT and ^3CT states by a supramolecular strategy for the molecular design of efficient TADF emitters unlike the conventional covalently linked systems. We believe that the present study has a momentous scope to harness triplet

excitons from purely organic phosphors with remarkable efficiency, tunable emission and less synthetic efforts.

6.9. Experimental Section:

6.9.1. General Methods:

NMR Measurements: ^1H and ^{13}C NMR spectra were recorded on a BRUKER AVANCE-400 fourier transformation spectrometer with 400 and 100 MHz respectively. The spectra were calibrated with respect to the residual solvent peaks. The chemical shifts are reported in parts per million (ppm) with respect to TMS. Short notations used are, s for singlet, d for doublet, t for triplet, q for quartet and m for multiplet.

Optical Measurements: Electronic absorption spectra were recorded on Jasco V-750 UV-Visible spectrophotometer and emission spectra were recorded on FLS1000 spectrometer, Edinburgh Instruments. Solution state UV-Vis and emission spectra were recorded in 10 mm path length cuvette. Fluorescence spectra of the films were recorded in front-face geometry to avoid self-absorption.

Lifetime Measurements and Quantum yield: Fluorescence lifetimes were performed on a Horiba Delta Flex time-correlated single-photon-counting (TCSPC) instrument. A 340 nm diode and 373 nm, 442 nm laser diode with a pulse repetition rate of 1 MHz was used as the light source. The instrument response function (IRF) was collected by using a scatterer (Ludox AS40 colloidal silica, Sigma-Aldrich). Phosphorescence lifetime ($\lambda_{\text{exc.}} = 340 \text{ nm}$ and 430 nm), gated emission and time-resolved excitation and emission were measured on FLS1000 spectrometer, Edinburgh Instruments equipped with a micro flash-lamp (μF2) set-up. Quantum yields were measured using an integrating sphere in the same instrument.

High Resolution Mass Spectrometry (HR-MS): HR-MS was carried out using Agilent Technologies 6538 UHD Accurate-Mass Q-TOFLC/MS.

High Performance Liquid Chromatography (HPLC): HPLC was carried out using Agilent 1260 infinity quaternary HPLC system equipped with analytical ZORBAX Eclipse plus C18 column ($4.6 \text{ mm} \times 100 \text{ mm}$, 3.5 micron).

Single Crystal X-ray Crystallography: Suitable single crystal of the **A+D₂** and **A+D₄** compound was mounted on a thin glass fibre with commercially available super glue.

Intensity data were collected Bruker D8 VENTURE diffractometer equipped with a PHOTON detector and graphite-monochromated Mo-K α radiation ($\lambda = 0.71073 \text{ \AA}$, 50 kV, 1mA) at 100 K. APEX III software was used to collect, reduce and integrate the raw data. The direct method was used for solving crystal structure, followed by full-matrix least-squares refinements against F2 (all data HKLF 4 format) using the SHELXL 2014/7^{R1} and difference Fourier synthesis and least-squares refinement revealed the positions of the non-hydrogen atoms. All nonhydrogen atoms were refined anisotropically and remaining hydrogen atoms were placed in geometrically constrained positions and refined with isotropic temperature factors, generally $1.2 \times U_{eq}$ of their parent atoms. Molecular structure drawings were prepared using the program Mercury (version 3.1). We have selected the best crystal; however, few alerts are generated and can't be resolved despite several attempts due to the weak diffraction of crystals.

Computational Details: Ground State (S_0) of donor-acceptor pairs (**A+D₅**) was optimized using density functional theory (DFT). We are not able to optimize other donor-acceptor pairs. Excitation energies were calculated using B3LYP functional with 6-31+g(d) basis set except for Br and I. For which we have used Lanl2dz functional with effective core potential. NTO calculations were done after TDDFT calculations. No solvent corrections were added in this work. The spin orbit coupling effect were considered to be a perturbation of scalar relativistic Kohn-Sham orbitals after SCF and TDDFT calculations (pSOC-TDDFT). The SOC matrix elements were calculated using B3LYP functional with a Slater type all-electron TZP basis set for all atoms as implemented in the ADF package.^[20] While the excited state calculations were performed using B3LYP exchange-correlation functional with the same basis sets as mentioned before.

6.9.2. Protocol for Sample Preparation:

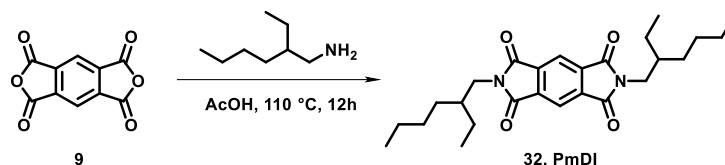
Protocol for co-crystal synthesis: We prepared saturated solutions of both donor and acceptors in chloroform and mixed them in a 1:1 molar ratio. Then acetonitrile was added into it as a bad solvent. The mixture was heated at 70 °C for ten minutes and then kept at room temperature for crystallization.

Protocol for sample preparation: All solution state studies were performed, keeping the final concentration of the samples to 0.05 mM and 0.1 mM from a stock solution of THF (1 mM). For thin films, acceptor molecules (1 mg) were mixed with 100 mg of PMMA.

This mixture was then heated at 50 °C for 10 minutes followed by sonication (5 minutes) to dissolve all the components thoroughly. Then, 0.5 mL of this solution was drop-casted on a clean quartz substrate. Finally, the drop-casted thin films were dried at 60 °C for 30 minutes before performing the photophysical studies. For the phosphorescence studies of the co-crystal, a small amount of the co-crystal was placed in between two quartz plates.

6.10. Synthetic Scheme and Procedures:

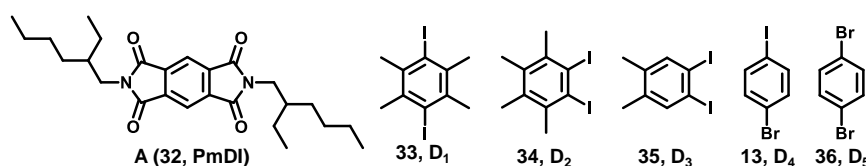
Pyromellitic dianhydride (PMDA) was purchased from Sigma Aldrich; Durene and 2-Ethylhexyl amine were purchased from Alfa-Aesar; 1-Bromo-4-iodobenzene and 1,4-Dibromobenzene were purchased from TCI, Acetic acid was purchased from Spectrochem and used without further purification.



Scheme 6. Synthetic scheme for **PmDI**.

Synthesis of PmDI: Pyromellitic dianhydride (**9**) (0.50 g, 2.4mmol) was taken in a 100 mL round bottom flask and 25 mL acetic acid was added into it and stirred at room temperature for 30 minutes. 2-Ethylhexylamine (0.66 g, 5.1 mmol) was added to the reaction mixture and the reaction mixture was allowed to reflux for 12 hours. Water was added to the reaction mixture to get white precipitate. The precipitate was then filtered and dried under vacuum for 10 hours. Column chromatography was performed using chloroform as an eluent to get the pure product as white solid (0.86 g, 85 % yield). ^1H NMR (CDCl_3 , 400 MHz), δ (ppm) = 8.26 (s, 2H), 3.64 (d, 4H, $J = 7.2$ Hz), 1.85 (t, 2H, $J = 6$ Hz), 1.55-1.26 (m, 16 H), 0.94-0.87 (m, 12 H); ^{13}C NMR (CDCl_3 , 100 MHz), δ (ppm) = 166.6, 137.2, 118.2, 42.6, 38.3, 30.6, 28.5, 23.9, 23.00, 14.0 10.4 HRMS (APCI): m/z calculated for $\text{C}_{26}\text{H}_{36}\text{N}_2\text{O}_4$: 440.2675: observed 440.2760 [M] $^+$.

Experimental Procedures: We have used the following acceptors and donors for the ^3CT and ^3LE phosphorescence studies. The donors D_1 ^[21], D_2 ^[22] and D_3 ^[23] were synthesized according to the literature procedures.



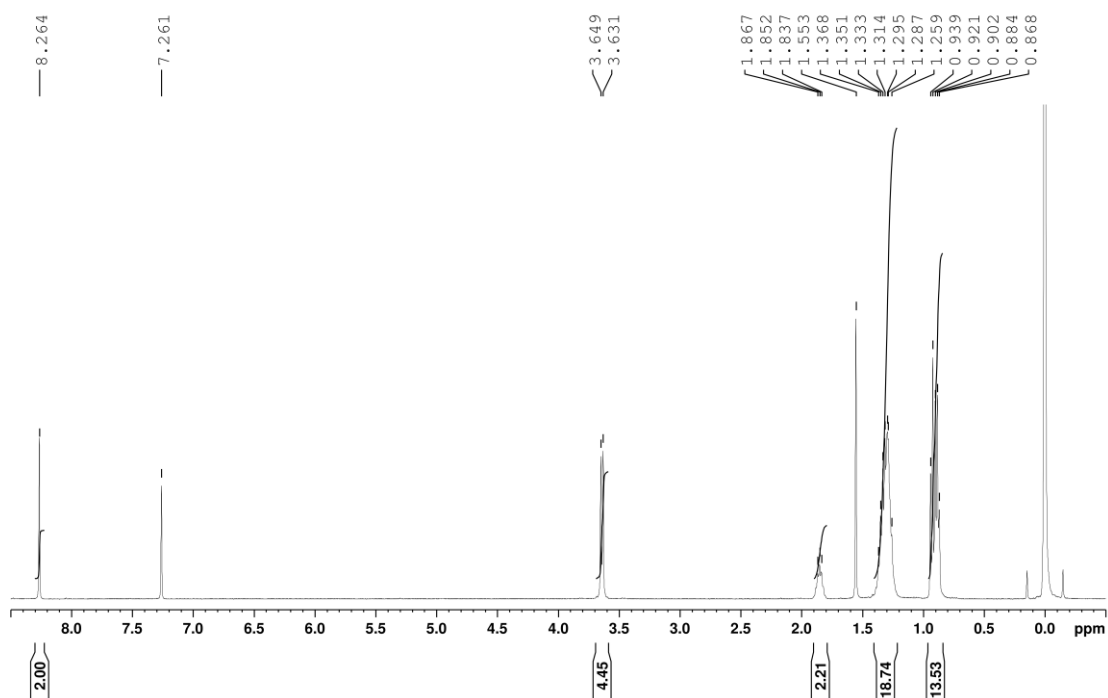


Figure 6.16. ^1H NMR spectrum of *PmDI* in CDCl_3 .

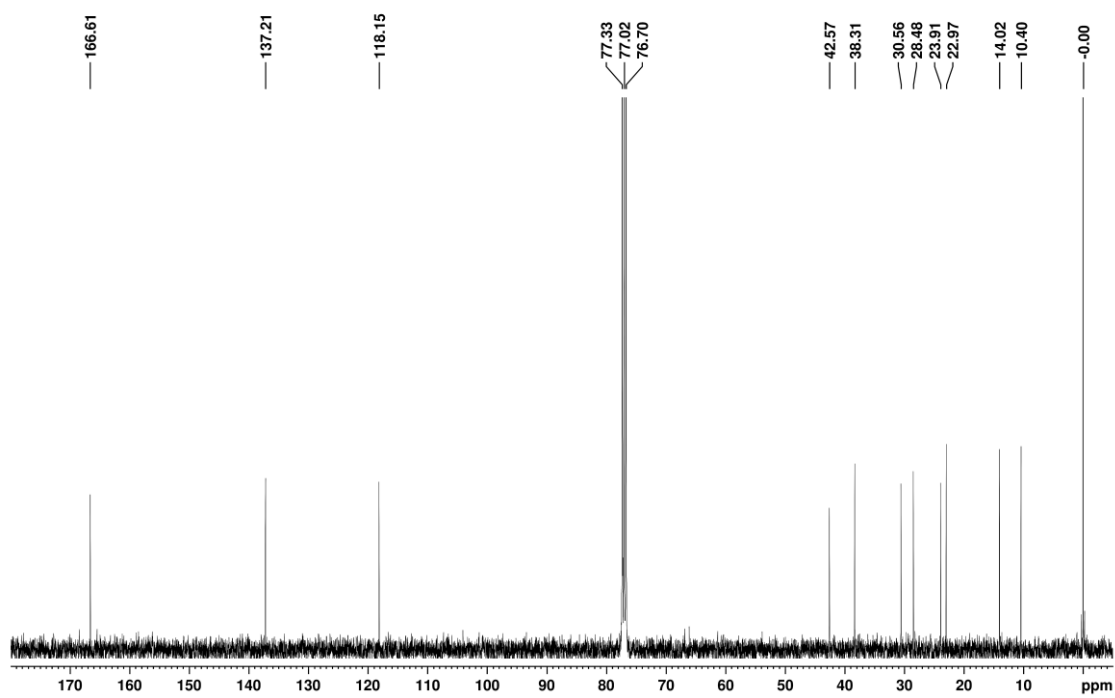


Figure 6.17. ^{13}C NMR spectrum of *PmDI* in CDCl_3 .

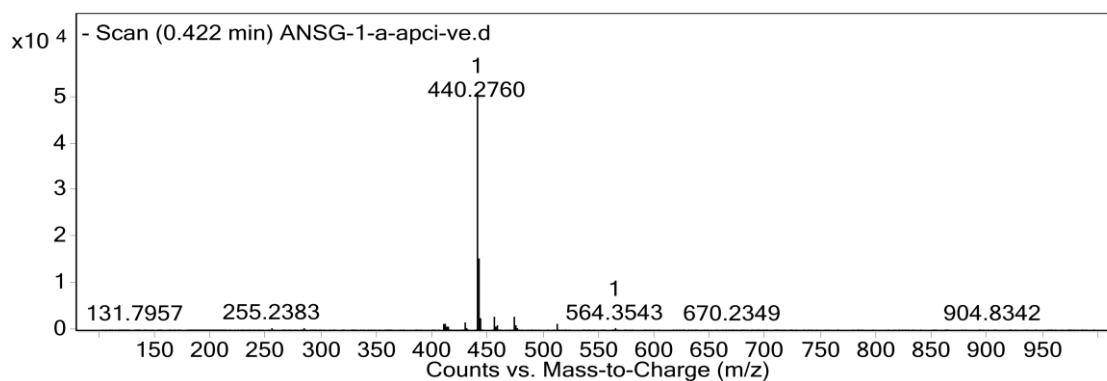


Figure 6.18. APCI-HR-MS spectrum of *PmDI*.

6.11. References:

- [1] a) S. Hirata, *Adv. Opt. Mater.* **2017**, *5*, 1700116; b) M. Y. Wong, E. Zysman-Colman, *Adv. Mat.* **2017**, *29*, 1605444; c) W. Zhao, Z. He, W. Y. Lam, Jacky, Q. Peng, H. Ma, Z. Shuai, G. Bai, J. Hao, B. Z. Tang, *Chem* **2016**, *1*, 592-602; d) S. Xu, R. Chen, C. Zheng, W. Huang, *Adv. Mater.* **2016**, *28*, 9920-9940; e) W. Zhao, Z. He, B. Z. Tang, *Nat. Rev. Mater.* **2020**, *5*, 869-885; f) X. Ma, J. Wang, H. Tian, *Acc. Chem. Res.* **2019**, *52*, 738-748; g) J. Yang, M. Fang, Z. Li, *Acc. Mater. Res.* **2021**, *2*, 644-654.
- [2] a) O. Bolton, K. Lee, J-H. Kim, K.Y. Lin, J. Kim, *Nat. Chem.* **2011**, *3*, 205-210; b) Z. An, C. Zheng, Y. Tao, R. Chen, H. Shi, T. Chen, Z. Wang, H. Li, R. Deng, X. Liu, W. Huang, *Nat. Mater.* **2015**, *14*, 685-690; c) P. Alam, T. S. Cheung, N. L. C. Leung, J. Zhang, J. Guo, L. Du, R. T. K. Kwok, J. W. Y. Lam, Z. Zeng, D. L. Phillips, H. H. Y. Sung, I. D. Williams, B. Z. Tang, *J. Am. Chem. Soc.* **2022**, *144*, 3050-3062; d) Q. Liao, Q. Gao, J. Wang, Y. Gong, Q. Peng, Y. Tian, Y. Fan, H. Guo, D. Ding, Q. Li, Z. Li, *Angew. Chem. Int. Ed.* **2020**, *59*, 9946-9951; e) J. Ren, Y. Wang, Y. Tian, Z. Liu, X. Xiao, J. Yang, M. Fang, Z. Li, *Angew. Chem. Int. Ed.* **2021**, *60*, 12335-12340.
- [3] a) D. Lee, O. Bolton, B. C. Kim, J. H. Youk, S. Takayama, J. Kim, *J. Am. Chem. Soc.* **2013**, *135*, 6325-6329; b) S. Kuila, S. Garain, S. Bandi, S. J. George, *Adv. Funct. Mater.* **2020**, *30*, 2003693; c) L. Gu, W. Ye, X. Liang, A. Lv, H. Ma, M. Singh, W. Jia, Z. Shen, Y. Guo, Y. Gao, H. Chen, D. Wang, Y. Wu, J. Liu, H. Wang, X.-Y. Zheng, Z. An, W. Huang, Y. Zhao, *J. Am. Chem. Soc.* **2021**, *143*, 18527-18535; d) Y. F. Zhang, Y. Su, H. W. Wu, Z. H. Wang, C. Wang, Y. Zheng, X. Zheng, L. Gao, Q. Zhou, Y. Yang, X. H. Chen, C. L. Yang, Y. L. Zhao, Large-Area, Flexible, Transparent, and Long-Lived Polymer-Based Phosphorescence Films. *J. Am. Chem. Soc.* **2021**, *143*, 13675-13685; e) Y. Su, Y.; Y. Zhang, Z. Wang, W. Gao, P. Jia, D. Zhang, C. Yang, Y. Li, Y. Zhao, *Angew.*

Chem. Int. Ed. **2020**, *59*, 9967-9971; f) S. Cai, Z. Sun, H. Wang, X. Yao, H. Ma, W. Jia, S. Wang, Z. Li, H. Shi, Z. An, Y. Ishida, T. Aida, W. Huang, *J. Am. Chem. Soc.* **2021**, *143*, 16256-16263.

[4] a) J. Wang, Z. D. Li, F. Lu, J. Wang, W. Hu, X. M. Cao, X. Ma, H. Tian, *J. Am. Chem. Soc.* **2018**, *140*, 1916-1923; b) Huang, X. Ma, H. Tian, *Angew. Chem. Int. Ed.* **2020**, *59*, 9928-9933; c) X. Yao, J. Wang, D. Jiao, Z. Huang, O. Mhirsi, F. Lossada, L. Chen, B. Haehnle, A. J. C. Kuehne, X. Ma, H. Tian, A. Walther, *Adv. Mater.* **2020**, 2005973; d) Z. Y. Zhang, Y. Chen, Y. Liu, *Angew. Chem. Int. Ed.* **2019**, *58*, 6028-6032; e) H. J. Yu, Q. Zhou, X. Dai, F. F. Shen, Y. M. Zhang, X. Xu, Y. Liu, *J. Am. Chem. Soc.* **2021**, *143*, 13887-13894; f) X. K. Ma, W. Zhang, Z. Liu, H. Zhang, B. Zhang, Y. Liu, *Adv. Mater.* **2021**, *33*, 2007476; g) Z. Li, Y. Han, F. Nie, M. Liu, H. Zhong, F. Wang, *Angew. Chem. Int. Ed.* **2021**, *60*, 8212-8219; (h) Z. Li, Y. Han, F. Wang, *Nat. Commun.* **2019**, *10*, 3735; h) S. Kuila, K. V. Rao, S. Garain, P. K. Samanta, S. Das, S. K. Pati, M. Eswaramoorthy, S. J. George, *Angew. Chem. Int. Ed.* **2018**, *57*, 17115-17119; i) S. Garain, B. C. Garain, M. Eswaramoorthy, S. K. Pati, S. J. George, *Angew. Chem. Int. Ed.* **2021**, *60*, 19720-19724.

[5] a) H. Uoyama, K. Goushi, K. Shizu, H. Nomura, C. Adachi, *Nature* **2012**, *492*, 234-238; b) Q. Zhang, H. Kuwabara, W. j. Potscavage, S. Huang, S.; Y. Hatae, T. Shibata, C. Adachi, *J. Am. Chem. Soc.* **2014**, *136*, 18070-18081.

[6] a) M. Kumar, K. V. Rao, S. J. George, *Phys. Chem. Chem. Phys.* **2014**, *16*, 1300-1313; b) A. Das, S. Ghosh, *Angew. Chem., Int. Ed.* **2014**, *53*, 2038-2054.

[7] a) A. S. Tayi, A. K. Shveyd, A. C.-H. Sue, J. M. Szarko, B. S. Rolczynski, D. Cao, T. J. Kennedy, A. Sarjeant, C. L. Stern, W. F. Paxton, W. Wu, S. K. Dey, A. C. Fahrenbach, J. R. Guest, H. Mohseni, L. X. Chen, K. L. Wang, J. F. Stoddart, S. I. Stupp, *Nature* **2012**, *488*, 485-489; b) A. Narayanan, D. Cao, L. Frazer, A. S. Tayi, A. K. Blackburn, A. C. H. Sue, J. B. Ketterson, J. F. Stoddart, S. I. Stupp, *J. Am. Chem. Soc.* **2017**, *139*, 9186-9191.

[8] a) Ferraris, J.; Cowan, D. O.; Walatka, V.; Perlstein, J. H. Electron Transfer in a New Highly Conducting Donor-Acceptor Complex. *J. Am. Chem. Soc.* **1973**, *95*, 948-949; b) H. Kuroda, T. Amano, I. Ikemoto, H. Akamatu, *J. Am. Chem. Soc.* **1967**, *89*, 6056-6063.

[9] a) Z. X. Zhu, A. C. Fahrenbach, H. Li, J. C. Barnes, Z. C. Liu, S. M. Dyar, H. C. Zhang, J. Y. Lei, R. Carmieli, A. A. Sarjeant, C. L. Stern, M. R. Wasielewski, J. F.

Stoddart, *J. Am. Chem. Soc.* **2012**, *134*, 11709-11720; b) Y. Liu, A. H. Flood, P. A. Bonvallet, S. A. Vignon, B. N. Northrop, H.-R. Tseng, J. O. Jeppesen, T. J. Huang, B. Brough, M. Baller, S. Magonov, S. Solares, W. A. Goddard, C.-M. Ho, J. F. Stoddart, *J. Am. Chem. Soc.* **2005**, *127*, 9745-9759.

[10] a) K. V. Rao, K. Jayaramulu, T. K. Maji, S. J. George, *Angew. Chem., Int. Ed.* **2010**, *49*, 4218-4222; b) E. A. Appel, F. Biedermann, U. Rauwald, S. T. Jones, J. M. Zayed, O. A. Scherman, *J. Am. Chem. Soc.* **2010**, *132*, 14251-14260; c) D. Jiao, J. Geng, X. J. Loh, D. Das, T. -C. Lee, O. A. Scherman, *Angew. Chem., Int. Ed.* **2012**, *51*, 9633-9637; d) E. A. Appel, J. del Barrio, X. J. Loh, O. A. Scherman, *Chem. Soc. Rev.*, **2012**, *41*, 6195-6214; e) K. Liu, C. Wang, Z. Li, X. Zhang, *Angew. Chem., Int. Ed.* **2011**, *50*, 4952-4956; f) Y. Liu, Y. Yu, J. Gao, Z. Wang, X. Zhang, *Angew. Chem., Int. Ed.* **2010**, *49*, 6576-6579.

[11] a) G. J. Gabriel, S. Sorey, B. L. Iverson, *J. Am. Chem. Soc.* **2005**, *127*, 2637-2640; b) V. J. Bradford, B. L. Iverson, *J. Am. Chem. Soc.* **2008**, *130*, 1517-1524; c) M. Wolffs, N. Delsuc, D. Veldman, N. Van Anh, R. M. Williams, S. C. J. Meskers, R. A. J. Janssen, I. Huc, A. Schenning, *J. Am. Chem. Soc.* **2009**, *131*, 4819-4829; d) K. Jalani, S. Dhiman, A. Jain, S. J. George, *Chem. Sci.* **2017**, *8*, 6030-6036.

[12] a) W. Zhu, R. Zheng, Y. Zhen, Z. Yu, H. Dong, H. Fu, Q. Shi, W. Hu, *J. Am. Chem. Soc.* **2015**, *137*, 11038-11046; b) J. -Y. Wang, J. Yan, L. Ding, Y. Ma, J. Pei, *Adv. Funct. Mater.* **2009**, *19*, 1746-1752.

[13] a) S. Iwata, J. Tanaka, S. Nagakura, *J. Chem. Phys.* **1967**, *47*, 2203-2209; b) H. Hayashi, S. Nagakura, S. Iwata, *Mol. Phys.* **1967**, *13*, 489-490.

[14] C. Kulkarni, G. Periyasamy, S. Balasubramanian, S. J. George, *Phys. Chem. Chem. Phys.* **2014**, *16*, 14661-14664.

[15] a) N. Sakai, J. Mareda, E. Vauthey, S. Matile, *Chem. Commun.* **2010**, *46*, 4225-4237; b) F. Würthner, S. Ahmed, C. Thalacker, T. Debaerdemaeker, *Chem. Eur. J.* **2002**, *8*, 4742-4750.

[16] a) S. Garain, S. Kuila, B. C. Garain, M. Kataria, A. Borah, S. K. Pati, S. J. George, *Angew. Chem. Int. Ed.* **2021**, *60*, 12323-12327; b) S. Garain, S. Sarkar, B. C. Garain, S. K. Pati, S. J. George, *Angew. Chem. Int. Ed.* **2022**, DOI: 10.1002/anie.202115773; c) A.

Manthanath, V. C. Wakchaure, K. C. Ranjeesh, T. Das, K. Vanka, T. Nakanishi, S. S. Babu, *Angew. Chem., Int. Ed.* **2019**, *58*, 2284-2288.

[17] C. Reichardt, *Chem. Rev.* **1994**, *94*, 2319-2358.

[18] a) Y. Takashima, V. M. Martínez, S. Furukawa, M. Kondo, S. Shimomura, H. Uehara, M. Nakahama, K. Sugimoto, S. Kitagawa, *Nat. Commun.* **2011**, *2*, 168; b) V. Martínez-Martínez, R. S. Llano, S. Furukawa, Y. Takashima, I. L. Arbeloa, S. Kitagawa, *Chem Phys Chem* **2014**, *15*, 2517-2521.

[19] a) H. Tsujimoto, D.-G. Ha, G. Markopoulos, H. S. Chae, M. A. Baldo, T. M. Swager, *J. Am. Chem. Soc.* **2017**, *139*, 4894-4900; b) C. M. Tonge, Z.M. Hudson, *J. Am. Chem. Soc.* **2019**, *141*, 13970-13976; c) Q. Li, J. Hu, J. Lv, X. Wang, S. Shao, L. Wang, X. Jing, F. Wang, *Angew. Chem. Int. Ed.* **2020**, *59*, 20174-20182; d) L. Sun, W. Hua, Y. Liu, G. Tian, M. Chen, M. Chen, F. Yang, S. Wang, X. Zhang, Y. Luo, W. Hu, *Angew. Chem., Int. Ed.* **2019**, *58*, 11311-11316.

[20] a) Gaussian 16, Revision C.01, Frisch, M. J.; Trucks, G. W.; Schlegel, H. B.; Scuseria, G. E.; Robb, M. A.; Cheeseman, J. R.; Scalmani, G.; Barone, V.; Petersson, G. A.; Nakatsuji, H.; Li, X.; Caricato, M.; Marenich, A. V.; Bloino, J.; Janesko, B. G.; Gomperts, R.; Mennucci, B.; Hratchian, H. P.; Ortiz, J. V.; Izmaylov, A. F.; Sonnenberg, J. L.; Williams-Young, D.; Ding, F.; Lipparini, F.; Egidi, F.; Goings, J.; Peng, B.; Petrone, A.; Henderson, T.; Ranasinghe, D.; Zakrzewski, V. G.; Gao, J.; Rega, N.; Zheng, G.; Liang, W.; Hada, M.; Ehara, M.; Toyota, K.; Fukuda, R.; Hasegawa, J.; Ishida, M.; Nakajima, T.; Honda, Y.; Kitao, O.; Nakai, H.; Vreven, T.; Throssell, K.; Montgomery, J. A., Jr.; Peralta, J. E.; Ogliaro, F.; Bearpark, M. J.; Heyd, J. J.; Brothers, E. N.; Kudin, K. N.; Staroverov, V. N.; Keith, T. A.; Kobayashi, R.; Normand, J.; Raghavachari, K.; Rendell, A. P.; Burant, J. C.; Iyengar, S. S.; Tomasi, J.; Cossi, M.; Millam, J. M.; Klene, M.; Adamo, C.; Cammi, R.; Ochterski, J. W.; Martin, R. L.; Morokuma, K.; Farkas, O.; Foresman, J. B.; Fox, D. J. Gaussian, Inc., Wallingford CT, 2016; b) A. D.Becke, *J. Chem. Phys.* **1993**, *98*, 1372; c) C. Lee, W. Yang, R. G. Parr, *Phys. Rev. B* **1988**, *37*, 785-789; d) B. Miehlich, A. Savin, H. Stoll, H. Preuss, *Chem. Phys. Lett.* **1989**, *157*, 200-206; e) S. Hirata, M. Head-Gordon, *Chem. Phys. Lett.* **1999**, *314*, 291-299; f) G. Scalmani, M. J. Frisch, *J. Chem. Phys.* **1996**, *57*, 281-293; g) ADF2017, SCM, Theoretical Chemistry, Vrije Universiteit, Amsterdam, The Netherlands, <http://www.scm.com>.

[21] D. Cao, M. Hong, A. K. Blackburn, Z. Liu, J. M. Holcroft, J. F. Stoddart, J. F. *Chem. Sci.* **2014**, *5*, 4242-4248.

[22] S. M. Luo, K. A. Stellmach, S. M. Ikuzwe, D. D. Cao, *J. Org. Chem.* **2019**, *84*, 10362-10370.

[23] X. Huang, M. Hu, X. Zhao, C. Li, Z. Yuan, X. Liu, C. Cai, Y. Zhang, Y. Hu, Y. Chen, *Org. Lett.* **2019**, *21*, 3382-3386.

PART B

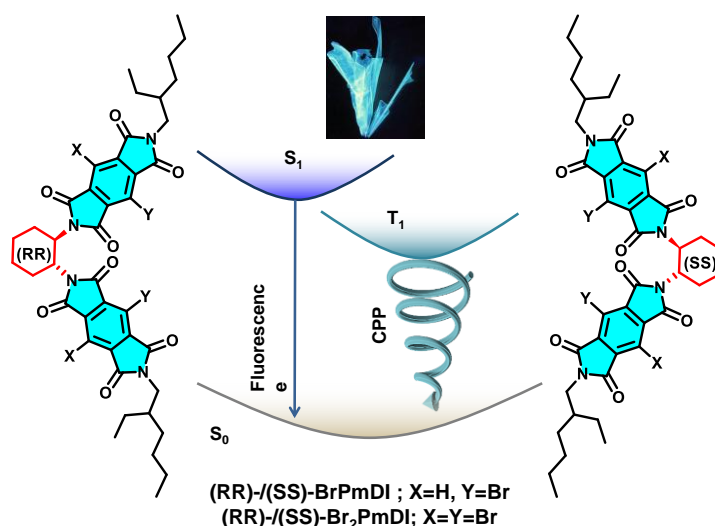
CHAPTER 7.1
**Circularly Polarized Phosphorescence from Pyromellitic
Diimides**

CHAPTER 7.1

Circularly Polarized Phosphorescence from Pyromellitic Diimides*

Abstract

Chiral organic phosphors with circularly polarized room temperature phosphorescence (CPP) provide new prospects to the realm of circularly polarized luminescence (CPL) materials, owing to the long-lived triplet states and persistent emission. Although several molecular designs show efficient room temperature phosphorescence (RTP), realization of ambient organic CPP remains a formidable challenge. Herein, we introduce a chiral bischromophoric phosphor design to realize ambient CPP emission by appending molecular phosphors to chiral diaminocyclohexane core. Thus, solution processable polymer films of the *trans*-1,2-diaminocyclohexane (DAC) chiral cores with heavy-atom substituted pyromellitic diimide phosphors, exhibits one of the most efficient exclusive CPP emission with high phosphorescence quantum yield ($\sim 18\%$ in air and 46% under vacuum) and significant luminescence dissymmetry factor ($|g_{lum}| \sim 4.0 \times 10^{-3}$).



*Manuscript based on this work is published in *Angew. Chem. Int. Ed.* **2022**, *61*, e2021157.

7.1.1. Introduction:

Chiral organic chromophores with circularly polarized luminescence (CPL) have been an active field of research in the optoelectronics realm due to their potential in various optical displays and bioimaging.^[1] However, most of the molecular designs for organic CPL have been based on chiral fluorophores^[2a-1] and chiral thermally activated delayed fluorophores.^[2m] In this context, the emerging research field of ambient organic phosphors,^[3,4] which displays room temperature phosphorescence, offers a new dimension to attain CPL and is an auspicious substitute to the toxic metal based chiral organometallic phosphors.^[5] However, circularly polarized phosphorescence (CPP) from purely organic systems is relatively unexplored, as it requires elegant molecular designs, which cater to both chiral induction and stabilization of triplets. Thus, the recent efficient examples of organic CPP systems utilize the restriction of motions of well-known chiral phosphors either in the crystalline state or in a host matrix.^[6] In a pioneering report, Hirata and co-workers have demonstrated CPP by incorporating metal-free chiral binaphthyl phosphors into amorphous steroid matrix.^[6a] Chen, Huang, and co-workers have shown persistent CPP in powders by appending known phosphors to chiral ester chains.^[6b] More recently, CPP emission in an amorphous state has also been realized independently by the groups of Zhao^[6d] and Ma,^[6e] by attaching axial chiral phosphors to polymer chains. However, further advancement of ambient chiral phosphors certainly demands generalized molecular designs with improved CPP efficiency and solution processability.

In this chapter we have shown mirror image cyan (~495 nm) CPP emission with significant luminescence dissymmetry factor of $|g_{lum}|$ of $\sim 1.3-4.0 \times 10^{-3}$ and high phosphorescence quantum yield of ~10-18% under ambient conditions (42-46% under vacuum) from the enantiomeric mono-bromo **(RR)/(SS)-BrPmDI** and di-bromo **(RR)/(SS)-Br₂PmDI** bischromophoric PmDIs in PMMA matrix. Such intense RTP emission with one of the highest quantum yield (~48 %) in the short-wavelength region of the visible spectrum is unprecedented.

7.1.2. Molecular Design:

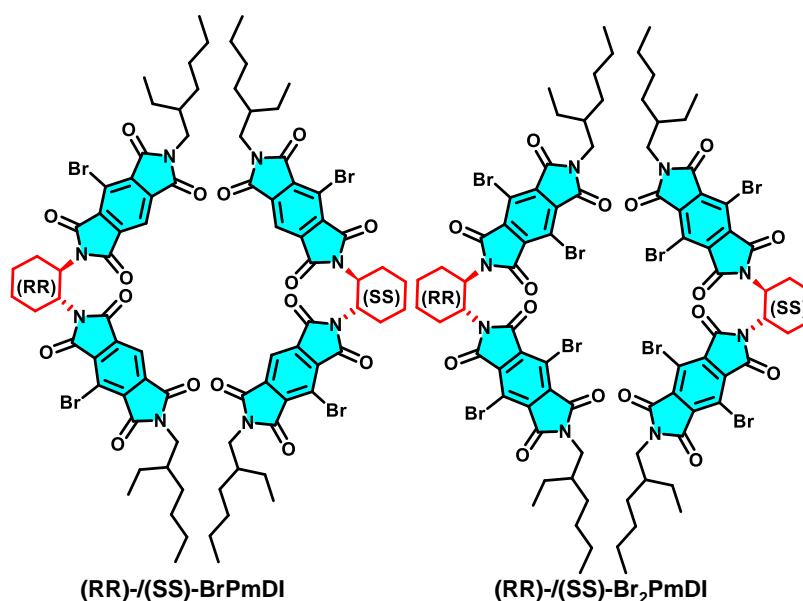


Figure 7.1.1. Molecular structure of (RR)-/(SS)-BrPmDI and (RR)-/(SS)-Br₂PmDI.

The chiral phosphors (RR)-/(SS)-BrPmDI and (RR)-/(SS)-Br₂PmDI were synthesized through statistical imidation reaction of the mono-bromo/di-bromo pyromellitic anhydride with (1R,2R)-(-)-1,2-diaminocyclohexane or (1S,2S)-(+)-1,2-diaminocyclohexane and 2-ethylhexylamine (See Scheme 7.1 and 7.2). Chiral diaminocyclohexane (DAC) derived bischromophoric design has been explored as an efficient molecular strategy to impart strong chirality bias for the asymmetric organization of the fluorophores.^[2a-e,7] This molecular design has been extensively used to construct helical chromophoric assemblies with interesting chiroptical and optoelectronic functions.^[2a,b] Although, circularly polarized fluorescence has been well established using bischromophoric systems,^[2a-e] the extension of this molecular design to realize chiral emission from triplet states is seldom attempted. With this perspective, in this chapter we introduce the bischromophoric chiral phosphor design by appending small molecular phosphors to the chiral DAC core, to realize solution-processable, ambient CPP with high quantum yield and good luminescence dissymmetry factor i.e., $|g_{lum}|$. Recently, we have contributed to the burgeoning field of ambient RTP phosphors, with a variety of arylene diimide derivatives, as they exhibit good inter-system crossing (ISC) efficiency by virtue of multiple imide groups in its backbone, with heavy halogen atoms in the core.^[8] Among various arylene diimides, pyromellitic diimides (PmDI) possess excellent triplet quantum yields and we have recently reported efficient ambient

RTP from heavy-atom substituted PmDIs in the crystalline state.^[8a] Thus, the bichromophoric molecular design presented here to realize ambient CPP consists of enantiomeric DAC chiral cores, functionalized with heavy atom substituted pyromellitic diimide (PmDI) phosphors (Figure 7.1.1). Presence of multiple carbonyl groups and heavy-atoms associated with the chiral bichromophoric design, which would enhance the spin-orbit coupling and ISC rate to realize phosphorescence in their monomeric states.

7.1.3. Spectroscopic Studies in Solution-state:

First, we have performed detailed photophysical studies of **(RR)-BrPmDI** and **(RR)-Br₂PmDI** in tetrahydrofuran (THF) ($[c] = 0.05$ mM, 25 °C), in which the phosphors exist in monomeric state. Both the derivatives showed the π - π^* absorption band in the 280 to 400 nm region (Figures 7.1.2a,d). The circular dichroism (CD) spectra of enantiomeric mono-bromo derivative **(RR)-/(SS)-BrPmDI** in THF showed a mirror image signal with maxima at 342 and 277 nm (anisotropy factor, $g_{CD} = 1.5 \times 10^{-4}$), while the di-bromo derivative **(RR)-/(SS)-Br₂PmDI** showed CD signal with maxima at 372, 337 and 293 nm ($g_{CD} = 1.7 \times 10^{-4}$), suggesting the induction of chirality to the pyromellitic chromophores from the chiral DAC core (Figures 7.1.2c,d).

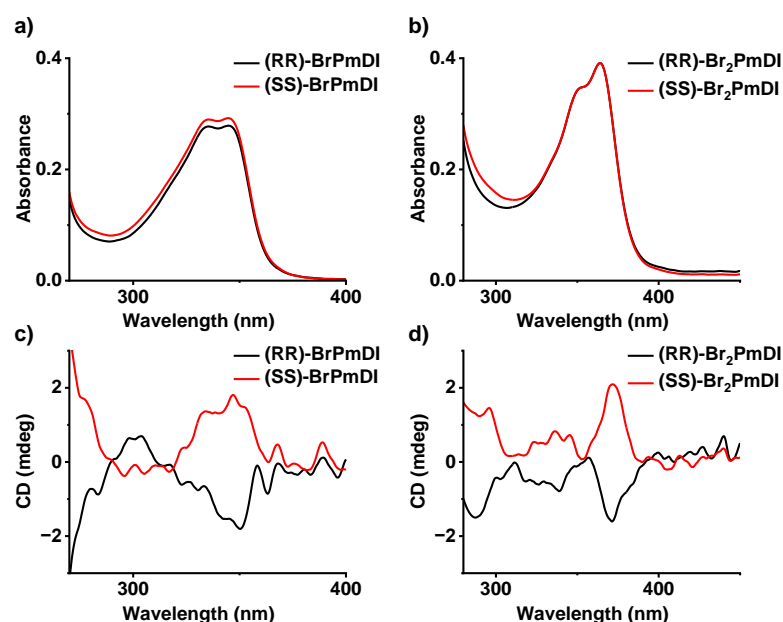


Figure 7.1.2. Absorption and their corresponding mirror image CD spectra of a, c) **(RR)-BrPmDI/(SS)-BrPmDI** and b, d) **(RR)-Br₂PmDI/(SS)-Br₂PmDI** in THF ($[c] = 0.05$ mM, $l = 10$ mm).

The corresponding emission spectra in THF showed sharp vibrational features with maxima at 404 nm and 385 nm with an average lifetime of 4.3 ns and 3.1 ns for **(RR)-BrPmDI** and **(RR)-Br₂PmDI**, respectively indicative of the locally excited fluorescence nature of the emission (Figures 7.1.3a,d,b,e). However, no phosphorescence emission and long lifetime decay were observed at room temperature in solution state (THF), due to the non-radiative decay paths associated with the triplets via vibrational or oxygen mediated quenching. However, emission spectra of both the derivatives at 77 K (THF glassy matrix) exhibited strikingly different emission characteristics with a red-shifted band in the 425 to 650 nm region (Figures 7.1.3a,d). Time-resolved emission decay profiles revealed a high average lifetime of 31.5 ms and 7.2 ms for **(RR)-BrPmDI** and **(RR)-Br₂PmDI**, respectively, pointing towards the triplet stabilization and phosphorescence emission in the glassy matrix due to reduced vibrational deactivation (Figures 7.1.3c,f).

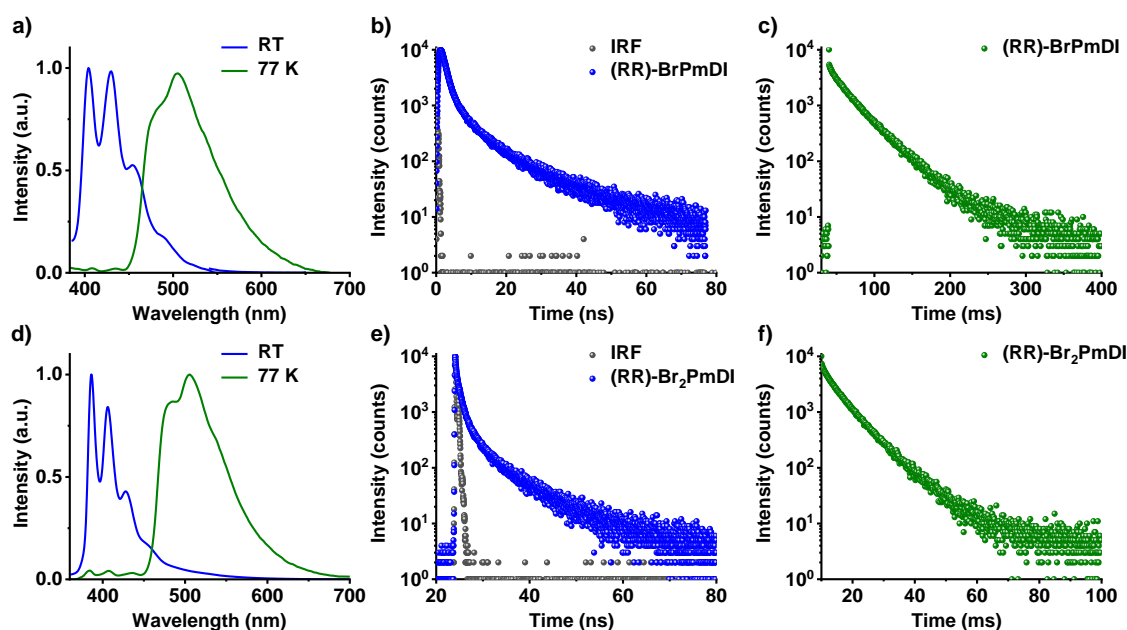


Figure 7.1.3. Steady-state emission at room-temperature (blue line) and at 77 K (green line) of a) **(RR)-BrPmDI** and d) **(RR)-Br₂PmDI** in THF. Fluorescence lifetime decay profiles of b) **(RR)-BrPmDI** ($\lambda_{exc.} = 286$ nm, $\lambda_{collected} = 410$ nm) and e) **(RR)-Br₂PmDI** ($\lambda_{exc.} = 373$ nm, $\lambda_{collected} = 410$ nm) in THF. Phosphorescence lifetime decay profiles of c, f) **(RR)-BrPmDI** and b) **(RR)-Br₂PmDI** ($\lambda_{exc.} = 310$ and 330 nm for **(RR)-BrPmDI**/**(RR)-Br₂PmDI** respectively, $\lambda_{collected} = 500$ nm).

7.1.4. Ambient Monomeric Room Temperature Phosphorescence in Polymer Matrix:

To realize ambient phosphorescence in the amorphous state, (R,R)-enantiomers of both phosphors were incorporated into PMMA matrix (1 wt.% with respect to PMMA), by drop-casting chloroform solution of the mixture on glass substrates. Interestingly, PMMA films of both the phosphors showed similar emission characteristics with that of the nascent molecules in frozen THF at 77 K, implying the ambient phosphorescence from the PMMA films (Figures 7.1.4a,d). Both **(RR)-BrPmDI** ($\lambda_{\text{exc.}} = 310$ nm) and **(RR)-Br₂PmDI** ($\lambda_{\text{exc.}} = 330$ nm) showed intense red-shifted emission band at the 425-650 nm region with a maximum around 495 nm along with a shoulder band in the 350-430 nm range (Figures 7.1.4a,d). Time-resolved emission decay profiles of both phosphors at the high energy shoulder emission ($\lambda_{\text{flu.}} = 380$ nm) showed short lifetimes (~ 2 ns and ~ 5 ns for **(RR)-BrPmDI** and **(RR)-Br₂PmDI** respectively), which points to its fluorescence nature (Figures 7.1.4b,e). On the other hand, the average lifetime of the red-shifted band at 500 nm is found to be in the millisecond regime for both the phosphors ($\tau_{\text{avg.}} = 1.6$ ms and 0.36 ms for **(RR)-BrPmDI** and **(RR)-Br₂PmDI**, respectively, $\lambda_{\text{phos.}} = 495$ nm), consistent with the phosphorescence nature of the emission (Figures 7.1.4c,f). Further, gated emission, with a delay time of 0.5 ms and time-resolved emission spectra reiterated the long-lived component of this emission with receded fluorescence intensity at the high energy end (Figures 7.1.4a,d).

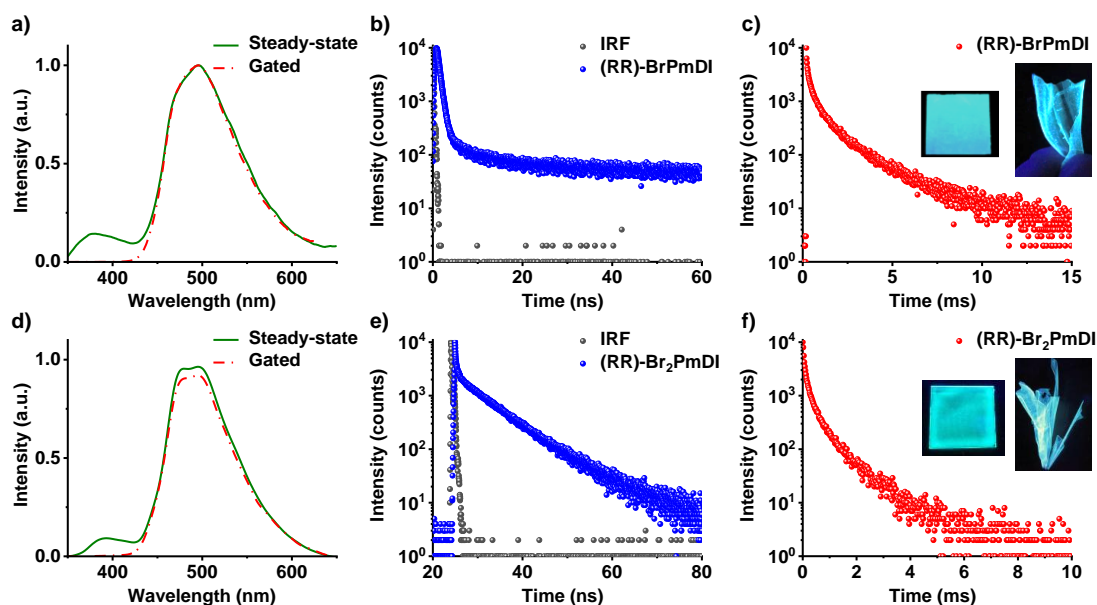


Figure 7.1.4. Steady-state and gated emission spectra (delay time = 0.5 ms) of the PMMA (1 wt.%) films of a) (RR)-BrPmDI and d) (RR)-Br₂PmDI. Fluorescence lifetime decay profiles (blue circles, $\lambda_{exc.} = 286$ nm and 373 nm for (RR)-BrPmDI/ (RR)-Br₂PmDI respectively, $\lambda_{collected} = 420$ nm) of b) (RR)-BrPmDI and e) (RR)-Br₂PmDI. Phosphorescence lifetime decay profiles (red circles, $\lambda_{exc.} = 310$ and 330 nm for (RR)-BrPmDI/ (RR)-Br₂PmDI respectively, $\lambda_{collected} = 500$ nm) of c) (RR)-BrPmDI and f) (RR)-Br₂PmDI. Inset of c) and f): Photographs of corresponding PMMA films on glass substrate and as free-standing sheets under UV light; all experiments were performed under air).

The temperature-dependent studies showed an increase in phosphorescence emission intensity and corresponding lifetime, with a decrease in temperature due to the reduced vibrational relaxation, which is expected for phosphorescence emission (Figure 7.1.5). The similarity of the phosphorescence emission of the PMMA films of these chiral PmDIs (1 wt.%) with that of the emission of control molecules, pyromellitic mono- and di-bromo derivatives without the chiral core, hints towards the monomeric nature of the phosphors in the PMMA matrix at low concentrations (1 wt.%) (Figures 7.1.6).

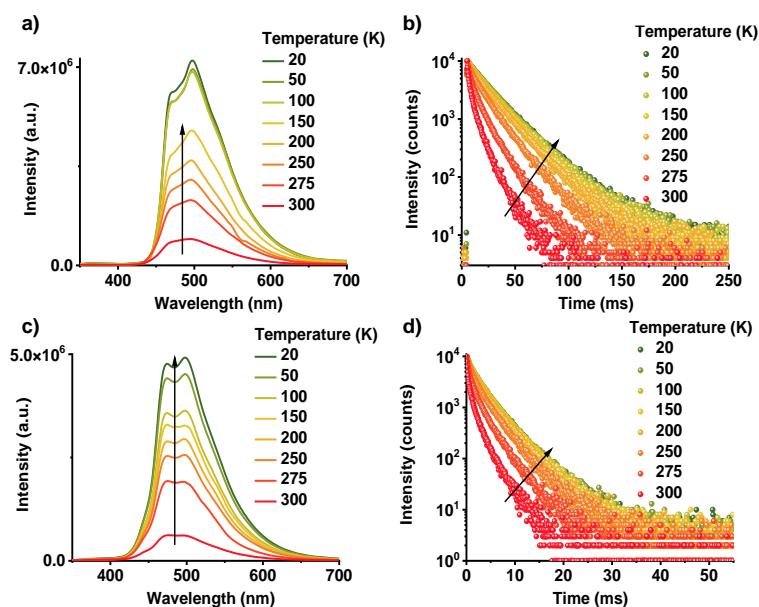


Figure 7.1.5. Temperature-dependent a,c) emission spectra and b,d) lifetime decay profiles of 1 wt.% (RR)-BrPmDI (1st row) and (RR)-Br₂PmDI (2nd row) doped in PMMA matrix ($\lambda_{exc.} = 310$ nm and 330 nm for (RR)-BrPmDI and (RR)-Br₂PmDI respectively $\lambda_{collected} = 500$ nm, $\tau_{avg.} = 23.4$ ms and 2.1 ms for (RR)-BrPmDI and (RR)-Br₂PmDI respectively at 20 K).

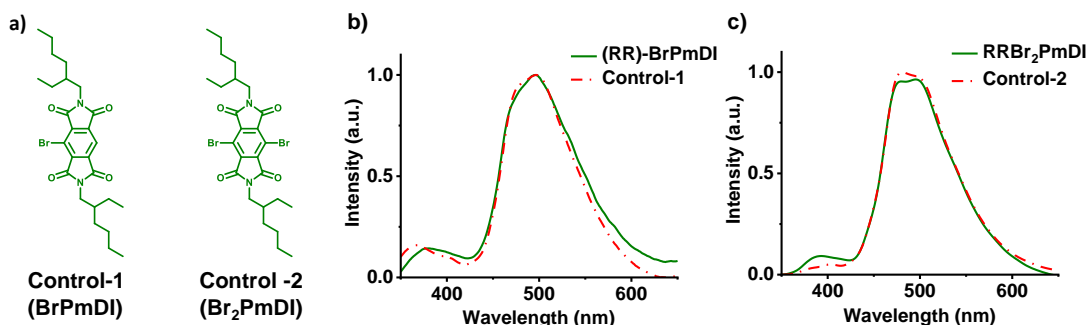


Figure 7.1.6. a) Molecular structure of the control molecules BrPmDI and Br₂PmDI. Spectral comparisons of b) (RR)-BrPmDI, and c) (RR)-Br₂PmDI with their corresponding control molecules (for all cases, 1 wt.% PmDI doped in PMMA matrix was used for experiments, $\lambda_{exc.} = 310$ nm and 330 nm for (RR)-BrPmDI and (RR)-Br₂PmDI, respectively.)

Increasing the doping concentration of the chiral PmDIs in the PMMA matrix (1 to 50 wt.%) showed a decrease in the phosphorescence intensity and lifetime, suggesting the aggregation caused quenching (Figures 7.1.7a-d). 1 wt.% PMMA films of (RR)-BrPmDI exhibited exceptional ambient stability (Figures 7.1.7e,f). PMMA films of

(RR)-BrPmDI and **(RR)-Br₂PmDI** (1 wt.%) show phosphorescence quantum yields (Φ_p) of $\sim 10.7\%$ and $\sim 17.5\%$ in the air. The significant increase in the phosphorescence emission intensity (3.9x and 2.5x folds for **(RR)-BrPmDI** and **(RR)-Br₂PmDI**, respectively) and phosphorescence lifetime (1.6 to 6.6 ms and 0.36 to 1.0 ms for **(RR)-BrPmDI** and **(RR)-Br₂PmDI**, respectively) of these films under vacuum when compared to that in air, further reaffirms the stabilization of triplets (Figure 7.1.8a-d). Accordingly, the Φ_p of **(RR)-BrPmDI** and **(RR)-Br₂PmDI** doped films showed a remarkable increase to $\sim 42\%$ and $\sim 46\%$, respectively, which renders them one of the most efficient chiral phosphors reported in the literature. As anticipated, the enantiomeric **(SS)-BrPmDI** and **(SS)-Br₂PmDI** exhibited similar phosphorescence spectral features under similar conditions. (Figures 7.1.9e,f).

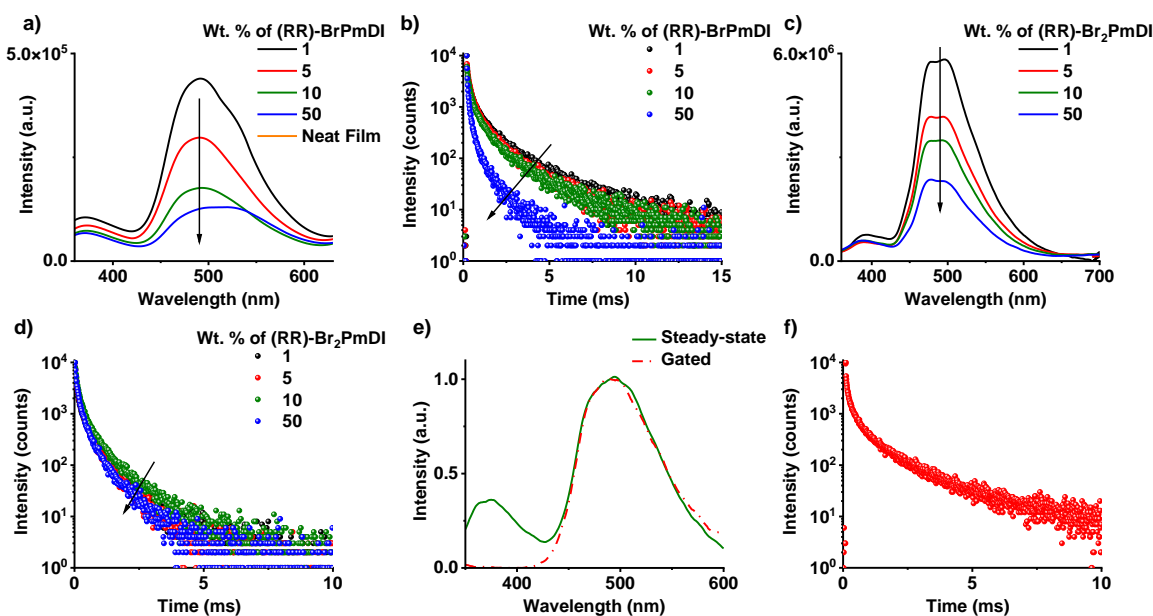


Figure 7.1.7. Composition-dependent studies of various wt.% **(RR)-BrPmDI**/**(RR)-Br₂PmDI** doped in PMMA matrix: Steady-state emission spectra of a) **(RR)-BrPmDI** and b) **(RR)-Br₂PmDI**. Phosphorescence lifetime decay profiles of c) **(RR)-BrPmDI** and d) **(RR)-Br₂PmDI**. ($\lambda_{exc.} = 310$ nm and 330 nm for **(RR)-BrPmDI** and **(RR)-Br₂PmDI** respectively, $\lambda_{collected} = 500$ nm). e) Normalized steady-state, gated emission spectra and f) lifetime decay profiles of **(RR)-BrPmDI** after 45 days in PMMA film ($\lambda_{exc.} = 310$ nm, $\lambda_{collected} = 500$ nm, delay time = 0.5 ms, 1 wt.% **(RR)-BrPmDI** in PMMA is used for the experiments, $\tau_{avg.} = 1.28$ ms).

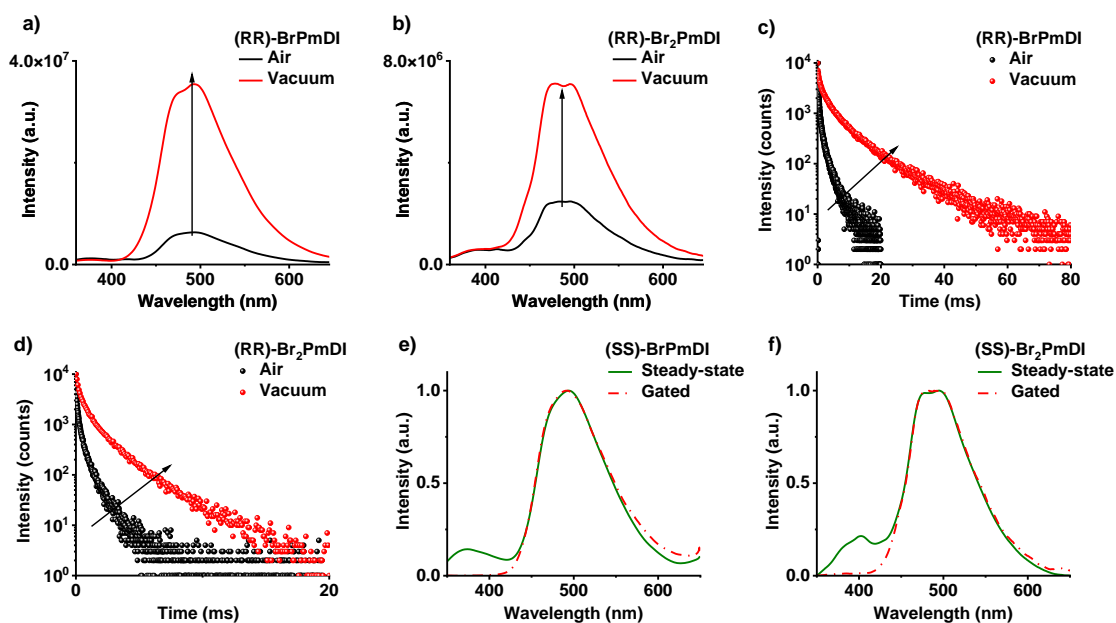


Figure 7.1.8. Steady-state emission spectra of a) **(RR)-BrPmDI** and b) **(RR)-Br₂PmDI** under air and vacuum in PMMA film. Phosphorescence lifetime decay profiles of c) **(RR)-BrPmDI** and d) **(RR)-Br₂PmDI** under air and vacuum in PMMA film. Normalized steady-state and gated emission spectra of e) **(SS)-BrPmDI** and f) **(SS)-Br₂PmDI** in PMMA film. ($\lambda_{exc.} = 310$ nm and 330 nm for **(RR)-/(SS)-BrPmDI** and **(RR)-/(SS)-Br₂PmDI** respectively, $\lambda_{collected} = 500$ nm, delay time = 0.5 ms, 1 wt.% **(RR)-/(SS)-BrPmDI-/(RR)-/(SS)-Br₂PmDI** in PMMA is used for all the experiments).

7.1.5. Theoretical Calculations:

To get the qualitative understanding of the ISC channels and SOC between singlet and triplet states of chiral PmDIs, time-dependent density functional theory (TDDFT) calculations using CAMB3LYP exchange-correlation functional were performed. (Figure 7.1.9). The TDDFT calculations showed that the main contributing ISC pathway is from S_1/S_2 ($n-\pi^*$) to T_3/T_4 ($\pi-\pi^*$), respectively for both the phosphors, which corroborates with El Sayed's rule (Figure 7.1.9). The spin-orbit coupling matrix element (SOCME) between $S_1 \rightarrow T_3$ and $S_2 \rightarrow T_4$ for **(RR)-BrPmDI** is calculated to be 27.8 cm^{-1} and 43.4 cm^{-1} , respectively (Figure 7.1.9). On the other hand, the SOCME between $S_1 \rightarrow T_3$, $S_1 \rightarrow T_4$ and $S_2 \rightarrow T_3$, $S_2 \rightarrow T_4$ are 500.9 cm^{-1} , 195.7 cm^{-1} and 197.0 cm^{-1} , 195.7 cm^{-1} , respectively for **(RR)-Br₂PmDI** (Figure 7.1.9). Thus, the strong SOCME with a faster ISC rate of the chiral phosphors results efficient ambient triplet yield.

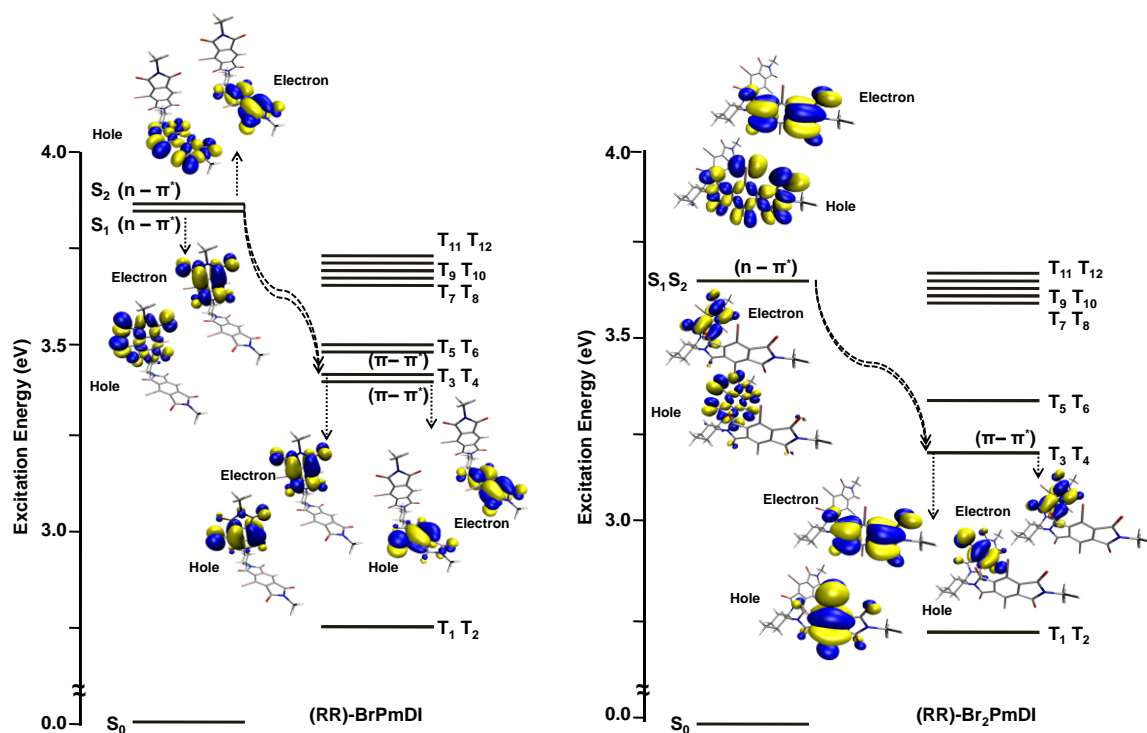


Figure 7.1.9. Relative excitation energies and their corresponding hole (below) and electron (above) wavefunctions of a) **(RR)-BrPmDI** and b) **(RR)-Br₂PmDI**, calculated using CAMB3LYP functional.

7.1.6. Circularly Polarized Phosphorescence in Processable Films:

Having established the RTP in chiral bischromophoric PmDIs, next, we investigated their chiroptical properties (Figures 7.1.10 and 7.1.11). The circular dichroism (CD) spectra of the PMMA films (1 wt.%) of enantiomeric **(RR)-/(SS)-BrPmDI** showed a mirror image CD spectrum with a $|g_{CD}|$ of $\sim 1.4 \times 10^{-4}$ (Figure 7.1.10). Thus, the CD studies clearly suggest the transfer of chirality bias from the chiral core to the intramolecular asymmetric organization of PmDI bischromophores in PMMA films (Figure 7.1.10).

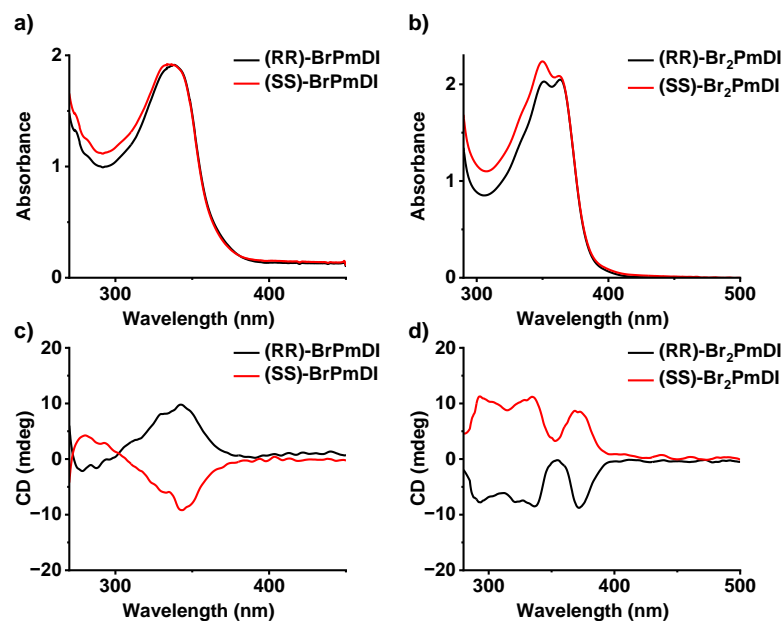


Figure 7.1.10. Absorption and their corresponding mirror image CD spectra of a, c) **(RR)-BrPmDI/(SS)-BrPmDI** and b, d) **(RR)-Br₂PmDI/(SS)-Br₂PmDI** in the PMMA (1 wt.%) films.

Chiral organization and the ambient phosphorescent nature of the PmDI phosphors in amorphous PMMA films motivated us to explore their excited state chiroptical properties. The CPL spectra of PMMA films of enantiomeric **(RR)-/(SS)-BrPmDI** and **(RR)-/(SS)-Br₂PmDI** derivatives showed mirror image CPL emission under ambient conditions (Figure 7.1.11). The CPL emission of both the phosphors with a maximum around 500 nm suggests exclusive triplet state contribution to yield pure mirror-imaged CPP emission (Figure 7.1.11). A similar sign of the CPP emission with that of the first Cotton-effect of the corresponding CD spectrum for the both the phosphors, suggest that the ground and excited states are having same electric or magnetic dipole transition moment (Figures 7.1.11 and 7.1.11). This was further validated by emission under ambient conditions. Additional linear dichroism (LD) experiments ruled out any LD contribution due to the macroscopic alignment of the phosphors in thin films to the observed chiroptical properties (Figure 7.1.12). Further, the magnitude of CPP could be evaluated by luminescence dissymmetry factor (g_{lum}), which is defined as $|g_{lum}| = 2 \times (I_L - I_R) / (I_L + I_R)$, where I_L and I_R present the emission intensity of the left-handed and right-handed circularly polarized light, respectively (Figure 7.1.11). Both the PmDI derivatives exhibit remarkably high CPP efficiency with a $|g_{lum}|$ of 1.3×10^{-3} and 4.0×10^{-3} for **(RR)-BrPmDI** and **(RR)-Br₂PmDI**, respectively.

It is noteworthy that CPP under ambient conditions has been effortlessly realized in the crystal state but rarely reported in the amorphous film state.^[6]

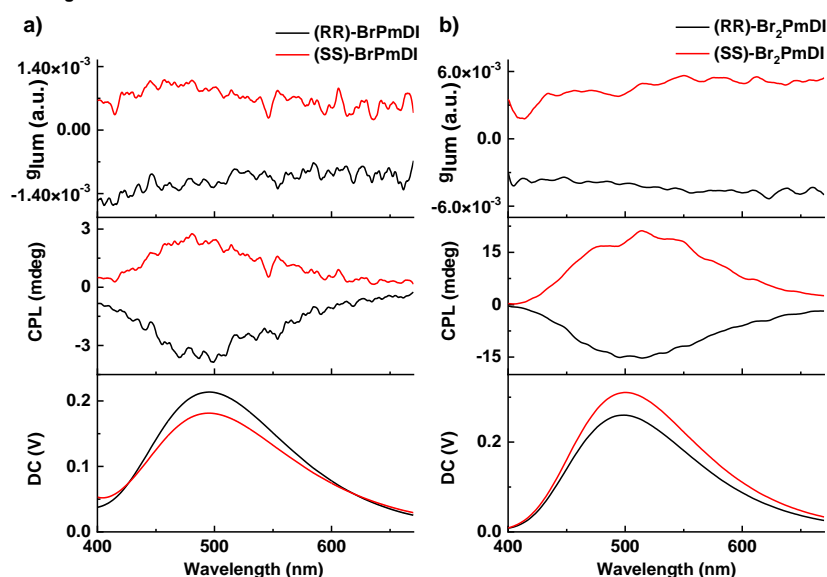


Figure 7.1.11. CPL, direct current (DC) spectra and dissymmetry factor ($|g_{lum}|$) of a) (RR)-BrPmDI / (SS)-BrPmDI and b) (RR)-Br₂PmDI / (SS)-Br₂PmDI ($\lambda_{exc.} = 310$ nm and 330 nm for BrPmDI and Br₂PmDI respectively, in all cases 1 wt.% PmDI in PMMA is used, all experiments were carried out in air).

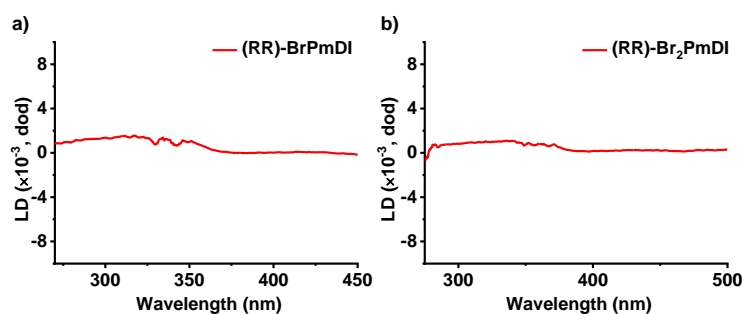


Figure 7.1.12. LD spectra of a) (RR)-BrPmDI, b) (RR)-Br₂PmDI in PMMA film (1 wt.% PmDI in PMMA is used).

7.1.7. Conclusions:

In conclusion, we have successfully introduced a chiral bischromophoric design to realize ambient CPP emission from molecular phosphors, which is well known in exciton coupling model systems and in the field of circularly polarized luminescence. The mono and dibromo substituted pyromellitic diimide phosphors appended to the chiral *trans*-1,2-diaminocyclohexane core showed ambient CPP emission in solution-processable

PMMA films, with excellent phosphorescence quantum yields of 10.7% and 17.5 % in air (42 % and 46 % under vacuum) and luminescence dissymmetry factor i.e., $|g_{lum}|$ of 1.3×10^{-3} and 4.0×10^{-3} , respectively. We envisage that the present design opens the door to investigation to the myriads of room temperature molecular phosphors to realize chiral phosphorescence emission.

7.1.8. Experimental Section:

7.1.8.1. General Methods:

NMR Measurements: ^1H and ^{13}C NMR ^1H and ^{13}C NMR spectra were recorded on a BRUKER AVANCE-400 Fourier transformation spectrometer with 400 and 100 MHz respectively. The spectra are calibrated with respect to the residual solvent peaks. The chemical shifts are reported in parts per million (ppm) with respect to TMS. Short notations used are, s for singlet, d for doublet, t for triplet, q for quartet and m for multiplet.

Optical Measurements: Electronic absorption spectra were recorded on a Perkin Elmer Lambda 900 UV-Vis-NIR spectrometer and emission spectra were recorded on FLS1000 spectrometer, Edinburgh Instruments. Solution state UV-Vis and emission spectra were recorded in 10 mm path length cuvette. Fluorescence spectra of films were recorded in front-face geometry to avoid self-absorption. Circular Dichroism (CD) spectra were recorded on a Jasco J-815 spectrometer where the sensitivity, time constant and scan rate were chosen appropriately. Circularly polarized luminescence (CPL) measurements were performed with a Jasco CPL-300 spectrometer. A scanning speed of 50 nm/min, excitation slit width of 4000 μM and emission slit width of 4000 μM , integration time (D.I.T) of 8 sec, and with multiple spectral accumulations were employed.

Lifetime Measurements and Quantum yield: Fluorescence lifetimes were performed on a Horiba Delta Flex time-correlated single-photon-counting (TCSPC) instrument. A 286 nm LED diode with a pulse repetition rate of 1 MHz was used as the light source. The instrument response function (IRF) was collected by using a scatterer (Ludox AS40 colloidal silica, Sigma-Aldrich). Phosphorescence lifetime ($\lambda_{exc.} = 310$ and 330 nm) and gated emission were measured on FLS1000 spectrometer, Edinburgh Instruments equipped with a micro flash-lamp (μF2) set-up. Quantum yield was measured using an integrating sphere in the same instrument.

Matrix-Assisted Laser Desorption Ionization (MALDI): MALDI was performed on a Bruker daltonics Autoflex Speed MALDI TOF System (GT0263G201) spectrometer using trans-2-[3-(4-tert-Butylphenyl)-2-methyl-2-propenylidene] malononitrile (DCTB) as the matrix.

Computational Details: Ground State (S_0) of **(RR)-BrPmDI** and **(RR)-Br₂PmDI** monomer molecules were optimized using density functional theory (DFT) and electronic absorption spectra was calculated using time-dependent density functional theory (TD-DFT) as implemented in the Gaussian 16 software.^[10a] Ground state (S_0) optimization and frequency calculations were performed employing B3LYP^[10b-d] exchange functional with 6-31+g(d) basis set except for Br for which LANL2DZ basis set was used with the corresponding effective core potential (ECP). While the excited state calculations were performed using long-range corrected CAM-B3LYP^[10e] exchange-correlation functional with the same basis sets as mentioned before and NTOs calculations were performed. NTOs were plotted with the isosurface value of ± 0.02 with the help of VMD. Ground state frequency calculations were performed to confirm the absence of any unstable normal mode. The solvent (THF) effects were taken into account using polarizable continuum model (PCM) through integral equation variant formalism.^[10f] The first singlet excited state (S_1) of monomers were optimized at the TD-DFT level of theory. While the first triplet excited states (T_1) were also optimized at the TD-DFT level of theory within the Tamn-Dancoff approximation (TDA), which overcomes the triplet instability issue.^[1g] The spin orbit coupling (SOC) effect was considered to be a perturbation of the scalar relativistic Kohn-Sham orbitals after SCF and TD-DFT calculations (pSOC-TDDFT).^[10g-j] The SOC matrix elements were calculated using B3LYP with a Slater-type all-electron TZP basis set for all atoms as implemented in the ADF package.^[10k]

7.1.8.2. Protocol of Sample Preparation:

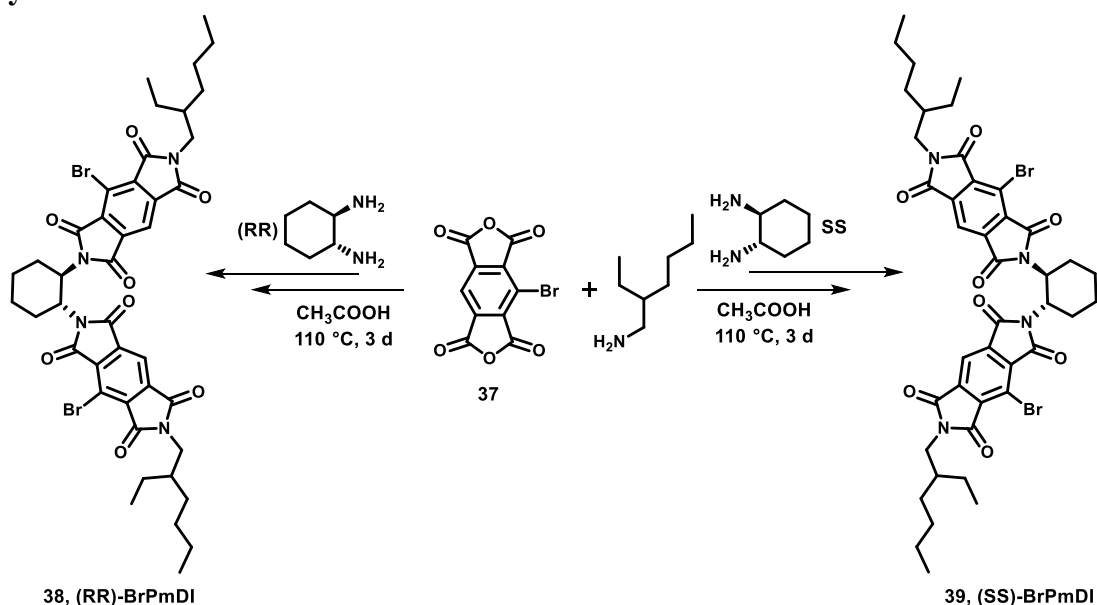
All solution state studies were performed keeping the final concentration of the samples to 0.05mM from a stock solution of THF (1 mM). For thin films, **(RR)-BrPmDI/(RR)-Br₂PmDI** or **(SS)-BrPmDI/(SS)-Br₂PmDI** molecules (3 mg each) were mixed with appropriate amount of PMMA (depending on the wt. ratio) in total 2 ml chloroform solution. (For example, 1 wt.% dye: PMMA consists of 3 mg dye in 300 mg PMMA). This mixture was then heated at 50 °C for 10 minutes followed by sonication (5 minutes)

to completely dissolve all the components. Then, 0.5 ml of this solution was drop-casted on a clean glass substrate and was dried at 60 °C for 30 minutes prior to the photophysical studies.

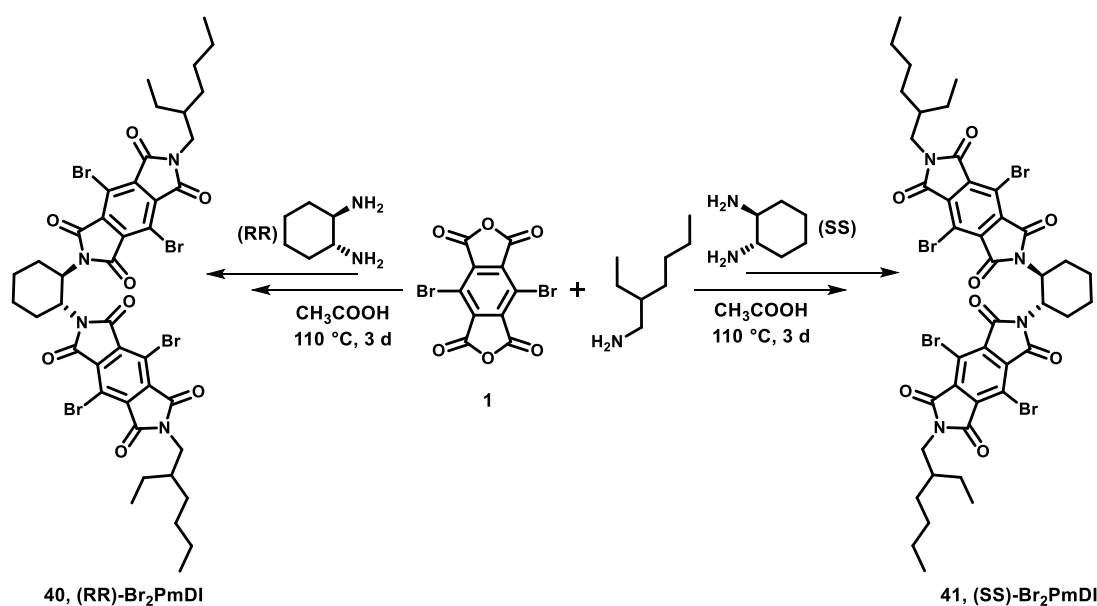
7.1.9. Synthetic Schemes and Procedures:

Materials: Pyromellitic dianhydride (PMDA) and [Bis(trifluoroacetoxy)iodo] benzene (BTI) was purchased from Sigma Aldrich; Durene, *n*-Butylamine and Potassium Permanganate were purchased from Alfa-Aesar; Pyridine, Acetic acid, Bromine and Iodine were purchased from Spectrochem and used without further purification.

Synthetic Scheme:



Scheme 7.1. Synthetic scheme for (RR)-BrPmDI and (SS)-BrPmDI.



Scheme 7.2. Synthetic scheme for (RR)-Br₂PmDI and (SS)-Br₂PmDI.

Synthetic Procedures:

Compound **37** and **1** were synthesized according to literature procedure.^[11]

Synthesis of (RR)-BrPmDI and (SS)-BrPmDI: Compound **37** (250 mg, 0.84 mmol) was taken in a 100 ml round bottom flask and 50 ml of acetic acid was added into it and stirred for 15 minutes at room temperature. Either (S,S)- or (R,R)- enantiomers of diaminocyclohexane (45 mg, 0.42 mmol) was mixed with 10 ml acetic acid and added drop wise into the reaction mixture and stirred at 110 °C for 3 days. The reaction mixture was cooled to room temperature and then 2-ethylhexylamine (109 mg, 0.84 mmol) was mixed with 10 ml acetic acid and added drop wise into the mixture and stirred at 110 °C for additional 12 hours. The completion of the reaction was monitored using thin layer chromatography. Subsequently, the reaction mixture was poured into ice-cold water to get the white precipitate. The solid was filtered and dried under vacuum for 10 hours, and column chromatography was performed using 15 % ethyl acetate in hexane (v/v) as an eluent to get the pure product as white solid.

(RR)-BrPmDI: ¹H NMR (400 MHz, CDCl₃, δ): 8.17-8.04 (b, 2H), 5.02 (d, 2H, *J* = 9.2 Hz), 3.59 (d, 4H, *J* = 7.6 Hz), 2.49 (b, 2H), 1.96-1.94 (m, 4H), 1.81-1.78 (m, 2H), 1.57 (b, 2H), 1.31-1.26 (m, 16H), 0.91-0.85 (m, 12H). ¹³C NMR (100 MHz, CDCl₃, δ): 163.8, 164.5, 164.4, 138.9, 135.0, 116.8, 115.8, 51.8, 42.7, 38.3, 30.5, 28.9, 28.5, 24.8, 23.9, 22.9, 14.0, 10.3; Yield = (67 mg) 9 %; Elemental analysis calculated for C₄₂H₄₆Br₂N₄O₈: C 56.39, H 5.18, N 6.26; found: C 56.63, H 5.37, N 6.29. MALDI-TOF (DCTB matrix, negative mode): m/z calculated for C₄₂H₄₆Br₂N₄O₈: 894.66, found: 894.24 [M]⁺.

(SS)-BrPmDI: ¹H NMR (400 MHz, CDCl₃, δ): 8.16-8.03 (b, 2H), 5.02 (d, 2H, *J* = 9.2 Hz), 3.59 (d, 4H, *J* = 7.2 Hz), 2.48 (b, 2H), 1.96-1.94 (m, 4H), 1.81-1.78 (m, 2H), 1.57-1.54 (b, 2H), 1.31-1.26 (m, 16H), 0.91-0.85 (m, 12H). ¹³C NMR (100 MHz, CDCl₃, δ): 164.9, 164.6, 164.5, 138.9, 134.9, 116.8, 115.8, 51.8, 42.7, 38.3, 34.2, 30.5, 28.5, 24.8, 23.9, 22.9, 22.4, 14.1, 10.4; Yield = (70 mg) 10 %; Elemental analysis calculated for C₄₂H₄₆Br₂N₄O₈: C 56.39, H 5.18, N 6.26; found: C 56.61, H 5.40, N 6.33. MALDI-TOF (DCTB matrix, negative mode): m/z calculated for C₄₂H₄₆Br₂N₄O₈: 894.66, found: 894.06 [M]⁺.

Synthesis of (RR)-Br₂PmDI and (SS)-Br₂PmDI: Compound **1** (310 mg, 0.83 mmol) was taken in a 100 mL round bottom flask and 50 mL of acetic acid was added into it and stirred for 15 minutes at room temperature. Either (SS)- or (RR) enantiomers of

diaminocyclohexane (45 mg, 0.42 mmol) was mixed with 10 ml acetic acid and added drop wise into the reaction mixture and stirred at 110 °C for 3 days. The reaction mixture was cooled to room temperature and then 2-ethyl hexyl amine (107 mg, 0.83 mmol) was mixed with 10 mL acetic acid and added drop wise into the mixture and stirred at 110 °C for 12 hours. The completion of the reaction was monitored by using thin layer chromatography. The reaction mixture was poured into ice-cold water to get the white precipitate. The solid was filtered and dried under vacuum for 10 hours, and column chromatography was performed using 25 % dichloromethane in chloroform (v/v) as an eluent to get the pure product as white solid.

(RR)-Br₂PmDI: ¹H NMR (400 MHz, CDCl₃, δ): 5.03 (d, 2H, *J* = 10 Hz), 3.59 (d, 4H, *J* = 6.8 Hz), 2.48-2.46 (m, 2H), 1.96-1.93 (m, 4H), 1.80-1.79 (m, 2H), 1.52-1.50 (m, 2H), 1.30-1.26 (m, 16H), 0.92-0.89 (m, 12H). ¹³C NMR (CDCl₃, 100 MHz), δ (ppm) = 163.6, 163.1, 136.2, 114.3, 51.9, 42.9, 38.2, 30.5, 29.7, 28.5, 24.8, 23.9, 22.9, 14.0, 10.3; Yield = (100 mg) 12 %; Elemental analysis calculated for C₄₂H₄₄Br₄N₄O₈: C 47.93, H 4.21, N 5.32; found: C 48.13, H 4.35, N 5.63. MALDI-TOF (DCTB matrix, negative mode): *m/z* calculated for C₄₂H₄₄Br₄N₄O₈: 1051.99, found: 1052.84 [M]⁻.

(SS)-Br₂PmDI: ¹H NMR (400 MHz, CDCl₃, δ): 5.03 (d, 2H, *J* = 10 Hz), 3.59 (d, 4H, *J* = 7.2 Hz), 2.48-2.46 (m, 2H), 1.96-1.93 (m, 4H), 1.80-1.79 (m, 2H), 1.52-1.50 (m, 2H), 1.30-1.26 (m, 16H), 0.92-0.88 (m, 12H). ¹³C NMR (CDCl₃, 100 MHz), δ (ppm) = 163.6, 163.1, 136.2, 114.3, 51.9, 42.9, 38.2, 30.5, 29.7, 28.5, 24.8, 23.9, 22.9, 14.0, 10.3; Yield = (95 mg) 11 %; Elemental analysis calculated for C₄₂H₄₄Br₄N₄O₈: C 47.93, H 4.21, N 5.32; found: C 48.11, H 4.32, N 5.43. MALDI-TOF (DCTB matrix, negative mode): *m/z* calculated for C₄₂H₄₄Br₄N₄O₈: 1051.99, found: 1052.33 [M]⁻.

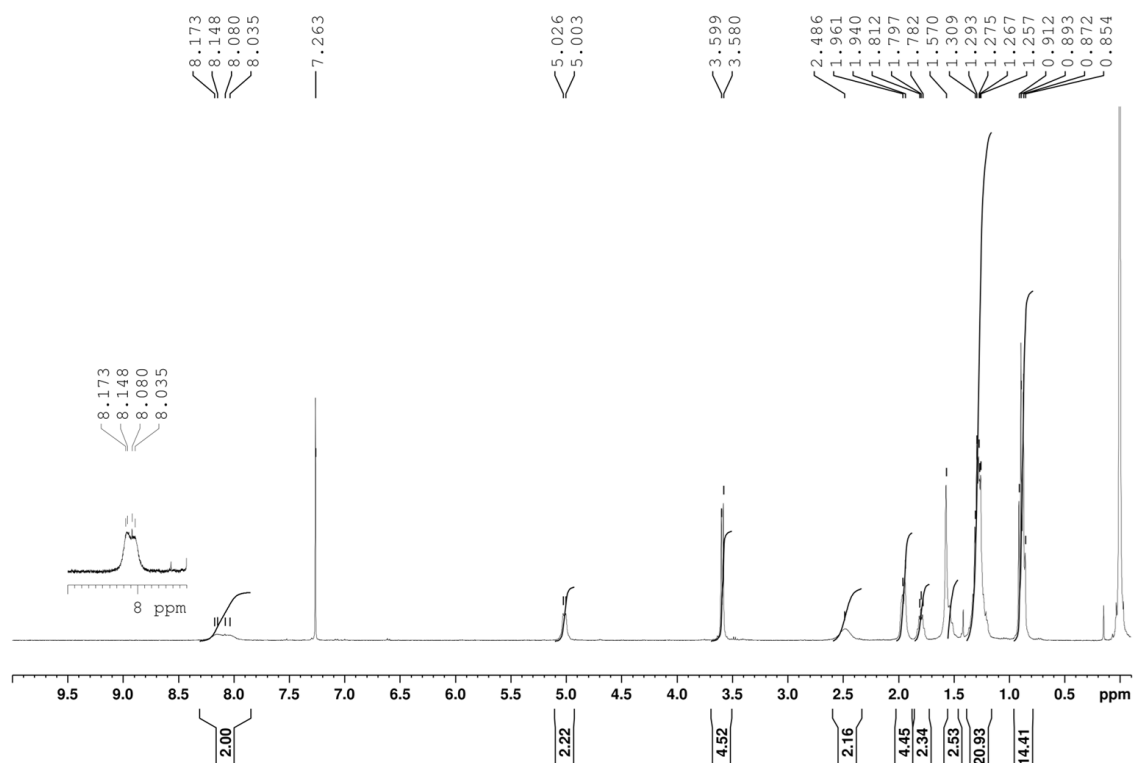


Figure 7.1.13. ¹H NMR spectrum of (RR)-BrPmDI in CDCl₃ at 25 °C.

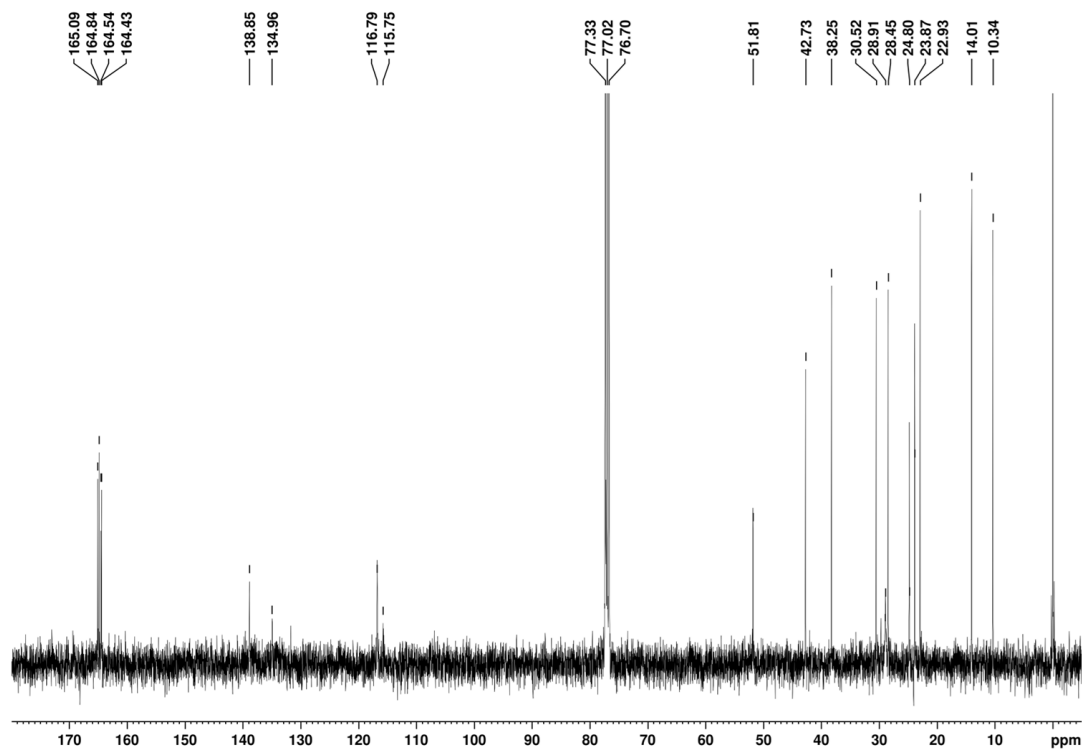


Figure 7.1.14. ¹³C NMR spectrum of (RR)-BrPmDI in CDCl₃ at 25 °C.

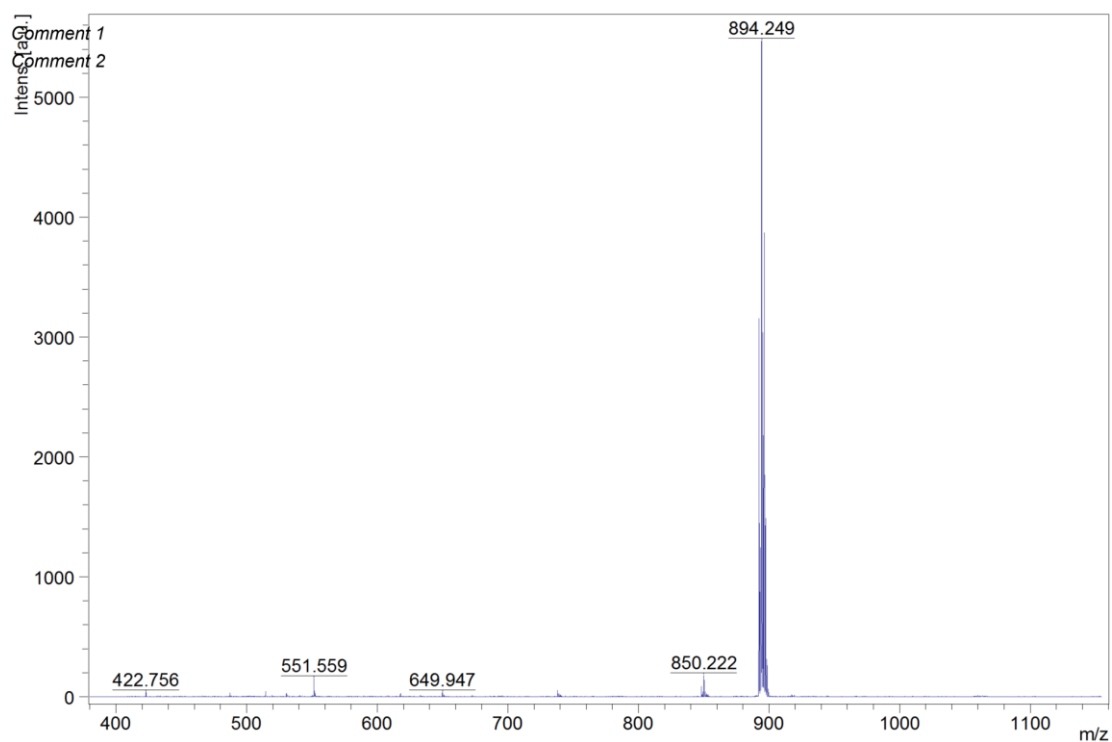


Figure 7.1.15. MALDI spectrum of *(RR)*-BrPmDI in DCTB matrix.

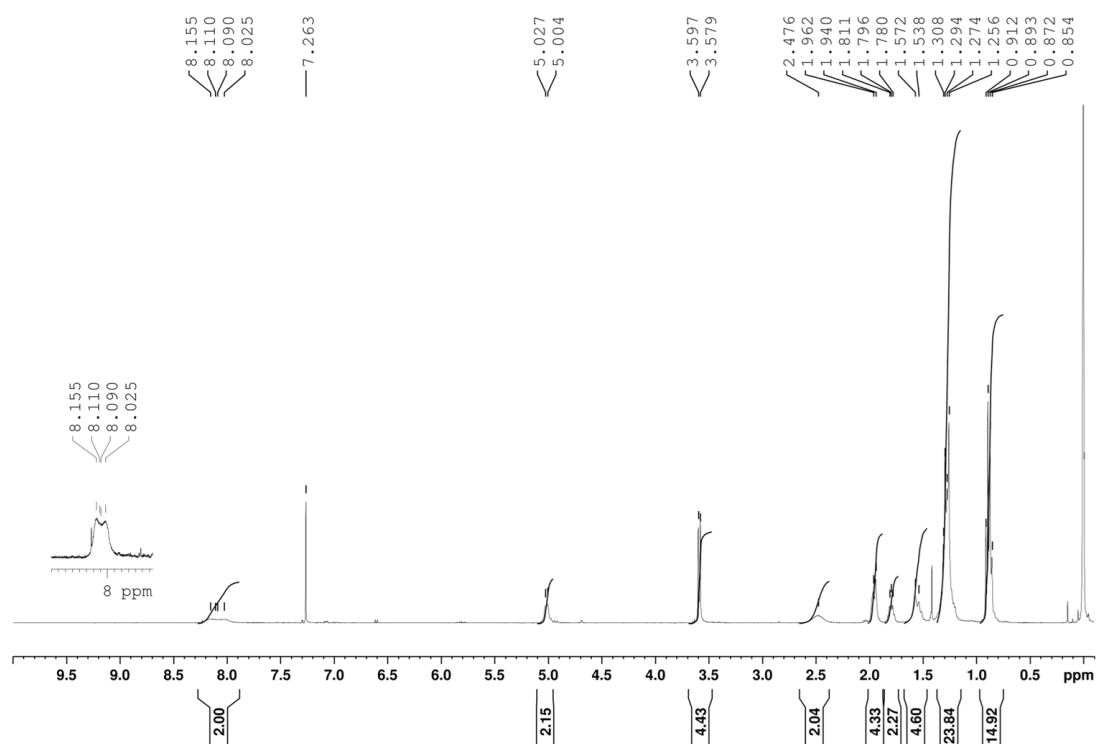


Figure 7.1.16. ^1H NMR spectrum of *(SS)*-BrPmDI in CDCl_3 at $25\text{ }^\circ\text{C}$.

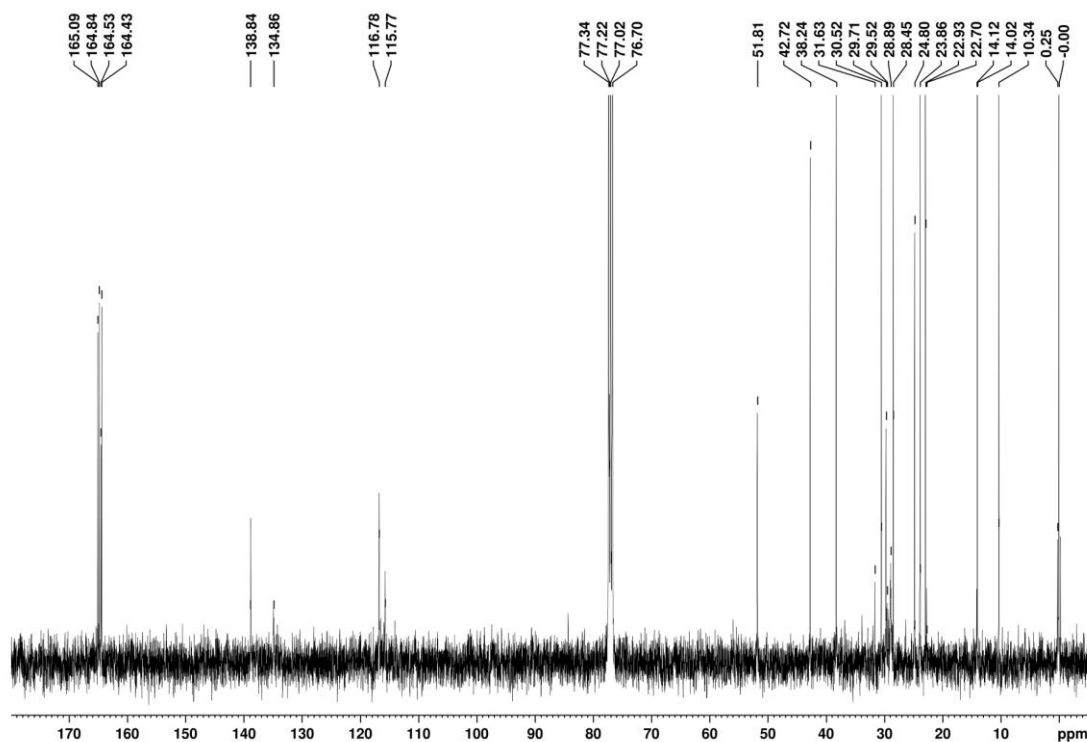


Figure 7.1.17. ^{13}C NMR spectrum of (SS)-BrPmDI in CDCl_3 at 25 °C.

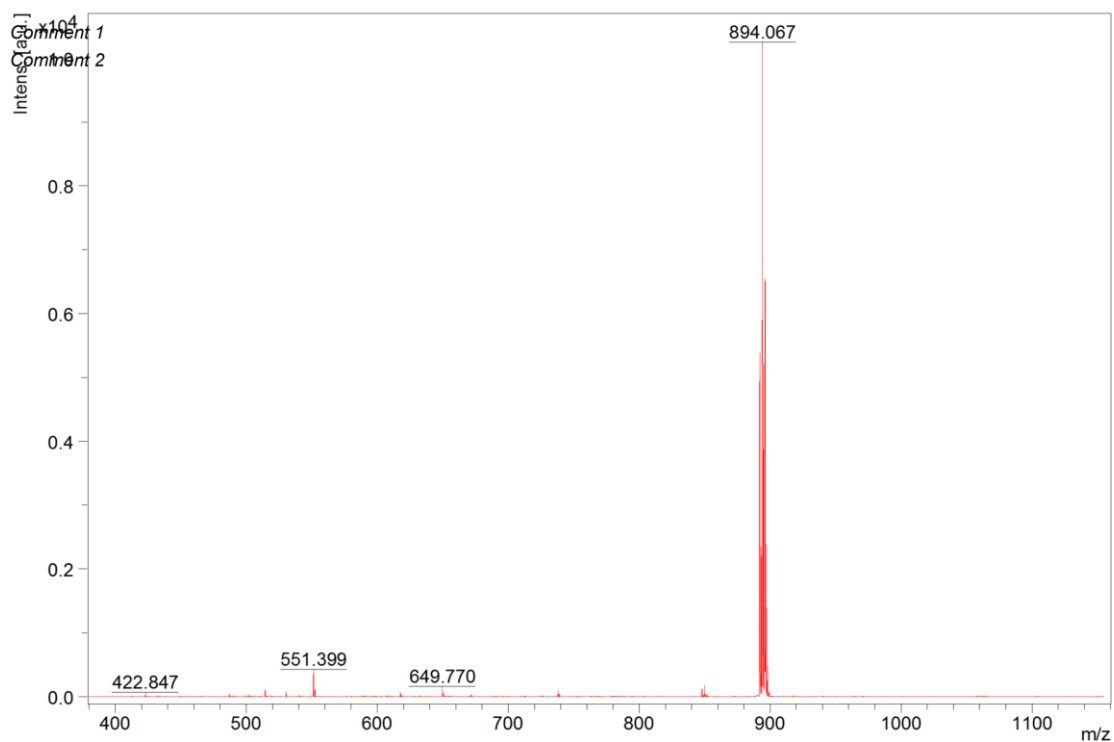


Figure 7.1.18. MALDI spectrum of (SS)-BrPmDI in DCTB matrix.

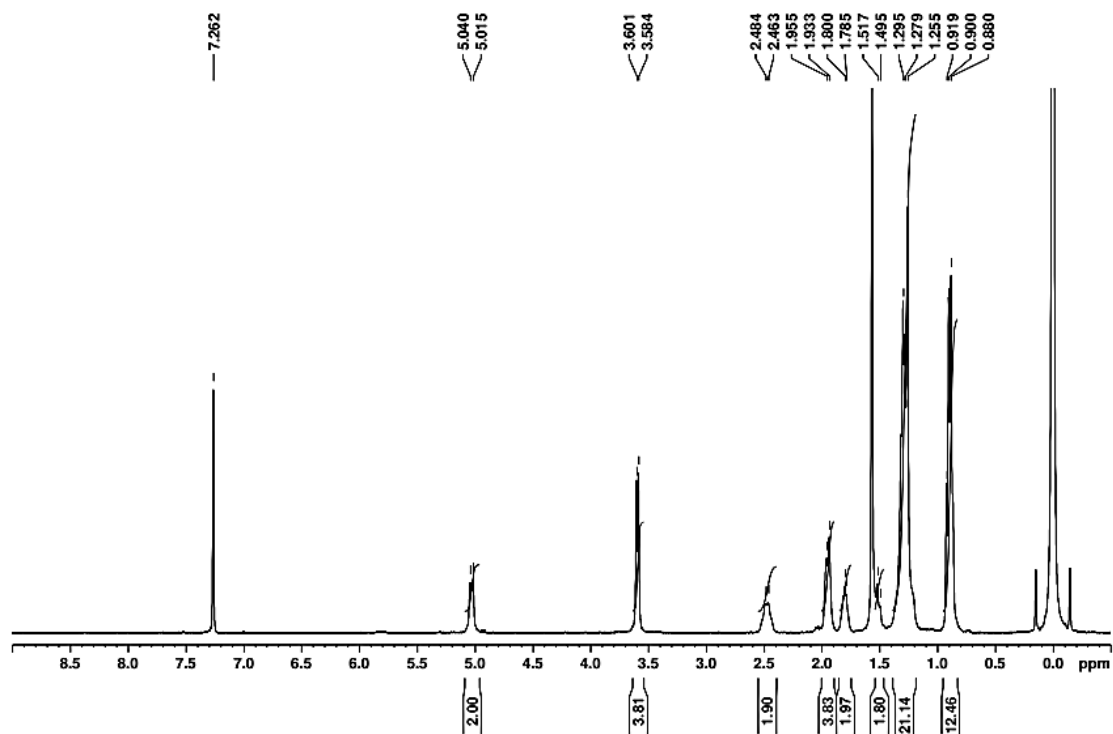


Figure 7.1.19. ^1H NMR spectrum of $(RR)\text{-Br}_2\text{PmDI}$ in CDCl_3 at 25°C .

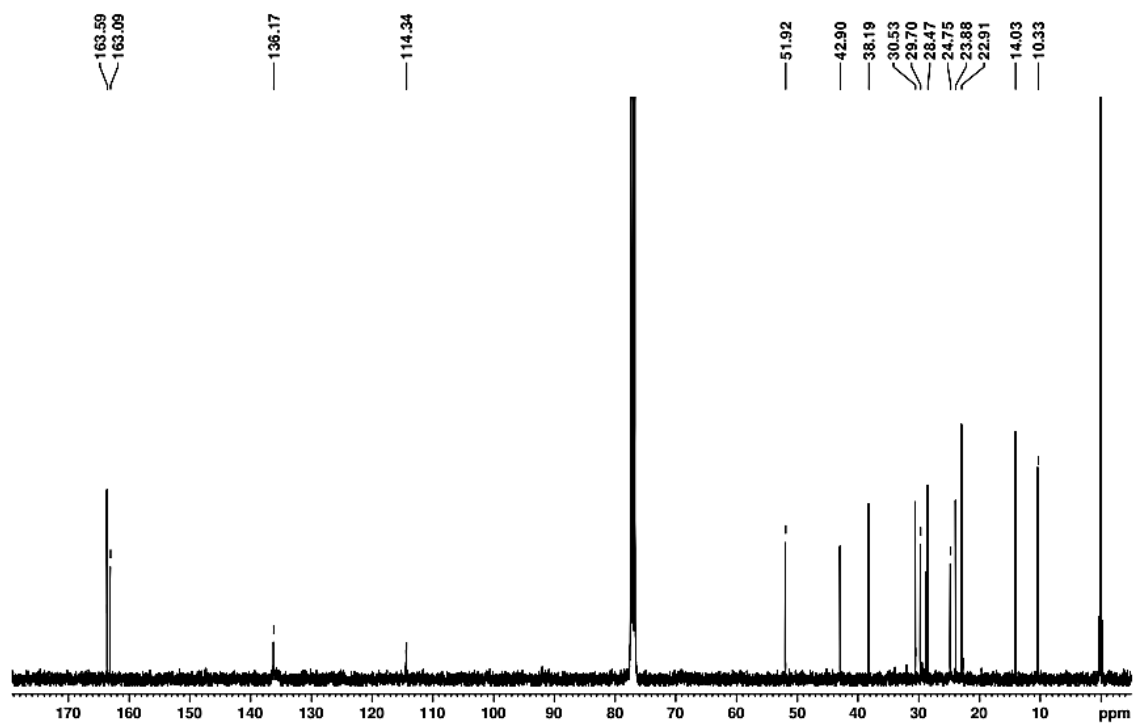


Figure 7.1.20. ^{13}C NMR spectrum of $(RR)\text{-Br}_2\text{PmDI}$ in CDCl_3 at 25°C .

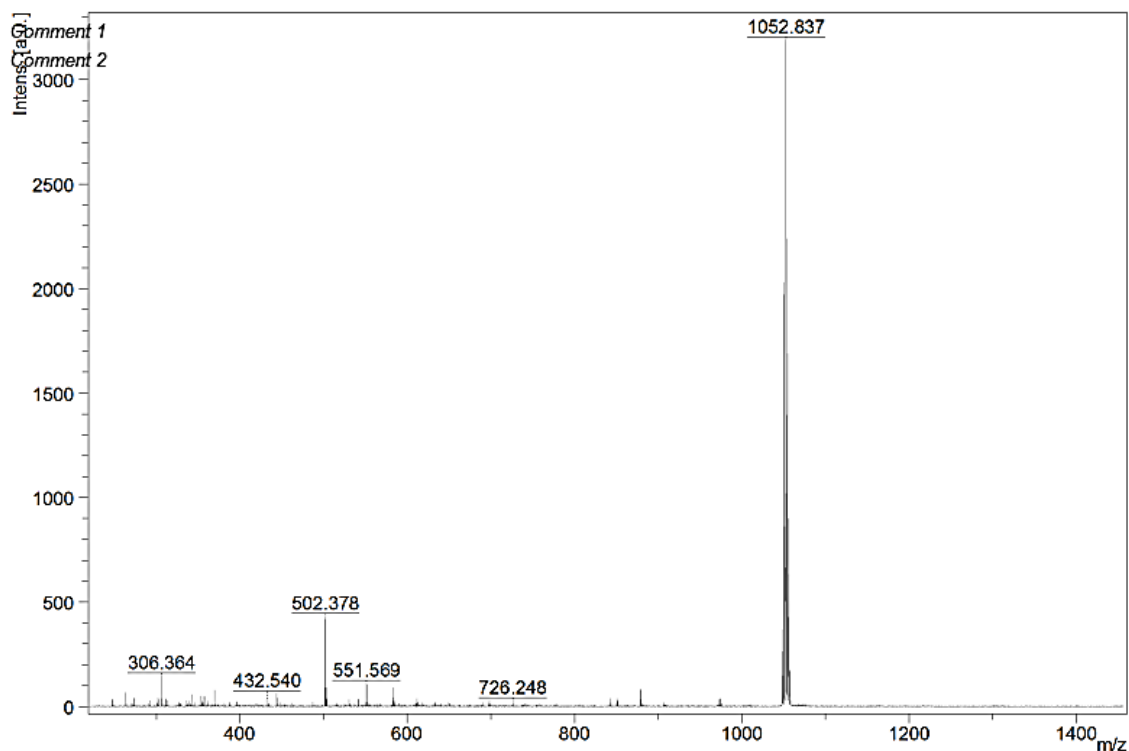


Figure 7.1.21. MALDI spectrum of *(RR)*-Br₂PmDI in DCTB matrix.

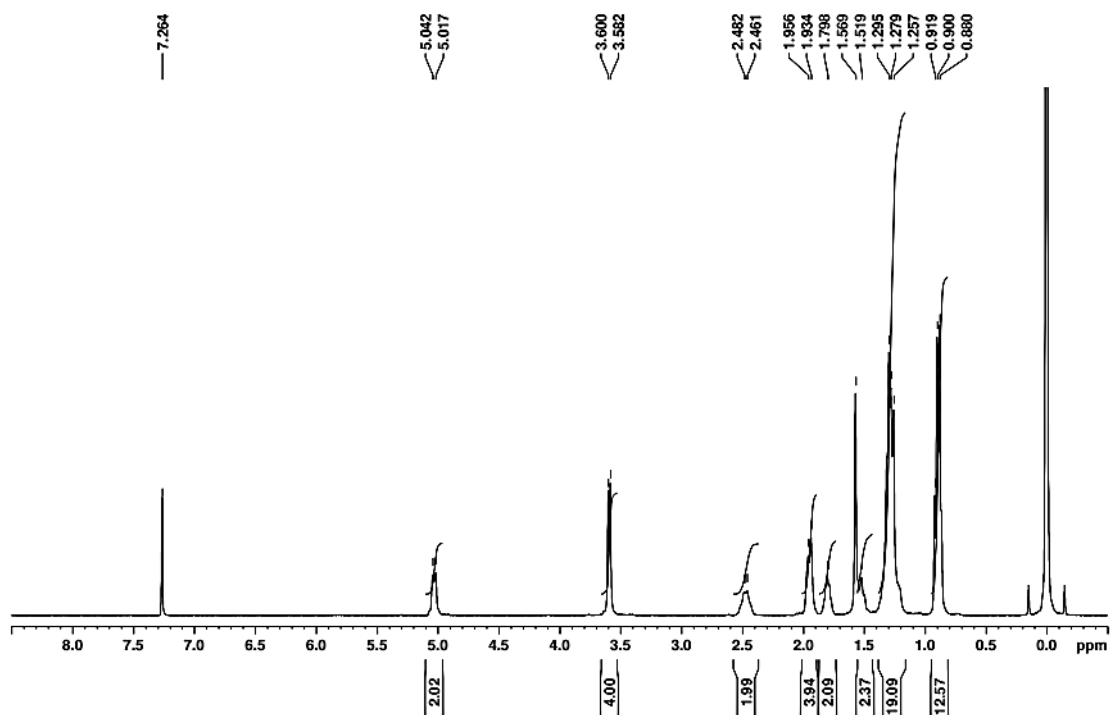


Figure 7.1.22. ¹H NMR spectrum of *(SS)*-Br₂PmDI in CDCl₃ at 25 °C.

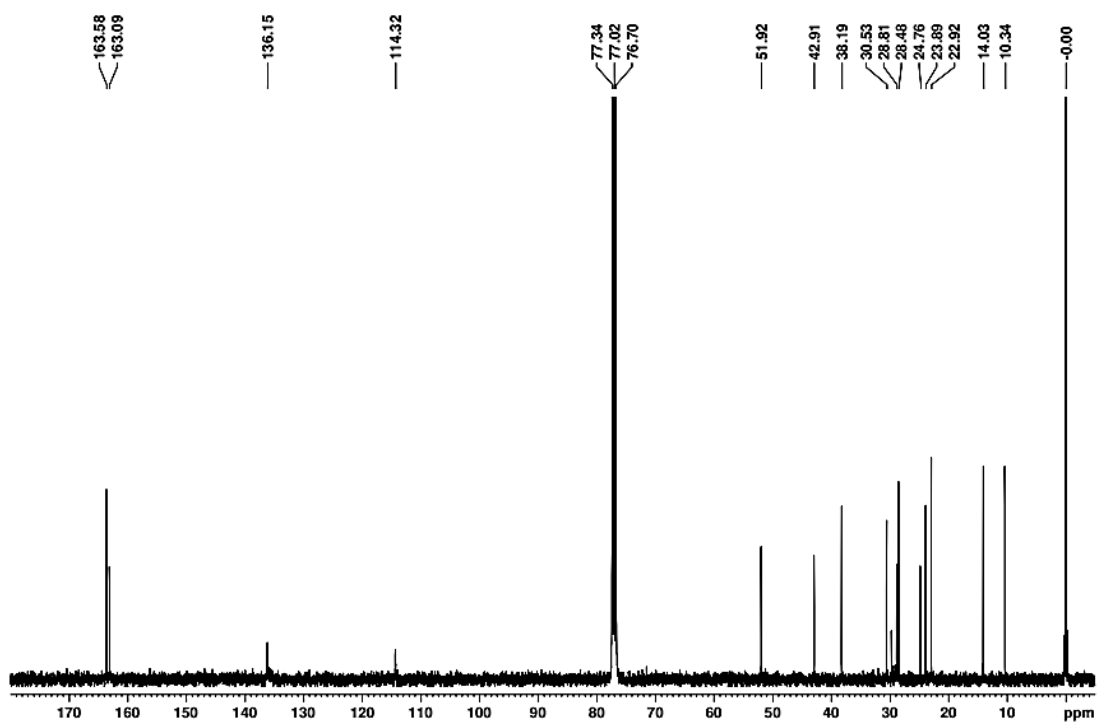


Figure 7.1.23. ^{13}C NMR spectrum of $(RR)\text{-Br}_2\text{PmDI}$ in CDCl_3 at $25\text{ }^\circ\text{C}$.

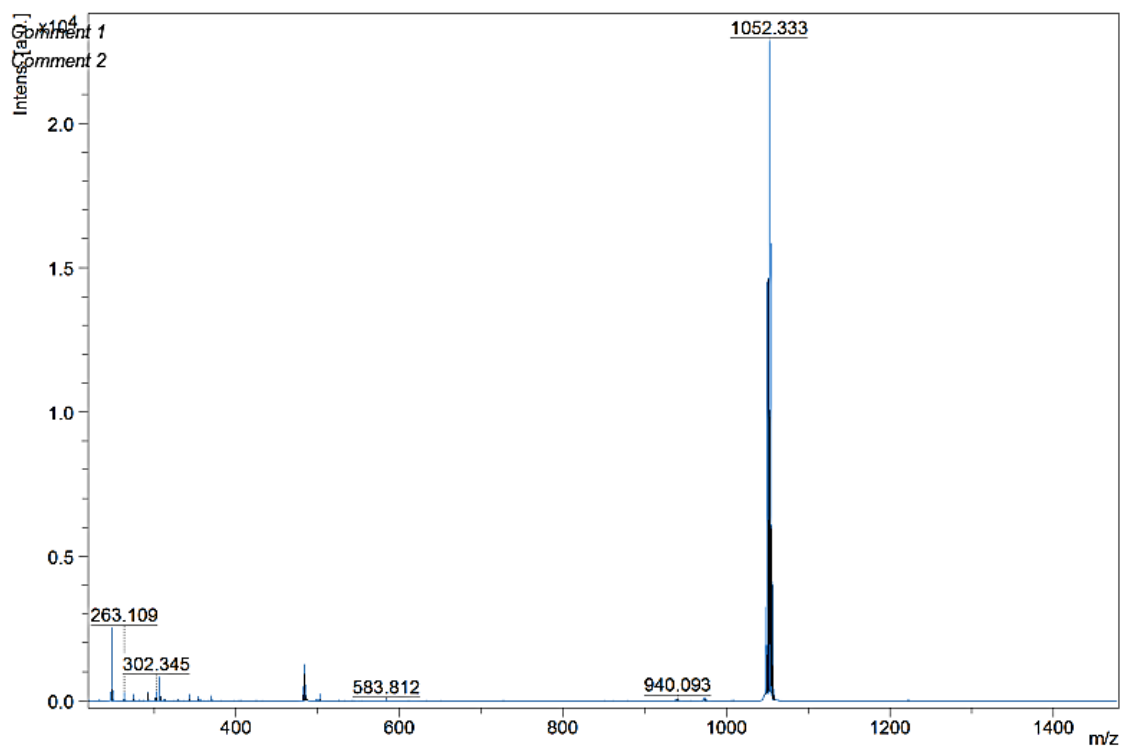


Figure 7.1.24. MALDI spectrum of $(SS)\text{-Br}_2\text{PmDI}$ in DCTB matrix.

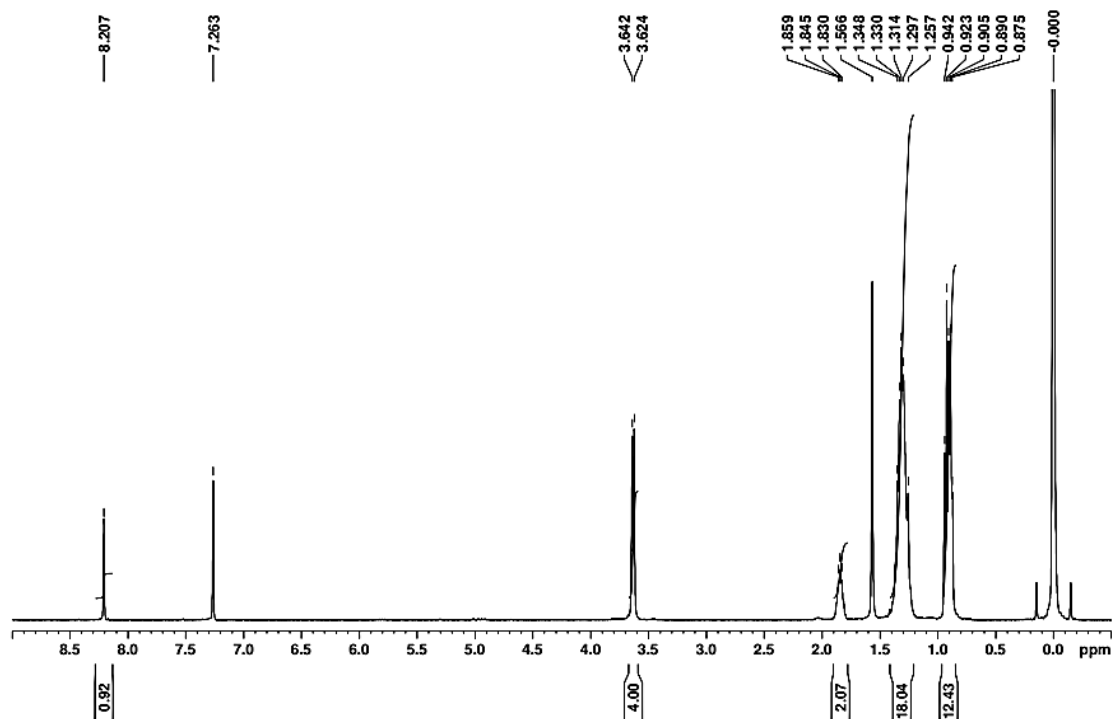


Figure 7.1.25. ^1H NMR spectrum of **BrPmDI** in CDCl_3 at $25\text{ }^\circ\text{C}$.

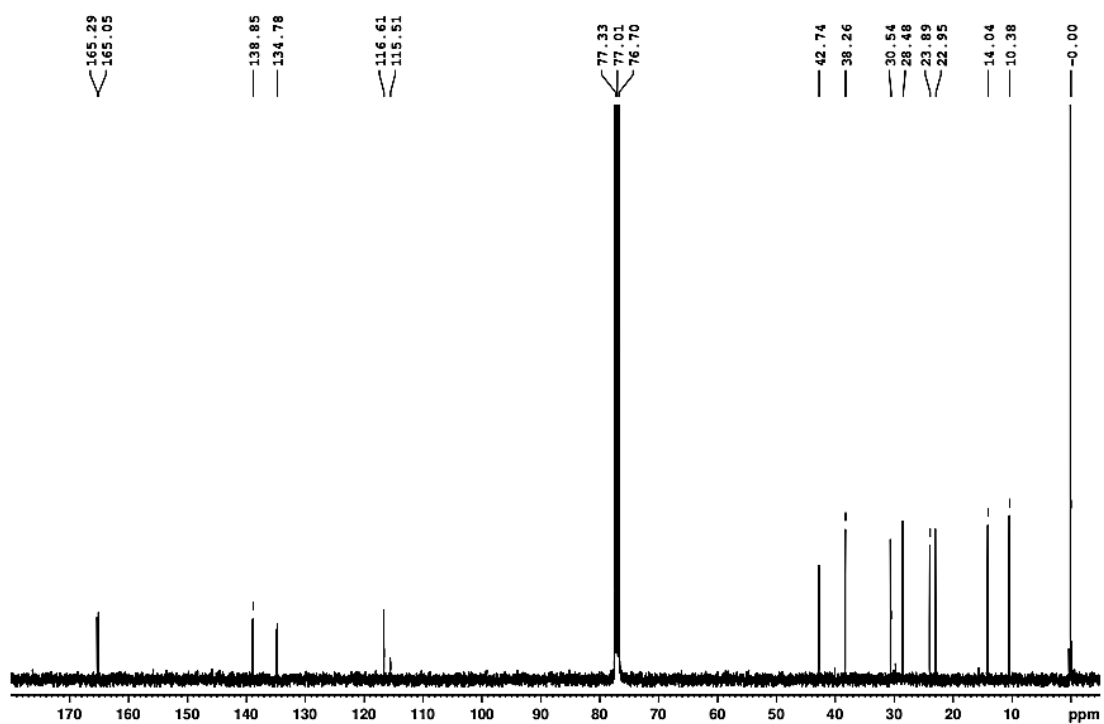


Figure 7.1.26. ^{13}C NMR spectrum of **BrPmDI** in CDCl_3 at $25\text{ }^\circ\text{C}$.

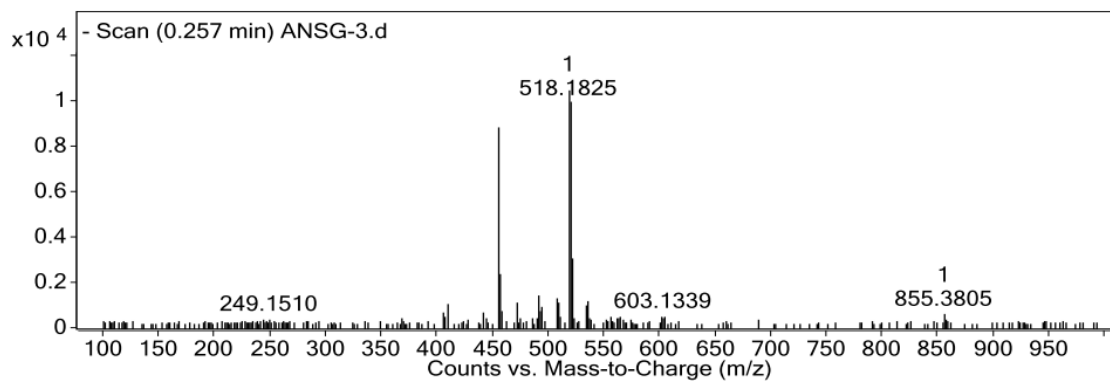


Figure 7.1.27. APCI-HR-MS spectrum of *BrPmDI*.

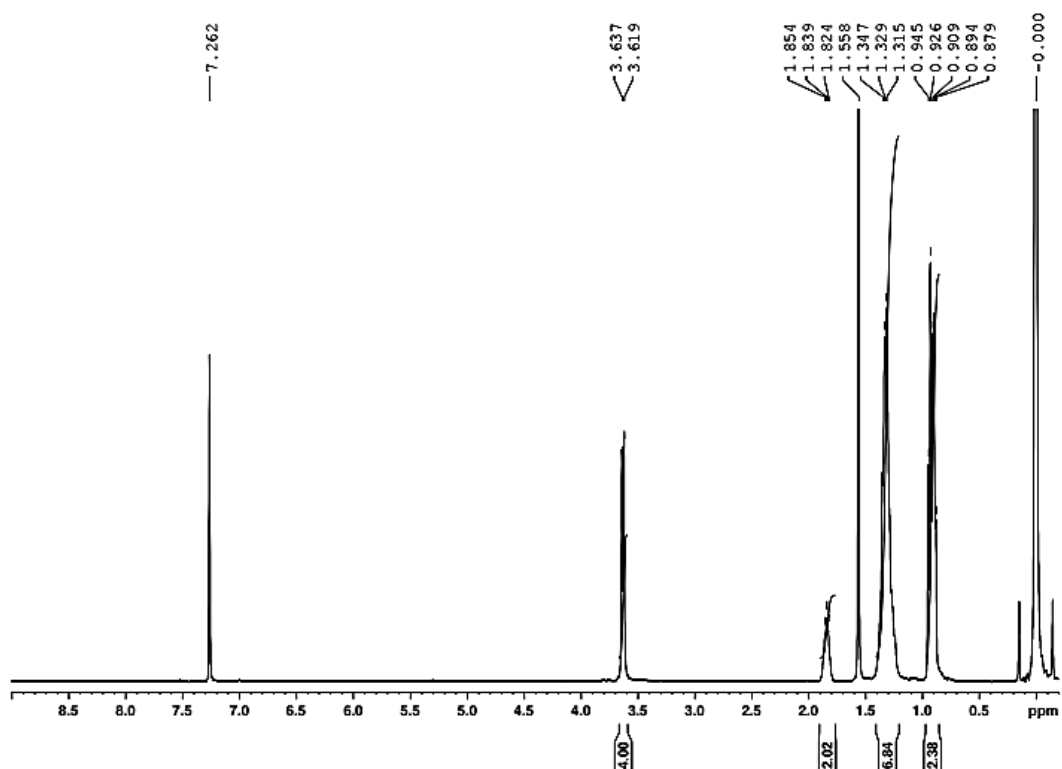


Figure 7.1.28. ¹H NMR spectrum of *Br₂PmDI* in CDCl₃ at 25 °C.

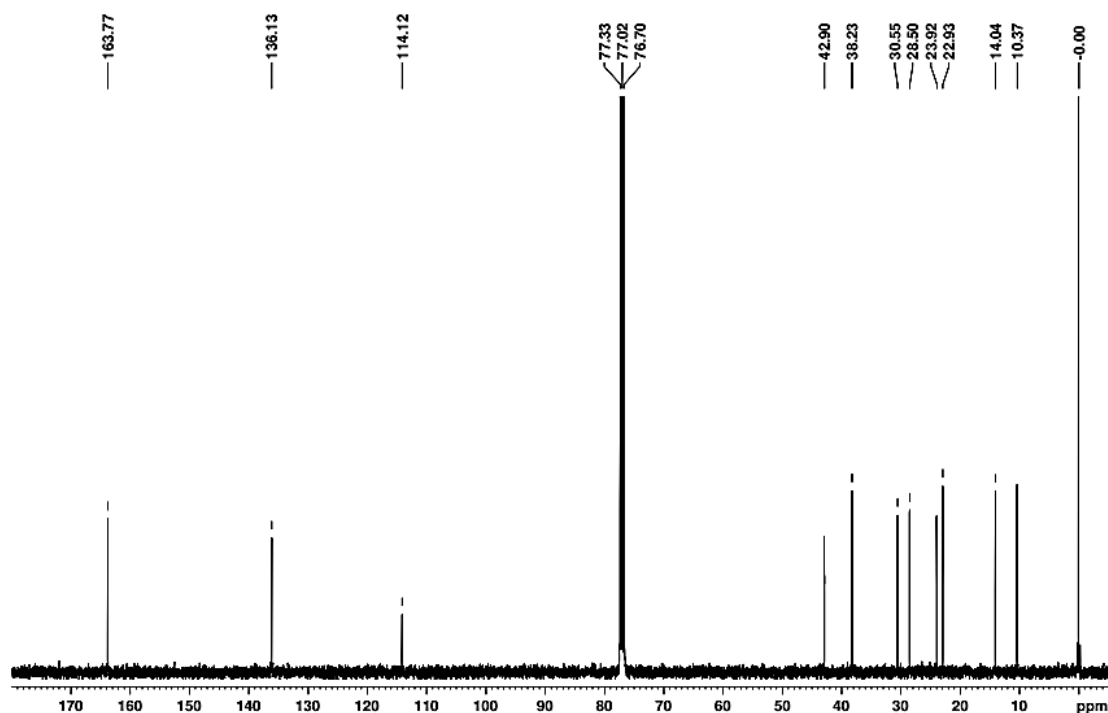


Figure 7.1.29. ^{13}C NMR spectrum of Br_2PmDI in CDCl_3 at $25\text{ }^\circ\text{C}$.

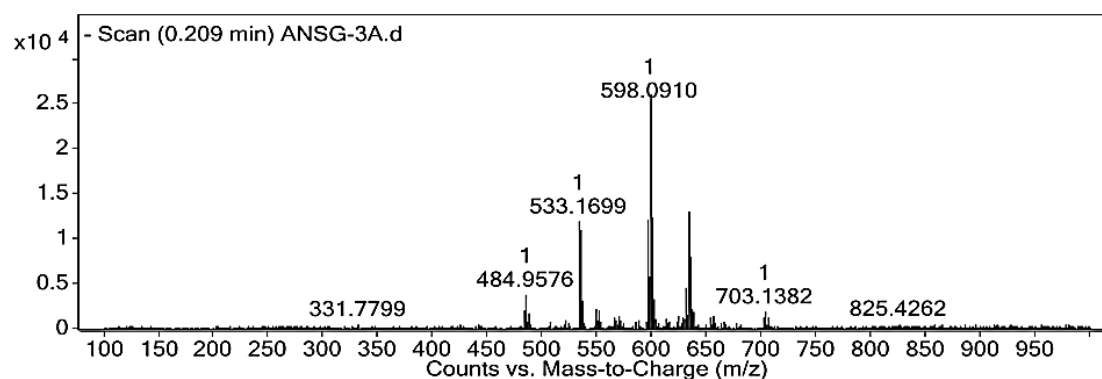


Figure 7.1.30. APCI-HR-MS spectrum of Br_2PmDI .

7.1.10. References:

[1] a) J. Han, S. Guo, H. Lu, S. Liu, Q. Zhao, W. Huang, *Adv. Opt. Mater.* **2018**, *6*, 1800538; b) X. Li, Y. Xie, Z. Li, *Adv. Photonics Res.* **2021**, *2*, 2000136; c) J. Roose, B. Z. Tang, K. S. Wong, *Small* **2016**, *12*, 6495-6512; d) Y. Sang, J. Han, T. Zhao, P. Duan, M. Liu, *Adv. Mater.* **2020**, *32*, 1900110; e) J. Kumar, T. Nakashima, T. Kawai, *J. Phys. Chem. Lett.* **2015**, *6*, 3445-3452; f) Y. Imai, Y. Nakano, T. Kawai, J. Yuasa, *Angew. Chem. Int. Ed.* **2018**, *57*, 8973-8978.

[2] a) J. Kumar, H. Tsumatori, J. Yuasa, T. Kawai, T. Nakashima, *Angew. Chem. Int. Ed.* **2015**, *54*, 5943-5947; b) J. Kumar, T. Nakashima, H. Tsumatori, T. Kawai, *J. Phys.*

Chem. Lett. **2014**, *5*, 316-321; c) S. Sarkar, B. Narayan, S. J. George, *Chem Nano Mat* **2020**, *6*, 1169-1174; d) S. Hu, L. Hu, X. Zhu, Y. Wang, M. Liu, *Angew. Chem. Int. Ed* **2021**, *60*, 19451-19457; e) H. Zhang, J. Han, X. Jin, P. Duan, *Angew. Chem. Int. Ed.* **2021**, *60*, 4575-4580; *Angew. Chem.* **2021**, *133*, 4625-4630; f) S. Zheng, J. Han, X. Jin, Q. Ye, J. Zhou, P. Duan, M. Liu, *Angew. Chem. Int. Ed* **2021**, *60*, 22711-22716; g) E. E. Greciano, R. Rodríguez, K. Maeda, L. Sánchez, *Chem. Commun.* **2020**, *56*, 2244-2247; h) Z. Li, Y. Han, F. Nie, M. Liu, H. Zhong, F. Wang, *Angew. Chem. Int. Ed.* **2021**, *60*, 8212-8219; i) K. Takaishi, K. Iwachido, R. Takehana, M. Uchiyama, T. Ema, *J. Am. Chem. Soc.* **2019**, *141*, 6185-6190; j) K. Takaishi, S. Murakami, K. Iwachido, T. Ema, *Chem. Sci.* **2021**, *12*, 14570-14576; k) J. Wade, J. R. Brandt, D. Reger, F. Zinna, K. Y. Amsharov, N. Jux, D. L. Andrews, M. J. Fuchter, *Angew. Chem. Int. Ed.* **2021**, *60*, 222-227; l) P. Liao, S. Zang, T. Wu, H. Jin, W. Wang, J. Huang, B.Z. Tang, Y. Yan, *Nat. Commun.* **2021**, *12*, 1-9; m) M. Li, S. H. Li, D. Zhang, M. Cai, L. Duan, M. K. Fung, C. F. Chen, *Angew. Chem. Int. Ed.* **2018**, *57*, 2889-2893.

[3] a) W. Zhao, Z. He, J. W. Y. Lam, Q. Peng, H. Ma, Z. Shuai, G. Bai, J. Hao, B. Z. Tang, *Chem* **2016**, *1*, 592-602; b) S. Xu, R. Chen, C. Zheng, W. Huang, *Adv. Mater.* **2016**, *28*, 9920-9940; c) S. Hirata, *Adv. Opt. Mater.* **2017**, *5*, 1700116; d) T. Zhang, X. Ma, H. Wu, L. Zhu, Y. Zhao, H. Tian, *Angew. Chem. Int. Ed.* **2020**, *59*, 11206-11216; e) W. Zhao, Z. He, B. Z. Tang, *Nat. Rev. Mater.* **2020**, *5*, 869-885; f) A. D. Nidhankar, Goudappagouda, V. C. Wakchaure, S. S. Babu, *Chem. Sci.* **2021**, *12*, 4216-4236; g) Q. Li, Y. Tang, W. Hu, Z. Li, *Small* **2018**, *14*, 1801560.

[4] a) W. Z. Yuan, X. Y. Shen, H. Zhao, J. W. Y. Lam, L. Tang, P. Lu, C. Wang, Y. Liu, Z. Wang, Q. Zheng, J. Z. Sun, Y. Ma, B. Z. Tang, *J. Phys. Chem. C* **2010**, *114*, 6090-6099; b) O. Bolton, K. Lee, H.-J. Kim, K. Y. Lin, J. Kim, *Nat. Chem.* **2011**, *3*, 205-210; c) Z. An, C. Zheng, Y. Tao, R. Chen, H. Shi, T. Chen, Z. Wang, H. Li, R. Deng, X. Liu, W. Huang, *Nat. Mater.* **2015**, *14*, 685-690; *130*, 8129-8133; d) A. D. Nidhankar, Goudappagouda, D. S. Mohana Kumari, S. K. Chaubey, R. Nayak, R. G. Gonnade, G. V. P. Kumar, R. Krishnan, S. S. Babu, *Angew. Chem. Int. Ed.* **2020**, *59*, 13079-13085; e) J. Ren, Y. Wang, Y. Tian, Z. Liu, X. Xiao, J. Yang, M. Fang, Z. Li, *Angew. Chem. Int. Ed.* **2021**, *60*, 12335; f) Q. Liao, Q. Gao, J. Wang, Y. Gong, Q. Peng, Y. Tian, Y. Fan, H. Guo, D. Ding, Q. Li, Z. Li, *Angew. Chem. Int. Ed.* **2020**, *59*, 9946-9951; g) Y. Su, Y. Zhang, Z. Wang, W. Gao, P. Jia, D. Zhang, C. Yang, Y. Li, Y. Zhao, *Angew. Chem. Int.*

Ed. **2020**, *59*, 9967-9971; h) Z.-Y. Zhang, W.-W. Xu, W.-S. Xu, J. Niu, X.-H. Sun, Y. Liu, *Angew. Chem. Int. Ed.* **2020**, *59*, 18748-18754; i) Z.-Y. Zhang, Y. Chen, Y. Liu, *Angew. Chem. Int. Ed.* **2019**, *58*, 6028-6032; j) S. Kuila, S. Garain, S. Bandi, S. J. George, *Adv. Funct. Mater.* **2020**, *30*, 2003693; k) S. Kuila, S. J. George, *Angew. Chem. Int. Ed.* **2020**, *59*, 9393-9397; l) D. Li, F. Lu, J. Wang, W. Hu, X.-M. Cao, X. Ma, H. Tian, *J. Am. Chem. Soc.* **2018**, *140*, 1916-1923; m) Z. Li, Y. Han, F. Wang, *Nat. Commun.* **2019**, *10*, 3735; n) J. Xu, A. Takai, Y. Kobayashi, M. Takeuchi, *Chem. Commun.* **2013**, *49*, 8447-8449.

[5] a) W. Hao, Y. Li, M. Liu, *Adv. Optical Mater.* **2021**, 2100452; b) G. Park, H. Kim, H. Yang, K. R. Park, I. Song, J. H. Oh, C. Kim, Y. You, *Chem. Sci.* **2019**, *10*, 1294-1301; c) E. S. Gauthier, L. Abella, N. Hellou, B. Darquie, E. Caytan, T. Roisnel, N. Vanthuyne, L. Favereau, M. Srebro-Hooper, J. A. G. Williams, J. Autschbach, J. Crassous, *Angew. Chem. Int. Ed.* **2020**, *59*, 8394-8400.

[6] a) S. Hirata, M. Vacha, *J. Phys. Chem. Lett.* **2016**, *7*, 1539-1545; b) H. Li, H. Li, W. Wang, Y. Tao, S. Wang, Q. Yang, Y. Jiang, C. Zheng, W. Huang, R. Chen, *Angew. Chem. Int. Ed.* **2020**, *59*, 4756-4762; c) W. Chen, Z. Tian, Y. Li, Y. Jiang, M. Liu, P. Duan, *Chem. Eur. J.* **2018**, *24*, 17444-17448; d) L. Gu, W. Ye, X. Liang, A. Lv, H. Ma, M. Singh, W. Jia, Z. Shen, Y. Guo, Y. Gao, H. Chen, D. Wang, Y. Wu, J. Liu, H. Wang, Y.-X. Zheng, Z. An, W. Huang, Y. Zhao, *J. Am. Chem. Soc.* **2021**, doi: 10.1021/jacs.1c08118; e) R. Liu, B. Ding, D. Liu, X. Ma, *Chem. Eng. J.*, **2021**, *421*, 129732; f) M. Xu, X. Wu, Y. Yang, C. Ma, W. Li, H. Yu, Z. Chen, J. Li, K. Zhang, S. Liu, *ACS Nano* **2020**, *14*, 11130-11139.

[7] a) M. de Loos, J. van Esch, R. M. Kellogg, B. L. Feringa, *Angew. Chem. Int. Ed.* **2001**, *40*, 613-616; b) B. Narayan, K. K. Bejagam, S. Balasubramanian, S. J. George, *Angew. Chem. Int. Ed.* **2015**, *54*, 13053-13057; c) A. Sarkar, S. Dhiman, A. Chalishazar, S. J. George, *Angew. Chem. Int. Ed.* **2017**, *56*, 13767-13771; d) S. Sarkar, A. Sarkar, S. J. George, *Angew. Chem. Int. Ed.* **2020**, *59*, 19841-19845; e) S. Sarkar, A. Sarkar, A. Som, S. S. Agasti, S. J. George, *J. Am. Chem. Soc.*, **2021**, *143*, 11777-11787.

[8] a) S. Garain, S. Kuila, B. C. Garain, M. Kataria, A. Borah, S. K. Pati, S. J. George, *Angew. Chem. Int. Ed.* **2021**, *60*, 12323-12327; b) S. Kuila, K. V. Rao, S. Garain, P. K. Samanta, S. Das, S. K. Pati, M. Eswaramoorthy, S. J. George, *Angew. Chem. Int. Ed.* **2018**, *57*, 17115-17119; c) S. Garain, B. C. Garain, M. Eswaramoorthy, S. K. Pati, S. J.

George, *Angew. Chem. Int. Ed.* **2021**, *60*, 19720-19724, d) S. Kuila, S. Garain, G. Banappanavar, B. C. Garain, D. Kabra, S. K. Pati, S. J. George, *J. Phys. Chem. B* **2021**, *125*, 4520-4526.

[9] a) D. Cao, M. Hong, A. K. Blackburn, Z. Liu, J. M. Holcroft, J. F. Stoddard, *Chem. Sci.* **2014**, *5*, 4242-4248. b) K. Kanosue, S. Ando, *ACS Macro Lett.* **2016**, *5*, 1301-1305.

[10] a) Gaussian 16, Revision A.03, M. J. Frisch, G. W. Trucks, H. B. Schlegel, G. E. Scuseria, M. A. Robb, J. R. Cheeseman, G. Scalmani, V. Barone, G. A. Petersson, H. Nakatsuji, X. Li, M. Caricato, A. V. Marenich, J. Bloino, B. G. Janesko, R. Gomperts, B. Mennucci, H. P. Hratchian, J. V. Ortiz, A. F. Izmaylov, J. L. Williams; F. Ding; F. Lipparini, F. Egidi, J. Goings, B. Peng, A. Petrone, T. Henderson, D. Ranasinghe, V. G. Zakrzewski, J. Gao, N. Rega, G. Zheng, W. Liang, M. Hada, M. Ehara, K. Toyota, R. Fukuda, J. Hasegawa, M. Ishida, T. Nakajima, Y. Honda, O. Kitao, H. Nakai, T. Vreven, K. Throssell, J. A. Montgomery Jr., J. E. Peralta, F. Ogliaro, M. J. Bearpark, J. J. Heyd, E. N. Brothers, K. N. Kudin, V. N. Staroverov, T. A. Keith, R. Kobayashi, J. Normand, K. Raghavachari, A. P. Rendell, J. C. Burant, S. S. Iyengar, J. Tomasi, M. Cossi, J. M. Millam, M. Klene, C. Adamo, R. Cammi, J. W. Ochterski, R. L. Martin, K. Morokuma, O. Farkas, J. B. Foresman, D. J. Fox, Gaussian, Inc., Wallingford CT, **2016**; b) A. D. Becke, *J. Chem. Phys.* **1993**, *98*, 1372; c) C. Lee, W. Yang, R. G. Parr, *Phys. Rev. B* **1988**, *37*, 785; d) B. Miehlich, A. Savin, H. Stoll, H. Preuss, *Chem. Phys. Lett.* **1989**, *157*, 200; e) T. Yanai, D. P. Tew, N. C. Handy, *Chem. Phys. Lett.* **2004**, *393*, 1-3. f) A. D. Becke, *J. Chem. Phys.* **1993**, *98*, 1372-1377; g) S. Hirata, M. Head-Gordon, *Chem. Phys. Lett.* **1999**, *314*, 291; h) E. van Lenthe, R. Van Leeuwen, E. J. Baerends, *Int. J. Quant. Chem.* **1996**, *57*, 281; i) E. van Lenthe, J. G. Snijders, E. J. Baerends, *J. Chem. Phys.* **1996**, *105*, 6505; j) F. Wang, T. Ziegler, E. van Lenthe, S. van Gisbergen, E. J. Baerends, *J. Chem. Phys.* **2005**, *122*, 204103; k) ADF2017, SCM, *Theoretical Chemistry*, Vrije Universiteit, Amsterdam, The Netherlands, <http://www.scm.com>.

[11] a) D. Cao, M. Hong, A. K. Blackburn, Z. Liu, J. M. Holcroft, J. F. Stoddard, *Chem. Sci.* **2014**, *5*, 4242-4248; b) S. Garain, S. Kuila, B. C. Garain, M. Kataria, A. Borah, S. K. Pati, S. J. George, *Angew. Chem. Int. Ed.* **2021**, *60*, 12323-12327; c) K. Kanosue, S. Ando, *ACS Macro Lett.* **2016**, *5*, 1301.

CHAPTER 7.2

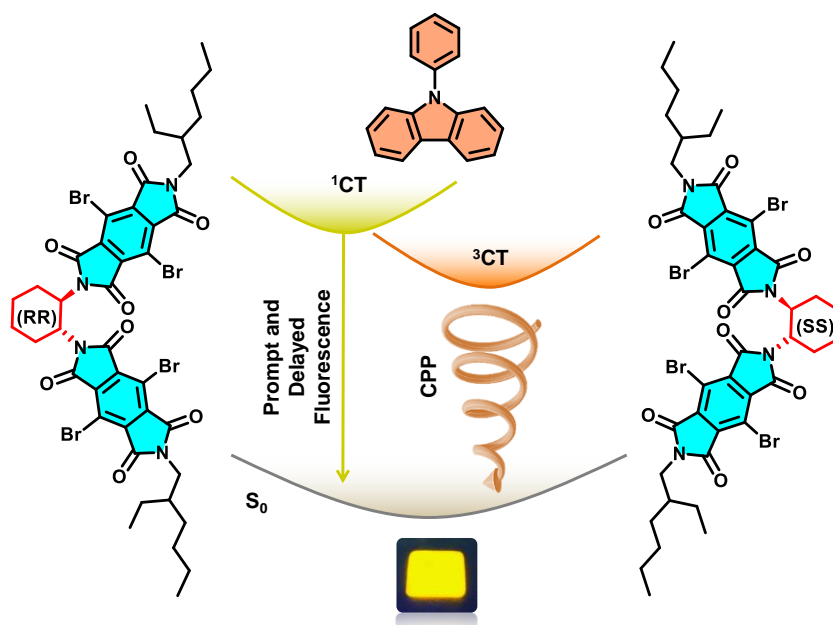
Circularly Polarized Room Temperature Phosphorescence from Charge-Transfer State Via Non-covalent Donor- Acceptor Approach

CHAPTER 7.2

Circularly Polarized Room Temperature Phosphorescence from Charge-Transfer State Via Non-covalent Donor- Acceptor Approach*

Abstract

Achieving phosphorescence from long-lived CT states via intermolecular donor-acceptor molecular design is challenging. In this chapter, we are presenting CPP from triplet CT state. To realize the CPP from ^3CT state, we used a bis-chromophoric molecular design with *trans*-1,2-diaminocyclohexane chiral core and heavy bromo substituted pyromellitic diimides phosphor as acceptor and phenyl carbazole as an achiral donor. The resultant, solution-processable films exhibit the most efficient CPP emission with high phosphorescence quantum yield ($\sim 40\%$ in air) and significant luminescence dissymmetry factor ($|g_{\text{lum}}| \sim 1.5 \times 10^{-2}$). We hypothesized that CT-based intermolecular donor-acceptor molecular design helps us to achieve efficient CPP with high $|g_{\text{lum}}|$ value.



*Manuscript based on this work is under preparation.

7.2.1. Introduction:

Efficient circularly polarized luminescence (CPL) materials are important in the optoelectronic community due to their several applications in flat panel 3D technology, chiral sensing, spintronics, optical imaging, and photoelectric devices.^[1] Also, CPL emitters are in the front of CP light-emitting diodes (CPLEDs) as they can reduce the reflectance from the surrounding without a polarizer and quarter waveplate.^[1] However, most of the CPL active materials are organometallic lanthanide complexes, as they have high luminescence dissymmetry factor ($|g_{lum}|$), due to large the magnitudes of magnetic transition moments.^[1h,k] Although there are several reports of CPL active small organic molecules, most are fluorescence emitters and show low $|g_{lum}|$ due to their low magnetic and high electric dipole transition moments.^[1h] In this regard, scientific community is eagerly trying to increase the $|g_{lum}|$ value further via different strategies like Up-conversion,^[2a] Förster resonance energy transfer (FRET),^[2b-d] and charge-transfer (CT)^[2e-f] for further advancement of the field. However, triplet harvesters having CPL emission is an efficient progress nowadays in the optoelectronic realm as 100 % internal quantum efficiency could be achieved theoretically.^[3] In this regard, CPL active TADF materials are growing very fast; however, most of them are efficient under inert conditions, and also, their emission is dominated by prompt fluorescence.^[4] Hitherto achieving efficient solution-processable organic phosphor is still difficult and is an active research area nowadays due to their potential to replace the unstable toxic organometallic phosphors.^[5,6] However, CPL active purely organic phosphors are rare and seldom reported,^[7] as they require an elegant molecular design strategy consisting of efficient phosphor with a strong chiral induction motif. Although there are a few reports of purely organic circularly polarized phosphorescence (CPP), they all suffer from meager quantum efficiency and low $|g_{lum}|$ value.^[7] In this regard, our group made a significant contribution to the field of organic phosphors using novel arylene diimides,^[8] especially pyromellitic diimides.^[9] This smallest member of arylene diimide received attention till date for being used in electron-deficient semiconductors.^[10] Although, we have utilized these pyromellitic diimides as efficient triplet harvesters and processable circularly polarized phosphorescence (CPP) emitter in PMMA matrix with $|g_{lum}|$ of 4×10^{-3} .^[9c] However, efficient CPP emission with high quantum yield and high $|g_{lum}|$ is required to advance the field further.

This chapter presents efficient CPP emission from a charge-transfer triplet (^3CT) state with a high $|g_{\text{lum}}|$ value to alleviate this scenario and we have achieved efficient CT phosphorescence with a very high quantum yield of 40 % in air. Further, excited state chiroptical properties reveal the highest efficient CPP emitter with $|g_{\text{lum}}|$ of 1.5×10^{-2} , which is the first report of the CPP from the triplet CT state till date.

7.2.2. Molecular Design:

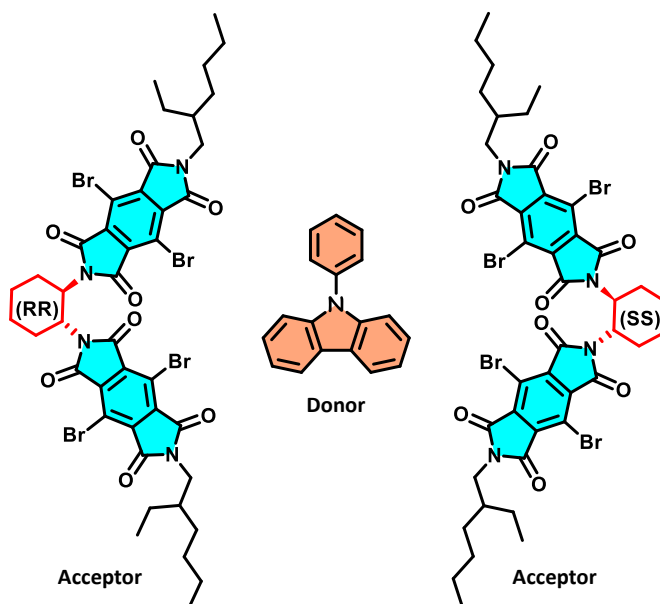


Figure 7.2.1. Molecular structure of *(RR)/(SS)-Br₂PmDI* (acceptor) and *CzPh* (donor).

Recently our group came up with a novel ^3CT phosphorescence concept via a non-covalent donor-acceptor strategy where heavy-atom substituted donor or acceptor is essential for significant spin-orbit coupling between singlet and triplet CT state (chapter 6). To achieve the CPP from the CT state, we have used our bis-chromophoric molecular design with trans-1,2-diaminocyclohexane chiral core with heavy bromo substituted pyromellitic diimides phosphor (*(RR)/(SS)-Br₂PmDI*) as an acceptor and achiral phenyl carbazole (*CzPh*) as a donor (Figure 7.2.1). We envisage the formation of CT interaction between donor and acceptor with significant enhancement of $|g_{\text{lum}}|$ value by decreasing electrical transition dipole moment and increasing magnetic transition dipole moment.^[2e,f]

7.2.3. Formation of CT Complex:

First, we have mixed the donor-acceptor molecules in a 2:1 molar ratio in chloroform, and observed a significant color change from a colorless solution of the donor and acceptor to brown color of the mixture solution at a very high concentration ($[c] = 0.1$ mM) (Figure 7.2.2a). The results indicate mutual CT interaction between donor and acceptor. We have further probed the CT interaction by ^1H NMR experiments where significant up-field shift of the donor aromatic proton was observed, which justifies the CT interaction between **(RR)-Br₂PmDI** and **CzPh** (Figures 7.2.2b,c). However, the CT state is non-emissive in nature in the solution state.

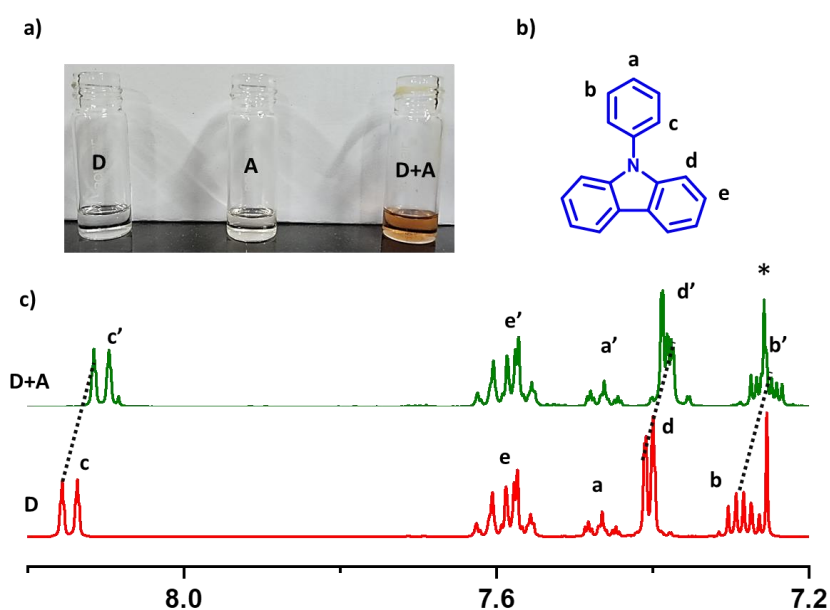


Figure 7.2.2. a) Photographs of **(RR)-Br₂PmDI** (A), **CzPh** (D) and **D-A** pair in CHCl_3 . b) Molecular structure of **D**. c) Partial ^1H NMR spectra (aromatic region) of **D** (red line) and 2:1 molar ratio of **D+A** pair (400 MHz, CDCl_3) ($[c] = 0.1$ M).

7.2.4. Spectroscopic Studies in Thin Films: Formation of ^3CT state:

We have spin-coated the 2:1 molar ratio of **D-A** on a clean quartz slide to harvest the triplets. Interestingly, we observed red-shifted band formation in the excitation spectra compared to the individual **D** and **A** (**D** and **A** doped in the PMMA matrix at very low concentration, $\lambda_{\text{monitored}} = 500$ nm for individual **D** and **A** and $\lambda_{\text{monitored}} = 600$ nm for **D-A** pair) due to the formation of the CT complex (Figure 7.2.3a). Corresponding emission spectra show a broad emission band with a maximum of 590 nm ($\lambda_{\text{exc.}} = 340$ nm) (Figure 7.2.3b). The CT nature of the orange emission is proved by the selective excitation at the

red-shifted band in the excitation spectra ($\lambda_{\text{exc.}} = 480$ nm) that showed the same spectral features similar to excitation at the LE band ($\lambda_{\text{exc.}} = 340$ nm) (Figure 7.2.3b). Further time-resolved emission decay experiments showed an average lifetime of 0.88 μs , hinting towards the triplet contribution to the emission ($\lambda_{\text{exc.}} = 405$ nm, $\lambda_{\text{collected}} = 600$ nm) (Figure 7.2.3c). The triplet contribution of the delayed emission is further confirmed by performing the emission and lifetime decay measurement in the absence of oxygen (Figures 7.2.3c,d). Significant increment of the emission intensity (3.4x fold) and lifetime (from 0.88 μs to 1.13 μs) under vacuum compared to air attested triplet contribution to the total delayed emission (Figures 7.2.3c,d). However, to understand the delayed nature of the emission, we have performed a temperature-dependent study (Figures 7.2.3e,f). Intensified emission and prolonged lifetime upon decreasing the temperature suggested the phosphorescence nature of the delayed emission (Figures 7.2.3e,f). The formation of the CT band in the excitation spectra of the **D-A** complex assuaged us to investigate the CT nature of the orange phosphorescence (^3CT) emission. To understand the LE or CT phosphorescence nature in detail, we have studied the individual donor and acceptor doped in the PMMA matrix at very low concentration (1wt.% with respect to PMMA). However, increasing the emission intensity and lifetime upon decreasing the temperature for both processable polymer films of donor and acceptor suggests the phosphorescence nature of the emission (Figure 7.2.4a-d). Further, the sharp vibrational of the emission for both donor and acceptor attested to the LE phosphorescence nature of the emission (Figures 7.2.4a,d). It is very interesting to mention here that the phosphorescence emission of the donor-acceptor pair is highly red-shifted ($\lambda_{\text{max.}} = 590$ nm) compared to the individual donor ($\lambda_{\text{max.}} = 441$ nm) and acceptor ($\lambda_{\text{max.}} = 500$ nm) confirmed the CT phosphorescence of the donor-acceptor pair (Figure 7.2.4e). Further, time-resolved emission experiments suggest the exclusive formation of the ^3CT state in the phosphorescence emission as there is no change in the spectral maximum upon time evolution ($\lambda_{\text{exc.}} = 480$ nm) (Figure 7.2.4f). The absolute phosphorescence quantum yield is measured to be 40 % for the **D-A** pair. We hypothesize the presence of delayed contribution to the total emission due to the proximity of the ^1CT and ^3CT states (Figures 7.2.5a,b). It is noteworthy that, when we made a closer look into the temperature-dependent lifetime decay profile, we found a small TADF emission contribution (Figure 7.2.5b). There is a decrease in the lifetime decay component upon increasing temperature attested to TADF contribution to the total emission (Figure 7.2.5b). A similar

phosphorescence emission and lifetime decay was observed for the 2:1 molar ratio of **D** (**CzPh**)-**A** ((**SS**)-**Br₂PmDI**) (Figure 7.2.5c,d).

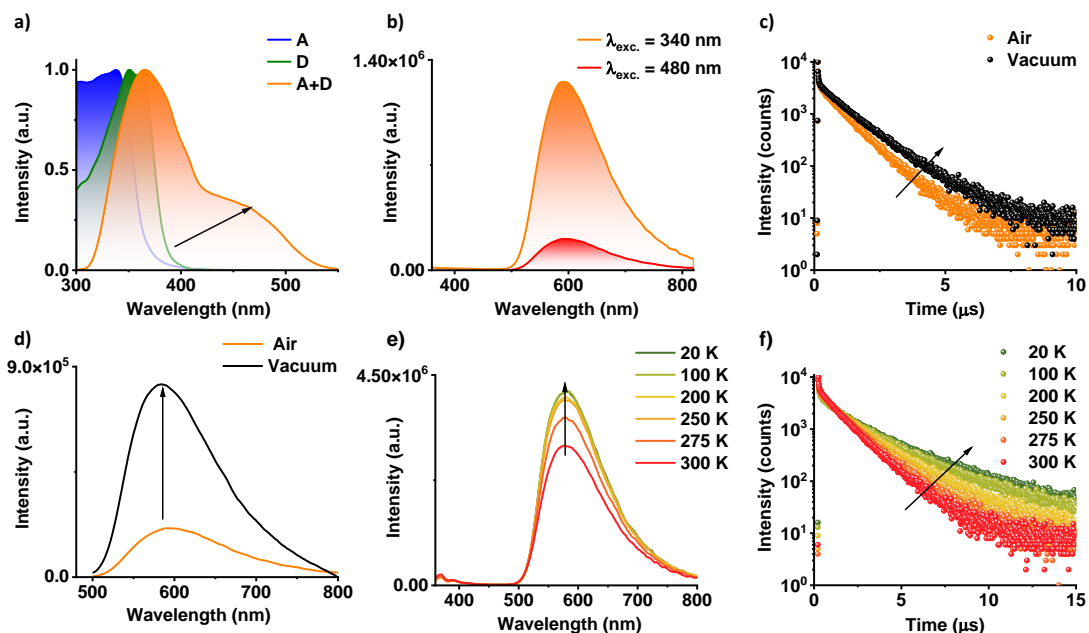


Figure 7.2.3. ³CT Phosphorescence studies of the **A**, **D**, and **A+D** pair. a) Normalized excitation spectra of individual **D** and **A** ($\lambda_{\text{monitored}} = 500 \text{ nm}$, 1 wt. % of **D** and **A** doped PMMA film is used) and **A+D** pair ($\lambda_{\text{monitored}} = 600 \text{ nm}$), which shows the red-shifted band for **A+D** pair compared to individual components suggesting the formation of CT complex. b) Steady-state emission spectra of the **A+D** pair show the highly emissive nature upon excited at 340 nm and selective excitation at the CT band ($\lambda_{\text{exc.}} = 480 \text{ nm}$). c) Lifetime decay profiles ($\lambda_{\text{exc.}} = 405 \text{ nm}$, $\lambda_{\text{collected}} = 600 \text{ nm}$) and d) steady-state emission spectra ($\lambda_{\text{exc.}} = 480 \text{ nm}$) and of **A+D** pair showed intensified lifetime and emission under vacuum suggesting triplet contribution to the emission. e) Steady-state emission spectra ($\lambda_{\text{exc.}} = 340 \text{ nm}$) and f) corresponding lifetime decay profiles ($\lambda_{\text{exc.}} = 405 \text{ nm}$, $\lambda_{\text{collected}} = 600 \text{ nm}$) of **A+D** pair in different temperatures, suggesting the phosphorescence nature of the emission. (For all cases (**RR**)-**Br₂PmDI** is the **A** (acceptor)).

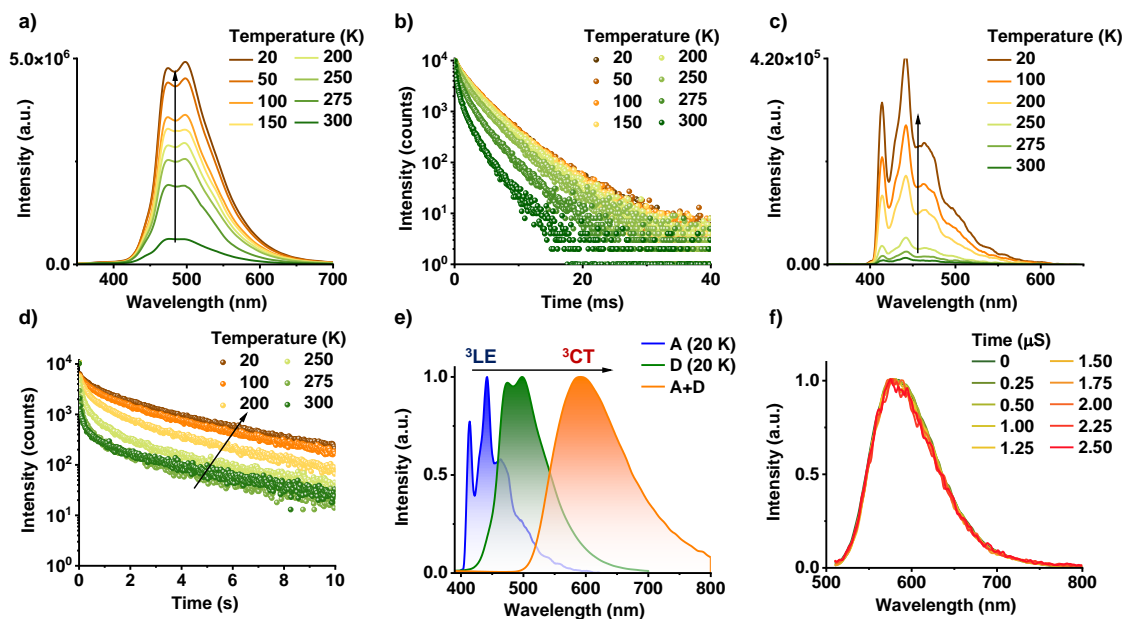


Figure 7.2.4. a) Steady-state emission spectra ($\lambda_{exc.} = 340$ nm) and corresponding b) lifetime decay profiles ($\lambda_{exc.} = 340$ nm, $\lambda_{collected} = 500$ nm) of **A** at different temperatures, suggesting the ³LE phosphorescence nature of the emission. c) Delayed emission spectra ($\lambda_{exc.} = 300$ nm, delay time = 0.5 ms) and d) lifetime decay profiles ($\lambda_{exc.} = 300$ nm, $\lambda_{collected} = 430$ nm) of **D** at different temperatures, suggesting the ³LE phosphorescence nature of the emission. e) Delayed emission spectra of **D**, and **A** alone in PMMA matrix (1 wt.% of **A** doped in PMMA matrix) show ³LE phosphorescence, and **A+D** in air show ³CT phosphorescence (delay time = 0.5 ms for **A**, **D**). f) Time-resolved emission spectra upon selective excitation at the CT band ($\lambda_{exc.} = 405$ nm) of **A+D** pair (For all cases (**RR**)-**Br₂PmDI** is the **A** (acceptor)).

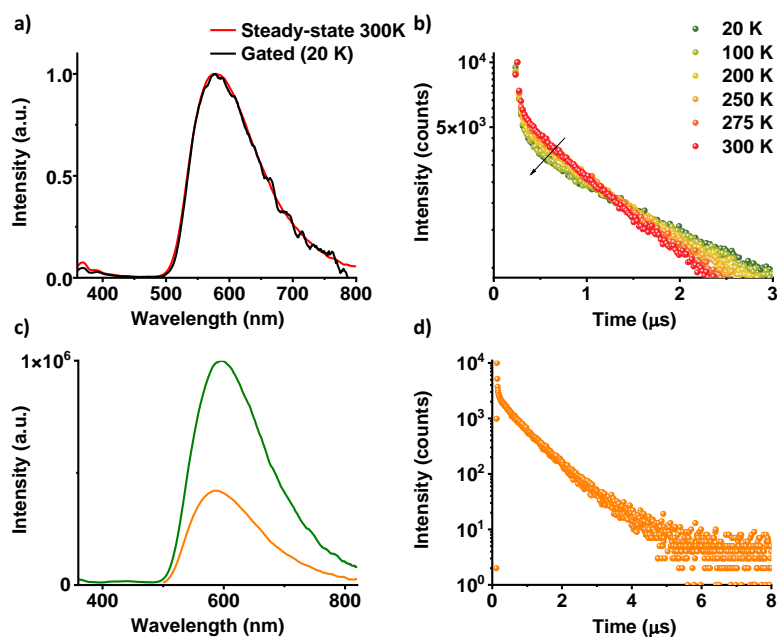


Figure 7.2.5. a) Steady-state and gated emission spectra ($\lambda_{exc.} = 340$ nm, delay time = 50 μ s) of **D-A** pair. b) Temperature dependent lifetime decay profiles of **D-A** pair ($\lambda_{exc.} = 405$ nm, $\lambda_{collected} = 600$ nm) showing TADF contribution. c) Steady-state emission spectra of the **A** ((**SS**)-**BrPmDI**)+**D** pair show the highly emissive nature upon excited at 340 nm and selective excitation at the CT band ($\lambda_{exc.} = 480$ nm). d) Lifetime decay profile of **A** ((**SS**)-**Br₂PmDI**)+**D** pair ($\lambda_{exc.} = 405$ nm and $\lambda_{collected} = 600$ nm).

7.2.5. Chiroptical Properties in Thin Films: Circularly Polarized Phosphorescence from Charge-transfer State:

Here we have used chiral heavy-atom substituted bischromophoric PmDIs ((**RR**)/(**SS**)-**Br₂PmDI**) as **A** and **CzPh** as a **D** to achieve CPP emission from the CT state. To accomplish that, first, we have established the ³CT phosphorescence nature of the donor-acceptor pair (Figures 7.2.4, 7.2.5). Next, we have performed circular dichroism (CD) study of the of enantiomeric (**RR**)-/(**SS**)-**BrPmDI** (**A**) and **CzPh** (**D**) pair (Figures 7.2.6a,b). CD spectra showed a mirror image CD signal with a $|g_{CD}|$ of 1.66×10^{-4} , suggesting the transfer of strong chiral bias from the chiral core (Figure 7.2.6b). Efficient phosphorescence from CT state and its potent to give CPP emission by reducing electrical transition dipole moment made us more curious to perform chiroptical properties in the excited state. Upon executing the chiroptical experiment in the excited state, we have observed a mirror image CPL signal with a maximum of 590 nm under ambient conditions ($\lambda_{exc.} = 340$ nm) (Figure 7.2.6).

Interestingly, we have achieved a very high CPP efficiency ($|g_{lum}|$) of 0.8×10^{-2} (Figure 7.2.6b). To increase the $|g_{lum}|$ further, we have coated the spin-coated film with polyvinyl alcohol (PVA), which reduces oxygen diffusion.^[12] We observed that emission intensity (3.23x) and lifetime (0.88 μ s to 1.00 μ s) increases significantly upon PVA coating (Figure 7.2.7a,b). We envisaged that PVA coating would help to increase the $|g_{lum}|$ value further. PVA is known to reduce triplet quenching via restricting the oxygen diffusion.^[12] As a result, significant enhancement in emission intensity and lifetime was observed upon PVA coating (Figure 7.2.7a). Upon performing the CPP experiments with the PVA coated film, we observed increment with $|g_{lum}|$ value from 0.8×10^{-2} to 1.2×10^{-2} (Figures 7.2.7c). Further, to avoid any macroscopic alignment of the phosphors in thin films, we have performed linear dichroism (LD) experiments. The observed results suggest the systems have negligible LD contribution to the chiroptical properties (Figure 7.2.6). Further rotation-dependent experiments ($\phi = 0^\circ, 90^\circ$ with respect to the direction of excitation light) were also performed to rule out the phosphors' macroscopic alignment (Figure 7.2.8). It is noteworthy to mention that CPP from purely organic phosphors is the systems have negligible LD contribution to the chiroptical properties (Figure 7.2.6). Further rotation-dependent experiments ($\phi = 0^\circ, 90^\circ$ with respect to the direction of excitation light) were also performed to rule out the phosphors' macroscopic alignment (Figure 7.2.8). It is noteworthy to mention that CPP from purely organic phosphors is rare and seldom reported, and CPP from charge-transfer triplet state is not reported in the literature till now.

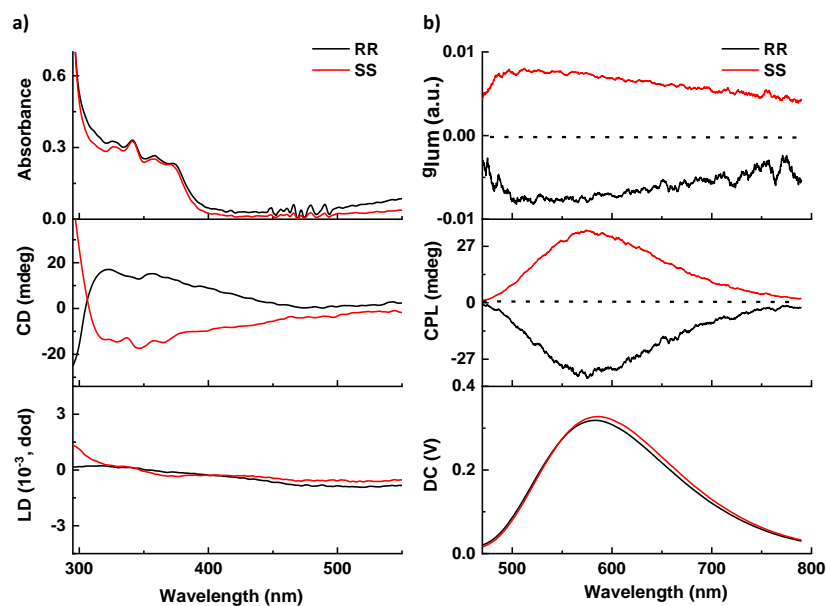


Figure 7.2.6. a) Absorption and their corresponding mirror image CD, LD spectra, and b) CPL, direct current (DC) spectra and dissymmetry factor ($|g_{lum}|$) for the spin-coated films of A ((RR)-Br₂PmDI/(SS)-Br₂PmDI)+D pair. ($\lambda_{exc.} = 340$ nm, all experiments were carried out in air).

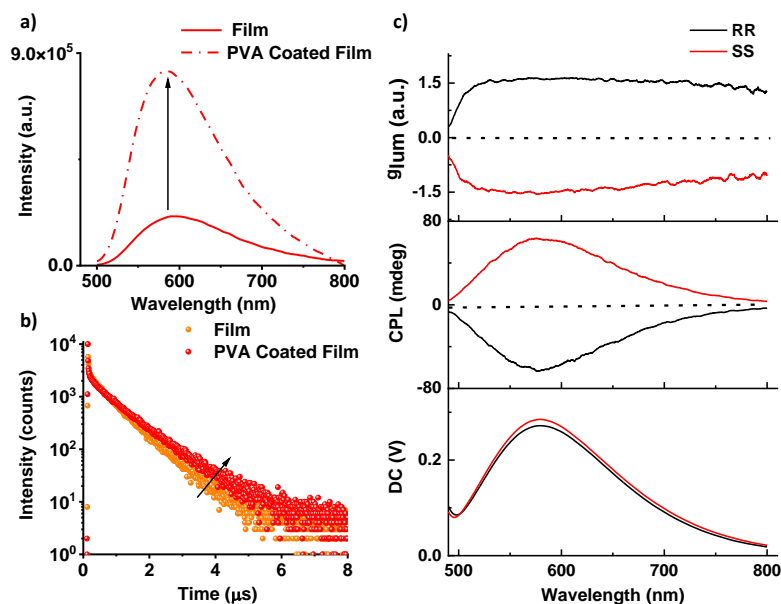


Figure 7.2.7. a) Steady-state emission spectra ($\lambda_{exc.} = 480$ nm) and b) lifetime decay profiles ($\lambda_{exc.} = 405$ nm, $\lambda_{collected} = 600$ nm) of A+D pair show intensified emission and lifetime upon PVA coating. c) CPL, direct current (DC) spectra and dissymmetry factor ($|g_{lum}|$) for the PVA coated films of A ((RR)-Br₂PmDI/(SS)-Br₂PmDI) + D pair. ($\lambda_{exc.} = 340$ nm, all experiments were carried out in the air).

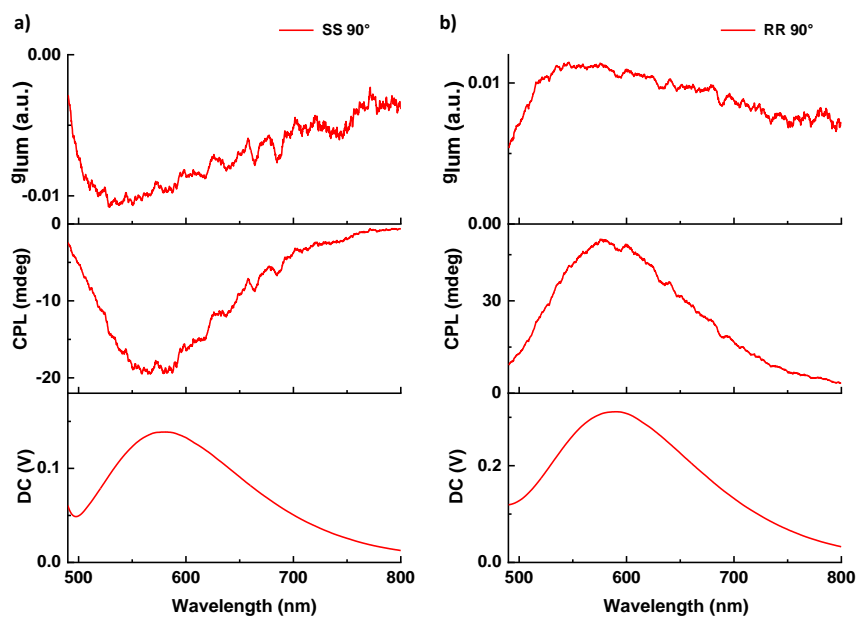


Figure 7.2.8. Direct current (DC), and CPL spectra and plot of dissymmetry factor versus wavelength of a) (RR)-Br₂PmDI and b) (SS)-Br₂PmDI after 90° rotation of the film to the direction of light irradiation.

7.2.6. Conclusions:

In conclusion, we have achieved room-temperature CT phosphorescence from organic donor-acceptor molecules via a non-covalent strategy using chiral heavy atom substituted pyromellitic diimide as the acceptor and achiral phenyl carbazole as donors. The ¹H NMR and detailed spectroscopic studies analyses CT complexation between donor and acceptor. Further phosphorescence studies of the individual donor, acceptor, and temperature-dependent studies of the donor-acceptor pair reveal the ³CT phosphorescence nature of the emission. The well-known excitonic coupling model system, i.e., bis-chromophoric molecular design of the acceptor and CT strategy, helped us achieve efficient CPP phosphorescence emission for the first time with very high luminescence dissymmetry of 1.5×10^{-2} with excellent phosphorescence quantum yield (40 %) in air.

7.2.7. Experimental Section:

7.2.7.1. General Methods:

Optical Measurements: Electronic absorption spectra were recorded on a Perkin Elmer Lambda 900 UV-Vis-NIR spectrometer and emission spectra were recorded on FLS1000 spectrometer, Edinburgh Instruments. Solution state UV-Vis and emission spectra were recorded in 10 mm path length cuvette. Fluorescence spectra of films were recorded in front-face geometry to avoid self-absorption. Circular Dichroism (CD) spectra were recorded on a Jasco J-815 spectrometer where the sensitivity, time constant and scan rate were chosen appropriately. Circularly polarized luminescence (CPL) measurements were performed with a Jasco CPL-300 spectrometer. A scanning speed of 50 nm/min, excitation slit width of 4000 μM and emission slit width of 4000 μM , integration time (D.I.T) of 8 sec, and with multiple spectral accumulations were employed.

Lifetime Measurements and Quantum yield: Fluorescence lifetimes were performed on a Horiba Delta Flex time-correlated single-photon-counting (TCSPC) instrument. A 340 nm diode and 373 nm, 442 nm laser diode with a pulse repetition rate of 1 MHz were used as the light source. The instrument response function (IRF) was collected using a scatterer (Ludox AS40 colloidal silica, Sigma-Aldrich). Phosphorescence lifetime ($\lambda_{\text{exc.}} = 340 \text{ nm}$ and 430 nm), gated emission and time-resolved excitation and emission were measured on FLS1000 spectrometer, Edinburgh Instruments equipped with a micro flash-lamp (μF2) set-up. Quantum yields were measured using an integrating sphere in the same instrument.

7.2.7.2. Protocol of Sample Preparation:

Protocol for sample preparation: All solution state studies were performed, keeping the final concentration of the samples 0.1 mM in CHCl_3 (1 mM). For the phosphorescence studies of the **D+A** pair, 50 μL of the stock solution was spin coated on a quartz plate. For individual **D** and **A** thin films, **D** or **A** molecules (1 mg) were mixed with 100 mg of PMMA. This mixture was then heated at 50 $^\circ\text{C}$ for 10 minutes followed by sonication (5 minutes) to dissolve all the components thoroughly. Then, 0.5 mL of this solution was drop-casted on a clean quartz substrate. Finally, the drop-casted thin films were dried at 60 $^\circ\text{C}$ for 30 minutes before performing the photophysical studies.

7.2.8. Synthetic Scheme and Procedures:

The synthetic of the Acceptors is shown in the previous chapter 7.1. and the donor was synthesized according to the literature procedures.^[9b, 13]

7.2.9. References:

[1] a) R. Farshchi, M. Ramsteiner, J. Herfort, A. Tahraoui, H. T. Grahn, *Appl. Phys. Lett.* **2011**, *98*, 162508; b) C. S. Wang, H. S. Fei, Y. Qiu, Y. Q. Yang, Z. Q. Wei, *Appl. Phys. Lett.* **1999**, *74*, 19-21; c) D.-Y. Kim, *J. Korean Phys. Soc.* **2006**, *49*, 505-508; d) C. Wagenknecht, C.-M. Li, A. Reingruber, X.-H. Bao, A. Goebel, Y.-A. Chen, Q. Zhang, K. Chen, J.-W. Pan, *Nat. Photonics* **2010**, *4*, 549-552. e) J. Han, S. Guo, H. Lu, S. Liu, Q. Zhao, W. Huang, *Adv. Opt. Mater.* **2018**, *6*, 1800538; f) X. Li, Y. Xie, Z. Li, *Adv. Photonics Res.* **2021**, *2*, 2000136; g) J. Roose, B. Z. Tang, K. S. Wong, *Small* **2016**, *12*, 6495-6512; h) Y. Sang, J. Han, T. Zhao, P. Duan, M. Liu, *Adv. Mater* **2020**, *32*, 1900110; i) J. Kumar, T. Nakashima, T. Kawai, *J. Phys. Chem. Lett.* **2015**, *6*, 3445-3452; j) Y. Imai, Y. Nakano, T. Kawai, J. Yuasa, *Angew. Chem. Int. Ed.* **2018**, *57*, 8973-8978; k) G. Albano, G. Pescitelli, L. Di Bari, *Chem. Rev.* **2020**, *120*, 10145-10243.

[2] a) J. Han, P. Duan, X. Li, M. Liu, *J. Am. Chem. Soc.* **2017**, *139*, 9783-9786; b) L. Ji, Y. Sang, G. Ouyang, D. Yang, P. Duan, Y. Jiang, M. Liu, *Angew. Chem., Int. Ed.* **2019**, *58*, 844-848; c) D. Yang, P. Duan, L. Zhang, M. Liu, *Nat. Commun.* **2017**, *8*, 15727; c) J. Wade, J. Brandt, D. Reger, F. Zinna, K. Amsharov, N. Jux, D. Andrews, M. J. Fuchter, *Angew. Chem., Int. Ed.* **2021**, *60*, 222-227; e) J. Han, D. Yang, X. Jin, Y. Jiang, M. Liu, P. Duan, *Angew. Chem. Int. Ed.* **2019**, *58*, 7013-7019; f) S. Inagaki, K. Yamamura, K. Nakasuji, T. Nakazawa, I. Murata, *J. Am. Chem. Soc.* **1981**, *103*, 2093-2094.

[3] a) S. Hirata, *Adv. Opt. Mater.* **2017**, *5*, 1700116; b) M. Y. Wong, E. Zysman-Colman, *Adv. Mat.* **2017**, *29*, 1605444. c) H. Uoyama, K. Goushi, K. Shizu, H. Nomura, C. Adachi, *Nature* **2012**, *492*, 234-238; d) Q. Zhang, H. Kuwabara, W. j. Potscavage, S. Huang, S.; Y. Hatae, T. Shibata, C. Adachi, *J. Am. Chem. Soc.* **2014**, *136*, 18070-18081.

[4] a) M. Li, S. H. Li, D. Zhang, M. Cai, L. Duan, M. K. Fung, C. F. Chen, *Angew. Chem. Int. Ed.* **2018**, *57*, 2889-2893; b) M. Li, Y.-F. Wang, D. Zhang, L. Duan, C.-F. Chen, *Angew. Chem., Int. Ed.* **2020**, *59*, 3500-3504; c) N. Sharma, E. Spuling, C. M. Mattern, W. Li, O. Fuhr, Y. Tsuchiya, C. Adachi, S. Bräse, I. D. W. Samuel, E. Zysman-Colman, *Chem. Sci.* **2019**, *10*, 6689-6696. d) S.-Y. Yang, Y.-K. Wang, C.-C. Peng, Z.-G. Wu, S.

Yuan, Y.-J. Yu, H. Li, T.-T. Wang, H.-C. Li, Y.-X. Zheng, Z.-Q. Jiang, L.-S. Liao, *J. Am. Chem. Soc.* **2020**, *142*, 17756-17765.

[5] (c) W. Zhao, Z. He, W. Y. Lam, Jacky, Q. Peng, H. Ma, Z. Shuai, G. Bai, J. Hao, B. Z. Tang, *Chem* **2016**, *1*, 592-602; (d) S. Xu, R. Chen, C. Zheng, W. Huang, *Adv. Mater.* **2016**, *28*, 9920-9940; (e) W. Zhao, Z. He, B. Z. Tang, *Nat. Rev. Mater.* **2020**, *5*, 869-885; (f) X. Ma, J. Wang, H. Tian, *Acc. Chem. Res.* **2019**, *52*, 738-748; (g) J. Yang, M. Fang, Z. Li, *Acc. Mater. Res.* **2021**, *2*, 644-654.

[6] a) O. Bolton, K. Lee, J.-H. Kim, K.Y. Lin, J. Kim, *Nat. Chem.* **2011**, *3*, 205-210; b) Z. An, C. Zheng, Y. Tao, R. Chen, H. Shi, T. Chen, Z. Wang, H. Li, R. Deng, X. Liu, W. Huang, *Nat. Mater.* **2015**, *14*, 685-690; c) P. Alam, T. S. Cheung, N. L. C. Leung, J. Zhang, J. Guo, L. Du, R. T. K. Kwok, J. W. Y. Lam, Z. Zeng, D. L. Phillips, H. H. Y. Sung, I. D. Williams, B. Z. Tang, *J. Am. Chem. Soc.* **2022**, *144*, 3050-3062; d) Q. Liao, Q. Gao, J. Wang, Y. Gong, Q. Peng, Y. Tian, Y. Fan, H. Guo, D. Ding, Q. Li, Z. Li, *Angew. Chem. Int. Ed.* **2020**, *59*, 9946-9951; e) J. Ren, Y. Wang, Y. Tian, Z. Liu, X. Xiao, J. Yang, M. Fang, Z. Li, *Angew. Chem. Int. Ed.* **2021**, *60*, 12335-12340; f) D. Lee, O. Bolton, B. C. Kim, J. H. Youk, S. Takayama, J. Kim, *J. Am. Chem. Soc.* **2013**, *135*, 6325-6329; g) Y. F. Zhang, Y. Su, H. W. Wu, Z. H. Wang, C. Wang, Y. Zheng, X. Zheng, L. Gao, Q. Zhou, Y. Yang, X. H. Chen, C. L. Yang, Y. L. Zhao, *J. Am. Chem. Soc.* **2021**, *143*, 13675-13685; h) Y. Su, Y.; Y. Zhang, Z. Wang, W. Gao, P. Jia, D. Zhang, C. Yang, Y. Li, Y. Zhao, *Angew. Chem. Int. Ed.* **2020**, *59*, 9967-9971; i) S. Cai, Z. Sun, H. Wang, X. Yao, H. Ma, W. Jia, S. Wang, Z. Li, H. Shi, Z. An, Y. Ishida, T. Aida, W. Huang, *J. Am. Chem. Soc.* **2021**, *143*, 16256-16263; j) J. Wang, Z. D. Li, F. Lu, J. Wang, W. Hu, X. M. Cao, X. Ma, H. Tian, *J. Am. Chem. Soc.* **2018**, *140*, 1916-1923; k) Huang, X. Ma, H. Tian, *Angew. Chem. Int. Ed.* **2020**, *59*, 9928-9933; (c) X. Yao, J. Wang, D. Jiao, Z. Huang, O. Mhirsii, F. Lossada, L. Chen, B. Haehnle, A. J. C. Kuehne, X. Ma, H. Tian, A. Walther, *Adv. Mater.* **2020**, 2005973; l) Z. Y. Zhang, Y. Chen, Y. Liu, *Angew. Chem. Int. Ed.* **2019**, *58*, 6028-6032; m) H. J. Yu, Q. Zhou, X. Dai, F. F. Shen, Y. M. Zhang, X. Xu, Y. Liu, *J. Am. Chem. Soc.* **2021**, *143*, 13887-13894; n) X. K. Ma, W. Zhang, Z. Liu, H. Zhang, B. Zhang, Y. Liu, *Adv. Mater.* **2021**, *33*, 2007476; o) Z. Li, Y. Han, F. Nie, M. Liu, H. Zhong, F. Wang, *Angew. Chem. Int. Ed.* **2021**, *60*, 8212-8219; p) Z. Li, Y. Han, F. Wang, *Nat. Commun.* **2019**, *10*, 3735.

[7] a) S. Hirata, M. Vacha, *J. Phys. Chem. Lett.* **2016**, *7*, 1539-1545; b) H. Li, H. Li, W. Wang, Y. Tao, S. Wang, Q. Yang, Y. Jiang, C. Zheng, W. Huang, R. Chen, *Angew. Chem. Int. Ed.* **2020**, *59*, 4756-4762; c) W. Chen, Z. Tian, Y. Li, Y. Jiang, M. Liu, P. Duan, *Chem. Eur. J.* **2018**, *24*, 17444-17448; d) L. Gu, W. Ye, X. Liang, A. Lv, H. Ma, M. Singh, W. Jia, Z. Shen, Y. Guo, Y. Gao, H. Chen, D. Wang, Y. Wu, J. Liu, H. Wang, Y.-X. Zheng, Z. An, W. Huang, Y. Zhao, *J. Am. Chem. Soc.* **2021**, doi: 10.1021/jacs.1c08118; e) R. Liu, B. Ding, D. Liu, X. Ma, *Chem. Eng. J.*, **2021**, *421*, 129732; f) M. Xu, X. Wu, Y. Yang, C. Ma, W. Li, H. Yu, Z. Chen, J. Li, K. Zhang, S. Liu, *ACS Nano* **2020**, *14*, 11130-11139; g) H. Li, J. Gu, Z. Wang, J. Wang, F. He, P. Li, Y. Tao, H. Li, G. Xie, W. Huang, C. Zheng, R. Chen, *Nat. Commun.* **2022**, *13*, 429; h) X. Pan, A. Zheng, X. Yu, Q. Di, L. Li, P. Duan, K. Ye, P. Naumov, H. Zhang, *Angew. Chem. Int. Ed.* **2022**, e202203938; i) W. Huang, C. Fu, Z. Liang, K. Zhou, Z. He, *Angew. Chem. Int. Ed.* **2022**, e202202977.

[8] a) S. Kuila, K. V. Rao, S. Garain, P. K. Samanta, S. Das, S. K. Pati, M. Eswaramoorthy, S. J. George, *Angew. Chem. Int. Ed.* **2018**, *57*, 17115-17119; b) S. Garain, B. C. Garain, M. Eswaramoorthy, S. K. Pati, S. J. George, *Angew. Chem. Int. Ed.* **2021**, *60*, 19720-19724; c) S. Kuila, A. Ghorai, P. K. Samanta, R. B. K. Siram, S. K. Pati, K. S. Narayan, S. J. George, *Chem. Eur. J.* **2019**, *25*, 16007-16011.

[9] a) S. Garain, S. Kuila, B. C. Garain, M. Kataria, A. Borah, S. K. Pati, S. J. George, *Angew. Chem. Int. Ed.* **2021**, *60*, 12323-12327; b) S. Garain, S. Sarkar, B. C. Garain, S. K. Pati, S. J. George, *Angew. Chem. Int. Ed.* **2022**, DOI: 10.1002/anie.202115773; c) S. Kuila, S. Garain, G. Banappanavar, B. C. Garain, D. Kabra, S. K. Pati, S. J. George, *J. Phys. Chem. B* **2021**, *125*, 4520-4526.

[10] a) Q. Zheng, J. Huang, A. Sarjeant, H. E. Katz, *J. Am. Chem. Soc.* **2008**, *130*, 14410-14411; b) S. Kola, J. H. Kim, R. Ireland, M.-L. Yeh, K. Smith, W. Guo, H. E. Katz, *ACS Macro Lett.* **2013**, *2*, 664-669.

[11] a) S. Kuila, S. Garain, S. Bandi, S. J. George, *Adv. Funct. Mater.* **2020**, *30*, 2003693; b) S. Kuila, S. J. George, *Angew. Chem. Int. Ed.* **2020**, *59*, 9393-9397; c) M. Louis, H. Thomas, M. Gmelch, A. Haft, F. Fries, S. Reineke, *Adv. Mater.* **2019**, *31*, 1807887; d) H. Thomas, D. L. Pastoetter, M. Gmelch, T. Achenbach, A. Schlögl, M. Louis, X. Feng, S. Reineke, *Adv. Mater.* **2020**, *32*, 2000880; e) A. Kirch, M. Gmelch, S. Reineke, *J. Phys. Chem. Lett.* **2019**, *10*, 310-315.

[12] M. Gmelch, H. Thomas, F. Fries, S. Reineke, *Sci. adv.* **2019**, *5*, eaau7310.

[13] L. Gan, K. Gao, X. Cai, D. Chen, S.-J. Su, *J. Phys. Chem. Lett.* **2018**, *9*, 4725-4731.

CURRICULUM VITAE

Swadhin Garain was born on August 15, 1993, in Dubrajpur, Birbhum, West Bengal. He finished his B. Sc. in chemistry from Visva-Bharati University, West Bengal, in 2015.



Subsequently, he moved to the Indian Institute of Technology Madras, Chennai, Tamil Nadu, in 2015 to pursue his M. Sc. in Chemical Science. After finishing his M. Sc., he joined Jawaharlal Nehru Centre for Advanced Scientific Research (JNCASR) as a Ph. D. student under Prof. Subi J. George in 2017. His research work at Supramolecular Chemistry Laboratory focused on Ambient Triplet Harvesting via Phosphorescence and Delayed fluorescence from purely organic chromophores.

PUBLICATIONS

From Thesis:

1. Anion- π -Induced Room Temperature Phosphorescence from Emissive Charge-Transfer States. **S. Garain**, S. M. Wagalgave, A. A. Kongasseri, B. C. Garain, S. N. Ansari, G. Sardar, D. Kabra, S. K. Pati, S. J. George, *J. Am. Chem. Soc.* **2022**, *144*, 10854-10861.
2. Chiral Arylene Diimide Phosphors: Circularly Polarized Ambient Phosphorescence from Bischromophoric Pyromellitic Diimides. **S. Garain**, S. Sarkar, B. Chandra Garain, S. K. Pati, S. J. George, *Angew. Chem. Int. Ed.* **2022**, *Angew. Chem. Int. Ed.* **2022**, *61*, e2021157.
3. Light-Harvesting Supramolecular Phosphors: Highly Efficient Room Temperature Phosphorescence in Solution and Hydrogels. **S. Garain**, B. C. Garain, M. Eswaramoorthy, S. K. Pati, S. J. George, *Angew. Chem. Int. Ed.* **2021**, *60*, 19720-19724.
4. Arylene diimide phosphors: aggregation modulated twin room temperature phosphorescence from pyromellitic diimides. **S. Garain**, S. Kuila, B. C. Garain, M. Kataria, A. Borah, S. K. Pati, S. J. George, *Angew. Chem. Int. Ed.* **2021**, *60*, 12323-12327.
5. Biasing the Excited State Manifold via Non-covalent Donor-Acceptor Approach **S. Garain**, S. N. Ansari, A. A. Kongasseri, B. C. Garain, S. K. Pati, S. J. George, (Chemical Sciences under revision).
6. Delayed Fluorescence via Triplet-triplet Annihilation from a Pyromellitic Diimide Phosphor. **S. Garain**, A. Sree. S, B. C. Garain, A. K. Singh, S. S. Behera, S. N. Ansari, S. C. Peter, K. S. Narayan, S. K. Pati, S. J. George (Manuscript under preparation).
7. Thermally Activated Delayed Fluorescence: Color Tunable Delayed Fluorescence from Core-substituted Pyromellitic Diimides. **S. Garain**, S. M. Wagalgave, S. J. George, (Manuscript under preparation).
8. Circularly Polarized Room Temperature Phosphorescence from Charge-Transfer State Via Non-covalent Donor-Acceptor Approach. **S. Garain**, S. J. George, (Manuscript under preparation).

9. Anion- π Induced Charge-transfer Emission from Cationic Naphthalene Diimide. **S. Garain**, S. Pradhan, S. N. Ansari, B. C. Garain, S. Kuila, S. K. Pati, S. S. Agasti, S. J. George, (Manuscript under preparation).

Other Publications:

1. All-Organic, Temporally Pure White Afterglow in Amorphous Films Using Complementary Blue and Greenish-Yellow Ultralong Room Temperature Phosphors. S. Kuila,* **S. Garain**,* S. Bandi, S. J. George, *Adv. Funct. Mater.* **2020**, *30*, 2003693. (* Equal contribution)

2. Ambient, tunable room temperature phosphorescence from a simple phthalimide phosphor in amorphous polymeric matrix and in crystalline state. **S. Garain**, A. K. Singh, S. C. Peter, S. J. George, *Mater. Res. Bull.* **2021**, *142*, 111420.

3. Room temperature phosphorescence from heavy atom free benzophenone boronic ester derivatives. **S. Garain**, S. Kuila, A. Sinhababu, S. J. George, *Bull. Mater. Sci.* **2020**, *43*, 318.

4. Ambient Room Temperature Phosphorescence and Thermally Activated Delayed Fluorescence from a Core-Substituted Pyromellitic Diimide Derivative. S. Kuila, **S. Garain**, G. Banappanavar, B. C. Garain, D. Kabra, S. K. Pati, S. J. George, *J. Phys. Chem. B*, **2021**, *125*, 4520-4526.

5. Aqueous phase and amorphous state room temperature phosphorescence from a small aromatic carbonyl derivative. S. Kuila, **S. Garain**, M. Eswaramoorthy, S.J. George, *Mater. Res. Express*, **2019**, *6*, 124003.

6. Aqueous phase and amorphous state room temperature phosphorescence from a small aromatic carbonyl derivative. S. Kuila, K. V. Rao, **S. Garain**, P. K. Samanta, S. Das, S. K. Pati, M. Eswaramoorthy, S. J. George, *Angew. Chem. Int. Ed.* **2018**, *57*, 17115-17119.

7. Effect of Photonic Band Gap on Photoluminescence in a Dye-Doped Blue Phase Liquid Crystal. N. Khatun, V. Sridurai, R. K. Gupta, S. Nath, M. B. Kanakala, **S. Garain**, A. S. Achalkumar, C. V. Yelamaggad, G. G. Nair, *J. Phys. Chem. B*, **2021**, *125*, 11582-11590.